REPORT DOCUMENTATION PAGE

Public reporting burden for this collection of information is estimated to average 1 hour per response, including the gathering and maintaining the data needed, and completing and reviewing the collection of information. Send cc collection of information, including suggestions for reducing this burden, to Washington Headquarters Services, l Davis Highway, Suite 1204, Arlington, VA 22202-4302, and to the Office of Management and Budget, Paperwork Reduction Project (0704-0188), Washington...

1. AGENCY USE ONLY (Leave Blank)	2. REPORT DATE Sept. 30, 1998	3. REPORT TYPE AND DATES COVERED Final Report for grant period 15 Apr 93 through 15 Apr 97

4. TITLE AND SUBTITLE The Influence of Alloying and Processing on the Microstructure and Properties of Monolithic Beta-NiAl	5. FUNDING NUMBERS N/A

6. AUTHORS
M.J. Kaufman
R. Abbaschian

7. PERFORMING ORGANIZATION NAME(S) AND ADDRESS(ES) University of Florida Department of Materials Science and Engineering 128 Rhines Hall, Bldg 184 Gainesville, FL 32611	8. PERFORMING ORGANIZATION REPORT NUMBER 4910 4509 464-12

9. SPONSORING / MONITORING AGENCY NAME(S) AND ADDRESS(ES) AFOSR/NC 110 Duncan Avenue Suite B115 Bolling AFB DC 20332-0001	10. SPONSORING / MONITORING AGENCY REPORT NUMBER F49620-93-1-0309

11. SUPPLEMENTARY NOTES

12a. DISTRIBUTION / AVAILABILITY STATEMENT Approved for public release; distribution unlimited.	12b. DISTRIBUTION CODE

13. ABSTRACT (Maximum 200 words)
The overall objective of this program was to provide a fundamental understanding of the effects of alloying and processing on the microstructure-property-processing relationships of monolithic b-NiAl. The emphasis was to determine the factors that affect both the low and high temperature compound by studying single crystals, bicrystals and polycrystals of selected alloys. Modeling of the solidification behavior was performed with the goal of understanding better the role of processing parameters on contamination and its effects on mechanical properties. Furthermore, the effects of interstitials, microalloying additions, thermal and constitutional vacancies, deviations from stoichiometry, processing defects/inhomogeneities and precipitate phases on both the low and high temperature properties of NiAl and how these are affected by processing history were examined in some detail. It is shown that b-NiAl is a reasonably well-behaved material that is both soft (low resistance to dislocation motion) and brittle (low fracture strength). This combination of intrinsic properties makes it difficult to develop NiAl into a viable engineering material. Specifically, while it is possible to strengthen NiAl using traditional methods, the stronger alloys have reduced toughness. Conversely, approaches for toughening are even less obvious since the intrinsic reason for the low toughness is not related to a lack of dislocation mobility but rather to the lack of a sufficient number of operative slip systems needed to avoid the build-up of stress at stresses concentrations. Finally, the results indicate that the brittle to ductile transition in NiAl should be interpreted with caution.

14. SUBJECT TERMS	15. NUMBER OF PAGES
	16. PRICE CODE

17. SECURITY CLASSIFICATION OF REPORT Unclassified	18. SECURITY CLASSIFICATION OF THIS PAGE Unclassified	19. SECURITY CLASSIFICATION OF ABSTRACT Unclassified	20. LIMITATION OF ABSTRACT UL

NSN 7540-01-280-5500

Standard Form 298 (Rev. 2-89)
Prescribed by ANSI Std. Z39-1
298-102

19981016 003

The Influence of Alloying and Processing on the Microstructure and Properties of β-NiAl

Table of Contents

19981016 003

The Influence of Alloying and Processing on the Microstructure and Properties of β-NiAl

AFOSR URI Grant No. F49620-93-1-0309

R. Abbaschian, R.T. DeHoff, F. Ebrahimi, M.J. Kaufman, R.E. Reed-Hill and E.D. Verink
Dept. of Materials Science and Engineering, University of Florida

A. Kumar
Dept. of Mechanical Engineering, Univeristy of Florida

W. Shyy
Dept. of Aerospace Engineering, Mechanics and Engineering Science, University of Florida

A.J. Melmed
Dept. of Materials Science and Engineering, Johns Hopkins University

This constitutes the final report on AFOSR URI Grant F49620-93-0309 which was performed at the University of Florida and Johns Hopkins University. This report is divided into a summary section that indicates the program goals followed by a summary of bullets highlighting some of the accomplishments that resulted from this work. A short description of some of the more recent efforts follows. The research students involved in this program are then described followed by a listing of papers, patents and presentations. Copies of the manuscripts are included at the end.

1.0 Objective

The purpose of this study was to develop a more fundamental understanding of the microstructure and properties of β-NiAl. Specifically, the dependence of mechanical properties on such things as alloying additions, interstitial impurities, deviations from stoichiometry, prestrain, specimen geometry and orientation and thermal-mechanical history were investigated with the goal of 1) extending our knowledge base concerning this material and 2) use this knowledge as a starting point for developing strategies aimed at enhancing the properties of alloys based on this compound.

2.0 Approach

The approach of this program was divided into four thrust areas. Thrust 1 dealt with the solidification processing of NiAl alloys using various techniques such as vacuum induction melting and casting, levitation melting, containerless zone melting and Bridgman growth. After establishing that the Bridgman-grown crystals had high purities, this techniques was focused on almost exclusively.

The focus of Thrust 2 was on developing a more thorough understanding of the influence of the various parameters alluded to above on both the microstructure and corresponding mechanical properties of β-NiAl as a function of temperature and strain rate. Both tension and compression tests were performed on a variety of alloy compositions, specimen geometries and orientations. For the tensile tests, it was shown that rectangular specimens provide more useful information than cylindrical specimens as will be described below.

The last two thrust areas complemented the first two by 1) applying a variety of analytical methods to characterize the materials (Thrust 3) and 2) by studying the static and cyclic oxidation behavior of the more promising alloys (Thrust 4) developed in the first two thrusts. Thus, such methods as

2

analytical transmission electron microscopy, atom probe/field ion microscopy (APFIM), internal friction (for interstitial diffusion mechanisms), ion implantation, secondary ion mass spectroscopy (SIMS), resistivity measurements and various other methods were used as needed.

3.0 Highlights

3.1 Thrust 1 - Solidification Studies and Single Crystal Growth

- NiAl single crystals produced at UF by the Bridgman growth method contained low interstitial concentrations and appeared to be of comparable quality to the zone-refined crystals produced by Prof. Ben Oliver at the University of Tennessee.

- Published a book: Shyy, W., Thakur, S.S., Ouyang, H., Liu, J. and Blosch, E, Computational Techniques for Complex Transport Phenomena, Cambridge University Press, New York, (1997), xviii + 321 pages.

- Comprehensive capabilities to compute solidification/melting, conjugate heat transfer (conduction/convection/radiation), and fluid dynamics in geometries directly relevant to a crystal growing device were developed and applied to the NiAl system.

- Coordinated experimental and computational investigations of the solidification dynamics in the UF Bridgman growth apparatus were performed and indicated the advantages of such efforts for making more useful modifications to the growth apparatus.

- NiAl appears to undergo considerable metastable superheating during levitation melting studies. Such behavior is quite unusual and has not been documented previously to our knowledge.

3.2 Thrust 2 - Microstructure/Property Studies

- NiAl single crystals deform readily by cube slip on {110} or {100} planes and there is no significant difference between the CRSS of cube slip on these planes for high purity NiAl.

- The glide of cube dislocations occurs readily in high purity NiAl although the edge components have lower mobility than the screw segments. Cross slip occurs readily in high purity NiAl and leads to the formation of jogs, dipoles and elongated loops.

- In the highest purity material, the dislocations develop into patches elongated along the edge orientations whereas in lower purity material or high purity NiAl containing quenched-in thermal vacancies, the dislocations and debris are more uniformly distributed throughout the material.

- Impurities, solute atoms, constitutional defects and thermal vacancies all lead to increased resistance to dislocation motion, increased work hardening rate and decreased ductility. The work hardening rate at ambient temperatures for high purity NiAl in the single slip orientation is quite low and extends to the highest strains achieved to date.

- The decrease in yield stress with temperature is less abrupt in the higher purity NiAl oriented along the hard orientation compared with the commercially pure and Si-doped NiAl. Silicon does not strongly influence the slip behavior in the case of <001>-oriented crystals.

- High tensile elongations (approaching 35% at room temperature) are possible in single crystals of high purity NiAl at both sub-ambient and ambient temperatures when the specimen geometry and purity are controlled.

- At intermediate temperatures, the elongations frequently exceed 200%. This has been correlated with lower initial flow stress, decreasing work hardening rates and increasing strain rate sensitivities with increasing temperature. The fracture surfaces after such high elongations are still brittle in nature.

- The previous bullet suggests that the brittle to ductile transition (BDT) should be interpreted with caution as high tensile elongations does not necessarily correlate with classical ductile behavior. In fact, the sensitivity of the tensile elongation to the strain rate suggests that NiAl will be brittle at all temperatures if the strain rate is sufficiently high. This was confirmed in the recent study at General Electric by Walston and Darolia.

- Above the temperature of maximum elongation, localized necking occurs due to the decreased work hardening rate. Even so, the fractures are still brittle except for the samples that neck to a chisel point in which case the local stress concentrations never reached the fracture stress.

- The soft, brittle nature of NiAl appears to be reasonably well understood at this point. Thus, the conventional approaches for enhancing the strength of monolithic NiAl will lead to even lower toughnesses while those attempts to enhance the toughness will result in lower strengths. The only viable approach appears to involve the utilization of ductile reinforcements such as those produced in the directionally solidified eutectics studied by various investigators. However, the question arises as to why one would choose to start with a soft, brittle matrix instead of something strong and tough?

- Although it is not clear that NiAl will ever be used as a structural material, it is of interest for fundamental studies where it is desirable to maintain single or double slip of cube dislocations over large amounts of plastic strain. As mentioned below, some fundamental studies of bicrystals were performed in the current study and more are planned.

3.3 Thrust 3 - Other Characterization Studies

- The atom probe/field ion microscopy studies indicated apparent segregation of carbon to the cores of dislocations as expected based on some of the strain aging studies performed by Weaver .

4

4.0 Recent Results

4.1 Thrust 1 - Solidification Studies and Single Crystal Growth

As alluded to above, the Bridgman growth system became the method of choice for producing both single crystals and bicrystals of the NiAl alloys of interest. Wet chemical analysis as well as traditional interstitial analyses indicated that the purities of the UF crystals were readily controllable; this was confirmed by the low critical resolved shear stresses (CRSS) measured in the mechanical property studies. The composition of a typical UF crystal is compared with those reported by other investigators in Table 1. Note that the silicon concentration was substantially lower than that reported by other investigators and that the interstitial contents are comparable to the zone-refined material made by Oliver and coworkers at the University of Tennessee (Weaver et al. paper). Besides the high purity crystals, we have also grown crystals of NiAl-5%Be; NiAl-2%Ta; NiAl-Zr; NiAl-Si, NiAl-Si-Zr and NiAl-C.

Table 1. The chemical compositions of the binary NiAl single crystals grown in this and previous studies. The compositions are in atom percent or atom ppm.

Ni	Al	Si	C, ppm	O, ppm	N, ppm	S, ppm	Source
50	50	.007	50	80	<10	<10	Present work
50.2	49.8	.06	<36	<27	<31	<13	Weaver et al.
50.4	49.5	.1	25	130	<5	<3	Hack et al.
50.1	49.9	N/R	N/R	120	N/R	N/R	Takasugi et al.

In addition to the single crystals grown for the URI studies, we have supplied crystals to a variety of researchers from various laboratories including Oak Ridge National Laboratory, Los Alamos National Laboratories, NASA-Lewis Research Center, Johns Hopkins University, The University of Chicago, The University of Michigan, Michigan Technological University, Michigan State University, Florida State University, North-Rhein Technical University (Germany), and The Institute of Metal Physics (Russia). We also extended our efforts to grow bicrystals as this area is of interest for fundamental deformation studies based on the single crystal results described below. We grew a variety of bicrystals such as the one shown schematically in Figure 1 where the solidification directions for the two grains were both <001> but where the boundary was misoriented by a 45° rotation about the <001> growth axis, i.e., where the boundary is approximately parallel to the (100) of grain 1 and the (110) of grain 2 (see Fig. 1). It is noted here that the grain boundary tends to wander somewhat during bicrystal growth but should be sufficient for most of the studies of this type where the specimen size is small. The results of some preliminary studies on the bicrystal samples are described in the paper by LeBleu et al.

Theoretical Studies

The large scale production of high quality crystals and alloys involves several complex physical mechanisms typical of solidification processes. These include heat and mass transport, dynamics of moving interfaces, geometrical configurations, material thermo-physical properties and the non-linear coupling among them. These phenomena are extremely complicated and can not be predicted by simple analyses or models. For example, the temperature distribution in crystal growth systems, such as the Bridgman system, is highly complex and is influenced by:

(i)   Melt/crystal phase change in the ampoule region;

(ii) Conduction among various components of the furnace, the alumina wall and the copper base;

(iii) Convection in the melt and the encapsulating argon gas;

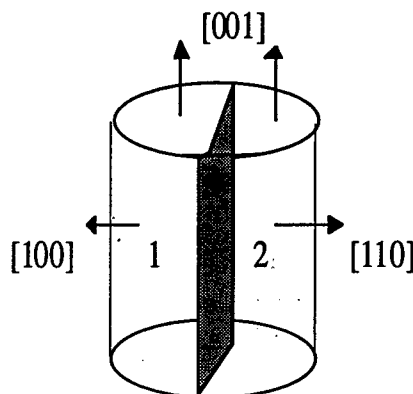(iv) Radiation between the heater and the ampoule wall.

Figure 1. Schematic of the bicrystals grown in the present study. The seeds for these bicrystals were cut from single crystal boules and oriented relative to each other in order to produce the desired orientations.

These complications have traditionally resulted in simplified analyses carried out under quite restrictive assumptions such as idealized geometry, assumed boundary conditions, and constant thermo-physical properties; in these reduced models, important convection modes created by buoyancy and capillary effects, critical in many solidification processes, are often neglected. First-principles-based computational tools can be very valuable for helping us gain physical insight and, based on this insight, improve and optimize the process design. They offer a framework for a convenient and relatively inexpensive platform for performing parametric studies to cover the entire range of processing conditions. In the following, we highlight a coordinated computational and experimental study conducted at the University of Florida dealing with the growth of NiAl in the Bridgman system.

As shown in Figures 6 and 7 in the paper by Hong, et al., the temperature distribution along the NiAl centerline and the ampoule outer wall obtained from the computational simulation matches the experimental measurements quite well overall. Satisfactory agreement is observed for all six ampoule positions, especially for the temperature along the outer alumina wall. This implies that the simplified radiation model we currently used for computing the heat flux between the alumina outer wall and the heater is sufficiently accurate, and the boundary condition of constant heat flux at the heater bottom is reasonable. Along the ampoule centerline, agreement between experimental data and computational results is good for the three higher ampoule positions of H=43 mm, H=59 mm and H=67 mm, but worsens for the three lower ampoule positions. This trend is explained in more detail below.

The streamfunctions and isotherm distributions for two selected ampoule positions, one at a higher location (H=43 mm) and the other at a lower location (H=87 mm) were calculated using the models described. For the higher ampoule position, the ampoule base region is contained inside the furnace hot zone. Since the treatment of radiation heat transfer and the boundary conditions appear to be reasonable there, the computed thermal distribution of this region is accurate. Accordingly, the predicted temperature profiles along the NiAl centerline match very well with the experimental results. At the lower ampoule position, the ampoule base region has been pulled out of the furnace hot zone. In this case, since the boundary condition at the outer wall of this region is still specified as a constant heat flux, this is no longer accurate. Furthermore, as the thermal distribution inside

6

the ampoule is very sensitive to the isotherm change near the ampoule base, it is not surprising that the deviations between the numerical results and experimental data along the NiAl centerline exist.

We have also developed a unified macro-micro model to deal with the issue of inadequate numerical resolution for the entire range of the length sacles (in the continuum model) during solidification.

4.2 Thrust 2 - Microstructure/Property Studies

The majority of the work performed on this grant was geared towards determining more clearly the basis for why NiAl is both soft and brittle at room temperature, i.e., whether these are intrinsic properties or related to some extrinsic effect such as contamination, thermal history, etc. Specifically, the question of why high purity NiAl, which has a very low CRSS (50-60 MPa for the higher purity crystals) when oriented for single (e.g., tensile axis (TA) parallel to <112>) or double (e.g., TA parallel to <011>) slip, fractures after elongations typically below 5% were largely unanswered when this program began. In addition, it was also unclear why NiAl single crystals microalloyed with Fe, Mo and Ga displayed higher elongations than the binary material in the study by Darolia et al. (1) and why the <110> (double slip) orientation appeared to be better than the single slip orientations. Consequently, the studies were initially geared towards characterizing the high purity UF crystals thereby establishing a baseline from which to operate. The results indicate that the CRSS vs. temperature behavior of high purity crystals is similar to that characteristic of bcc metals (Fig. 2). Furthermore, the RT CRSS values were ~50±5 MPa for both single slip (tensile axis ~[$\bar{5}$57]) and double slip (TA~[011]) orientations (Fig. 3) indicative of the high purity of the UF crystals. In spite of the similar CRSS values however, the work hardening rates (WHR) varied as expected with the double slip orientation exhibiting a considerably higher WHR. This implies that the deformation behavior is not unlike most high purity metals. These results have been described in greater detail in the various papers written by Prof. Kaufman and his group.

In spite of the reasonably well-understood deformation behavior of NiAl prior to fracture, the fracture process has been a more difficult issue to understand and control. Specifically, it has been found that the tensile elongation depends strongly on temperature and strain rate, whether the specimens are oriented for single or double slip and whether they are "constrained" during the deformation process. For example, rectangular tensile specimens oriented for single slip exhibit considerably higher RT elongations when the constraints that limit the natural specimen rotation are minimized. This is apparent in Table 2 where the "Face (110)" notation refers to a "less-constrained" geometry than the "Side (110)" notation (2). Based on these results, it is apparent that the varying elongations typically observed in single crystal NiAl alloys in soft orientations are due to a combination of factors which include 1) specimen geometry/constraints, 2) hardening due to impurities (obvious from the CRSS values), and 3) surface perfection/defects among other things. It is also noted that elongations as high as 10% at -100°C were achieved in the UF crystals (TA~[$\bar{5}$57] with the optimized specimen geometry.

At higher temperatures, the elongations of the soft oriented crystals exhibit a high peak in elongation in most cases similar to that reported by Takasugi et al. (4) and Lahrman et al (5). Because of the enhanced RT elongations, the peaks in elongation in the UF material are not as sharp (Fig. 4) and so the transition from brittle to ductile behavior (the BDTT) is not as well defined as is "typically" the case. In fact, the fractures of the specimens exhibiting the highest elongations remain brittle indicating that caution should be used in defining the BDTT in NiAl.

In order to understand the behavior more thoroughly, careful analyses of the specimens undergoing the high tensile elongations were performed by examining the specimen during
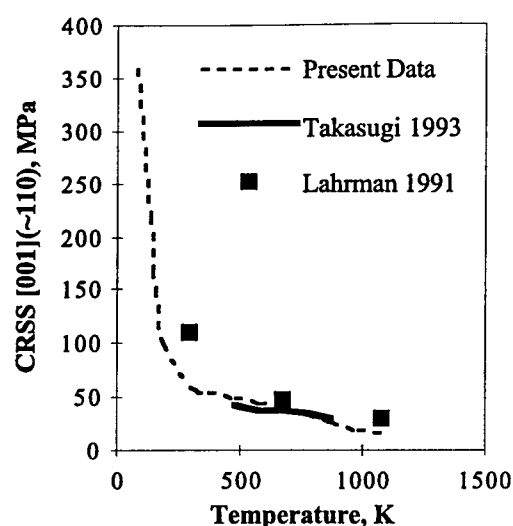
Figure 2 - CRSS vs. temperature for the [001]($\bar{1}$10) slip system taken from tests on [$\bar{1}$11] specimens.

Figure 3 - Stereographic projection with the relevant directions indicated. Both $\bar{5}$57 (single slip) and 011 (double slip) orientations have Schmid factors ~0.5.

Sample Description	$\sigma_{0.2\%}$ MPa	Elong. %	σ_f. MPa
Side (110)	140	6.2	205
15 mm gage	132	4.5	184
	127	10.3	196
	137	15.0	239
	134	12.6	221
	141	2.5	183
Face (110)	101	16.6	196
15 mm gage	98	9.4	158
	100	22.0	195
	97	12.1	215
	94	26.0	203
	105	13.9	188
Face (110)	115	17.9	218
10 mm gage	114	33.9	266
	109	16.2	190

Table 2. Mechanical properties of NiAl crystals tested parallel to <$\bar{5}$57> at room temperature.

interrupted tensile tests. For the highest elongation tests, typical load-elongation curves appear as shown in Figure 5a. The interrupted examination revealed that the initial "drop" in load corresponds to the formation of a localized neck; this neck continues to localize and then stops as work hardening increases the flow stress locally. Based on these intermediate observations, it is possible to draw approximate shear stress-shear-strain curves; the results (Fig. 5b) imply that the shear stress does not drop; rather, it plateaus during the propagation of the localized band across the gage length and then increases again during continued deformation due to normal strain hardening throughout the gage length. During this deformation, the material is relatively resistant to necking and tends to undergo extensive elongation. These observations are consistent with the recent theoretical work by Haehner (6, 7) who used a dynamic dislocation model to predict the behavior of Lüders bands in both single crystals and polycrystals. In spite of these large elongations, the ensuing fracture is still brittle in appearance. The drop-off in the elongation at elevated temperatures (Fig. 4) can be correlated with an increased tendency for the material to neck prior to fracture (Fig. 6). When the strain rate sensitivity and work hardening rates were examined as a function of temperature, it became obvious that the strain rate sensitivity increases with increasing temperature whereas the work hardening rate drops off presumably due to dynamic recovery effects. However, the drop in work hardening rate
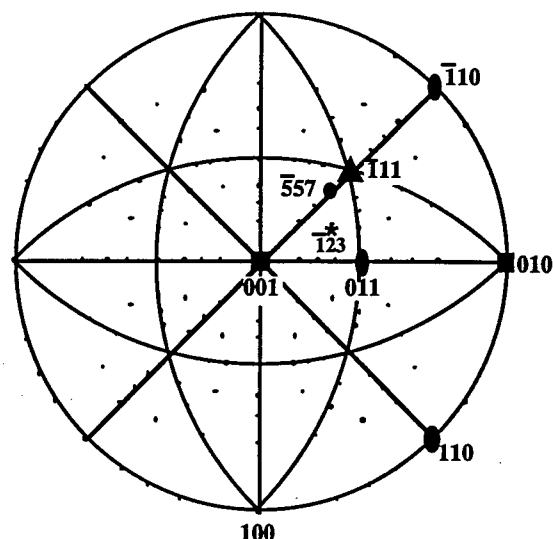
outweighs the increase in SRS resulting in the increased tendency for the necks to localize the deformation and lead to fracture at shorter total elongations.

The influence of small additions of silicon to the NiAl has been examined in order to understand 1) the influence of a substitutional addition on the properties of NiAl and 2) it's influence on static and dynamic strain aging. The results indicate that silicon does harden NiAl and lowers the
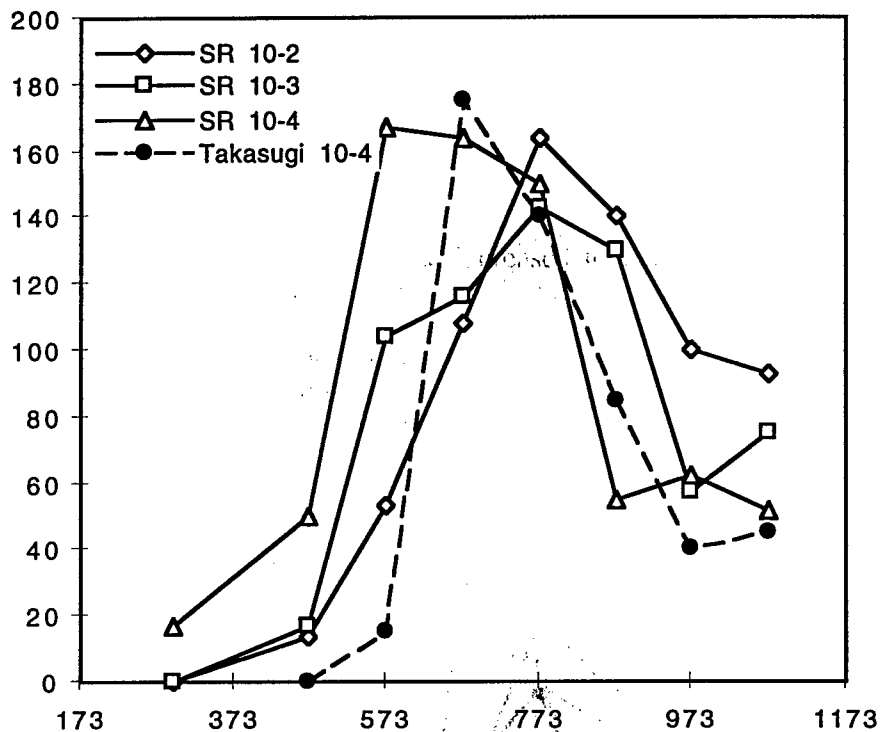
Figure 4 - Elongation vs. temperature of <111> crystals tested at three different strain rates.
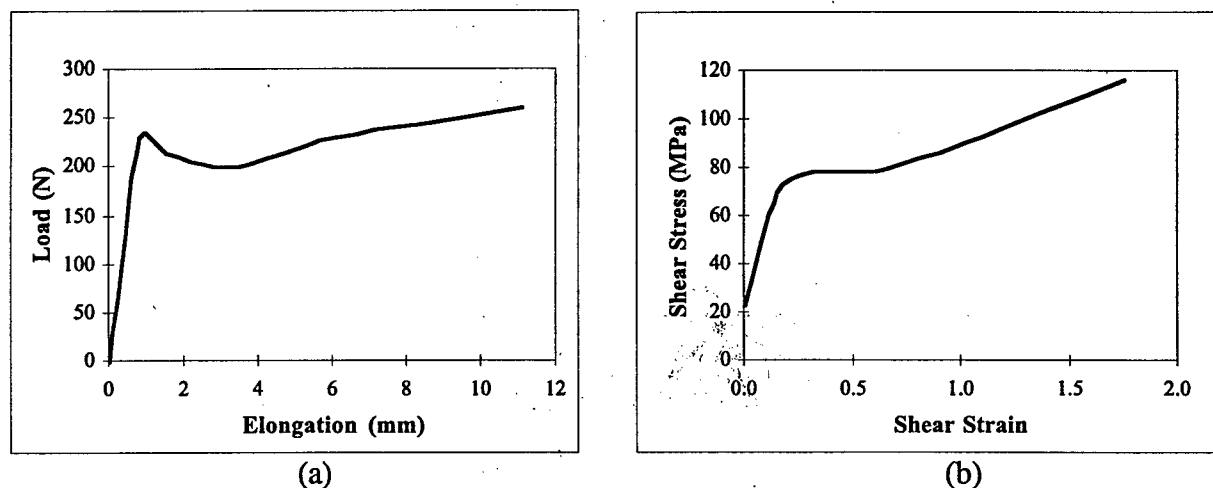

(a)   (b)

Figure 5 - (a) Load vs. elongation for <$\bar{1}$11> crystal tested at 573K. (b) Shear stress vs. shear strain of same taking into account both "Lüders" band propagation (actual area) and specimen rotation during elongation. Strain rate = 10^{-3} s^{-1}.
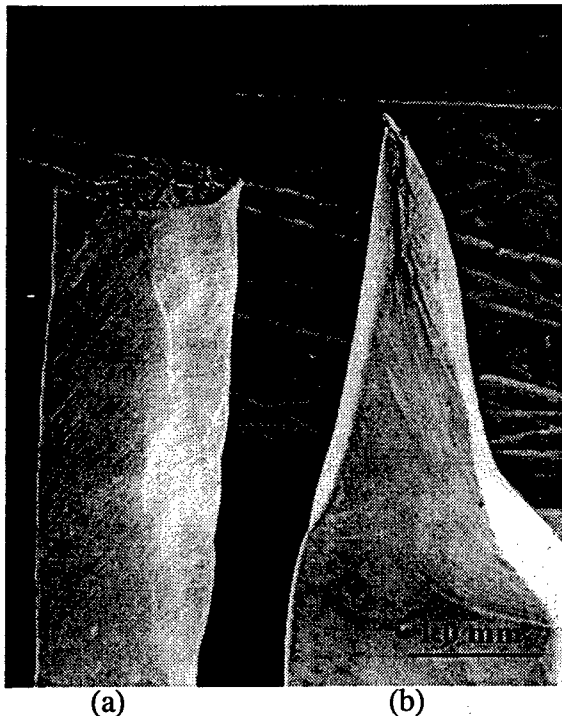
9

Figure 6 - Scanning electron micrographs of [$\bar{1}$11] samples tested at (a) 573K (strain rate = 10^{-3} s^{-1}) and (b) 873K (strain rate = 10^{-4} s^{-1}) showing the greater necking at the higher temperatures.

maximum elongations observed. In addition, it does exacerbate the effect of carbon on SSA and DSA although the mechanism remains unclear at this time.

Because of the dependence of the elongation vs. temperature behavior on strain rate, it was decided to analyze the BDTT as a function of displacement rate using double-notch tensile specimens. Figure 7 shows the fracture toughness vs. temperature behavior for three different displacement rates and it is clear that the apparent BDTT depends on temperature in a manner consistent with the tensile results. This implies that thermally activated processes are responsible for the transition from brittle to ductile behavior and, as already mentioned above, the definition of a BDTT should be used with caution as the fractures on both sides of the BDTT are brittle in nature.

In terms of modeling, our efforts have been focused on understanding plastic deformation in the low and intermediate temperature regime, as a function of the temperature T and strain rate. Procedures have been developed for correctly resolving the observed flow stress σ into its component parts, an effective

stress, σ^*, and an athermal internal stress, σ_μ. It has been shown that a power law, derived by substituting the form of the enthalpy function suggested by Yokobori, $H=-H°\ln(\sigma^*/\sigma_0)$ where $H°$ and σ_0 are constants, into the thermally activated strain rate equation, can describe the dependence of σ^* on both temperature and strain rate. Further, the addition of a dynamic strain aging (DSA) component σ_{DSA} to σ^* explains the apparent independence of σ on strain rate and temperature, in the so called "plateau" region in the σ vs T curve. Research is currently in progress for a better understanding of the reasons for the existence of σ_μ as this is important to its correct estimation.

Our previous efforts delineate the procedures for looking at stress strain data based on the power law and illustrate them with analyses of published data in single phase Nb (bcc) and Ti (hcp) as well as two-phase Ti-6Al-4V alloy.

Another analysis of published data covering a wide range of T and orders of magnitude of strain rate, along the above lines is being readied for publication at this writing. These data are on commercially pure Mo (bcc) and on an α–Ti-Al alloy. The conclusions reached by us are substantially different from those of the original authors, who evaluated σ_μ and σ^* incorrectly.

A critical evaluation of the various methods employed to measure σ_μ has also been done. These methods, which consist of stress relaxation or strain rate cycling experiments, suffer from practical limitations in their applicability. The more popular back-extrapolation method is predicated upon the mistaken belief that σ^* becomes athermal in the plateau region in the σ versus T curve. It is our contention that this interpretation of the so-called plateau is incorrect and that the apparent

independence of σ^* on strain rate and temperature can be explained by the presence of DSA. An erroneous estimate of σ_μ (and hence σ^*) renders all further data analysis moot.
The factors contributing to σ_μ are known to include grain size, prestrain, composition and elastic modulus. We hope to explain the values of σ_μ and its temperature dependence in terms of the grain size and prestrain for data on commercially pure Ti.
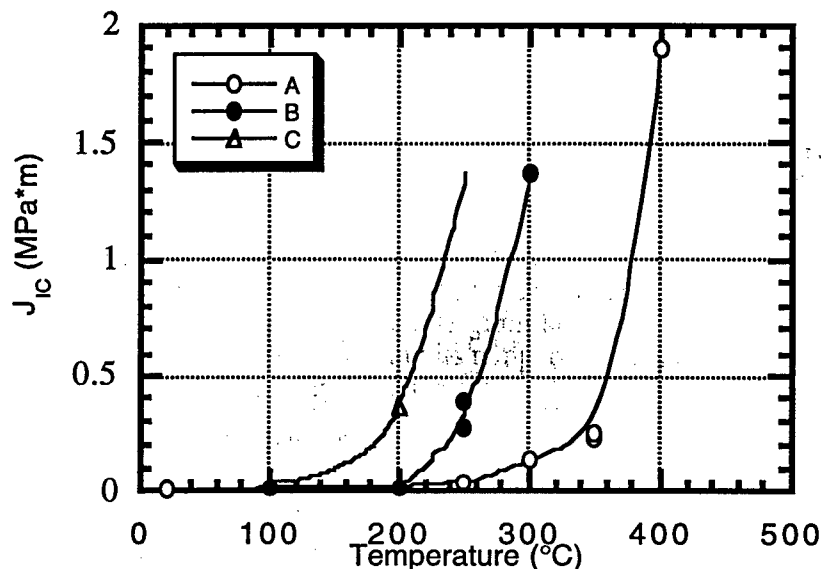

Figure 7 - Effect of displacement rate on the "BDTT" of NiAl crystals tested at (a) 2 x10^{-2}mm/sec (b) 2 x10^{-4}mm/sec (c) 2 x10^{-5}mm/sec.

Thrusts 3 - Other Characterization Studies There have been a variety of methods utilized in the present study in order to understand more clearly the structure/property relations in NiAl. Among these, APFIM studies have been used to determine if carbon does segregate to dislocations as suspected based on the SSA and DSA studies. Figure 8 displays one such measurement where it is apparent that indeed there is a higher concentration of carbon at the core of the dislocations. This is being pursued further under more controlled conditions with and without the addition of silicon.

In addition to the APFIM studies, Hanrahan and Verink have utilized ion implantation, thermal processing and SIMS profiling to study diffusion, site occupation (of carbon in NiAl), and interactions (e.g., carbon and iron). The results have been inconclusive as pointed out in previous publications and reports on this subject although the approach is still of interest.

4.4. References

1. R. Darolia, D.F. Lahrman, R.D. Field, A.J. Freeman, in *High Temperature Ordered Intermetallic Alloys III*. C.T. Liu, A.I. Taub, N.S. Stoloff, C.C. Koch, Eds. (Materials Research Society, Boston, 1989).

2. V.I. Levit, I.A. Bul, J. Hu and M.J. Kaufman, *Scripta Mater.* **34**, 1935-1930 (1996).

3. V.I. Levit, J. Hu, I.A. Bul, J.S. Winton and M.J. Kaufman, Challenges in the Development and Application of β-NiAl as a Structural Material, In Press (1996).

4. T. Takasugi, J. Kishino, S. Hanada, *Acta. Metall. Mater.* **41**, 1009-1020 (1993).

5. Lahrman, R.D. Field, R. Darolia, The Effect of Strain Rate on the Mechanical Properties of Single Crystal NiAl, L.A. Johnson, D.P. Pope, J.O. Stiegler, Eds., High-Temperature Ordered Intermetallic Alloys IV (Materials Research Society, Boston, Mass. 1991), vol. 213, pp. 603-607.

6. P. Haehner, *Appl. Phys.* A **58**, 41-48 (1994).

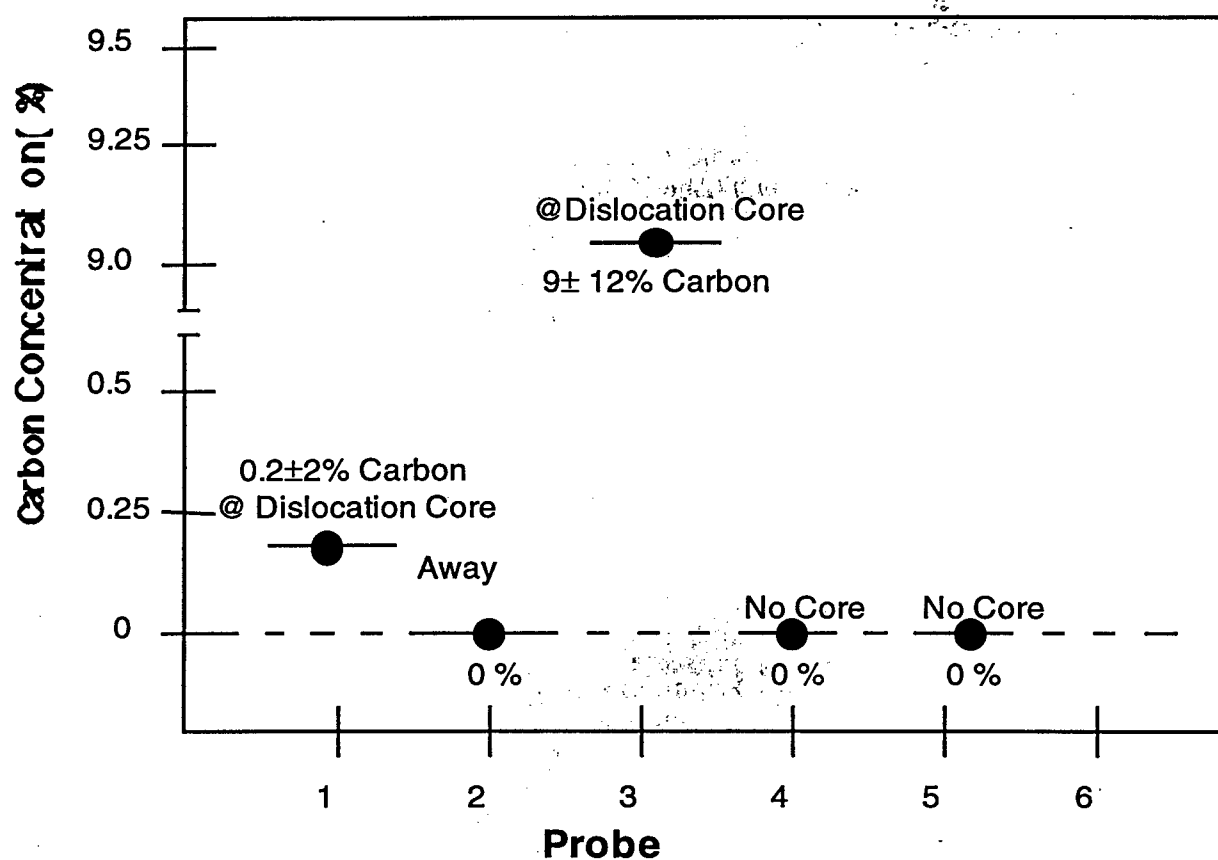7. P. Haehner, *Appl. Phys.* A **58**, 49-58 (1994).

Figure 8 - APFIM mass spectra from NiAl. The upper spectrum is a summation of our data from the dislocation core, and the lower spectrum is a summation of the data from an undisturbed region some distance away from the dislocation.

12

5.0 List of Publications

5.1 Thrust 1

1. "Computational Fluid Dynamics with Moving Boundaries" W. Shyy, H.S. Udaykumar, M.M. Rao and R.W. Smith, Taylor and Francis, Washington, DC, (1996) xviii + 286 pages.

2. "The Computer-Aided Analysis of Directional Solidification Processes" W. Shyy, *J. of Metals* **48** (1996) 24.

3. "*ELAFINT*: A Mixed Eulerian-Lagrangian Method for Fluid Flow With Complex and Moving Boundaries" H.S. Udaykumar, W. Shyy and M.M. Rao, *International Journal for Numerical Methods in Fluids,* **22** (1996) 691.

4. "Multi-Zone Simulation of Bridgman Growth Process of β-NiAl Crystal" H. Ouyang and W. Shyy, *International Journal of Heat and Mass Transfer,* **39** (1996) 2039.

5. Moving Boundary Computation of the Float Zone Process" M.M. Rao and W. Shyy, *International Journal for Numerical Methods in Engineering,* **40** (1997) pp.1231-1261; also in *Transport Phenomena in Materials Processing and Manufacturing,* ASME HTD-Vol. 336/FED-Vol. 240, pp.295-303 (1996).

6. "Simulation and Measurement of a Vertical Bridgman Growth System for β-NiAl Crystal," H. Ouyang, W. Shyy, V. Levit, and M.J. Kaufman, *International Journal of Heat and Mass Transfer,* Vol. 40, (1997) 2293-2305, also in *Transport Phenomena in Materials Processing and Manufacturing,* ASME HTD-Vol. 336/FED-Vol. 240, pp.73-83 (1996).

7. "Applications of Multi-Level Simulation of Bridgman Growth Process for β-NiAl and CdTe Crystals," H. Ouyang, H. and W. Shyy, 1996 TMS Annual Meeting, 1996 EPD Congress (Proceedings of Sessions and Symposia sponsored by the Extraction and Processing Division), G.W. Warren (ed.), pp.707-723, The Minerals, Metals & Materials Society, Warrendale, PA, (1996).

8. "Multi-Resolution Computations for Fluid Flow and Heat/Mass Transfer" W. Shyy, J. Liu J. and H. Ouyang in *Advances in Numerical Heat Transfer,* W.J. Minkowycz and E.M. Sparrow (editors), **1** (1997) pp.137-169, Taylor & Francis, Washington, DC.

9. "Computational Techniques for Complex Transport Phenomena," W. Shyy, S.S. Thakur, H. Ouyang, J. Liu, and E. Blosch, Cambridge University Press, New York, (1997), xviii + 321 pages.

10. "Superheating Behavior of NiAl," N.S. Kulkarni and K.T. Hong, *Metallurgical and Materials Transactions A,* **29A** (1998) 2221-2225.

5.2 Thrust 2

1. "Application of a Method for Determination of the Internal Stress in Polycrystaline NiAl," M.L. Weaver and M.J. Kaufman, *Scripta Met.* **31** (1994) 745-750.

2. "Effect of Crystallographic Orientationon the Fracture Toughness of NiAl Single Crystals", S. Shrivastava and F. Ebrahimi, MRS Symposium Proceedings, 1995, Vol. 364, Part I, pp. 431-436.

13

3. "Crack Path in Single Crystals," F. Ebrahimi and S. I. Hussain, *Scripta Metall. Mater.*, 1995, Vol. 23, pp. 1507-1511.

4. "On Evaluating the Flow Stress in Niobium of Commercial Purity" R.E. Reed-Hill and M.J. Kaufman, *Acta Metall. et Mater.*, **43**, 1731 (1995).

5. "The Effects of Interstitial Content, Heat Treatment, and Prestrain on the Tensile Properties of NiAl," M.L. Weaver, R.D. Noebe, J.J. Lewandowski, B.F. Oliver, and M.J. Kaufman, *Mat. Sci. & Engr.*, **A192/193** (1995) 179-185.

6. "Modeling Flow Stresses and Strain Rate Sensitivities Using Low Temperature Deformation Data" C.V. Iswaran, R.E. Reed-Hill, V.I. Levit and M.J. Kaufman, *Scripta Metall. et Mater.*, **32**, 941 (1995).

7. "A Power Law Model for the Flow Stress and Strain-Rate Sensitivity in CP Titanium" R.E. Reed-Hill, C.V. Iswaran and M.J. Kaufman, *Scripta Metall. et Mater.*, **33**, 157 (1995).

8. "The Influence of Iron on the Physical and Mechanical Properties of β-NiAl," Y.J. Lim, K.T. Hong, V. Levit and M.J. Kaufman, *Mat. Res. Soc. Symp. on High Temperature Ordered Intermetallic Alloys - VI*, **364**, (1995).

9. "The Influence of Mo On the Physical and Mechanical Properties of Single Crystalline NiAl," J. Hu, V. Levit and M.J. Kaufman, *Mat. Res. Soc. Symp. on High Temperature Ordered Intermetallic Alloys - VI*, **364**, (1995).

10. "The Effects of Interstitial Content and Annealing on the Flow and Fracture Behavior of Polycrystalline β-NiAl," M.L. Weaver, V.I. Levit, M.J. Kaufman and R.D. Noebe, *Mat. Res. Soc. Symp. on High Temperature Ordered Intermetallic Alloys-VI*, **364**, (1995) 425-430.

11. "Kinetics of Static Strain Aging in Polycrystalline NiAl-Based Alloys " M.L. Weaver, M.J. Kaufman and R.D. Noebe, *Intermetallics* **4** (1996), 121-129.

12. "Manifestations of Dynamic Strain Aging in Soft-Oriented NiAl Single Crystals," M.L. Weaver, M.J. Kaufman and R.D. Noebe, *Metall. Trans. A*, **27**A (1996) 3542-3557.

13. "Observations of Static Strain-Aging in Polycrystalline NiAl," M.L. Weaver, R.D. Noebe and M.J. Kaufman, *Intermetallics*, **4** (1996) 533-542.

14. "High Tensile Elongation of β-NiAl Single Crystals at 293 K," V.I. Levit, I.A. Bul, J. Hu and M.J. Kaufman *Scripta Materialia* , **34** (12), 1925-1930, 1996.

15. "The Influence of C and Si on the Flow Behavior of NiAl Single Crystals," M.L. Weaver, R.D. Noebe, and M.J. Kaufman, *Scripta Materialia.*, **34** (6), 941-948, 1996.

16. "Nature of Slip During Indentation on {100} Surface of NiAl," F. Ebrahimi, A. Gomez, and T. G. Hicks, *Scripta Metall. et Mater.*, **35** (1996) 337-342.

17. "Brittle-to-Ductile Transition in Polycrystalline NiAl," F. Ebrahimi and G.T.Hoyle, *Acta Materialia*, 45 (1997) 4193-4204.

18. "Effect of Prestraining on the Brittle-to-Ductile Transition of NiAl Single Crystals," S. Shrivastava and F. Ebrahimi, *Mat. Res. Soc. Symp. on High Temperature Ordered Intermetallic Alloys - VII*, 1997, Vol. 460, pp. 393- 398.

19. "Crack Initiation in Brittle-to-Ductile Transition Regime of NiAl Single Crystals," F. Ebrahimi and S. Shrivastava, *Materials Science and Engineering*, **239**-240 (1997) 386-392.

20. "Brittle-to-Ductile Transition in NiAlSingle Crystal," F. Ebrahimi and S. Shrivastava, *Acta Materialia*, **46** (1998) 1493-1502.

21. "Influence of Interstitials on the Mechanical Properties of Metallic Materials" R.E. Reed-Hill, C.V. Iswaran and M.J. Kaufman, *Metall. and Mater. Trans. A*, **27A** (1996) 3524-3529.

22. "An Analysis of the Flow Stress of a Two Phase Alloy System, Ti-6Al-4V" R.E. Reed-Hill, C.V. Iswaran and M.J. Kaufman, *Metall. and Mater. Trans. A*, **47** (1996) 1-6

23. "Challenges in the Development and Application of β-NiAl as a Structural Material" V.I. Levit, J. Hu, I.A. Bul, J.S. Winton and M.J. Kaufman in *Processing and Design Issues in High Temperature Materials*, ed. N.S. Stoloff and R.H. Jones, TMS Proceedings of the Engineering Foundation Conference, Davos, Switzerland, May 1996, pp. 185-194.

24. "Mechanisms of High Tensile Elongation in NiAl Single Crystals at Intermediate Temperatures," V.I. Levit, J.S. Winton, Yu. N.Gornostyrev and M.J. Kaufman, *Proceedings of ReX'96: The Third International Conference on Recrystallization and Related Phenomena* Edited by Terry R. McNelley Monterrey, CA, USA, 637-644, 1996.

25. "Concerning the Evaluation of the Internal Stress During Plastic Deformation," C.V. Iswaran, R.E. Reed-Hill, and M.J. Kaufman, *Proc. Johannes Weertman Symposium*, R.J. Arsenault, et al (eds.), TMS Conference Proceedings, Anaheim, CA, February 4-8, 1996, pp. 449-454.

26. "Simulation of Grain Boundary Instabilities During Hot Straining," A.V. Kaptsan, Yu.N. Gornostyrev, V.I. Levit and M.J. Kaufman, *Proceedings of ReX'96: The Third International Conference on Recrystallization and Related Phenomena* Edited by Terry R. McNelley Monterrey, CA, USA, 571-578, 1996.

27. "On Determining the Internal Stress Using Hall-Petch Data," R.E. Reed-Hill, C.V. Iswaran, and M.J. Kaufman, *Scripta Met.*, **36** (12) (1997) 1361-1366.

28. "Development of NiAl Single Crystals and Their Mechanical Properties," M.J. Kaufman, V.I. Levit, I.A. Bul, J. Hu and J.S. Winton, *Proc. of International Symposium on Nickel and Iron Aluminides: Procesing, Properties and Applications*, Materials Week, 1996, Cincinnati, Ohio, 117-122, 1997.

29. "Strain Aging Behavior in NiAl Microalloyed with Interstitial and Substitutional Solutes," M.L. Weaver, R.D. Noebe and M.J. Kaufman, *Mat. Res. Soc. Symp. on High Temperature Ordered Intermetallic Alloys - VII*, **460**, (1997) pp. 499-504.

30. "Tensile Behavior of β-NiAl: Intrinsic vs. Extrinsic Properties," V.I. Levit and M.J. Kaufman, *Structural Intermetallics 1997*, ed. by M.V. Nathal, R. Darolia, C.T. Liu, P.L. Martin, D.B. Miracle, R. Wagner and M. Yamaguchi, Seven Springs, PA, USA, (1990) 683-690.

31. "Simulation of Deformation in NiAl Single Crystals," C. Yang and A.V. Kumar, Proceedings of the International Mechanical Engineering Conference and Exposition 1998, ASME Materials Division, MAT-5B, 1997.

32. "Tensile Properties of NiAl Bicrystals," J.B. LeBleu, Jr., P.R. Mei, V.I. Levit, and M.J. Kaufman, *Scripta Materialia*, **38** (1998) 415-422.

33. "Investigation of Localized Deformation in NiAl Single Crystals", A.V. Kumar, C. Yang, and Y.B.R sasubmitted to *Journal of Engineering Materials and Technology*, 1998.

34. "Study of Work Hardening Models for Single Crystals Using 3D Finite Element Analysis", submitted to the *International Journal of Plasticity*, 1998.

35. "Texture Evolution in NiAl," K.E. Harris, F. Ebrahimi and H. Garmestani *Journal of Materials Science and Engineering*, (in press).

36. "Effects of Purity on the Properties of β-NiAl Single Crystals," J. Hu, V.I. Levit and M.J. Kaufman, to be published in TMS Proceedings of Symposium on *Interstitial and Substitutional Effects on Intermetallics*, 1998 Rosemont, IL Fall Meeting.

37. "Investigation of Strain Hardening in NiAl Single Crystals Using Three-Dimensional FEA Models," A.V. Kumar and C. Yang, submitted to *Journal of Engineering Materials and Technology*, 1998.

5.3 Thrusts 3 and 4

1. "Nano-chemical Analysis of a Dislocation Core" A.J. Melmed, N.C. Tambakis, M.J. Kaufman, J. Hu and V.I. Levit, *Zeit. f. Physikalishe Chemie*, **202** (1997) 197-203.

2. "Oxidation Kinetics of Ion Implanted NiAl" R.J. Hanrahan Jr., D.P. Butt, and S.P. Withrow, *in Surface Modification Technologies IX*, T.S. Sudarshan, W. Reitz, and J. Stiglich, eds. 209-219 TMS, (1996).

3. "A Study of the 'Pest' Phenomenon in NbAl₃" R.J. Hanrahan Jr., E. Lambers, M. Puga-Lambers and S.P. Withrow *in Elevated Temperature Coatings: Science and Technology I*, N.B. Dahotre, J. Hampikian and J.J. Stiglich eds. TMS (1996).

4. "Chemical Potential Shifts Due to Capillarity – Unary Systems," N. Kulkarni and R.T. DeHoff, *Acta Materialia*, **45** (1997) 4963-4968.

6.0 Students and Staff Supported

6.1 PhD Students:

1. Robert Hanrahan, now a staff member at Los Alamos National Laboratory

2. Jian Hu, now a Post-Doc at Auburn University

3. N. Kulkarni, finishing dissertation at U. of Florida

4. Yong Jin Lim, Returned to his company in S. Korea

5. Tom Lushby, finishing dissertation at Johns Hopkins

6. Hong Ouyang, now with Pratt and Whitney in West Palm Beach, FL

7. M. Rao, now with ACRI in Cincinnati, Ohio.

8. Sanjay Shrivastava, Ingersoll-Rand, Manufacturing Development Eng., The Torrington Company, 3975 Steve Reynolds Blvd., Norcross, GA 30093

9. Chulho Yang, Working as Post Doctoral research associate at Georgia Institute of Technology.

10. Igor Bul, left before finishing to take job in the electronic materials industry in Los Angeles, CA.

11. Mark Weaver, now an assistant professor at the University of Alabama, Tuscaloosa, AL.

12. Andy Duncan, now at Westinghouse - Savannah River Site in Aiken, SC.

6.2 Masters Students

1. Todd Hoyle, now with the Department of Transportation in Gainesville, FL

2. Vijay B. R. Seelam, now working at Altair Engineering, Inc in Detroit.

3. N.C. Tambakis, now at Computer Science Corp., College Park, MD.

4. Jeff Winton, now with Intel in Phoenix.

5. Manas Lakshmipathy, finishing thesis and looking for a job.

6. Tolga Ornek, now at American University, Washington, DC.

7. Bruce Bouchard, now with Honda in Columbus, OH.

6.3 Undergraduate Students:

1. Trevor Hicks now at Westinghouse, Pittsburgh, PA

2. Roswitha Schneider, now at Pratt and Whitney, West Palm Beach, FL.

3. Jonathan McEldowney, worked at Pratt and Whitney, West Palm Beach, FL after graduation; now deceased.

4. Matthew Parks, now at Pratt and Whitney, West Palm Beach, FL.

5. Carla Cloutier, graduate student at the University of Michigan.

6. Stephen Mayers, now at Pratt and Whitney, West Palm Beach, FL.

7. John Molloy, now with Motorola in Austin, TX.

8. Phillip Maggio, now at Norton in Massachussetts.

9. James LeBleu, now at Exxon, Houston, TX.

6.4 Other Staff

1. Vladimir Levit, research scientist now with AS&M (on-site contractor at NASA, Langley), Hampton, VA.

2. K.T. Hong, was a visiting scientist and returned to Korea Institute of Science and Technology (KIST) in Seoul, Korea.

3. Paulo Mei, worked for 1.5 years on his sabbatical from Campinas University in Brazil.

4. Coimbatore Iswaran, post-doc who still works in the department with myself and Prof. Reed-Hill.

7.0 REPRINTS, PREPRINTS OF MANUSCRIPTS

Computational Techniques for Complex Transport Phenomena

W. Shyy
University of Florida

S. S. Thakur
University of Florida

H. Ouyang
Atchison Casting Corp.

J. Liu
Western Atlas Logging Services

E. Blosch
Northrop-Grumman

The Computer-Aided Analysis of Directional Solidification Processes

Wei Shyy

Computer-aided modeling and simulation has become a viable tool in enhancing the physical understanding of solidification processes. This tool also has the unique capability of enabling the user to extrapolate a given materials processing technique from a small-sized laboratory set-up to a large production size, yielding improved process design. However, most solidification processes are very complicated in nature; both physical models and geometrical complexities pose stringent computing requirements. Recent progress made in modeling, computing, and process simulation is highlighted in this article.

INTRODUCTION

The large-scale production of high-quality crystals and alloys involves several complex physical mechanisms typical of solidification processes. These include heat and mass transport, the dynamics of moving interfaces, geometrical configurations, material thermophysical properties, and non-linear coupling among them. These phenomena are extremely complicated and cannot be predicted by simple analyses or models. For example, the Bridgman growth system is one of the directional solidification configurations frequently employed for producing large single crystals from the melt.[1,2] A schematic of the growth system, currently being used to produce single crystals of β-NiAl, is shown in Figure 1.

The temperature distribution in crystal growth systems such as the Bridgman system is highly complex and is influenced by several factors. As shown in Figure 1, the furnace is composed of two parts: the enclosure, which is filled with argon and contains the heater (T4), and the ampoule containing the melt, the growing crystal, and the cooler (T1). The ampoule is made of alumina and rests on a copper support. The enclosure remains stationary during the growth process, and the ampoule is pulled out to control the growth speed of the crystal. In order to model this crystal growth process, the following phenomena are of key importance and need to be resolved adequately: melt/crystal phase change within the ampoule region; conduction among various components of the furnace, the alumina wall, and the copper base; convection in the melt and the encapsulated gas argon; and radiation between the heater and the ampoule wall.

These complications have traditionally resulted in simplified analyses carried out under quite restrictive assumptions such as idealized geometry, assumed boundary conditions, and constant thermophysical properties; in these

> **Computational tools can be very valuable for gaining physical insight and, based on this insight, improving and optimizing the process design.**

reduced models, important convection modes created by buoyancy and capillary effects (critical in many solidification processes) are also often neglected. General understanding of transport processes and macroscopic properties in crystal growth during the last three decades has improved substantially. However, a comprehensive model of the crystal-growth process has to account for the complex geometry, temperature and phase-dependent material properties, buoyancy-driven convection and its influence on the melt/crystal interface, and the resulting thermal distribution within the crystal. In particular, process scale-up from small laboratory experiments to large production is not well addressed in theory.

Computational tools can be very valuable for gaining physical insight and, based on this insight, improving and optimizing the process design. They offer a framework for a convenient and relatively inexpensive platform for performing parametric studies to cover the entire range of processing conditions.

Two case studies are discussed to illustrate the practical utility of a computational tool. The cases presented include the Bridgman growth of β-NiAl crystals, based on a multizone approach to optimize the use of computing resources, and the continuous ingot casting process of Ti-6Al-4V, where Marangoni convection, natural convection, turbulence, and solidification all interact actively within the mold.

BRIDGMAN GROWTH OF β-NiAl CRYSTAL

β-NiAl is an intermetallic that is currently being investigated as a promising high-temperature structural material for application in the next generation of aircraft engines and structural components.
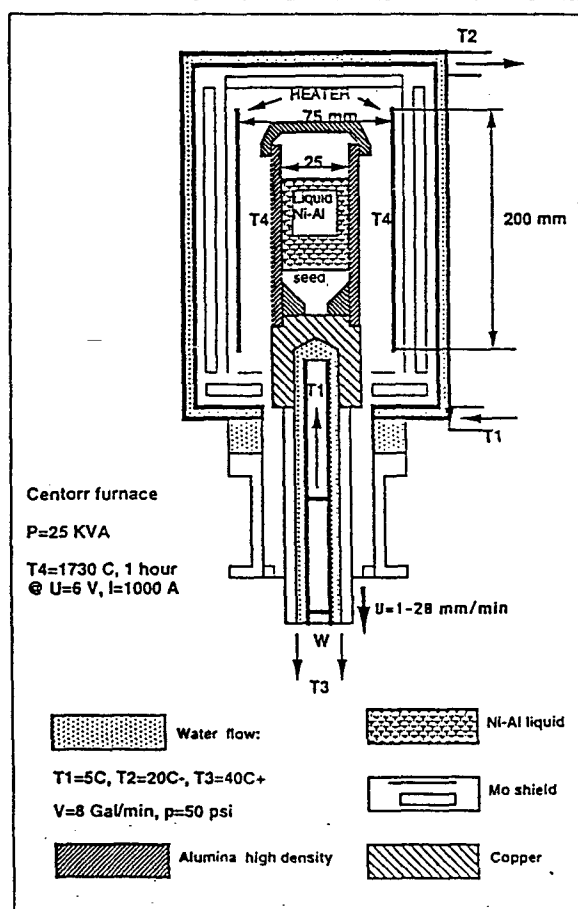

Figure 1. A schematic of vertical Bridgman furnace for growing β-NiAl.

COMPUTER-AIDED MODELING

Time Scale

One issue intrinsic to the solidification process is the presence and interaction of different length and time scales in the system. To illustrate this point, consider three dimensionless parameters encountered during many practically important solidification processes. One such parameter is the Grashof number

$$(Gr)_T = \frac{\rho^2 g \beta_T \Delta T l^3}{\mu^2}$$

where g is gravitational acceleration, ρ is the characteristic density, l is the characteristic length scale of the melt, ΔT is the characteristic temperature variation in the melt, β_T is the coefficient of thermal expansion, and μ is the dynamic viscosity. The Grashof number measures the relative importance of buoyancy force and viscous dissipation within the melt. Thus, it characterizes the magnitude of buoyancy-induced convection within the melt during solidification.

Another parameter is the Marangoni number

$$Ma = \frac{\left(\frac{d\sigma}{dT}\right)\Delta T \, l}{\mu \alpha_t}$$

where σ is surface tension and α_t is thermal diffusivity of the melt. The Marangoni number is a measure of the importance of surface tension relative to viscous and

thermal diffusion in heat, mass, and momentum transfer within the melt; it appears when free surfaces exist in the solidification process.

Another is the Stefan number

$$St = \frac{C_p \Delta T}{\Delta h_{l-s}}$$

where C_p is the specific heat of the melt and Δh_{l-s} is the latent heat of fusion. The Stefan number measures the magnitude of superheat with respect to that of latent heat. It dictates the rate of solidification.

An inspection reveals that these dimensionless parameters scale differently with respect to the geometrical dimensions of the solidification component:

$$(Gr)_T \sim l^3$$
$$Ma \sim l$$
St is independent of l

Hence, in practical terms, it is virtually impossible to conduct a laboratory experiment that can maintain the same values of all the dimensionless parameters since a change of length scale of the melt impacts different dimensionless parameters differently. In other words, between laboratory and production scales, the relative dominance of different transport mechanisms (e.g., molecular diffusion and buoyancy- and surface-tension-driven convection) changes.[3] No experiments have been reported that can claim that a strict similarity of the transport processes between solidification facilities of

different length scales can be maintained via the change of, for example, ΔT, μ, and α to accommodate the variation in l. It must be observed that the Prandtl number and Schmidt numbers, the latter measuring the ratio of kinematic viscosity and mass diffusivity, should also be unchanged to study the transport characteristics in a given processing condition, thus substantially restricting flexibility in choosing a substitute material that is easier to handle in a laboratory set-up.

Computational Modeling

With the experimental difficulties mentioned for scaling issues in reproducing the actual operating conditions, it becomes clear that computational modeling can be immensely useful. Through such modeling, one can first assess the predictive capability via validating against carefully conducted laboratory measurements and then extend the calculations to the conditions directly relevant to actual production. Besides the scaling aspect, computer-aided modeling can contribute to other important process-related issues as well. For example, it can be used to assess the impact of environmental perturbations, to optimize the geometrical configuration of processing equipment, and to regulate thermal scheduling and heat-transfer distribution during the solidification process. Much progress has been made in modeling of the various aspects of materials processing and solidification (e.g., References 3–15).

It is now well established that computer-aided process simulation based on fundamental physical laws can play a critical role in helping engineers assess the impact of scale extrapolation; however, before confidence can be gained in extrapolating computational results to actual production, considerable assessment and research must be carefully conducted to understand the strengths and weaknesses of a given theoretical model. This requirement is most critical because it directly links model development and experimental observation. Figure A shows a schematic of an experimentally assessed model development effort; it is clear that many steps are needed before a laboratory experimental set-up and a computational tool can be applied effectively to predict and control large-scale manufacturing process improvement.

Our understanding of the fluid flow and thermal transport aspects of solidification processing can be substantially enhanced with the aid of computer graphics. Multidimensional views of transport phenomena in complex geometries have yielded valuable insight that is difficult to obtain by other means. Despite the many potential pitfalls of relying on numerical solutions to study flowfields and transport mechanisms, by carefully exercising a well-defined comparison between prediction and measurement, the level of the numerical and physical accuracy of a given calculation can, in general, be established. Hence, based on this assessment, one can further study the various aspects of the flowfields that are not easily amenable to direct experimental measurements. It is this unique capability of the computational tool that can most impact engineering practice.

Several important aspects of computational algorithms need to be addressed before a practical simulation tool can be developed;[3] these aspects include formulation of the field equations solver; choice of the coordinate system and primary velocity variables; issues of grid layout, boundary treatment, and the role of global mass conservation; convection and diffusion treatments; and solution procedure and convergence. A critical issue that must be considered early in the development of the computational framework is related to the choice of algorithms for solving the system of fluid-flow equations involving several dependent variables; this requires the extra consideration of the coordination of the coupling and signal propagation among the equations. There are many existing algorithms capable of solving the fluid flow, heat, and mass-transport equations needed for process simulation.[3,16–20]
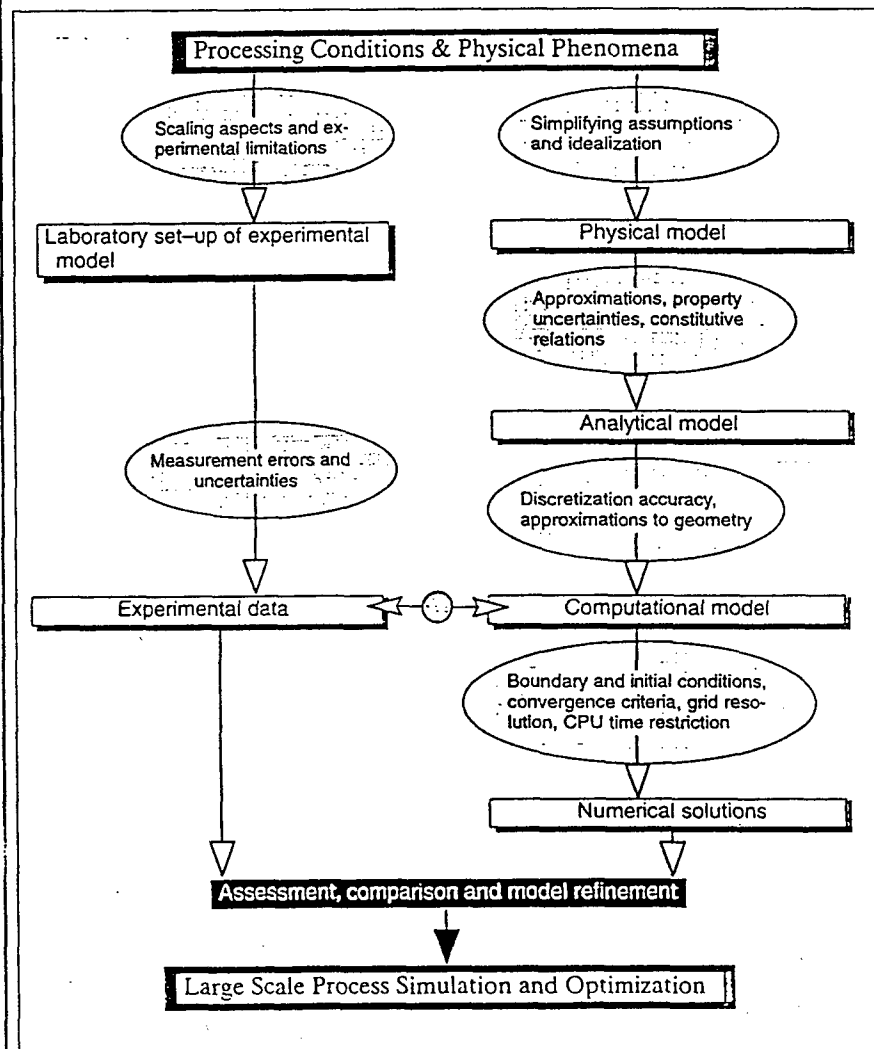

Figure A. An outline of an experimentally assessed model development effort.
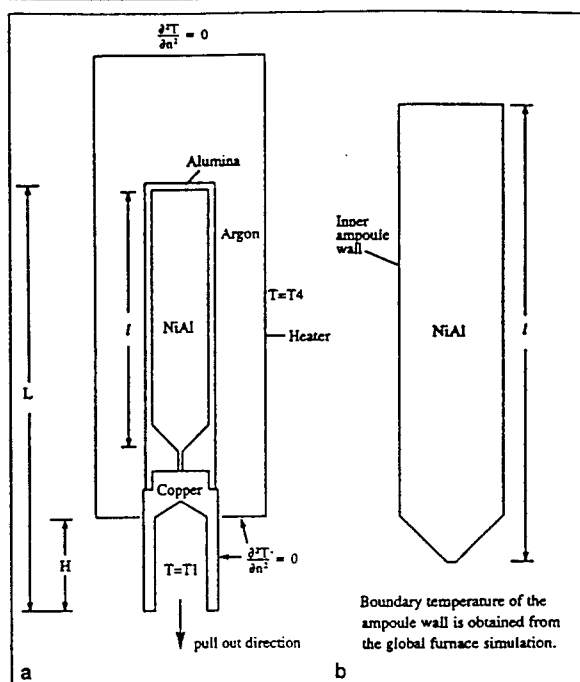
Figure 2. Layout and boundary conditions for (a) the global furnace model and (b) the refined ampoule model. H measures the ampoule position as it is pulled out. The total length of the ampoule part, between the top of alumina and the bottom of copper, is 185 mm while the length of the ampoule is 113.5 mm.

NiAl is especially attractive because of its low density, high thermal conductivity, high melting temperature, and superior isothermal and cyclic oxidation resistance.[21,22] However, it has two major drawbacks—low toughness at room temperature and low strength at high temperature. These deficiencies need to be resolved before NiAl can be used in structural applications.
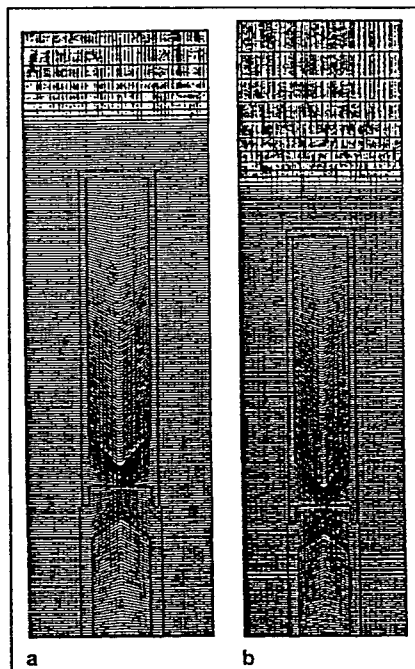
The results of this case study are part of an ongoing effort to grow high-purity single crystals of NiAl of a controlled composition and under controlled environments. To formulate this problem with combined heat transfer and phase change in a geometrically complex domain, a set of unified governing equations that describe conduction, convection, and phase-change phenomena over the entire geometry of the system can be derived and solved.[3,23]

As depicted in Figure 1, the combination of the furnace enclosure and the ampoule presents a very complicated geometry. To render the computations tractable and to simultaneously obtain adequate resolution in the ampoule region, a two-level strategy is employed. Level one simulates the entire domain and is referred to as the global furnace model. Level two concentrates on the ampoule region and obtains its boundary conditions from the level one or the global simulation. With this two-level strategy, the user can obtain useful information at the global level and yet obtain adequate resolution at the melt/crystal interface. Figure 2 demonstrates the two-level strategy devised for the present Bridgman growth process. To solve the governing equations, the control-volume technique employing a nonorthogonal body-fitted coordinate system has been adopted.[3,23]

In order to take into account the relative displacement of the ampoule as the growing crystal is pulled out of the furnace, three simulations have been performed at the global level involving three different locations of the ampoule. A multizone patched grid method has been employed to generate the grid system needed for global (furnace) level simulations. Sample grid distributions are presented in Figures 3a and 3b for H = 40 mm and 80 mm, respectively, where H indicates the position of the ampoule within the furnace. The global furnace (level one) simulations were conducted for three different ampoule positions in order to estimate the effects of geometric variations as the crystal is pulled out of the furnace. Calculations were conducted for H = 40 mm (151 × 213 grid), 80 mm (151 × 216 grid), and 120 mm (151 × 219 grid). In all cases, there were 51 × 103 points in the ampoule region. Based on this resolution, the ampoule region is then computed again with a better resolution; the boundary conditions needed for this level two simulation are extracted from the results obtained from the level one solutions.

Figure 4 shows the stream function (a–c) and the isotherm distribution (d–f) for each of the three ampoule locations. The streamline pattern arises as a result of buoyancy-driven convection. It may be observed that the convection pattern in the encapsulating gas is quite weak, and the convective heat transfer into the ampoule is negligible compared to the radiative effect from the heater. As the ampoule translates downward, the convection within the ampoule becomes slightly weaker and the melt/crystal interface becomes convex towards the melt. It is difficult to predict the strength and detailed characteristics of the convective field within the furnace because the geometry is complicated and the bound-

Figure 3. Grid distributions for the global furnace model of (a) H = 40 mm (grid size = 151 × 213), and (b) H = 80 mm (grid size = 151 × 213).

Figure 4. Stream functions (a–c) and isotherms (d–f) of the global furnace simulations for (a and d) H = 40 mm, (b and e) H = 80 mm, and (c and f) H = 120 mm. Inside the NiAl melt: a—S_{max} = 0.0506, ΔS = 0.0053; b—S_{max} = 0.0513, ΔS = 0.0054; c—S_{max} = 0.0532; ΔS = 0.0056. Inside the argon gas: a—S_{max} = 0.0239, ΔS = 0.0053; b—S_{max} = 0.00243; ΔS = 0.00054; c—S_{max} = 0.00196; ΔS = 0.00056. In d–f, T_{melt} = 0.95, ΔT = 0.02.
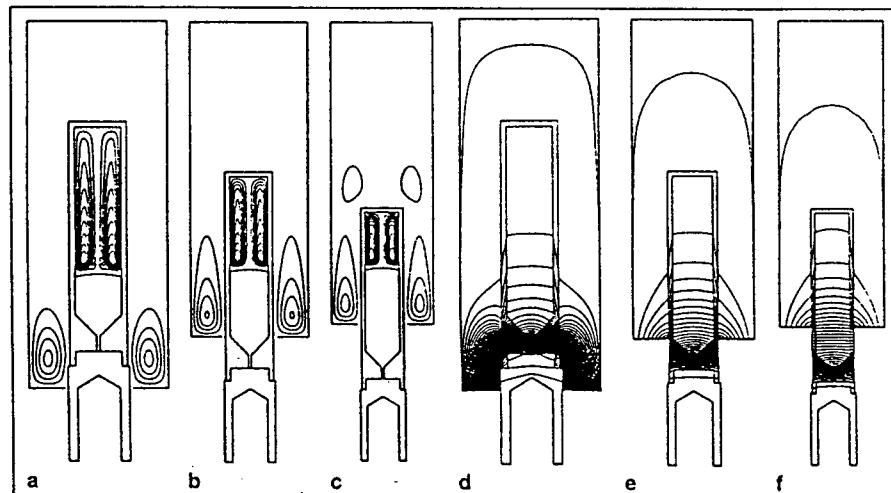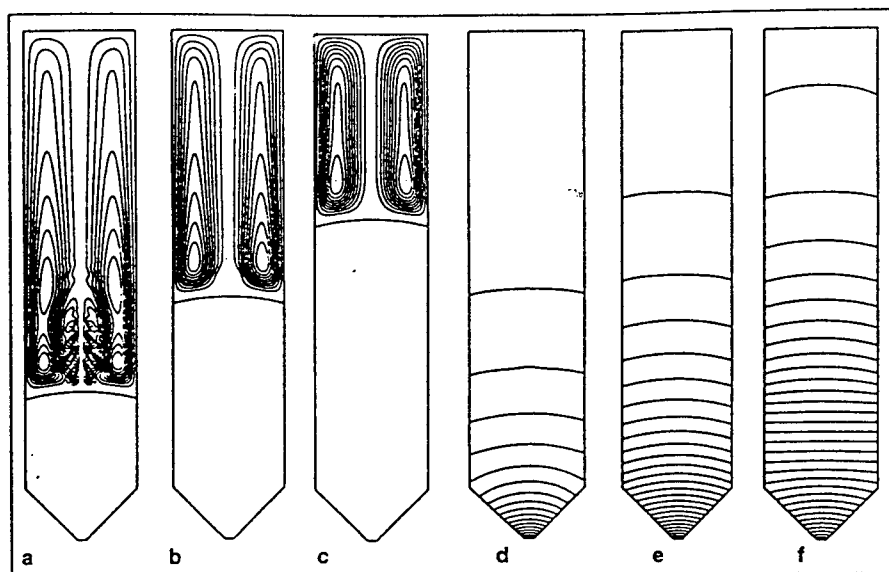
Figure 5. Stream functions (a–c) and isotherms (d–f) of the refined ampoule simulations for (a and d) H = 40 mm, (b and e) H = 80 mm, and (c and f) H = 120 mm. a—S_{max} = 0.0445; ΔS = 0.0048. b—S_{max} = 0.0541; ΔS = 0.0057. c—S_{max} = 0.0560; ΔS = 0.0059. d–f—T_{melt} = 0.95; ΔT = 0.02.

ary conditions vary with the ampoule movement. Nevertheless, it is clear that the isotherm pattern changes significantly as the crystal is drawn down and the temperature gradients at the base of the crystal decrease in magnitude.

The refined ampoule (level two) simulation was conducted using the ampoule wall temperature distribution (obtained from level one) as the boundary condition. The grid resolution within the ampoule has been increased to 101 × 154 from 51 × 103 used at level one. Stream function and isotherm contours are shown in Figure 5. Noticeable differences can be observed between the convection patterns in Figure 5 (a–c) and Figure 4 (a–c) and, more significantly, the convection strengths are different, especially for H = 40 mm. At this ampoule position, more detailed secondary vortical structure in the central region above the solid-melt interface can be clearly observed from the refined solutions depicted in Figure 5 (a–c); at the global level [Figure 4 (a–c)], such characteristics are less pronounced. This assessment shows that a fine grid is needed to capture convection-dominated phenomena, thereby justifying the two-level approach taken in this study.

Figure 6 contrasts the melt/crystal interface obtained from the two-level simulation for all three ampoule locations. It may be observed that the differences between the coarse grid (level one) and the fine grid (level two) calculations are most significant when the melt volume decreases (i.e., as the crystal is pulled out). This observation reinforces the trends exhibited in the stream-function plots mentioned previously. The sensitivity to grid refinement increases as the melt volume decreases because of the constraining effect of the top wall. Since interface positions at the ampoule wall

are the same between the two grid levels, it is significant that the temperature distributions predicted on them are different, resulting in different melt/crystal curvatures. This aspect impacts on the detailed distribution of temperature gradients in the interface region, resulting in different microstructures of the crystal.

INGOT CASTING OF Ti-6Al-4V

Titanium alloys have been extensively used in the fan and compressor sections of gas-turbine power plants; however, there has long been a concern regarding the quality of the alloys used for these critical components, specifically involving melt-related defects. The current state of fundamental understanding of titanium alloys is such that even for the widely used Ti-6Al-4V there is a lack of concrete knowledge regarding its solidi-

fication characteristics. Intensive efforts have been made worldwide[24–31] to advance understanding of the processing characteristics and their impact on the microstructural composition of these important materials. The normal operating conditions of these processes are such that many transport mechanisms are present in the solidification process, including buoyancy-induced convection, surface tension-induced (Marangoni) convection, turbulence, combined conduction-radiation heat transfer, and, most critically, their interactions with the movement of the solidification front.

A schematic illustration of an operational system is shown in Figure 7a, where the raw materials are initially melted with an external heat source in a water-cooled melting hearth before the molten metal is cast into ingots. The modeled geometry as well as conditions of the ingot casting are sketched in Figure 7b. For the case considered, the material is Ti-6Al-4V with an ingot diameter of 0.432 m and a 0.457 m height of the copper mold.

In studying the convection mechanisms, both the buoyancy effect within the melt and the thermocapillary effect on the pool surface need to be included. In estimating the strength of buoyancy-induced convection, one can use the thermal Rayleigh number, $(R\alpha)_T$, as an indicator. The thermal Rayleigh number is defined as

$$(R\alpha)_T = (Gr)_T \cdot Pr$$

Here, we chose the characteristic length R to be the ingot radius R = 0.216 m and the representative kinematic viscosity to be the value at the liquidus temperature, T_{liq} (1,898 K), which is about 10^{-6} m²/s. Hence, under the normal gravity level on earth, a thermal Rayleigh number of $(R\alpha)_T \sim 10^{10} \Delta\rho/\rho$ results. With a density variation of around ten percent, as is the
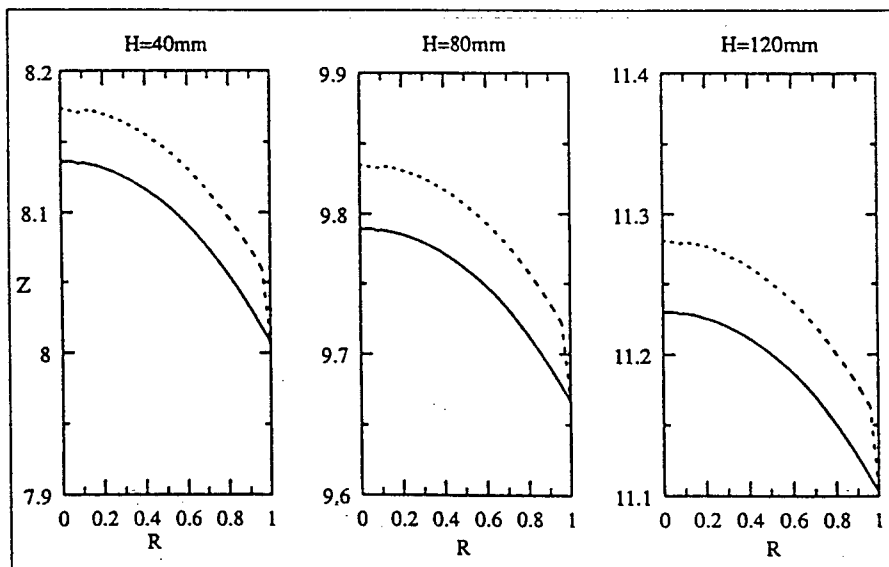

Figure 6. A comparison of the melt/solid interface positions between global furnace (dashed line) and refined ampoule (solid line) models.

case here, thermal Rayleigh number is of the order of 10^9. Regarding the thermocapillary aspect, based on the same length scale and the appropriate material properties, it is estimated that the Marangoni number is of the order of 10^6. Hence, the flows are expected to be well within the turbulent regime.

The Favre-averaged Navier-Stokes equations of mass continuity, momentum, and energy transport along with a k-ε two-equation turbulence closure[32] modified to account for the low Reynolds number effect in the mushy zone[30,31] are the basis of the computations reported here. Collective and individual effects of buoyancy and surface tension on convection can be investigated and their interaction with solidification studied. The results presented correspond to two casting speeds: -2×10^{-4} m/s (455 kg/h) and -4×10^{-4} m/s (910 kg/h). The negative sign indicates a downward casting direction. Figure 8 shows predicted isotherms and liquid-fraction distribution across the mushy zone under two casting speeds. The model predicts a thick mushy zone based on the mean temperature as a result of the convection effect, and the zone thickness varies with the change of casting speed. Within the half domain of the cross section, the model predicts that contrarotating eddies appear due to the combined effects of surface tension and buoyancy. The liquidus line in both solutions is approximately flat, and its depth appears insensitive to the variation of the casting speed. It is noted that under the same thermal energy conditions, the mushy zone yielded by the pure conduction transport is generally thinner in order to maintain required heat flow rates by pure molecular transport (i.e., conduction). With the inclusion of convection, the heat-transfer rates in both the bulk melt and upper mushy zone are now enhanced by macroscopic flow motion; the degree of heat-transfer enhancement depends, of course, on the local

Figure 9. Effect of casting speed on stream function as predicted by modified k–ε turbulence model for (a) $u_{cast} = -2 \times 10{-4}$ m s⁻¹ and (b) $u_{cast} = -4 \times 10^{-4}$ m s⁻¹ ($\Delta\psi = 5 \times 10{-2}$ kg/m s).

convection strength. In the bulk melt as well as the upper mushy zone where convection is vigorous, turbulence plays a dominant role in overall heat transfer and, accordingly, in these regions the temperature distribution is smeared and the overall thermal gradients are substantially reduced.

Toward the solidus line, however, the increasing presence of solidified dendrites within the mushy zone dampens convection, and the thermal conduction again becomes the controlling mechanism. This change of dominant transport mechanisms from liquidus to solidus lines explains why in regions close to the solidus lines the temperature gradients are high, resulting in small mushy-zone thicknesses encompassing large variations of the liquid fraction, while, on the other hand, the temperature gradients are low close to the liquidus lines, resulting in much increased mushy-zone thicknesses there. Figure 9 shows the distribution of the corresponding stream function under the two casting speeds. Although the patterns of the distributions appear qualitatively the same for both speeds, it is clear that the higher the casting speed, the deeper the convection penetrates into the mushy zone.
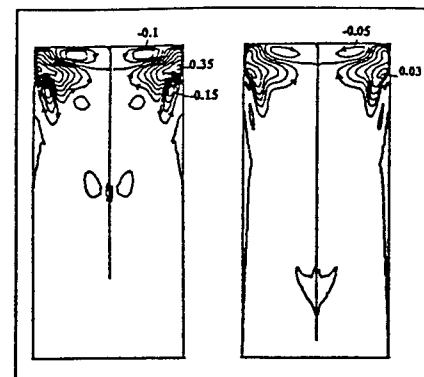
A Ti-6Al-4V ingot was cast in an electron-beam melting process with a casting rate of about -1.8×10^{-4} m/s. A small amount of copper was added to the ingot mold pool near the end of the casting process to mark the pool profile for subsequent ingot macroetch evaluation. Because it reduces the melting temperature, the copper probably caused some of the solid (particularly in the mushy zone) to remelt. Since there was insufficient heat available to remelt much of the solid, the profile indicated by macroetching is probably close to the solidus line. The orientation of the columnar dendritic structure that does not contain copper suggests that the macroetch profile at least approximates the solidus line.

The modified k–ε turbulence model

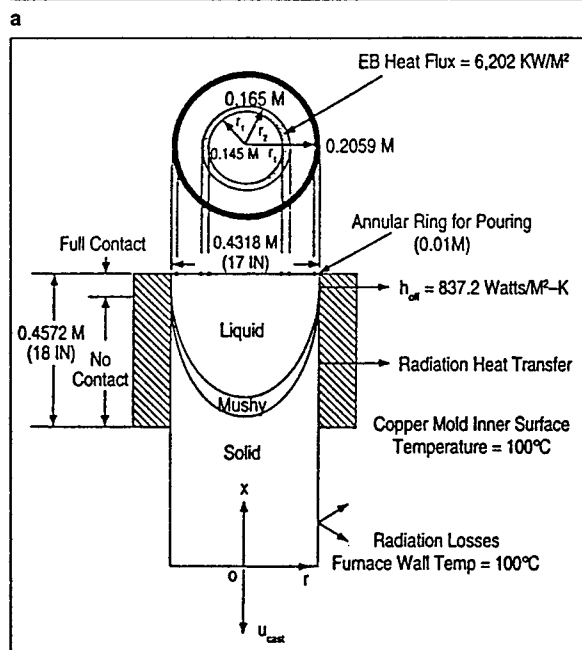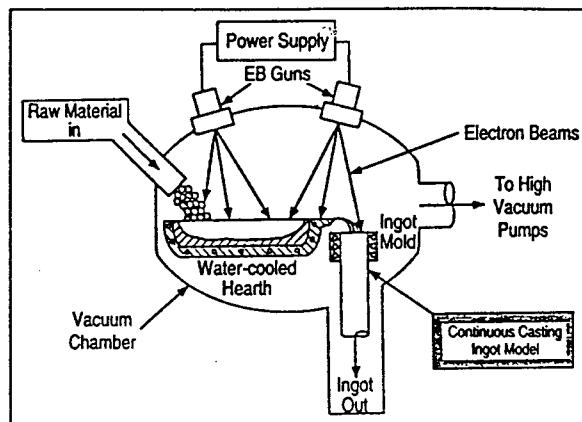Figure 7. A (a) schematic of a cold-hearth electron-beam melting ingot casting system and an (b) ingot model schematic and boundary conditions.
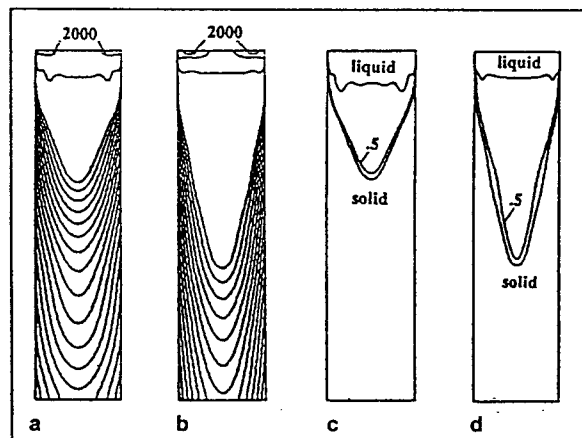

Figure 8. Effect of casting speed on temperature (a and b— $\Delta T = 50$ K) and liquid-fraction contours (c and d) as predicted by modified k–ε turbulence model for (a) $u_{cast} = -2 \times 10^{-4}$ m s⁻¹ and (b) $u_{cast} = -4 \times 10^{-4}$ m s⁻¹.

prediction for the solidus line profile (Figure 9) has features that correlate to features observed on the macroetch profile. The bulge outward in the upper portion of the pool qualitatively appears in both profiles. The high curvature at the bottom of the macroetch pool profile also corresponds closely to the prediction. The predicted pool depth is roughly proportional to the casting rate. Therefore, the pool depth predicted by the modified k-ε turbulence model is 55 cm with the -1.8×10^{-4} m/s casting rate, which closely approximates the macroetch profile depth of 53 cm.

CONCLUSIONS

While computer-aided modeling and simulation has already made contributions to various materials processing techniques, numerous unresolved issues remain (e.g., treatment of extreme scale disparity caused by capillarity and momentum/heat/mass transfer, integration between thermofluid transport and phase change nonequilibrium, and tracking of irregularly shaped moving solid-melt interfaces).[3] With continuing and rapid progress, simulation and design capabilities will improve accordingly.

References

1. J.C. Brice, *Crystal Growth Processes* (London: Blackie, 1986).
2. A.W. Vere, *Crystal Growth* (New York, NY: Plenum, 1987).
3. W. Shyy, *Computational Modeling for Fluid Flow and Interfacial Transport* (Amsterdam, Netherlands: Elsevier, 1994).
4. F. Rosenberger, *Fundamentals of Crystal Growth I* (New York, NY: Springer-Verlag, 1979).
5. R.A. Brown, "Theory of Transport Processes in Single Crystal Growth from the Melt," *A.I.Ch.E. Journal* 34 (1988), pp. 881–911.
6. M.E. Glicksman, S.R. Coriell, and G.B. McFadden, "Interaction of Flows with the Crystal-Melt Interface," *Annual Review of Fluid Mechanics*, 18 (1986), pp. 307–335.
7. J.S. Langer, "Instabilities and Pattern Formation in Crystal Growth," *Review of Modern Physics*, 52 (1980), pp. 1–28.
8. M. Flemings, *Solidification Processing* (New York, NY: McGraw-Hill, 1974).
9. J. Szekely, *Fluid Flow Phenomena in Metals Processing* (New York, NY: Academic Press, 1979)
10. L Sawada, H. Tanaka, and M. Tanaka, "Status of Computational Fluid Dynamics and Its Application to Materials Manufacturing," *MRS Bulletin*, XIX (1994), pp. 14–19.
11. C. Beckermann and R. Viskanta, "Mathematical Modeling of Transport Phenomena During Alloy Solidification," *Appl. Mech. Rev.*, 46 (1993), pp. 1–27.
12. S.H. Davis, "Hydrodynamic Interactions in Directional Solidification," *J. Fluid Mech.*, 212 (1990), pp. 241–262.
13. D.T.J. Hurle, ed., *Handbook of Crystal Growth*, vol. 1 A and B (Amsterdam, Netherlands: North-Holland, 1993).
14. P.J. Prescott and F.P. Incropera, "Binary Solid-Liquid Phase Change with Fluid Flow," vol. IX, *Advances in Transport Processes*, ed. A.S. Mujumdar and R.A. Mashelkar (Amsterdam, Netherlands: Elsevier, 1993), pp. 57–101.
15. M. Rappaz, "Modeling of Microstructure Formation in Solidification Processes," *International Mat. Rev.*, 34 (1989), pp. 93–123.
16. D.A. Anderson, J.C. Tannehill, and R.H. Pletcher, *Computational Fluid Mechanics and Heat Transfer* (Washington, D.C.: Hemisphere, 1984).
17. C.A.J. Fletcher, *Computational Techniques for Fluid Dynamics*, vol. 2, (New York, NY: Springer-Verlag, 1988).
18. C. Hirsch, *Numerical Computation of Internal and External Flows*, vol. 2 (New York, NY: Wiley, 1990).
19. W.J. Minkowycz et al., *Handbook of Numerical Heat Transfer* (New York, NY: Wiley, 1988).
20. O.C. Zienkiewicz and R.L. Taylor, *The Finite Element Method*, 4th ed., vol. 2 (New York, NY: McGraw-Hill, 1991).
21. S. Sen and D.M. Stefanescu, "Melting and Casting Processes for High-Temperature Intermetallics," *JOM*, 43 (5) (1991), pp. 30–32.
22. R. Darolia, "NiAl Alloys for High-Temperature Structural Applications," *JOM*, 43 (3) (1991), pp. 44–49.
23. W. Shyy et al., *Computational Fluid Dynamics with Moving Boundaries* (Washington, D.C.: Hemisphere, 1996).
24. H. Hayakawa et al., "Solidification Structure and Segregation in Cast Ingots of Titanium Alloy Produced by Vacuum Arc Consumable Electrode Method," *ISIJ International*, 31 (1991), pp. 775–784.
25. A. Kagawa, M. Hirata, and Y. Sakamoto, "Solute Partition on Solidification of Nickel-Base Ternary Alloys," *J. Mater. Sci.*, 25 (1990), pp. 5063–5069.
26. R. Sellamuthu and A.F. Giamei, "Measurement of Segregation and Distribution Coefficients in MAR-M200 and Hafnium-Modified MAR-M200 Superalloys," *Metall. Tran.*, 17A (1986), pp. 419–428.
27. C.E. Shamblen and G.B. Hunter, "Titanium Base Alloys Clean Melt Process Development," *Proc. of the 1989 Vacuum Metallurgy Conference*, ed. L.W. Lherbier and J.T. Cordy (Warrendale, PA: Iron & Steel Society, 1989), pp. 3–11.
28. W. Shyy et al., "Modeling of Turbulent Transport and Solidification during Continuous Ingot Casting," *Int. J. Heat Mass Trans.*, 35 (1992), pp. 1229–1245.
29. W. Shyy et al., "Effect of Turbulent Heat Transfer on Continuous Ingot Solidification," *ASME J. of Eng. Mat. and Tech.*, 115 (1993), pp. 8–16.
30. M.A. Taha and W. Kurz, "About Microsegregation of Nickel Base Superalloys," *Z. Metallkde.*, 72 (1981), pp. 546–549.
31. D.W. Tripp and A. Mitchell, "Segregation and Hot-Topping of Titanium Alloy Ingots," *Proc. of the 1989 Vacuum Metallurgy Conference*, ed. L.W. Lherbier and J.T. Cordy (Warrendale, PA: Iron & Steel Society, 1989), pp. 83–89.
32. B.E. Launder and D.B. Spalding, "The Numerical Computation of Turbulent Flow," *Comput. Meths. Appl. Mech. Engrg.*, 3 (1974), pp. 269–289.

ABOUT THE AUTHOR

Wei Shyy earned his Ph.D. in aerospace engineering at the University of Michigan in 1982. He is currently a professor in and chair of the Department of Aerospace Engineering, Mechanics, and Engineering Science at the University of Florida. Dr. Shyy is also a member of TMS.

For more information, contact W. Shyy, University of Florida, 231 Aerospace Building, Gainesville, Florida 32611; (904) 392-6416; fax (904) 392-7303; e-mail wss@tiger.aero.ufl.edu.

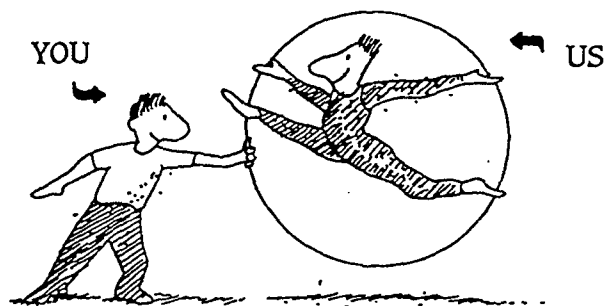# Multi-zone simulation of the Bridgman growth process of β-NiAl crystal

HONG OUYANG and WEI SHYY†

Department of Aerospace Engineering, Mechanics and Engineering Science, University of Florida,
Gainesville, FL 32611, U.S.A.

Abstract—A computational model has been developed for the Bridgman growth process of β-NiAl crystal. The model accounts for heat transfer in the whole furnace system, including the encapsulated fluid between the heater and the ampoule, conjugate heat transfer around and within the ampoule, and phase change dynamics between melt and crystal. To handle the geometrical and physical complexities of the crystal growth processes, a two-level approach has been developed. At the global furnace level, combined convection/conduction/radiation calculations with realistic geometrical and thermal boundary conditions are made inside the whole system. Refined calculations are then made within the ampoule, with the boundary conditions supplied by the global furnace simulations. The present multi-level model can help improve the predictive capabilities for crystal growth techniques by optimizing the use of the computing resources; it allows one to probe the effects of different physical and geometrical variables on the crystal quality.
Copyright © 1996 Elsevier Science Ltd.

1. INTRODUCTION

β-NiAl is an intermetallic that is currently being investigated as a promising high temperature structural material for application in the next generation of aircraft engines and structural components. NiAl is especially attractive because of its low density, high thermal conductivity, high melting temperature, superior isothermal and cyclic oxidation resistance [1]. However, it has two major drawbacks; low toughness at room temperatures and low strength at high temperatures [2]. These deficiencies need to be resolved before NiAl can be used in structural applications. The current study is part of an ongoing effort to grow high purity single crystals of NiAl with controlled compositions and under controlled conditions. This would be the starting point in fundamental and detailed studies directed towards understanding the behavior of this material.

The Bridgman growth system is one of the directional solidification configurations that are useful for producing large size single crystals from the melt [3]. The advantage of the Bridgman system is that the temperature gradients can be controlled, making it possible to achieve unidirectional solidification. This study is directed towards the prediction of the thermal characteristics of a Bridgman growth system that has and is currently being used to produce single crystals of NiAl. A schematic of the growth system is shown in Fig. 1.

The temperature distribution in crystal growth

systems, such as the Bridgman system, is highly complex and is influenced by several factors such as varying thermo-physical properties and multiple heat transfer modes, namely, conduction, convection and radiation. These complications have traditionally resulted in simplified analyses carried out under quite restrictive assumptions of simplified geometry, assumed boundary conditions, constant thermo-physical properties and neglecting important convection modes such as buoyancy driven convection. Our general understanding of the transport process and macroscopic properties of the crystal growth during the last three decades has improved substantially. However, quantitative prediction of the performance of specific crystal growth devices is not yet feasible. Efforts have been made in the research community to develop such predictive capabilities. For example, Brown [4] reviewed calculations, conducted by his research group using the finite element method, of the temperature field in the melt, crystal, and ampoule, the location of melt/crystal and melt/ambient surfaces during crystal growth. Shyy [5] previewed many of the possible factors that contribute to the solidification and heat transport, such as natural convection, Marangoni convection, solute concentration, turbulence and capillarity, at both macroscopic and morphological scales. In all these aspects, active investigations are being made to address the issues of the interfacial dynamics in conjunction with the macroscopic solute segregation and melt oscillation [5–7], and microscopic morphological evolution [5, 8–10]. In this study we have attempted to realistically model the system taking into account complex geometry,

---

† Author to whom correspondence should be addressed.

NOMENCLATURE

A	permeability coefficient	T	dimensionless temperature
C_p	specific heat	$T1$	cooler temperature
f	fluid fraction	$T4$	heater temperature
f_e	ratio of distances between points $E–e$ and between points $e–P$, used for harmonic interpolation	T_a	temperature of the ampoule outer wall
		T_h	temperature of the heater, $T_h = T4$
		ΔT	reference temperature scale, $\Delta T = T4–T1$
g	gravitational acceleration		
H	ampoule position within the furnace	u	dimensionless radial velocity
ΔH_0	latent heat of NiAl	w	dimensionless axial velocity
k	thermal conductivity	z	dimensionless axial coordinate.
P	dimensionless pressure		
Pr_0	Prandtl number based on NiAl properties at 300 K		

Greek symbols

α	thermal diffusivity
β	thermal expansion coefficient
ε_a	emissivity of the ampoule outer wall
ε_h	emissivity of the heater
μ	viscosity
ϱ	density
σ	Stefan–Boltzmann constant, 5.67×10^{-8} [W m^{-2} k^{-4}].

q	radiation heat flux between ampoule outer wall and heater
R_0	reference length scale based on ampoule inner radius
Ra_0	Rayleigh number based on NiAl properties at 300 K
r	dimensionless radial coordinate
r_a	radial position of the ampoule outer wall
r_h	radial position of the heater
St_0	Stefan number based on NiAl properties at 300 K
Su	source term accounting for phase change in the radial momentum equation
Sw	source term accounting for phase change in the axial momentum equation
t	dimensionless time

Subscripts

E	node index of the east unknown control volume E
P	node index of the present unknown control volume P
e	east surface of the present control volume P
a	ampoule
h	heater
0	reference scale.

temperature and phase dependent material properties, buoyancy driven convection and its influence on the melt/crystal interface and the thermal distribution within the crystal.

In the following, we first formulate the physical phenomena that is involved in this Bridgman growth process for β-NiAl, then develop the numerical strategy to solve this problem, and finally present the simulation results and the corresponding findings.

2. FORMULATION AND COMPUTATIONAL STRATEGY

Figure 1 shows the schematic of a practical designed vertical Bridgman furnace for growing β-NiAl [11] that we chose for our current numerical simulation. For the purposes of our calculation, the furnace is composed of two parts:

    (i) the enclosure, filled with argon, containing the heater ($T4$) and;

    (ii) the axisymmetric ampoule containing the melt, the growing crystal and the cooler ($T1$).

The ampoule is made of alumina and rests on a copper support. The enclosure stays stationary during the growth process and the ampoule is pulled out to control the growth speed of the crystal.

The following phenomena are of key importance and need to be resolved adequately:

- melt/crystal phase change in the ampoule region;
- conduction among various components of the furnace, the alumina wall and the copper base;
- convection in the melt and the encapsulated gas argon;
- radiation between the heater $T4$ and the ampoule wall.

(i) Governing equations

To formulate this problem with combined heat transfer and phase change in a geometrically complex

Centorr furnace

P=25 KVA

T4=1730 C, 1 hour
@ U=6 V, I=1000 A

Water flow:

T1=5C, T2=20C-, T3=40C+

V=8 Gal/min, p=50 psi

Ni-Al liquid

Mo shield

Alumina high density

Copper
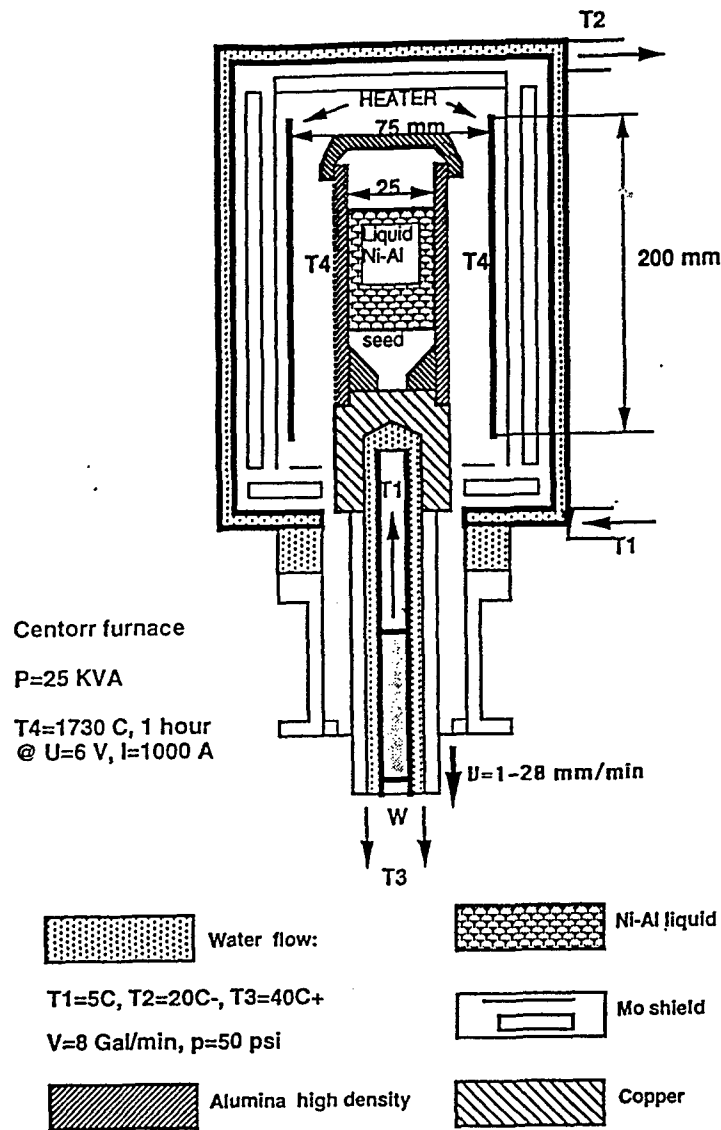
Fig. 1. Schematic of vertical Bridgman growth furnace for growing β-NiAl.

domain, we have derived and solved a set of unified governing equations that describes the conduction, convection and phase change phenomena over the entire geometry of the system. The dimensionless, axisymmetric, Navier–Stokes and energy equations, incorporating variable thermal conductivities and the Boussinesq approximation are:

(i) Continuity equation

$$\frac{\partial}{\partial r}\left(\frac{\varrho}{\varrho_0}ru\right)+\frac{\partial}{\partial z}\left(\frac{\varrho}{\varrho_0}rw\right)= 0, \qquad (1)$$

where u and w are, respectively, the velocity components along the radial and axial direction.

(ii) Momentum equation
r-momentum:

$$\frac{\partial}{\partial t}\left(\frac{\varrho}{\varrho_0}ru\right)+\frac{\partial}{\partial r}\left(\frac{\varrho}{\varrho_0}ruu\right)+\frac{\partial}{\partial z}\left(\frac{\varrho}{\varrho_0}rwu\right)= -r\frac{\partial P}{\partial r}$$

$$+Pr_0\left\{\frac{\partial}{\partial r}\left(\frac{\mu}{\mu_0}r\frac{\partial u}{\partial r}\right)+\frac{\partial}{\partial z}\left(\frac{\mu}{\mu_0}r\frac{\partial u}{\partial z}\right)\right\}-Pr_0\left(\frac{\mu}{\mu_0}\right)\frac{u}{r}+Su.$$

$$(2)$$

z-momentum:

$$\frac{\partial}{\partial t}\left(\frac{\varrho}{\varrho_0}rw\right)+\frac{\partial}{\partial r}\left(\frac{\varrho}{\varrho_0}ruw\right)+\frac{\partial}{\partial z}\left(\frac{\varrho}{\varrho_0}rww\right)$$

$$= -r\frac{\partial P}{\partial z}+Pr_0\left\{\frac{\partial}{\partial r}\left(\frac{\mu}{\mu_0}r\frac{\partial w}{\partial r}\right)+\frac{\partial}{\partial z}\left(\frac{\mu}{\mu_0}r\frac{\partial w}{\partial z}\right)\right\}$$

$$+Ra_0Pr_0\left(\frac{\varrho}{\varrho_0}\right)\left(\frac{\beta}{\beta_0}\right)rT+Sw. \qquad (3)$$

Table 1. Thermodynamic and transport properties

Material	ϱ (kg m^{-3})	μ (kg m^{-1} s^{-1})	k (W m^{-1} K^{-1})	C_p (J kg^{-1} K^{-1})	β (K^{-1})
NiAl	5950	0.005	75	660	1.52×10^{-5}
Argon	0.487	5.42×10^{-5}	0.0427	520	8.33×10^{-4}
Alumina	3975	†	‡	765	—
Copper	8930	†	‡	386	—

$\Delta H_0 = 688$ kJ kg^{-1}.
† Assigned big values.
‡ Varied with temperature (see Fig. 4).

(iii) Energy equation

$$\left\{\frac{\partial}{\partial t}\left(\frac{\varrho}{\varrho_0}\frac{Cp}{Cp_0}rT\right)+\frac{\partial}{\partial r}\left(\frac{\varrho}{\varrho_0}\frac{Cp}{Cp_0}ruT\right)+\frac{\partial}{\partial z}\left(\frac{\varrho}{\varrho_0}\frac{Cp}{Cp_0}rwT\right)\right\}$$

$$=\left\{\frac{\partial}{\partial r}\left(\frac{k}{k_0}r\frac{\partial T}{\partial r}\right)+\frac{\partial}{\partial z}\left(\frac{k}{k_0}r\frac{\partial T}{\partial z}\right)\right\}$$

$$-\frac{1}{St_0}\left\{\frac{\partial}{\partial t}\left(\frac{\varrho}{\varrho_0}rf\right)+\frac{\partial}{\partial r}\left(\frac{\varrho}{\varrho_0}ruf\right)+\frac{\partial}{\partial z}\left(\frac{\varrho}{\varrho_0}rwf\right)\right\}, \quad (4)$$

where the term with Ra_0 in equation (3) comes from the Boussinesq approximation for treating the buoyancy effect, Su, Sw in equations (2) and (3) and the terms with fluid fraction f in equation (4) are appropriate source terms to account for the phase change, ϱ, μ, Cp, k and β are the density, viscosity, specific heat, conductivity and coefficient of thermal expansion, respectively. Ra_0, Pr_0 and St_0 are the Rayleigh number, Prandtl number and Stefan number, respectively. Their definitions are

$$Ra_0 = \frac{\text{Buoyancy force}}{\text{Viscous force}} = \frac{\varrho_0 g\beta_0 \Delta T R_0^3}{\alpha_0 \mu_0} \quad (5)$$

$$Pr_0 = \frac{\text{Kinematic viscosity}}{\text{Heat diffusivity}} = \frac{\mu_0/\varrho_0}{\alpha_0} \quad (6)$$

$$St_0 = \frac{\text{Sensible heat}}{\text{Latent heat}} = \frac{Cp_0 \Delta T}{\Delta H_0}, \quad (7)$$

where α_0, ϱ_0, μ_0, Cp_0, k_0 and β_0 are chosen reference material properties for nondimensionalization. g is gravitational acceleration, ΔH_0 is the reference latent heat, R_0 is the reference length, and ΔT is the reference temperature. In this study, we chose the properties of β-NiAl at 300 K as the reference properties, the radius of ampoule inner wall R_0 as the reference length and

the difference between the highest and the lowest temperature in the furnace, $\Delta T = T4-T1$, as the reference temperature scale. The estimated dimensionless parameters for our current calculation are

$$Ra_0 = 3.2 \times 10^4 \quad Pr_0 = 4.4 \times 10^{-2} \quad St_0 = 1.7. \quad (8)$$

Furthermore, the original parameters of the material properties for different material regions, which have been listed in Table 1, are converted correspondingly into dimensionless form as listed in Table 2.

(ii) Two-level modeling strategy

It may be observed from Fig. 1 that the combination of the furnace enclosure and the ampoule presents a very complicated geometry. To render the computations tractable and simultaneously obtain adequate resolution in the ampoule region, a two-level strategy is employed. Level 1 simulates the entire domain and is referred to as the global furnace model. Level 2 concentrates on the ampoule region and obtains its boundary conditions from the level 1 or the global simulation. With this two-level strategy, we can obtain useful information at the global level and yet obtain adequate resolution at the melt/crystal interface. Figure 2 demonstrates the application of the two-level strategy to the present simulation. To solve the governing equations, the control volume technique employing a non-orthogonal body-fitted coordinate system has been adopted [5, 12, 13]. A proven and robust pressure-based algorithm is then used to iterate the discretized form of the governing equations to the steady state [12, 14].

Table 2. Dimensionless thermodynamic and transport properties

Material	ϱ/ϱ_0	$Pr_0(\mu/\mu_0)$	k/k_0	C_p/C_{p0}	$Ra_0/Pr_0(\beta/\beta_0)$ (ϱ/ϱ_0)
NiAl	1.0	4.4×10^{-2}	1.0	1.0	1.4×10^3
Argon	8.2×10^{-5}	4.77×10^{-5}	5.7×10^{-4}	0.79	6.32
Alumina	0.67	†	‡	1.16	—
Copper	1.5	†	‡	0.58	—

† Assigned big values.
‡ Varied with temperature (see Fig. 4).

$$\frac{\partial^2 T}{\partial n^2} = 0$$

Alumina

Argon

$T=T4$

Heater

NiAl

l

L

Inner
ampoule
wall

NiAl

l

Copper

$T=T1$

$\frac{\partial^2 T}{\partial n^2} = 0$

pull out direction

Boundary temperature of the
ampoule wall is obtained from
the global furnace simulation.

(a) Global furnace model   *(b) Refined ampoule model*
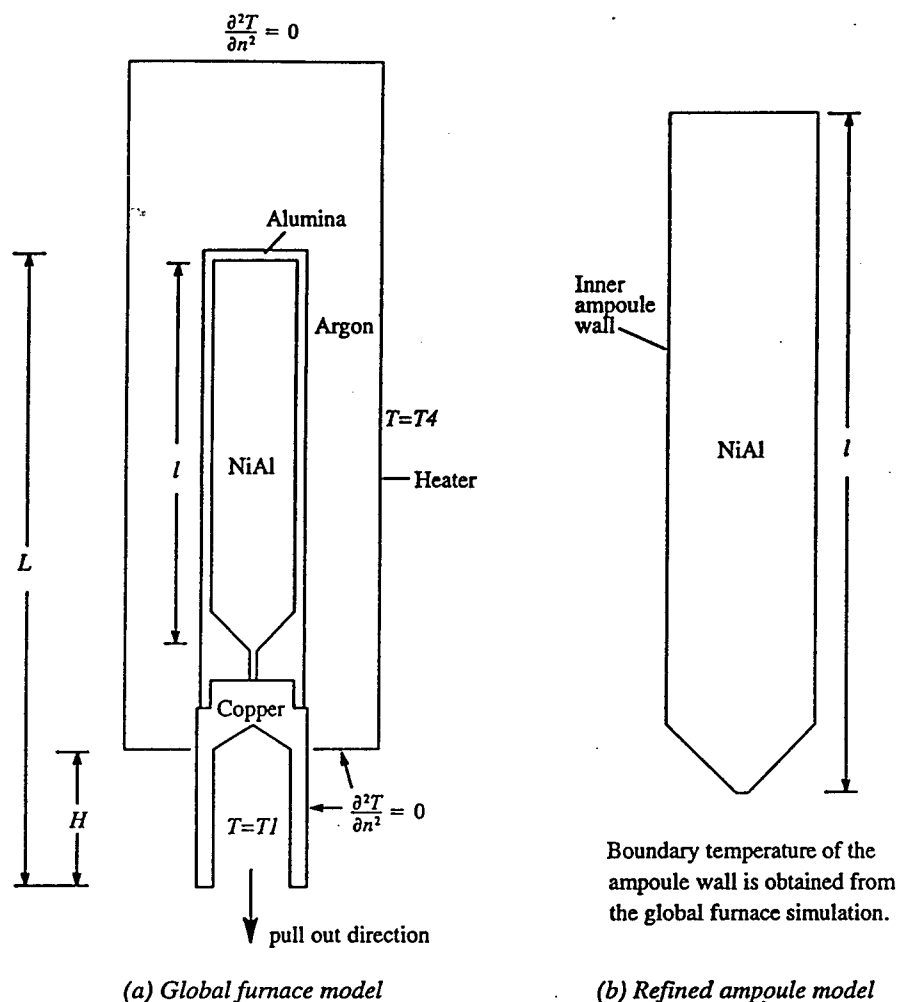
Fig. 2. Layout and boundary conditions for (a) the global furnace model, and (b) the refined ampoule model used in the present numerical simulation, where H measures the ampoule position as it is pulled out. The total length of the ampoule part, between the top of alumina and the bottom of copper, is $L = 185$ mm, while the length of the ampoule is $l = 113.5$ mm.

(iii) The treatment of phase change

In the modeling of the melt/solid interface region, phase change needs to be considered along with the coupled mass and heat transport. Special treatment thus need to be taken to account for the release of latent heat during solidification [5, 15, 16]. As is shown in equation (4), an enthalpy based method has been adopted in the energy equation through the implementation of the fluid fraction f in the source term. Here, f is defined to be 1 in the region of melt, zero in the region of solid, and varies continuously between zero and unity when the material undergoes phase change. In addition, Su and Sw are included in the momentum equations (2) and (3) to enforce the velocity in the solid to match the pull rate of the crystal. The approach taken here is the inclusion of Darcy-type source terms in the momentum equations [5, 15]. Thus the phase change material in the solid/melt interface region is considered to be a porous medium, with the porosity changing from zero to unity as the material

melts. For pure materials, the porosity changes abruptly as the phase change occurs, but to ensure numerical stability, a continuous variation is imposed. Here, the source terms have the form: $Su = -Au$ and $Sw = -Aw$, where A varies as a function of the fluid fraction f from zero in the liquid phase to infinity in the solid phase [15, 17].

(iv) The interpolation of material properties

The calculations conducted in this study take into account the variation of material properties with temperature, such as thermal conductivity, at the ampoule walls and at the melt/crystal interface. Abrupt changes in material properties may be expected at the interfaces between two media and the interpolation for material properties must be handled carefully in order to obtain numerical solutions. The usual approach taken is linear interpolation,

$$k_e = f_e k_P + (1 - f_e) k_E, \qquad (9)$$

where f_e designates the ratio of distances between points $E-e$ and between points $e-P$, with E, P, and e representing, respectively, the east-side unknown node, the present unknown node, and the east-side control surface of the present unknown cell P. Here, a standard arithmetic averaging with $f_e = 0.5$ is chosen for interpolation within the same material media. However, this does not handle abrupt changes at the interface between the two media. Hence, following Patankar [14], a harmonic interpolation based on a one-dimensional flux conservation is used as follows:

$$k_e = \frac{1}{(1-f_e)/k_P + f_e/k_E}. \tag{10}$$

This treatment has been compared with the flux balance approach [18] and is found to be equally robust and accurate; but simpler to implement.

(v) Radiation effect

The radiation heat flux between the heat ($T4$) and the outer wall of the ampoule is handled by the following simplified treatment [19]:

$$q = \frac{\sigma(T_a^4 - T_h^4)}{(1/\varepsilon_a) + \left(\dfrac{1-\varepsilon_h}{\varepsilon_h}\right)(r_a/r_h)}, \tag{11}$$

where $\sigma = 5.67 \times 10^{-8}$ W m^{-2} K^4 is the Stefan–Boltzmann constant, T_a, r_a, and ε_a are temperature, radial position and emissivity for the ampoule outer wall and T_h, r_h and ε_n are the corresponding variables for the heater. The heater is considered to be a black body, so $\varepsilon_h = 1.0$. For the alumina wall of the ampoule, $\varepsilon_a = 0.8$ and for the copper wall, $\varepsilon_a = 0.6$. The expression for the boundary condition at the outer ampoule wall is given by,

$$-k\frac{\partial T}{\partial r}\bigg|_{\text{ampoule}} = -k\frac{\partial T}{\partial r}\bigg|_{\text{argon}} + q, \tag{12}$$

where the left hand side represents the heat flux into the ampoule wall and the right hand side represents the heat flux due to convection and conduction from the encapsulating gas and the radiation from the heater.

3. RESULTS AND DISCUSSION

In the following, we present the results of steady state calculations for the Bridgman growth of NiAl. The geometry of the calculation domain is shown in Fig. 2a, b. In order to optimize computational costs without sacrificing accuracy and resolution in the melt/crystal region, the simulation was conducted at two levels. Level 1 is the global furnace simulation involving the entire domain. Level 2 is a refined ampoule simulation and takes its boundary conditions based on the global simulation. It will be shown later that the global simulation is relatively insensitive to

the details of the interface morphology. We also try to take into account the relative displacement of the ampoule as the growing crystal is pulled out of the furnace. Therefore, three simulations have been performed at the global level involving three different locations of the ampoule. A multi-zone patched grid method has been employed to generate the grid system needed for global (furnace) level simulations. Sample grid distributions have been shown in Fig. 3a, b for $H = 40$ and 80 mm, where H indicates the position of the ampoule within the furnace. The global furnace (Level 1) simulations were conducted for three different ampoule positions in order to estimate the effects of geometric variations as the crystal is pulled out of the furnace. Calculations were conducted for $H = 40$ mm (151×213 grid), 80 mm (151×216 grid) and 120 mm (151×219 grid). In all cases, there were 51×103 points in the ampoule region. Based on this resolution, the ampoule region is then computed again with a better resolution; the boundary conditions needed for this Level 2 simulation are extracted from the results obtained from the Level 1 solutions. In the following sections, we will first show that consideration of realistic material property variation, as, e.g. functions of temperature, is essential to obtain a faithful simulation; we will then discuss the solutions obtained for different ampoule locations on both Level 1 and Level 2.

(i) The global furnace simulation

Figure 4 shows the variation of thermal conductivity of alumina and copper with temperature [20]. Figures 5 and 6 show the stream function and the isotherm distribution, respectively, for each of the three ampoule locations. The streamline pattern arises as a result of buoyancy driven convection. It may be observed that the convection pattern in the encapsulating gas is quite weak and the convective heat transfer into the ampoule is negligible compared to the radiative effect from the heater. As the ampoule translates downward, the convection within the ampoule gets slightly weaker and the melt/crystal interface becomes convex towards the melt. It is difficult to predict the strength and detailed characteristics of the convective field within the furnace because the geometry is complicated and the boundary conditions vary with the ampoule movement. Nevertheless, it is clear that the isotherm pattern changes quite significantly as the crystal is drawn down and the temperature gradients at the base of the crystal decrease in magnitude. To shed some light on the role played by the variations of the transport properties, with respect to temperature, calculations have also been conducted with the material properties held fixed to the reference values at 300 K, a practice employed in some modeling work. While the general patterns of stream functions and isotherms seem insensitive, some critical aspects of the solutions are substantially affected. As an illustration, Fig. 7 shows the differences in the temperature distribution along the centerline and
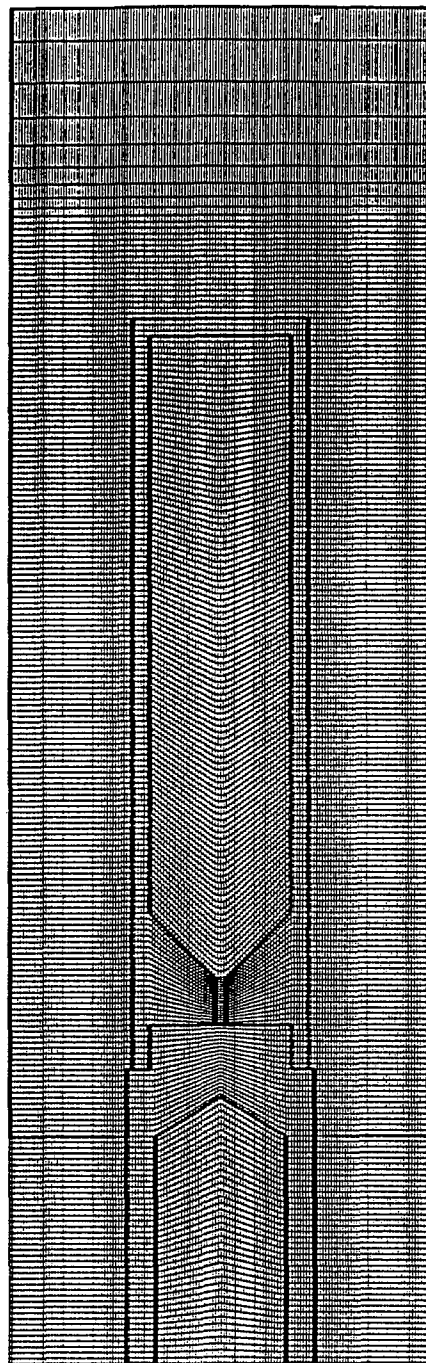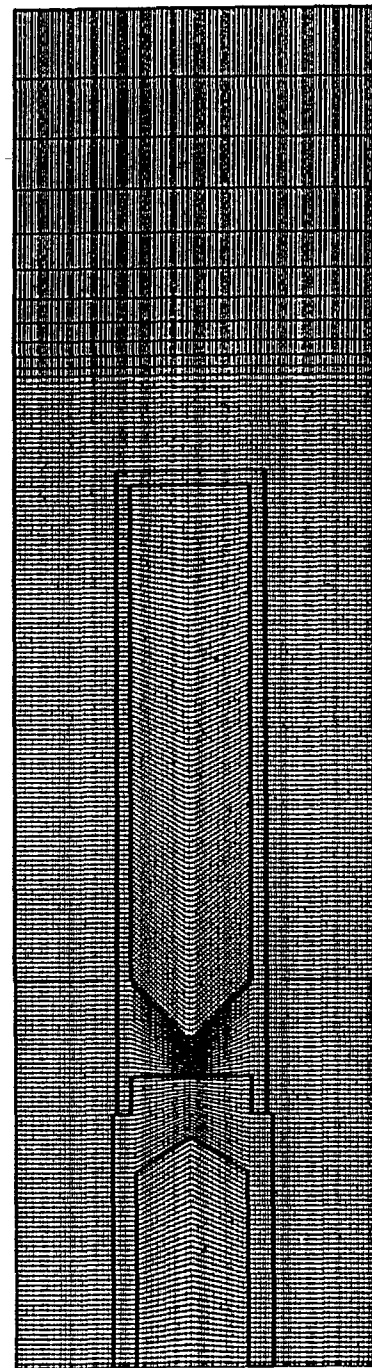
(a) Grid of H=40mm   (b) Grid of H=80mm

Fig. 3. Grid distributions for the global furnace model of (a) $H = 40$ mm (grid size = 151 × 213), and (b) $H = 80$ mm (grid size = 151 × 216).

the inner wall of the ampoule, between the variable properties and constant properties simulations. Noticeable differences have been observed: for example, a 50% difference exists along the bottom wall of the ampoule. The differences exhibited in Fig. 7 impact the temperature distribution in the crystal and its accurate prediction is necessary to understand its implications on crystal quality.
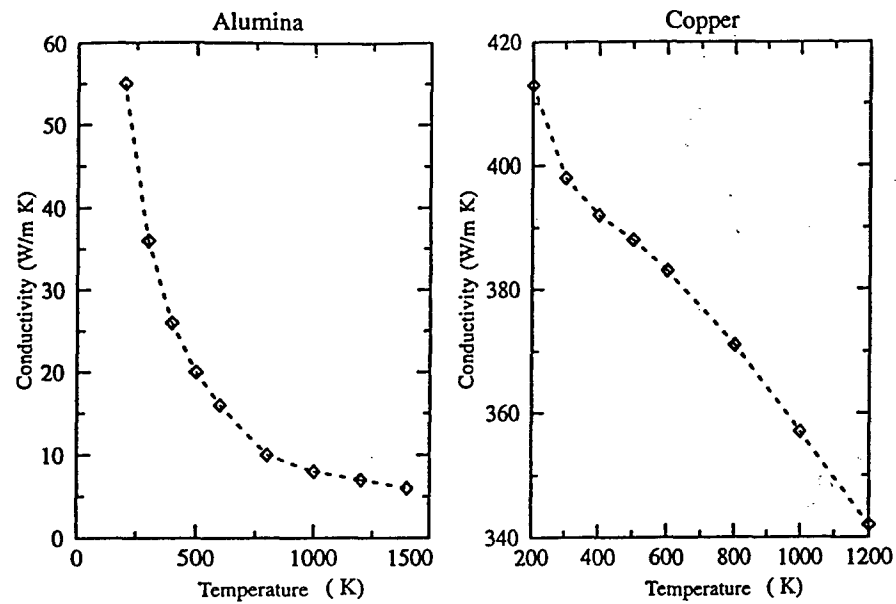
Fig. 4. Dependency of thermal conductivities of alumina and copper on temperature (*Perry's Chemical Engineerings' Handbook*, 1984).

(i)	*(ii)*	*(iii)*
Inside the NiAl melt $S_{max}=0.0506, \Delta S=0.0053$	Inside the NiAl melt $S_{max}=0.0513, \Delta S=0.0054$	Inside the NiAl melt $S_{max}=0.0532, \Delta S=0.0056$
Inside the Argon gas $S_{max}=0.0239, \Delta S=0.0053$	Inside the Argon gas $S_{max}=0.00243, \Delta S=0.00054$	Inside the Argon gas $S_{max}=0.00196, \Delta S=0.00056$

Fig. 5. Solution characteristics of the global furnace simulation for three different H. (i) $H = 40$ mm; (ii) $H = 80$ mm; (iii) $H = 120$ mm. Stream function.

(i)   *(ii)*   *(iii)*

$T_{melt}=0.95$ $\Delta T=0.02$ $T_{melt}=0.95$ $\Delta T=0.02$ $T_{melt}=0.95$ $\Delta T=0.02$

Fig. 6. Solution characteristics of the global furnace simulation for three different H. (i) $H = 40$ mm; (ii) $H = 80$ mm; (iii) $H = 120$ mm. Isotherms.

——— Variable conductivity

----- Constant conductivity (based on the values at T=300 K)

Fig. 7. Comparison of the temperature profiles of the global furnace model with variable and constant thermal conductivities of alumina and copper for $H = 80$ mm.

<div align="center">

(i)

S_{max}=0.0445
ΔS=0.0048

(ii)

S_{max}=0.0541
ΔS=0.0057

(iii)

S_{max}=0.0560
ΔS=0.0059

</div>

Fig. 8. Solution characteristics of the refined ampoule simulation for three different H. (i) $H = 40$ mm;
(ii) $H = 80$ mm; (iii) $H = 120$ mm. Stream function.

(ii) The refined ampoule simulation

The refined ampoule (Level 2) simulation was conducted using the ampoule wall temperature distribution, obtained from Level 1, as the boundary condition. The grid resolution within the ampoule has been increased to 101×154 from 51×103 used at Level 1. Stream function and isotherm contours are presented in Figs. 8 and 9, respectively. Noticeable differences may be observed between the convection patterns in Fig. 5(i–iii) and Fig. 8(i–iii), and more significantly, the convection strengths are different, especially for $H = 40$ mm. At this ampoule position, the more detailed secondary vortical structure in the central region above the solid–melt interface can be clearly observed from the refined solutions depicted in Fig. 8; at the global level, as shown in Fig. 5, such characteristics are less pronounced. This assessment shows that a fine grid is needed to capture convection dominated phenomena, thus justifying the two level approach taken in this study.

Figure 10 contrasts the melt/crystal interface obtained from the two level simulation for all three ampoule locations. It may be observed that the differences between the coarse grid (Level 1) and the fine grid (Level 2) calculations are most significant when the melt volume decreases (as the crystal is pulled out). This observation just reinforces the trends exhibited in the stream function plots mentioned previously. The sensitivity to grid refinement increases as the melt volume decreases because of the constraining effect of the top wall. Since the interface positions at the ampoule wall are the same between the two grid levels, it is significant that the temperature distributions predicted on them are different, resulting in different melt/crystal curvatures. This aspect impacts on the detailed distribution of temperature gradients in the interface region, resulting in a different micro-structure of the crystal.

To further illustrate the usefulness of the multi-level approach, a fine grid simulation of the $H = 40$ mm case, corresponding to Fig. 5(i) and Fig. 6(i), was carried on a refined grid of 223×284 nodes (73×154 nodes in the ampoule region). This represents a substantial refinement over the grid system shown in Fig.

(i)

$T_{melt}=0.95$
$\Delta T=0.02$

(ii)

$T_{melt}=0.95$
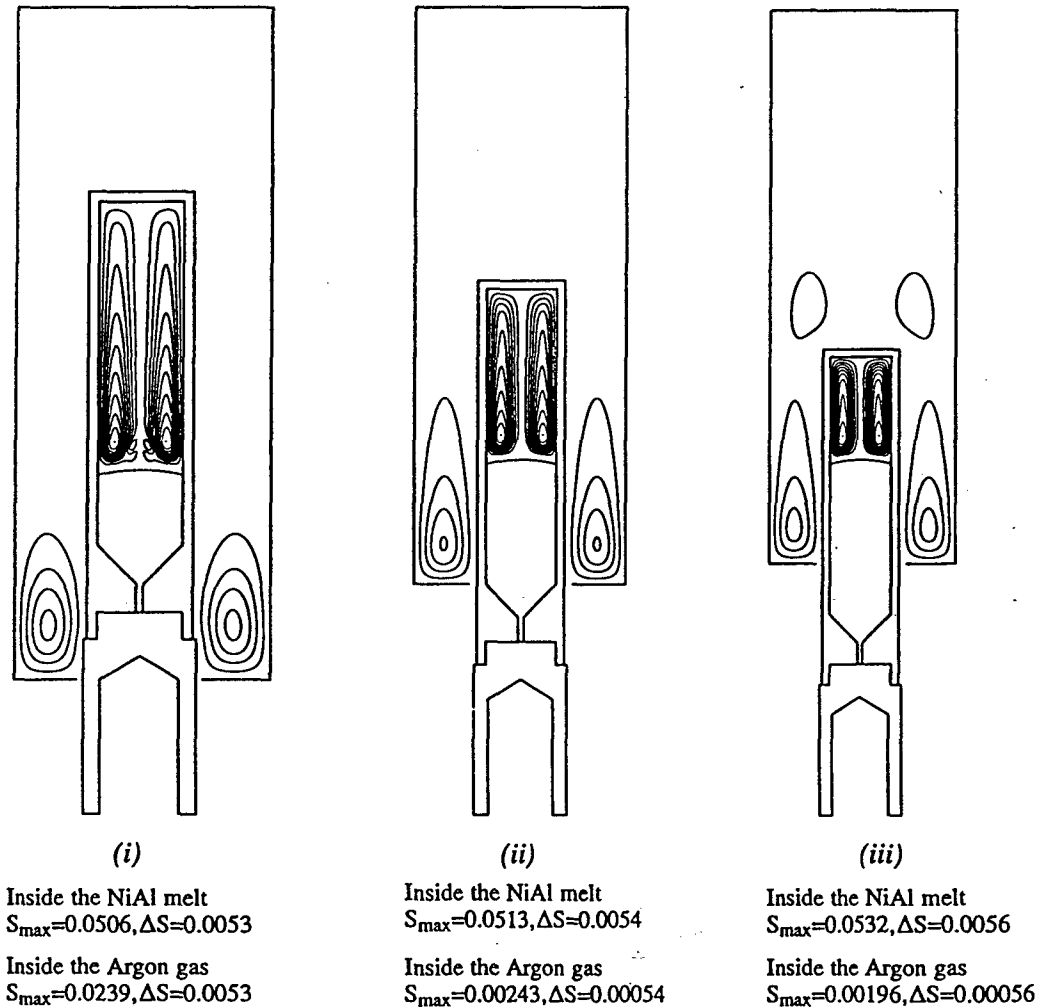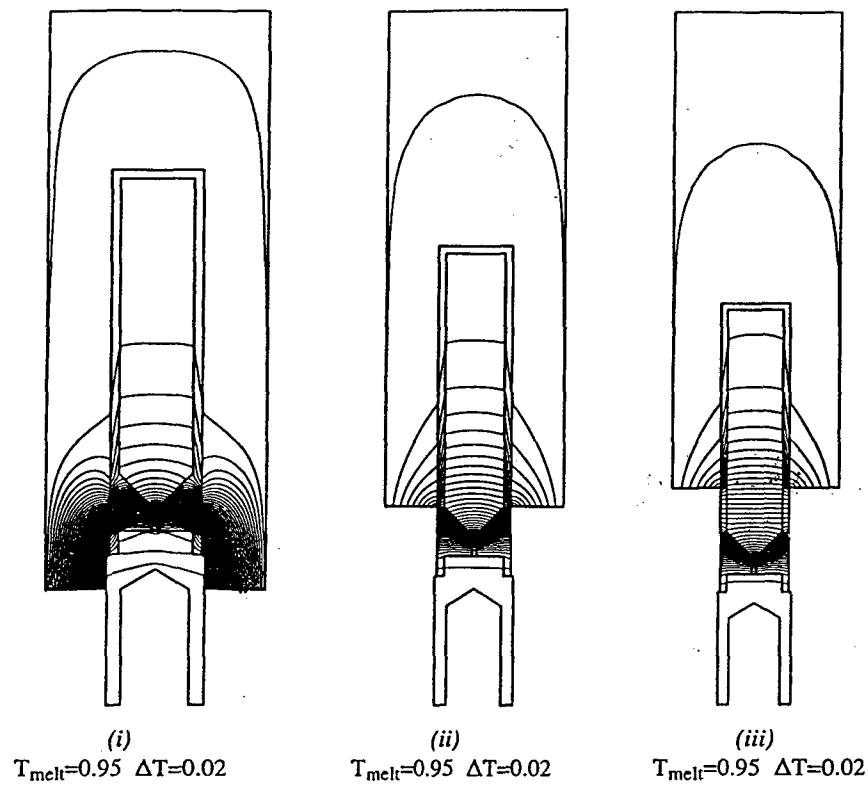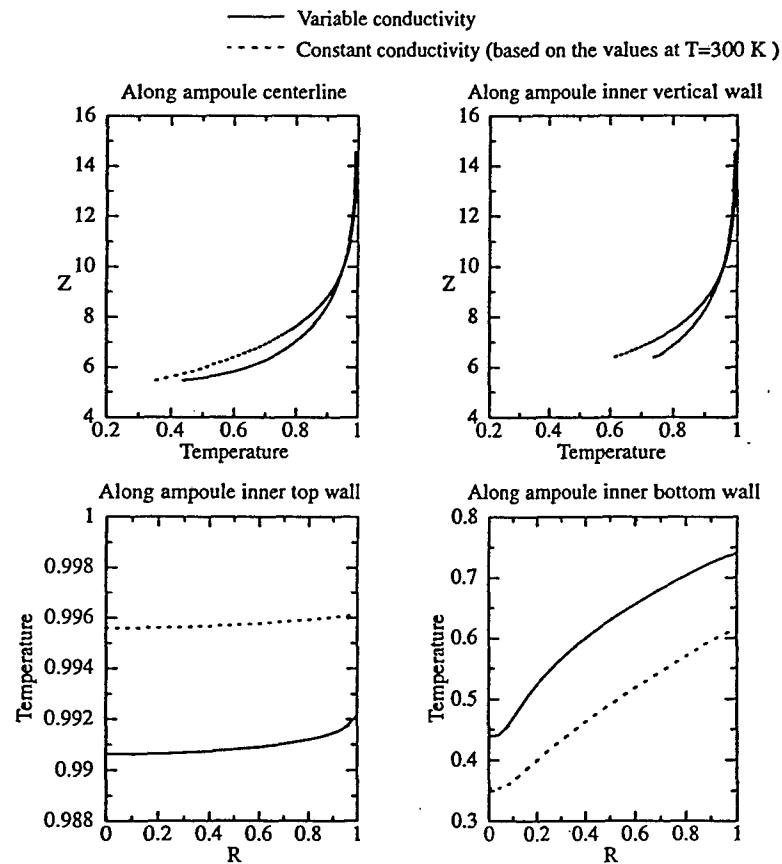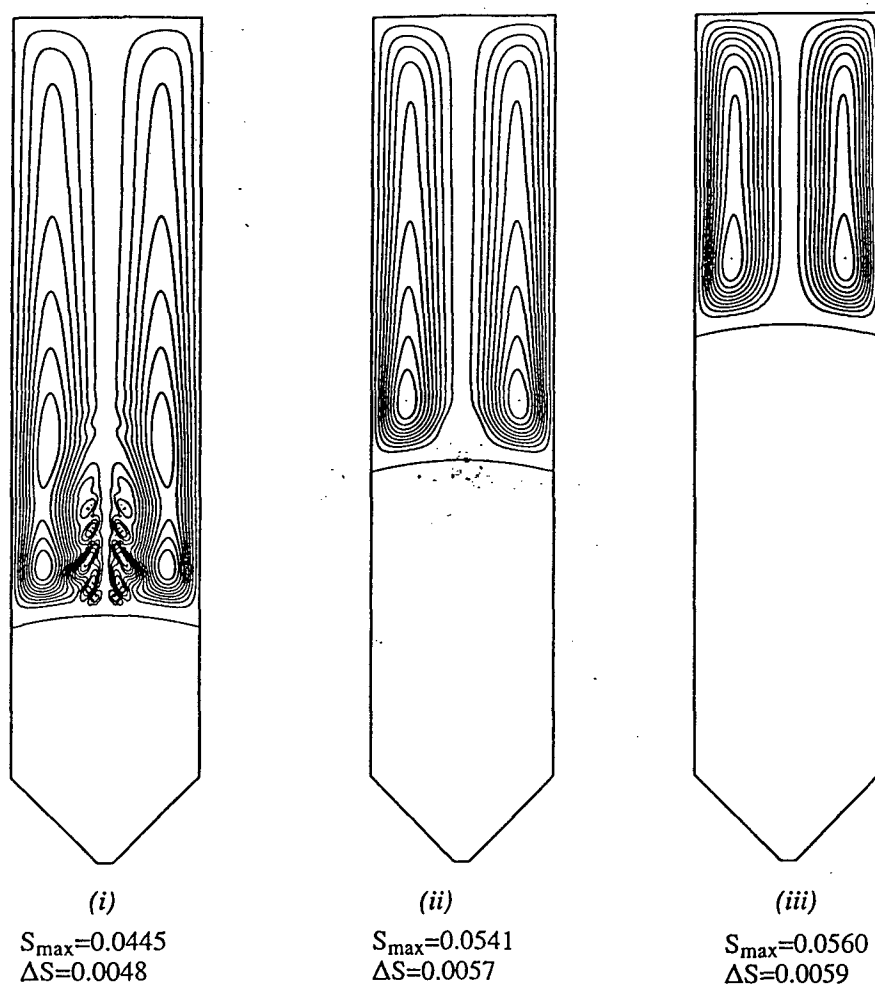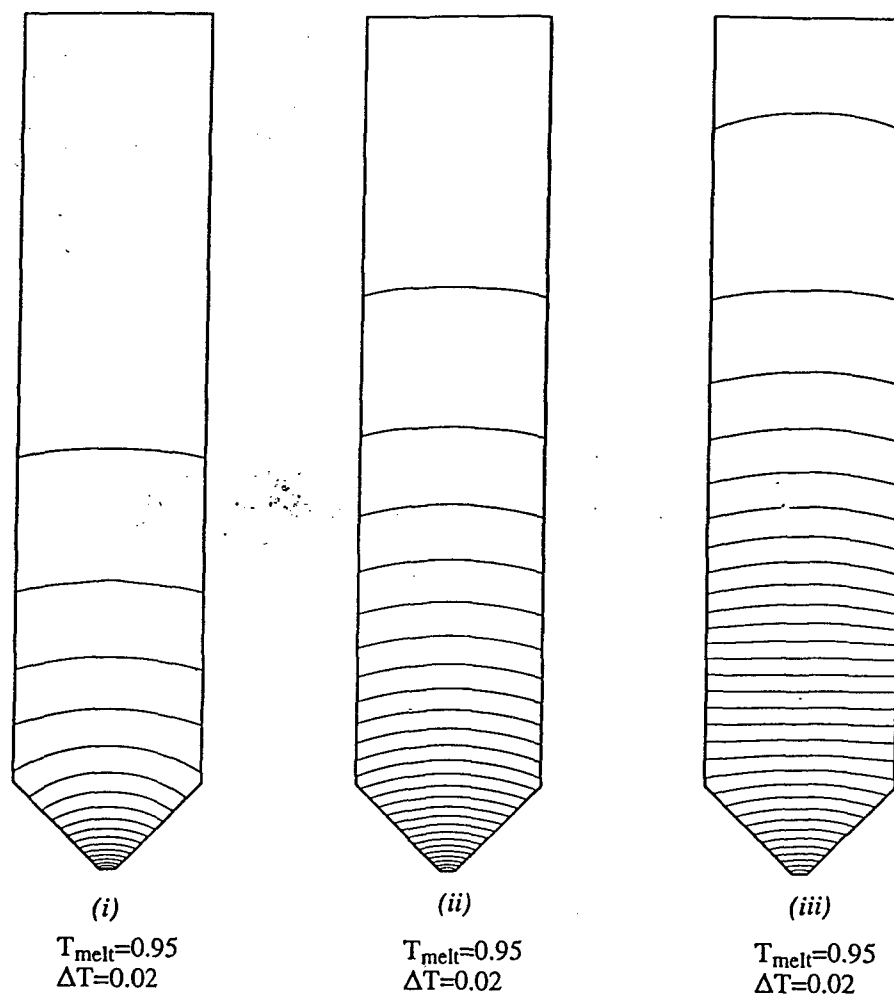$\Delta T=0.02$

(iii)

$T_{melt}=0.95$
$\Delta T=0.02$

Fig. 9. Solution characteristics of the refined ampoule simulation for three different H. (i) $H = 40$ mm; (ii) H 80 mm; (iii) $H = 120$ mm. Isotherms.

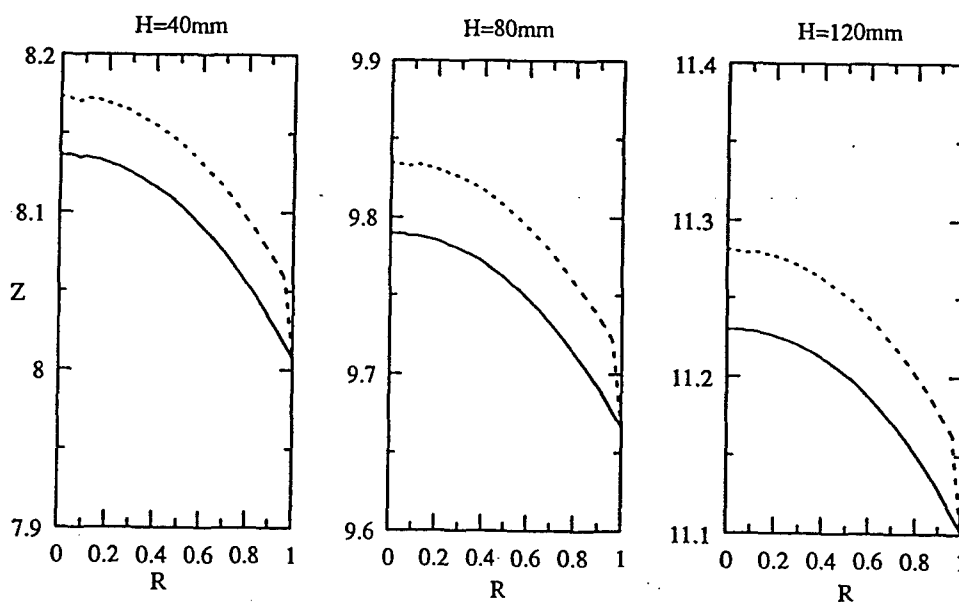- - - - Global furnace model   ———— Refined ampoule model

Fig. 10. Comparison of the melt/solid interface positions between the global furnace and refined ampoule models.
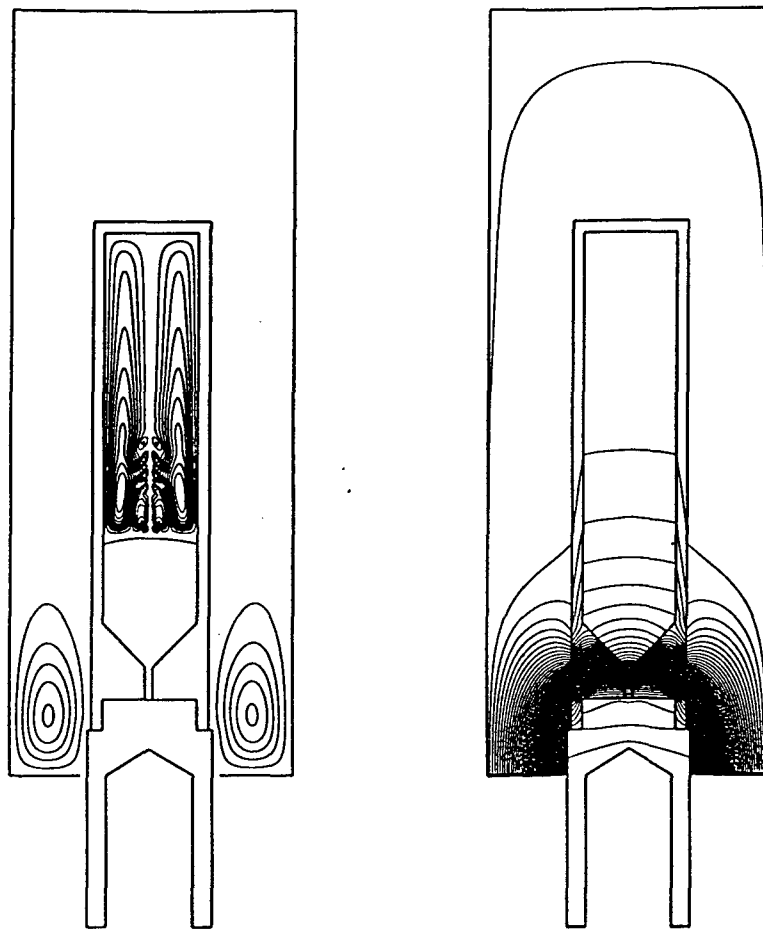
Inside the NiAl melt: $S_{max}=0.0418, \Delta S=0.0044$ $T_{melt}=0.95$ $\Delta T=0.02$
Inside the Argon gas: $S_{max}=0.0242, \Delta S=0.0044$

Fig. 11. Solution characteristics of the global furnace simulation for $H = 40$ mm with grid size: 223×284.

3a with 151×213 nodes (51×103 nodes in the ampoule region). Figure 11(i) and (ii) show the streamfunction and isotherms, respectively, obtained on this fine grid system. It can be observed that the fine grid solution captures more details of the convection pattern within the ampoule. Differences can be noted between the solutions presented in Figs. 5 and 6 and those presented in Fig. 11; more secondary vortical structures are captured on the fine grid. The fine grid solution is closer to the refined ampoule simulation (Figs. 8 and 9) than to the coarse grid solutions from the global furnace simulation. The fine grid results of the global furnace simulation clearly demonstrate the economy of the multi-level approach; instead of resorting to a fine grid distribution at the global level, carrying out the refined ampoule simulation yields the desired accuracy economically.

Correlations between the thermal characteristics in the combined crystal/melt region and the microscopic structure of NiAl are not well established at the present time. However, the capability established in this work to predict the solidification dynamics and thermal field will aid the development of such critical information.

4. CONCLUSION

Accurate and realistic numerical simulations have been carried out for a vertical Bridgman crystal growth system for the single crystal growth of NiAl. All three heat transfer modes—conduction, convection and radiation—have been taken into account with reasonable resolutions. A two-level simulation has been performed to simultaneously achieve accuracy as well as computational economy. At the global level, the entire system consisting of the enclosure, heaters and the ampoule have been considered. However, it was desirable to improve the grid resolution within the ampoule to capture the dynamics of the melt/crystal interface. Thus, a refined ampoule simulation was performed using the solution from the Level 1 simulation as the boundary condition for the

Level 2 simulation. This enables an accurate treatment of the solidification dynamics within the ampoule and the heat transfer through the crystal. It is evident that this kind of multi-level approach, with appropriate matching of boundary conditions, is necessary to achieve accuracy at reasonable computing costs.

It has also been shown that variations of the material properties need to be considered in order to achieve a realistic simulation. Significant errors exist for simulations carried out assuming constant material properties. Accurate property data are not readily available in the literature, but have been shown to be necessary to predict the temperature distribution within the crystal growth system.

The predictions reported in the present work are of value in improving our understanding of the growth process and will be of help in controlling the growth parameters in order to achieve the desired melt/crystal interface shape which has implications on the composition and quality of the resulting crystal.

REFERENCES

1. S. Sen and D. M. Stefanescu, Melting and casting processes for high-temperature intermetallics, *JOM* May, 20–32 (1991).
2. R. Darolia, NiAl alloys for high-temperature structural applications, *JOM* March, 44–49 (1991).
3. J. C. Brice, *Crystal Growth Processes*. Blackie, London (1986).
4. R. A. Brown, Theory of transport processes in single crystal growth from the melt, *A.I.Ch.E.J.* 34, 881–911 (1988).
5. W. Shyy, *Computational Modeling for Fluid Flow and Interfacial Transport*. Elsevier, Amsterdam (1994).
6. F. Rosenberger, *Fundamentals of Crystal Growth*. Springer, New York (1979).
7. M. J. Crochet, F. T. Greyling and J. J. Van Schaftinger, Numerical simulation of horizontal Bridgman growth I: two-dimensional flow, *Int. J. Numer. Meth. Fluids* 7, 27–49 (1987).
8. M. E. Glicksman, S. R. Coriell and G. B. McFadden, Interaction of flows with the crystal-melt interface, *Ann. Rev. Fluid Mech.* 18, 307–335 (1986).
9. J. S. Langer, Instabilities and pattern formation in crystal growth, *Rev. Modern Phys.* 52, 1–28 (1980).
10. H. S. Udaykumar and W. Shyy, Simulation of interfacial instabilities during solidification; part I: conduction and capillarity effects, *Int. J. Heat Mass Transf.* 11, 2057–2075 (1995).
11. M. J. Kaufman and V. Levit, Private communication (1994).
12. W. Shyy, S. S. Tong and S. M. Correa, Numerical recirculating flow calculation using a body-fitted coordinate system, *Numer. Heat Transfer* 8, 99–113 (1985).
13. M. E. Braaten and W. Shyy, A study of recirculating flow computation using body-fitted coordinates: consistency aspects and mesh skewness, *Numer. Heat Transfer* 9, 559–574 (1986).
14. S. V. Patankar, *Numerical Heat Transfer and Fluid Flow*. Hemisphere, Washington, D.C. (1980).
15. V. Voller, Implicit finite-difference solutions of the enthalpy formulation of Stefan problems, *IMA J.* 5, 201–214 (1985).
16. W. Shyy and M. M. Rao, Enthalpy based formulations for phase-change problems with application to G-jitter, *Microgravity Sci. Tech.* 7, 41–49 (1994).
17. W. Shyy and M.-H. Chen, Steady-state natural convection with phase change, *Int. J. Heat Mass Transfer* 33, 2545–2563 (1990).
18. W. Shyy and J. Burke, A study of iterative characteristics of convective-diffusive and conjugate heat transfer problems, *Numer. Heat Transfer* 26B, 21–37 (1994).
19. R. Siegel and J. R. Howell, *Thermal Radiation Heat Transfer*. Hemisphere, Washington, D.C. (1981).
20. R. H. Perry, D. W. Green and J. O. Maloney (eds), *Perry's Chemical Engineerings' Handbook* (6th Edn). McGraw-Hill, New York (1984).

MOVING BOUNDARY COMPUTATION
OF THE FLOAT-ZONE PROCESS

MADHUKAR M. RAO AND WEI SHYY

Department of Aerospace Engineering, Mechanics and Engineering Science, 231 Aero Building, University of Florida, Gainesville, FL 32611, U.S.A.

SUMMARY

A computational capability has been developed to predict the free surface shape, heat transfer and melt–crystal interface shapes in float-zone processing. A moving boundary, second order, finite volume, incompressible Navier–Stokes solver has been developed for the fluid flow and heat transfer calculations. The salient features of the approach include solving the dynamic form of the Young–Laplace equation for the free surface shape, dynamic remeshing to fit the free boundary, a flexible, multi–block, grid generation procedure and the enthalpy method to capture the melt–crystal and the melt–feed interfaces without the need for explicit interface tracking. Important convective heat transfer modes; natural convection and thermocapillary convection have been computed. It is shown that, whereas the overall heat transfer is not substantially affected by convection, the melt–crystal interface shape acquires significant distortion due to the redistribution of the temperature field by the thermocapillary and buoyancy-induced convective mechanisms. It is also demonstrated that the interaction of natural and thermocapillary convection can reduce the melt–crystal interface distortion if they act in opposing directions. It is found that the meniscus deformation can cause the height of the zone to increase but the qualitative nature of the melt–solid interface shapes are not significantly affected. Results are compared with literature to validate the predictive capability developed in this work. © 1997 by John Wiley & Sons, Ltd.

KEY WORDS: float zone; crystal growth; solidification; moving boundary; thermocapillary transport

1. INTRODUCTION

The float-zone technique is one of the candidate methods for growing single crystals. The main advantage of the float-zone process is that it is a containerless process and thus a main source of contamination is removed. Another advantage is the reduction of thermal stresses which are caused by differential thermal expansion between the crystal and the crucible. On earth, it is mainly limited by the size of the melt zone that can be achieved, since the hydrostatic pressure of the melt zone is balanced by the surface tension between the melt and the ambient fluid. Another problem is the loss of volatile components from the melt, which can be circumvented by the use of encapsulating fluids. Liquid encapsulants can also increase the maximum size of the melt zone that can be achieved. The formation of the meniscus during the melting process is a major concern in the successful operation of the float-zone technique and this aspect has been examined in detail by Shyy and Rao.[1]

Float-zone simulations have been carried out by many researchers at different levels of complexity. Kobayashi[2] computed thermocapillary convection under zero gravity conditions for

Moving Boundary Computation of the Float-Zone Process

Madhukar M. Rao
Wei Shyy

Department of Aerospace Engineering,
Mechanics and Engineering Science
University of Florida
Gainesville, FL 32611

Abstract

A computational capability has been developed to predict the free surface shape, heat transfer and melt–crystal interface shapes in float zone processing. A moving boundary, second order, finite volume, incompressible Navier–Stokes solver has been developed for the fluid flow and heat transfer calculations. The salient features of the approach include solving the dynamic form of the Young–Laplace equation for the free surface shape, dynamic remeshing to fit the free boundary, a flexible, multi–block, grid generation procedure and the enthalpy method to capture the melt–crystal and the melt–feed interfaces without the need for explicit interface tracking. Important convective heat transfer modes; natural convection and thermocapillary convection have been computed. It is shown that, whereas the overall heat transfer is not substantially affected by convection, the melt–crystal interface shape acquires significant distortion due to the redistribution of the temperature field by the thermocapillary and buoyancy–induced convective mechanisms. It is also demonstrated that the interaction of natural and thermocapillary convection can reduce the melt–crystal interface distortion if they act in opposing directions. It is found that the meniscus deformation can cause the height of the zone to increase but the qualitative nature of the melt/solid interface shapes are not significantly affected. Results are compared with literature to validate the predictive capability developed in this work.

Keywords:

Float Zone, Crystal Growth, Solidification, Moving Boundary, Thermocapillary Transport.

1. Introduction

The float zone technique is one of the candidate methods for growing single crystals. The main advantage of the float zone process is that it is a containerless process and thus a main source of contamination is removed. Another advantage is the reduction of thermal stresses which are caused by differential thermal expansion between the crystal and the crucible. On earth, it is mainly limited by the size of the melt zone that can be achieved, since the hydrostatic pressure of the melt zone is balanced by the surface tension between the melt and the ambient fluid. Another problem is the loss of volatile components from the melt, which can be circumvented by the use of encapsulating fluids. Liquid encapsulants can also increase the maximum size of the melt zone that can be achieved. The formation of the meniscus during the melting process is a major concern in the successful operation of the float zone technique and this aspect has been examined in detail by Shyy and Rao[1].

Float zone simulations have been carried out by many researchers at different levels of complexity. Kobayashi[2] computed thermocapillary convection under zero gravity conditions for two different Prandtl numbers, with and without crystal rotation while neglecting the deformation of the free surface. Kobayashi[3] extended the study to include buoyancy induced convection. Young and Chait[4] has presented asymptotic solutions for the temperature, concentration, and interface shapes in the limit of small aspect ratio and weak surface tension for a two dimensional float zone established in a vertical sheet. Neitzel et. al.[5] have computed thermocapillary convection in a float zone with a computed free surface shape. Chu and Chen[6] have obtained numerical solutions for float zone growth of Molybdenum (Mo) crystals with an imposed heat input profile rather than an imposed temperature profile. Again, they imposed the constraint of a fixed cylindrical free surface and concentrated their efforts on the details of the flow structure. Duranceau and Brown[7] developed a steady–state, thermal–capillary model where the free surface was computed as part of the solution. However, their model considered only heat conduction but not melt convection. Lan and Kou[8] have carried out coupled calculations of steady thermocapillary flow and natural convection under microgravity conditions for an $NaNO_3$ float zone with an imposed cylindrical shape of the free surface. Lan and Kou[9] extended this study to include the free surface deformation computed by solving the Young–Laplace equation with an imposed contact angle at the solidifying trijunction point. Lan and Kou[10] have also carried out a series of studies on float zones with rotation and counterrotation of the feed and crystal. The have found that due to the resulting melt rotation the height of the zone can be reduced significantly by reducing the power input. The forced convection in the melt due to rotation helps to prevent freezing of the melt at the centerline. This is especially useful for non–electrically conducting materials such as $NaNO_3$ since electromagnetic levitation forces cannot be used to stabilize the zone.

Chan and Choi[11] and Chan[12] have modeled the convective heat transfer, solidification and free surface deformation during float zone growth of Titanium Carbide (TiC) by induction heating. Mühlbauer et. al.[13] have simulated the growth of large Silicon crystals by the needle–eye technique with the unknown interface shapes determined as a coupled thermal-electromagnetic-hydrodynamic problem. For their problem, buoyancy induced convection and forced convection due to crystal rotation dominated thermocapillary convection in the float zone. The effect of dopant segregation in float zone growth of KNO_3 doped $NaNO_3$ crystals has been considered by Lan and Kou[14] at zero gravity. The have found that the shape of the melt/crystal interface is significantly affected by the radial dopant segregation, especially at the centerline. Also, with increasing strength of thermocapillary convection, the segregation decreases. They also obtained a similar effect with fast counterrotation of the crystal – feed system. Lan[15] computed steady, convective heat transfer and interface shapes in a float zone using Newton's iterations. This study employed a mass conservation scheme to determine the free surface shape as opposed to a fixed contact angle condition.

Transient computations of g–jitter induced convection in a Bismuth Silicate (BSO) float zone have been studied by Chen et. al.[16]. However, they constrained the free surface to a nondeformable cylindrical shape and imposed a fixed, parabolic temperature distribution on the free surface and did not consider phase change/solidification effects. Grugel et. al.[17] have carried out experimental investigations of vibration on the solidification characteristics in a $NaNO_3$ float zone. They found that vibration suppressed thermocapillary convection resulting in flatter interfaces as evidenced by the improved uniformity of the microstructural morphology presumably due to the opposing effects of thermocapillary and buoyancy driven convection set up the by effect of body forces due to vibration. Hu et. al.[18] have carried out experiments on the onset of oscillatory thermocapillary flow in a half zone to determine the relationship between the liquid bridge volume and the critical Marangoni number measured in terms of the critical temperature difference. Tang and Hu[19] carried out corresponding numerical simulations on a two dimensional half zone. Lee et. al.[20] have performed experiments to investigate oscillatory thermocapillary flow. They found that three dimensional oscillatory flow appears when the Marangoni number exceeds a critical value. The flow modes were found to be strongly dependent on the aspect ratio rather than on the Marangoni number. The flow oscillations, thermal oscillations and the free surface deformations had the same frequencies. Yeckel et. al.[21] have simulated heat and momentum transport in the vertical float zone refinement of two dimensional silicon sheets. They found that Marangoni convection dominates over buoyancy driven flow and the solid–liquid interfaces depart considerably from a planar shape. Levenstam et. al.[22] have carried out experimental and theoretical studies to determine the critical Reynolds number for transition to oscillatory flow in a silicon float zone. They found that as the Reynolds number increases, the flow transitions from a steady two dimensional state to a three dimensional state and then to an unsteady flow.

In this study, a numerical methodology has been developed to treat fluid flow and heat transfer in the float zone process for single crystal growth. A moving boundary approach has been developed to handle the free surface between the melt and ambient gas. The solidification interfaces between the growing crystal and its melt have been treated using the enthalpy method discussed in Shyy and Rao[23], Shyy[24] and Shyy et. al.[25] as opposed to the studies described above where the solid – liquid interfaces as well as the free surface were explicitly tracked. The enthalpy method makes it unnecessary to explicitly track the solid–liquid interfaces, thus the grid generation requirements are less stringent. The free surface has been computed by solving the dynamic form of the Young–Laplace equation coupled with a mass conservation condition. The SIMPLE algorithm in body–fitted coordinates[24] has been utilized to solve the convective heat transport problem.

2. Governing Equations and Boundary Conditions

2.1 Transport Processes

The Navier–Stokes equations of continuity, momentum and energy can be written in a cylindrical coordinate system and specialized to the axisymmetric case as follows:

continuity:
$$\frac{\partial(\varrho r)}{\partial t} + \frac{\partial(\varrho r u)}{\partial r} + \frac{\partial(\varrho r v)}{\partial y} = 0 \tag{1a}$$

r–momentum:
$$\frac{\partial(\varrho r u)}{\partial t} + \frac{\partial(\varrho r u u)}{\partial r} + \frac{\partial(\varrho r u v)}{\partial y} = -r\frac{\partial p}{\partial r} + \left[\frac{\partial}{\partial r}\left(\mu r\frac{\partial u}{\partial r}\right) + \frac{\partial}{\partial y}\left(\mu r\frac{\partial u}{\partial y}\right)\right]$$
$$-\frac{2\mu u}{r} - Ar(u - u_{cast}) \tag{1b}$$

y–momentum
$$\frac{\partial(\varrho r v)}{\partial t} + \frac{\partial(\varrho r u v)}{\partial r} + \frac{\partial(\varrho r v v)}{\partial y} = -\frac{\partial(rp)}{\partial y} + \left[\frac{\partial}{\partial r}\left(\mu r\frac{\partial v}{\partial r}\right) + \frac{\partial}{\partial y}\left(\mu r\frac{\partial v}{\partial y}\right)\right]$$
$$-(\varrho - \varrho_{ref})rg - Ar(v - v_{cast}) \tag{1c}$$

energy:
$$\frac{\partial(r\varrho C_p T)}{\partial t} + \frac{\partial(r\varrho C_p u T)}{\partial r} + \frac{\partial(r\varrho C_p v T)}{\partial y} = \left[\frac{\partial}{\partial r}\left(kr\frac{\partial T}{\partial r}\right) + \frac{\partial}{\partial y}\left(kr\frac{\partial T}{\partial y}\right)\right]$$
$$- L\left[\frac{\partial(\varrho r f)}{\partial t} + \frac{\partial(\varrho r u f)}{\partial r} + \frac{\partial(\varrho r v)}{\partial y}\right] \tag{1d}$$

where the source terms in the energy equation arise from the enthalpy formulation for phase change problems[24]. The effect of property variation in the domain has been taken into account and the properties in the mushy zone are given by,

thermal conductivity: $\qquad k_{mush} = f\, k_l + (1 - f)\, k_s$ (2a)

density: $\qquad \varrho_{mush} = f\, \varrho_l + (1 - f)\, \varrho_s$ (2b)

where the subscripts 'l' and 's' indicate the liquid and solid phases respectively and f is the liquid fraction. The D'arcy law term is used to drive the velocities in the solid to equal the casting or pulling rate given by $\vec{V}_{cast}$. The D'arcy coefficient is given by[24],

$$A = C\left(\frac{1 - f^2}{f^3 + q}\right)$$ (2c)

where C is a large number and q is a small number. For a pure material they can be chosen quite arbitrarily so as to drive the velocity in the solid region to the casting rate while retaining numerical stability. The liquid fraction is modeled as a linear function of the temperature within the phase change interval and is set to zero in the solid

$$f = \begin{cases} 0 & , \quad T < T_s \\ \dfrac{T - T_s}{2\,\varepsilon} & , \quad T_s \le T \le T_l \\ 1 & , \quad T > T_l \end{cases}$$ (2d)

and unity in the liquid. For a pure material, the phase change interval, 2ε, is chosen so as to spread the numerical mushy zone over one or two computational cells in order to achieve numerical stability as described in Shyy et. al.[25]. As regards the numerical implementation, a choice of either the T–based or the H–based method is available[23,25]. All the calculations in this work employ the T–based method.

2.2 Boundary Conditions

(i) Thermal Boundary Conditions

Heat transfer to the system is controlled by radiation and convective transfer from the ambient, i.e.,

$$- k\nabla T \cdot \hat{n}\big|_{r=R} = h(T - T_{amb}) + \varepsilon\sigma(T^4 - T^4_{amb})$$ (3a)

where $r = R$ designates the surface of the melt/crystal/feed system. T_{amb} is the imposed temperature distribution due to the heater. Following Duranceau and Brown[7] and Lan[15], T_{amb} is modeled as a Gaussian distribution given by

$$T_{amb} = (T_p - T_\infty) \exp\left(-\left(\frac{y - y_p}{a}\right)^2\right) + T_\infty \tag{3b}$$

where T_p is the heater temperature located at position y_p, T_∞ is the ambient temperature far away from the heater and a is the half width of the distribution.

(ii) Free Surface Treatment

For liquids bounded by a free or deformable boundary where a temperature gradient exists along the interface, a surface shear stress is generated by the surface tension gradient. Thus, the force balance can be written as,

$$\mu \, \nabla \, (\vec{V} \cdot \vec{t}) \cdot \vec{n} = \frac{\partial \gamma}{\partial T} \, \nabla T \cdot \vec{t} \tag{4a}$$

where the surface tension gradient is proportional to the temperature gradient and gives rise to the normal derivative of the tangential velocity at the free surface. $\vec{V}$ is the velocity vector, $\vec{n}$ is the unit normal vector to the free surface, and $\vec{t}$ is the unit tangent vector to the free surface. The convection strength is described, in nondimensional terms, by the Marangoni number,

$$Ma = \left|\frac{d\gamma}{dT}\right| \frac{\Delta T \, r_b}{\mu \alpha} \tag{4b}$$

which is obtained by nondimensionalizing Eq. (4a) with a temperature scale, ΔT, length scale, r_b, and a velocity scale given by α/r_b, where α is the thermal diffusivity of the melt and μ is its viscosity. This dimensionless parameter represents the strength of the velocity gradients generated by the shear stress due to the surface tension gradient.

The velocity boundary conditions for the momentum equations are obtained by solving Eq. (4a), in conjunction with the fact that the meniscus is a material surface, i.e.,

$$\frac{\partial F}{\partial t} + u \frac{\partial F}{\partial r} + v \frac{\partial F}{\partial y} = 0 \tag{5a}$$

where $F(x, y, t) = 0$ describes the equation of the meniscus. This can be written as,

$$\vec{V} \cdot \hat{n} = 0 \tag{5b}$$

in a moving grid system generated to fit a moving and deforming meniscus. Equations (4a) and (5b) are solved simultaneously to obtain the boundary velocities at the free surface.

(iii) Symmetry

Since axisymmetry is assumed, the centerline is taken to a symmetry boundary. Thus, at $r = 0$,

$$\begin{aligned} u &= 0 \\ \frac{\partial v}{\partial r} &= 0 \\ \frac{\partial T}{\partial r} &= 0 \end{aligned} \tag{6}$$

6

2.3 Governing Equations for a Deformable Meniscus

The meniscus shape obeys the Young–Laplace equation obtained by balancing the hydrostatic pressure, hydrodynamic pressure and viscous normal stress terms against the surface tension force, i.e.,

$$\Delta\varrho\, g\, y - P_L - P_d + 2\mu\frac{\partial v_n}{\partial n} = \gamma(T)\left[\frac{r''}{(1+r'^2)^{3/2}} - \frac{1}{r\,(1+r'^2)^{1/2}}\right] \qquad (7a)$$

where $r = r(y)$ describes the free surface shape. Here, $\Delta\varrho$ is the density difference between the melt and the ambient fluid, g is the acceleration due to gravity, γ is the temperature dependent surface tension between the melt and the ambient fluid. The term on the right hand side represents the product of the temperature dependent surface tension and the free surface curvature. The left hand side represents the hydrostatic pressure, the hydrodynamic pressure, P_d, and the viscous normal stress generated by the fluid motion. In addition, there is a pressurization parameter, P_L, that must be determined as part of the solution either by satisfying a contact angle condition at the solidifying interface or by a mass conservation constraint.

The dynamic form of the Young–Laplace equation, Eq. (7a), can be nondimensionalized as follows:

$$Bo\, Y - We\, P_d - P_L + Ca\frac{\partial V_n}{\partial n} = \left(1 - \left|\frac{d\gamma}{dT}\right|\frac{\Delta T}{\gamma_0}\right)\left[\frac{R''}{(1+R'^2)^{3/2}} - \frac{1}{R(1+R'^2)^{1/2}}\right]$$

$$(7b)$$

where the Bond number, Bo, is defined as

$$Bo = (\Delta\varrho\, g\, r_b^2)/(\gamma_0) \qquad (8a)$$

describes the force balance between the hydrostatic pressure and the surface tension, the Weber number, We,

$$We = (\varrho\, \alpha^2)/(\gamma_0\, r_b) \qquad (8b)$$

describes the relative magnitudes of the inertia and surface tension, and the Capillary number, Ca,

$$Ca = (2\,\mu\,\alpha)\big/(\gamma_0\, r_b) \qquad (8c)$$

describes the relative magnitudes of the viscous normal stress and the surface tension. Here, α is the thermal diffusivity of the melt, μ is the viscosity of the melt and r_b is a characteristic length scale typically taken to be radius of the melting feed.

Equation (7a) may be solved with the following boundary conditions:

(i) Fixed radius at the melting feed.

$$r(y = h_c) = r_b \qquad (9)$$

and either

(ii) Fixed radius at the solidifying crystal,

$$r(y = 0) = r_c \qquad (10a)$$

or fixed contact angle at the solidifying crystal

$$r'(y = 0) = \tan(\pi/2 - \phi_c) \qquad (10b)$$

assuming downward pulling as is the case in the problem considered subsequently. Equation (10a) has been used in all the cases considered in this study for the purpose of comparison with the solutions available in literature. Here, $y = 0$ describes the location of the melting feed and $y = h_c$ is the height of the meniscus, ϕ_c is the contact angle between the meniscus and the solidifying crystal and r_c is the radius of the growing crystal.

3. Computational Methodology

3.1 Moving Grid Procedure

Equations (1a–d) are transformed into a moving grid body fitted coordinate system as follows: The transformation may be expressed as

$$\begin{aligned} \xi &= \xi(x, y, t) \\ \eta &= \eta(x, y, t) \end{aligned} \qquad (11a)$$

The continuity equation in nonorthogonal coordinates then becomes,

$$\frac{\partial}{\partial t}(Jr\varrho) + \frac{\partial(\varrho r U)}{\partial \xi} + \frac{\partial(\varrho r V)}{\partial \eta} = 0 \qquad (11b)$$

where r is the radial coordinate which is identical to x in the following treatment. The separation between r and x is maintained for the ease of application to a two dimensional Cartesian coordinate system as opposed to a cylindrical coordinate system considered here.

$$\begin{aligned} U &= (u - \dot{x}) \, y_\eta - (v - \dot{y}) \, x_\eta \\ V &= (v - \dot{y}) \, x_\xi - (u - \dot{x}) \, y_\xi \end{aligned} \qquad (11d)$$

are the contravariant velocity components and $\dot{x}$ and $\dot{y}$ are the radial and vertical components of the grid velocity vector respectively. The determination of the Jacobian, J, will be explained subsequently. The momentum equations then become
r–momentum:

$$\begin{aligned} \frac{\partial(J\varrho r u)}{\partial t} + \frac{\partial(\varrho r U u)}{\partial \xi} + \frac{\partial(\varrho r V u)}{\partial \eta} &= - \left\{ ry_\eta \frac{\partial p}{\partial \xi} - ry_\xi \frac{\partial p}{\partial \eta} \right\} + \\ &\quad \frac{\partial}{\partial \xi}\left[\frac{\mu}{J} r\left(q_1 u_\xi - q_2 u_\eta \right) \right] + \\ &\quad \frac{\partial}{\partial \eta}\left[\frac{\mu}{J} r\left(q_2 u_\xi - q_3 u_\eta \right) \right] + S_u(\xi, \eta) \cdot J \cdot r \end{aligned} \qquad (11e)$$

y−momentum:

$$\frac{\partial(Jr\varrho v)}{\partial t} + \frac{\partial(\varrho rUv)}{\partial \xi} + \frac{\partial(\varrho rVv)}{\partial \eta} = - \left\{ x_\xi \frac{\partial(rp)}{\partial \eta} - x_\eta \frac{\partial(rp)}{\partial \xi} \right\} +$$

$$\frac{\partial}{\partial \xi}\left[\frac{\mu}{J}r\left(q_1 v_\xi - q_2 v_\eta\right)\right] + \frac{\partial}{\partial \eta}\left[\frac{\mu}{J}r\left(q_2 v_\xi - q_3 v_\eta\right)\right] - \tag{11f}$$

$$(\varrho - \varrho_{ref})\, g \cdot J \cdot r + S_v(\xi,\eta) \cdot J \cdot r$$

along x and y directions respectively, where x_η, y_η and so on are the metrics of the transformation and q_1, q_2 and q_3 are defined as

$$\begin{aligned}
q_1 &= x_\eta^2 + y_\eta^2 \\
q_2 &= x_\xi x_\eta + y_\xi y_\eta \\
q_3 &= x_\xi^2 + y_\xi^2
\end{aligned} \tag{11g}$$

Following Shyy[24], the metric terms x_η, y_η and so on are evaluated as the projected lengths of the control volume in the physical space in order to ensure conservative treatment.

3.2 Determination of the Jacobian

The Jacobian of the transformation is defined as,

$$J = x_\xi y_\eta - x_\eta y_\xi \tag{12}$$

which can be interpreted as the volume of the computational cell (Shyy 1994). However, in a moving grid system, the Jacobian has to satisfy the geometric conservation law which can be derived by considering the transformed continuity equation. Consider an uniform flowfield with $\varrho = 1$, $u = 1$ and $v = 1$. Such a flowfield identically satisfies the continuity equation (1a) and is required to satisfy the transformed continuity equation (11b). Equation (11b) then becomes

$$\frac{\partial[Jr]}{\partial t} + \frac{\partial\left[r\left(\dot{y}\,x_\eta - \dot{x}\,y_\eta\right)\right]}{\partial \xi} + \frac{\partial\left[r\left(\dot{x}\,y_\xi - \dot{y}\,x_\xi\right)\right]}{\partial \eta} = 0 \tag{13}$$

The Jacobian is thus computed by a backward Euler difference in time based on the geometric quantities such as the radial coordinate and the metric as shown above. The methodology is an extension of the procedure described in Shyy et. al.[25] to the cylindrical coordinate system.

3.3 Meshing Procedure

For moving boundary problems like the float−zone simulation, it is essential to maintain an adequate resolution in the liquid zone, even as the grid deforms to track the changing geometry. Adequate resolution in the liquid zone is necessary in order to (a) stabilize the calculation, (b) maximize the accuracy of the convective heat transfer and phase change computations, and (c) accurately capture the meniscus deformation and faithfully represent the curved geometry of the

domain. At the same time, it is desirable that the grid generation process be fast and robust, i.e., ensure that the grid distribution is smooth, avoid excessive skewness, allow good control of the grid spacing and that the mapping between the physical domain and the computational domain is invertible.

In this work, a block structured approach with an algebraic grid generation procedure has been taken to enable fast grid generation. A typical float–zone domain can be divided into three logical subdomains: (a) the crystal, (b) the melt and (c) the feed rod, as illustrated in Fig. 1. Subdomains (a) and (c) are highly stretched to fit the long crystal and the feed rod. Thus, the material in subdomains (a) and (b) is entirely solid during the solution process. Subdomain (b), however, encloses the melt zone. Thus, phase change and convective heat transfer occur entirely in subdomain (b). It is also to be noted that subdomain (b) has an $O(1)$ aspect ratio which dictates the choice of the interpolation and distribution functions chosen for the algebraic grid generation procedure.

Due to the varying and sometimes conflicting requirements listed above, the grid in each block or subdomain is generated separately and subsequently assembled together into a single grid system at each iteration of the solution procedure. In each subdomain, the grid is generated algebraically by using appropriate interpolation functions and distribution parameters, checked for integrity and only then is the assembly procedure invoked to create a single grid system. The algebraic generation procedure is relatively inexpensive; as opposed to the solution of quasi–linear elliptic equations and has been found to be robust as well in the present problem. However, careful choice of the

Subdomain (c): the feed.

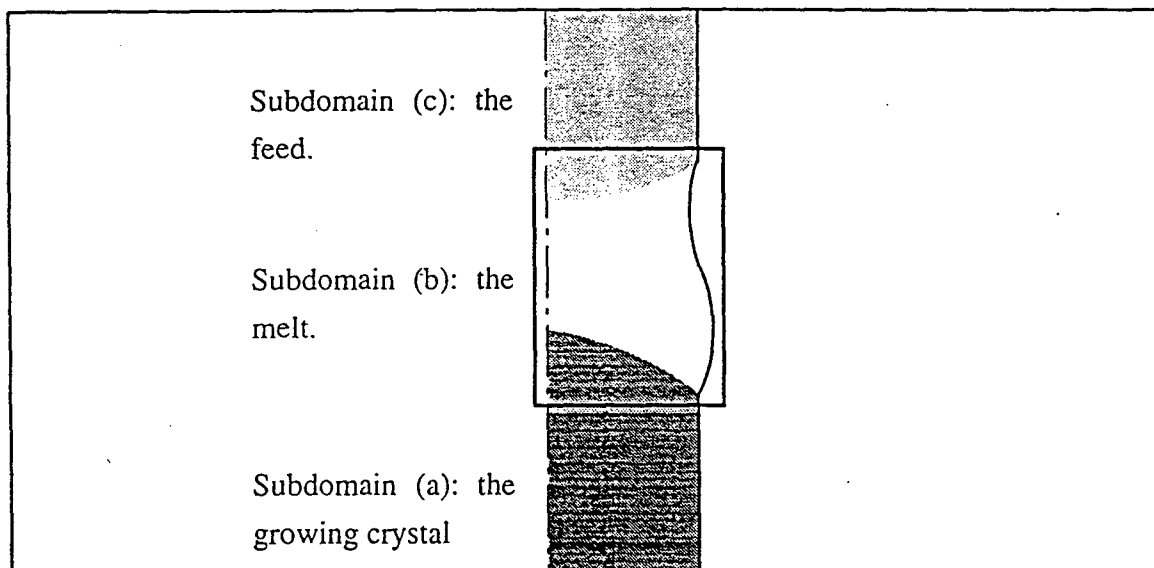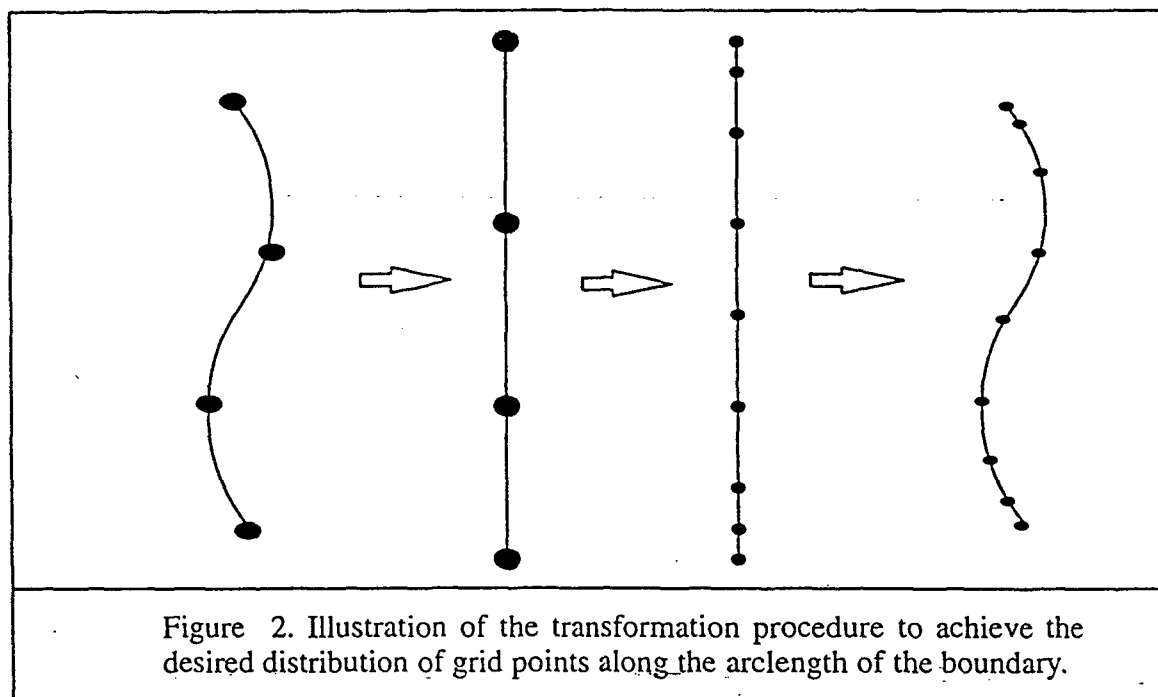Subdomain (b): the melt.

Subdomain (a): the growing crystal

Figure 1. Illustration of the domain and its partition into three blocks for the purpose of grid generation. Block 2 enclosing the phase change region is boxed for illustration. The extent of block 2 into the solid regions can be adjusted to track the height variation of the zone.

distribution parameters and interpolation functions is necessary to ensure smoothness and concentration of grid lines close to the interfaces.

The calculation domain is divided into contiguous, non–overlapping blocks and the meshing procedure is carried out separately in each block. For convenience, it is required that each block consist only of four sides. The sides may be specified either as straight lines or by sequence of (x,y) pairs describing a curve. The curve may be specified or computed; the only requirement is that it does not intersect itself. For instance, in the melt zone, the meniscus shape is computed by numerically integrating the dynamic form of the Young–Laplace equation. The detailed procedure is as follows:

(a) Divide the domain into contiguous blocks of four sides each. Each block is described by a non–intersecting curve. For the float–zone calculations, it is convenient to divide the domain into three blocks; the first block consisting of the crystal, the second block consisting of the feed rod and the third block enclosing the melt and the phase change region.

(b) For each side, compute the arclength from the sequence of (x,y) pairs describing the curve. The required number of grid points are then distributed along the arclength of each side as illustrated in Fig. 2. A variety of choices exist for the distributing function. In this study, it was found convenient to use cubic and exponential clustering functions depending on the geometry of the individual block. The cubic polynomial allows a fixed number of grid points to be distributed with specified end points as well as specified end spacings. The exponential clustering is suitable for highly stretched

Figure 2. Illustration of the transformation procedure to achieve the desired distribution of grid points along the arclength of the boundary.

subdomains, allowing the end points to be matched alongwith the spacing at one end. The spacing at the other end is determined by the function. The exponential clustering is described by

$$\frac{s - s_1}{s_N - s_1} = \frac{\exp(\alpha\ \xi) - 1}{\exp(\alpha) - 1} \tag{14a}$$

where $\xi = \frac{i - 1}{N - 1}$, N being the number of grid points that need to be accommodated within $s_1 \leq s \leq s_N$. The coefficient, α, is determined by specifying the spacing at one end, i.e. as the root of

$$\frac{\Delta s_1}{s_N - s_1} = \frac{\exp(\alpha\ \Delta\xi) - 1}{\exp(\alpha) - 1} \tag{14b}$$

where the root is determined by an iterative procedure. The quantities ξ and η are the transformed and normalized coordinates in the computational plane and are defined as,

$$\xi = \frac{i - 1}{N_i - 1} \tag{14c}$$

and

$$\eta = \frac{j - 1}{N_j - 1} \tag{14d}$$

where N_i is the number of grid points along the ξ direction and N_j the number of grid points along the η direction. The ability to match the spacing at one end allows a smooth variation of the grid spacing between the different subdomains.

(c) The resulting boundary distribution is then verified by ensuring that all the newly formed arclength elements have a positive length. This step is necessary when using high order polynomials such as the cubic clustering because of potentially oscillatory behavior between the colocation points.

(d) The newly formed arclength distribution is mapped back to the x–y plane via cubic spline interpolation. This completes the generation of the boundary distribution for each subdomain.

(e) The internal grid distribution is generated for each block by transfinite interpolation. For transfinite interpolation, use of linear basis functions has been found to be robust and efficient. The quality of the grid is determined mostly by the boundary distribution since using low order interpolation polynomials does not give rise to oscillatory tendencies. The disadvantage is that it is does not provide additional control of the interior grid distribution which is necessary to ensure grid orthogonality.

$$\vec{r}(\xi, \eta) = \xi\ \vec{r}(0, \eta) + (1 - \xi)\ \vec{r}(1, \eta) + \eta\ \vec{r}(\xi, 0) + (1 - \eta)\ \vec{r}(\xi, 1) - \xi\ \eta\ \vec{r}(0, 0) -$$
$$\xi\ (1 - \eta)\ \vec{r}(0, 1) - (1 - \xi)\ \eta\ \vec{r}(1, 0) - (1 - \xi)\ (1 - \eta)\ \vec{r}(1, 1) \tag{15}$$

where $\vec{r} = x\ \hat{i} + y\ \hat{j}$

12

(f) The grid is checked for zero Jacobians and convexity of the control volumes. Loss of convexity implies excessive distortion of the quadrilateral that constitutes the control volume. Loss of convexity is tested by taking the cross product of pairs of adjacent sides of the control volume and ensuring that the angle between them is not greater than π radians. Appropriate error recovery measures, described later, are taken if such situations are encountered.

(g) The various subdomains are combined together to form a single grid.

3.4 Deformable Meniscus

The meniscus shape is computed by integrating the dynamic Young–Laplace equation described earlier. As shown in Fig. 3, the meniscus is discretized into finite domains on the underlying grid points. The dynamic Young–Laplace equation is then integrated over the finite domains in a manner analogous to the discretization of the transport equations over the control volume. The derivatives in the equation are approximated by piecewise linear interpolation functions effectively giving rise to a second order central difference scheme for all the terms in the dynamic Young–Laplace equation.

The discretized dynamic form of equation (7a) can now be written in the form

$$ap\ r_i = as\ r_{i-1} + an\ r_{i+1} + b \qquad (16a)$$

in the notation popularized by Patankar[26], where

$$as = \frac{\gamma}{\Delta y_{i-1/2} \left(1 + r'^2\right)^{3/2}\Big|_{y\ =\ y_{j-1/2}}} \qquad (16b)$$

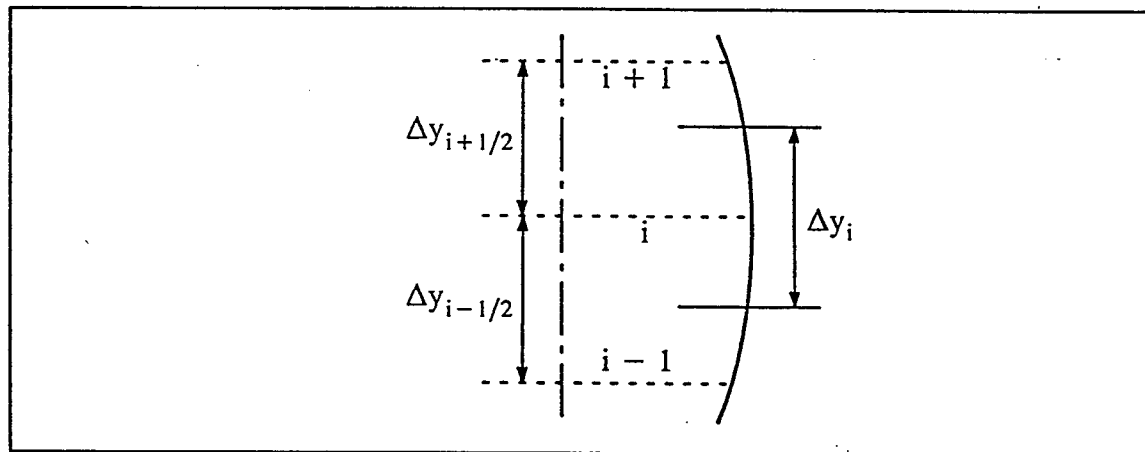$$an = \frac{\gamma}{\Delta y_{i+1/2} \left(1 + r'^2\right)^{3/2}\Big|_{y\ =\ y_{j+1/2}}} \qquad (16c)$$

Figure 3. Illustration of the differencing procedure for the Young–Laplace equation.

$$ap = as + an \qquad (16d)$$

and the source term is given by

$$b = \varrho_i \, g \left[\frac{y_{i+1}}{4} + \frac{y_{i-1}}{4} + \frac{y_i}{2} - y_{ref} \right] - P_{d_i} - P_L + \frac{\gamma}{r_i \left(1 + r'^2\right)^{1/2}}\Bigg|_{y=y_i} \qquad (16e)$$

where all the first derivative terms, r', are evaluated using central differences over the nearest half grid points and the term P_{d_i} includes the contribution from the inertia and viscous stress effects due to melt convection.

The equation system (16) is conveniently solved using a tridiagonal solver. However, since the coefficients are non–linear, successive substitution is employed as the outer iteration. During the course of the iterations, underrelaxation is employed to ensure convergence. Underrelaxation is first applied to the non–linear first derivative terms,

$$r'^k = \omega_r \, \delta r^k + (1 - \omega_r) \, r'^{k-1} \qquad (17a)$$

where k denotes the iteration number. Underrelaxation is also applied to the shape update as follows:

$$ap = ap/\omega_m \qquad (17b)$$

$$b = b + (1 - \omega_m) \, ap \, r_i \qquad (17c)$$

to ensure diagonal dominance before solving the tridiagonal system.

3.5 Convergence Criteria

Convergence criteria for terminating the non–linear iterations consists of examining the residuals summed over the entire field as well as the 1–norm of the solution variation with iterations. The residual is always scaled/normalized by the solution and is defined as,

$$Res = \sum_i \left[\frac{an \, r_{i+1} + as \, r_{i-1} - ap \, r_i + b}{ap} \right] \Bigg/ \sum_i |r_i| \qquad (18)$$

The 1–norm is defined as,

$$\| r \| = \frac{\sum_i \left| r_i^k - r_i^{k-1} \right|}{\sum_i \left| r_i^{k-1} \right|} \qquad (19)$$

and is an auxiliary indicator of convergence. Both, the residual averaged over the total number of control volumes, as well as the L_1–norm are required to be less than 10^{-4}.

3.6 Global Mass Conservation

Meniscus shapes are determined by adjusting the value of P_L so as to satisfy the constraint of global mass conservation. In this study, a target domain mass is determined by considering the

14

domain to be initially a solid cylinder. As melting progresses, a mass deficit builds up due to density differences between the melt and the solid. The meniscus shape is adjusted to reduce the mass deficit to zero via manipulation of P_L.

First, the mass deficit is determined,

$$\Delta M = M_{domain} - \int_{Vol} \varrho \, dV \tag{20}$$

The meniscus is then required to satisfy a volume constraint,

$$V_m = \pi \int r \, dy + \frac{\Delta M}{\varrho_l} \tag{21}$$

The required value of P_L is determined by finding the root of

$$\mathcal{F}(P_L) = V_m - \pi \int r \, dy = 0 \tag{22}$$

3.7 Root Finding Procedure

(i)   The root is bracketed between two extreme values of P_L by a linear search for a zero crossing of $\mathcal{F}(P_L)$. It is helpful to carry out exploratory computations to arrive at reasonable guess values for the step size as well as the initial guess for P_L.

(ii)   The secant method is used to locate the root. If a pathological situation is encountered where the secant method does not converge, the procedure automatically switches over to the bisection method.

3.8 Remeshing Procedure

Once a meniscus profile is obtained satisfying the dynamic form of the Young–Laplace equation and the global mass conservation constraint, the domain has to be remeshed as the grid moves to fit the meniscus. It is possible to underrelax the grid movement in order to stabilize the transport calculations. Again, an algebraic procedure is adopted whereby the x–coordinates of the control volumes are determined by using transfinite interpolation.

(i)   Carry out linear transfinite interpolation to determine the x–coordinates of the grid points using the x–component of Eq. (15).

(ii) Check the grid for zero Jacobians and loss of convexity of the control volumes. The error recovery procedure is described next.

3.9 Error Recovery

It is possible to encounter zero Jacobians during the iterative process if the height of the zone decreases so that the grid gets excessively squashed. In such a case, the algorithm prints a warning

message and continues the calculations without updating the grid. To prevent this from occurring it is possible to specify a minimum zone height below which the vertical component of grid motion is suppressed. Loss of convexity usually occurs if the meniscus computation diverges due lack of existence of solutions in the required parameter range – especially if the zone height becomes excessively large. An appropriate parameter range can be approximately determined by solving the static form of the Young–Laplace equation to generate an existence map over the desired parameter range[23] and utilizing such a map to generate appropriate initial guesses. Such a procedure will be described in detail in the results section.

3.10 Grid Underrelaxation

For most cases, grid underrelaxation is necessary in order to ensure a smooth and oscillation free convergence history. The vertical and radial components of the grid deformation are underrelaxed separately and the corresponding underrelaxation parameters are denoted by ω_r and ω_y respectively. Typical values of ω_r range from 0.4 to 0.7 depending on the estimated height of the melt zone. The vertical component, however, needs to be underrelaxed substantially. The value of ω_y has been varied from 0 (no deformation in the y–direction) to 1 (no underrelaxation) in an attempt to quantify its effect on the solution history. Typical values used are in the range of 0.05 to 0.1 to ensure convergence of the solution. Care is taken to ensure that the melt zone is completely enclosed by the refined grid region comprising subdomain (b) as illustrated in Fig. 2 by tracking the location of the subdomain boundaries with respect to the phase boundaries during the iterative process and also by an a posteriori estimation after the solution has been obtained.

4. Results and Discussion

4.1 Test Problem

The test problem used to develop and test the algorithm is the float zone growth of Sodium Nitrate crystal ($NaNO_3$) crystals heated using a ring heater. The steady state solutions for pure heat conduction, meniscus shapes, natural and Marangoni convection are available in literature[8,9,15]. These solutions provide a reference point for comparison and assessment.

An initially cylindrical rod of $NaNO_3$ is heated at the center by radiation from a ring heater which causes it to start melting and form a float zone. The meniscus deformation depends on the length of the molten zone and also on the density change during melting as the meniscus deforms to conserve mass. The rod is then pulled downwards to simulate the crystal growth processes. Since the length of the rod is set to 40 times its radius, the melt zone occupies only a small fraction of the domain. The physical properties of $NaNO_3$ are shown in table 1. Other relevant geometrical and physical parameters are presented in table 2.

Table 1. Physical properties of $NaNO_3$	
Melting temperature, T_m	579.8 K
Latent heat, L	182 J g^{-1}
Thermal conductivity (solid), k_s	$5.65 \times 10^{-3} + 33.5\ (T - 503) \times 10^{-7}$ W cm^{-1} K^{-1}
Thermal conductivity (liquid), k_l	$5.65 \times 10^{-3} + 33.5\ (T - T_m) \times 10^{-7}$ W cm^{-1} K^{-1}
Specific heat, $C_{ps} = C_{pl}$	$1.255 + 2.18\ (T - 373) \times 10^{-3}$ J g^{-1} K^{-1}
Surface tension gradient, $\partial\gamma/\partial T$	-0.056 dyn cm^{-1} K^{-1}
Surface tension, γ	$119.96 - 0.056\ (T - T_m)$ dyn cm^{-1}
Dynamic viscosity, μ	$0.0302 - 1.533 \times 10^{-4}\ (T - T_m)$ g cm^{-1} s^{-1}
Thermal expansion coefficient, β	6.6×10^{-4} K^{-1}
Density (solid), ϱ_s	2.118 g cm^{-1}
Density (liquid), ϱ_l	1.904 g cm^{-1}

Table 2. Geometrical and physical parameters	
r_b (radius)	0.2 cm
y_p (heater location)	4.0 cm
a (width of heater profile)	0.3 cm
T_∞	298 K
T_p (heater temperature)	813 K, 913 K
ε (emissivity)	0.7
h (heat transfer coefficient)	4.6×10^{-4} W cm^{-2} K^{-1}

In order to accommodate the enthalpy method, the melting temperature is distributed over a finite phase change interval given by

$$2\,\varepsilon \ = \ 0.2\,K \tag{23}$$

4.2 Nondimensional Parameters

The material properties and the geometrical parameters presented in tables 1 and 2 above enable the estimation of important nondimensional parameters for the system. Based on an estimated temperature scale, $\Delta T = T_{max} - T_m = 20K$, length scale, $r_b = 0.2$cm, and the material properties given in table 1, the following nondimensional parameters can be obtained:

Prandtl number $\qquad Pr = \dfrac{\nu}{\alpha} \ = \ 9.2$

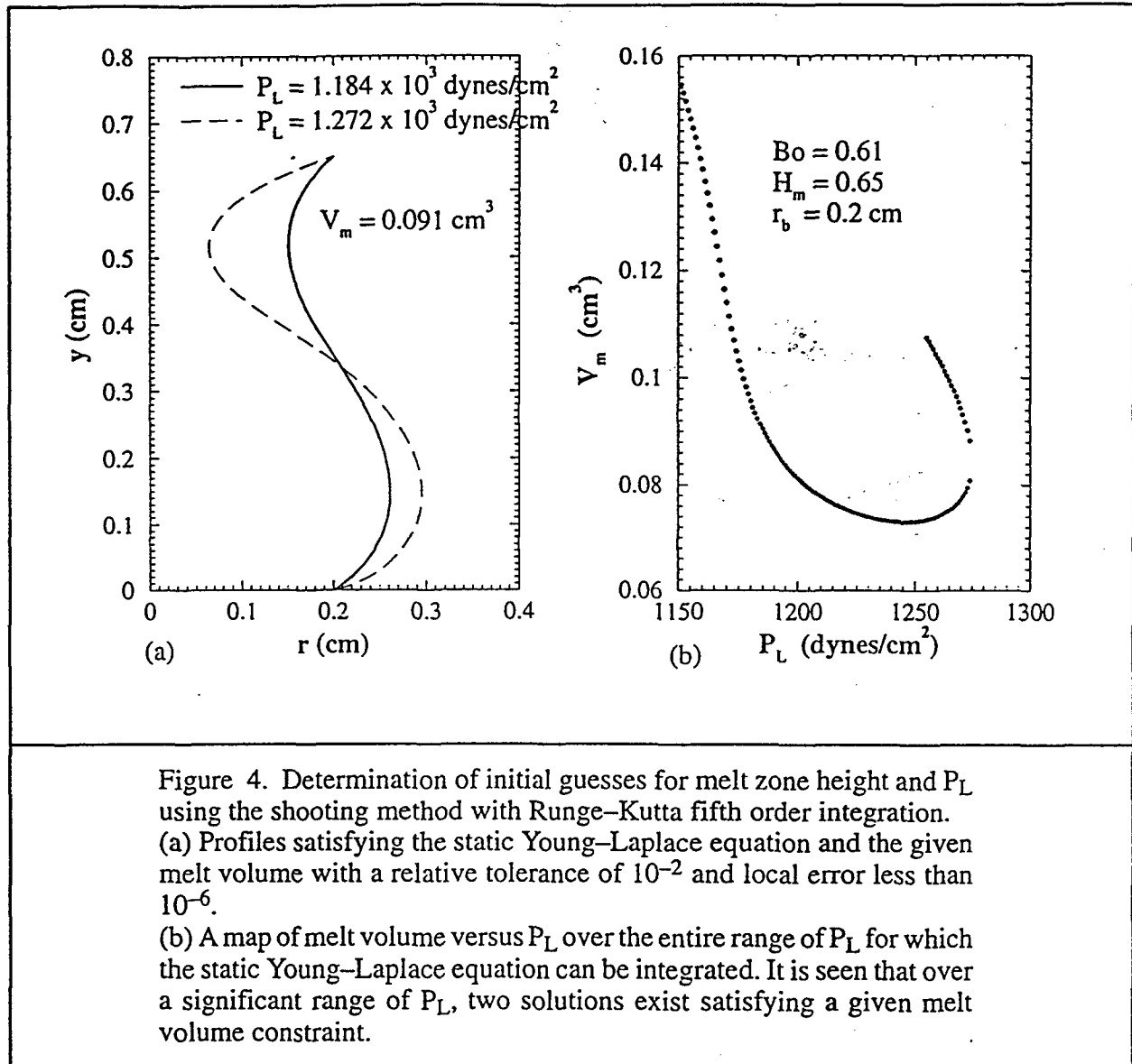Grashof number $\qquad \dfrac{g\beta\Delta T r_b^3}{\nu^2} \ = \ 411$

17

Rayleigh number	$Ra = Gr\, Pr = 3781$
Marangoni number	$Ma = 4752$
Stefan number	$St = \dfrac{C_p \Delta T}{\Delta H} = 0.3$
Bond number	$Bo = \dfrac{\Delta \varrho g r_b^2}{\gamma_0} = 0.61$
Capillary number	$Ca = \dfrac{2\mu\alpha}{\gamma_0 r_b} = 3.8 \times 10^{-6}$
Weber number	$We = \dfrac{\varrho\alpha^2}{\gamma_0 r_b} = \ = 2.4 \times 10^{-7}$
Biot number	$\dfrac{h\, r_b}{k} = 0.02$
Radiation number	$\dfrac{\varepsilon \sigma r_b \Delta T^3}{k} = 3.7 \times 10^{-6}$

A conduction–capillarity solution obtained by setting the heater temperature to 913 K has been chosen to present some of the features of the algorithm and its implementation, and to characterize the interaction between the grid movement, meniscus deformation and heat conduction terms in the discretized energy equation.

4.3 Estimation of Meniscus Shape and P_L

The meniscus calculations need a starting procedure to determine the initial guesses for the melt zone height and the corresponding guess value of P_L. The procedure is as follows:

(i) Determine an initial estimate of the melt zone height. This was done by computing a pure heat conduction solution for a cylindrical geometry, i.e., with the meniscus shape held fixed.

(ii) Using the guessed height, the static Young–Laplace equation is solved using an adaptive fifth order Runge–Kutta method and the shooting technique to generate all possible profiles over the entire range of P_L for which solutions exist. The relative local error (Shyy 1994) is maintained below 10^{-6} by comparing with the corresponding fourth order Runge–Kutta technique and varying the step size accordingly.

(iii) Figure 4(a) shows the map of melt volume, V_m, versus P_L over the entire range of available solutions. It is evident that over the range of interest, two solutions exist even for the static Young–Laplace equation. Figure 4(b) shows the meniscus profiles satisfying the volume constraint with a relative tolerance of 10^{-2}.

(iv) Figures 4(a) and (b) are used to guide the initial guesses for P_L and the limiting values for the meniscus volume for the float zone computations. Such a procedure ensures operation in the range where the solutions to the Young–Laplace equation exist.

Figure 4. Determination of initial guesses for melt zone height and P_L using the shooting method with Runge–Kutta fifth order integration.
(a) Profiles satisfying the static Young–Laplace equation and the given melt volume with a relative tolerance of 10^{-2} and local error less than 10^{-6}.
(b) A map of melt volume versus P_L over the entire range of P_L for which the static Young–Laplace equation can be integrated. It is seen that over a significant range of P_L, two solutions exist satisfying a given melt volume constraint.

4.4 Conduction–Capillarity Solution

Two sets of calculations with different initial guesses and grid underrelaxation parameters were carried out to investigate the coupling between the grid movement, boundary deformation and heat conduction. First, a conduction solution was obtained with the heater temperature set to 913 K and by imposing a cylindrical shape on the meniscus. This was then used as an initial guess for the conduction–capillarity problem which allowed the meniscus shape to deform in accordance with the Young–Laplace equation. No underrelaxation was used when updating the meniscus shape or the grid. Figure 5 shows the convergence characteristics of this procedure. Figure 5(a) shows the history of the monitored quantities, H_m – the zone height at the free surface, and H_c – the zone height at the centerline. Figures 5(b) and (c) show the history of P_L and the melt volume, V_m, respectively. The

residual of the energy equation and the 1—norms of the temperature, x, and y components of the grid deformation are shown in Fig. 5(d–f). The highly oscillatory trend in the solution characteristics is evident and this procedure cannot yield a solution.

The second set of calculations used an initially solid rod at room temperature, 300 K, as the initial guess. Figure 6 shows the effect of various grid underrelaxation factors on the convergence characteristics. Figures 6(a–c) shows the history of H_m for grid underrelaxation factors over a range, $0 \leq \omega_y \leq 1$. $\omega_y = 1$ indicates that the vertical component of grid deformation was not underrelaxed and $\omega_y = 0$ indicates that the vertical component of grid deformation was completely suppressed. It is evident that grid underrelaxation in the range, $0.1 \leq \omega_y \leq 0.05$ is sufficient to suppress the oscillatory behavior. Complete suppression of the vertical component of grid deformation yields the smoothest but the slowest convergence characteristics.

Figure 7 shows the solution features. It is observed that the meniscus profile and the zone height are very close to the profile shown in Fig. 4a. The hydrostatic pressure causes the melt to bulge outwards near its base and to 'neck' inwards near the top. Figure 7(a) shows the computed grid and
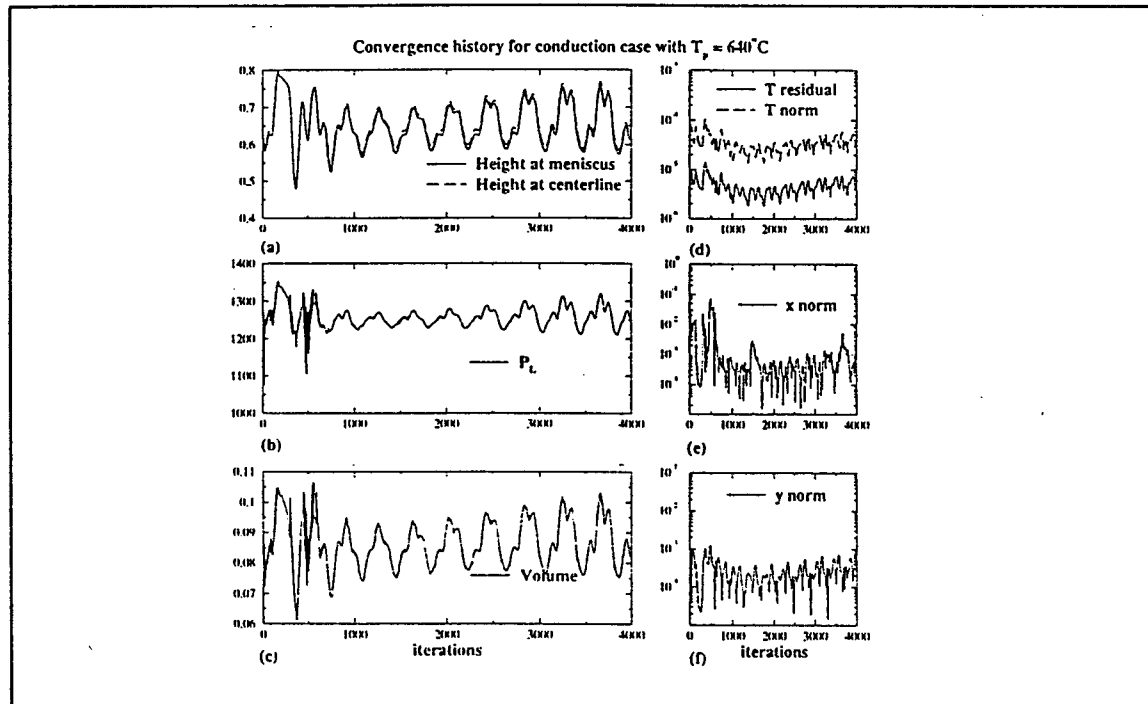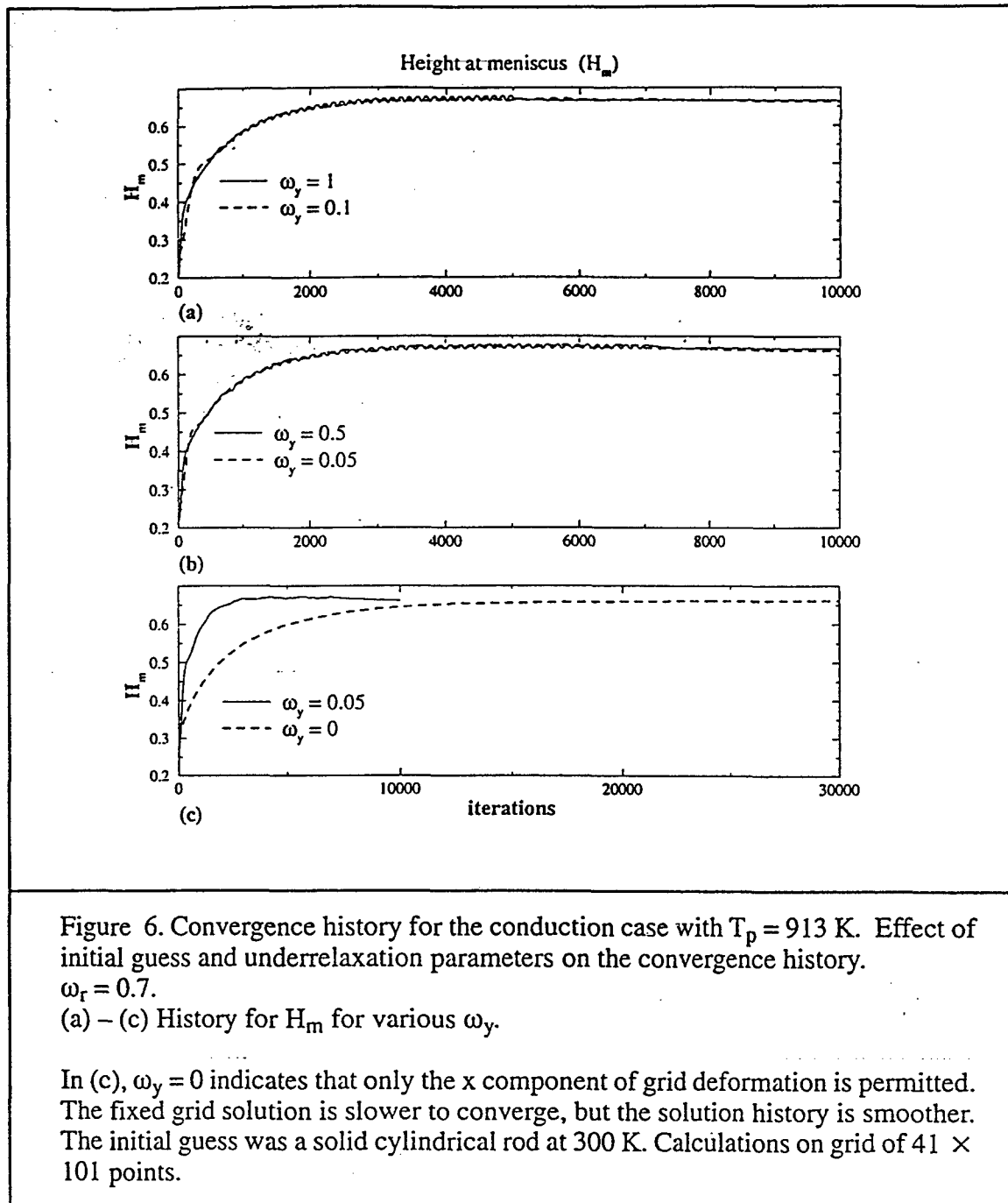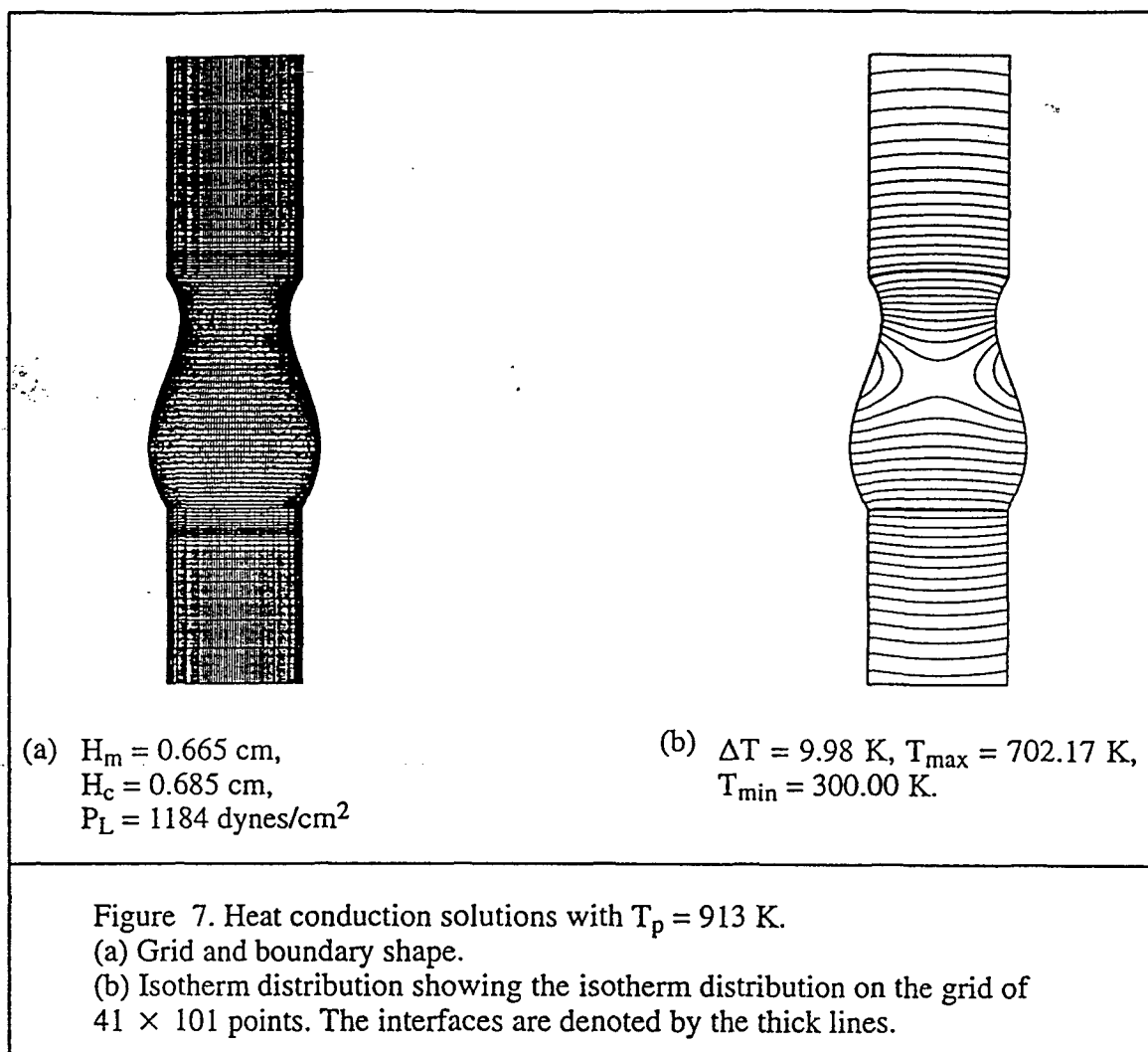

Figure 5. Convergence history for the conduction case with $T_p = 913$ K. Effect of initial guess and underrelaxation parameters on the convergence history. A conduction solution was obtained by imposing a cylindrical meniscus shape. The converged solution was then used as the initial guess for the conduction – capillary solution. The grid motion and boundary deformation were not underrelaxed, i.e., $\omega_y = \omega_r = 1$.

Figure 6. Convergence history for the conduction case with $T_p = 913$ K. Effect of initial guess and underrelaxation parameters on the convergence history. $\omega_r = 0.7$.
(a) – (c) History for H_m for various ω_y.

In (c), $\omega_y = 0$ indicates that only the x component of grid deformation is permitted. The fixed grid solution is slower to converge, but the solution history is smoother. The initial guess was a solid cylindrical rod at 300 K. Calculations on grid of 41 × 101 points.
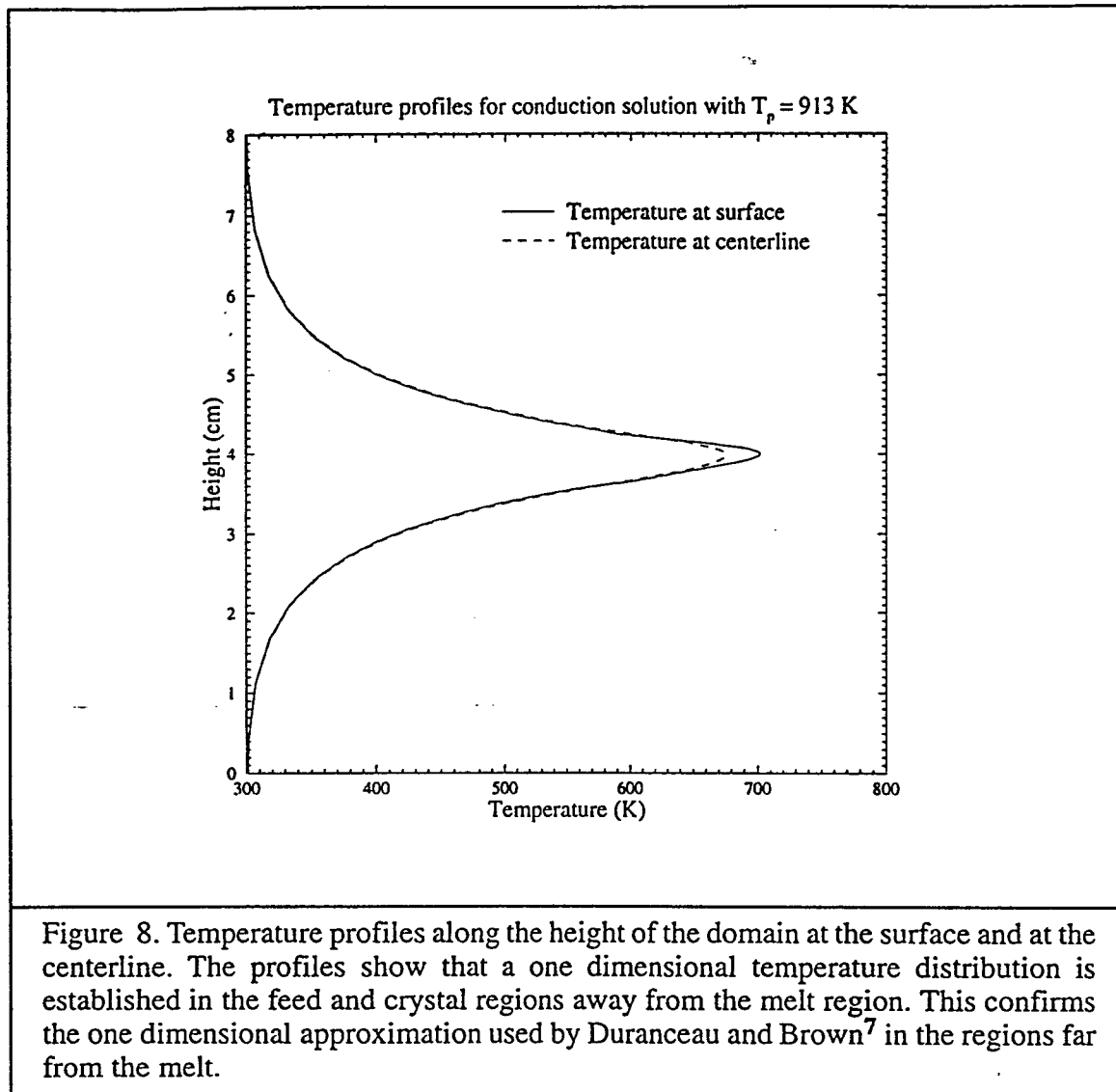
the free surface shape. Figure 7(b) shows the corresponding isotherms. The phase interfaces are illustrated by the thick lines in Fig. 7(b). The melt/crystal interface at the base of the zone is quite flat whereas the melt/feed interface at the top is slightly concave towards the melt. Figure 8 shows the temperature profiles along the entire height of the domain. The temperature profile at the surface is shown by the solid line and the profile at the centerline is shown by the dashed line. It is observed that the temperature distribution in the solid regions becomes essentially one dimensional away from the melt zone. This confirms the assumption made by Duranceau and Brown[7] in their

(a) $H_m = 0.665$ cm,
$H_c = 0.685$ cm,
$P_L = 1184$ dynes/cm^2

(b) $\Delta T = 9.98$ K, $T_{max} = 702.17$ K,
$T_{min} = 300.00$ K.

Figure 7. Heat conduction solutions with $T_p = 913$ K.
(a) Grid and boundary shape.
(b) Isotherm distribution showing the isotherm distribution on the grid of
41×101 points. The interfaces are denoted by the thick lines.

conduction–capillarity model which imposed a one dimensional temperature distribution in regions far from the melt zone in order to reduce the computational load. The present computations help to justify this assumption and also designate the regions in which a one dimensional distribution can be prescribed.

5. Grid Refinement Study and Assessment

A series of calculations have been conducted with parameters chosen so as to facilitate comparison with the solutions of Lan[15]. The heater temperature was set to 813 K. Starting with the conduction–capillarity solution, the effects of buoyancy induced convection and thermocapillary convection have been successively incorporated. For all computations, the convergence history of important quantities such as the height of the zone at the free surface, H_m, the height of the zone at the centerline, H_c, and the heat flux balance has been monitored. These calculations employ the second order accurate central difference scheme for the convection and diffusion terms in the

Figure 8. Temperature profiles along the height of the domain at the surface and at the centerline. The profiles show that a one dimensional temperature distribution is established in the feed and crystal regions away from the melt region. This confirms the one dimensional approximation used by Duranceau and Brown[7] in the regions far from the melt.

discretized form of the Navier–Stokes equations. These calculations were carried out to assess the present computations with those of Lan[15] in terms of accuracy and numerical diffusion. The study by Lan[15] and the other works cited, have used a first order upwind scheme to discretize the convection terms.

5.1 Grid

Two grids have been used for the accuracy assessment, a grid of 41 × 101 points and a refined grid of 81 × 181 points.
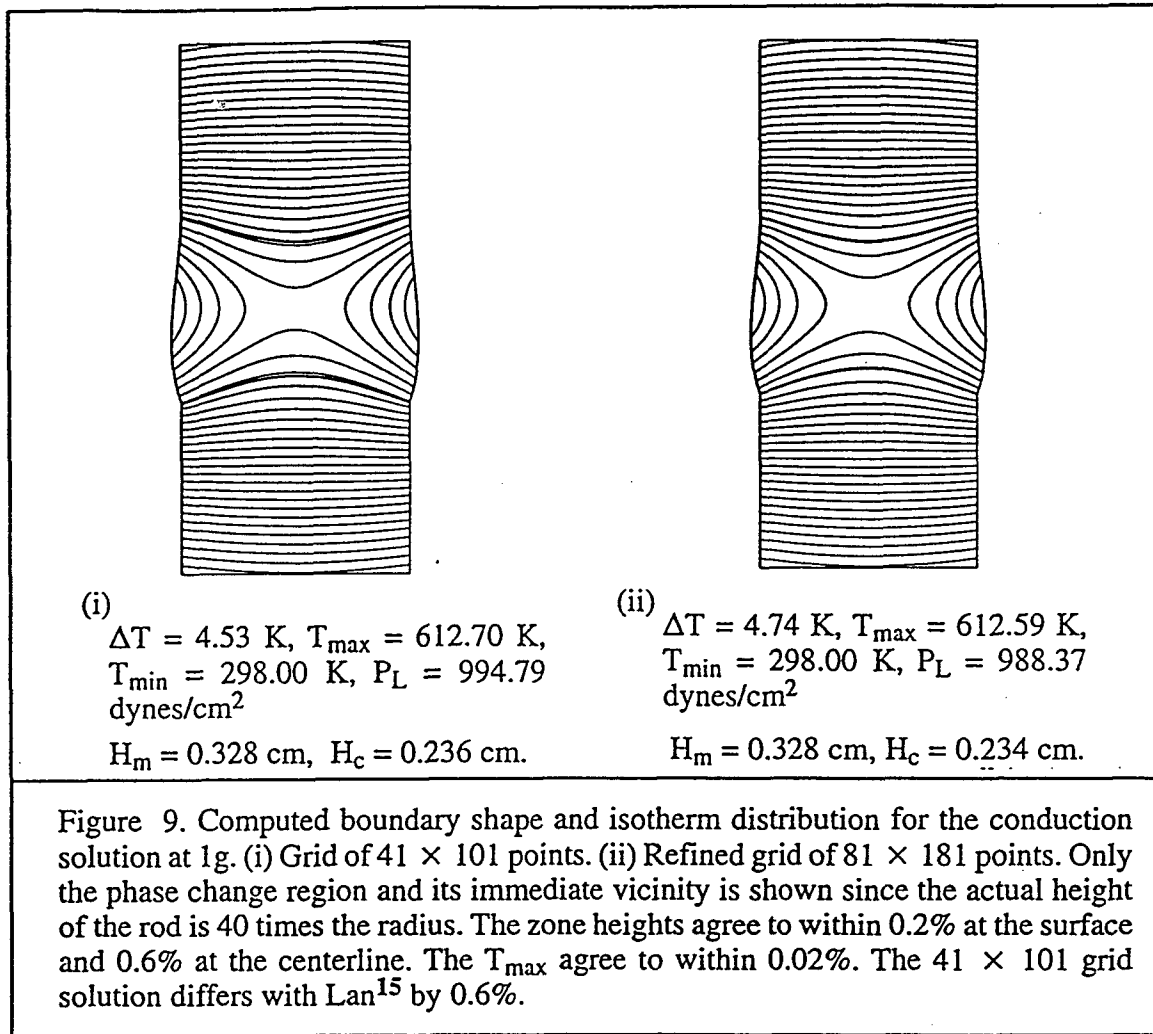
(i) 41 × 101 grid

This grid has 41 points in the radial direction with a spacing of 0.002 cm at the meniscus and 0.008 cm at the symmetry boundary distributed by fitting a cubic polynomial. In the vertical direction, the phase change zone has 61 points distributed by a cubic polynomial with the spacings at each end set to 0.007 cm. The feed and crystal zones have 21 points each, distributed according to the exponential clustering by matching the spacings to the phase change zone. The grid in the phase change zone extends beyond the location of the trijunction points by 0.02 cm.

(ii) 81 × 181 grid

This grid has 81 points in the radial direction with a spacing of 0.001 cm at the meniscus and 0.004 cm at the symmetry boundary distributed by fitting a cubic polynomial. In the vertical direction, the phase change zone has 121 points distributed by a cubic polynomial with the spacings at each end set to 0.003 cm. The feed and crystal zones have 31 points each, distributed according to the exponential clustering by matching the spacings to the phase change zone. The grid in the phase change zone extends beyond the location of the trijunction points by 0.03 cm.

5.2 Heat Conduction Calculations

The initial guess was a solid cylindrical rod at 300 K. Initially, the meniscus deformation was not permitted and a cylindrical meniscus shape was imposed. A converged solution was obtained for this configuration when the zone height stopped varying and the residual for the energy equation, averaged over the control volumes, was less than 10^{-5}. This was used as the initial guess for the subsequent set of calculations with the meniscus shape computed by integrating the Young–Laplace equation. The zone height is a very sensitive indicator of solution convergence since it occupies a small fraction of the overall length of the domain. Calculations have been carried out with the meniscus shapes computed under both normal and under microgravity (0g) conditions to assess the impact of meniscus shape on the solution.
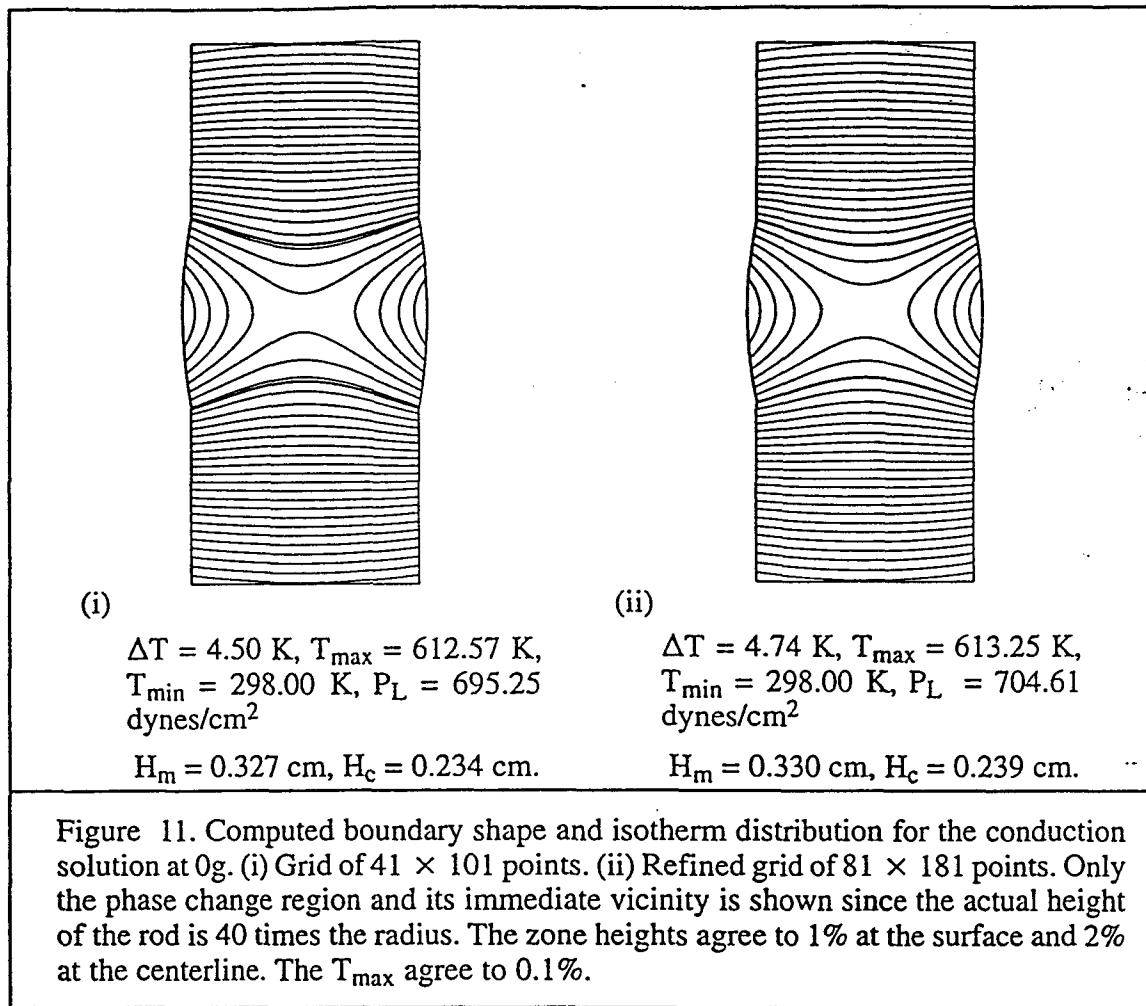
Figure 9 (i) and (ii) show the computed shape and isotherm distribution obtained on the 41 × 101 grid and the 81 × 181 grid respectively. The zone heights and the maximum temperature, T_{max}, agree to within 0.6% and 0.2% respectively, establishing the grid independent nature of the converged solutions. The solid – liquid interfaces are shown by the thick lines. The meniscus has a pronounced bulge at the base of the zone due to the combined action of gravity and the density change due to phase change. The solid liquid interfaces show mild convexity towards the melt. The solution on the 41 × 101 grid agrees with the solution of Lan[15], the difference in T_{max} being less than 0.6%. Figure 10 (a) and (b) show that the temperature profiles obtained on the 41 × 101 grid and the 81 × 181 grid are identical. Figure 10(c) and (d) show that the temperature distribution in the feed and crystal regions becomes one–dimensional far away from the zone.

(i)
$\Delta T = 4.53$ K, $T_{max} = 612.70$ K, $T_{min} = 298.00$ K, $P_L = 994.79$ dynes/cm^2

$H_m = 0.328$ cm, $H_c = 0.236$ cm.

(ii)
$\Delta T = 4.74$ K, $T_{max} = 612.59$ K, $T_{min} = 298.00$ K, $P_L = 988.37$ dynes/cm^2

$H_m = 0.328$ cm, $H_c = 0.234$ cm.

Figure 9. Computed boundary shape and isotherm distribution for the conduction solution at 1g. (i) Grid of 41 × 101 points. (ii) Refined grid of 81 × 181 points. Only the phase change region and its immediate vicinity is shown since the actual height of the rod is 40 times the radius. The zone heights agree to within 0.2% at the surface and 0.6% at the centerline. The T_{max} agree to within 0.02%. The 41 × 101 grid solution differs with Lan[15] by 0.6%.

Figures 11 and 12 correspond to the microgravity condition. The most significant impact of microgravity on the conduction solution is on the meniscus shape. The meniscus shape now resembles a circular arc due to the absence of gravity and the solution displays symmetry about the heater location. Figure 11 shows the computed boundary shape and the isotherm distribution and also establishes the grid independence of the solutions on the 41 × 101 grid and the 81 × 181 grid. It is worth noting that the value of P_L required to maintain mass conservation in the molten zone decreases from the normal gravity case shown in Figure 9. Figure 12 compares the temperature profiles between the 41 × 101 and the 81 × 181 grids showing grid independence of the solution.

5.3 Buoyancy Driven Convection

Figures 13 – 15 show the effect of buoyancy driven convection on the solution characteristics. Thermocapillary convection has been suppressed by imposing a zero shear stress condition on the free surface. Convergence was declared when the residuals were less than 10^{-5} for the momentum equations and 10^{-7} for the energy equation. The 1–norm of the solution was less than 10^{-5} for all

Figure 10. (a) and (b) Temperature profiles showing comparison between coarse grid of 41 × 101 points and fine grid of 81 × 181 points along the entire height of the domain. (a) Temperature profile along the surface. (b) Temperature profile along the centerline.
(c) and (d) Comparison of Temperatures along the surface and the centerline. (c) 41 × 101 grid, (d) 81 × 181 grid.

the dependent variables. This is adequate for the purpose of accuracy assessment and comparison with the solutions of Lan[15]. The streamfunction is shown in Figure 13. The maximum streamfunction, Ψ_{max}, differs by less than 2%. The present solution on the 41 × 101 grid differs by 8% from the maximum streamfunction reported in Lan[15]. Figure 14 shows the corresponding isotherms. The maximum temperature, T_{max}, occurring on the free surface differs by 0.05% between the solutions and 0.4% from the solution of Lan[15]. Figure 15 (a) and (b) show identical temperature profiles for the solutions on 41 × 101 and 81 × 181 grids indicating grid independence of the solution. Figures 15(a) and (b) may be contrasted with the conduction case illustrated in Figures 10(a) and (b) showing the decrease in T_{max} due to the effectiveness of convection in heat transport. The effect of natural convection is to cause the heated melt to rise along the free surface, transfer heat to the melt–feed interface, and sink at the centerline towards the melt–crystal interface. This

26

(i)

ΔT = 4.50 K, T_{max} = 612.57 K, T_{min} = 298.00 K, P_L = 695.25 dynes/cm^2

H_m = 0.327 cm, H_c = 0.234 cm.

(ii)

ΔT = 4.74 K, T_{max} = 613.25 K, T_{min} = 298.00 K, P_L = 704.61 dynes/cm^2

H_m = 0.330 cm, H_c = 0.239 cm.

Figure 11. Computed boundary shape and isotherm distribution for the conduction solution at 0g. (i) Grid of 41 × 101 points. (ii) Refined grid of 81 × 181 points. Only the phase change region and its immediate vicinity is shown since the actual height of the rod is 40 times the radius. The zone heights agree to 1% at the surface and 2% at the centerline. The T_{max} agree to 0.1%.

causes the melt–feed interface to acquire a more distorted shape compared with the conduction solution, and the melt–crystal interface to become flatter over most of the region except close to the meniscus. The distortion of the isotherms and the upward shift in the location of T_{max} is due to the convective action. Since the Prandtl number is high, even a modest Grashof number results in a significant impact on the temperature distribution. The higher temperature gradients evident at the base of the zone also indicate that the heating takes place close to the bottom of the zone. The zone is translated upward as compared with the conduction solution due to the enhancement of heat transfer through the upper half of the domain and its suppression through the lower half.

5.4 Thermocapillary Convection

In the following set of calculations, the effect of thermocapillary convection is taken into account. As will be demonstrated, the Marangoni effect has a significant impact on the temperature distribution and the phase interfaces within the melt zone. The actual Marangoni numbers in this particular system are in the region of 5000, however, numerical stability constrained the calculations

Temperature profiles for conduction solution and deforming meniscus at 0g

Figure 12. (a) and (b) Temperature profiles showing comparison between coarse grid of 41 × 101 points and fine grid of 81 × 181 points along the entire height of the domain. (a) Temperature profile along the surface. (b) Temperature profile along the centerline.
(c) and (d) Comparison of Temperatures along the surface and the centerline. (c) 41 × 101 grid, (d) 81 × 181 grid.

to a Marangoni number of 500. Grid independence and accuracy assessments have been carried out. Computations have been carried out to assess the impact of meniscus deformation on the solid – liquid interface shape and zone size. Calculations have also been conducted to simulate float zone growth under zero–gravity conditions to simulate float zone processing in orbit. In all subsequent calculations, the convergence criteria has been set to less than 10^{-4} for the momentum equations and to less than 10^{-6} for the energy equations while ensuring that the 1–norm of the solution was less than 10^{-5}. These criteria either meet or exceed the convergence criteria specified in the literature cited previously.

(i) Normal Gravity

(a) Cylindrical meniscus

A conduction calculation with the imposed cylindrical meniscus was used as the initial guess. Figure 16(a) shows the streamfunction and Figure 16(b) shows the computed isotherms. The

(i)
$\Psi_{max} = 2.706 \times 10^{-3}$ g/s,
$\Delta\Psi = 1.87 \times 10^{-4}$ g/s

(ii)
$\Psi_{max} = 2.654 \times 10^{-3}$ g/s
$\Delta\Psi = 1.84 \times 10^{-4}$ g/s
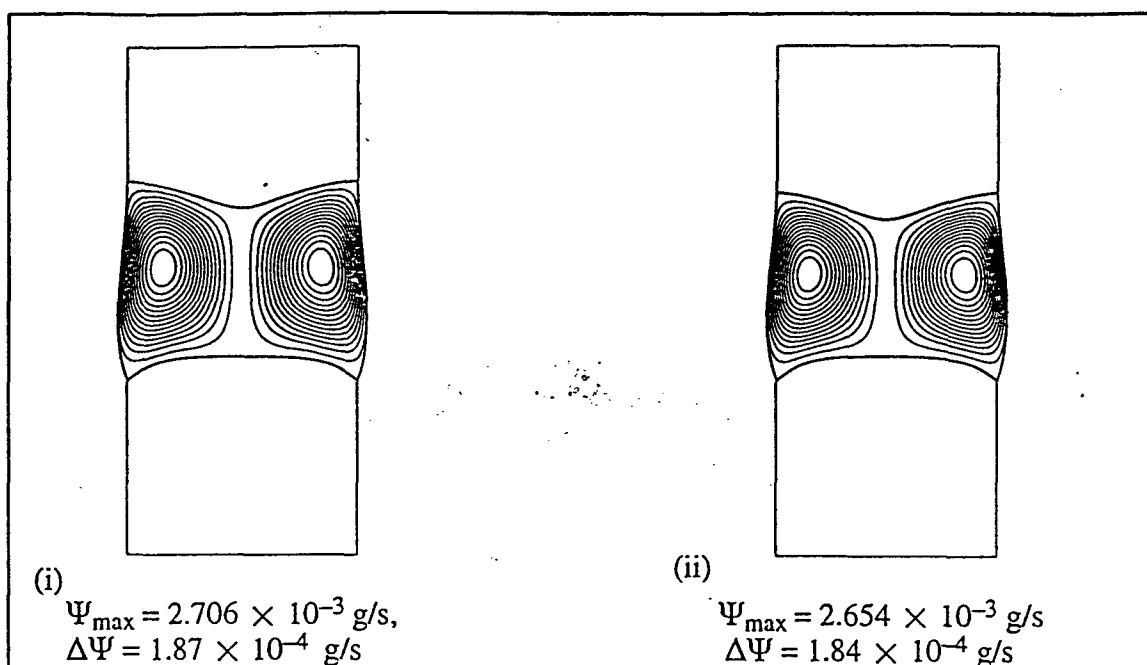
Figure 13. Streamfunction and phase interfaces on (i) 41 × 101 and (ii) 81 × 181 grids. (i) and (ii) differ by less than 2%.
The 41 × 101 grid solution differs from Lan[15] by 8%.

(i)
$\Delta T = 3.99$ K, $T_{max} = 601.03$ K,
$T_{min} = 301.23$ K
$H_m = 0.344$ cm, $H_c = 0.257$ cm
$P_L = 995.46$ dynes/cm^2

(ii)
$\Delta T = 4.07$ K, $T_{max} = 600.76$ K,
$T_{min} = 300.93$ K
$H_m = 0.335$ cm, $H_c = 0.244$ cm
$P_L = 995.31$ dynes/cm^2.
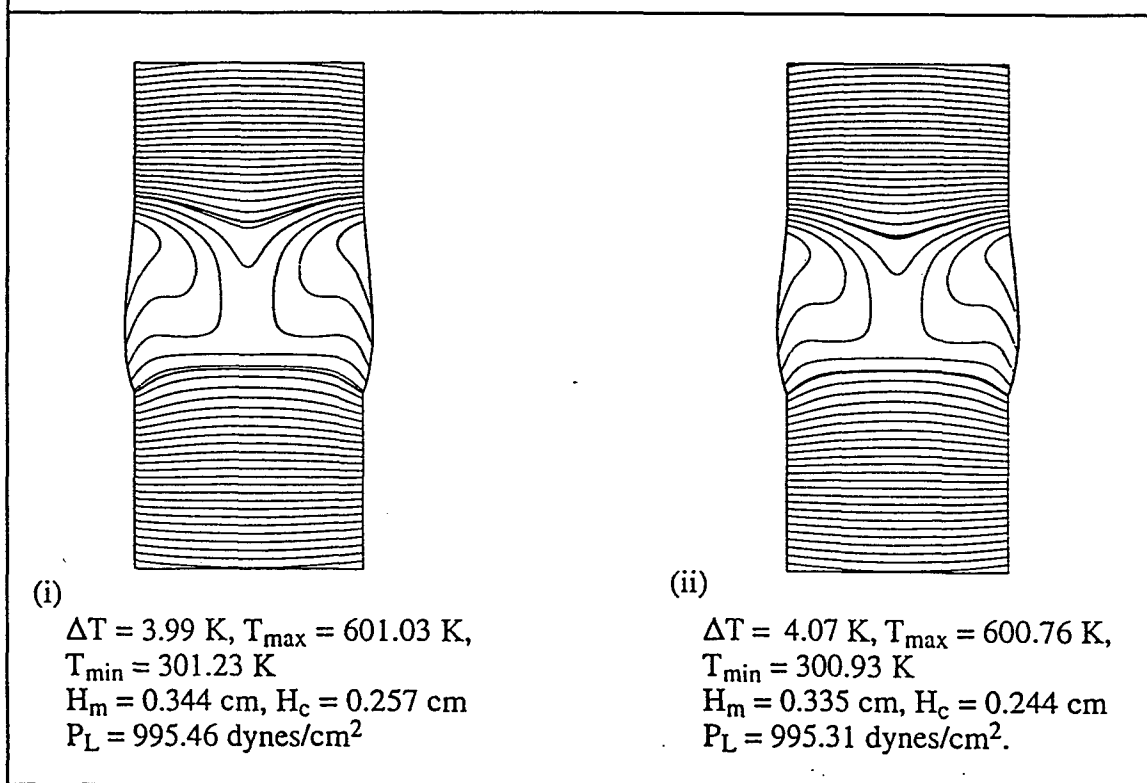
Figure 14. Isotherms on (i) 41 × 101 and (ii) 81 × 181 grids. T_{max} differs by 0.05%.
The 41 × 101 grid solution differs from the solution of Lan[15] by 0.4%.

Figure 15. (a) and (b) Temperature profiles showing comparison between coarse grid of 41 × 101 points and fine grid of 81 × 181 points along the entire height of the domain. (a) Temperature profile along the surface. (b) Temperature profile along the centerline.
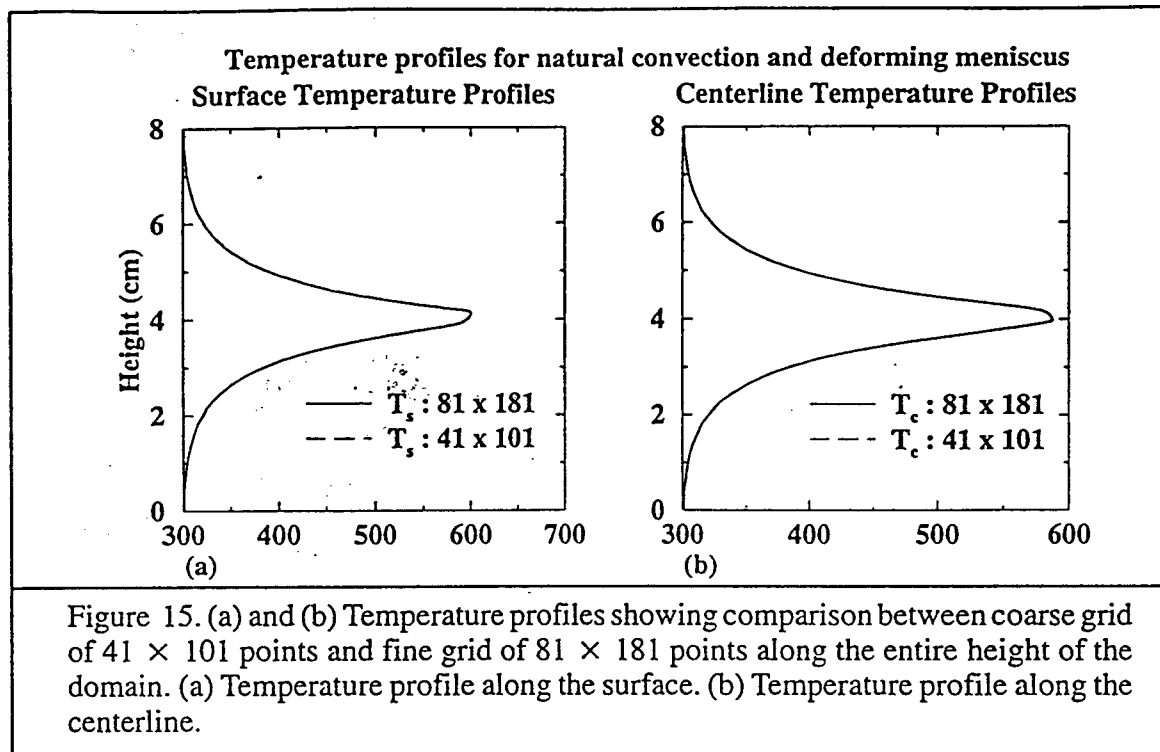
streamfunction pattern shows the interaction between natural and thermocapillary convection. Two large convection rolls are apparent in the upper half of the domain where the thermocapillary convection aids natural convection. In the lower part of the zone, two small counter–rotating loops are formed where the thermocapillary effect opposes natural convection. The isotherm plots show that the location of T_{max} is displaced upwards and its value is less as compared with the conduction case. The distortion of the phase interfaces is clearly evident especially away from the centerline. Figure 17(a) and (b) provide a comparison of the temperature profiles on the two grid resolutions considered. The temperature distribution is almost identical on the two grids.

(b) Deformed meniscus

The previous calculation is used as the starting guess and now the meniscus is allowed to deform according to the requirement of mass conservation and the Young–Laplace equation. Figure 18(a) shows the streamfunction on the 41 × 101 grid and the 81 × 181 grid. Figure 18(b) shows the corresponding isotherms. Allowing the meniscus to deform increases the free surface area thereby increasing the convection strength of all the four convection cells in the domain. Since the maximum Temperature, T_{max}, is virtually unaffected, this implies a larger heat flux through the domain resulting in a taller melt zone. The increased strength of the upper convection rolls also causes the melt–crystal interface at the lower end of the melt zone to become flatter at the centerline, but acquire increased distortion close to the free surface. The maximum streamfunction differs by 9.7% between the solutions on the grid of 41 × 101 points and the grid of 81 × 181 points. Figure 19(a)

(i)
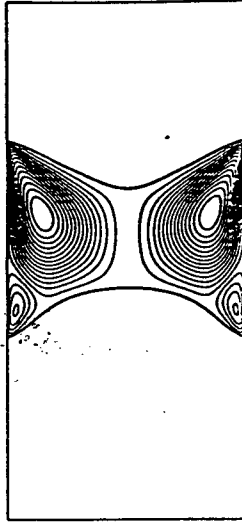
$\Psi_{max} = 1.733 \times 10^{-3}$ g/s,
$\Delta\Psi = 1.20 \times 10^{-4}$ g/s
$\Psi_1 = -4.433 \times 10^{-4}$ g/s

(ii)
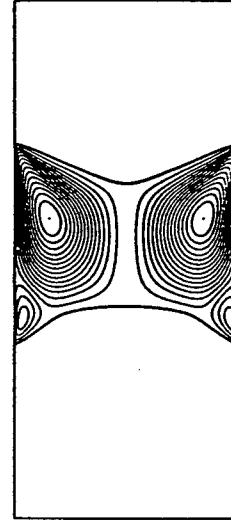
$\Psi_{max} = 2.242 \times 10^{-3}$ g/s
$\Delta\Psi = 1.55 \times 10^{-4}$ g/s
$\Psi_1 = -4.840 \times 10^{-4}$ g/s

(a) Streamfunction and phase interfaces on (i) 41 $\times$ 101 and (ii) 81 $\times$ 181 grids.

(i)
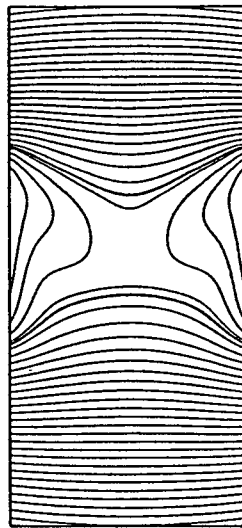
$\Delta T = 3.90$ K, $T_{max} = 596.97$ K,
$T_{min} = 300.85$ K
$H_m = 0.331$ cm, $H_c = 0.166$ cm

(ii)
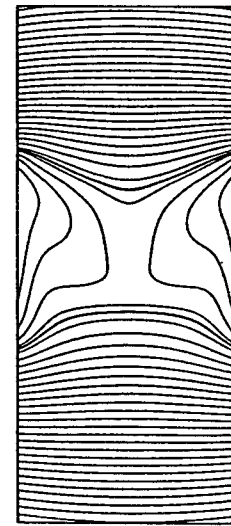
$\Delta T = 4.04$ K, $T_{max} = 597.81$ K,
$T_{min} = 300.94$ K
$H_m = 0.365$ cm, $H_c = 0.223$ cm

(b) Isotherms on (i) 41 $\times$ 101 and (ii) 81 $\times$ 181 grids.

Figure 16. Solution for Ma = 500, 1g, and fixed cylindrical meniscus.

Figure 17. (a) and (b) Temperature profiles showing comparison between coarse grid of 41 × 101 points and fine grid of 81 × 181 points along the entire height of the domain. (a) Temperature profile along the surface. (b) Temperature profile along the centerline.
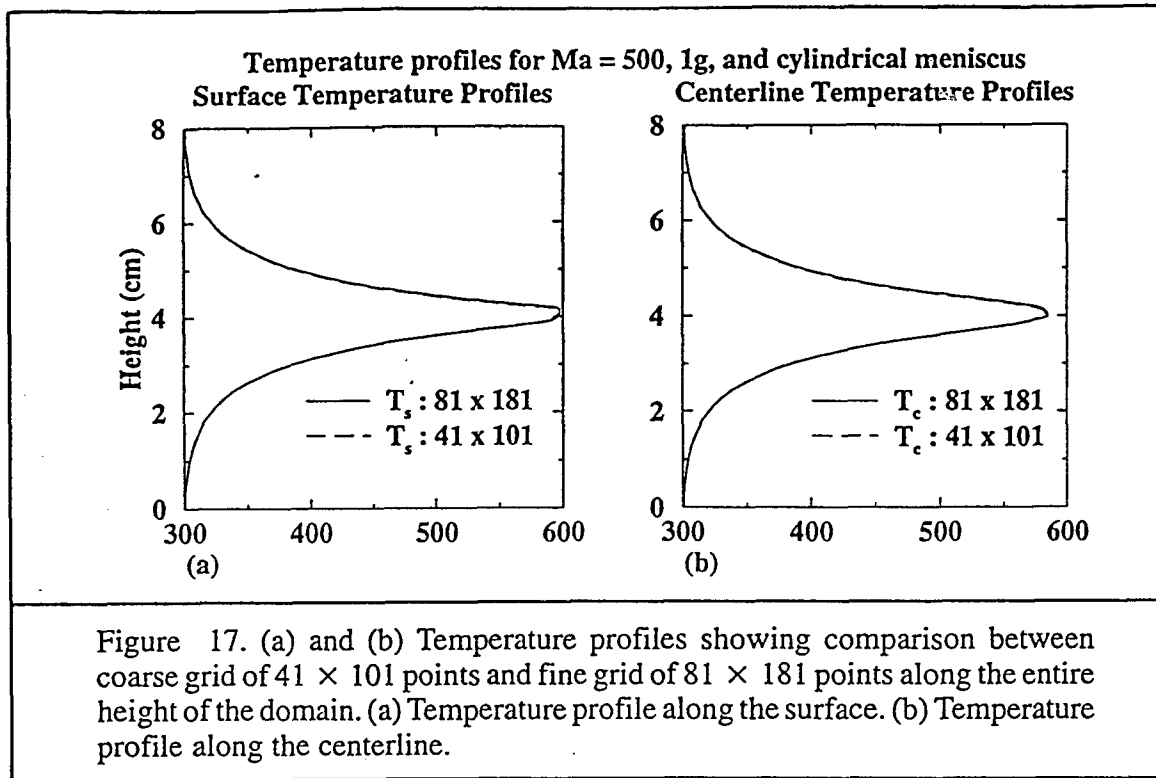
and (b) compare the temperature profiles of the two solutions which are indistinguishable. Figure 19(c) and (d) show the upward displacement of the location of T_{max} as compared with the conduction solutions and the establishment of the one dimensional temperature distribution in the feed and crystal regions away from the melt zone.

(ii) Zero Gravity

(a) Cylindrical meniscus

A conduction solution with an imposed cylindrical meniscus was used as the initial guess. Figure 20(a) shows the streamfunction and Figure 20(b) the isotherm distribution. It is immediately evident that the solution is symmetrical about y = 4 cm which is the heater location. Four counter–rotating flow loops are evident in the melt zone and these convection rolls cause the isotherm distribution to be pulled towards the free surface. Convection suppresses heat transfer to the centerline causing the characteristic convexity of the phase interfaces towards the melt. The maximum streamfunction is lower than that in the normal gravity case, but the flattening effect of natural convection on the melt–crystal interface is absent. Figure 21(a) and (b) compare the temperature profiles on the two grids and it may be observed that the two solutions are nearly identical.

(i)
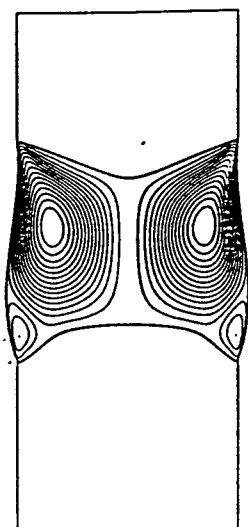
$\Psi_{max} = 2.880 \times 10^{-3}$ g/s,
$\Delta\Psi = 1.99 \times 10^{-4}$ g/s
$\Psi_1 = -4.975 \times 10^{-4}$ g/s

(ii)
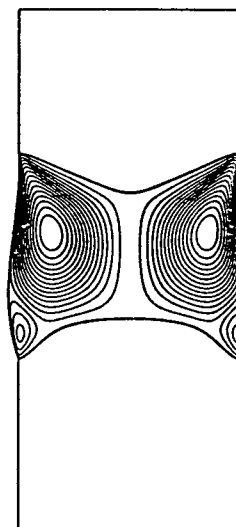
$\Psi_{max} = 2.623 \times 10^{-3}$ g/s
$\Delta\Psi = 1.81 \times 10^{-4}$ g/s
$\Psi_1 = -5.160 \times 10^{-4}$ g/s

(a) Streamfunction and phase interfaces on (i) 41 × 101 and (ii) 81 × 181 grids.

(i)
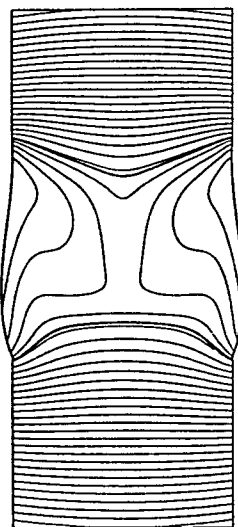
$\Delta T = 4.01$ K, $T_{max} = 598.66$ K,
$T_{min} = 301.33$ K
$H_m = 0.394$ cm, $H_c = 0.260$ cm.
$P_L = 1011.47$ dynes/cm^2.

(ii)
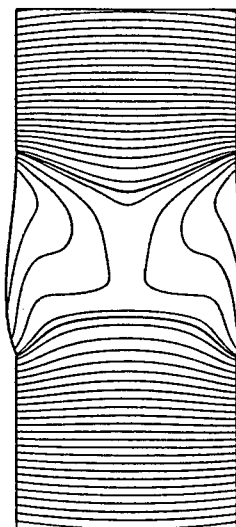
$\Delta T = 4.07$ K, $T_{max} = 597.87$ K,
$T_{min} = 300.94$K
$H_m = 0.372$ cm, $H_c = 0.227$ cm
$P_L = 1011.52$ dynes/cm^2.

(b) Isotherms on (i) 41 × 101 and (ii) 81 × 181 grids.

Figure 18. Solution for Ma = 500, 1g, and computed meniscus.

33

Figure 19. (a) and (b) Temperature profiles showing comparison between coarse grid of 41×101 points and fine grid of 81×181 points along the entire height of the domain. (a) Temperature profile along the surface. (b) Temperature profile along the centerline.
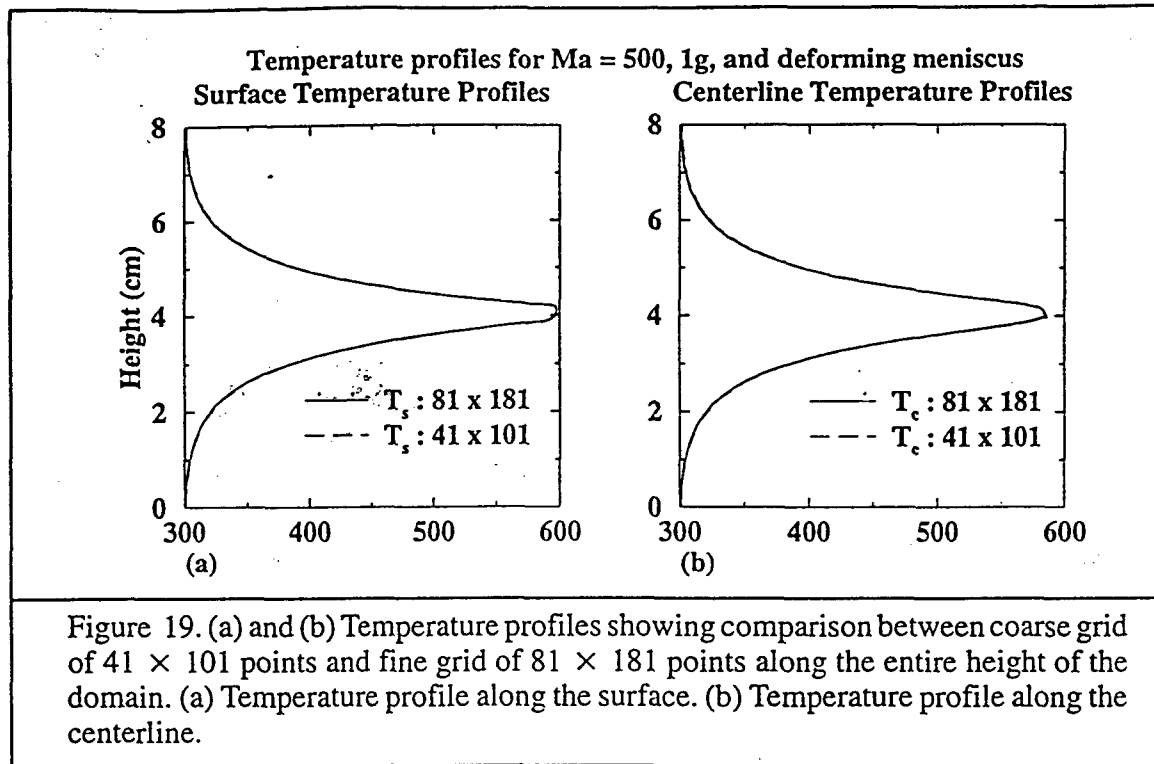
(b) Deformed meniscus

The previously computed solution was used as the initial guess and the meniscus was allowed to deform in response to the needs of global mass conservation and the Young–Laplace equation. For this case, momentum residuals of less than 5×10^{-4} could not be achieved on the grid of 41×101 points. Figure 22(a) shows the streamfunction and Figure 22(b) shows the isotherm distribution on the grid of 41×101 and 81×181 points. It is observed that the convection rolls increase in strength since the meniscus deformation results in a larger surface area over which the surface tension gradients can act. These factors also result in a larger heat flux being transported through the domain and the height of the melt zone to increase. The maximum streamfunction differs by 6.6% between the solution on the 41×101 grid and 81×181 grid. Figure 23(a) and (b) show that the temperature profiles obtained on the two grids are identical.

5.5 CPU Time

The CPU time for a computation that includes meniscus deformation is approximately 0.2 ms per iteration per grid point on a single cpu DEC AlphaStation 200 166 MHz workstation and approximately 46 μs on a single cpu of the CRAY YMP.

34

(i)
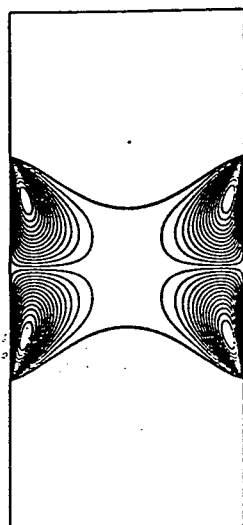
$\Psi_{max} = 1.013 \times 10^{-3}$ g/s,
$\Delta\Psi = 7.00 \times 10^{-5}$ g/s

(ii)
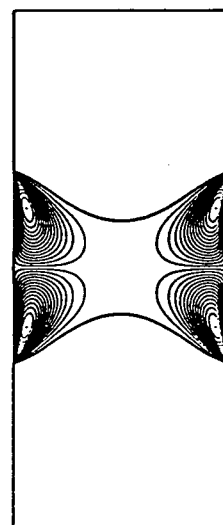
$\Psi_{max} = 0.954 \times 10^{-3}$ g/s
$\Delta\Psi = 6.58 \times 10^{-5}$ g/s

(a) Streamfunction and phase interfaces on (i) 41 × 101 and (ii) 81 × 181 grids.

(i)
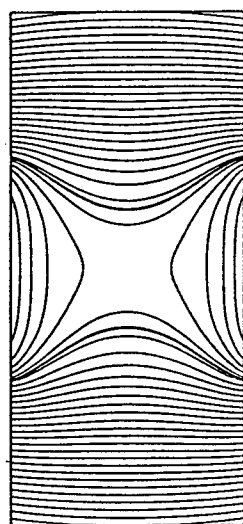
$\Delta T = 3.65$ K, $T_{max} = 600.18$ K,
$T_{min} = 298.00$ K
$H_m = 0.374$ cm, $H_c = 0.199$ cm

(ii)
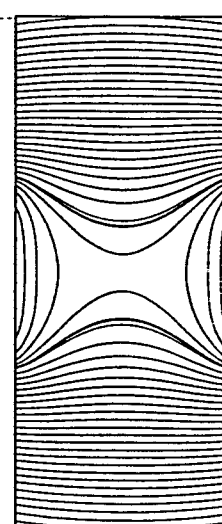
$\Delta T = 4.14$ K, $T_{max} = 599.50$ K,
$T_{min} = 298.00$ K
$H_m = 0.356$ cm, $H_c = 0.173$ cm

(b) Isotherms on (i) 41 × 101 and (ii) 81 × 181 grids.

Figure 20. Solution for Ma = 500, 0g, and fixed cylindrical meniscus.

Figure 21. (a) and (b) Temperature profiles showing comparison between coarse grid of 41 × 101 points and fine grid of 81 × 181 points along the entire height of the domain. (a) Temperature profile along the surface. (b) Temperature profile along the centerline.
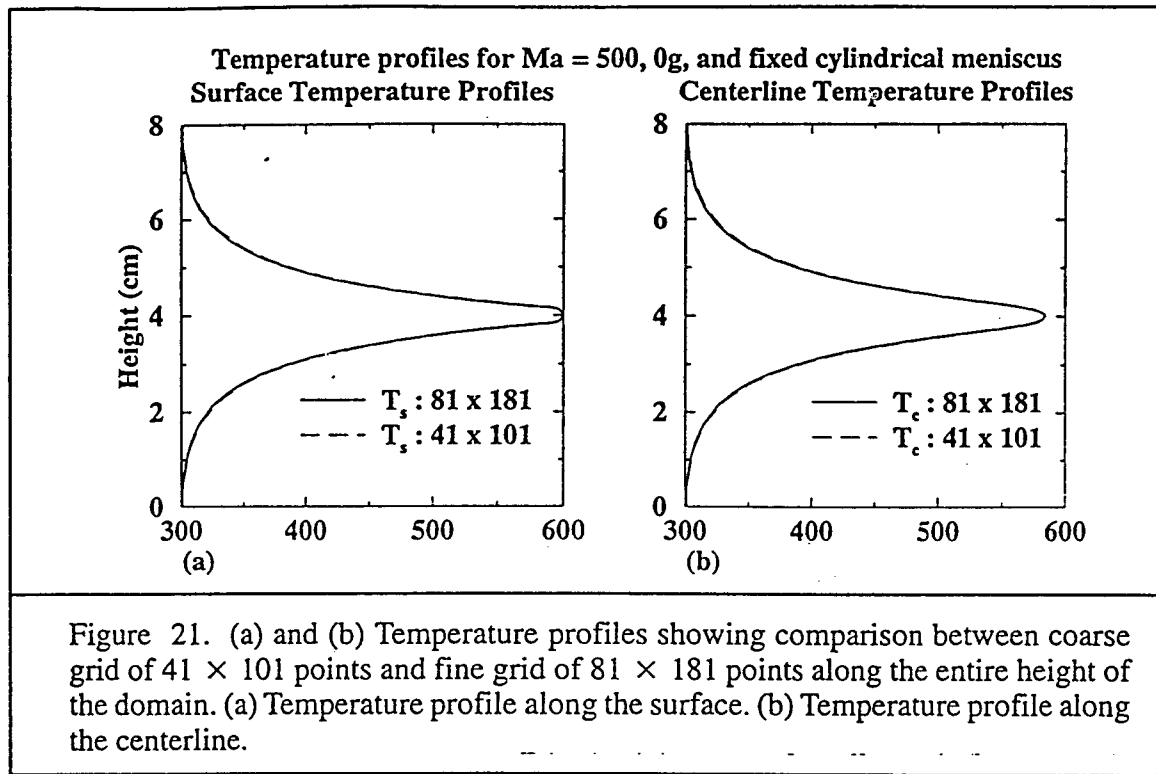
6. Conclusion

A moving boundary technique has been developed in the context of the SIMPLE algorithm and the enthalpy method for the computation of convective heat transfer and solidification in the float zone. A general multi–block technique for algebraic grid generation has been developed to fit curved free surfaces and adaptively enclose the phase change regions in solidification processes. Underrelaxation procedures have been developed to ensure the stability of the numerical procedure. Care has been taken to ensure that grid quality is maintained after the grid generation procedure with appropriate error recovery in case of failure of the grid generation procedure.

Computations have been carried out to assess the robustness, stability and accuracy of the convective heat transfer and phase change computations via grid refinement and comparison with the solutions of Lan[15]. The solutions of Lan[15] were based on front tracking rather than the enthalpy method, used the streamfunction–vorticity formulation of the Navier–Stokes equations as opposed to the primitive variables formulation used in the present work, and employed first order upwind schemes for the convection schemes rather than the second order central difference scheme employed in this study. It is found that for the conduction–capillarity and buoyancy driven convection calculations, grid independent solutions can be obtained even on 41 x 101 grids. However, when thermocapillary convection is taken into account, grid refinement from the 41 x 101 grid to the 81 x 181 grid exhibits quantitative differences although not qualitative differences. Good

(i)

$\Psi_{max} = 1.170 \times 10^{-3}$ g/s,
$\Delta\Psi = 8.07 \times 10^{-5}$ g/s

(ii)

$\Psi_{max} = 1.097 \times 10^{-3}$ g/s
$\Delta\Psi = 7.57 \times 10^{-5}$ g/s

(a) Streamfunction and phase interfaces on (i) 41 × 101 and (ii) 81 × 181 grids.

(i)

$\Delta T = 3.63$ K, $T_{max} = 600.89$ K,
$T_{min} = 298.00$ K
$H_m = 0.406$ cm, $H_c = 0.219$ cm
$P_L = 642.25$ dynes/cm^2

(ii)

$\Delta T = 4.23$ K, $T_{max} = 599.95$ K,
$T_{min} = 300.91$K
$H_m = 0.381$ cm, $H_c = 0.183$ cm
$P_L = 654.94$ dynes/cm^2.

(b) Isotherms on (i) 41 × 101 and (ii) 81 × 181 grids.
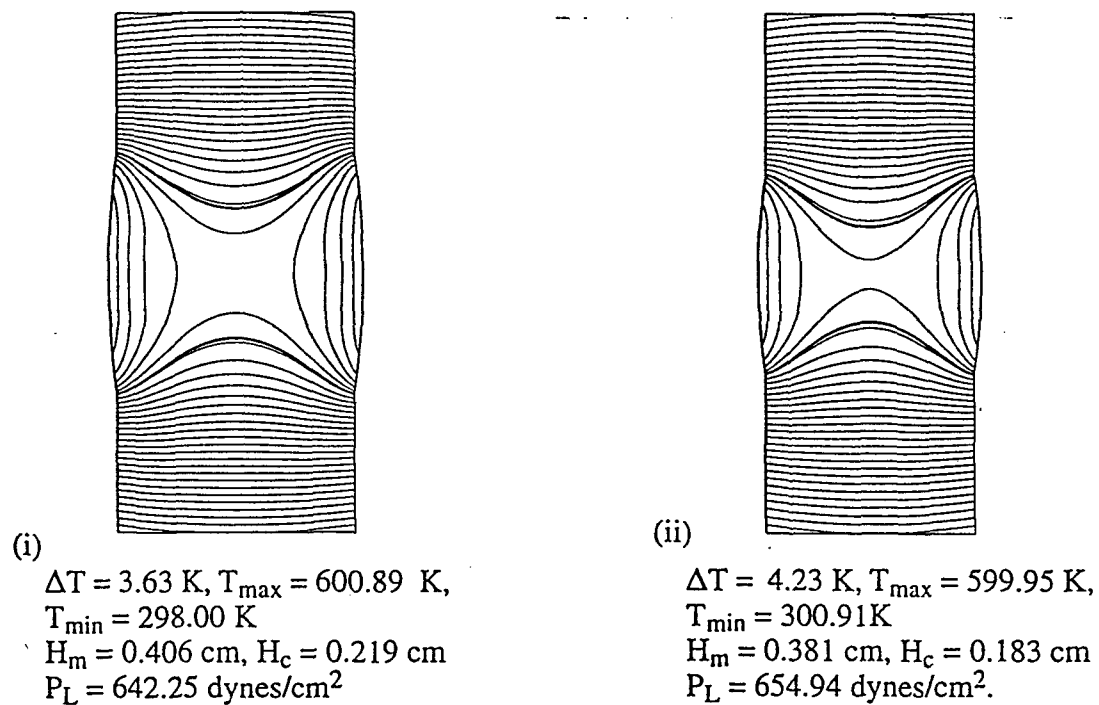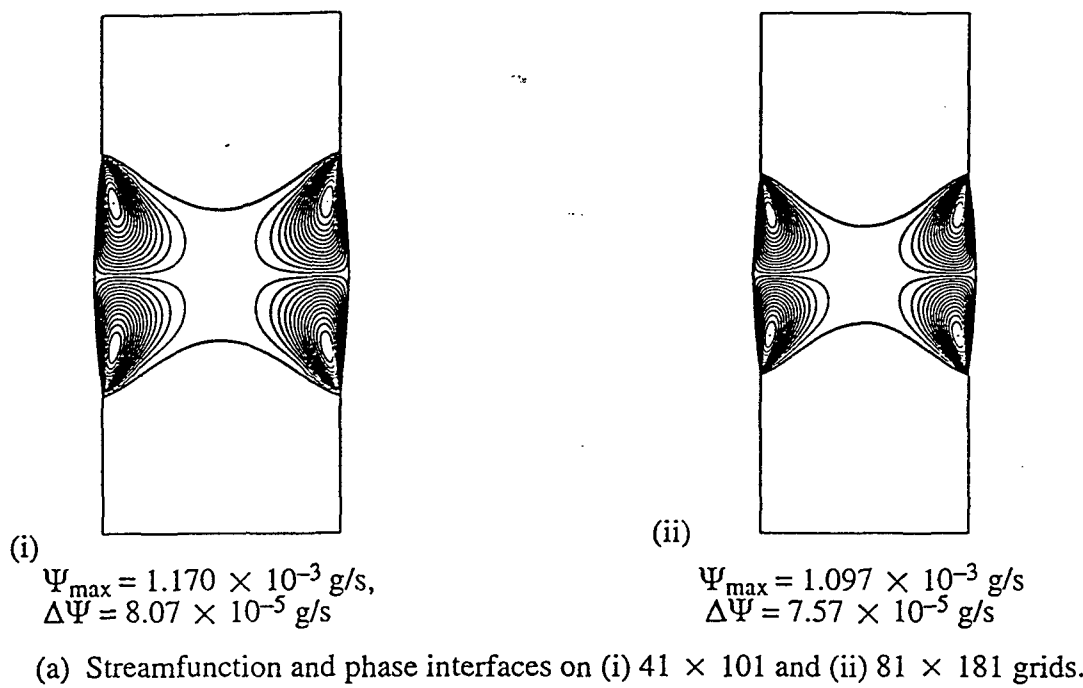
Figure 22. Solution for Ma = 500, 0g, and computed meniscus.

Temperature profiles for Ma = 500, 0g, and deforming meniscus

Figure 23. (a) and (b) Temperature profiles showing comparison between coarse grid of 41 × 101 points and fine grid of 81 × 181 points along the entire height of the domain. (a) Temperature profile along the surface. (b) Temperature profile along the centerline.
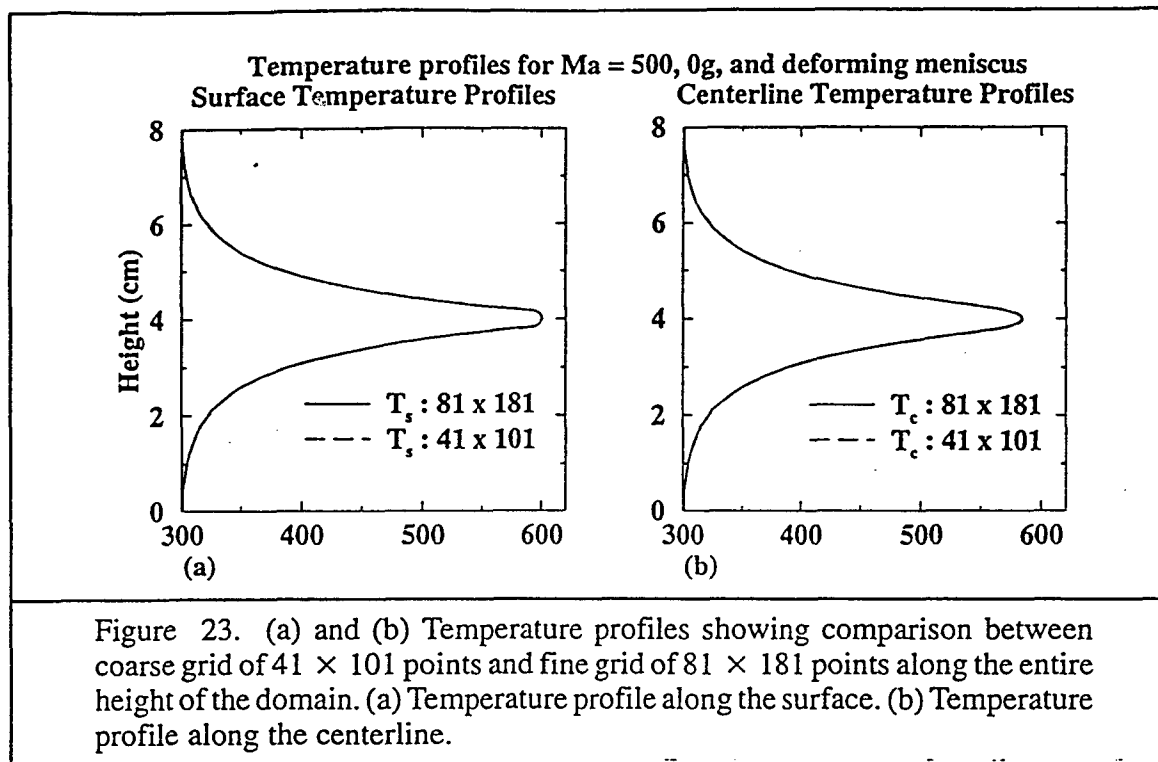
comparison has been obtained with the solutions of Lan[15] for the conduction–capillarity and natural convection solutions with similar boundary shapes and grid distributions.

Computations have been carried out to assess the impact of free surface deformation as well as microgravity environment on the float zone. The free surface deformation results in a larger surface area at the meniscus resulting in a higher strength of thermocapillary convection as well as an increase in the heat flux through the system. Thus, for the parameters and regimes considered in this study, the free surface deformation has a quantitative but not qualitative impact on the melt zone. The microgravity environment, on the other hand, results in a suppression of buoyancy induced convection as well as a significant impact on the meniscus shape. However, at the operating parameters considered in this study, the microgravity environment does not offer any significantly reduced convection since the surface tension gradient is always present due to the thermal inhomogeneities along the meniscus.

The difference between the present study and the previous studies lies in the use of the enthalpy method as opposed to interface tracking and the use of a flexible, multi–block grid generation procedure that, in conjunction with the use of the enthalpy method, can adapt to a wide range of zone lengths including the fully solid case. The procedure has been designed to accommodate unsteady computations, to be presented in a subsequent study, which can use a fully solid rod as the initial condition. A front tracking procedure as formulated by previous studies[9,15] cannot handle the small zone sizes that will be present initially. The use of the enthalpy method in this study makes it

unnecessary to fit the solid – liquid interfaces giving additional flexibility. This study also uses higher order convection schemes – the second order central difference scheme as opposed to the first order upwind scheme used in the previous studies. Grid refinement studies have been carried out employing substantially higher grid resolutions than the previous studies. The study indicates that higher grid resolutions are needed to due to the high strength of thermocapillary convection in the present system.

Acknowledgments

References

1. Shyy, W. and Rao, M. M. 1995 "Calculation of Meniscus Shapes and Transport Processes in Float Zone," *Intl. J. of Heat and Mass Transf.*, 38, pp 2281 – 2295.

2. Kobayashi, N 1984 "Computer Simulation of the Steady Flow in a Cylindrical Floating Zone under Low Gravity," *J. Crystal Growth*, 66, pp. 63 – 72.

3. Kobayashi, N 1988 "Steady Convection caused by the Temperature Inhomogeneity in a Cylindrical Floating Zone," *Japanese J. Appl. Phys.*, 27, pp. 20 – 24.

4. Young, G. W. and Chait, A. 1990 "Surface Tension Driven Heat, Mass and Momentum Transport in a Two-Dimensional Float Zone," *J. Crystal Growth*, 106, pp. 445 – 466.

5. Neitzel, G. P., Hyer, J. R. and Jankowski, D. F. 1990 "Thermocapillary Convection in a Model Float–Zone," AIAA Paper No. 90–0406.

6. Chu, C.-F. and Chen, J.-C. 1995 "Numerical Computation of Fluid Flow of Floating-Zone Crystal Growth of Molybdenum," *Intl. J. Heat Mass Transf.*, 38, pp. 1841 – 1853.

7. Duranceau, J. L. and Brown, R. A. 1986 "Thermal-Capillary Analysis of Small-Scale Floating Zones," *J. Crystal Growth*, 75, pp. 367 – 389.

8. Lan, C. W. and Kou, S. 1990 "Thermocapillary Flow and Melt/Solid Interfaces in Floating-Zone Crystal Growth under Microgravity," *J. Crystal Growth*, 102, pp. 1043 – 1058.

9. Lan, C. W. and Kou, S. 1991 "Heat Transfer, Fluid Flow and Interface Shapes in Floating-Zone Crystal Growth," *J. Crystal Growth*, 108, pp. 351 – 366.

10. Lan, C. W. and Kou, S. 1992 "Shortened Floating Zone Crystal Growth under Normal Gravity," *J. Crystal Growth*, 119, pp. 281 – 291.

11. Chan, Y. T. and Choi, S. K. 1992 "Numerical Simulations of Inductive–Heated Float–Zone Growth," *J. Appl. Phys.*, 72, pp. 3741 – 3749.

12. Chan, Y. T. 1995 "Crystal Growth," in *Computational Modeling in Semiconductor Processing*, M. Meyyappan (editor), Artech House, Boston.

13. Mühlbauer, A., Muiznieks, A., Virbulis, J., Lüdge, A., and Riemann, H. 1995 "Interface Shape, Heat Transfer and Fluid Flow in the Floating Zone Growth of Large Silicon Crystals with the Needle–eye Technique," *J. Crystal Growth*, 151, pp. 66 – 79.

14. Lan, C. W. and Kou, S. 1993 "Effect of Rotation on Radial Dopant Segregation in Microgravity Floating-zone Crystal Growth," *J. Crystal Growth*, **133**, pp. 309 – 321.

15. Lan, C. W. 1994 "Newton's Method for solving Heat Transfer, Fluid Flow and Interface Shapes in a Floating Molten Zone," *Intl. J. Numer. methods Fluids*, **19**, pp. 41 – 65.

16. Chen, H., Saghir, M. Z., Quon, D. H. H. and Chehab, S. 1994 "Numerical Study on Transient Convection in Float Zone Induced by g–jitters," *J. Crystal Growth*, **142**, pp. 362 – 372.

17. Grugel, R. N., Shen, X. F., Anilkumar, A. V. and Wang, T. G. 1994 "The Influence of Vibration on Microstructural Uniformity during Floating–Zone Crystal Growth," *J. Crystal Growth*, **142**, pp. 209 – 214.

18. Hu, W. R., Shu, J. Z., Zhou, R. and Tang, Z. M. 1994 "Influence of Liquid Bridge Volume on the Onset of Oscillation in Floating Zone Convection. I. Experiments," *J. Crystal Growth*, **142**, pp. 379 – 384.

19. Tang, Z. M. and Hu, W. R. 1994 "Influence of Liquid Bridge Volume on the Onset of Oscillation in Floating Zone Convection. II. Numerical Simulation," *J. Crystal Growth*, **142**, pp. 385 – 391.

20. Lee, J., Lee, D.–J. and Lee, J. H. 1995 "On the Mechanism of Oscillation in a Simulated Floating Zone," *J. Crystal Growth*, **152**, pp. 341 – 346.

21. Yeckel, A., Salinger, A. G. and Derby, J. J. 1995 "Theoretical Analysis and Design Considerations for Float–Zone Refinement of Electronic Grade Silicon Sheets," *J. Crystal Growth*, **152**, pp. 51 – 64.

22. Levenstam, M., Amberg, G., Carlberg, T. and Andersson, M. 1996 "Experimental and Numerical Studies of Thermocapillary Convection in a Floating Zone like Configuration," *J. Crystal Growth*, **158**, pp. 224 – 230.

23. Shyy, W. and Rao, M. M. 1994 "Enthalpy Based Formulations for Phase Change Problems with Application to g–jitter," AIAA Paper No. 93–2831, also *Microgravity Sci. and Tech.*, 7, pp. 441–491.

24. Shyy, W. 1994 *Computational Modeling for Fluid Flow and Interfacial Transport*, Elsevier, Amsterdam, The Netherlands.

25. Shyy, W., Udaykumar, H. S., Rao, M. M., and Smith, R. W. 1996 *Computational Fluid Dynamics with Moving Boundaries*, Taylor & Francis, Washington, D. C.

26. Patankar, S. V. 1980 *Numerical Heat Transfer and Fluid Flow*, Hemisphere Publishing Corporation, Washington, D. C.

Simulation and measurement of a vertical Bridgman growth system for β-NiAl crystal

H. OUYANG† and W. SHYY‡

Department of Aerospace Engineering, Mechanics and Engineering Science, University of Florida, Gainesville, FL 32611, U.S.A.

and

V. I. LEVIT and M. J. KAUFMAN

Department of Materials Science and Engineering, University of Florida, Gainesville, FL 32611, U.S.A.

Abstract—A coordinated theoretical and experimental study of the temperature distribution inside a customized vertical Bridgman system for growing β-NiAl crystal has been conducted. The theoretical model accounts for the combined effects of phase change dynamics, the coupled heat transfer processes of conduction, convection and radiation, variable material properties, and complex geometry pertaining to the system. Comparisons between numerical predictions and experimental measurements show satisfactory agreement. The accuracy of the melting temperature of NiAl with stoichiometric composition, along with important processing parameters such as interface curvatures and temperature gradients across the interface, have been discussed in detail. Also assessed are possibilities of improving the solidification process, including coating the ampoule outer wall with a material of high radiative emissivity or decreasing the ampoule wall thickness. ©

1. INTRODUCTION

The physical and mechanical properties of nickel aluminum (NiAl) depend strongly on both composition and temperature [1–6]. At stoichiometric composition (50 at.% Ni, 50 at.% Al), NiAl has its lowest yield strength and highest ductility, while transition temperature from brittle to ductile behavior (BDTT) is at a minimum [2]. Impurity content and deviations from stoichiometry can significantly change these properties. For example, it has been found that single crystal NiAl with improved purity [1] or with small (<1%) additions of iron, gallium or molybdenum [5] yields substantial increase of ductility at room temperature. As far as the temperature effect is concerned, it has been widely recognized that NiAl, like most other intermetallics, has the drawbacks of poor ductility at room temperature and low strength at elevated temperature, despite its many other superior advantages such as low density, high thermal conductivity and high melting temperature [2, 5–6]. These problems need to be resolved before NiAl will be useful in structural applications as a high temperature material.

The present work represents part of a systematic effort conducted with the goal of understanding the behavior of NiAl from two aspects, i.e. the influence of alloying and processing on the structure and properties of NiAl. Alloying mostly deals with the procedure of additions of certain elements or other precipitates to the single crystal for the purpose of property enhancement. Processing, on the other hand, is mainly concerned with the change of thermal conditions by factors such as selection of ampoule materials, setup of heating and cooling temperatures, and variation of growth speed. The current study is focused on the processing conditions in a vertical Bridgman system for growing single crystal β-NiAl, having a composition of 50 at.% Ni, 50 at.% Al, with a B2 (CsCl) crystal structure. The information obtained facilitates a better understanding of the various processing parameters, which, in turn, offer guidance to adjust the processing environment for enhancing crystal quality and composition control.

In the present study, initially, the raw material of NiAl is vacuum induction melted and chill cast into a rod with a desired size. The rod is then removed from the chill mold, placed in a high density refractory (e.g. alumina) ampoule, which is situated on top of a water cooled ram (e.g. copper), remelted and then directionally solidified by slowly withdrawing the ampoule/ram assembly from the hot zone. In most cases, a single crystal seed is placed between the chill and the feedstock in order to preselect the orientation of the single crystal NiAl. Figure 1 (a) shows the schematic of such a Bridgman system. Several physical mech-

---

† Current Address: Atchison Casting Corporation, Quaker Alloy Division, Myerstown, PA 17067, U.S.A.

‡ Author to whom correspondence should be addressed.

NOMENCLATURE

C_p	specific heat	$T1$	coolant temperature
g	gravitational acceleration	$T4$	heater temperature
H	ampoule position within the furnace	TC1, TC2	thermocouple reading
		TC3, TC4	thermocouple reading
ΔH	latent heat	u	radial velocity component
k	thermal conductivity	w	axial velocity component
P	static pressure	z	axial coordinate
R	radial position from the reference point of the ampoule (see Fig. 1)	Z	axial position from the reference point of the ampoule (see Fig. 1).
r	radial coordinate		
Su, Sw	source terms in the momentum equations	Greek symbols	
		β	thermal expansion coefficient
T	temperature	μ	viscosity
T_{ref}	reference temperature	ϱ	density.
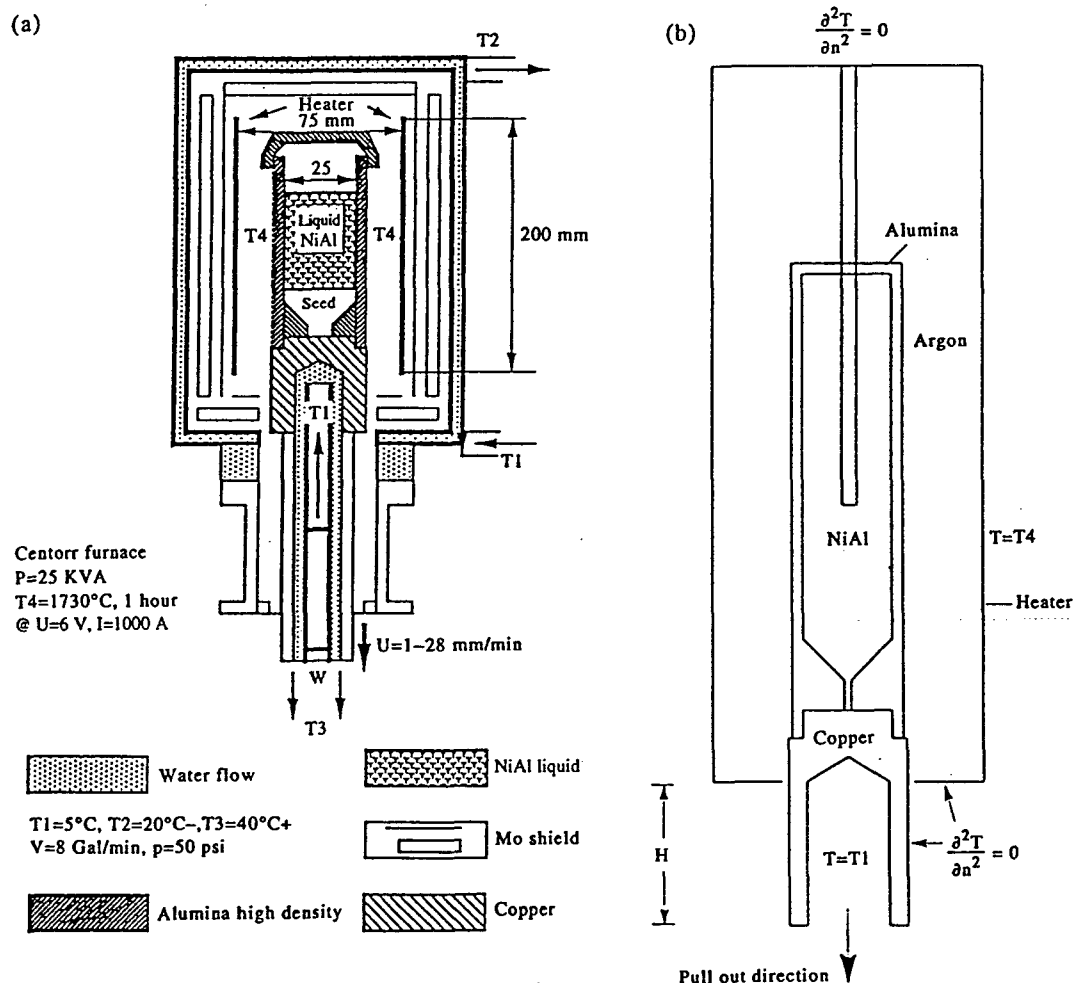
Fig. 1. Vertical Bridgman growth system for β-NiAl crystal: (a) schematic of actual design; (b) layout and boundary conditions extracted from (a) for numerical simulation, where H measures the ampoule position with respect to the heater baseline as it is pulled out, $T4 = 1800°C$ and $T1 = 10°C$.

anisms can be identified in this system and are of key importance to the processing conditions. These include the phase change dynamics between the NiAl melt/solid interface, heat conduction across the ampoule wall and the copper ram, convection in the melt and in the encapsulated argon gas, and radiation between the outer ampoule wall and the heater, which is held at T4, surrounding the ampoule.

We have developed a numerical model to simulate the thermal and solidification characteristics of this system, accounting for the coupled heat transfer processes, complex geometry, as well as variable material properties [7, 8]. To validate this model, experimental measurements of temperature profiles at designated locations in a vertical Bridgman growth system for β-NiAl single crystal have been made and compared with the predictions. To help optimize the thermal conditions for growing single crystal β-NiAl with desired properties, parametric variations have also been considered in numerical simulations. Furthermore, the exact melting temperature of NiAl does not seem to have been ascertained; combining the computational and experimental information, the correct value of the melting temperature is assessed.

2. EXPERIMENTAL PROCEDURE

2.1. System set-up

Figure 1(a) shows the schematic of the current vertical Bridgman growth system, which is axisymmetric. Compared to the previous work [7, 8], in this study, the ampoule inner diameter has been increased from 25 to 29 mm diameter to grow a larger crystal. The feedstock of NiAl was prepared by vacuum induction melting and chill casting into a 28 mm diameter rod, with a 5 mm diameter hole in the center to allow for installation of a thermocouple.

Four Type C tungsten–rhenium thermocouples with 3 mm diameter were installed for measuring the temperature profiles and furnace hot zone temperature during the crystal growth process. Figure 2 shows the detailed arrangement of these thermocouples. Thermocouple 1 (TC1) was positioned along the centerline of the NiAl feedstock. To protect this thermocouple from corrosion and contaminating the crystal during the melting process, it was enclosed by an alumina tube using a 3 mm inner diameter and 5 mm outer diameter and a tip length of 6.5 mm. This arrangement also allows thermocouple 1 to translate vertically along the NiAl centerline. Thermocouple 2 (TC2) was positioned along the outer ampoule wall and was also allowed to translate vertically. In addition, thermocouples 3 and 4 (TC3 and TC4) were fixed horizontally at about one-half height of the heater. They were used to help monitor the thermal condition in the furnace hot zone during the entire crystal growth process. All thermocouples were calibrated before the installation. However, it has to be mentioned that the confidence limit for type C thermal couple is 1%.

The relative positions of the various components in the system were measured with respect to the baseline of the sealing frame as shown in Fig. 1(a) and Fig. 2. While the relative positions of the ampoule and thermocouples are taken with respect to the bottom of the heater, shown in Fig. 2 by the horizontal radial axis R. The ampoule position is denoted by H, which is initially set as 43 mm. As the ampoule is pulled down, this number increases. h denotes the tip positions of thermocouple 1 or 2. Because of the interior complexity and small scale of the current system, the measurement of positions is estimated to have a confidence limit of ± 1 mm.

2.2. Temperature measurement

In the course of making temperature measurements, the system was first heated for about 3.5 h until TC3 and TC4 reached 1740°C. Then the system was held for another 30–45 min to allow the NiAl feedstock to melt. Next, the ampoule/ram assembly was withdrawn from the furnace and stopped at designated positions to allow TC1 and TC2 to take measurements at different positions, as described next.

After the NiAl feedstock was melted, the alumina tube with thermocouple TC1 was moved down through the melt until it stopped and touched the melt/solid interface. Hence, the interface position for the initial ampoule position of $h = 43$ mm could be located. Thereafter, the alumina tube remained at this position, while TC1 was allowed to translate vertically. Once temperature readings from TC1 and TC2 were stable, TC1 and TC2 were moved to a new height and the corresponding temperatures obtained. For the convenience of measurement, TC1 and TC2 were always moved in tandem. After measurements at various h positions were made, the ampoule/ram assembly was withdrawn and stopped at a designated new ampoule position, e.g. $H = 59$ mm, where temperatures were once again measured. This process was repeated until the desired number of ampoule positions were measured. In the present work, temperature profiles, along the NiAl centerline and the ampoule outer wall, were measured for a total of six ampoule positions, $H = 43, 59, 67, 77, 87$ and 97 mm. Table 1 and Fig. 3 summarize the data collected. The number of data points collected decreases as the ampoule is pulled out (H increases), since the thermocouples traverse a smaller length. In addition, the interface position was only obtained for the first ampoule position of $H = 43$ mm. The measured interface position, with respect to the bottom line of the heater (R axis), is 75 mm. This number is checked once again after the experiment when the solidified NiAl ingot was broken and the position of the tip trace of the alumina tube was measured. The result showed that the confidence limit for the interface measurement is about ± 2 mm. During the entire experimental process, a stable furnace temperature of 1740 ± 1°C was maintained by manually adjusting the input power about a baseline value of 7 kW.
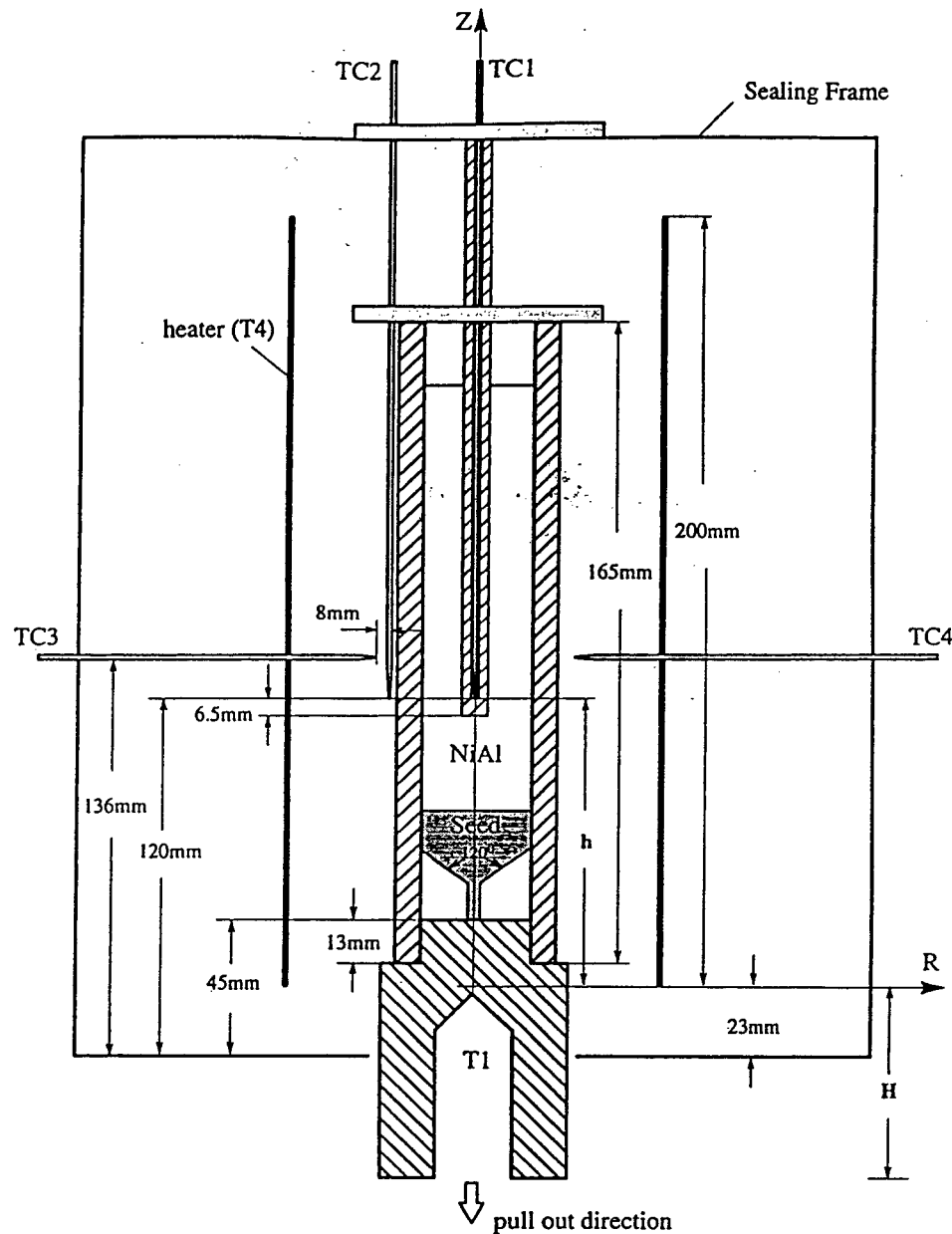
Fig. 2. Setup of thermocouples for the experimental measurement of temperature.

2.3. *Experimental observations*

From Table 1 and Fig. 3, it can be seen that the temperature measured along the outer ampoule wall can be up to 1796°C, which is higher than the value of 1740°C measured by TC3/TC4. Even at the same height, the temperature value at the ampoule outer wall is about 40°C higher than that of TC3/TC4, although their horizontal gap is only about 8 mm as shown in Fig. 2. It is also observed that, when TC3 or TC4 touches the ampoule outer wall, it yields the same temperature as that is measured by TC2. However, when TC3 or TC4 is pulled horizontally away from the

ampoule, its temperature reading drops significantly. The cause of this substantial discrepancy of temperature is unclear at present, but might be explained by the effect of radiation. Figure 4 shows this situation more clearly in a top view of the system. It can be seen that the tips of TC3 and TC4 both face directly to the ampoule wall instead of the heater, hence they receive less radiation from the heater than TC2, resulting in a lower temperature. In addition, it is also observed from Fig. 3 that the temperature gradient in the axial direction is higher at the lower portion of the ampoule than at the higher portion of the ampoule. As the

Table 1. Temperature vs thermal couple positions (h) for different ampoule positions (H)

H [mm]	Thermocouple 1 (located along the NiAl centerline)					
43	h [mm]	82	88	98	108	118
	T [°C]	1737	1752	1766	1774	1778
59	h [mm]	63	78	88	98	108
	T [°C]	1734	1762	1774	1779	1782
67	h [mm]	56	68	83	93	103
	T [°C]	1733	1758	1773	1782	1784
77	h [mm]	54	58	68	78	88
	T [°C]	1752	1758	1772	1780	1785
87	h [mm]	54	63	73	83	
	T [°C]	1762	1773	1780	1780	
97	h [mm]	54	58	68	73	
	T [°C]	1767	1770	1778	1780	

H [mm]	Thermocouple 2 (located along the ampoule outer wall)					
43	h [mm]	82	88	98	108	118
	T [°C]	1780	1786	1791	1795	1796
59	h [mm]	54	63	78	88	98	108
	T [°C]	1761	1773	1787	1791	1793	1793
67	h [mm]	56	68	83	93	103
	T [°C]	1773	1783	1792	1794	1795
77	h [mm]	54	58	68	78	88
	T [°C]	1779	1782	1788	1793	1794
87	h [mm]	54	63	73	83	
	T [°C]	1779	1787	1790	1793	
97	h [mm]	54	58	68	73	83	93
	T [°C]	1782	1784	1789	1790	1793	1794

ampoule is pulled out (H increases), temperature profiles along both the NiAl centerline and the ampoule outer wall become more unified.

3. COMPARISON WITH NUMERICAL SIMULATION

3.1. Modeling considerations

We have mentioned before that, in the vertical Bridgman system, there exists complicated physical phenomena of phase change, conduction, convection and radiation heat transfer, variable material properties and complex geometry. Previously, we have developed a comprehensive numerical model that could take into account all these factors [7, 8]. In the present effort, we compare the modeling predictions by this method with experimental results. In order to accomplish this, several modifications to the model have been made to meet the specific conditions adopted in the current experiment.

First, as explained previously, the geometry of the experimental system had to be changed to accommodate the thermocouples. The inserted alumina tube along the NiAl centerline has a diameter about one sixth of the ampoule inner diameter of 29 mm. Hence, the interference caused by the alumina tube had to be considered.

The second change is in boundary condition specification. In the previous study [7, 8], we used
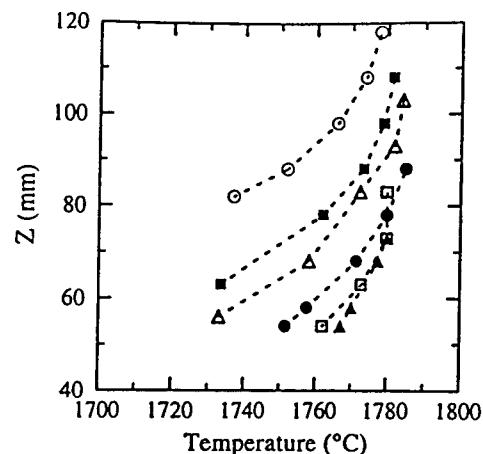
(a)
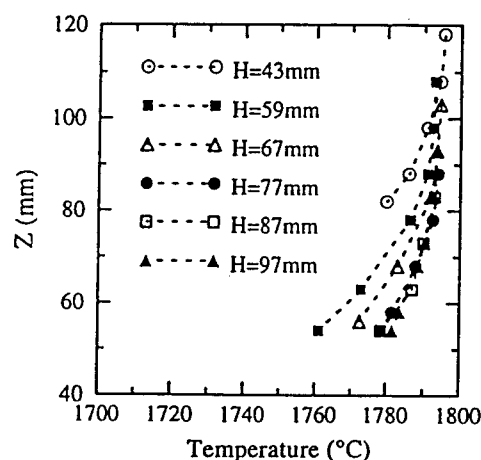
(b)

Fig. 3. Experimental result of temperature profiles along: (a) the NiAl centerline; and (b) the ampoule outer wall for different ampoule position H.

$T4 = 1740$°C as the heater boundary condition, which is actually the temperature measured by TC3/TC4. From the aforementioned experimental set-up, the heater temperature cannot be directly measured. However, the highest temperature along the ampoule outer wall was measured by TC2 to be 1796°C. Therefore, the heater temperature T4 can be estimated to be 1800°C, based upon previous numerical results which showed a 3–5°C difference in temperature between the heater and the alumina wall. The cooling water temperature ranged from 5 to 10°C (city water). When the cooling water reaches the copper ram, it will be warmed up somewhat, so we use the upper limit of $T1 = 10$°C as the cooling boundary condition. For the rest of the boundaries in the furnace, temperature boundary conditions are difficult to give directly. Estimation can be made, though, according to the experimental characteristics. We have mentioned that, during the entire crystal growth process, the furnace hot
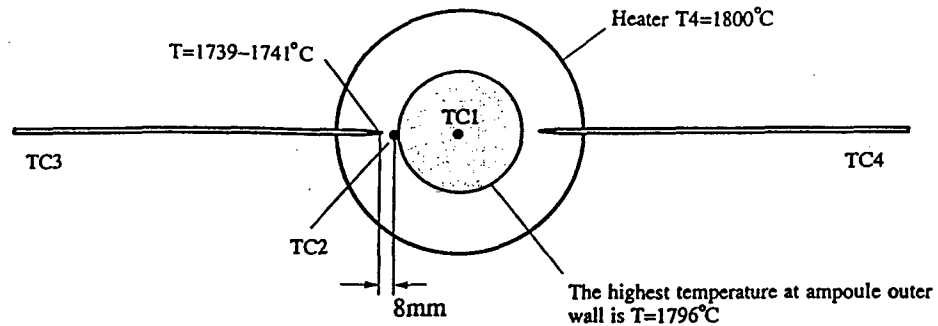
Fig. 4. The top view of the arrangement of thermocouples in the NiAl furnace.
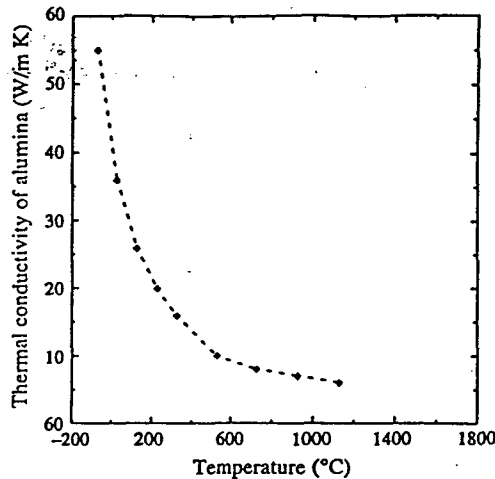

Fig. 5. Dependency of thermal conductivity of alumina on temperature.

zone temperature was maintained at a stable value of 1740°C by manually adjusting the stable power input. In other words, a constant heat flux condition is imposed for the remaining furnace boundaries, i.e. $\partial T^2/\partial n^2 = 0$.

The third consideration is the accurate specification of the material properties as functions of temperature. This is a very important factor in obtaining accurate numerical results. As shown in Table 1 and Fig. 3, the majority of the alumina ampoule is exposed to a temperature range above 1700°C, which exceeds the upper threshold (1127°C) of conductivity as a function of temperature, $k(T)$, shown in Fig. 5 [9]. Therefore, in this modeling effort, conductivity of alumina above $T = 1127$°C has been estimated by extrapolation of the gradient of $k(T)$ at $T = 1127$°C.

3.2. Modeling result

A similar set-up of the computational domain as adopted in ref. [8] is applied here, except that the alumina tube has been considered in this case, shown in Fig. 1(b). The governing equations, in conjunction with the enthalpy formulation for phase change, Boussinesq approximation for buoyancy effect and variable material properties, are given as:

(i) Continuity equation

$$\frac{\partial}{\partial r}(\varrho r u) + \frac{\partial}{\partial z}(\varrho r w) = 0. \tag{1}$$

(ii) Momentum equation
r-momentum

$$\frac{\partial}{\partial t}(\varrho r u) + \frac{\partial}{\partial r}(\varrho r u u) + \frac{\partial}{\partial z}(\varrho r w u)$$

$$= -r\frac{\partial P}{\partial r} + \left\{ \frac{\partial}{\partial r}\left(\mu r \frac{\partial u}{\partial r}\right) + \frac{\partial}{\partial z}\left(\mu r \frac{\partial u}{\partial z}\right) \right\}$$

$$-\mu\frac{u}{r} + Su \tag{2}$$

z-momentum

$$\frac{\partial}{\partial t}(\varrho r w) + \frac{\partial}{\partial r}(\varrho r u w) + \frac{\partial}{\partial z}(\varrho r w w)$$

$$= -r\frac{\partial P}{\partial z} + \left\{ \frac{\partial}{\partial r}\left(\mu r \frac{\partial w}{\partial r}\right) + \frac{\partial}{\partial z}\left(\mu r \frac{\partial w}{\partial z}\right) \right\}$$

$$+ \varrho r g\beta(T - T_{ref}) + Sw. \tag{3}$$

(iii) Energy equation

$$\varrho C_p \left\{ \frac{\partial}{\partial t}(rT) + \frac{\partial}{\partial r}(ruT) + \frac{\partial}{\partial z}(rwT) \right\}$$

$$= \frac{\partial}{\partial r}\left(kr\frac{\partial T}{\partial r}\right) + \frac{\partial}{\partial z}\left(kr\frac{\partial T}{\partial z}\right)$$

$$-\Delta H \left\{ \frac{\partial}{\partial t}(\varrho r f) + \frac{\partial}{\partial r}(\varrho r u f) + \frac{\partial}{\partial z}(\varrho r w f) \right\}. \tag{4}$$

The radiation heat transfer between the heater and the ampoule outer wall comes into play via boundary conditions. The detailed account of the formulation and the numerical solution of these equations can be found in refs. [7, 8]. As the pulling speed of the current crystal growth process is about 1–2 mm per h, steady-state computations are most likely sufficient.

3.2.1. Comparison of temperature profiles. Figures 6 and 7 show that the temperature distribution along the NiAl centerline and the ampoule outer wall obtained from the computational simulation matches
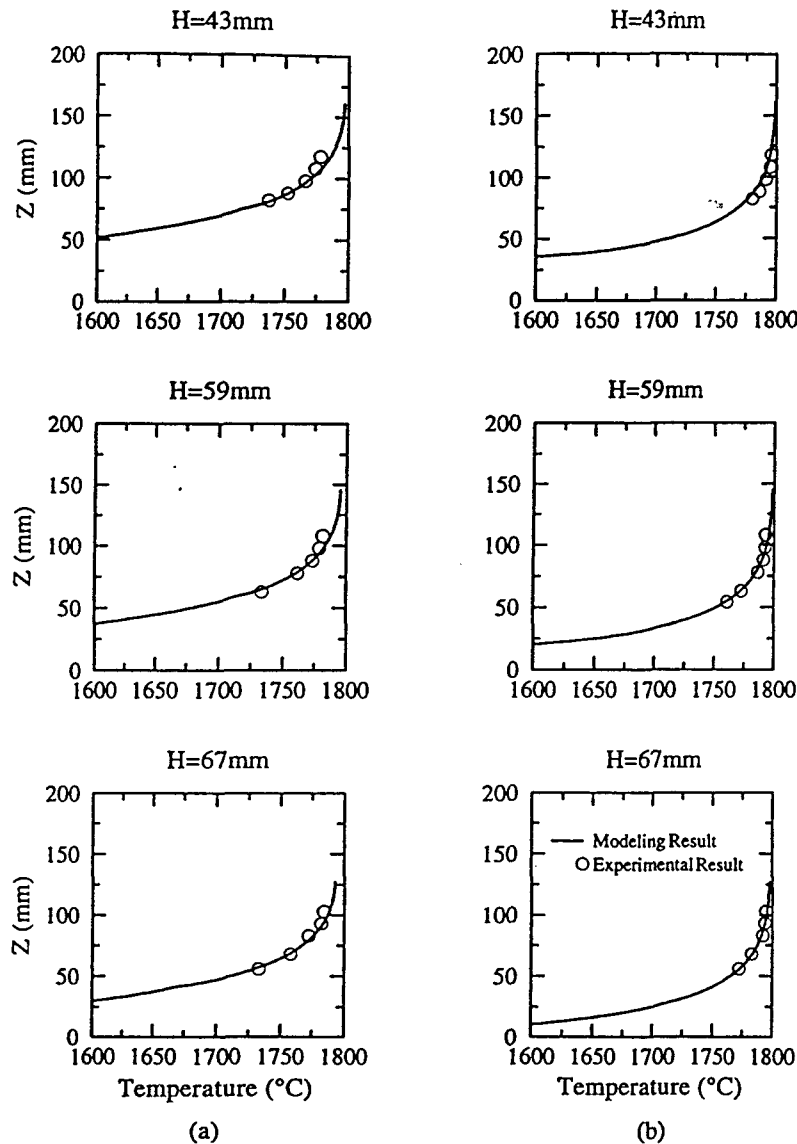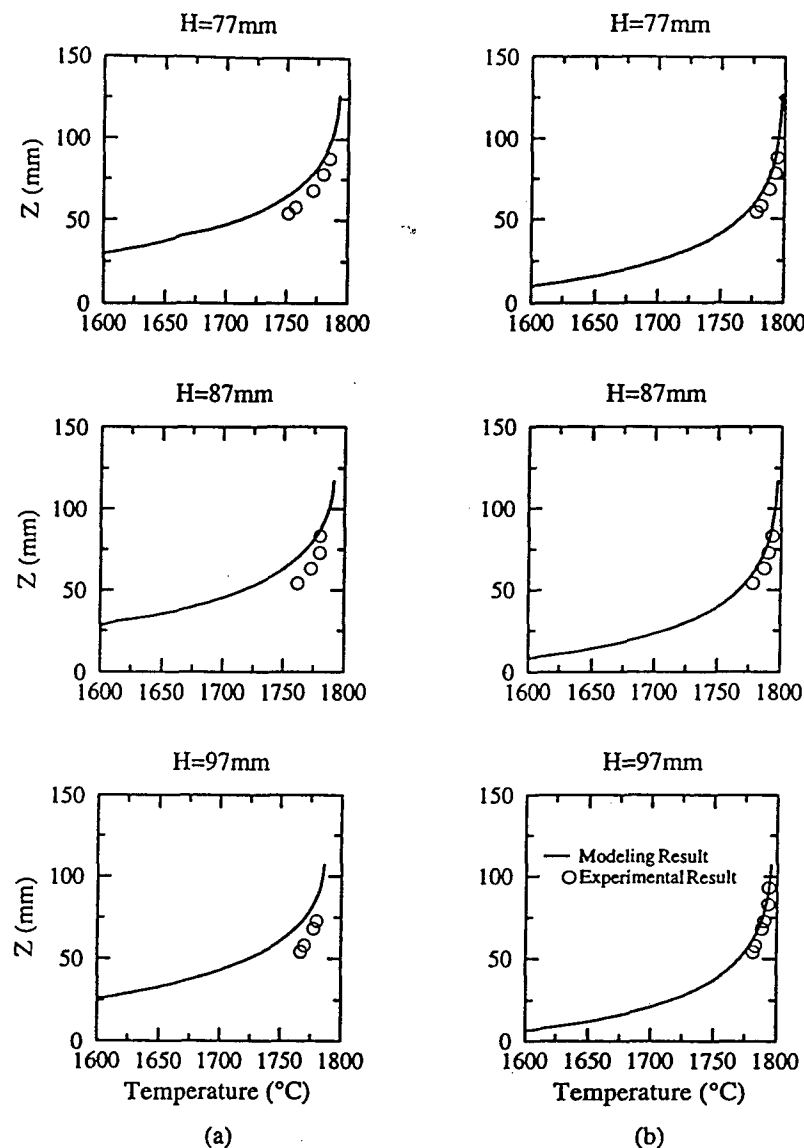
Fig. 6. Comparisons of temperature profiles along: (a) the NiAl centerline; and (b) the ampoule outer wall between the modeling result and the experimental data for the three higher ampoule positions of $H = 43$ mm, $H = 59$ mm and $H = 67$ mm.

the experimental measurements well overall. Satisfactory agreement is observed for all six ampoule positions, especially for the temperature along the outer alumina wall. This implies that both the simplified radiation model currently in use for computing the heat flux between the alumina outer wall and the heater, and the boundary condition of constant heat flux at the heater bottom are reasonable. Along the ampoule centerline, agreement between experimental data and computational results is good for the three higher ampoule positions of $H = 43$ mm, $H = 59$ mm and $H = 67$ mm, but worsens for the three lower ampoule positions. This trend is explained in more detail below.

Figure 8 shows the streamfunctions and isotherm distributions for two selected ampoule positions, one

at a higher location ($H = 43$ mm) and the other at a lower location ($H = 87$ mm). For the higher ampoule position, Fig. 8(a) shows that the ampoule base region is contained inside the furnace hot zone. Since the treatment of radiation heat transfer and boundary conditions appear reasonable there shown by Fig. 6(b) and Fig. 7(b), the computed thermal distribution of this region is also accurate. Accordingly, the predicted temperature profile along the NiAl centerline matches very well with experimental results. At the lower ampoule position, Fig. 8(b) shows clearly that the ampoule base region has been pulled out of the furnace hot zone. In this case, the boundary condition at the outer wall of this region is still specified as a constant heat flux, which is no longer accurate. Furthermore, as the thermal distribution inside the

Fig. 7. Comparisons of temperature profiles along: (a) the NiAl centerline; and (b) the ampoule outer wall between the modeling result and the experimental data for the three lower ampoule positions of $H = 77$ mm, $H = 87$ mm and $H = 97$ mm.

ampoule is very sensitive to the isotherm change near the ampoule base, it is not surprising to observe in Fig. 7 some deviations between numerical results and experimental data along the NiAl centerline. Improvement of the modeling accuracy can be obtained by specifying realistic boundary condition at the outer ampoule wall as it is pulled out of the furnace. The temperature distribution along the ampoule outer wall in the furnace hot zone, though, is not influenced by this effect.

3.2.2. *Melting temperature of β-NiAl.* The melting temperature of NiAl at stoichiometric composition is reported in the literature as $Tmelt = 1638°C$ [2, 3]. However, the accuracy of this value seems questionable. Since the pulling speed of the ampoule is slow and the convective strength within the melt is rather weak, solutions obtained with the steady-state conduction analysis are quite close to the full simulation for the present case. Based on the experimental data and conduction analysis, we are able to make a direct evaluation of the melting temperature of β-NiAl and compare it with the value adopted in the literature. The established melting temperature is also consistent with the solutions obtained by including the convective effect.

For the ampoule position of $H = 43$ mm, we measured the interface position by moving the alumina tube through the NiAl melt until it touched the solid/melt interface, which was found to be $h_{interf} = 75$ mm. It is noted that, since the tip of TC1 is separated from the interface by the closed end of the alumina tube (with a thickness of 6.5 mm shown in Fig. 2),

streamfuction   isotherm

(a) H=35mm

Fig. 9. The estimation of melt/solid interface temperature of
β-NiAl.

streamfuction   isotherm
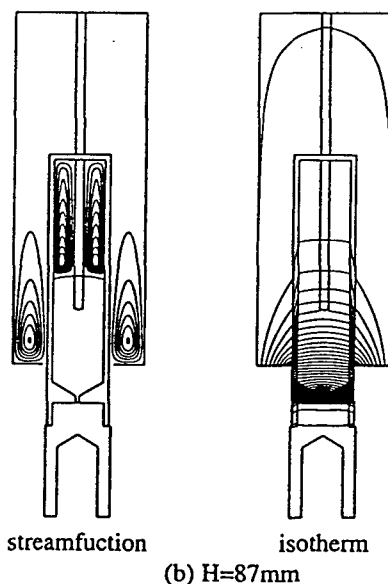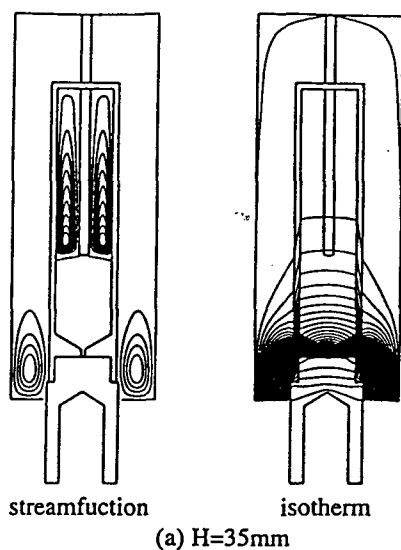
(b) H=87mm

Fig. 8. Solution characteristics of NiAl furnace for selected
ampoule positions of: (a) $H = 43$ mm; and (b) $H = 87$ mm.

the temperature reading of TC1 is not the melt/solid
interface temperature. However, the detailed tem-
perature profile along the entire ampoule centerline
can be obtained from our numerical results. Com-
bining these two results, the interface temperature of
NiAl can be determined by interpolation, as shown in
Fig. 9, yielding $T_{interf} = 1716°C$. This result is surpris-
ing, as this value is at least 70°C higher than the
melting temperature of NiAl widely reported in the
literature. Walston and Darolia [10] have also
reported recently an observation of NiAl melting tem-
perature as high as 1682°C. Although T_{melt} could not
be determined directly in this study, the above esti-
mation does seem to have its merit. Since the current
numerical model correlates well with the experimental

data, the temperature profile we used for interpolating
the interface temperature is likely to be accurate. It is
noted that type C thermocouples have a confidence
limit up to 1%, and hence can possibly result in about
18°C uncertainty in the present temperature measure-
ment. The confidence limit of the solid/melt interface
measurement is ± 2 mm. Considering all possible
errors that might effect the measurements of tem-
perature and interface position, the melting tem-
perature we obtained for the NiAl sample at stoi-
chiometric composition is still noticeably higher than
1638°C reported in the literature.

4. ASSESSMENT OF PROCESSING CONDITIONS VIA NUMERICAL MODELING

β-NiAl with high purity and improved mechanical
property of high tensile elongation at room tem-
perature has been produced routinely with the current
design of the vertical Bridgman system [1]. Therefore,
it is valuable to describe the detailed characteristics of
the processing conditions that are suitable for growing
high quality single crystal NiAl. Furthermore, based
on the numerical simulation, we will also provide
suggestions to improve design of the furnace com-
ponents.

4.1. Simulation of actual vertical Bridgman growth system

Based on the satisfactory comparison between
experimental and numerical results obtained for the
case with thermocouples, we now turn our attention
to the actual growth process without inserting the
alumina tube. Figure 10 shows the solution charac-
teristics of the stream function and isotherm at differ-
ent ampoule positions. The convective fields in the
melt are of very similar patterns at all ampoule
positions, and the maximum velocity varies little. The
convective strength in the encapsulated argon gas
change more noticeably, but the maximum velocity
there is at least one or two orders of magnitude smaller

(i)   *(ii)*   *(i)*   *(ii)*   *(i)*   *(ii)*

In the NiAl melt $U_{max}=1.06$ *mm/s*   *In the NiAl melt* $U_{max}=1.05$ *mm/s*   *In the NiAl melt* $U_{max}=1.04$ *mm/s*

(a) H=43mm   *(b) H=59mm*   *(c) H=67mm*
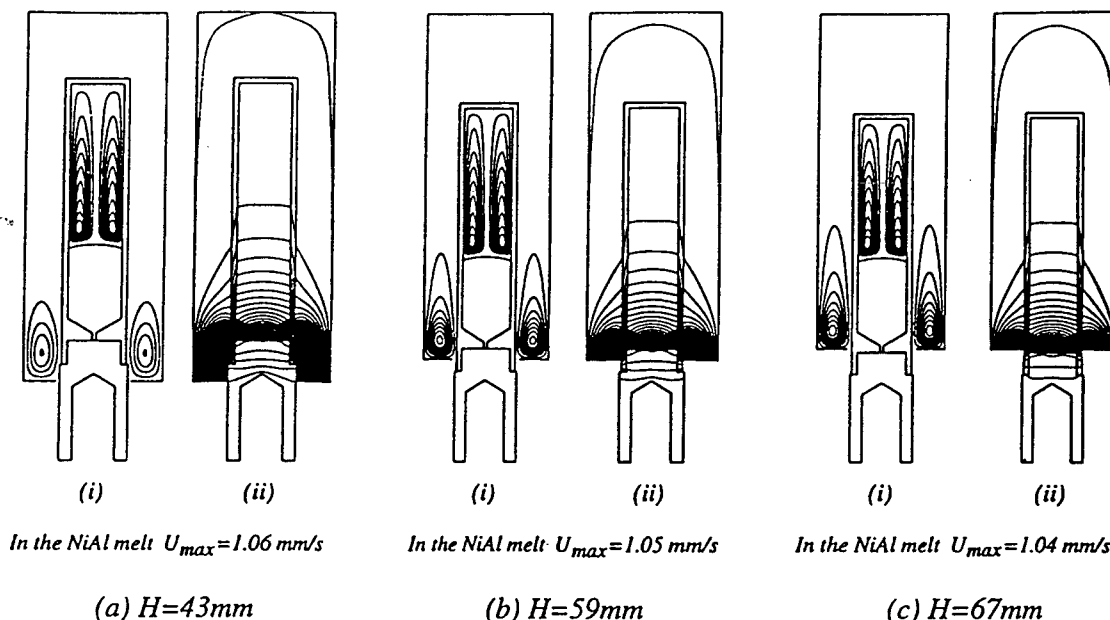
Fig. 10. Solution characteristics of (i) streamfunctions and (ii) isotherm in an actual vertical Bridgman growth system for NiAl crystal for different ampoule positions: (a) $H = 43$ mm; (b) $H = 59$ mm; and (c) $H = 67$ mm.

than that in the melt due to the higher Grashof number. As already discussed, the convective effects in the current crystal growth system are not strong. This is a desirable condition, for otherwise isotherms can be greatly distorted by convection which will cause nonuniform thermal gradients across the interface.

It has been recognized in the literature that, for crystal growth from the melt in the vertical Bridgman growth system, a slightly convex (toward the melt) liquid–solid interface can help prevent spontaneous nucleation at the ampoule wall. In addition, high temperature gradients across the interface and uniform distributions of thermal conditions along the interface are desirable for obtaining high purity crystals [11–13]. In the following, these aspects are further discussed.

Figure 11 shows the interface shape and the vertical temperature gradient across the interface at different ampoule positions. Due to the similar convective patterns, the interface shapes and temperature gradients obtained at ampoule positions are also close to each other. The difference between the centerline and inner ampoule wall locations is about 2 mm, and the gradients are all maintained within the range of 3.16–3.35°C mm^{-1}. Because of the convective effect in the melt, the temperature gradient at the interface centerline is about 5% higher than that at the inner ampoule wall. Figure 12 explains this situation more clearly, in which the interface characteristics with and without convection are compared. It is observed that convection causes the interface position to be moved up about 0.5%, which is quite small. However, it causes the temperature gradient across the interface to vary more noticeably (5%) along the interface, as shown in Fig. 12(b).

4.2. Suggestions for design improvement

In this section, we will vary design parameters with the goal of improving processing conditions in the vertical Bridgman growth system. Since convection has been found to be insignificant to affect the isotherm distributions within the melt in the present setup, it is not included in order to save computational time. Parameters such as the ampoule emissivity, the geometry of the ampoule base, the thermal conductivity of the ram, and the ampoule wall thickness have been adjusted and their influence on the interface curvature and temperature gradient are compared. In the following, possible modification that might lead to the improvement of the interface conditions are listed.

- Case 1: the original design will be treated as the base case;
- Case 2: increase the emissivity of the ampoule outer wall from 0.8 to 1.0. This can be achieved in reality by, for example, coating the alumina ampoule outer wall with high emissivity and high melting temperature materials;
- Case 3: decrease the ampoule base angle from 120 to 100 degrees, as shown in Fig. 2;
- Case 4: use a higher thermal conductivity material for the chill ram. For example, replace copper by silver;
- Case 5: decrease the ampoule outer diameter by 2 mm.

Figure 13 shows the interface characteristics resulting from the variations of these parameters. It is observed that most of these variations can lead to certain increases of the temperature gradient across

H=43mm

H=43mm

H=59mm
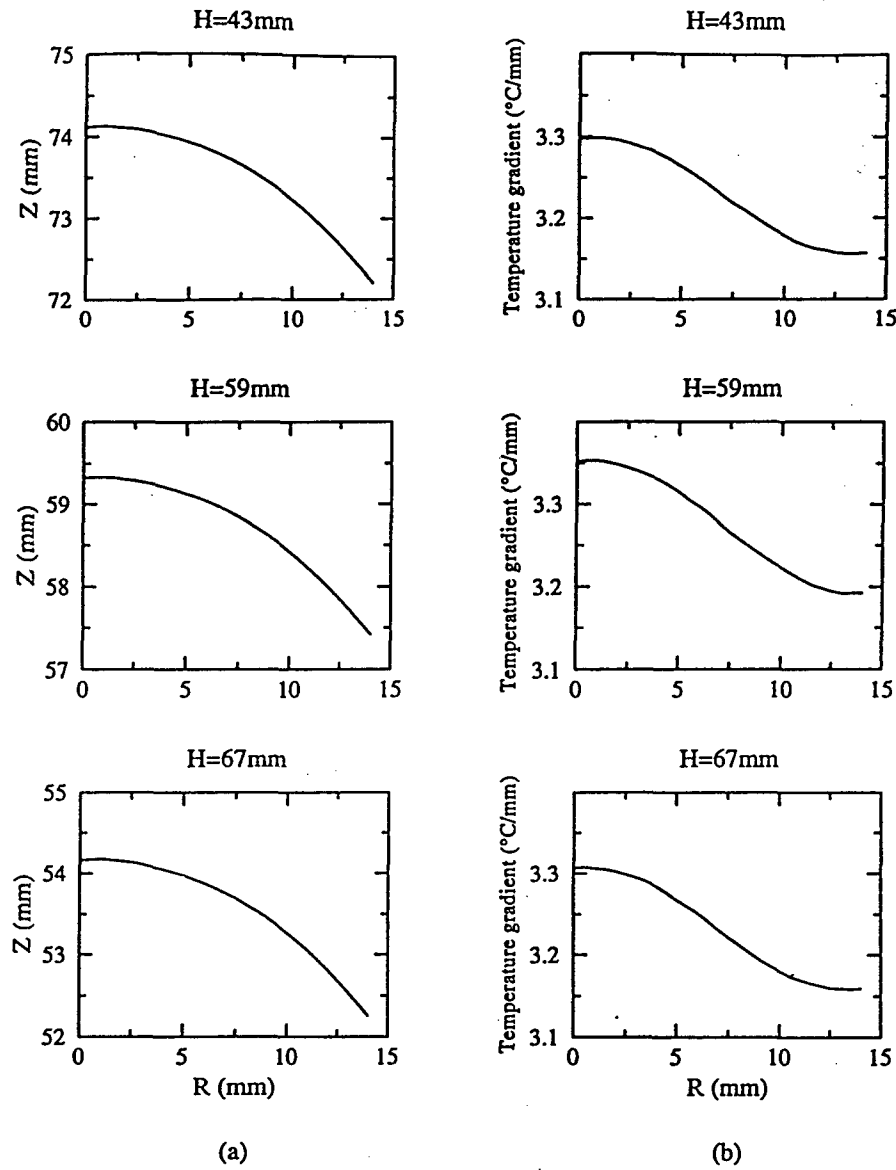
H=59mm

H=67mm

H=67mm

Fig. 11. (a) Interface characteristics; and (b) vertical temperature gradient across the interface for three ampoule positions of $H = 43$ mm, $H = 59$ mm and $H = 67$ mm.
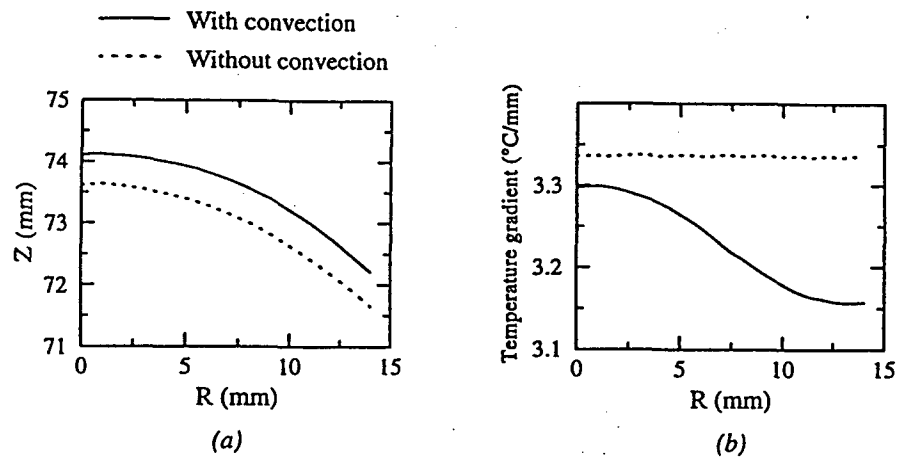
——— With convection

- - - - - Without convection

(a)   *(b)*

Fig. 12. Comparison of: (a) interface characteristics; and (b) temperature gradient across the interface between solutions with convection and without convection effects for the ampoule position of $H = 43$ mm.
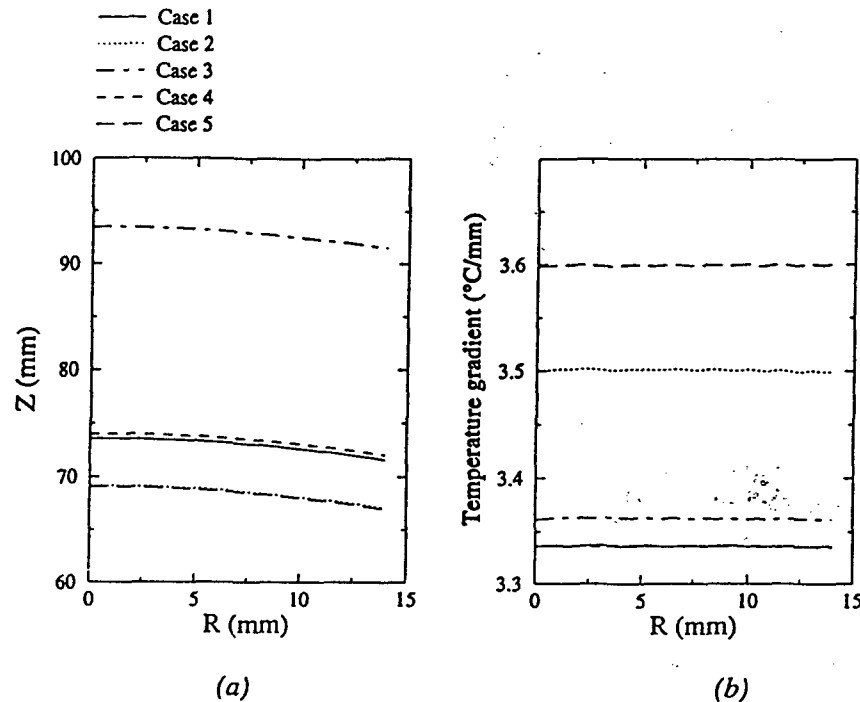
Fig. 13. Effects of variations in processing parameters on the interface characteristics by solutions without convection: (a) interface position; and (b) temperature gradient across the interface.

the solid/melt interface, which is desirable. In particular, for Cases 2 and 5, i.e. the increase of emissivity of the ampoule outer wall and the decrease of the ampoule thickness, the increase of the temperature gradient is more prominent. However, the change of the ram material to one with a higher conductivity (Case 4) seems not to influence the interface conditions much. It is interesting to observe that the interface curvature seems to be insensitive to these parametric variations. The locations of the interface, though, become lowered for Cases 2 and 5, higher for Case 3, and nearly unchanged for Case 4. It is desirable to further explore these factors by inspecting the quality of the crystal growth with these design modifications.

There are also other possible variations in furnace design that can potentially improve the processing condition near the interface. For example, it is obvious that an increase in heater temperature (T4) or a decrease of the cooling temperature (T1) helps increase the temperature gradient inside the system. However, care needs to be taken here because of the convection effect. It is observed from Fig. 12 that convection tends to cause the nonuniform distribution of temperature gradient along the interface, which is undesirable. Thus, any variations that can lead to increased convection strength should be made carefully.

5. CONCLUSION

In this study, we have conducted a detailed analysis of thermal conditions in a vertical Bridgman growth

system for the β-NiAl single crystal. In this system, there are strongly coupled effects of phase change, conduction, convection and radiation heat transfer, variable material properties as functions of temperature, and complex geometry and boundary conditions. Therefore, optimization of the processing conditions for crystal growth is a very challenging task. In this study, we have coordinated computational and experimental efforts to first validate our theoretical model, then offer insight into possible design improvements. For example, we have shown that coating the ampoule outer wall with a high emissivity material, or decreasing the ampoule wall thickness can be advantageous. We have also found that the melting temperature of β-NiAl is around 1716°C, which is about 70°C higher than that reported in the literature. Because the high melting temperature of NiAl is one of its strongest attributes, the accurate definition of the melting temperature is of great interest. This important aspect should be further investigated.

REFERENCES

1. Levit, V. I., Bul, I. A., Hu, J. and Kaufman, M. J., High tensile elongation of β-NiAl single crystals at 293 K. Scripta Metallurgy Material, 1995 (submitted).
2. Noebe, R. D., Bowman, R. R. and Nathal, M. V., Physical and mechanical properties of the B2 compound NiAl. International Material Review, 1993, 38(4), 193–232.

3. Vedula, K., Pathare, V., Aslandis, I. and Titran, R., Alloys based on NiAl for high temperature applications. *Material Research Society Symposium Proceedings*, 1985, 39, 411–421.

4. Takasugi, T., Watanabe, S. and Hanada, S., The temperature and orientation dependence of tensile deformation and fracture in NiAl single crystals. *Material Science Engineering*, 1992, A149, 183–193.

5. Darolia, R., NiAl alloys for high-temperature structural applications. *JOM*, 1991, 44–49.

6. Sen, S. and Stefanescu, D. M., Melting and casting processes for high-temperature intermetallics. *JOM*, 1991, 30–32.

7. Shyy, W., Udaykumar, H. S., Rao, M. M. and Smith, R. W., *Computational Fluid Dynamics with Moving Boundaries*. Taylor and Francis, Washington, D.C., 1996.

8. Ouyang, H. and Shyy, W., Multi-zone simulation of the Bridgman growth process of β-NiAl crystal. *Inter-*

national Journal of Heat and Mass Transfer, 1996, 39, 2039–2051.

9. Perry, R. H., Green, D. W. and Maloney, J. O., *Perry's Chemical Engineerings' Handbook*, 6th edn. McGraw-Hill, New York, 1984.

10. Walston, W. S. and Darolia, R., Effect of alloying on physical properties of NiAl. *MRS Symposium Proceedings*, 1995, 28, 237–242.

11. Sen, S., Konkel, W. H., Tighe, S. J., Bland, L. G., Sharma, S. R. and Taylor, R. E., Crystal growth of large-area single-crystal CdTe and CdZnTe by the computer-controlled vertical modified-Bridgman process. *Journal Crystal Growth*, 1988, 86, 111–117.

12. Brown, R. A., Theory of transport processes in single crystal growth from the melt. *A.I.Ch.E. Journal*, 1988, 34, 881–911.

13. Kurz, W. and Fisher, D. J., *Fundamentals of Solidification*. Trans Tech Publications Ltd, Switzerland, 1989.

8. P. E. Cantonwine & H. N. G. Wadley, "The Effect of Fiber Matrix Reactions on the Interface Properties in a SCS-6/Ti-24Al-11Nb Composite", Comp. Eng. 4(1), (1994), 67-80.

9. R.Gampala, D.M.Elzey and H.N.G.Wadley, "Plastic Deformation of Asperities during Consolidation of Plasma Sprayed Metal Matrix Composite Monotapes", Acta metall. 42, 3209, (1994).

10. R.Gampala, D.M.Elzey and H.N.G.Wadley, "Power-law Creep Blunting of Contacts and Its Implications for Consolidation Modeling", Acta metall. (In Press, 1995).

11. B. Derby and M. F. Ashby, "A Microstructural Model for Primary Creep", Acta Metall. 35(6), 1349, (1987).

12. Z. Mroz and Trampczynski, "On the Creep Hardening Rule for Metals with a Memory of Maximal Prestress", Int. J. Solids Structures, 20, 467, (1984).

13. R. K. Penny and D. L. Marriott, "Design for Creep", McGraw Hill, UK, (1971).

14. N.Ogbonna, N.A.Fleck and A.C.F.Cocks, "Transient Creep Analysis of ball Indentation", Int. J. Mech. Sci. (In Press, 1995).

15. A.F.Bower et al., "Indentation of a Power-law Creeping Solid", Proc. R. Soc. Lond. A 441, 97, (1993).

16. R.Hill, "Similarity Analysis of Creep Indentation Tests", Proc. R. Soc. Lond. A436, 617, (1992).

17. ABAQUS [1984] developed by Hibbitt, Karlsson & Sorensen, Providence, RI.

APPLICATIONS OF MULTI-LEVEL SIMULATION OF BRIDGMAN GROWTH PROCESS FOR β-NiAl AND CdTe CRYSTALS

Hong-Ouyang and Wei Shyy

Department of Aerospace Engineering,
Mechanics and Engineering Science,
University of Florida, Gainesville, FL 32611

Abstract

A unified computational model has been developed for the Bridgman growth processes of β-NiAl and CdTe crystals. To handle the geometrical and physical complexities, a two-level approach has been developed. At the global level, conjugate heat transfer, phase change dynamics, and variable material properties along with the realistic geometries and thermal boundary conditions are accounted for inside the entire crystal growth system. Refined calculations are then made within the ampoule, with the boundary conditions supplied by the global simulations. This model can optimize the use of computational source, help understand solidification behaviors, and improve designs of crystal growth system.

Figure 1. Vertical Bridgman growth system for β–NiAl crystal. (a) Schematic of practical design. (b) Layout and boundary conditions extracted from (a) for current numerical simulation, in which (i) is the global model and (ii) is the refined model. The total length of the ampoule housing, between the top of alumina section and the bottom of copper section, is L=14.8, while the length of ampoule is l=9.08, after being scaled by the ampoule inner radius of 12.5mm.

(b)

(i) Global model   (ii) Refined model

pull out direction

$\frac{\partial^2 T}{\partial n^2} = 0$

$T = T1$

Copper

Enclosure Wall (Heater) $T = T1$

NiAl

Argon

Alumina

$\frac{\partial^2 T}{\partial n^2} = 0$

Boundary temperature of the ampoule wall is obtained from the global furnace simulation

Inner ampoule wall

NiAl

(a)

Center furnace

P≈25 KVA

Ta=1730 C, 1 hour

θ U≈4 V, I≈1000 A

U=1–28 mm/min

200 mm

Copper
Alumina High density
V≈8 Ca/min, p≈50 psi
Ni–Al liquid
No shield
T1=SC, T2=20C, T3=40C*
Water flow

Introduction

β–NiAl is an intermetallic that is currently being investigated as a promising high temperature structural material for application in the next generation of aircraft engines and structural components. NiAl is especially attractive because of its low density, high thermal conductivity, high melting temperature, superior isothermal and cyclic oxidation resistance [1]. However, it has two major drawbacks; low toughness at room temperatures and low strength at high temperatures [2]. These deficiencies need to be resolved before NiAl can be used in structural applications.

CdTe, on the other hand, is important and unique in such applications as gamma–ray and x–ray detectors, lenses and electro–optic modulators [3]. Especially, CdTe and its solid solution systems (Cd, Zn)Te and Cd(Te, Se) are the most favored substrate materials for the infrared detector material cadimium mercury telluride (Hg$_{1-x}$Cd$_x$Te) [4]. However, CdTe has low thermal conductivity (k≈1.5 W/m K) and low critical resolved shear stress (CRSS≈0.5 x 10^{-3} dynes/m^2), which make it very sensitive to minor variations in thermal condition and prone to formation of dislocations [5]. At present, CdTe has not made as significant an impact as Silicon because it is expensive and difficult to grow.

The Bridgman growth system is one of the directional solidification configurations that are useful for producing large size single crystals from the melt [6]. The advantage of the Bridgman system is that the temperature gradients can be controlled, making it possible to achieve unidirectional solidification. In two separate efforts, we have been developing computational tool for predicting the solidification processes of NiAl and CdTe. The NiAl system in actual growth is shown in Fig. 1(a) [7]. Figure 2 shows schematic of two Bridgman configurations that are underdevelopment for growing CdTe, in which one has a flat base ampoule and the other has a semi–spherical base ampoule [8]. Although those two materials are of distinctly different thermo–physical properties and practical applications, they are considered together to demonstrate that a unified predictive capability can be developed according to the physical mechanisms, instead of the individual predictive materials, involved in the solidification processes. Our goals are to understand the solidification characteristics of NiAl and to seek stable controls of crystal growth process of CdTe.

Crystal growth in a vertical Bridgman system is a highly complex process and is influenced by many factors, such as phase change dynamics, varying thermo–physical properties and multiple heat transfer modes of conduction, convection and radiation. These complications have traditionally resulted in unrealistic analyses carried out under such assumptions as simplified geometry, assumed boundary conditions, constant thermo–physical properties and neglects of buoyancy driven convection. In this effort, we attempt to realistically accounted for all these factors that are present in a Bridgman NiAl or CdTe system. Accordingly, a two–level approach previously developed is employed to achieve computational accuracy and economy [9, 10]. In what follows, we first present the computational formulation, and their implication on crystal growth.

Computational Formulation and Strategy

Figure 1 shows the schematic of actual vertical Bridgman system for growing β–NiAl crystal [7]. It can be seen that the ampoule is made of alumina and rests on a copper support. The enclosure (heater 74) remains stationary during the growth process and the ampoule is pulled out to control the growth speed of NiAl. Figure 2 shows two configuration designs of vertical Bridgman growth system for CdTe crystal, one with a flat base ampoule and the other with a semi–spherical base ampoule. Differed from Fig. 1, the heating units of CdTe system are not shown in Fig.2 as they are applied very closely to the enclosure wall. Hence schematic of thermal boundary conditions are given. During the growth process of CdTe, these thermal profiles are kept invariant while the configurations shown in Fig. 2 are slowly pulled out of the heating units. Nevertheless, common
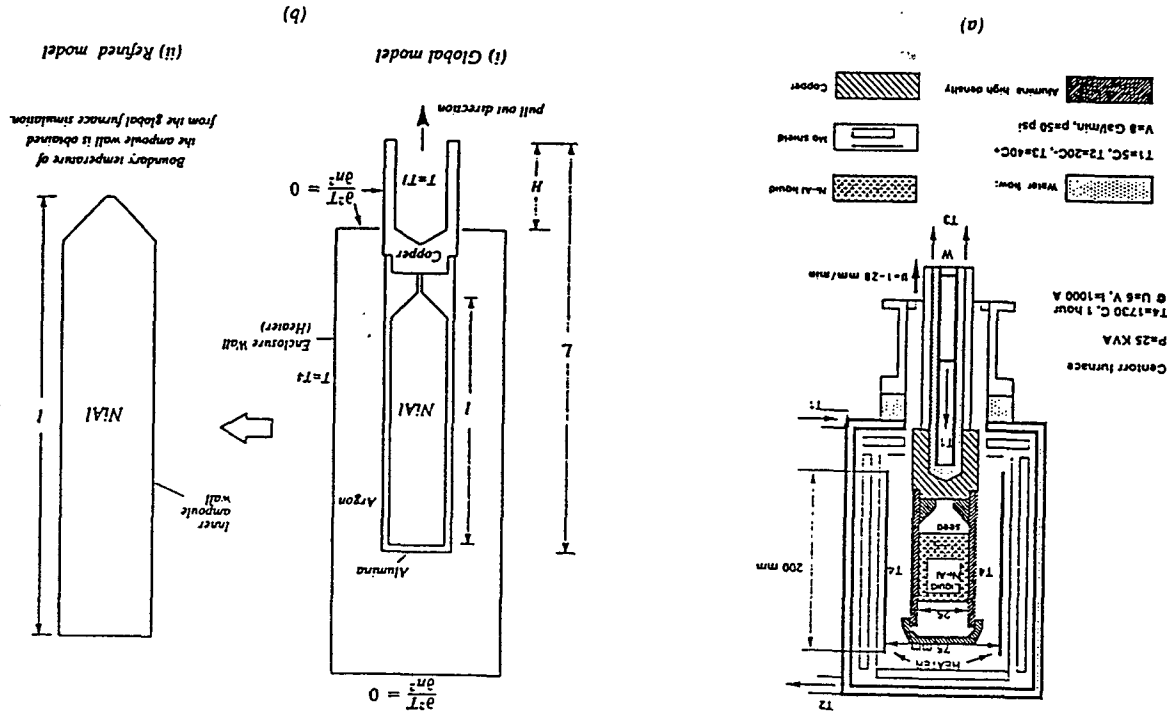
features are identified for both NiAl and CdTe systems in that they are all axisymmetric and are basically composed of two regions:

1. The enclosure region, consisting of the enclosure wall, ampoule support and encapsulated gas, and
2. The ampoule region, containing NiAl or CdTe melt and crystal.

The following physical phenomena are of key importance in all three configurations and need to be resolved adequately.

- Phase change within ampoules;
- Heat conduction within enclosure walls and ampoule supports;
- Convection in melts and in encapsulated gases;
- Radiation between outer ampoule walls and inner enclosure walls.

Governing Equations

To account for the combined effects of heat transfer, phase change, variable materials properties and complex geometries of the vertical Bridgman growth system, we have derived a unified set of transport equations that are equally valid in phase change, solid, liquid and gas regions [9]. In dimensionless form, these equations cast in axisymmetric coordinates, incorporating the Boussinesq approximation are:

(i) Continuity equation

$$\frac{\partial}{\partial t}\left(\frac{\varrho}{\varrho_0}\right) + \frac{\partial}{\partial r}\left(\frac{\varrho}{\varrho_0}ru\right) + \frac{\partial}{\partial z}\left(\frac{\varrho}{\varrho_0}rv\right) = 0 \qquad (1)$$

(ii) Momentum equation

r-momentum:

$$\frac{\partial}{\partial t}\left(\frac{\varrho}{\varrho_0}ru\right) + \frac{\partial}{\partial r}\left(\frac{\varrho}{\varrho_0}ruu\right) + \frac{\partial}{\partial z}\left(\frac{\varrho}{\varrho_0}rvu\right) =$$
$$-r\frac{\partial P}{\partial r} + \mathrm{Pr}_0\left\{\frac{\partial}{\partial r}\left(\frac{\mu}{\mu_0}r\frac{\partial u}{\partial r}\right) + \frac{\partial}{\partial z}\left(\frac{\mu}{\mu_0}r\frac{\partial u}{\partial z}\right)\right\} - \mathrm{Pr}_0\left(\frac{\mu}{\mu_0}\right)\frac{u}{r} + Su \qquad (2)$$

z-momentum:

$$\frac{\partial}{\partial t}\left(\frac{\varrho}{\varrho_0}rv\right) + \frac{\partial}{\partial r}\left(\frac{\varrho}{\varrho_0}ruv\right) + \frac{\partial}{\partial z}\left(\frac{\varrho}{\varrho_0}rvv\right) =$$
$$-r\frac{\partial P}{\partial z} + \mathrm{Pr}_0\left\{\frac{\partial}{\partial r}\left(\frac{\mu}{\mu_0}r\frac{\partial v}{\partial r}\right) + \frac{\partial}{\partial z}\left(\frac{\mu}{\mu_0}r\frac{\partial v}{\partial z}\right)\right\} + Ra_0\mathrm{Pr}_0\left(\frac{\varrho}{\varrho_0}\right)\left(\frac{\beta}{\beta_0}\right)rT + Sw \qquad (3)$$

(iii) Energy equation

$$\left\{\frac{\partial}{\partial t}\frac{\varrho}{\varrho_0}\frac{C_p}{C_{p_0}}rT + \frac{\partial}{\partial r}\frac{\varrho}{\varrho_0}\frac{C_p}{C_{p_0}}ruT + \frac{\partial}{\partial z}\frac{\varrho}{\varrho_0}\frac{C_p}{C_{p_0}}rvT\right\} =$$
$$\left\{\frac{\partial}{\partial r}\left(\frac{k}{k_0}r\frac{\partial T}{\partial r}\right) + \frac{\partial}{\partial z}\left(\frac{k}{k_0}r\frac{\partial T}{\partial z}\right)\right\} - \frac{1}{St_0}\left\{\frac{\partial}{\partial r}\frac{\varrho}{\varrho_0}rf + \frac{\partial}{\partial r}\frac{\varrho}{\varrho_0}ruf + \frac{\partial}{\partial z}\frac{\varrho}{\varrho_0}rvf\right\} = \qquad (4)$$

The three dimensionless parameters resulted from the present scaling procedure are the Stefan number St_0, Prandtl number Pr_0, and Rayleigh number Ra_0. The reference length scale for nondimensionalization is the inner radius of the ampoule and the reference temperature scale is the dif-

711

710

Figure 2. Schematic of global and refined models, along with the thermal boundary conditions, for two configurations of vertical Bridgman growth system for CdTe crystal. (a) The flat base ampoule base configuration. (b) The semi-spherical base ampoule base configuration.
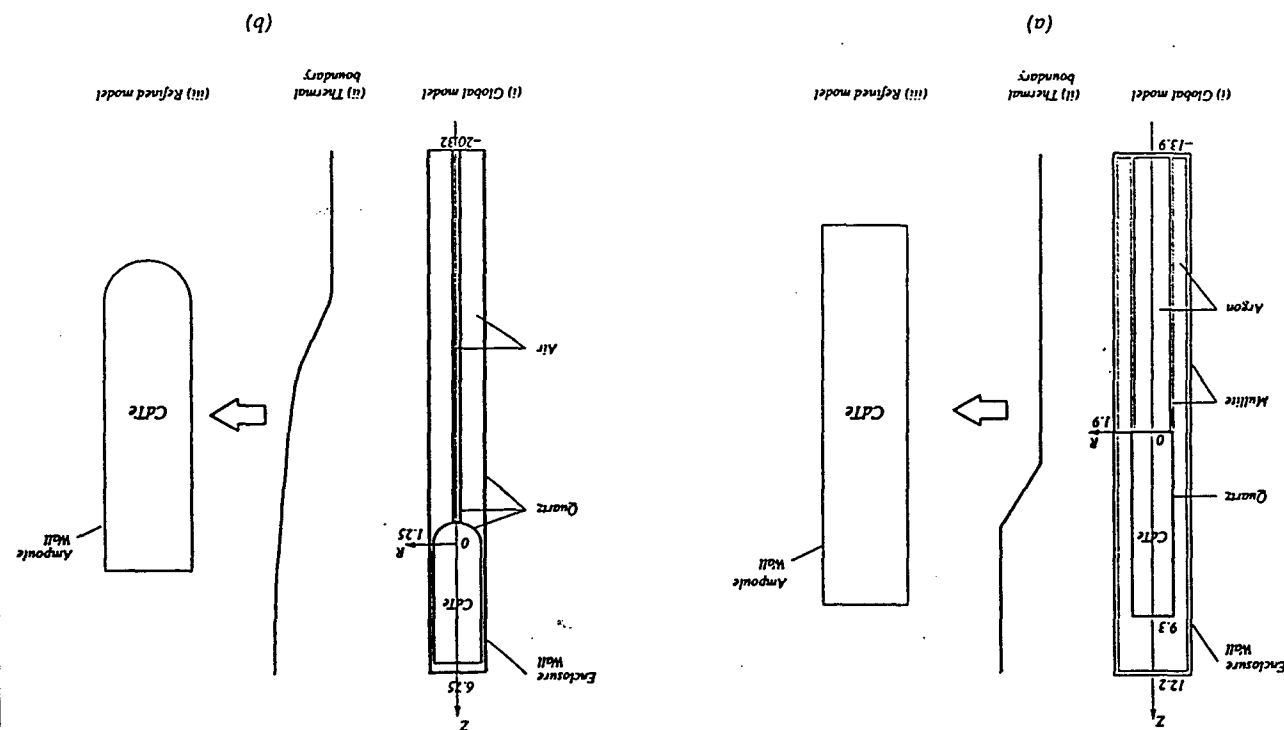
ference between the maximum and minimum temperatures in corresponding Bridgman configurations.

In addition, ρ_0, μ_0, C_{p0}, k_0 and β_0 are reference scales of material properties of density, viscosity, thermal capacity, conductivity and expansion coefficient, based on liquid NiAl or CdTe crystals at room temperature, and are given in Table 1. ΔH is the latent heat. It is noticed that the conductivity of CdTe is significantly smaller than that of NiAl, which implies that the crystal growth process of CdTe is much more sensitive to temperature variations than that of NiAl and is more difficult to control.

To solve the above governing equations, a control volume technique employing non-orthogonal body-fitted coordinate system, with the pressure-based algorithm, has been adopted. Details of this algorithm can be found in Refs. [11-13].

Table 1 Material Properties of NiAl and CdTe

Material	ρ (kg/m³)	μ (kg/m-s)	k (W/m-K)	C_p (J/kg-K)	β (K⁻¹)	ΔH (kJ/kg)	T_{melt} (K)
NiAl	5950	5.0×10^{-3}	75	660	1.5×10^{-5}	688	1911
CdTe	5680	2.5×10^{-3}	1.5(s) 3.0(l)	160(s) 187(l)	5.0×10^{-4}	209.2	1365

s: solid   l: liquid

Two-Level Modeling Strategy

Figures 1 and 2 show that the geometries of the current crystal growth systems are very complex. To render the computations tractable and to obtain an adequate resolution within the ampoule to resolve the melt-solid interface region, a two-level modeling strategy previously developed [9, 10] is employed. In this modeling strategy, Level 1, accounting for the entire configuration is referred to as the global model; Level 2, concentrating on the ampoule region, deduces its boundary conditions from the Level 1 solution and is referred to as the refined model. With this two-level strategy we can economically obtain useful information at the global level, while assessing the resolution refinement within the ampoule to investigate the details of the melt/crystal interface characteristics. Figure 1(b) and Figure 2(a) and (b) demonstrate the application of the two-level strategy of the present simulation.

The Treatment of Phase Change and Material Properties

In modeling the solidification process, due treatment needs to be taken to account for the release of latent heat during phase change. As is shown in Eq. (4), an enthalpy-based method [11, 14-15] has been adopted in the energy equation through the implementation of the fluid fraction f in the source term. Here f is defined to be 1 in liquid phase, 0 in solid phase, and varies continuously between the two phases. Although the melting temperature given in Table 1 is uniquely defined, in the present model, phase change is considered to take place between $T_{melt}-\delta T$ and $T_{melt}+\delta T$ in order to incorporate the notion of "mushy zone". δT is a specified small range of dimensionless temperature for numerical stability, taken as 10^{-3} at present. In practice the mushy zone thickness is very thin compared to the typical dimension of a computational cell, ensuring faithful representation of the interface characteristics.

To handle both solid and liquid regions simultaneously, the source terms, S_u and S_w, are included in the momentum equations (2) and (3), to ensure that the velocity in solid matches the pull rate in the ampoule region.

of the crystal. The approach taken here is the inclusion of Darcy-type source terms in the momentum equations [11, 14-15]. Thus the source terms have the form: $S_u = -A u$ and $S_w = -A w$ where A varies as a function of the fluid fraction f from zero in the liquid phase to infinity in the solid phase [14, 16], i.e. $A=K_0(1-f)^2/f^3$, where K_0 is a permeability constant, taken as 2.5×10^6 here.

Jumps in transport and mechanical properties appear among different materials. Following Patankar [13], a harmonic interpolation based on a one-dimensional flux conservation is used. This treatment has been compared with the flux balance approach [17] and is found to be equally robust and accurate but simpler to implement. The mathematical expression adopted here can be found in Ref. [9].

Radiation Effect

The radiation heat flux between the inner wall of the enclosure and the outer wall of the ampoule is handled by adopting the heat flux formulation between two infinite concentrate cylinders [18]. The simplified treatment has the form

$$q = \frac{\sigma (T_a^4 - T_e^4)}{(1/\varepsilon_a) + \left(\frac{1-\varepsilon_e}{\varepsilon_e}\right)(r_a/r_e)} \tag{5}$$

where σ is the Stefan-Boltzmann constant, T_a, r_a, and ε_a are the temperature, radius and emissivity of the ampoule outer wall and T_e, r_e and ε_e are corresponding variables at the inner wall of the enclosure. The expression for the boundary condition at the outer wall of the ampoule is given by,

$$-k\frac{\partial T}{\partial r}\Big|_{ampoule} = -k\frac{\partial T}{\partial r}\Big|_{argon\ or\ air} + q \tag{6}$$

where the left hand side represents the heat flux into the ampoule wall and the right hand side represents the heat flux due to convection and conduction from the encapsulating gas and the radiation from the enclosure.

Results and Discussion

A unified computational software has been developed to simulate vertical Bridgman growth processes for both NiAl and CdTe crystals. The geometrical effects and the interplay of physical properties on crystal growth characteristics are investigated. For the NiAl system, the actual parameters of $Ra_q=3.2 \times 10^4$, $Pr_q=4.4 \times 10^{-2}$, and $St_q=1.7$, based on the liquid NiAl properties at room temperature are adopted. For the CdTe system, as two configuration designs need to be simulated, consistent parameters of $Ra_q=1.0 \times 10^5$, $Pr_q=0.4$, and $St_q=0.2$ are employed for both configurations. A multi-zone patched grid method has been employed to generate the grid systems needed for global model. Sample grid distributions for both NiAl and CdTe systems are shown in Fig. 3.

The Simulation of NiAl system

In this case, the global simulations (Level 1) were conducted for three different ampoule positions in order to estimate the effects of geometric variations as the crystal is pulled out of the heater, i.e. $H=3.2$, $H=6.4$ and $H=9.6$. For all positions, there were 51×103 grid points in the ampoule region.
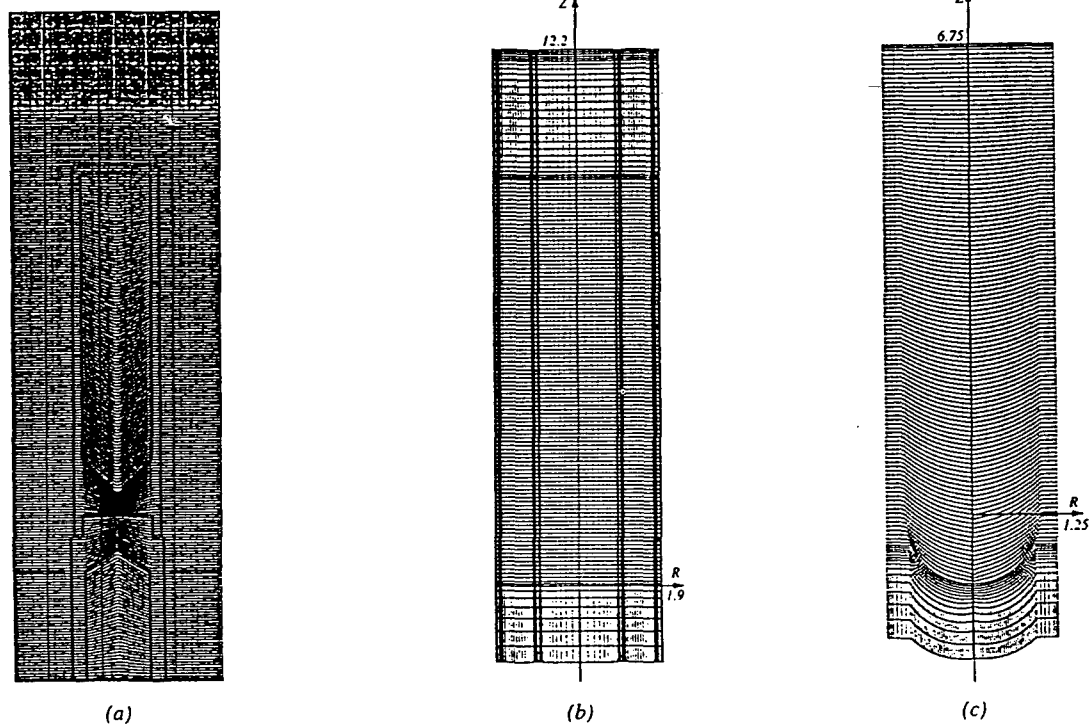
Figure 3. Global grid distributions for (a) the NiAl system of H=3.2 with a total grid size of 151x213 and 51x103 inside ampoule, (b) the flat base CdTe configuration around the ampoule region with a total grid size of 79x167 and 31x101 inside ampoule, and (c) the semi-spherical CdTe configuration around the ampoule region with a total grid size of 79x175 and 61x110 inside ampoule.
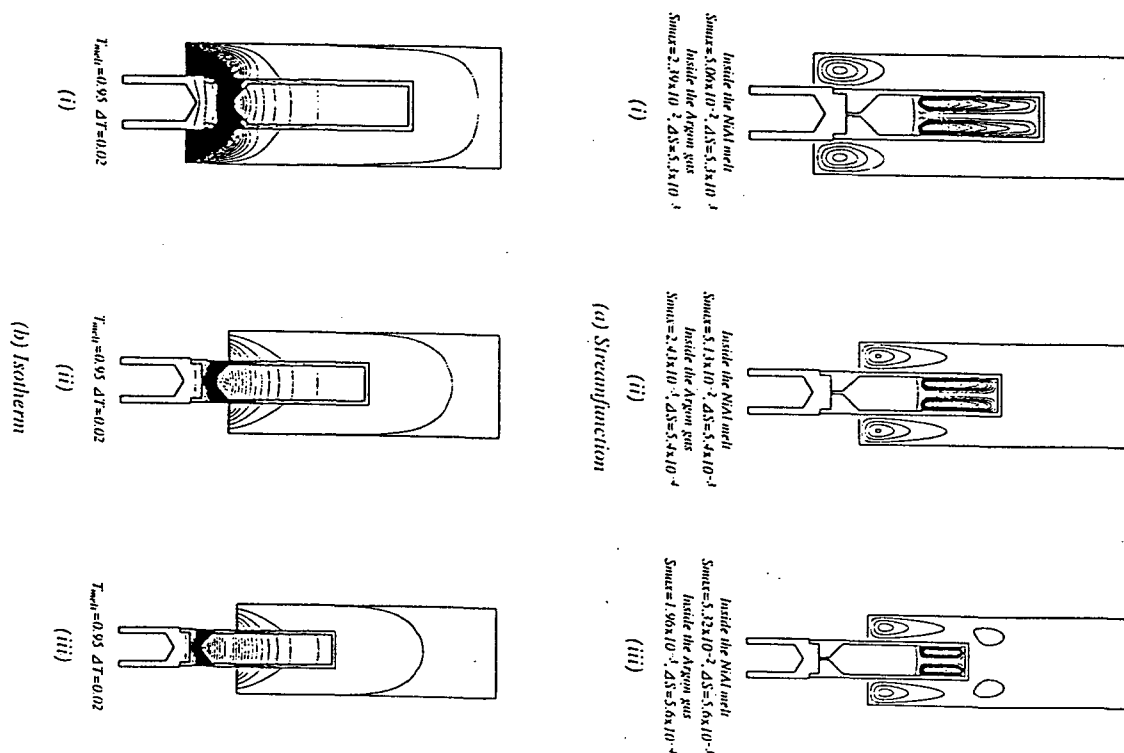

Figure 4. Solution characteristics of the global simulation of NiAl system for three different H. (i) H=3.2 (ii) H=6.4 (iii) H=9.6. $Ra_q=3.2\times10^4$, $Pr_q=4.4\times10^{-2}$, and $St_q=1.7$

Figure 4 show the streamfunction and isotherm distributions, respectively, for each of the three ampoule positions. It may be observed that, in the encapsulated gas region, the convection pattern is quite weak and the convective heat transfer into the ampoule is negligible compared to the radiative effect from the heater. Nevertheless, its isotherm pattern changes quite significantly. As the crystal is drawn downward, the temperature gradients at the base region decrease in magnitude. Within the ampoule region though, both convection and interface develop quite stable. As the crystal is pulled downward, convection strength gets slightly stronger and the melt/crystal interface shape keeps convex towards the melt for all positions.

The refined ampoule simulation (Level 2) was then conducted using the ampoule wall temperature distribution, obtained from Level 1, as the boundary condition. The grid resolution within the ampoule has been increased to 101 x 154 from 51 x 103 used at Level 1. Figure 5 presents the streamfunction and isotherm contours. Noticeable differences may be observed between the convection patterns in Fig. 4 and Fig. 5. Especially for H=3.2, more detailed secondary vortical structure in the central region above the solid–melt interface is clearly observed from the refined solutions.

This characteristics of secondary vortical structure can also be captured by global refined calculation, as is shown in Fig. 6 for H=3.2. However, this global refinement requires a total grid size of 223x284 over the entire domain to achieve the 73x154 grid points inside ampoule. Compared with the single ampoule refinement of 101x154 grid points, the computational cost of global refinement is about four times higher. This indicates that the current multi-level approach is necessary to achieve computational accuracy as well as economy.

Inside the NiAl melt
$Smax=4.18 \times 10^{-2}, \Delta S=4.4 \times 10^{-3}$
Inside the Argon gas
$Smax=2.42 \times 10^{-3}, \Delta S=4.4 \times 10^{-3}$

(a) Streamfunction

$T_{melt}=0.95 \ \Delta T=0.02$

(b) Isotherm

717

Figure 6. Solution characteristics of the global refined simulation of NiAl system for H=3.2 with a total grid size of 223x284. $Ra_0=3.2 \times 10^4$, $Pr_0=4.4 \times 10^{-2}$, and $St_0=1.7$

$Smax=4.45 \times 10^{-2}, \Delta S=4.8 \times 10^{-3}$
(i)

$Smax=5.41 \times 10^{-2}, \Delta S=5.7 \times 10^{-3}$
(ii)

$Smax=5.60 \times 10^{-2}, \Delta S=5.9 \times 10^{-3}$
(iii)

(a) Streamfunction

$T_{melt}=0.95 \ \Delta T=0.02$
(i)

$T_{melt}=0.95 \ \Delta T=0.02$
(ii)

$T_{melt}=0.95 \ \Delta T=0.02$
(iii)

(b) Isotherm

716

Figure 5. Solution characteristics of the refined ampoule simulation of NiAl system for three different H. (i) H=3.2 (ii) H=6.4 (iii) H=9.6. $Ra_0=3.2 \times 10^4$, $Pr_0=4.4 \times 10^{-2}$, and $St_0=1.7$

719

Isotherm

Stream Function

Smax=0.427

(ii)

Stream Function

Isotherm

Inside the CdTe melt, Smax=0.406
Inside the Argon gas, Smax=8x10⁻³

(i)

(a) Flat base ampoule configuration

Isotherm

Stream Function

Smax=0.162

(ii)

Stream Function

Isotherm

Inside the melt Smax=0.157
Inside the air Smax=5.84x10⁻²

(i)

(b) Semi-spherical base ampoule configuration

Figure 9. Solution characteristics of (i) the global and (ii) the refined simulations of CdTe system for (a) the flat base ampoule configuration and (b) the semi-spherical base ampoule configuration. $Ra_0=10^5$, $Pr_0=0.4$, $St_0=0.2$, and $k_l=2k_s$.

† *Streamfunction inside encapsulated gase and inside CdTe melt are not drawn by the same scales.*

Copper

Conductivity (W/m K)

Temperature (K)

Alumina

Conductivity (W/m K)

Temperature (K)

Figure 7. Dependency of thermal conductivities of alumina and copper on temperature.

— Variable conductivity
···· Constant conductivity (based on the values at room temperature)

Along ampoule centerline

Along ampoule inner vertical wall

Along ampoule inner top wall

Along ampoule inner bottom wall

Temperature

Z

R

Figure 8. Comparison of temperature profiles of the global simulation of NiAl system with variable and constant thermal conductivities of alumina and copper for $\Pi=6.4$.

718

The Simulation of CdTe System

In addition, it is mentioned that our current model can fully account for the dependency of material properties on temperature as well as on phases. However, limited by the data available to us, only variations of thermal conductivities of alumina and copper with respect to temperature, as are given in Fig. 7 [19], are considered in the current simulation of NiAl system. To demonstrate the influence of the property variations, a calculation was also conducted with thermal conductivities of alumina and copper held fixed to the reference values at room temperature, a practice employed in some modeling work. While the general patterns of streamfunction and isotherm seem insensitive, some critical aspects of the solutions are substantially different. For example, Figure 8 shows the differences in the temperature distribution along the centerline and the inner wall of the ampoule, between the cases with variable conductivities and with constant conductivities; a 50 % difference is observed along the bottom wall of the ampoule.

The Simulation of CdTe System

Figures 9(a) shows the solution characteristics obtained by the global model and the refined model for the flat base configuration of CdTe system. For the refined model, the grid size within the ampoule region is increased to 161x101 from 31x101 nodes used by the global model. It is observed that both models predicted similar convective and isothermal features except that the refined model captured two additional recirculation cells near the top region. Figures 9(b) shows the results for the semi-spherical base configuration. For the refined model, the grids within the ampoule region are increased to 121x219 from 61x110 nodes used by the global model. Again almost identical distributions of streamfunction and isotherm within the ampoule region are achieved by both models. These agreements indicates that accurate solutions have been obtained with the present grid resolution. In the case of NiAl, the two-level model offers improved spatial resolution; here, it helps ascertain the numerical accuracy.

—— Flat base system　· · · Semi-spherical system
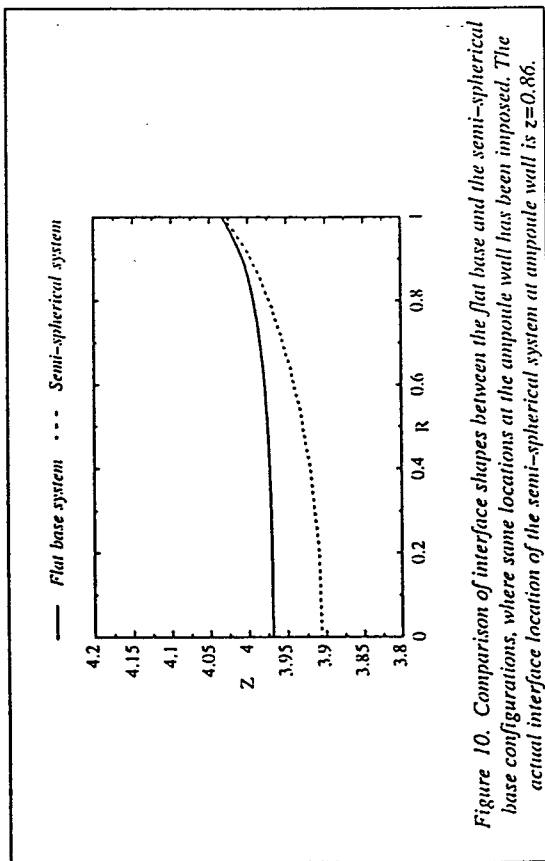
Figure 10. Comparison of interface shapes between the flat base and the semi-spherical base configurations, where same locations at the ampoule wall has been imposed. The actual interface location of the semi-spherical system at ampoule wall is z=0.86.

To show the impact of the ampoule configuration on interface characteristics, Figure 10 compares the interface curvature obtained by the flat base and by the semi-spherical base configurations by imposing their locations on the ampoule wall together. This comparison shows that a concave interface appears in both configurations. Despite the dramatic change in ampoule geometries, the

---

change of the interface curvature is rather small. The difference of the interface position at the ampoule center is only about 5%. Thus at this point, no obvious improvement of one design over the other is achieved by changing the ampoule geometry.

In addition, by comparing the streamfunction and the isotherm in Fig. 9(a) and (b), it is observed that in both configurations minor cells appear in the region close to the interface due to the concave shape of the interface. Nevertheless, the main convection cells assume very different features between the two configurations. In Fig. 9(b), the convection cells are more stretched over the whole melt domain and their magnitudes are smaller. This is because the thermal boundary condition applied to this configuration is distributed more smoothly. However, the change of the main convection characteristics does not seem to substantially influence the interface curvature.

Stream Function

Isotherm

$Smax=0.430$

(a)

$k_l=2k_s$
$k_l=k_s$

(b)
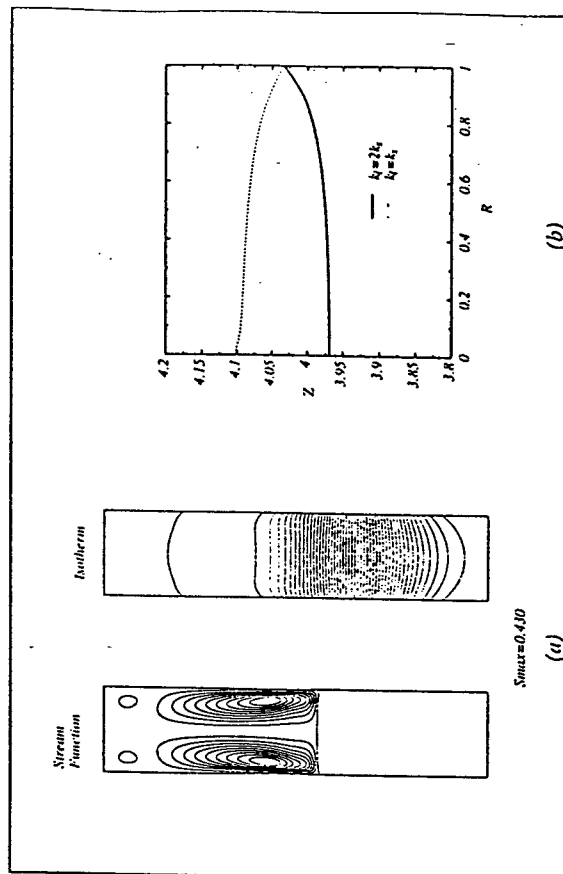
Figure 11. Solution characteristics of the refined model with constant conductivity of CdTe, i.e. $k_l=k_s$, for the flat base ampoule configuration. (a) Streamfunction and isotherm. (b) Comparisons of interface characteristics between $k_l=k_s$ and $k_l=2k_s$.

Finally, one of the major aspect of CdTe is its thermal conductivity of melt is twice that of the solid, i.e. $k_l=2k_s$ [8]. This aspect is investigated now. In fig. 11, we present a refined ampoule solution with a constant conductivity of CdTe, i.e. $k_l=k_s$, and compared their interface characteristics. It is striking to observe that the interface shape changes from concave to convex due to the change in the thermal conductivity. While the comparison between Fig. 9(a) and Fig. 11(a) shows that the main convective pattern in the melt is largely unchanged, the two smaller cells near the interface region observed with $k_l=2k_s$ no longer exist with $k_l=k_s$.

Conclusion

Numerical simulation has been carried out for the single crystal growth of β-NiAl and CdTe in three different configurations of vertical Bridgman system. All three heat transfer modes, conduction, convection and radiation, and the complex geometry of the entire system consisting of the enclosure wall, encapsulated gas and the ampoule have been considered. Accordingly, a two-level

simulation has been performed to simultaneously achieve accuracy as well as computational economy. At the global level, the entire system consisting of the enclosure, the ampoule support and the ampoule is fully considered. However, it is desirable to improve the grid resolution within the ampoule to capture the detailed characteristics of the melt/crystal interface. Thus, a refined ampoule simulation was performed using the solution from the global simulation as the boundary condition, enabling an accurate treatment of solidification dynamics within the ampoule, and heat transfer through the crystal.

Furthermore, by the simulation of NiAl system, it is shown that variations of material properties need to be considered in order to achieve a realistic solution. Significant errors exist for simulations carried out assuming constant material properties. Accurate property data are not readily available in the literature, but have been shown to be necessary to predict the temperature distribution within the crystal growth system. For the CdTe system, it is found that both the flat base and the semi-spherical base configurations produce slightly concave solid–melt interface which is apparently undesirable. Furthermore, the curvature of the melt/crystal interface seems to depend strongly on the variations in thermal conductivities between melt and crystal.

The predictions reported in the present work are of value in improving our understanding of the growth process and will be of help in controlling the growth parameters in order to achieve the desired melt/crystal interface shape, which has implications on the composition and quality of the resulting crystal.

Acknowledgment

References

1. S. Sen and D. M. Stefanescu, "Melting and Casting Processes for High–Temperature Intermetallics," JOM, May (1991), 30–32.

2. R. Darolia, "NiAl Alloys for High–Temperature Structural Applications," JOM, March (1991), 44–49.

3. K. Zanio, "Cadmium Telluride," Semiconductors and Semimetals, eds. R.K. Willardson and A.C. Beer (New York: Academic Press, 1978), Vol. 13.

4. M. Pfeiffer and M. Mühlberg, "Interface Shape Observation and Calculation in Crystal Growth of CdTe by the Vertical Bridgman Method," J. Crystal Growth, 118 (1992), 269–276.

5. R.A. Brown, "Theory of Transport Processes in Single Crystal Growth from the Melt," A.I.Ch.E. J., 34 (1988), 881–911.

6. J. C. Brice, Crystal Growth Processes, (London, U.K.: Blackie, 1986).

7. M. J. Kaufman and V. Levit, Private Communication, University of Florida, Gainesville, FL, 1994.

8. Y. Pang, Private communication, BDM Inc, McLean, VA, 1994.

9. H. Ouyang and W. Shyy, "Multi–level Simulation of Bridgman Growth of β–NiAl," Accepted for publication in Int. J. Heat Mass Transf. (1995).

10. H. Ouyang and W. Shyy, "Numerical Simulation of Bridgman Growth of CdTe," To be published (1995).

11. W. Shyy, Computational Modeling for Fluid Flow and Interfacial Transport, (Amsterdam, The Netherlands: Elsevier, 1994).

12. W. Shyy, S.S. Tong and S.M. Correa, "Numerical Recirculating Flow Calculation using a Body–Fitted Coordinate System," Numer. Heat Transf., 8 (1985), 99 –113.

13. S.V. Patankar, Numerical Heat Transfer and Fluid Flow, (Washington, D.C.: Hemisphere, 1980).

14. V. Voller, "Implicit Finite–Difference Solutions of the Enthalpy Formulation of Stefan Problems," IMA J., 5 (1985), 201–214.

15. W. Shyy, H.S. Udaykumar, M.M. Rao and R.W. Smith, Computational Fluid Dynamics with Moving Boundaries, (Washington, D.C.: Taylor and Francis, 1995).

16. W. Shyy and M.–H. Chen, "Steady–State Natural Convection with Phase Change," Int. J. Heat Mass Transf., 33 (1990), 2545–2563.

17. W. Shyy and J. Burke, "A Study of Iterative Characteristics of Convective–Diffusive and Conjugate Heat Transfer Problems," Numer. Heat Transf., 26B (1994), 21–37.

18. R. Siegel and J.R. Howell, Thermal Radiation Heat Transfer, (Washington, D.C.: Hemisphere, 1981).

19. R. H. Perry, D. W. Green and J. O. Maloney (editors), Perry's Chemical Engineerings' Handbook (6th edn), (New York: McGraw–Hill, 1984).

MULTI-RESOLUTION COMPUTATIONS FOR FLUID FLOW AND HEAT/MASS TRANSFER

W. Shyy
J. Liu
H. Ouyang

1 INTRODUCTION

Complex fluid flow and heat/mass transfer problems encountered in natural and man–made environments are characterized by both geometric and dynamic complexities. For example, the geometric configuration of a jet engine, a heart, or a crystal growth device is irregular; to analyze the heat and fluid flow in these devices, *geometric complexity* is a major issue. From the analytical point of view, *dynamic complexity* is a well established characteristic of fluid dynamics and heat/mass transfer. Dynamic complexity results from the disparities of the length, time, and velocity scales caused by the presence of competing mechanisms such as, e.g., convection, conduction, body forces, chemical reaction, and surface tension; these mechanisms are often coupled and nonlinear. A case in point is the classical boundary layer theory originated by Prandtl [1, 2], whose foundation is built upon the realization that the ratio of viscous and convective length and time scales can differ by orders of magnitude for high Reynolds number flows. With sufficiently high Reynolds number, or other appropriate non–dimensional parameters, such as Rayleigh or Marangoni number [3], turbulence appears, and there exists a wide spectrum of scales, ranging from the global one dictated by the flow configuration, to the smallest one where turbulent energy is dissipated into heat [4–6]. In addition to these standard textbook materials, relevant examples abound in nature and in engineering practice. A timely example can be drawn from materials solidification and processing. It is well established that the interaction of transport mechanisms in

the melt with the solidification process can have a strong effect on the resulting structure and properties of the material, the main reason being that these mechanisms create multiple length and time scales in the physical system [3, 7–10]. For example, based on dimensional analysis, several length scales can be identified in a system containing binary species; extra scales will appear in systems containing more species. First, the length scales important for the solidification process can be summarized as:

1. capillary length, $d = \gamma/L$ where γ is the surface tension, L is the latent heat of fusion,
2. thermal diffusion length scale, $\delta_T = \alpha/V_n$, where α is the thermal diffusivity of the melt, and V_n is the growth speed of the solid–melt interface,
3. solutal diffusion length scale, $\delta_s = D/V_n$, where D is the mass diffusivity of the melt, and
4. convective length scale, δ_v.

For most technologically important materials, due to the disparity of Schmidt and Prandtl numbers, Sc > O(1) and Pr < O(1), the following relative order of magnitudes can be identified among these length scales,

$$O(d) \ll O(\delta_s) < O(\delta_v) < O(\delta_T)$$

Most of the work published in this area deals with the issues confined within a particular range of scales. At the microscopic level, work has been conducted by many researchers to analyze and simulate the formation, growth and evolution of the solid–liquid interface where the mechanisms at the morphological length scale are considered [11–18]. Physical mechanisms such as capillarity and diffusion are important to consider. At the macroscopic level, where convective and diffusive effects on momentum, heat and mass transport are important, limited analyses have been made to study the solidification problem, without accounting for the smaller length scales such as capillarity [19–30]. In order to treat the physical processes involving different scales, one needs to devise separate scaling procedures for each physical regime, as well as to find ways to couple these scales in a coherent manner so as to optimize the utilization of computing resources.

Generally speaking, two classes of multi-scale problems exist. In the first class, small scales occupy distinct regions in space so that the large and small scales need only be matched or patched together; the boundary layer theory is a good example where the viscous, small scale effect is confined only in the vicinity of the solid boundary. Methods such as singular perturbation and matched asymptotic expansion have been developed during the last several decades to deal with such problems [2, 31]. In the second class, the disparate scales coexist throughout the entire domain and interact with one another everywhere; turbulence is a classical example where the macroscopic and microscopic scales are present simultaneously and, in fact, exchange energy via the cascading process [4]. Analytical techniques such as the renormalization group (RNG) method, originally developed for treating the critical phenomena involving phase change, has been recently applied to treat

broader physical problems such as turbulent fluid flows [32, 33], yielding some success.

A computational framework will be presented herein. The overall strategy is based on the concept of multi–resolution, to enable one to deal with fluid flow and heat/mass transfer problems involving both *geometric and dynamic complexities*. For both types of complexities, while the generation of the grid system, the discretization of the governing differential equations, and the efficiency of the solution procedure are all part of the challenge, *the key to overall success is an effective coordination among them*. The materials presented are guided by the viewpoint that a pragmatic, multiple–resolution modeling and computational strategy capable of handling the existence of distinguishable competing mechanisms, acting at disparate scales and speed is very desirable. Specifically, the computational challenge in the present context, is to develop:

1. a *computational capability* for solving general transport equations to simulate the physical phenomena at both macroscopic and microscopic scales;
2. a modeling strategy based on *scale patching* that is capable of handling the mutual influence between different scales, in the form of, for example, modified source terms, effective transport properties such as diffusivities, or boundary conditions, and
3. a *resolution patching* capability based on multi–block techniques to allow different scales, or geometrical details, to be patched together if different numerical resolutions are needed in different spatial domains.

In the following, details of these challenges are elucidated. Our current efforts in developing a multiple–resolution computational strategy in a thermo–fluid system will be presented. Both modeling concepts for linking the multiple scales and the numerical techniques for handling data communication and for resolving transport characteristics, in the context of *scale patching and resolution patching*, will be discussed in a detailed manner. Physical examples will also be presented to help illustrate the issues involved.

2 NUMERICAL METHODS FOR TRANSPORT EQUATIONS

Before presenting other specific aspects of the multiple–resolution computational technique, some background about the solution technique for the general fluid flow equations will be useful.

2.1 Governing Equations and Numerical Algorithm

To facilitate our discussion, the 2–D steady state, incompressible, constant property, Navier–Stokes equations are used:

$$\frac{\partial}{\partial x}(\varrho u) + \frac{\partial}{\partial y}(\varrho v) = 0 \tag{1}$$

$$\frac{\partial}{\partial x}(\varrho uu) + \frac{\partial}{\partial y}(\varrho vu) = -\frac{\partial p}{\partial x} + \frac{\partial}{\partial x}\left(\mu\frac{\partial u}{\partial x}\right) + \frac{\partial}{\partial y}\left(\mu\frac{\partial u}{\partial y}\right) \tag{2}$$

$$\frac{\partial}{\partial x}(\varrho uv) + \frac{\partial}{\partial y}(\varrho vv) = -\frac{\partial p}{\partial y} + \frac{\partial}{\partial x}\left(\mu\frac{\partial v}{\partial x}\right) + \frac{\partial}{\partial y}\left(\mu\frac{\partial v}{\partial y}\right) \tag{3}$$

With the introduction of coordinate transformation $\xi = \xi(x,y)$, $\eta = \eta(x,y)$, the equations above are then cast into the curvilinear coordinates [3],

$$\frac{\partial}{\partial \xi}(\varrho U) + \frac{\partial}{\partial \eta}(\varrho V) = 0 \tag{4}$$

$$\frac{\partial}{\partial \xi}(\varrho Uu) + \frac{\partial}{\partial \eta}(\varrho Vu) = -y_\eta\frac{\partial p}{\partial \xi} + y_\xi\frac{\partial p}{\partial \eta} + \frac{\partial}{\partial \xi}\left[\frac{\mu}{J}(q_1 u_\xi - q_2 u_\eta)\right]$$
$$+ \frac{\partial}{\partial \eta}\left[\frac{\mu}{J}(-q_2 u_\xi + q_3 u_\eta)\right] \tag{5}$$

$$\frac{\partial}{\partial \xi}(\varrho Uv) + \frac{\partial}{\partial \eta}(\varrho Vv) = +x_\eta\frac{\partial p}{\partial \xi} - x_\xi\frac{\partial p}{\partial \eta} + \frac{\partial}{\partial \xi}\left[\frac{\mu}{J}(q_1 v_\xi - q_2 v_\eta)\right]$$
$$+ \frac{\partial}{\partial \eta}\left[\frac{\mu}{J}(-q_2 v_\xi + q_3 v_\eta)\right] \tag{6}$$

where

$$U = uy_\eta - vx_\eta, \quad V = vx_\xi - uy_\xi \tag{7}$$

$$q_1 = x_\eta^2 + y_\eta^2, \quad q_3 = x_\xi^2 + y_\xi^2 \tag{8}$$

$$q_2 = x_\xi x_\eta + y_\xi y_\eta, \quad J = x_\xi y_\eta - x_\eta y_\xi \tag{9}$$

A staggered grid system is adopted, as shown in Fig. 1, for discretization of the above equations. Scalar variables, such as P, are located at the center of the control volume. Both u and U are located at the midpoints of the east and west faces of the control volume. Both v and V are located at the midpoints of the north and south faces of the control volume. In terms of the notation shown in Fig. 1, for a node P enclosed in its cell and surrounded by its neighbors N, S, E and W, the finite-difference approximation to the momentum equations can be obtained by taking the integral of the momentum equations over the control volume. By arbitrarily taking $\Delta\xi = \Delta\eta = 1$, the resulting momentum equations yield:

$$\left[\varrho Uu + y_\eta p - \frac{\mu}{J}(q_1 u_\xi - q_2 u_\eta)\right]\Big|_w^e + \left[\varrho Vu - y_\xi p - \frac{\mu}{J}(-q_2 u_\xi + q_3 u_\eta)\right]\Big|_s^n = 0 \tag{10}$$
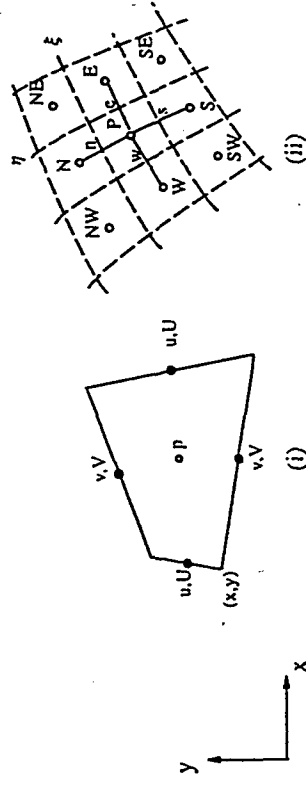
Figure 1 Staggered grid and notation for curvilinear grid system. (i) Configuration of a staggered grid system. (ii) Curvilinear grid system.

$$\left[\varrho Uv - x_\eta p - \frac{\mu}{J}(q_1 v_\xi - q_2 v_\eta)\right]\Big|_w^e + \left[\varrho Vv + x_\xi p - \frac{\mu}{J}(-q_2 v_\xi + q_3 v_\eta)\right]\Big|_s^n = 0 \tag{11}$$

Furthermore, the above equations can be put into a generalized form as:

$$\left[\varrho U\Phi - \frac{\mu}{J}(q_1\Phi_\xi - q_2\Phi_\eta)\right]\Big|_w^e + \left[\varrho V\Phi - \frac{\mu}{J}(-q_2 u_\xi + q_3\Phi_\eta)\right]\Big|_s^n = S \cdot J \tag{12}$$

where Φ is the general dependent variable and S is the source term. With appropriate finite difference schemes representing the convective and diffusive terms at the control volume boundaries, the discretized equation relating the variable at a central point P to its neighboring values is obtained [34],

$$A_P\Phi_P = A_E\Phi_E + A_W\Phi_W + A_S\Phi_S + A_N\Phi_N + S_v \tag{13}$$

where the coefficients result from different numerical schemes chosen in the course of discretization. The pressure terms and the cross-derivative portion of the viscous terms, due to the non-orthogonal grid effects, are taken into the source term, S_v. Specifically, if the central-difference scheme is used for the convection and diffusion terms, the coefficients are :

$$A_E = \frac{\mu}{J}q_1|_e - \frac{1}{2}\varrho U|_e \tag{14}$$

$$A_W = \frac{\mu}{J}q_1|_w + \frac{1}{2}\varrho U|_w \tag{15}$$

$$A_N = \frac{\mu}{J}q_3|_n - \frac{1}{2}\varrho V|_n \tag{16}$$

$$A_S = \frac{\mu}{J}q_3|_s + \frac{1}{2}\varrho V|_s \tag{17}$$

$$A_P = A_E + A_W + A_N + A_S \tag{18}$$

The continuity equation can be written in a similar discretized form over each control volume as follows:

$$(y_\eta \varrho u - x_\eta \varrho v)_e - (y_\eta \varrho u - x_\eta \varrho v)_w - (y_\xi \varrho u - x_\xi \varrho v)_n + (y_\xi \varrho u - x_\xi \varrho v)_s = 0 \tag{19}$$

Let u^* and v^* be the intermediate velocity components with a given distribution of pressure, p^*. Since in general the mass continuity equation is not satisfied by this intermediate velocity field, the pressure p^* must be corrected. The corrected pressure is obtained from [35]

$$p = p^* + p' \tag{20}$$

where p' is called the pressure correction. The corresponding velocity corrections u' and v' can be introduced in a similar manner:

$$u = u^* + u' , \quad v = v^* + v' \tag{21}$$

To derive the pressure-correction equation, u' and v' are obtained from the momentum equations as follows:

$$u_P^* = \sum_{i=E,W,N,S} \frac{A_i^u}{A_P^u} u_i^* + D^u + (B^u p_\xi' + C^u p_\eta') \tag{22}$$

$$v_P^* = \sum_{i=E,W,N,S} \frac{A_i^v}{A_P^v} v_i^* + D^v + (B^v p_\xi' + C^v p_\eta') \tag{23}$$

where D^u and D^v are, respectively, the cross-derivative viscous terms in the u- and v- momentum equations, and

$$B^u = -\frac{y_\eta}{A_P^u}, \quad C^u = \frac{y_\xi}{A_P^u}$$
$$B^v = \frac{x_\eta}{A_P^v}, \quad C^v = -\frac{x_\xi}{A_P^v} \tag{24}$$

The velocity components are thus corrected by the following formulas:

$$u = u^* + (B^u p_\xi' + C^u p_\eta') \tag{25}$$

$$v = v^* + (B^v p_\xi' + C^v p_\eta') \tag{26}$$

Subsequently, the corresponding correction forms for U and V are obtained by substituting Eqs. (25–26) into Eq. (7)

$$U = U^* + (B^u y_\eta - B^v x_\eta) p_\xi' + (C^u y_\eta - C^v x_\eta) p_\eta' \tag{27}$$

$$V = V^* + (B^v x_\xi - B^u y_\xi) p_\xi' + (C^v x_\xi - C^u y_\xi) p_\eta' \tag{28}$$

where U^* and V^* are calculated based on u^* and v^*. It is noted that the continuity equation, Eq. (19), can also be written in the following finite-difference form:

$$(\varrho U)_e - (\varrho U)_w + (\varrho V)_n - (\varrho V)_s = 0 \tag{29}$$

To retain a five-point approximation in the pressure-correction equation, the p_η' term in Eq. (27) and the p_ξ' term in Eq. (28) are dropped, leading to the following simplified correction equations for U and V:

$$U = U^* + (B^u y_\eta - B^v x_\eta) p_\xi' \tag{30}$$

$$V = V^* + (C^v x_\xi - C^u y_\xi) p_\eta' \tag{31}$$

These equations are then substituted into Eq. (29) to obtain the following pressure-correction equation:

$$a_P p_P' = a_E p_E' + a_W p_W' + a_N p_N' + a_S p_S' + S_P \tag{32}$$

$$a_P = a_E + a_W + a_N + a_S \tag{33}$$

$$S_P = (\varrho U^*)_w - (\varrho U^*)_e + (\varrho V^*)_s - (\varrho V^*)_n \tag{34}$$

with the coefficients given by:

$$a_E = \varrho \left(\frac{y_\eta^2}{A_P^u} + \frac{x_\eta^2}{A_P^v} \right)_e \tag{35}$$

$$a_W = \varrho \left(\frac{y_\eta^2}{A_P^u} + \frac{x_\eta^2}{A_P^v} \right)_w \tag{36}$$

$$a_N = \varrho \left(\frac{x_\xi^2}{A_P^u} + \frac{y_\xi^2}{A_P^v} \right)_n \tag{37}$$

$$a_S = \varrho \left[\frac{x_\xi^2}{A_P^v} + \frac{y_\xi^2}{A_P^v} \right]_s \qquad (38)$$

2.1.1 Boundary condition for the momentum equations. At solid walls, the no-slip conditions are applied, i.e., the fluid velocities at solid walls are the same as the wall velocity. At inlets, the velocity distributions are prescribed. At outlets, the velocity gradients along the streamwise direction are taken as zero.

2.1.2 Boundary conditions for the pressure correction equation. Usually, two types of boundary conditions can be adopted for the pressure correction equation. If the pressure is known at the boundary, the pressure correction is zero there. If the velocity is known at the boundary, then, according to Eq. (30) or Eq. (31)

$$U = U^* \text{ or } V = V^* \qquad (39)$$

or

$$p'_\xi = 0 \text{ or } p'_\eta = 0 \qquad (40)$$

i.e., the Neumann type of boundary condition is applied to the pressure correction equation. At outlets, where usually the velocity is not known, the Neumann type of boundary condition is applied iteratively by updating the exit velocity based on the global mass conservation [3, 36].

3 SCALE PATCHING: MODELING CONCEPTS

3.1 Overall Strategy

In this section we describe the aspects of scale patching with the multiple-resolution model. For problems involving disparate length and time scales, it is desirable to account for the micro-scale effects via a filtering procedure in the macroscopic equations. The micro-scale terms, which represent the averaged effect viewed from the length and time scales appropriate to the macroscopic transport equations, are modeled based on the information generated from the ensembles of simulations conducted at the microscopic scale. The local conditions resulting from the solutions of the equations at the macroscopic scale, on the other hand, will be used as either the boundary conditions, effective transport properties, or the modified source terms for the microscopic analyses. Such a two-way coupling can proceed until both scales have yielded definitive solutions.

The fundamental tenet behind the scale patching is to treat the the macroscopic and microscopic scales separately. However, the two levels must communicate in some manner in order to produce a meaningful result; hence, some form of modelling to connect the two levels is required. Here, we will discuss some of the possibilities which have been considered in the design of the communication

Solve Global Flow Problem With a *Best Guess* Approach for Micro-Scales

Solve Micro-Scale Problem At Given Locations

Construct "Map" Relating Locally Computed Micro-Scale Characteristics To Modify e.g., Source Terms In Macro-Scale Equations

Solve Macro-Scale Flow Problem With Modified Source Terms Resulting from Micro-Scale Model
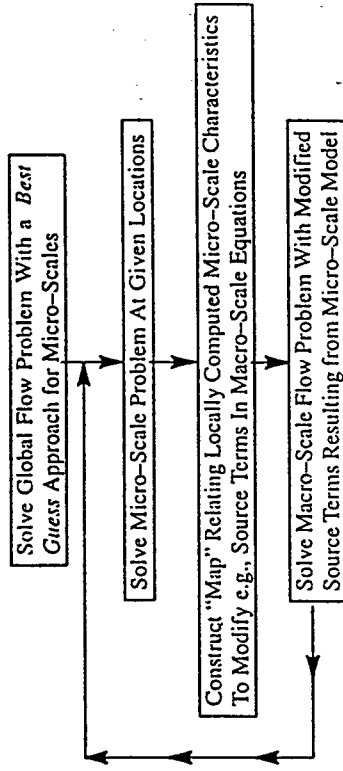
Figure 2 Flowchart for the coupled macro-micro computational procedure.

link between the two solution levels. At the macro-scale level, no detailed knowledge of the exact geometrical characteristics of particular roughness elements is known. In general, modifications are introduced into the governing equations to account for the micro-scale effects. The basic solution methodology can be described as follows. For reference, a flowchart of the solution process is shown in Fig. 2.

The first step in the scale patching process is the solution of the system of the governing equations on the macro-scale grid without consideration of the micro-scale characteristics. To link the two scales, one can construct a "map" relating the micro-scale features to the modifications, such as added sources terms or effective transport properties, required in the governing equations for the macro-scale. Once an initial solution has been obtained at the macro-scale, several micro-scale problems at multiple locations in the domain of interest can be set up and solved independently, using the boundary conditions from the global solution at these locations. From these solutions, the micro-scale characteristics can be correlated with the macro-scale solutions, such as local temperature and velocity fields and liquid fraction, and a map constructed. Using a limited number of micro-scale solutions, a complete map can be formed via curve fitting. From this map the micro-scale information at each location can be determined and the modifications in the macro-scale governing equations can be prescribed. This idea has been developed in some areas; for example, models of large-eddy simulations for turbulent fluid flows [37, 38] express the *subgrid-scale* terms according to the information obtained from the *large-scale* field. For more complex problems, a stochastic approach can be taken to construct a set of transport equations for the probability density function (pdf) of the variables of interest. For instance, for phase change problems, this procedure can be used to represent information such as the solidus volume fraction and the dendritic spacings in the interface region, according to the temporal and spatial information from the macroscopic model. The resulting pdf can be used, in turn, by the macroscopic model to define the phase change characteristics in the interface region. The macro-scale solution is then solved again,

oxidation resistance [43]. However, it has two major drawbacks; low toughness at room temperatures and low strength at high temperatures [44]. These deficiencies need to be resolved before NiAl can be used in structural applications. CdTe, on the other hand, is important and unique in such applications as gamma–ray and x–ray detectors, lenses and electro-optic modulators [45]. Furthermore, CdTe and its solid solutions (Cd, Zn)Te and Cd(Te, Se) can be used as the substrate for the infrared detector material, cadmium mercury telluride (Hg$_{1-x}$Cd$_x$Te) [46]. However, CdTe has low thermal conductivity ($k \approx 1.5$ W/m K) and low critical resolved shear stress (CRSS $\approx 0.5 \times 10^{-3}$ dynes/m^2), which make it very sensitive to minor variations in thermal condition and prone to formation of dislocations [47]. At present, CdTe has not made as significant an impact as Silicon because it is expensive and difficult to grow.

The Bridgman growth system is one of the directional solidification configurations that are useful for producing large size single crystals from the melt [48]. The advantage of the Bridgman system is that the temperature gradients can be controlled, making it possible to achieve unidirectional solidification. In the following, both NiAl and CdTe crystals will be considered. Figure 3a shows the schematic of actual design of the vertical Bridgman system for growing NiAl crystal [49]. The ampoule containing the melt and the crystal is made of alumina and rests on a copper support. The enclosure (heater 74) remains stationary during the growth process and the ampoule is pulled out to control the growth speed of NiAl. Figure 4 shows two designs of the vertical Bridgman growth system for CdTe, one with a flat base ampoule and the other with a semi–spherical base ampoule [50]. During the growth process, the thermal boundary profiles shown in Fig. 4 are kept stationary while the ampoule is pulled out of the enclosure.

From Fig. 3 and Fig. 4, it is clear that crystal growth in a vertical Bridgman system is a highly complex process and different physical phenomena occur at different scales. First, at the global scale, i.e. the entire system, there is conduction within enclosure walls and ampoule supports, convection in melts and in encapsulated gases and radiation between outer ampoule walls and inner enclosure walls. Secondly, at the ampoule scale, i.e. the ampoule region, there are the melt/solid phase change process and interfacial dynamics. Finally, at the interface, there is the morphological evolution as crystals are solidified. At present, our major goals are to investigate the influence of global processing conditions on the interfacial characteristics of pure crystal growth. A two–level scale patching strategy is developed for this purpose [51]. In this strategy, Level 1, accounting for the entire configuration is referred to as the global model; Level 2, concentrating on the ampoule region, is referred to as the refined model. Level 1 maps its boundary conditions to Level 2 via linear interpolation. With this two–level strategy we can economically obtain useful information at the global level, while assessing the resolution refinement within the ampoule to investigate the details of the melt/crystal interface characteristics. Figure 3b and Figs. 4a and 4b demonstrate the application of the two–level strategy of the present simulation.

For the NiAl system, the global simulations (Level 1) were conducted for three different ampoule positions in order to estimate the effects of geometric variations as the crystal is pulled out of the heater, i.e. $H=3.2$, $H=6.4$ and $H=9.6$.
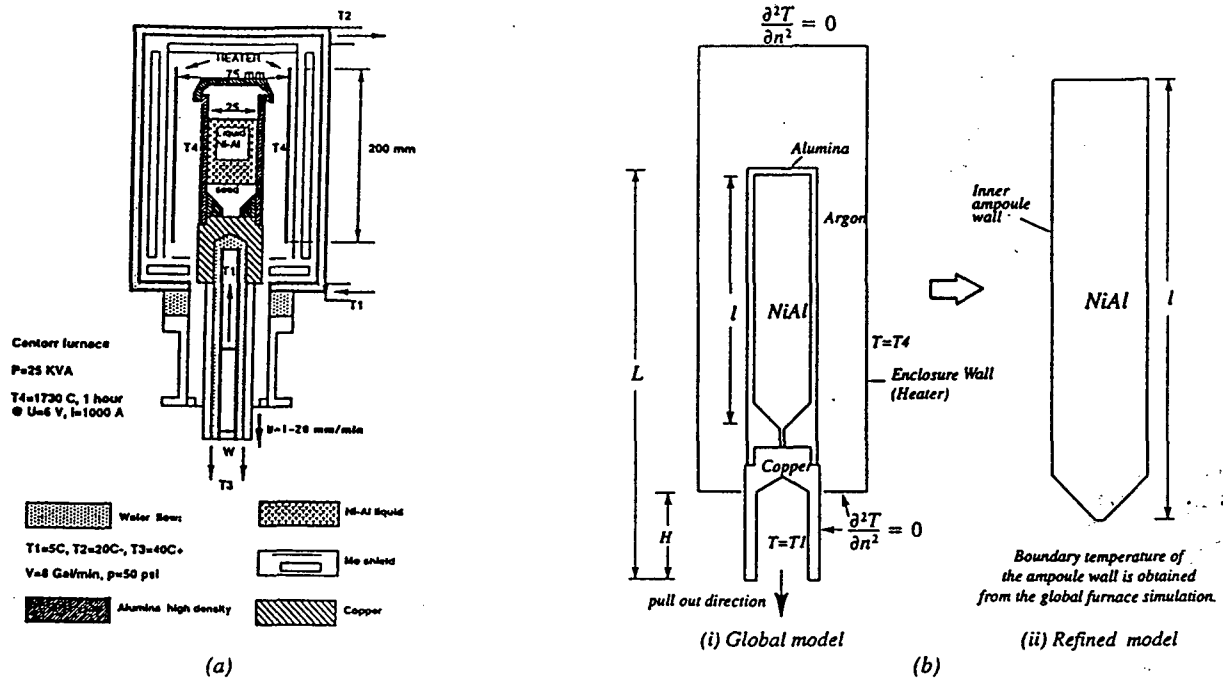
---

this time, including the information via modifications to the governing equations deduced from the macro–micro map, and the whole process is repeated.

3.2 Case Studies

In the following we present two physical applications employing the multiple–resolution model. The first case involves solidification of engineering materials from the melt, while the second case is motivated by fluid machinery flows. The solidification problem involves substantial geometric complexities with multiple physical mechanisms, including all three modes of heat transfer, and phase change; a multi–resolution approach at the macroscopic scales is considered. For the turbomachinery flow problem to be presented, many solid objects are present; in order to handle all the necessary details economically, a two–level model is devised.

3.2.1 Crystal growth using Bridgman technique. As already mentioned, during materials solidification, a wide disparity of the length scales exists, ranging from those resulting from the balance between convection and conduction/diffusion, to those from the balance between capillarity and conduction. With today's computing resources, no computational technique can resolve all the important length scales within the continuum regime. Accordingly, a multi–scale modeling strategy has to be devised. This is an actively researched area. For relevant references, the readers can consult Refs. [39–41], and the references cited therein. In virtually all the published studies employing the macro/micro modeling, the field equations governing the conservation laws of mass, momentum, and energy are solved at the macroscopic level, namely, at the convection and diffusion scales, while some descriptions of microscopic phenomena such as nucleation, undercooling and grain growth kinetics are adopted to supply the information needed by the macroscopic scale model. For example, Wang and Beckermann [41] have derived a set of macroscopic governing equations based on information averaged over microscopic scales. Consequently, the closure issue appears; in other words, additional relations supplementing the averaged macroscopic governing equations are needed to account for the phase change characteristics at the microscopic scale. Li and Anyalebechi [40] have followed a similar philosophy; however, they have used the macroscopic conservation equations in a simpler form, retaining the macro–micro coupling only via the heat release term during solidification.

These studies have helped our understanding of macro–micro modeling in simplified contexts. A key aspect which needs to be improved is the treatment of the physical process at the microscopic scale. The approach taken to date in this regard is to take existing relations obtained in more idealized set-ups. Oftentimes, the macroscopic effect on the microscopic scale is not fully accounted for. For example, it is now established that convection affects growth dynamics at the morphological levels [42]; such information is generally missing from the existing empirical correlations. In the following example, this aspect is illustrated via the simulation of vertical Bridgman growth process of NiAl and CdTe crystals.

NiAl is an intermetallic compound currently being investigated as a promising high temperature structural material because of its low density, high thermal conductivity, high melting temperature, superior isothermal and cyclic

Figure 3 Vertical Bridgman growth system for β–NiAl crystal. (a) Schematic of practical design. (b) Layout and boundary conditions extracted from (a) for current numerical simulation, in which (i) is the global model and (ii) is the refined model. The total length of the ampoule housing, between the top of alumina section and the bottom of copper section, after being scaled by the ampoule inner radius of 12.5mm, is L=14.8, while the length of ampoule is l=9.08.
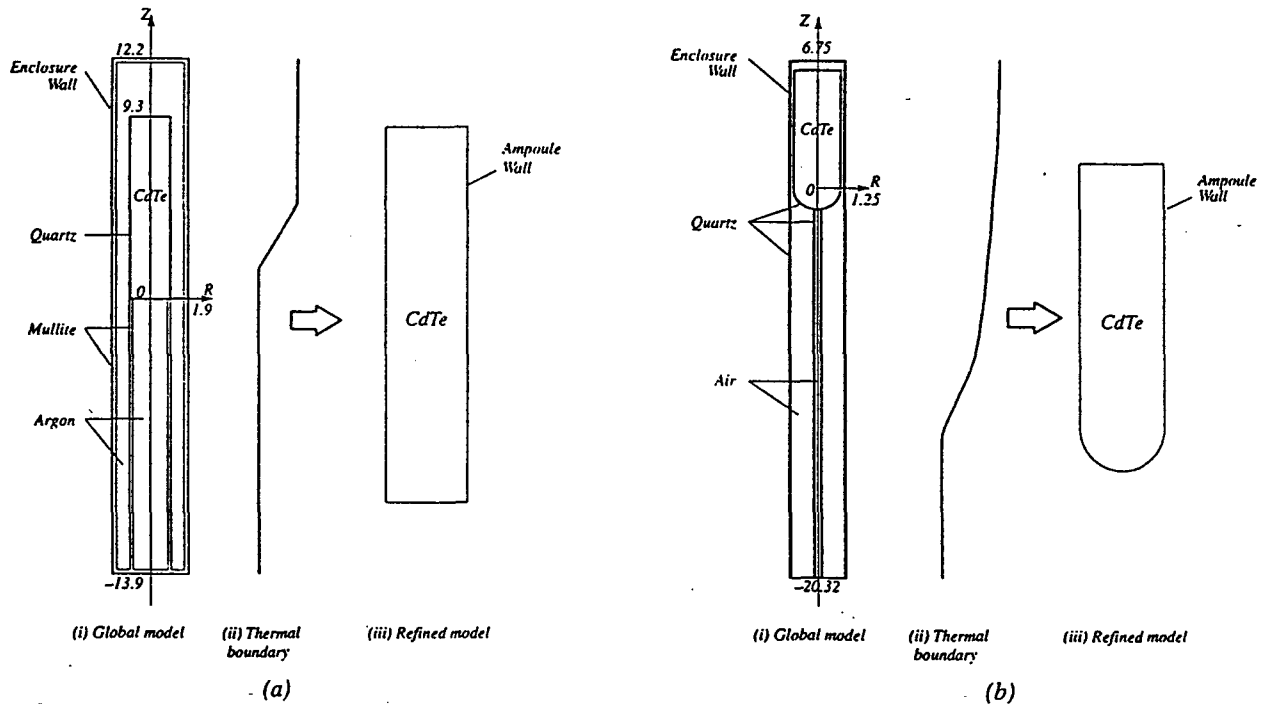
Figure 4 Schematic of global and refined models, along with the thermal boundary conditions, for two configurations of vertical Bridgman growth system for CdTe crystal. (a) The flat base ampoule configuration. (b) The semi–spherical base ampoule configuration.
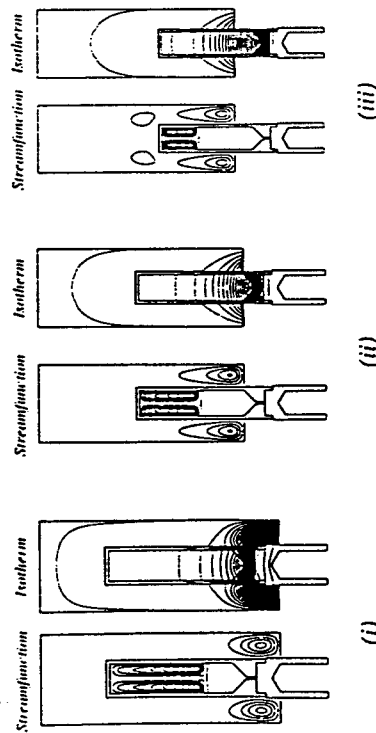
(i)   (ii)   (iii)

Figure 5 Solution characteristics of the global simulation of NiAl system for three different H. (i) H=3.2 (ii) H=6.4 (iii) H=9.6. $Ra_0=3.2 \times 10^4$, $Pr_0=4.4 \times 10^{-2}$, and $St_0=1.7$.

For all positions, there were 51 x 103 grid points in the ampoule region. Figure 5 shows the streamfunction and isotherm distributions, respectively, for each of the three ampoule positions. The dimensionless parameters are: Rayleigh number, Ra_0 = 3.2x10^4. Prandtl number, Pr_0 = 4.4 x 10^{-2}, and Stefan number, St_0 = 1.7 [51]. It is observed that, in the encapsulated gas region, the convection pattern is quite weak and the convective heat transfer into the ampoule is negligible compared to the radiative effect from the heater. Nevertheless, its isotherm pattern changes quite significantly. As the crystal is drawn downward, the temperature gradients at the base region decrease in magnitude. As the crystal is pulled downward, convection strength increases slightly and the melt/crystal interface shape remains convex towards the melt for all positions. To better resolve convection characteristics at the ampoule region, the grid resolution within the ampoule is increased to 101 x 154 from 51 x 103 used at Level 1; the refined ampoule simulation (Level 2) is conducted on this grid using the boundary conditions deduced from Level 1. Figure 6 presents the streamfunction and isotherm contours. Noticeable differences may be observed between the convection patterns in Fig. 5 and Fig. 6. For H=3.2, more detailed secondary vortical structure in the central region above the solid–melt interface is clearly observed from the refined solutions. These characteristics of the secondary vortical structure can also be captured by a globally refined calculation, as shown in Fig. 7 for H=3.2. However, this global refinement requires a total grid size of 223x284 over the entire domain to achieve the 73x154 grid points inside the ampoule. Compared with the single ampoule refinement of 101x154 grid points, the computational cost of global refinement is about four times higher. This indicates that the current multi–level approach is necessary to achieve desirable computational with reduced resources.

In the present CdTe system, the dimensionless parameters are: Rayleigh number 10^5, Prandtl number 0.4, and Stefan number 0.2. Figure 8a shows the convection characteristics obtained by the global model and the refined model for the

(i)   (ii)   (iii)
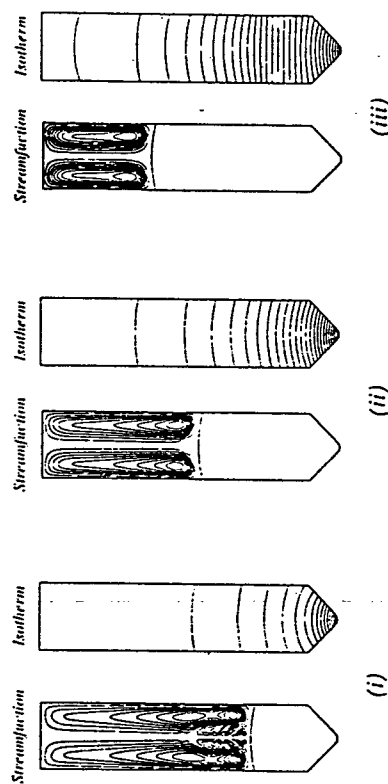
Figure 6 Solution characteristics of the refined ampoule simulation of NiAl system for three different H. (i) H=3.2 (ii) H=6.4 (iii) H=9.6. $Ra_0=3.2 \times 10^4$, $Pr_0=4.4 \times 10^{-2}$, and $St_0=1.7$.

flat base configuration of CdTe system. For the refined model, the grid size within the ampoule region is increased to 161x101 from 31x101 nodes used by the global model. It is observed that both models predict similar convective and isothermal features except that the refined model captures two additional recirculation cells near the top region. Figure 8b shows the results for the semi–spherical base configuration. For the refined model, the grids within the ampoule region are increased to 121x219

Inside the NiAl melt
$Smax=4.18 \times 10^{-2}$, $\Delta S=4.4 \times 10^{-3}$

Inside the Argon gas
$Smax=2.42 \times 10^{-3}$, $\Delta S=4.4 \times 10^{-3}$

$T_{melt}=0.95$ $\Delta T=0.02$

(a) Streamfunction   (b) Isotherm
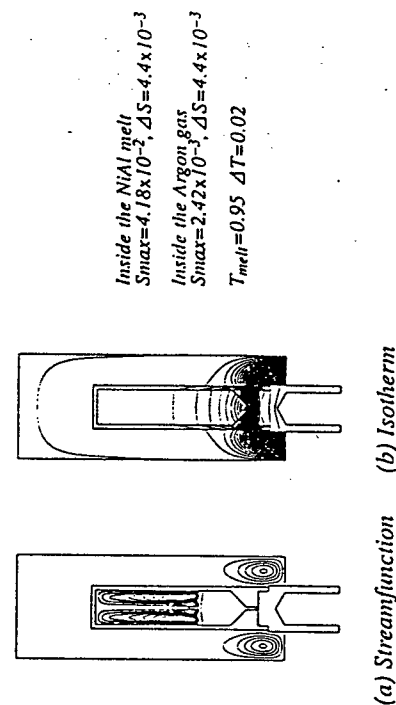
Figure 7 Solution characteristics of the global refined simulation of NiAl system for H=3.2 with a total grid size of 223x284. $Ra_0=3.2 \times 10^4$, $Pr_0=4.4 \times 10^{-2}$, and $St_0=1.7$.

(i)   (ii)

(a) *Flat base ampoule configuration*

(i)   (ii)

(b) *Semi-spherical base ampoule configuration*
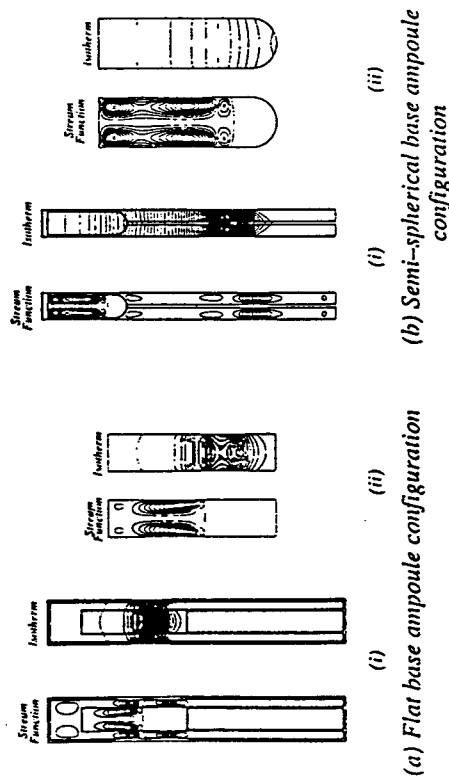
Figure 8   Solution characteristics of (i) the global and (ii) the refined simulations of CdTe system for (a) the flat base ampoule configuration and (b) the semi-spherical base ampoule configuration. $Ra_0=10^5$, $Pr_0=0.4$, $St_0=0.2$, and $k_l=2k_s$.

† *Streamfunction inside encapsulated gas and inside CdTe melt are not drawn by the same scales.*

from 61×110 nodes in the global model. Again virtually identical distributions of the streamfunction and isotherm within the ampoule region are achieved by both models. These agreements indicate that accurate solutions can be obtained with the present grid resolution. In the case of NiAl, the two-level scale patching offers improved resolution; here, it helps ascertain the numerical accuracy.

3.2.2 Turbulent flow in a passage with multiple Solid objects. In this section, we report a case study to illustrate an application that truly utilizes the multi-level simulations to construct a map to link the physical phenomena at different scales. The problem considered is a three-dimensional turbulent flow within a device containing large curvature and a number of solid objects. The flow device investigated here is a spiral casing of a hydraulic turbine power plant. As schematically illustrated in Fig. 9a, the spiral casing is a passage of 360° turning that directs water, coming from the dam, to enter from one end, and to exit circumferentially along the radially inward direction. The distributor, consisting of a cascade of stay vanes and wicket gates, is housed in the outlet region of the casing. In the present example, there are twenty-four pairs of airfoils to control the mass-flux distribution and the angle of the water. Water, after leaving the distributor, enters the runner to drive the shaft and produce usable power. Representative geometries and grid distributions are shown in Fig. 9b and c for casing and distributor, respectively.

The flow in a combined spiral casing and distributor is difficult to model and predict. Since the spiral casing and the distributor closely affect each other, both must

Plan view

Elevation view

(a) Plan view and elevation view of a spiral case.

Cross section A

Cross section B

Cross section C

Cross section D

(b) Flow domain and body-fitted grid system of a spiral case.

(c) Flow domain and body-fitted grid system of a distributor.
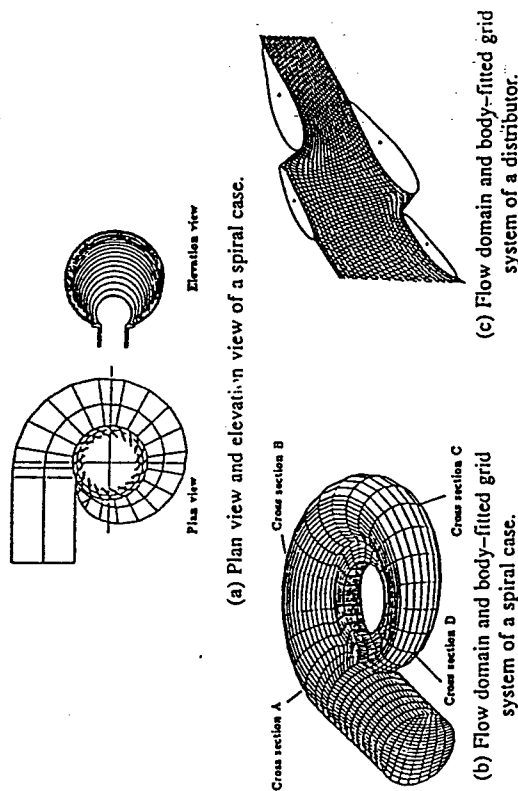
Figure 9   Schematic of turbine and spiral casing.

be treated in a coupled manner. We have found that in the computational model, without taking an appropriate account of the presence of the distributor, the flow in a spiral casing can be persistently oscillatory due to the lack of dissipation of the flow kinetic energy in the exit region. However, from the viewpoint of aiding the design practice for such devices on a routine basis, it is not practical to model the whole spiral casing and distributor combination simultaneously with adequate grid resolution. In view of these considerations, instead of solving the whole problem all at once, an alternative method is devised utilizing different grid resolutions to satisfy the different needs of physical modeling in casing and in distributor. To predict the overall characteristics of the flow in the spiral casing, while accounting for the geometry of the casing in detail, it is not necessary to consider each individual airfoil element of the distributor. On the other hand, from the viewpoint of the distributor flow analysis, only the inlet condition of the distributor is needed from the global spiral casing flow analysis. Hence, the two-level modeling strategy is very appropriate to adopt in the present case:

1.   To predict the flow characteristics inside the spiral casing, the distributor region is treated as a porous medium with the details of individual airfoils being smeared out;

2.   Within the distributor region, analysis is conducted for flow between each pair of wicket gates and stay vanes to determine the local distributor performance and to provide input to the porous medium treatment.

The information is exchanged and coupled between the two levels.

The Reynolds-averaged three-dimensional Navier–Stokes equations, with an extra inclusion of the porous medium treatment based on Darcy's law, have been used. The equations for mass continuity and momentum conservation of the incompressible fluid are:

$$\nabla \cdot \bar{q} = 0 \qquad (41)$$

$$\bar{q} \cdot \nabla \bar{q} = -\frac{1}{\rho}\nabla p + \nu_{eff}\nabla^2 \bar{q} - K\bar{q} \qquad (42)$$

where $\bar{q}$ is the velocity vector with three velocity components, ν_{eff} is the effective viscosity, and K is the Darcy's coefficient whose magnitude regulates the resistance exerted by the presence of porous medium in the distributor region. In the present case, K is zero everywhere except in the distributor region. Within the distributor region, K varies according to the nature (e.g., number, shape, and thickness) of the airfoils, and the local angles of attack of the incoming flow. In order to determine K, the distributor flow analysis [52] is conducted for flow in a passage bounded by a cascade of airfoils, as shown in Fig. 9. Since the inlet flow angles of the distributor vary along the circumferential direction, individual analysis for the flow between each pair of wicket gates and stay vanes is made with the inlet flow condition supplied by the spiral casing flow analysis. The total pressure loss profile of the distributor flow along the circumference of the spiral casing is then used to correlate the Darcy's coefficient, K. In the present work, the value of K is taken to be proportional to the second power of the total pressure loss. This choice is made according to the relative agreement observed between the computation and the measurement for a base geometry and flow condition. The proportionality constant is fixed by trying to match the prediction with the experimental measurement at one operating point. Once the correlation formula is determined, calculation is made to model other operating conditions without changing any of the constants. In summary, the global casing model supplies the inlet condition to the local distributor flow analysis; the total pressure loss predicted by the distributor model, in turn, yields guidance to determine the distribution of K in the porous medium treatment. Such a global-local iterative procedure continues till convergence is reached at both levels simultaneously.

Figure 10 shows the total pressure loss in the distributor as a function of the angle of attack. Under the favorable condition (25-degrees or higher), the flow is attached, resulting in a small amount of total pressure loss. As the inlet flow angle is reduced to, say, 15-degrees, flow is no longer attached and separation appears in the region above the stay vane. Hence, the flow under such a condition produces a larger total pressure loss. With the inlet flow angle further reduced to, say, 10-degrees, massive separation results from the larger adverse pressure gradient, which also produces noticeable streamline curvatures downstream of the separation zone. The loss is obviously the highest for the lowest flow angle.

One of the key features in the present work is the supply of the inlet flow profiles of the distributor computation by the spiral casing analysis. The distributor flow analysis, in turn, yields information of the total losses within the distributor
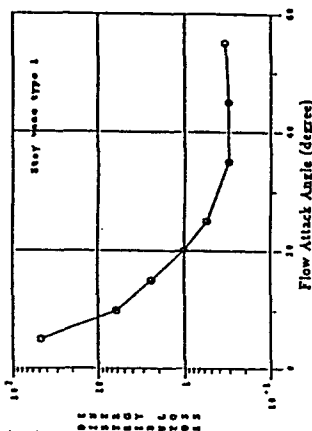
Figure 10 Total pressure loss in the distributor as a function of angle of attack.

region. Based on this information, Darcy's resistance term is devised to represent the presence of the distributor. It is noted that, throughout the whole casing, the inlet angle of the distributor flow varies substantially along the circumferential direction. Figure 11 shows two profiles of inlet angle of the distributor flow, one at the mid-height location of the casing and the other averaged over the whole height of each cross-section of the casing. The variation of the angle of attack of the distributor flow results from the change of flow rate along the circumferential direction of the casing, and the nonuniform total pressure loss within the distributor region.

As already stated, in the present model, Darcy's coefficient is determined from the local total pressure loss in the distributor region. Figure 12 exhibits three K profiles at different heights, from bottom to mid-height of the casing, along the circumferential direction. In the upstream portion of the casing, the inlet flow angles are low, resulting in higher values of K for the distributor region. In the middle circumferential portion of the casing, as indicated by Fig. 11, the inlet angles of the distributor flow produce favorable conditions, resulting in lower total pressure loss and, accordingly, lower values of K. Towards the end, the inlet angles of the distributor flow vary substantially from bottom (high angle) to mid-height (low angle), and hence causes large differences in K to appear there.
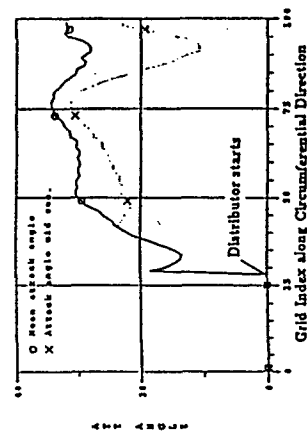
Figure 11 Variation of flow angle of attack in upstream of distributor.
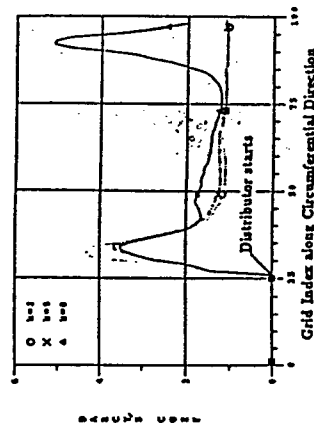
Figure 12   Distribution of Darcy's coefficient along circumferential direction.

Based on the combined casing/distributor flow analysis, a complete solution can be obtained for the whole passage. The numerical solutions have been compared to the in-house experimental measurements made with pitot tubes for various aspects of flow characteristics. We first compare the numerical prediction with the experimental measurement for the distributions of the static pressure, radial and tangential velocity components at two cross-sectional planes. The data shown in Fig. 13 are for physical quantities predicted and measured on the cross-sectional planes A and B of Fig. 9 ; the plots are shown along the radial direction, from the outside wall (left end of figure) to the outlet (right end of figure) of the casing along the mid-height line. Figure 13 illustrates the range of agreement between the numerical prediction and the experimental measurement. Qualitatively, the static pressure generally decreases from the outside wall (upstream) toward the casing/distributor outlet (downstream). With regard to the velocity components, they also increase in magnitude along the same direction until reaching the distributor region. Within the

(a) At mid-height of cross section A.

(b) At mid-height of cross section B.
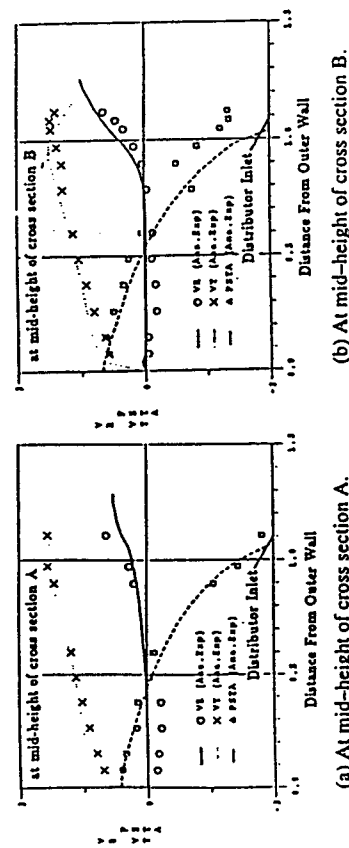
Figure 13   Comparison between prediction and experiment for static pressure, radial and tangential velocity components along radial direction. (symbols: measurements; lines: prediction)

distributor region, the radial velocity component increases in magnitude while the tangential velocity component becomes smaller, indicating that the flow is evolving toward a two-dimensional behavior due to the flow acceleration caused by the distributors. More information can be found in Ref. [3].

4 RESOLUTION PATCHING: MULTI-BLOCK GRID

In Section 3, modeling strategies have been presented to help bridge the needs for resolving both geometrical and dynamical complexities in the context of the single-grid computation. These strategies enable one to reduce the requirements of computing resources while achieving necessary resolutions. However, there are also occasions which require that the multiple resolutions on different zones of the entire domain be reached simultaneously in the course of the single-level computations. For example, in certain regions, the flow field may contain features such as high velocity and temperature gradients, as well as geometric complexities which can not be treated separately, such as in the Bridgman crystal growth examples. To handle such circumstances, a multi-block grid method is a very useful technique, which allows different number and density of grid points to be distributed in different regions, without forcing the grid lines to be continuous in the entire domain. The multi-block structured grid can alleviate some of the difficulties because (1) it can reduce the topological complexity of a single structured grid system by employing several grid blocks, permitting each individual grid block to be generated independently so that both geometry and resolution in the boundary region can be treated more satisfactorily; (2) grid lines need not be continuous across grid interfaces, and local grid refinement and adaptive redistribution can be conducted more easily to accommodate different physical length scales present in different regions; (3) the multi-block method also provides a natural route for parallel computations.

4.1 Overview of the Multi-Block Technique

Multi-block structured grids can be broadly classified as either patched grids [53] or overlapping grids [54]. Patched grids are individual grid blocks of which two neighboring blocks are joined together at a common grid line without overlap. With overlapping grids, the grid blocks can be arbitrarily superimposed on each other to cover the domain of interest. Compared to patched grids, overlapping grids are more flexible to generate and can be more easily fitted to complex geometry, but information transfer between the blocks is more complicated and flux conservation is more difficult to maintain. For both grid arrangements, the issues of interface treatment regarding both conservation laws and spatial accuracy need to be addressed. For flow problems involving discontinuities or sharp gradients, it is well know that it is often advantageous to use a numerical scheme in conservation form. The need for accurate conservative grid interfaces is illustrated by Benek et al. [55]. Rai [53, 56] has developed a conservative interface treatment for patched grids and has conducted calculations demonstrating the shock capturing capability with

discontinuous grid interface. Berger [57] gives a discussion of conservative interpolation in overlapping grids. Chesshire and Henshaw [58, 59] have conducted analyses on grid interface treatment and develop data structures for conservative interpolation on general overlapping grids. They solve slow and fast moving shock problems, with both conservative and non-conservative interpolation and find that, with the appropriate form of artificial viscosity, both conservative and non-conservative interface schemes give good results. Part–Enander and Sjogreen [60] also compare the effects of both conservative and non-conservative interpolation on slow moving shock problems. They find that the non-conservative interpolation can lead to a large error; in their approach, the conservative interpolation alone is not stable, and the conservative flux interpolation with a characteristic decomposition along with a non-linear filter is necessary to produce a satisfying solution. Meakin [61] investigates the spatial and temporal accuracy of the interface overlapping method for moving body problems and suggests that the issue with interface treatment is not necessarily one of conservative versus non-conservative treatment, but one of grid resolution. The issue of an accurate and conservative treatment of discontinuous grids is also investigated [62]. Other related work can be found in Refs. [65,66]. From the literature cited above, it can be seen that several factors can affect the solution quality for a shock problem involving discontinuous grid interfaces, e.g., the order of interpolation, accuracy, conservative or non-conservative interpolation, convection schemes (or forms of artificial viscosity), and grid resolution. Which factor (or combination of several different factors) has the most critical effect is still not clear. Ideally, the physical conservation laws should be satisfied in the entire domain, but when discontinuous grids are encountered, to what extent should flux be conserved is still an open question. For some problems, compromise has to be made between maintaining flux conservation and interpolation accuracy consistently in both the grid interface and the interior regions. All these problems need to be investigated further.

For multi-block computation of incompressible flow, the maintenance of mass conservation across discontinuous grid interfaces is also an important issue. Some efforts have been made with different methods of interface treatment for mass flux. For example, 2–D incompressible flow problems have been computed by employing the patched grids [65–67]. In those methods, the grid interface arrangements are either continuous or one coarse grid including integer number of fine grids, so that the maintenance of mass conservation across the grid interface is relatively easy. Several authors [68–71] have solved the flow problems using overlapping grids by employing direct interpolation of the dependent variables across the grid interface. The extent of satisfaction of mass conservation there depends solely on the order of the interpolation methods used. Yung et al. [72] and Tu and Fuchs [73] have used a different mass correction method to achieve global mass conservation across the grid interface, but the effects of those methods on solution accuracy is hard to judge. Wright and Shyy [74] have developed a pressure–based multi-block method based on the discontinuous, overlapped grid technique for solving the incompressible Navier–Stokes equations in a Cartesian grid system. A locally conservative interface scheme, with first order accuracy, is devised to ensure that local and global conservation of mass and momentum fluxes

are maintained. This overlapped grid methodology has been extend to non-orthogonal curvilinear coordinates [75]. The related work about domain decomposition and parallel computation methods can be found in Gropp and Keyes [76, 77]. Although much progress has been made in this field, some fundamental issues remain unsolved. For mass flux treatment, an interface scheme with global mass conservation may not be sufficient to yield accurate solution: On the other hand, a locally conservative interface scheme may have difficulties in maintaining an equal accuracy between the interface and interior regions. Furthermore, for incompressible flow computations, the pressure is generally known up to an arbitrary constant. When the flow solver is applied to multi-block grids, how to couple pressure fields in different blocks, and at the same time maintain mass flux conservation across the interface is an important question.

In the following, the issues of conservation and accuracy of the interface treatment in a multi-block method is investigated for incompressible, viscous flow computations on general curvilinear staggered grids. Effects of non-conservative and conservative treatments for mass flux, either only globally along the whole grid interface or locally in each computational cell, on solution accuracy are discussed. A scheme based on interpolation with local conservative correction method for mass flux at the grid interfaces is devised. Two different ways to couple pressure fields between adjacent blocks are discussed. The approaches investigated can handle both patched and overlapped grids in the same manner.

4.2 Interface Treatment for Momentum Equations

In the current multi-block computational method, the entire flow domain can be decomposed into several subdomains (or blocks). Within each block, a structured grid is generated. Two different blocks can either patch together or overlap over several grid layers. In the present approach, the grid lines between the adjacent blocks can be discontinuous, and, if necessary, multiple number of blocks can simultaneously overlap at the same location [3, 74]. At grid interfaces, the grid lines of a given block are extended to the adjacent block by two cells to accomodate the need for constructing upwind convection schemes.

4.2.1 Direct interpolation of dependent variables. For the momentum equations, at the internal boundary, both velocity and pressure boundary conditions are needed. If the south boundary is the internal boundary, for example, in the u–momentum equation, i.e., Eq. (11), the total momentum flux

$$F = \varrho V u - y_\xi p - \frac{\mu}{J}(-q_2 u_\xi + q_3 u_\eta) \quad (43)$$

needs to be evaluated at the grid interface. For smooth flow fields, the direct interpolation of dependent variables from the adjacent block should be satisfactory. With the extended grid points, the dependent variables u, v and p can be interpolated from the adjacent block, and the geometric quantities y_ξ, q_2, q_3 and J can also be evaluated with the grid values in both blocks.

4.2.2 Interpolation of momentum fluxes. For problems involving large flow gradients, the conservative treatment of momentum fluxes is often desirable. Here, to analyze the interpolation of momentum fluxes as the internal boundary condition at the grid interface, consider the flux at the south boundary again. As indicated by Eq. (43), momentum flux F includes convection, diffusion and pressure terms. One straightforward way is to directly interpolate flux F as a whole, from the adjacent block, and then put the flux into the source term of Eq. (13). But momentum flux F includes gradient terms u_ξ and u_η, and a direct interpolation of these gradient terms admits solutions where an arbitrary constant may be added to the solution on each grid, rendering the solution non-uniform [78]. In the current treatment, the flux F is split into two terms, as indicated by Eq. (44), and the two terms are treated separately.

$$F = \left[\varrho V u - y_\xi p\right] - \left[\frac{\mu}{J}(-q_2 u_\xi + q_3 u_\eta)\right] \qquad (44)$$
$$\qquad\quad (i) \qquad\qquad\qquad (ii)$$

The first term in F is interpolated directly from the adjacent block, and is put into the source term in Eq. (13). For the second term, u itself is interpolated from the adjacent block, and gradient terms u_ξ and u_η at the interface are evaluated with the u values in both blocks. In this way, the problem of non-uniqueness is eliminated, and at the same time, the convection and pressure fluxes can be interpolated directly from the adjacent block. In the present interface treatment, the nonlinear part and the diffusion part of the total momentum flux are treated separately. While the nonlinear parts are interpolated totally from the adjacent block, the evaluation of the diffusion flux employs the velocity components from both blocks to avoid creating non-unique solutions. With these interface treatments, both overlapped and patched grids can be handled.

4.3 Interface Treatment for Pressure Correction Equation

Two alternative interface boundary conditions are devised for the pressure-correction equation. With the first treatment, the mass flux at the interface is taken as the boundary condition for the pressure-correction equation. Suppose the south face of a pressure-correction control volume is at the interface, as illustrated in Fig. 14. The p' equation for that control volume is as below,

$$a_P p'_P = a_E p'_E + a_W p'_W + a_N p'_N + S_P \qquad (45)$$

$$a_P = a_E + a_W + a_N \qquad (46)$$

$$S_P = (\varrho U^*)_w - (\varrho U^*)_e + (\varrho V^*)_s - (\varrho V^*)_n \qquad (47)$$

where $(\varrho V)_s$ is the mass flux from the south face at the interface, presumably known, which is interpolated conservatively from solutions on the adjacent block and is put
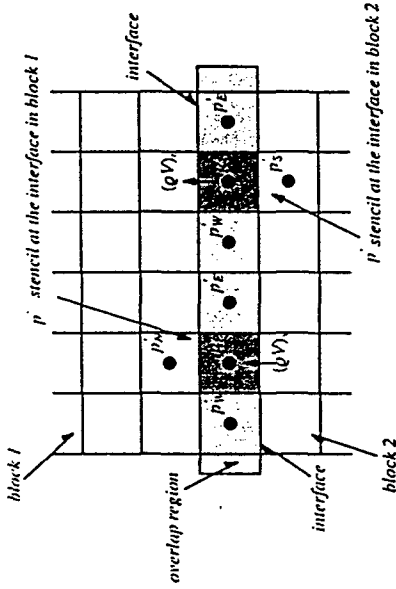
Figure 14   Interface layout with one grid layer overlap.

into the source term. The term $a_S p'_S$ is no longer present in the p' equation for that control volume. Conversely, for the corresponding control volume at the interface of the adjacent block, the north face of the pressure-correction control volume is at the interface. The corresponding p' equation is as below,

$$a_P p'_P = a_E p'_E + a_W p'_W + a_S p'_S + S_P \qquad (48)$$

$$a_P = a_E + a_W + a_S \qquad (49)$$

$$S_P = (\varrho U^*)_w - (\varrho U^*)_e + (\varrho V^*)_s - (\varrho V^*)_n \qquad (50)$$

where $(\varrho V)_n$ is interpolated conservatively and $a_N p'_N$ is no longer present. So, on both sides of the grid interface, the boundary conditions for p' equation are implemented via the mass flux (ϱV) and are of the Neumann type. In other words, the pressure fields in different blocks are independent of one another. To make the pressure field compatible in the entire flow domain, the reference pressure in each block resulting from the Neumann boundary condition is adjusted according to the total momentum flux balance at a common line in the overlap region between the blocks [3, 74]. This treatment is called method NN (meaning Neumann–Neumann conditions). It is noted that when evaluating the a_E and a_W terms, whose expressions are shown in Eqs. (35) and (36), the A_P^v term as shown in Eqs. (14)–(18), is taken from the average of four surrounding values from the corresponding $v -$ momentum equations, two of which are at the interface. The associated (ϱU) and (ϱV) are evaluated from the values within the block and the interpolated values in the adjacent block; the $\mu q_1/J$ and $\mu q_3/J$ are evaluated from the grid points within the current block and the extended fictitious points in the adjacent block.
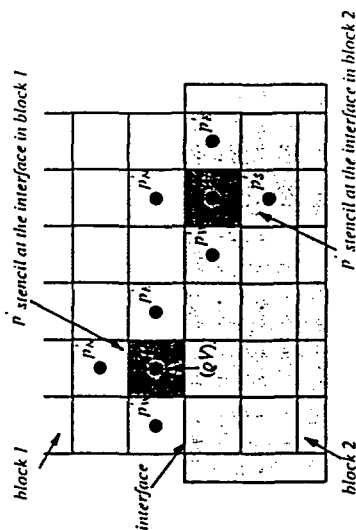
Figure 15 Interface layout without overlap.

In the alternate method, for the p' equation, on one side of the interface, the interpolated and locally conserved mass flux normal to the interface, say, $(\rho V)_n$, is still used as the boundary condition in grid block 1, as shown in Fig. 15. On the other side of the interface, in the adjacent block, instead of $(\rho V)_n$, p_N is interpolated from grid block 1, as the boundary condition, as illustrated in Fig. 15. With this new treatment, the different grid blocks at the interface may overlap or patch together. In this arrangement, the grid lines at the interface of one block are extended to the adjacent block to form fictitious grid points. The metric coefficients of the curvilinear grid system at the interface are evaluated accordingly by interpolation. Whenever needed, the unknowns, e.g., u, v and p are interpolated from the adjacent block to facilitate computations at the interface. The transport coefficient a_N is evaluated at the interface as below:

$$a_N = \rho \left[\frac{x_\xi^2}{A_P^v} + \frac{y_\xi^2}{A_P^u} \right]_n \tag{51}$$

The term $(A_P^u)_n$ is the average from the values at four surrounding u – locations. At the interface, the two locations are outside the current block, as illustrated in Fig. 16. To compute the A_P^u, at those two locations, whose expression is shown in Eqs. (14)–(18), the terms (ρU) and (ρV) are interpolated at the extended grid points, and $\mu q_1/J$ and $\mu q_3/J$ are evaluated using both the physical grid points within the current block and the extended fictitious points in the adjacent block. The same method is applied when evaluating the $(A_P^v)_n$ term at the interface. The source term S_P still has its original form given by Eq. (34), in which, $(\rho V^*)_n$ is actually computed using the v value at the interface and the u values within the current block and interpolated v values outside the block. In summary, at one side of the interface, the (ρV) term is computed, while at the other side, it is interpolated. The one grid layer overlap is no longer needed to facilitate the mutual updating, as shown in Fig. 16. It is also noted
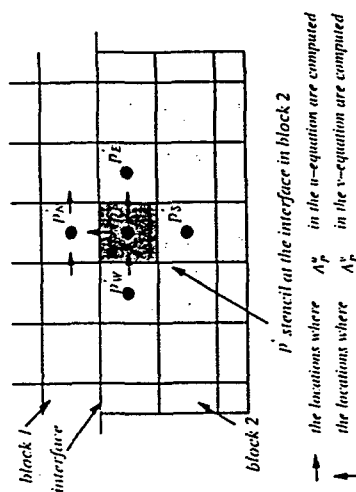
Figure 16 Interpolation stencil for pressure correction equation at grid interface.

that with the new treatment, the boundary condition is of Neumann type on one side and Dirichlet type on the other side. Since the pressure fields across the interface are tightly coupled together, the adjustment for the pressure field between blocks is no longer needed. This treatment is called method DN, standing for Dirichlet–Neumann conditions. In both methods, the contravariant velocities are interpolated conservatively; as will be demonstrated later, linear interpolation with local conservative correction is found to be satisfactory for interior nodes.

4.4 Conservative Treatment for Mass Flux

In this subsection, a method of conservative interpolation of mass flux is presented. Suppose a portion of an interface corresponds to the width of a single control volume of the coarse grid 1, and to the width of several control volumes of the fine grid 2, indexed from i=1 to imax. This scenario is shown schematically in Fig. 17, where $\overline{V}_c$ is the contravariant velocity component normal to the grid face, normalized by the control volume face length S_c, at the coarse grid control volume face; and $\overline{V}_f$ represents the contravariant velocity component, normalized by the control volume face length S_{fi} at the fine grid control volume face. From the fine grid to coarse grid, $\overline{V}_c$ can be obtained as:
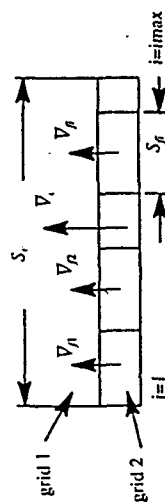
Figure 17 Notations used in two-block interface (subscript c and f designate coarse and fine grid quantities, respectively).

$$\nabla S_c = \sum_{i=1}^{imax} \nabla_{fi} S_{fi} \qquad (52)$$

Equation (52) is for the constant density flow. It can be easily extended to account for density variations. For the sake of simplicity, this aspect is neglected in the current discussion. In this way, the flux into the coarse grid control volume is uniquely determined from the corresponding fine grid fluxes conservatively. Conversely, given the coarse grid flux $\nabla_c S_c$, the conservation constraint yields the follow:

$$\sum_{i=1}^{imax} \nabla_{fi} S_{fi} = \nabla_c S_c \qquad (53)$$

In this situation, conservation does not provide unique values for the ∇_{fi}. A certain distribution has to be chosen to determine each ∇_{fi}. As a first approximation, ∇_{fi} is obtained using the linear (or quadratic) interpolation of the normalized contravariant velocity in the coarse grid. The interpolated value is denoted as $\overline{V}_{fi}$. With the first approximation, Equation (52) is not satisfied. Then the fine grid fluxes are scaled so that the total flux obtained is $\nabla_c S_c$. Accordingly, the values ∇_{fi} at the fine grid boundary are computed as follows:

$$\nabla_{fi} S_{fi} = \frac{|\overline{V}|S_{fi}}{\sum_{i=1}^{imax}|\overline{V}|S_{fi}} \nabla_c S_c \qquad (54)$$

From Eq. (54), it can be seen that Eq. (52), which expresses flux conservation from coarse grid to fine grid, is satisfied and the flux distribution is close to that determined by the interpolation employed.

If the grid interface is not exactly matched in the sense of a coarse control volume face adjoining an integer number of fine grid control volume faces, a split–merge procedure is devised. The control volume in grid 2 can be split into smaller sub–control volumes. In this manner, from control volumes in grid 1 and sub–control volumes in grid 2, the locally conservative treatment can still be applied on a cell by cell basis, after the interpolation and correction have been conducted. After that, the fluxes at the split sub–control volume faces will be merged back to get the flux at the original control volume face. From grid 2 to grid 1, this same split–merge treatment is also applicable. The only extra work in this procedure is to create some arrays to store the intermediate information. Thus, the interface can be treated no matter what kind of interface arrangement is encountered. This linear (quadratic) interpolation with local correction treatment is not limited to the mass flux, it can also be applied to the momentum flux conservative treatment.

block 1
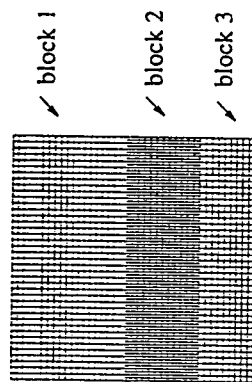
block 2

block 3

Figure 18 Three–block grid with 41x21, 81x13 and 41x11 nodes for block 1, 2 and 3, respectively.

4.5 Assessment of Interface Methods

4.5.1 Comparison of conservative and non–conservative treatments. In this subsection, the conservative and non–conservative treatments of mass flux with different accuracies are tested and compared. The test problem is the lid-driven cavity flow problem with Re=1000. First, a 3–block discontinuous Cartesian grid configuration with different grid resolutions is used. A grid system of 41x21, 81x13 and 41x11 grid points for block 1, 2 and 3 respectively, as shown in Fig. 18 is first employed. Here, the interface between block 1 and 2 coincides with the cavity horizontal center line. The second grid system doubles the grid resolutions of the first grid system, and has 81x41, 161x23 and 81x21 grid points in each block, respectively. The third grid system doubles the grid resolution in x direction of the second grid system and has 161x41, 321x23 and 161x21 grid points in three blocks. To clarify the terminology, the multi–block grid for the whole flow domain is called "grid system" here. Each grid system consists of several blocks. The first grid system described above is denoted as the coarse grid system, the second as the median grid system, and the third as the fine grid system. The three grid systems share the same topological characteristics in each block. We have created these three grid systems to investigate the interplay of interface treatment and overall grid resolutions. The grid layouts are not ideally suitable for the present recirculating flow, they are purposely set up to test the relative merits of different interface treatments. For all the test cases presented in this section, the second–order central difference is used for convection, diffusion and pressure terms. Furthermore, the Neumann–Neumann (NN) interface condition is employed in all the cases studied in this subsection. The Dirichlet–Neumann condition will be investigated in next subsection.

Case 1. *The Cartesian velocity components u and v and the contravariant velocity components U and V are linearly interpolated at the grid interfaces. Total momentum fluxes across the interfaces are conserved via the pressure adjustment. No mass conservation is enforced across the grid interfaces.* The computations are conducted over the coarse, median and fine grid systems. Figures 19a and 19b show the u–component distributions along the vertical center line and v–component

(a) u velocity along the vertical center line (b) v velocity along the horizontal center line

(c) pressure distribution at the interface between block 1 and 2 on the fine grid system.
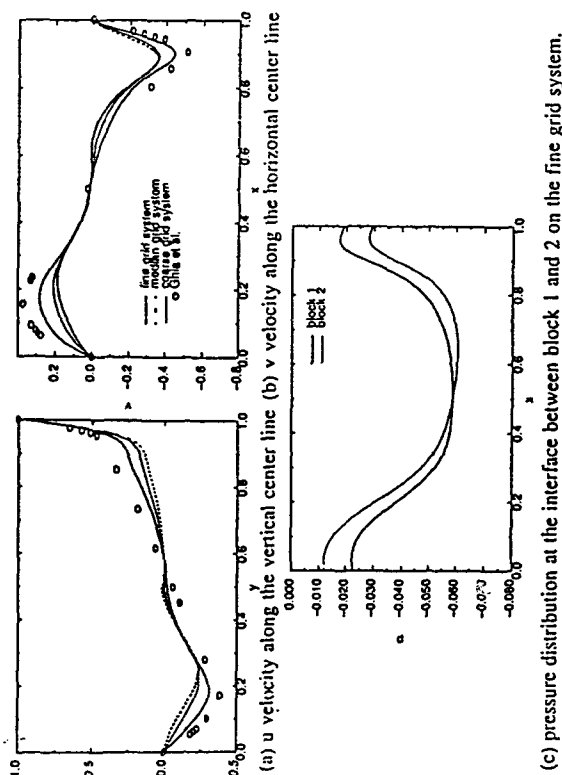
Figure 19 Solution profiles based on linear interpolation for U and V without mass conservation correction.

distributions along the horizontal center line. They are compared with the corresponding benchmark solution reported by Ghia et al. [79]. It can be seen that the solutions for all the three grid systems have substantial discrepancies with respect to the benchmark values. Although, in general, the solutions improve as the grids are refined, the overall performance of all three systems are unsatisfactory. For this problem, on a single, uniform grid, a 81x81 grid system can yield very accurate solution [80, 81]; it is unsatisfactory to observe that with the present multi–block interface treatment, solutions are less accurate on finer grids. Figure 19c shows the interface pressure distribution computed on block 1 and 2. The pressure in each block has been adjusted according to the total momentum balance at the interface. The absolute value of the pressure has no practical meaning. For a well converged solution, the pressures from different blocks are expected to have the same distributions at the interface; in the current case, even with fine grid system, the discrepancy between the two pressure distributions is obvious.

Case 2. *Both the Cartesian velocity components u and v and the contravariant velocity components U and V are quadratically interpolated, but still without enforcing mass conservation.* This procedure is of higher interpolation accuracy than that in case 1; however, neither has conservative treatment. The motivation here is to test the role of interpolation accuracy. Although improvement has been obtained, discrepancy between solutions on two blocks still exists. It appears that a non–conservative interface treatment is prone to creating difficulties.

Case 3. Since the non-conservative linear and quadratic interpolations for the contravariant velocities do not lead to a satisfactory solution even for a very fine grid,

(a) u velocity along the vertical center line (b) v velocity along the horizontal center line.
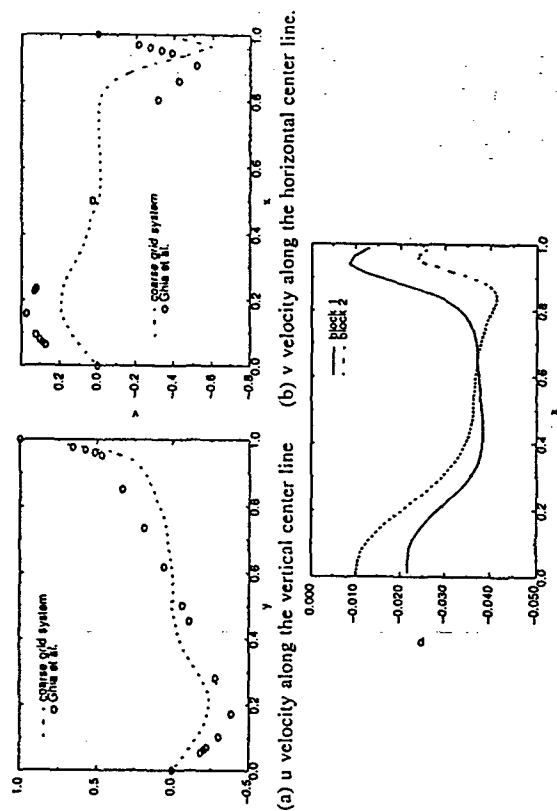
(c) pressure distribution at the interface between block 1 and 2 on the coarse grid system.

Figure 20 Solution profiles based on linear interpolation with global correction of mass conservation for U and V on the coarse grid system.

a conservative interface treatment is tested next. In this case, *the Cartesian velocity components u and v are linearly interpolated. The contravariant velocities U and V are linearly interpolated first, followed by a global correction procedure for mass flux as discussed previously.* The computation is conducted for the coarse grid system only. The momentum and mass flux residuals reach to the level of 10^{-5}. As shown in Fig. 20, the solution is not satisfactory. It appears that the conservative interface treatment conducted at the global level cannot yield the correct solution either.

Case 4. *The Cartesian velocity components u and v are still linearly interpolated. The contravariant velocities U and V are interpolated based on the piecewise constant formula, which by nature is locally conservative with first order accuracy.* This treatment is implemented to investigate the effect of the local conservation on the solution. The computations are conducted on three grids. Figures 21a and 21b present the u and v component distributions for the coarse and median grids. Both u and v profiles agree well with the benchmark solutions. Figures 21c and 21d exhibit the pressure distributions at the interfaces of blocks 1 and 2 for two grid systems. The pressure distributions in the interface region obtained on different blocks agree with each other generally well, except for some oscillations in block 2. The cause of this nonphysical oscillation is that the mass flux distributions at the fine grid interface are assigned according to the piecewise constant formula. This distribution results in a series of stair–step mass flux profile at the interface of

(a) u velocity along the vertical center line.

(b) v velocity along the horizontal center line.

(c) pressure distribution at the interface between block 1 and 2 on the coarse grid system.

(d) pressure distribution at the interface between block 1 and 2 on the median grid system.
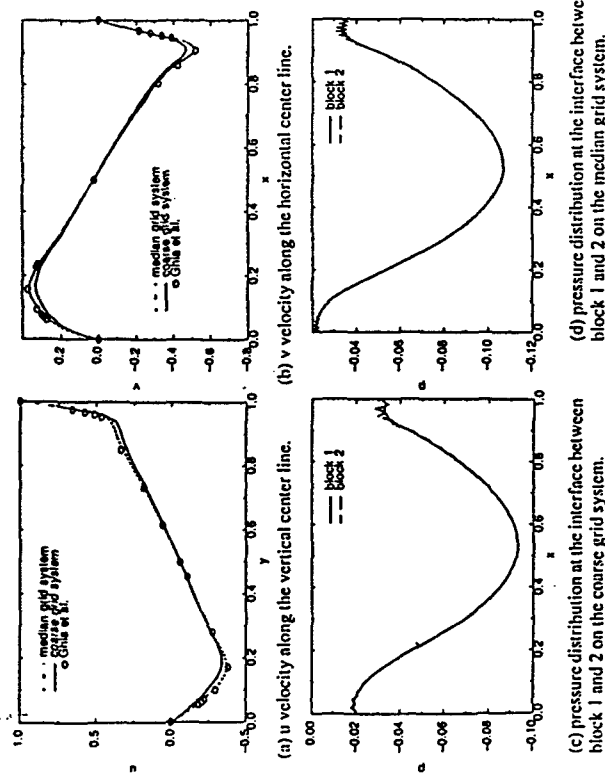
Figure 21 Solution profiles based on piecewise constant interpolation for U and V.

the fine block, forcing the pressure field to oscillate. This phenomenon is also likely to be responsible for the non–convergence of the fine grid solution.

Case 5. *The Cartesian velocity components u and v are linearly interpolated. The contravariant velocities U and V are linearly interpolated first, followed by a local correction to maintain the cell by cell mass conservation across the interfaces.* The tests are conducted for all three grid systems. Figures 22a and 22b show the u and v component distributions. The solution on the coarse grid system shows a very small discrepancy compared to the benchmark solution; the solution on the median and fine grid systems agree well with the benchmark solution. Figure 22c displays the pressure distributions at the interface of block 1 and 2 on the fine grid system. The two pressure profiles conform to each other very well. Clearly, a treatment of interface mass flux with local conservation and certain accuracy holds the key to obtaining an accurate solution.

Case 6. *The Cartesian velocity components u and v are quadratically interpolated. The contravariant velocities U and V are quadratically interpolated first, followed by a local correction to maintain the cell by cell mass conservation across the interfaces.* For the present flow problem, both the linear and quadratic interpolations with local correction give accurate solutions. Since the discretization scheme for the interior nodes are second–order accurate, it appears that a linear interpolation (aided by the follow–up local conservative correction) treatment is sufficient.

(a) u velocity along the vertical center line.

(b) v velocity along the horizontal center line.

(c) pressure distribution at the interface between block 1 and 2 on the fine grid system.
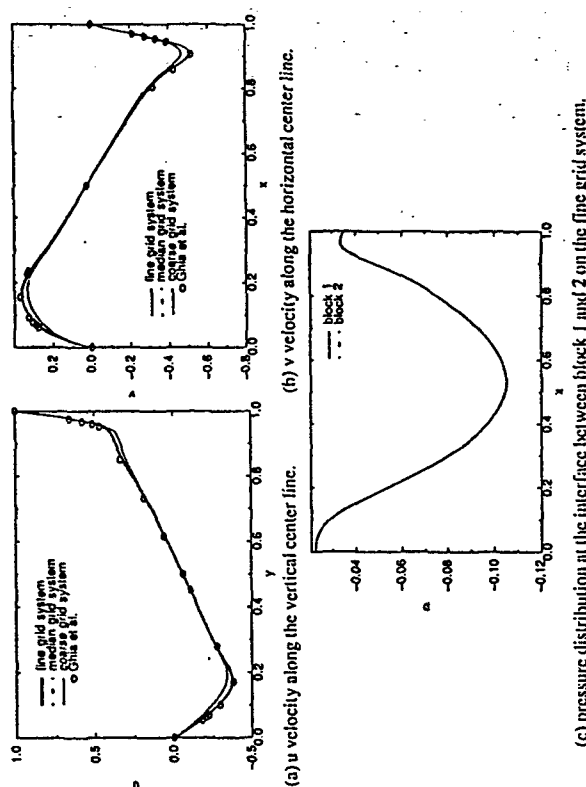
Figure 22 Solution profiles based on linear interpolation with local correction of mass conservation for U and V.

4.5.2 Comparison of two different boundary condition types for pressure correction equation. In this subsection, the NN and DN block interface conditions in the pressure correction equation are compared. The lid-driven cavity flow with Re=1000 is still used as the test case, with the flow domain partitioned into two grid blocks at the cavity horizontal center line. A grid system of 65x33 and 61x34 nodes is used for block1 and block 2, respectively. There is one grid layer overlap between the two blocks. The mass flux at the interface is estimated based on piecewise, linear interpolation with local conservative correction.

Figures 23a and 23b show the u–profile along the vertical center line and v–profile along the horizontal center line for both interface methods on the overlapped grid; they are compared with the corresponding benchmark solution reported by Ghia et al. [79]. It can be seen that the solutions produced by both methods are almost identical and conform very well with the benchmark solution. The profiles with method DN on a patched grid system of 65x33 and 61x33 nodes are also shown in Fig. 23. The velocity distributions on overlapped and patched grids are almost indistinguishable. It is noted that the discontinuous interface at the horizontal center line has no noticeable effect on the solutions. As discussed in the previous section, with the NN treatment, details of the interface schemes are critical in determining the solution accuracy; with the present DN scheme, solutions seem to be less sensitive to the details of the interface treatment.

(a) The u velocity along the vertical center line

(b) The v velocity along the horizontal center line
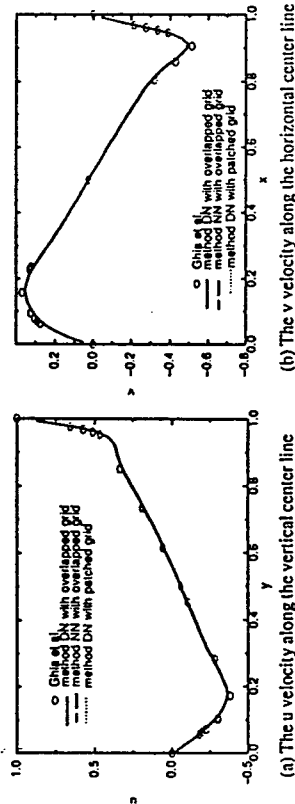
Figure 23 Comparison of three interface treatments on cavity flow calculations with Re=10^3. (The three interface treatments result in indistinguishable solutions).

5 CONCLUSION

In this article, the challenges for developing a computational framework and modeling strategy for handling fluid flow and heat/mass transfer problems with both geometric and dynamic complexities are presented. In our view, a major research in computational fluid dynamics and numerical heat transfer is to adequately simulate the physical phenomena at both macroscopic and microscopic scales, to formulate a modeling strategy that is capable of handling the mutual influence between different scales via scale patching, in the form of, for example, modified source terms or boundary conditions. To fulfill this goal, a matching procedure to allow different scales to be patched together if they occupy different spatial domain will be needed. Besides, a resolution patching procedure utilizing the multi-block technique can play a critical role; an account of the philosophy, modeling approach, and numerical algorithms that have been under development has been presented. It is hoped that this paper can help improve our handling of complex fluid flow and heat/mass transfer problems.

6 REFERENCES

1. H. Schlichting, *Boundary–Layer Theory*, 7th edition, McGraw–Hill, New, York, 1979.
2. M. Van Dyke, *Perturbation Methods in Fluid Mechanics*, annotated edition, Parabolic Press, Stanford, CA, 1975.
3. W. Shyy, *Computational Modeling for Fluid Flow and Interfacial Transport*, Elsevier, Amsterdam, The Netherlands, 1994.
4. H. Tennekes and J.L. Lumley, *A First Course in Turbulence*, The MIT Press, Cambridge, MA, 1972.

5. A.S. Monin and A.M. Yaglom, *Statiscal Fluid Mechanics*, 2 volumes, The MIT Press, Cambridge, MA, 1971 & 1975.
6. M.T. Landhal and E. Mollo–Christensen, *Turbulence and Random Processes in Fluid Mechanics*, Cambridge University Press, Cambridge, U.K., 1992.
7. J.S. Langer, Instabilities and Pattern Formation in Crystal Growth, *Rev. Modern Phys.*, vol. 52, pp. 1–28, 1980.
8. W. Kurz and D.J. Fisher, *Fundamentals of Solidification*, Trans. Tech. SA, Switzerland, 1984.
9. D.A. Kessler, J. Koplik and H. Levine, Pattern Selection in Fingered Growth Phenomena, *Advances in Physics*, vol. 37, pp. 255–339, 1988.
10. W. Shyy, H.S. Udaykumar, M.M. Rao, and R.W.Smith, *Computational Fluid Dynamics with Moving Boundaries*, Taylor and Francis, Washington, DC, 1996.
11. A.J. DeGregoria and L.W. Schwartz, A Boundary–Integral Method for Two–phase Displacement in Hele–Shaw Cells, *J. Fluid Mech.*, vol. 164, pp. 383–400, 1986.
12. S.–C. Huang and M.E. Glicksman, Fundamentals of Dendritic Solidification.I. Steady–State Tip Growth, *Acta Metall.*, 29, 701–715, and II. Development of Side–Branch Structure, *Acta Metall.*, vol. 29, pp. 717–734, 1981.
13. R. Kobayashi, Modeling and Numerical Simulations of Dendritic Crystal Growth, *Physica D*, vol. 63, pp. 410–423. 1993.
14. D.R. Lynch, Unified Approach to Simulation on Deforming Elements with Application to Phase Change Problem, *J. Comput. Phys.*, vol. 47, pp. 387–441, 1982.
15. G.B. McFadden and S.R. Coriell, Non–Planar Interface Morphologies During Unidirectional Solidification, *J. Crystal Growth*, vol. 84, pp. 371–388, 1987.
16. W.A. Tiller, *The Science of Crystallization: Microscopic Interfacial Phenomena*, Cambridge University Press, Cambridge, U.K., 1991.
17. H.S. Udaykumar and W. Shyy, Development of a Grid–Supported Marker Particle Scheme for Interface Tracking, *Numer. Heat Transfer*, Part B, vol.27, pp. 127–153, 1995.
18. A.A. Wheeler, B.T. Murray, and R.J. Schaefer, Computation of Dendrites using a Phase Field Model, *Physica D.*, vol. 66, pp. 243–262, 1993.
19. C. Beckermann and R. Viskanta, Double–Diffusive Convection due to Melting, *Int. J. Heat Mass Transf.*, vol. 31, pp. 2077–2089, 1988.
20. W.D. Bennon and F.B. Incropera, A Continuum Model for Momentum, Heat and Species Transport in Binary Solid–Liquid Phase Change Systems — I. Model Formulation, *Int. J. Heat Mass Transfer*, Vol. 10, pp. 2161–2170, 1987.
21. D. Canright and S.H. Davis, Buoyancy Effects of a Growing, Isolated Dendrite, *J. Crystal Growth*, vol. 114, pp. 173–189, 1991.
22. M.S. Christensen, W.D. Bennon and F.P. Incropera, Solidification of an Aqueous Ammonium Chloride Solution in a Rectangular Cavity—II. Comparison of Predicted and Measured Results. *Int. J. Heat Mass Transfer*, vol. 32, pp. 69–79, 1989.
23. A.B. Crowley, Mathematical Modeling of Heat Flow in Czochralski Crystal Growth, *IMA J. Appl. Math.*, vol. 30, pp. 173–189, 1983.

24. J.A. Dantzig, Modeling Liquid–Solid Phase Change with Melt Convection, *Int. J. Numer. Meths. Engrg.* vol. 28, pp. 1769–1785, 1989.

25. J.P. Garandet, T. Duffar, and J.J. Favier, On the Scaling Analysis of the Solute Boundary Layer in an Idealized Growth Configuration, *J. Crystal Growth*, vol. 106, pp. 437–444, 1990.

26. J.C. Heinrich, S. Felicelli, P. Nadapukar, and D.R. Poirier, Thermosolutal Convection during Dendritic Solidification of Alloys, Part II: Nonlinear Convection, *Metallurgical Transaction*, B vol. 20B, pp. 883–891, 1989.

27. D.T.J. Hurle, E. Jakeman and A.A.Wheeler, Hydrodynamics Stability of the Melt during Solidification of a Binary Alloy, *Phys. Fluids*, vol. 26, pp. 624–626, 1983.

28. D. Schwabe, Surface–Tension Driven Fluid Flow in Crystal Growth Melts, *Crystals*, vol. 11, pp. 75–112, Springer–Verlag, New York, 1988.

29. W. Shyy, Y. Pang, G.B. Hunter, D.Y. Wei, and M.-H, Chen, Modeling of Turbulent Transport and Solidification during Continuous Ingot Casting, *Int. J. Heat Mass Transf.*, vol. 35, pp. 1229–1245, 1992.

30. J. Szekely, *Fluid Flow Phenomena in Metals Processing*, Academic Press, New York, 1979.

31. R.E. Meyer and S.V. Parter (eds.), *Singular Perturbations and Asymptotics*, Academic Press, New York, 1980.

32. W.D. McComb, *The Physics of Fluid Turbulence*, Oxford University Press, Oxford, UK, 1990.

33. S.A. Orszag, V. Yakhot, W.S. Flanney, F. Boysan, D. Choudhury, J. Maruzewski and B. Patel, Renormalization Group Modeling and Turbulence Simulations, in *Near–Wall Turbulent Flows* (ed. R.M.C. So, C.G. Speziale and B.E. Launder), pp. 1031–1047, Elsevier, Amsterdam, The Netherlands, 1993.

34. W. Shyy, S.S. Tong and S.M. Correa, Numerical Recirculating Flow Calculation using a Body–Fitted Coordinate System, *Numer. Heat Transfer*, Vol. 8. pp. 99–113, 1985.

35. S.V. Patankar, *Numerical Heat Transfer and Fluid Flow*, Hemisphere, Washington D. C., 1980.

36. E. Blosch, W. Shyy, and R.W. Smith, The Role of Mass Conservation in Pressure–Based Algorithms, *Numer. Heat Transfer*, Part B, Vol. 24, pp. 415–430, 1994.

37. R.S. Rogallo and P. Moin, Numerical Simulation of Turbulent Flows, *Ann. Rev. Fluid Mech.*, vol. 16, pp. 99–137, 1984.

38. M. Lesieur, *Turbulence in Fluids*, Kluwer, Dordrecht, The Netherlands, 1990.

39. M. Rappaz, Modelling of Microstructure Formation in Solidification Processes, *Int. J. Heat Mass Transfer*, Vol. 34, pp. 93–123, 1995

40. B.Q. Li and P.N. Anyalebechi, Macro/Micro Modeling of Melt Flow and Microstructure Formation During Continuous Casting, in *Transport Phenomena in Solidification* (ed. C. Beckermann, H.P. Wang, L.A. Bertram, M.S. Sohal and S.I. Guceri), ASME, HTD–Vol. 284 & AMD–Vol. 182, pp. 97–107, New York, 1994.

41. C.Y. Wang and C. Beckermann, Multi-Scale/–Phase Modeling of Dendritic Alloy Solidification, in *Transport Phenomena in Solidification* (ed. C.

Beckermann, H.P. Wang, L.A. Bertram, M.S. Sohal and S.I. Guceri), ASME, HTD–Vol. 284 & AMD–Vol. 182, 75–95, New York, 1994.

42. M.E. Glicksman, M.B. Koss and E.A.Winsa, The Chronology of a Microgravity Spaceflight Experiment: 1DGE, *JOM*, August Issue, pp. 49–54, 1995.

43. S. Sen and D.M. Stefanescu, Melting and Casting Processes for High Temperature Intermetallics, *JOM*, May issue, pp. 30–32, 1991.

44. R. Darolia. NiAl alloys for High Temperature Structural Applications, *JOM*, March issue, pp. 44–49, 1991.

45. K. Zanio, Cadmium Telluride, in *Semiconductors and Semimetals* (ed. R.K. Willardson and A.C. Beer), Vol.13, Academic Press, New York, 1978.

46. M. Pfeiffer and M. Mühlberg, Interface Shape Observation and Calculation in Crystal Growth of CdTe by the Vertical Bridgman Method, *J. Crystal Growth*, Vol.118, pp. 269–276, 1992.

47. R.A. Brown, Theory of Transport Processes in Single Crystal Growth from the Melt, *A.I.Ch.E. J.*, vol. 34, pp. 881–911, 1988.

48. J.C. Brice, *Crystal Growth Processes*, Blackie, London, U.K. 1986.

49. M.J. Kaufman and V. Levit, *Private Communication*, University of Florida, Gainesville, FL, 1994.

50. Y. Pang, Private communication, BDM Inc, McLean, VA, 1994.

51. H. Ouyang and W. Shyy, Multi–level Simulation of Bridgman Growth of β–NiAl, Accepted for publication in *Int. J. Heat Mass Transf.*, 1995.

52. T.C. Vu and W. Shyy, Navier–Stokes Computation of Radial Inflow Turbine Distributor, *J. Fluid Engng.*, vol. 110, pp. 29–32, 1988.

53. M.M. Rai, A Conservative Treatment of Zonal Boundary for Euler Equation Calculations, *AIAA–84–0164*, 1984.

54. J.L. Steger, Thoughts on the Chimera Method of Simulation of Three–Dimensional Viscous Flow, in Proceedings, *Computational Fluid Dynamics Symposium on Aeropropulsion*, Cleveland, Ohio, *NASA CP–3078*, pp. 1–10, 1991.

55. J.A. Benek, J.J. Steger, and F.C. Dougherty, A Flexible Grid Embedding Technique with Application to the Euler Equations, *AIAA–83–1944–CP*, 1983.

56. M.M. Rai, A Implicit, Conservative, Zonal–Boundary Scheme for Euler Equation Calculations, *AIAA–85–0488*, 1985.

57. M.J. Berger, On Conservation at Grid Interfaces, *SIAM J. Numer. Anal.*, Vol. 24, No. 5, pp. 967–984, 1987.

58. G. Chesshire and W.D. Henshaw, Composite Overlapping Meshes for the Solution of Partial Differential Equations, *J. Comp. Phys.*, Vol. 90, pp. 1–64, 1990.

59. G. Chesshire and W.D. Henshaw, A Scheme for Conservative Interpolation on Overlapping Grids, *SIAM J. Sci. Comput.*, Vol. 15, No. 4, pp. 819–845, 1994.

60. E. Part–Enander and B. Sjogreen, Conservative and Non–Conservative Interpolation Between Overlapping Grids for Finite Volume Solutions of Hyperbolic Problems, *Comp. Fluids*, Vol. 23, pp. 551–574, 1994.

61. R.L. Meakin, On the Spatial and Temporal Accuracy of Overset Grid Methods for Moving Body Problems, *AIAA–94–1925*, 1994.

78. J. Wright and W. Shyy, Numerical Simulation of Unsteady Convective Intrusions in a Thermohaline Stratification, Accepted for publication in *Int. J. Heat Mass Transfer*, 1995.

79. U. Ghia, K.N. Ghia, and C.T. Shin, High–Re Solutions for Incompressible Flow Using the Navier–Stokes Equations and a Multigrid Method, *J. Comp. Phys.*, Vol. 48, pp. 387–411, 1982.

80. W. Shyy, S. Thakur, and J. Wright, Second–Order Upwind and Central Difference Schemes for Recirculating Flow Computation, *AIAA J.*, Vol. 30, pp. 923–932, 1992.

81. S. Thakur and W. Shyy, Some Implementational Issues of Convection Schemes for Finite Volume Formulations, Second–Order Upwind and Central Difference Schemes for Recirculating Flow Computation, *Numer. Heat Transfer*, Part B, Vol. 24, pp. 31–55, 1993.

62. Y. Kallinderis, Numerical Treatment of Grid Interfaces for Viscous Flows, *J. Comp. Phys.*, Vol. 98, pp. 129–144, 1992.

63. Y. Moon and M.–S. Liou, Conservative Treatment of Boundary Interfaces for Overlaid Grids and Multi–level Grid Adaptations, *AIAA–89–1980*, 1989.

64. Z.J. Wang, P. Buning and J. Benek, Critical Evaluation of Conservative and Non–Conservative Interface Treatment for Chimera Grids, *AIAA–95–0077*, 1995.

65. C.Y. Perng and R.L. Street, A coupled Multigrid–Domain–Splitting Technique for Simulating Incompressible Flow in Geometrically Complex Domains, *Int. J. Numer. Meths. Fluids*, Vol. 13, pp. 269–286, 1991.

66. Y.G. Lai, Y. Jiang and A.J. Przekwas, An Implicit Multi–Domain Approach for the Solution of Navier–Stokes Equations in Body–Fitted–Coordinate Grids, *AIAA–93–0541*, 1993.

67. S. Thakur, J. Wright, W. Shyy, J. Liu, H. Ouyang, and T. Vu, Development of Pressure–Based Composite Multigrid Method for Complex Fluid Flows, to appear *in Progress in Aerospace Sciences*, 1995.

68. R.L. Meakin and R.L. Street, Simulation of Environmental Flow Problems in Geometrically Complex Domain. Part 2: A Domain–Splitting Method, *Computer Meths. Appl. Mech. Eng.*, Vol. 68, pp. 311–331, 1988.

69. M. Hinatsu and J.H. Ferziger, Numerical Computation of Unsteady Incompressible Flow in Complex Geometry Using a Composite Multigrid Technique, *Intl. J. Numer. Meths. Fluids*, Vol. 13, pp. 971–997, 1991.

70. J.C. Strikwerda and C.D. Scarbnick, A domain Decomposition Method for Incompressible Viscous Flow, *SIAM J. Sci. Comput.*, Vol. 14, pp 49–67, 1993.

71. W.D. Henshaw, A Fourth–Order Accurate Method for the Incompressible Navier–Stokes Equations on Overlapping Grids, *J. Comp. Phys.*, Vol. 113, pp. 13–25, 1994.

72. C. Yung, T.G. Keith, Jr., and K.J. De Witt, Numerical Simulation of Axisymmetric Turbulent Flow in Combustors and Diffusers, *Int. J. Numer. Meths. Fluids*, Vol. 9, pp. 167–183, 1989.

73. J.Y. Tu and L. Fuch, Overlapping Grids and Multigrid Methods for Three–Dimensional Unsteady Flow Calculations in IC Engines, *Int. J. Numer. Meths. Fluids*, Vol. 15, pp. 693–714, 1992.

74. J. Wright and W. Shyy, A Pressure–Based Composite Grid Method for the Incompressible Navier–Stokes Equations, *J. Comp. Phys.*, Vol. 107, pp. 225–238, 1993.

75. W. Shyy, J. Liu, and J. Wright, Pressure–Based Viscous Flow Computation Using Multiblock Overlapped Curvilinear Grid, *Numer. Heat Transfer*, Vol. 25, pp. 39–59, 1994.

76. W.D. Gropp and D.E. Keyes, Domain Decomposition Methods in Computational Fluid Dynamics, *Int. J. Numer. Meths. Fluids*, Vol. 14, pp. 147–165, 1992.

77. W.D. Gropp and D.E. Keyes, Domain Decomposition with Local Mesh Refinement, *SIAM J. Sci. Stat. Comput.*, Vol. 13, No. 4, pp. 967–993, 1992.

ADVANCES IN
NUMERICAL HEAT TRANSFER

Volume 1

ADVANCES IN
NUMERICAL HEAT TRANSFER

Editors
W.J. Minkowycz, University of Illinois, Chicago, Illinois
E.M. Sparrow, University of Minnesota, Minneapolis, Minnesota

CONTENTS

v

Communications

Superheating Behavior of NiAl

NAGRAJ S. KULKARNI and KYUNG TAE HONG

The intermetallic compound NiAl has been widely studied for its possible use as a high-temperature structural material.[1] The preparation of NiAl alloys of controlled composition and stoichiometry has been recognized to be an important component in their continued development and understanding. Control of interstitial elements such as oxygen and carbon is necessary to minimize the effect of these elements on the mechanical properties of such intermetallics. A promising laboratory technique that can be used to circumvent these problems involves the containerless processing of metals and their alloys using electromagnetic levitation.[2,3] Compared to other conventional processing techniques, electromagnetic levitation processing offers several unique advantages,[2,3] such as (1) noncontamination of the melt since there is no contact with crucible materials; (2) homogeneity of the melt due to extremely efficient electromagnetic stirring and homogeneity of the solid due to rapid solidification; (3) rapid equilibration in metal-gas systems due to the large surface area of the melt exposed to the gas phase and to efficient stirring, thus permitting control of interstitial elements such as O, C, N, and H; and (4) laboratory survey work of unknown alloys and the investigation of basic phenomena such as melting, vaporization, nucleation, and solidification. Since only small samples weighing 1 to 2 g can be used during levitation processing, the application is limited to laboratory purposes. In the case of alloys that contain an element having a high vapor pressure (e.g., Al in NiAl), the technique is especially attractive since it permits control of the stoichiometry (Ni/Al atom ratio) by preferential evaporation of the high vapor pressure element. The present study describes an unusual superheating and transformation phenomenon observed during electromagnetic levitation processing of the intermetallic compound NiAl.

A high frequency generator was used to supply a sinusoidally varying power with frequencies ranging from 50 kHz to 5 MHZ to a step-down transformer, which in turn was used to supply currents of several hundred amps to a specially designed coaxial levitation coil (1/8-in. Cu tubing and 0.02-in. wall thickness). The resulting electromagnetic field was used for levitating and simultaneously internally heating (due to eddy current losses) a given sample. The sample was contained within a PYREX* glass tube for at-

*PYREX is a trademark of Corning Glass Works, Corning, NY.

mosphere control (Figure 1). The glass tube was housed in a suitable chamber, which facilitated rapid insertion and removal of samples. Since both heating and levitation de-

NAGRAJ S. KULKARNI, Graduate Student, is with the Department of Materials Science and Engineering, University of Florida, Gainesville, FL 32611. KYUNG TAE HONG is Principal Researcher with the Division of Metals, Korea Institute of Science and Technology (KIST), Seoul, Korea 136-791.
Manuscript submitted September 3, 1997.
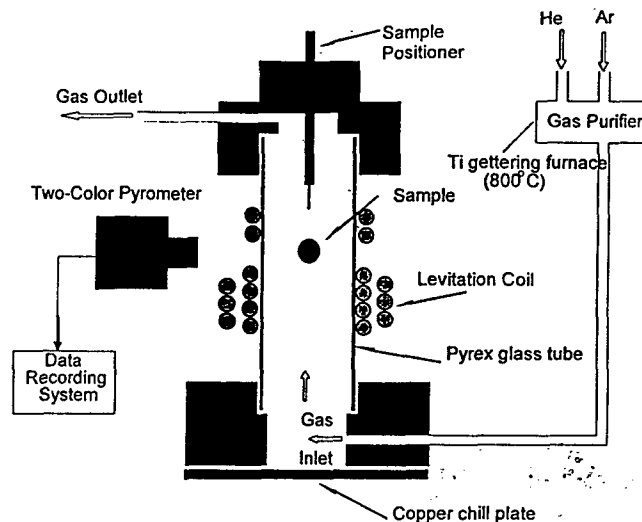
Fig. 1—Schematic representation of the electromagnetic levitation melting apparatus.

pend on the strength of the magnetic field, independent control of temperature was done by varying the flow rate of He gas (a highly conductive gas) in a mixture of purified Ar, while maintaining a constant power level for the duration of the experiment. The gases (initial purity 5 ppm O) were ultrapurified by passing them through a Ti gettering furnace at 800 °C. The purity of the gases was determined at a location just before their entry into the levitation chamber using a solid-state oxygen monitor.* The oxygen

*Centorr model 2D oxygen monitor, CENTORR Associates Inc., Suncook, NH.

monitor is a Voltaic cell of the concentration type and has yttria-stabilized zirconium dioxide as the cell electrolyte. The voltage of this cell depends on the ratio of the partial pressure of oxygen at the two electrodes and is given by the Nernst equation. The concentration of oxygen in air (20.95 pct or 209500 ppm) establishes the potential of the reference electrode. The monitor registered oxygen levels of $<10^{-20}$ atm. (10^{-14} ppm) for the ultrapurified gases used in this study. Such low levels of oxygen are achieved by the preferential oxidation of porous Ti in the gettering furnace (hence reducing the oxygen concentration in the gases) since the oxygen partial pressure of Ti in equilibrium with TiO_2 is $<10^{-35}$ atm at 800 °C, as seen from a standard Richardson–Ellingham stability diagram for the formation of oxides. This high-purity atmosphere protected the NiAl samples used in this study from oxidation. The gas flow lines and various fittings employed in the entire setup were made from stainless steel.

Small button-head NiAl samples weighing 1 to 2 g, that were used for levitation processing, were obtained from arc-melted NiAl ingots of known composition. The ingots were prepared by arc melting high-purity (99.99 pct) Ni and Al pellets of weighed proportions in an Ar atmosphere that was purified by passing through the Ti gettering furnace. Wet chemistry* and inductively coupled plasma emis-

*Nickel by dimethylglyoxime precipitation and Al by 8-hydroxyquinoline precipitation.
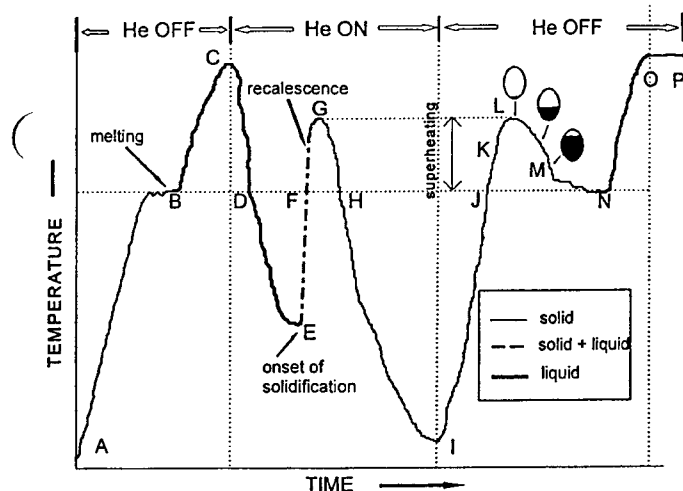
Fig. 2—Schematic of a typical output during levitation processing of NiAl alloys.

sion spectrometry (ICP)** analysis were employed to de-

**Perkin-Elmer ICP/5000 (Perkin-Elmer Physical Electronics, Eden Prairie, MN).

termine the Ni and Al contents. To ascertain the purity of the levitation chamber, combustion analysis† was used to

†Models CS444 for C and S; RH404 for H; and TC436AR for N, O, and Ar. Performed at LECO Corporation (St. Joseph, MI).

determine the concentrations of dissolved C, S, N, O, Ar, and H in a stoichiometric NiAl sample before and after levitation processing. It was found that the concentration of O reduced from 25 to 15 ppm, while that of C reduced from 25 to 2 ppm. The concentrations of the other elements were unchanged: N < 2 ppm, Ar < 5 ppm, S < 2 ppm, and H ≤ 2 ppm.

During levitation processing, the sample temperature was monitored continuously using a two-color ratio pyrometer*

*RatioScope III, Capintec Instruments, Inc., Pittsburgh, PA.

(narrow band filters centered around wavelengths of 0.81 and 0.95 μm) that was connected to a fast response chart recorder. The use of a ratio pyrometer was necessary since the emissivity of NiAl, both as a function of composition (i.e., stoichiometry) and temperature, was not known. In the case of a two-color pyrometer, the measured response depends on the ratio of the emissivities at the two wavelengths (colors). The standard practice is to calibrate the ratio pyrometer for a gray body for which the ratio response becomes independent of emissivity, since the emissivity ratio is always unity. Naturally, this introduces an error in the measurement of temperature for a material, where the emissivity ratio differs from unity at the selected wavelengths. However, in practice, it has been found that while the emissivities at each wavelength may vary widely as a function of temperature and state (phase), the ratio of emissivities at the selected wavelengths is relatively constant and rarely exceeds 1.05 for most materials. The ratio pyrometer has been traditionally used in the steel industry for temperature measurement under adverse viewing conditions. More recently, it has been widely used in laboratory supercooling and solidification studies in many systems, e.g., Fe-Ni[4] and

Ti-Al,[5] over a broad range of temperatures and states. In the present case, the accuracy of the ratio-pyrometer was determined by comparing the melting temperature of a stoichiometric NiAl sample with the value published in the literature (1638 °C).[6] The pyrometer reported the average temperature of the sample since its aperture was large enough to cover the entire sample. Usually, there was a temperature gradient of less than 10 °C along the vertical axis of the sample, the bottom being hotter than the top during the heating process. The sample could be quenched at any time by simply turning off the power. At all times, the sample could be visually observed with the aid of high-temperature viewing glasses.

A typical experiment that describes the observed phenomenon during levitation processing is explained with the aid of Figure 2. An NiAl sample was suspended in the melting chamber surrounded by the induction coil using an adhesive tape at the end of a specimen positioner. A continuous flow of purified Ar was maintained throughout the course of the experiment. During the heating stage, the He flow was turned off. The power was then turned on, which caused the sample to be dislodged from the tape, to levitate, and to heat up simultaneously. The specimen positioner along with the tape was withdrawn upward, where it remained for the duration of the experiment. The NiAl sample began to heat up (AB in Figure 2) and, at the melting point, transformed to the liquid state (B). This initial heating up took only about 15 to 20 seconds. The melting process corresponded to a plateau on the temperature time profile of the chart recorder. This is consistent with observations in the literature, where first-order transformations, such as the melting process, are indicated by a plateau on the time-temperature profile during electromagnetic levitation experiments.[4] After melting, the molten sample was superheated anyway from 150 up to 200 °C (BC in Figure 2) over the melting point and held at that temperature for a few seconds. High frequency oscillations that occurred in the liquid due to the electromagnetic stirring caused temperature fluctuations of ±5 °C that resulted in a wavy profile on the chart recorder. In contrast, the temperature of the solid sample could be controlled within ±1 °C and the time-temperature profile was quite smooth.

The molten liquid was then cooled by allowing a flow of a purified He-Ar mixture (CDE). Supercoolings ranging from 200 up to 250 °C (DE) could be achieved for most samples due to the suppression of nucleation in the containerless, high-purity (low O) environment of the melting chamber. Because of the large driving force available at high supercoolings, solidification of the entire sample occurred extremely rapidly resulting in an almost adiabatic temperature rise as the latent heat was released, a phenomenon commonly known as recalescence (EFG). For a pure metal such as nickel, while using this technique, the recalescence phenomenon results in the temperature of the sample rising to a few degrees Celsius below the melting point of the sample. However, in the case of NiAl samples, an extraordinary event occurred. The recalescence effect resulted in the sample temperature increasing several tens of degrees over the melting point (FG). Following the recalescence, since the He flow was still being maintained, the temperature of the solidified sample dropped to below 1000 °C (GHI).

The same sample was then reheated by turning off the
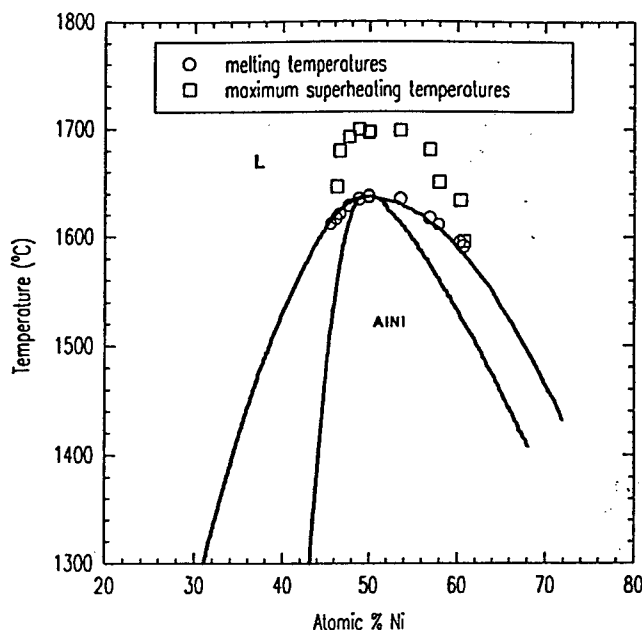
Fig. 3—Superheating effect in NiAl levitation processed alloys as a function of composition.

He flow (IJ). The NiAl solid sample appeared to be completely stable even after its temperature had risen well above its reported melting point (JKL). In fact, a superheated NiAl sample held at 45 °C over the melting point (K) for *30 minutes* showed no signs of melting or instability. This was clear both visually (no solid-liquid interface and no instability seen) and from the temperature profile on a chart recorder, which was smooth throughout. In contrast, at the onset of melting during the levitation heating process, a sample exhibits instability due to the varying responses of the electromagnetic field on the solid and liquid fractions of the sample (near B in Figure 2). The solid-liquid interface is also visible through the high-temperature viewing glasses at the onset of melting. A solid + liquid sample that is quenched by turning off the power and allowing the sample to freely fall either on the Cu base plate or in a water chamber directly below the Cu base plate loses its integrity, since there are no longer electromagnetic stabilizing forces that can preserve the shape of the sample. The solid-liquid interface is easily distinguished by microstructural examination of a quenched sample. In the present case, microstructural examination of a NiAl sample quenched from the superheated temperature confirmed that the sample in the superheated state was solid. The shape and integrity of the sample were unaltered by the quenching process.

Once the sample reached a certain critical superheating temperature (L), which was almost identical to the temperature increase upon recalescence (G), an interface appeared at the bottom of the sample (visually observed, see LM in Figure 2), indicating initiation of a transformation. With continued heat input, the interface advanced toward the top portion of the sample, leaving behind a transformed region in the bottom portion, which could be easily distinguished visually on account of its darker color (LMN). The average temperature of the sample *dropped* during the period of motion of this interface (LMN), although heat was still being continuously supplied, since the He flow was turned off. This suggested a peculiar *endothermic* transformation that was absorbing heat at a faster rate than was being supplied. Visual observation and the lack of any significant instability in levitation, as evident from the temperature profile, until almost the end of the transformation suggested that this transformation occurred in the solid state. By the time the interface had advanced completely to the top and the entire sample had transformed, the temperature had dropped to the *same* melting point (N) as that measured during the original heating stage (B). Following this, there was a great deal of instability that ultimately resulted in the sample melting at its melting point (N). Thus, it appeared that although the *path* followed during this heating stage (IJKLMN) was distinctly different from the initial heating stage (AB), the melting temperatures (B and N) were identical.

The entire process (A–N) was repeated a few times for the same sample as well as for other samples having the same composition. In each case, the identical phenomenon was observed and the same melting and superheating temperatures (±1 °C) were observed. The composition of a given sample was varied by simply holding the superheated liquid for a sufficient period of time (usually a few minutes) in the flowing Ar atmosphere (OP in Figure 2). Since Al in NiAl has a much higher vapor pressure than Ni, the composition of the NiAl sample shifted toward the Ni-rich side of the phase diagram due to the Al loss. In principle, a single sample of a known Al-rich composition (*e.g.*, 45 at. pct Ni) is enough to scan the relevant NiAl liquidus phase boundary (up to 60 at. pct Ni) around the stoichiometric composition. In practice, however, instabilities in levitation that resulted during the melting process or during the superheating of the liquid sometimes caused fusion between the sample and the walls of the melting chamber. Hence, a number of samples had to be used.

The NiAl phase exhibits congruent melting at the stoichiometric composition,[6] and the melting point at this composition is a maximum. The maximum melting temperature that was noted during the scan across the relevant NiAl phase region was 57 °C higher than the published value for the stoichiometric composition (1638 °C). This was not surprising since errors in measurement of absolute temperature using two-color ratio pyrometers are not uncommon and can arise from a variety of sources,[7] most notably the deviation of the emissivity ratio from unity. Hence, the emphasis was on *relative* measurements (relative to the melting or liquidus temperatures), while maintaining similar processing conditions for all compositions. The same offset of 57 °C was applied to all the melting and superheating temperatures that were recorded during the scan across the β NiAl phase region. The actual compositions were then extrapolated from the known liquidus temperatures of the NiAl phase diagram.[6] This procedure of determining the compositions from the known melting points seemed adequate since the extrapolated compositions for each sample corresponded quite well with the known weighed compositions.

Results of the study are plotted in Figure 3. The superheating effect occurred for compositions between approximately 45 to 60 at. pct Ni, with the maximum superheating of about 65 deg occurring close to the stoichiometric composition. The compositional dependence and the *asymmetry*

of the superheating behavior on either side of stoichiometry is also apparent and is indeed consistent with the asymmetric nature of NiAl in general, with respect to its liquidus ∼⁴ solidus as well as its physical properties such as density, tensile strength, hardness, etc.[1]

Our attempts in trying to quench in the unusual transformation proved unsuccessful. Solid superheating NiAl samples that were quenched during the transformation (LM in Figure 2) or at any stage of the heating process always corresponded to the ordered B2 NiAl crystal structure, as evident from powder X-ray diffraction analysis.* The shape

---

*APD 3720, Philips Electronic Instruments, Inc. (Mahwah, NJ).

---

and integrity of the sample were unaltered by the quenching process, either in water or on the Cu chill plate. Microstructural analysis also revealed no trace of any interface. It thus appeared that the kinetics of this transformation was extremely rapid. Further studies of this unusual transformation revealed that it was in fact reversible; if the He flow was turned on (instead of being turned off during the normal heating process) at stage M of the transformation, the interface moved from the top toward the bottom portion of the sample and completely disappeared as it approached L. The path MLKJI was followed in this case, and it appeared that the transformation in this reversed case was *exothermic*.

The similarities between our observations regarding this unusual transformation and those of Sykes and Jones[8] in their investigation of the order-disorder transformation[9] in the Cu₃Au system are indeed striking.* It is suggested that

---

*Sykes and Jones[8] make the following statements in their article: "It (ound that provided the specimen had a consistent scheme of order ghout each crystal at a temperature just below the critical temperature, then, although energy was continuously supplied to the specimen, its temperature-time curve in the neighborhood of the critical temperature showed first a maximum and then a minimum; in brief, an effect exactly opposite to the undercooling phenomena observed on cooling curves and generally produced by a change of phase. The fact that the temperature of the specimen falls, although heat energy is continuously supplied, proves that latent heat is absorbed at the critical temperature on heating."

---

this transformation in NiAl is an order-disorder transformation that appears to be associated with the superheating process in NiAl. Studies that have explored correlations between the heat of formation, the critical temperatures for disordering, the type of defect structure, and the melting point have suggested that NiAl, like many other intermetallic compounds (*e.g.*, NiGa, Ni₃Al,[10,11] FeAl, CoAl, *etc.*), has a virtual order-disorder transformation temperature well above its melting point.[12,13,14] It appears likely that the levitation processing of NiAl caused the order-disorder transformation to become more transparent, since one must expect an ordered material to undergo disordering before actually melting. The fact that the transformation occurred over a temperature range rather than at a fixed temperature is consistent with the transformation behavior of order-disorder transformations.[8,9] A comparison may also be made with β brass (CuZn), which has the same B2 crystal structure as NiAl, but has an order-disorder transition temperature that lies well below its melting point. It is known that (isordered state of the β brass structure is almost impossible to quench due to rapid second-order transformation kinetics.[15,16] This suggests that the unusual transformation

in NiAl, that we found impossible to retain by quenching, also had second-order kinetics.

We do not believe that our observations were affected by oxidation problems, since as discussed earlier, the purity of the levitation chamber had been verified both by using an oxygen monitor as well as by bulk chemical analysis of the oxygen content within the samples. The surfaces of the levitation processed samples appeared extremely clean and lustrous and exhibited a range of colors ranging from yellowish at the Ni-rich end (approximately 60 at. pct Ni) of the β phase region to silvery gray at the Al-rich end (approximately 45 at. pct Ni). Formation of an oxide scale would have resulted in a dull surface and the range of colors would not be evident. A depth profile analysis using Auger spectroscopy* confirmed that oxidation was not a

---

*Perkin-Elmer PHI 660 (Perkin-Elmer Physical Electronics, Eden Prairie, MN).

---

problem. We also discount the possibility that the rapid solidification of the undercooled melt during levitation processing (EG in Figure 2) could result in some nonequilibrium or disordered phase in NiAl that is somehow responsible for the unusual superheating behavior. X-ray analysis of our samples always corresponded to the ordered NiAl crystal structure, and there was no evidence of any other phases. Studies in the literature have also documented that attempts at trying to induce disorder in NiAl by rapid solidification from the melt have been unsuccessful.[17,18,19] Electron microprobe** analysis along a longitudinal section

---

**JEOL Superprobe 733 (Japan Electron Optics Ltd., Tokyo).

---

of a levitation processed sample did not reveal the presence of any unusual segregation or partitioning, the Ni/Al atomic ratio being constant throughout. Bulk density measurements of levitation processed samples using helium micropycnometry† were also consistent with those previously pub-

---

†Model MPY-1, Quantachrome Corporation, Boynton Beach, FL.

---

lished for NiAl.[20]

It seems logical to assume that the superheating and transformation that occurred during levitation processing were related to the high supercoolings (up to 250 °C) achieved in the liquid NiAl sample prior to the onset of rapid solidification. Stoichiometric NiAl samples, that were not levitation processed, did not show any significant superheating or any visual signs of a transformation and had a time-temperature profile indicated by path AB in Figure 2 during the heating process. However, when a stoichiometric NiAl sample, regardless of its prior processing history, was subjected to high supercoolings using levitation processing, it always exhibited the same superheating behavior followed by the unusual transformation. This suggested that the structure and properties of the supercooled NiAl liquid was different from the liquid that existed at the melting point, since the resulting solidified structures behaved differently with regard to the unusual transformation and superheating behavior. Indeed these differences have been well documented in the literature in terms of a change in the short-range order parameter in molten NiAl melts using X-ray diffraction, density, viscosity, surface energy, and interaction energy measurements.[21,22] Furthermore, the thermodynamic properties of liquid NiAl have been exper-

imentally determined by Stolz et al.[23] as a function of composition and temperature and have been well described using an association model.[19,24] The association model for NiAl[23] considers the molten state to consist of free atoms of Ni and Al that are in dynamic equilibrium with the associate having the stoichiometry NiAl. This dynamic equilibrium is assumed to be governed by the law of mass action. The concentration or the mole fraction of the NiAl associate is a function of both composition and temperature. Within the β NiAl phase region, it is expected that the stoichiometric composition (i.e., 50 at. pct Ni) would have the maximum concentration of the NiAl associate in the molten liquid. As compared to the liquid at the melting point, it is expected that at high supercoolings, the concentration of this associate would be much higher. The rapid solidification from the supercooled NiAl melt, having such an associated structure, appears to be responsible for the formation of NiAl samples that show this unusual superheating[25,26] and transformation behavior. The melting and solidification behaviors of NiAl need greater analysis in light of this study.

REFERENCES

1. D.B. Miracle: *Acta Metall. Mater.*, 1993, vol. 41, pp. 649-84.
2. W.A. Peifer: *J. Met.*, 1965, pp. 487-93.
3. E.C. Okress, D.M. Wroughton, G. Comenetz, P.H. Brace, and J.C.R. Kelly: *J. Appl. Phys.*, 1952, vol. 23, pp. 545-52.
4. R. Willnecker, D.M. Herlach, and B. Feuerbacher: *Appl. Phys. Lett.*, 1986, vol. 49, pp. 1339-41.
5. J.J. Valencia, C. McCullough, C.G. Levi, and R. Mehrabian: *Acta Metall.*, 1989, vol. 37, pp. 2517-30.
6. P. Nash, M.F. Singleton, and J.L. Murray: in *Phase Diagrams of Binary Nickel Alloys*, P. Nash, ed., ASM INTERNATIONAL, Metals Park, OH, 1991, vol. 1, pp. 3-11.
7. R.E. Spjut: *Noncontact Temperature Measurement*, NASA Conf. Pub. 2503, M.C. Lee, ed., NASA, Washington, DC, 1987, pp. 182-213.
8. C. Sykes and F.W. Jones: *Proc. R. Soc. A*, 1936, vol. 157, pp. 213-390.
9. F.C. Nix and W. Shockley: *Rev. Modern Phys.*, 1938, vol. 10, pp. 1-71.
10. R.W. Cahn, P.A. Siemers, J.E. Geiger, and P. Bardhan: *Acta Metall.*, 1987, vol. 35, pp. 2737-52.
11. R.W. Cahn, P.A. Siemers, and E.L. Hall: *Acta Metall.*, 1987, vol. 35, pp. 2753-764.
12. J.P. Neumann, Y.A. Chang, and H. Ipser: *Scripta Metall.*, 1976, vol. 10, pp. 917-22.
13. J.P. Neumann, Y.A. Chang, and C.M. Lee: *Acta Metall.*, 1976, vol. 24, pp. 593-604.
14. H. Assadi, M. Barth, A.L. Greer, and D.M. Herlach: *Acta Metall. Mater.*, 1998, vol. 46, pp. 491-500.
15. S.G. Cupschalk and N. Brown: *Acta Metall.*, 1967, vol. 15, pp. 847-56.
16. S.G. Cupschalk and N. Brown: *Acta Metall.*, 1968, vol. 16, pp. 657-66.
17. V.F. Bashev, I.S. Miroshnichenko, and F.F. Dotsenko: *Izv. Akad. Nauk SSSR, Met.*, 1989, vol. 6, pp. 55-58.
18. M. Barth, B. Wei, D.M. Herlach, and B. Feuerbacher: *Mater. Sci. Eng. A*, 1994, vol. 178, pp. 305-07.
19. R.N. Singh and N.H. March: in *Intermetallic Compounds: Principles and Practice*, J.H. Westbrook and R.L. Fleischer, eds., John Wiley and Sons, New York, NY, 1995, vol. 1, pp. 661-86.
20. A. Taylor and N.J. Doyle: *J. Appl. Crystallogr.*, 1972, vol. 5, pp. 201-15.
21. M.S. Petrushevskii, E.S. Levin, and P.V. Gel'd: *Russ. J. Phys. Chem.*, 1971, vol. 45, pp. 1719-21.
22. G.D. Ayushina, E.S. Levin, and P.V. Gel'd: *Russ. J. Phys. Chem.*, 1969, vol. 43, pp. 1548-51.
23. U.K. Stolz, I. Arpshofen, F. Sommer, and B. Predel: *J. Phase Equilibria*, 1993, vol. 14, pp. 473-78.
24. F. Sommer: *Z. Metallk.*, 1982, vol. 72, pp. 72-86.
25. R.W. Cahn: *Nature*, 1988, vol. 334, pp. 17-18.
26. V.K. Pecharsky, K.A. Gschneidner, Jr., and D. Fort: *Scripta Mater.*, 1996, vol. 35, pp. 843-48.

Ordering and Martensitic Transformations of Ni$_2$AlMn Heusler Alloys

Y. SUTOU, I. OHNUMA, R. KAINUMA, K. ISHIDA

The NiAlMn β alloys having a high M_s temperature are of interest as potential high-temperature shape memory

Y. SUTOU, Graduate Student, I. OHNUMA, Research Associate, R. KAINUMA, Associate Professor, and K. ISHIDA, Professor, are with the Department of Materials Science, Graduate School of Engineering, Tohoku University, Sendai 980-8579, Japan.
Manuscript submitted March 23, 1998.
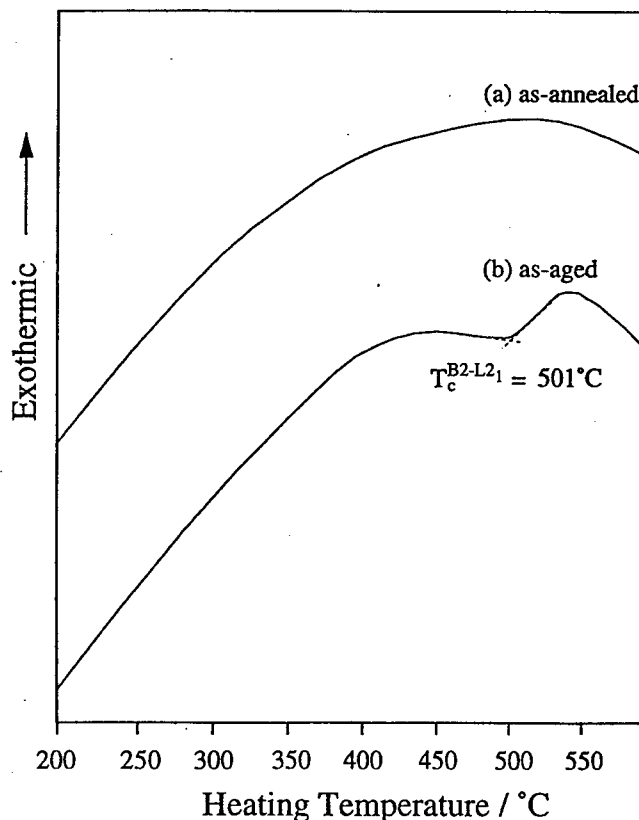
Fig. 1—DSC heating curves of (a) as-annealed and (b) as-aged Ni-25 at. pct Al-22.5 at. pct Mn alloys.

B2

(a)

200

011

$[01\bar{1}]_{B2}$

$L2_1$

(b)

400

111

000 · 022

$[01\bar{1}]_{L21}$

(c)

100nm
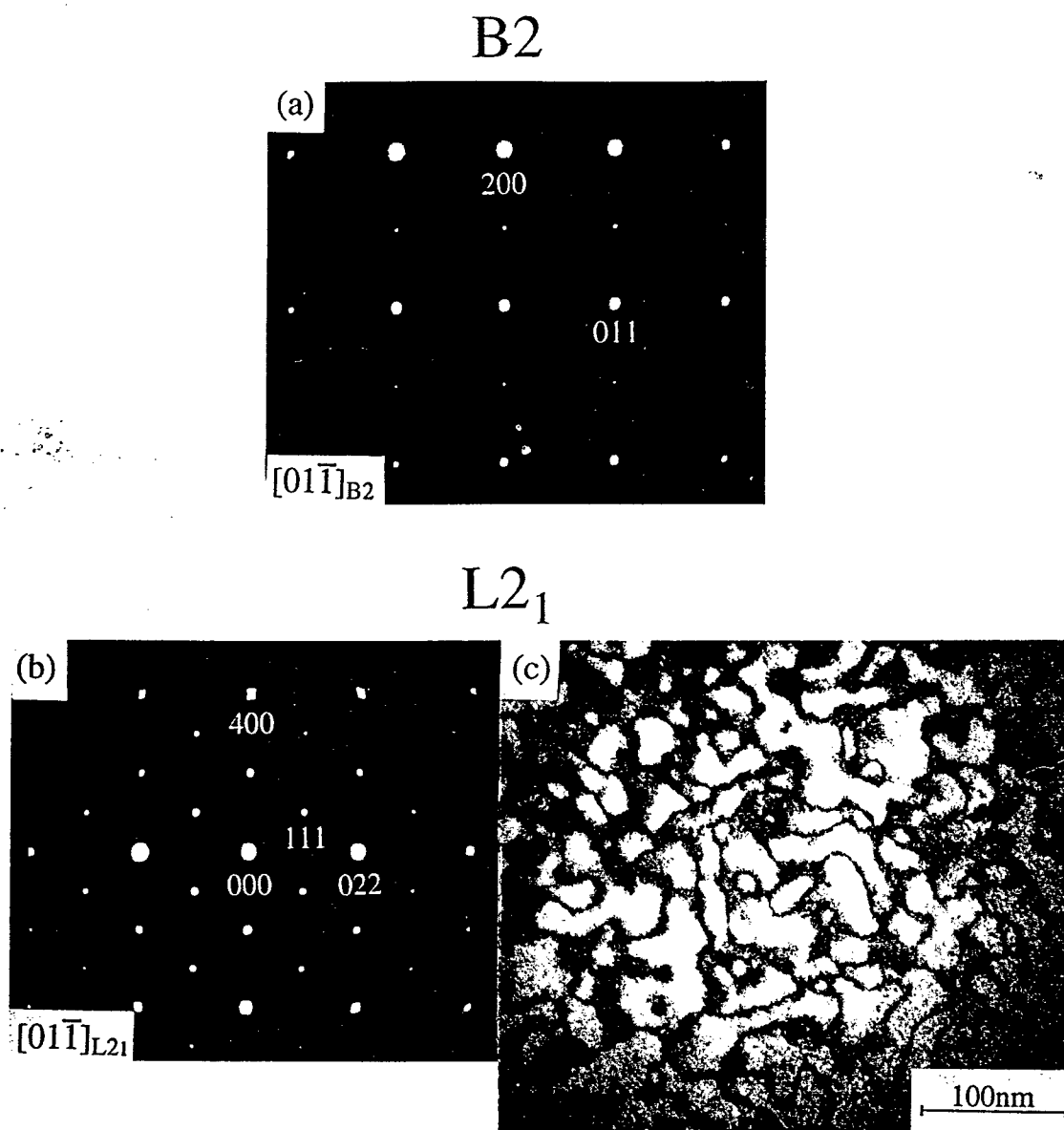
Fig. 2—Selected area diffraction patterns (SADPs) taken from (a) as-annealed and (b) as-aged Ni-25 at. pct Al-17.5 at. pct Mn alloy specimens. (c) TEM dark-field image taken from the $(111)_{L21}$ ordered reflection in the SADP (b) showing the APD structure of the $L2_1$ phase.

(SM) alloys.[1,2,3] The present authors have recently examined the details of martensitic transformation, such as the crystal structure of the parent and martensite phases and the M_s temperature and microstructure of the premartensite phase, in the Ni-Al-Mn alloys quenched from high temperatures over 1000 °C.[4] In these specimens quenched from the elevated temperatures, the crystal structure of the parent phase is always B2 (Ni(Al, Mn)) and the martensite phase shows a 2M ($L1_0$), 10M, 12M, or 14M (7R) structure or a mixture of them.[4,5,6] Very recently, Chernenko et al. pointed out that ferromagnetic NiGaMn SM alloys with a $L2_1$ (Ni_2GaMn: Heusler) structure have potential for use as a new type of smart materials whose SM properties can be controlled not only by temperature and stress, but also by magnetic field.[7] Since the $L2_1$ Heusler structure also appears in the stoichiometric Ni_2AlMn alloy,[8] it can be expected that the NiMnAl Heusler alloys exhibit unique properties similar to those of the NiMnGa alloys. However, there are very few reports on the stability of the $L2_1$ ordered

phase and the magnetic and SM properties of NiMnAl Heusler alloys.[8,9] It is the purpose of this article to report the results of our investigation of the order-disorder and martensitic transitions of Ni-Mn-Al Heusler alloys aged at low temperatures.

Single-phase β alloys of the Ni-Mn-Al ternary system were prepared in an induction furnace under an argon atmosphere by melting from pure metals of Ni (99.9 pct), Al (99.7 pct), and Mn (99.9 pct) in appropriate quantities. All the cast alloys were solution treated at 1000 °C for 72 hours and quenched in ice water; some alloys were then aged at 400 °C to obtain an ordered $L2_1$ structure. Details of the experimental procedures of transmission electron microscopic (TEM) and X-ray diffraction (XRD) examinations and differential scanning calorimetric (DSC) measurement are described in our previous article.[4]

Figure 1 shows the DSC heating curves of as-annealed and as-aged specimens. While there is no endothermic peak in the as-annealed specimen, an endothermic peak appears

Application of a Method for Determination of the Internal Stress in Polycrystalline NiAl

M.L. Weaver and M.J. Kaufman
Department of Materials Science and Engineering
University of Florida
Gainesville, Florida 32611

Introduction

The concept of the internal stress is widely accepted, however, its measurement has proven difficult. Originally Seeger assumed that the internal stress at low temperatures could be measured at the plateau of the flow stress versus temperature curve [1] . However, such assumptions are subject to conjecture because flow stress plateaus are typically associated with dynamic strain aging (DSA). As a result, deformation in the plateau region can involve interactions between dislocations, point defects and mobile solute atoms in addition to basic rate controlling mechanisms. Thus, it is difficult to build a definitive correlation of the plateau stress to the internal stress at temperatures below the plateau region.

Several stress relaxation techniques based on the empirical equation proposed by Li [2] have been applied to determine a variety of thermal activation parameters including the internal stress, σ_i, the effective stress, σ^*, the stress sensitivity exponent, m, and the density of mobile dislocations, ρ_m [3-5]. Unfortunately, inconsistencies have been noted when the results of such tests are analyzed by means of Li's equation, including negative values of m which have no physical significance [6,7].

Qian and Reed-Hill have developed a simplified approach for determining σ_i which implies a zero entropy of activation. The feasibility of this approach has been demonstrated for the commercial purity niobium data of Fries et al. [8,9], the experimental Nb-O data of Park et al. [10] and the Cu₃Sn data of Qian and Reed-Hill [11]. In this paper, the general approach is reviewed and an attempt is made to apply it to the polycrystalline Ni-48.9 at.%Al and Ni-43.0 at.%Al data of Pascoe and Newey [12,13].

Review of Qian and Reed-Hill's Model

The approach of Qian and Reed-Hill, which is based on the early relations of Orowan [14] and Johnston and Gilman [15] , has several assumptions and requirements:

(1)   it must be possible to evaluate the temperature and strain rate dependence of flow stress by a power law relationship of the form

$$\sigma^* = \sigma_0^*(\dot{\varepsilon}/\dot{\varepsilon}_0)^n \tag{1}$$

where the exponent n is the strain rate sensitivity measured under conditions where ε is directly proportional to the dislocation velocity v, σ^* is the effective component of the flow stress, $\dot{\varepsilon}$ is the base strain rate, and $\dot{\varepsilon}_0$ is a constant equal to $\rho_m \bar{b} v_0$. It is further assumed that n is given by $n = RT/H_0$ where R is the universal gas constant and H_0 is a material parameter with units of energy;

(2)   sufficient strain rate sensitivity and flow stress versus temperature data must exist at temperatures below the plateau region (*i.e.*, where DSA does not occur);

(3)   the temperature dependence of the elastic modulus must be known;

(4)   it is assumed that the temperature dependence of the internal stress is related to that of the elastic modulus by the equation

$$\sigma_i = \frac{\sigma_{i_0} \cdot E}{E_0} \tag{2}$$

(5)   the applied stress is assumed to be the sum of its internal, σ_i, and effective, σ^*, components. Thus,

$$\sigma = \sigma_i + \sigma^*. \tag{3}$$

In studies of strain aging the strain rate sensitivity, which was expressed above as n, may also be expressed as $s = d\sigma/d\ln\dot{\varepsilon}$. Considering the assumptions listed above, it can be shown that the strain rate sensitivity, s, is related to the flow stress and the strain rate by the following equation

$$s = \frac{RT}{H_0}\sigma_0^*(\dot{\varepsilon}/\dot{\varepsilon}_0)^{RT/H_0} \tag{4}$$

where σ_0^* is the effective stress at 0 K. Plotting s versus temperature yields a curve containing a single maximum as illustrated in Fig. 1. At the maximum of this curve it can be shown that the following relationships apply:

$$\sigma_{max}^* = \sigma_0^*/e \tag{5}$$

$$H_0 = \frac{RT_{max}\sigma_{max}^*}{s_{max}} \tag{6}$$

$$\dot{\varepsilon}_0 = \dot{\varepsilon}\exp\left(\frac{\sigma_{max}^*}{s_{max}}\right) \tag{7}$$

where e is the base of the natural logarithm, s_{max} the strain rate sensitivity peak, T_{max} the temperature at s_{max}, σ_{max} the effective stress at T_{max} and σ_0 the effective stress at 0 K. These relationships can be used in conjunction with equation 3 to derive the following expression for the internal stress at 0 K

$$\sigma_{i_0} = \frac{\sigma_0 - e\sigma_{max}}{\left(1 - \frac{e \cdot E_{max}}{E_0}\right)} \tag{8}$$

where σ_0 and σ_{max} can be extrapolated from the experimental data. Thus, only data concerning the temperature dependence of the elastic modulus is required to determine σ_{i_0}.

Application of the Model to β-NiAl

Pascoe and Newey [12,13] have published an extensive set of flow stress and strain rate sensitivity data between 77 K and 1550 K at a base strain rate of 2.2×10^{-4} s^{-1} for a variety of extruded and single crystal NiAl alloys. Nearly complete sets of data exist for polycrystalline Ni-48.9 at.%Al and Ni-43.0 at.%Al and these data are represented in Figs. 2 and 3. For Ni-48.9 at.%Al, the maximum in the strain rate sensitivity plot was judged to occur at $s_{max} = 23.57$ MPa and $T_{max} = 103$ K. For Ni-43.0 at.%Al, no definite maximum was given but it was assumed to occur at $s_{max} = 32.12$ MPa and $T_{max} = 150$ K which represents the first data point for this alloy. Extrapolating the flow stress data to 0 K we find $\sigma_0 = 2000$ MPa and $\sigma_{max} = 750$ MPa at 103 K for Ni-48.9 at.% Al and $\sigma_0 = 3100$ MPa and $\sigma_{max} = 1380$ MPa at 150 K for Ni-43.0 at.%Al. The temperature dependence of the elastic modulus has been found to vary significantly with processing technique but not with composition [16]. For this analysis we have adopted the recent equation of Hellman *et al.* [17] which was derived for a powder processed alloy of Ni-50.6 at.%Al. Assuming that this equation may be applied to off-stoichiometry extruded alloys, we describe the modulus as follows

$$E \text{ (GPa)} = 249.3 - 0.031T + 1 \times 10^{-5}T^2 \tag{9}$$

which yields values of $E_0 = 249.3$ GPa and $E_{max} = 246.2$ GPa for Ni-48.9 at.%Al and $E_0 = 249.3$ GPa and $E_{max} = 244.9$ GPa for Ni-43.0 at.%Al. Substituting these values into equations 6, 7 and 8 we determined internal stresses for both alloys as summarized in Table 1.

Table 1. Calculated values of σ_{i_0}, H_0 and $\dot{\varepsilon}_0$ for the data of Pascoe and Newey [12,13].

Alloy	σ_{i_0} (MPa)	H_0 J/mole	$\dot{\varepsilon}_0$ s^{-1}
Ni-43.0 at.% Al	389.9	38,442.4	5.4×10^9
Ni-48.9 at.% Al	35.0	26,927.6	9.1×10^9

A second method for determinating the constants H_0 and $\dot{\varepsilon}_0$ is from a plot of the strain-rate sensitivity n versus T [18]. A plot of n versus temperature should be linear where DSA is not a factor. Using the n versus

temperature data of Pascoe and Newey [12,13], we determined H_0 to be 58,561 J/mol for Ni-43.0 at.% Al and 23,077 J/mol for Ni-48.9 at .% Al which, for Ni-48.9 at.%Al, compares favorably with the data presented in Table 1. The poor correlation for Ni-43.0 at.%Al is attributed to a lack of sufficient low temperature data for this alloy.

The curves appearing in Figs. 2 and 3 were obtained by insertion of these parameters into equations 1 and 4. These curves are based upon original estimates of material parameters. No attempts have been made to improve the fit of the derived curves by adjustment of the original estimates of T_{max} and s_{max}. In view of the limited number of strain rate sensitivity measurements of Pascoe and Newey [12,13] near the strain rate sensitivity peak, there is good agreement between the analytical curves and the experimental data in regions where DSA is not a factor. The deviations of the calculated curves from the experimental data at temperatures above the start of the yield stress plateau may be explained in terms of a combination of DSA and dislocation drag [8]. It is well documented that minima in the temperature dependence of strain rate sensitivity (s or n) occur in the regime of DSA [19]. General agreement is observed between the NiAl data of Pascoe and Newey [12,13] and that for other metals and alloys. Examination of the n versus temperature plots for Ni-48.9 at.% Al and Ni-43.0 at.% Al, for example, reveals deviations from linearity which may be associated with strain aging. In addition, the locations of these deviations correspond well with the minima observed in the s versus temperature curves and the locations of the yield stress plateaus in the 0.2% yield stress versus temperature curves. Further evidence in support of these assertions are the observations of yield drops in Ni-48.9 at.% Al in the range 100 K to 500 K [12,13]. Such yield drops were absent upon unloading and immediate reloading but reappeared when the test specimen was unloaded and aged at 350 K for 1 hr; this behavior is often associated with static strain aging.

This method appears to work well for the available data up to approximately 600 K. If the general model is modified to take into account DSA, good agreement between the experimental s versus temperature curves and the actual data is observed up to the minima in this curve [20]. Above this temperature, the minimum in the s versus temperature passes through a well-defined peak. Similar peaks have been observed in Ti-O [21], Nb-O [10], and Cu_3Sn alloys [11]. It has been suggested that this peak is the result of deformation involving dislocation drag [8].

As a final note, the method for determining H_0 from n and s versus temperature curves also correlates very well for Pascoe and Newey's soft-oriented single crystal data. Unfortunately, there are insufficient data to effectively model s or the yield stress as a function of temperature presently and further work is needed in this area.

Conclusions

We conclude that the approach of Qian and Reed-Hill is useful for determining the internal stress in NiAl and for modeling the strain rate sensitivity and flow stress as a function of temperature and strain provided data is available below the regime of DSA and when the strain rate dependence of the flow stress can be approximated with a power law (equation 1).

Acknowledgments

References

1.   A. Seeger, in *Dislocations and the Mechanical Properties of Crystals*, J. C. Fisher, W. G. Johnston, R. Thomson and J. T. Vreeland, Eds., John Wiley and Sons, New York, (1957) p. 243.
2.   J. C. M. Li, *Canadian Journal of Physics* 45, 493 (1967).
3.   I. Gupta and J. C. M. Li, *Metallurgical Transactions* 1, 2323 (1970).
4.   H. Conrad and K. Okazaki, *Scripta Metallurgica* 4, 259 (1970).
5.   P. Rodriquez, *Journal of Materials Science* 3, 98 (1968).
6.   R. E. Reed-Hill and J. R. Donoso, *Scripta Metallurgica* 9, 1305 (1975).
7.   P. E. V. de Miranda, I. LeMay and S. N. Monteiro, *Scripta Metallurgica* 14, 1201 (1980).
8.   R. E. Reed-Hill and T. Zhu, *High Temp. Mater. and Proc.* 6, 93 (1984).
9.   J. F. Fries, B. Houssin, G. Cizeron and P. Lacombe, *Journal of the Less Common Metals* 33, 117 (1973).
10.   S. C. Park, L. P. Beckerman and R. E. Reed-Hill, *Metallurgical Transactions A* 14A, 463 (1983).
11.   K. W. Qian and R. E. Reed-Hill, *Acta Metallurgica* 31, 87 (1983).
12.   R. T. Pascoe and C. W. A. Newey, *Metal Science Journal* 5, 50 (1971).
13.   R. T. Pascoe and C. W. A. Newey, *Metal Science Journal* 2, 138 (1968).
14.   E. Orowan, *Proceedings of the Physical Society* 52, 8 (1940).
15.   W. G. Johnston and J. J. Gilman, *Journal of Applied Physics* 30, 129 (1959).
16.   R. D. Noebe, R. R. Bowman and M. V. Nathal, *International Materials Reviews* 38, 193 (1993).
17.   J. R. Hellman, D. A. Koss, C. A. Moose, R. R. Petrich and M. N. Kallas, in *HITEMP Review-1990* . 1990), pp. 41.
18.   R. E. Reed-Hill, personal communication (1994).
19.   J. D. Lubahn, *Transactions of the American Society for Metals* 44, 643 (1952).
20.   M. L. Weaver, unpublished research, University of Florida (1993).
21.   C. Yin, M. Doner and H. Conrad, *Metallurgical Transactions* 6A, 1901 (1975).
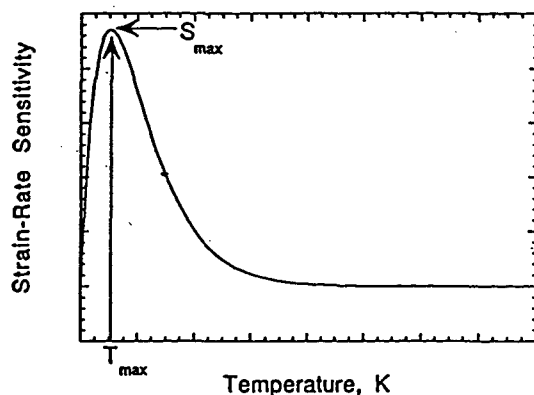
Fig. 1. Schematic representation of the variation of the strain rate sensitivity with temperature.

(a)   (b)
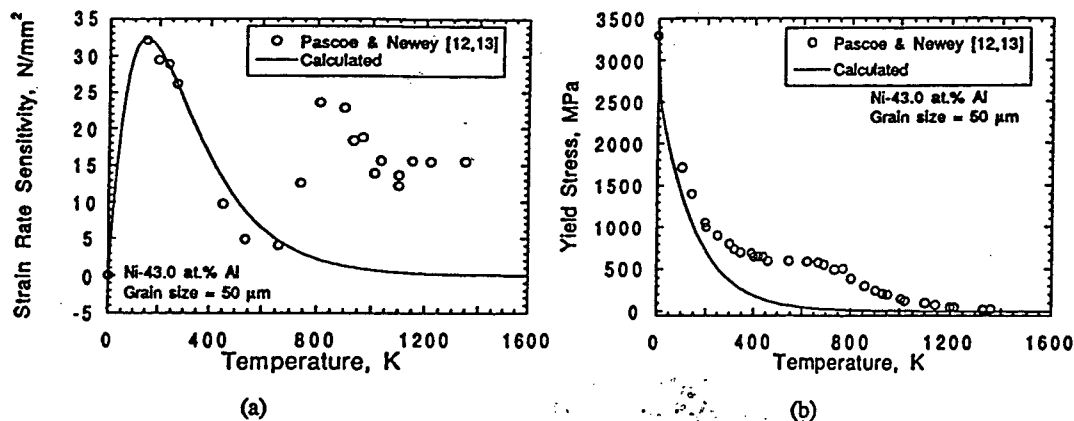
Fig. 2. The analytical strain rate sensitivity and 0.2% yield stress versus temperature curves for Ni-43.0 at.% Al deduced from the data of Pascoe and Newey [12, 13]. Base strain rate $2.2 \times 10^{-4} s^{-1}$. Their experimental data are also shown. (a) Strain rate sensitivity and (b) 0.2% yield stress.

(a)   (b)
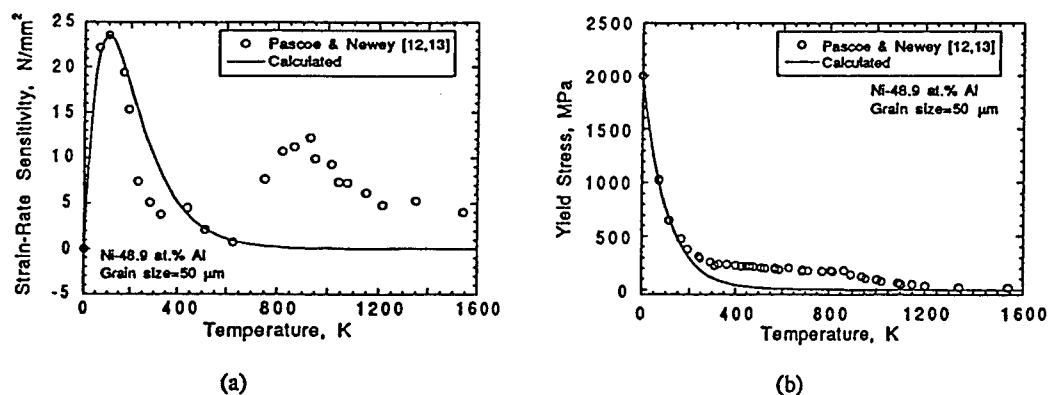
Fig. 3. The analytical strain rate sensitivity and 0.2% yield stress versus temperature curves for Ni-48.9 at.% Al deduced from the data of Pascoe and Newey [12, 13]. Their experimental data are also shown. Base strain rate $2.2 \times 10^{-4} s^{-1}$. (a) Strain rate sensitivity and (b) 0.2% yield stress.

EFFECT OF CRYSTALLOGRAPHIC ORIENTATION ON THE FRACTURE TOUGHNESS OF NiAl SINGLE CRYSTALS

S. SHRIVASTAVA AND F. EBRAHIMI
Department of Materials Science and Engineering, University of Florida, Gainesville. FL 32611

ABSTRACT

In the present study, single-edge notched bend specimens of NiAl single crystals were tested in {100}<010>, {101}<101>, and {101}<010> orientations before and after heat-treating the notched specimens at 1000°C for one hour. The fracture toughness data for the non heat-treated specimens were found to be consistent with the previous results. An increase in the fracture toughness of NiAl was observed in all orientations studied upon heat-treating the notched specimens. The toughness ratio for the two orientations obtained from the heat-treated notched specimens was found to be 1.2. This ratio is in agreement with the reported stress analysis considering the crack kinking in {100} oriented specimens. A detailed SEM analysis revealed that the electric discharge machine (EDM) cutting of the notch caused the formation of sharp microcracks at the notch front and also created internal stresses in the vicinity of the notch. The increase in toughness upon heat treatment is attributed to the modification of EDM damage.

INTRODUCTION

The fracture toughness as well as the ductile-to-brittle transition of NiAl single crystals depend on the crystallographic orientation.[1] It has been reported that the toughness of the specimens oriented with {100} as the crack plane is nearly twice the toughness of specimens having {110} as the crack plane. Chang et al.[1] reported that the crack in the {100} plane kinked macroscopically into the {110} plane during propagation and they attributed the doubling of the toughness to the halving of the normal stress on {110} plane, assuming that the stress ratio ahead of a crack is similar to an unnotched specimen. However, such an assumption may not be valid for the notched specimens.

Rigorous analysis[2] of elastic stresses for crack kinking suggests that the stress ratio for a kink angle of 45° is approximately 1.2 rather than 2. Another factor to consider is that the elastic modulus in the <100> direction is about half of that in the <110> direction in NiAl[3], which makes the critical elastic energy release rate for {100} fracture plane to be four times of that for {110} fracture plane. The purpose of the present study has been to investigate the cause of the fracture toughness anisotropy and to study the effect of heat treatment on the toughness anisotropy in NiAl single crystals.

MATERIALS AND EXPERIMENTAL PROCEDURES

Single crystals of NiAl were provided by General Electric, Aircraft Division in Cincinnati, Ohio. The as-received crystals had been homogenized in an argon filled vacuum furnace at

1350°C for 50 hours. The orientations of crystals were determined using Laue back-scattered x-ray diffraction technique.

Fracture toughness testing was conducted using single-edge-notch-bend (SENB) specimens. The rectangular bar specimens of 40 mm x 5 mm x 3 mm were cut and the notches were prepared using the electric discharge machine (EDM). The faces of the specimens were mechanically ground using SiC paper and polished up to 0.05μ Al_2O_3. The orientations of the specimens tested were {110} <110>, {110} <100>, and {100} <010>, where the given planes represent the plane of the notch and the given directions denote the direction of the crack profile. The notch shape, size and the damage introduced by EDM were characterized prior to performing the four point bend testing. Selected specimens were heat-treated either before or after making the notch for stress relieving. The heat treatment was carried out at 1000°C in argon atmosphere for one hour followed by furnace cooling under flowing argon.

The four point bend testing was conducted at a constant displacement rate of 0.001 mm/sec using a closed-loop hydraulic mechanical testing system. The fracture toughness K_Q was calculated using the relationship given in reference.[4]

The fracture surfaces were characterized using a scanning electron microscope. In selected specimens, after fracturing, one of the broken halves was cut in the middle and the plane normal to the notch plane was prepared using mechanical and electrolytic polishing for etch-pitting. Marble etchant was found to be a suitable etchant for etch-pitting.

RESULTS

The fracture toughness values were determined at room temperature and the results are presented in Table 1. The toughness data obtained for the non heat-treated samples are in good agreement with the previously reported values.[1,2] In these specimens, the {100} orientation consistently showed approximately twice the toughness of the {110} orientation. It was observed that the heat treatment of notched specimens resulted in an improvement of the fracture toughness in all the orientations studied. A higher magnitude of increase in toughness was observed for {110} fracture plane, for which the toughness was increased to twice the toughness of the non heat-treated specimen. Consequently, the difference in the fracture toughness of the two orientations was reduced. However, the heat treatment performed prior to making a notch did not improve the toughness.

The K_{JC} values were calculated based on the J-integral values and are also given in Table 1. The J-integral values were obtained from the area under the load-displacement curves of the four point bend test. As seen in Table 1, the K_{JC} values correlated with the K_Q values reasonably well. If J_c is considered to be the fracture criterion, the {100} orientation has an approximately four times the toughness of {110} plane in the non heat-treated condition. This ratio decreases to 2 in the heat-treated condition.

The fracture surfaces of all the orientations studied showed a distinct zone of the length of 30-50 μm adjacent to the notch front as shown in Figure 1(a). This zone comprised of two different planes forming steps as shown in a higher magnification fractograph [Figure 1(b)]. Figure 2 shows that these steps were formed in continuation of the cracks developed on the EDM notch surface. It can be noted that these microcracks are much sharper than the original notch. A study of an EDM notch prior to loading revealed that the cracks observed on the surface of the notch (see Figure 2) were formed during the EDM cutting. SEM analysis of the heat-treated samples showed that the fracture zone adjacent to the notch was oxidized upon heat

Table 1. Room temperature fracture toughness of NiAl single crystal.

Crystal No.	Speci-men No.	Orienta-tion	Heat Treat-ment	Jc (N/m)	E (GPa)	$K_{Jc}=\sqrt{JE}$ (MPa m$^{1/2}$)	K_Q (MPa m$^{1/2}$)
1	1	(101)[$\bar{1}$01]	No	154.5	184.5	5.33	5.77
2	2	(101)[010]	No	259.0	184.5	6.91	7.88
2	3	(101)[010]	Yes*	219.9	184.5	6.37	7.44
1	4	(101)[010]	Yes	736.3	184.5	11.58	14.76
1	5	(100)[010]	No	709.1	94.5	8.18	9.23
2	6	(100)[010]	Yes	1418.2	94.5	11.57	15.43
2	7	(100)[010]	Yes	1381.8	94.5	11.43	15.55

* This specimen was heat-treated before making a notch.
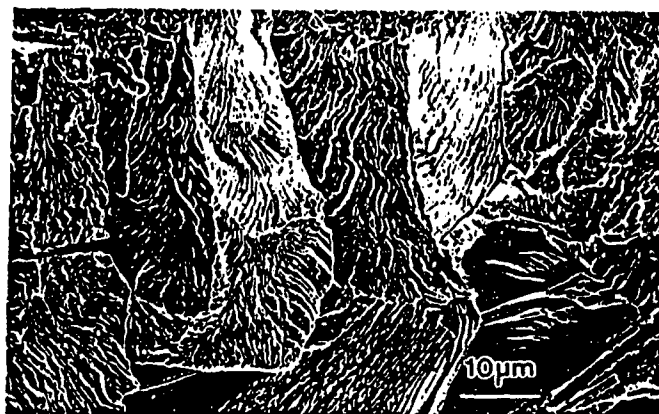
Figure 1. (a) {110}<101> fracture surface showing the presence of a distinct zone along the notch front (delineated by the dotted line); (b) A high magnification fractograph showing the step-like features in the fractograph presented in (a).
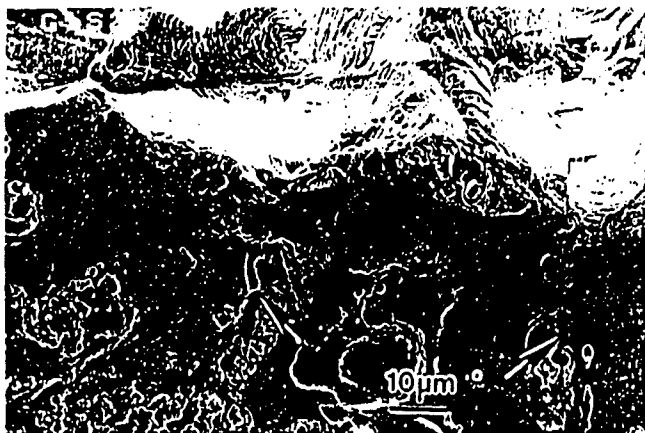
Figure 2 SEM fractograph of an area inside the notch showing the association of the step-like features present on the fracture surface with the microcracks (marked by arrows) produced by the EDM
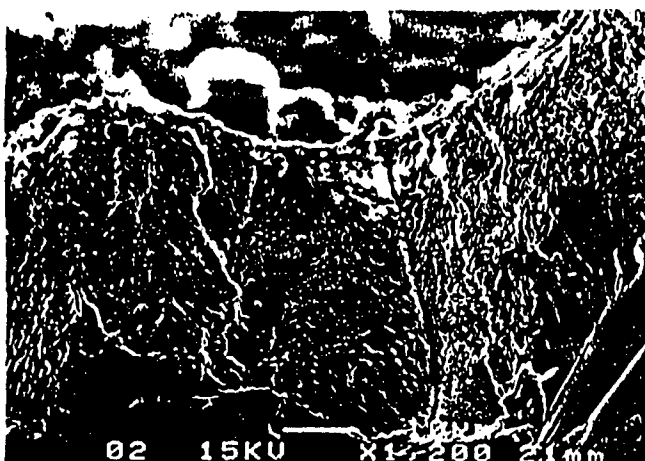
Figure 3: SEM fractograph showing the oxidation of the distinct zone in a heat-treated {110} <010> specimen.

treatment. The oxidized zone is shown in Figure 3. This observation suggests that this zone developed during making the EDM notch prior to loading the specimen.

DISCUSSION

Fracture toughness data show a significant increase in all the orientations studied, when tested after heat-treating the notched specimens. The ratio of $K_{()}$ values obtained for the two orientations decreased to 1.2 upon heat-treating the notched specimens which is in excellent agreement with the stress analysis for crack kinking [2] In a previous study[5], an increase in toughness has been reported upon annealing NiAl single crystals at 1300°C. However, in that study, the increase in toughness was attributed to the cooling rate effect. It was suggested that a fast cooling rate increases the number of mobile dislocations, which had been previously pinned by the interstitial atoms However, the absence of toughness enhancement in the sample

heat-treated prior to making the EDM notch suggests that in the present study the above mechanism does not operate

The toughness enhancement for the {100} orientation was much less than that for the {110} orientation. This observation suggests that the mechanism responsible for the gain in toughness should be orientation dependent. Similar to the evaluation of fracture toughness of glasses using indentation flaws[5,6], the increase in toughness may be attributed to the relief of residual stresses and/or blunting of the sharp crack front produced by the EDM process. The residual stresses present ahead of the notch front alter the stress distribution and therefore result in lower toughness values. Although, the mechanism by which the residual stresses are produced has not been fully investigated, preliminary results indicate generation of a high density of dislocations near the notch. A high density of etch-pits formed near the notch front on a {100} plane is shown in Figure 4. Recovery of these dislocations would result in a reduction in residual stresses. The lower elastic modulus in <100> direction and the possible higher plasticity associated with the {100} oriented fracture specimens can be responsible for creating a lower level of internal stresses and hence a higher toughness value. Upon heat treatment, hence, lower recovery of toughness is achieved in these specimens.

The present investigation suggests that the damage created by the EDM process of making a notch is important in evaluating the fracture toughness of materials and must be considered. The presence of a distinct zone adjacent to the notch on the fracture surface and the association of this zone with the microcracks created by the EDM are evidences of this damage. The formation of etch-pits around the notch is currently under further investigation and will be reported in a future paper.

Bergmann and Vehoff[8] have reported fracture toughness data for NiAl single crystal using fatigue pre-cracked and also using notched specimens. Their data for the {110} plane at low temperatures does not show any significant difference between the fracture toughness value obtained from the notched specimens and those from the fatigue pre-cracked specimens. In the present study, it was observed that the notches produced by the EDM have sharp cracks along the notch front, which can act as a starter crack for the fracture to occur. This may be the reason why no significant difference was observed between the low temperature toughness of the notched and the fatigue cracked NiAl single crystal
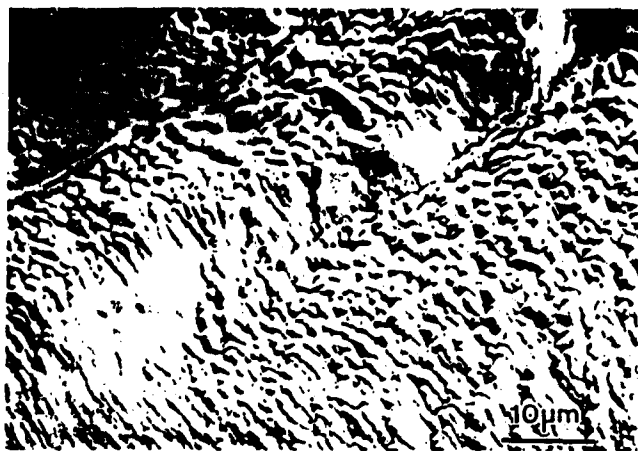
Figure 4. SEM micrograph showing the presence of etch pits near the EDM notch on {100} plane.

ACKNOWLEDGMENTS

REFERENCES

1. K.M. Chang, R. Darolia, and H.A. Lipsitt, Acta Metall. Mater. 40, 2727 (1992).
2. K. Palaniswamy and W.G. Knauss, in Mechanics Today, edited by S. Nemat-Nasser (Pergamon Press, 1978) pp. 4, 87.
3. R.J. Wasilewski, Trans. Metall. Soc. AIME 236, 455 (1966).
4. O.L. Towers, "Stress Intensity Factors, Compliance and Elastic Factors for Six Test Geometries," NBS Report #7709.01.81/249.1 (1981).
5. J.E. Hack, J.M. Brzeski, and R.Darolia, Scripta Metall. Mater. 27, 1259 (1992).
6. B.R. Lawn, K. Jakus, and A.C. Gonzalez, J. Am. Cer. Soc. 68 (1), 25 (1985).
7. K. Hirao and M. Tomazawa, J. Am. Cer. Soc. 70 (6), 377 (1987).
8. G. Bergmann and H. Vehoff, Scripta Metall. Mater. 30, 969 (1994).

CRACK PATH IN SINGLE CRYSTALS

Fereshteh Ebrahimi and S. I. Hussain
Materials Science and Engineering Department
University of Florida, Gainesville, FL 32611

Introduction

Consider a defect free elastic single crystal loaded uniaxially in tension along the [uvw] crystallographic direction. If one of the weakest crystallographic planes (minimum theoretical tensile strength planes) lies perpendicular to the loading axis then this plane will be the cleavage plane (in this paper cleavage plane is referred to any crystallographic plane on which fracture occurs by breaking atomic bonds) and the fracture strength may be estimated from the theoretical tensile strength of the material [1]. In the absence of thermal activation cleavage is expected to occur simultaneously on all of the cleavage planes, while thermal vibration may statistically cause the fracture to occur on a particular weakest plane. Recent molecular dynamics calculations confirm these concepts [2]. If the single crystal is oriented such that the normals to the weakest tensile planes make angles Φ_i with the uniaxial loading direction (where the value of i depends on the crystal symmetry) then fracture will occur on the planes for which the resolved normal stress reaches the fracture stress first.

A notch (or an inherent defect) creates an inhomogeneous local deformation field which depends on the specimen geometry as well as the remote applied displacement field. In the case of notched specimens a simple stress criterion for fracture based on the remote applied stress is not applicable. For isotropic elastic materials the fracture path may be determined as the path where (a) the elastic energy release rate is maximum [3-5], (b) the strain energy consumed is minimum (S criterion) [6], or (c) the local tensile stress intensification is maximum [7]. If the notch is loaded in mode I, these criteria are equivalent and predict that the crack should propagate on the same plane as the notch. However, when the crack is loaded under a mixed mode, the crack kinks out of the notch plane. The fracture path predictions made by these criteria, in this case, are also in good agreement .

Now let us consider a notched anisotropic material, such as a single crystal, loaded in mode I. Owing to the dependency of properties such as elastic constants, surface energy, and cleavage stress on crystallographic orientation, although the crack is remotely loaded in pure mode I, locally it may not propagate on the same plane as the notch. Indeed in many cases the crack kinks into other planes and propagates under a mixed mode. The purpose of this study has been to predict the fracture path in notched anisotropic single crystals. We have adopted the maximum elastic energy release rate criterion for determining the fracture path. The analysis has been performed for a simple cubic crystal, however, it can easily be extended to other crystal symmetries.

Analysis

Let us consider a sharply notched elastic single crystal with a simple cubic structure loaded in mode I as shown in Figure 1. The origin is chosen at the crack tip with the x-axis parallel to the notch profile. The crystallographic orientation of the crystal is presented by a radial distribution of the surface energy $\gamma_c(\theta)$, known as a crystal γ-plot [8]. In Figure 1 the [hkl] orientation, which is parallel to the notch

front, has been chosen to be a <100> type direction. The surface energy cusps, at which $d\gamma_c(\theta)/d\theta$ is discontinuous, locate the other two perpendicular <100> directions. The planar orientation of the crystal relative to the crack is defined by the angle Φ (rotation angle), which is the angle between the x-axis and the trace of one of the {100} planes. Note that both the fracture resistance and the applied local stress depend on the orientation, i.e. the θ angle in Figure 1. The fracture criterion based on the maximum energy release rate approach for a uniaxially loaded two dimensional problem can be expressed as [3]:

$$G = G(\theta,L) \qquad \gamma_c = \gamma_c(\theta)$$
$$\frac{\delta G}{\delta \theta} = 2 \frac{d\gamma_c}{d\theta} \qquad (1)$$
$$G(\theta^*,L^*) = 2 \gamma_c(\theta^*) \qquad (2)$$

where $G(\theta,L)$ represents the variation of the elastic energy release rate with load L and orientation angle θ, $\gamma_c(\theta)$ represents the variation of the surface energy with crystallographic orientation, and L^* and θ^* give the remote load and the incipient kink angle at the point of crack propagation.

The rate of release of energy at the tip of a kinked crack for plane strain condition can be approximated as [4]:

$$G(\theta) = (1 - v^2) (K_I^2 + K_{II}^2)/E \qquad (3)$$
$$K_I = C_{11}k_I$$
$$K_{II} = C_{21}k_I$$
$$C_{11} = (3 \cos\theta/2 + \cos 3\theta/2)/4$$
$$C_{21} = (\sin\theta/2 + \sin3\theta/2)/4$$

where K_I and K_{II} represent the stress intensity factors at the tip of the kinked crack in mode I and II, respectively, and k_I represents the stress intensity factor at the tip of the sharp notch.

The two dimensional variation of the surface energy with crystallographic orientation for a <100> zone axis (four-fold symmetry) of a cubic crystal was approximated by the following equation:

$$\gamma_c(\theta) / \gamma_0 = 1 + a(\sin 2(\theta \pm \Phi))^4 \qquad (4)$$

where γ_0 is the minimum value of surface energy, a is a geometrical factor. The $\gamma_c(\theta) / \gamma_0$ function is plotted for various values of a in Figure 2. The numerical method used for calculation required that the $\gamma_c(\theta)$ function to have a continuous derivative at all angles, and consequently no cusps were included in this function.

The Newton-Raphson numerical method for non linear systems was used to solve equations (1) and (2) simultaneously. Incorporation of anisotropy of elastic constants would have required that the equation for $G(\theta,L)$ and its derivative to be modified for each Φ angle. Due to the complexity of the problem as a first approximation we have ignored the elastic constant anisotropy in this paper.

Discussion

Figures (3) and (4) show the variation of the kink angle, θ^*, and the normalized fracture toughness $(G(0) / \gamma_0)$ as a function of the rotation angle Φ. Note that the applied load relates to the applied k_{II} and hence, toughness is given by $G(0)$ rather than $G(\theta^*)$. The results presented in Figure 3 indicate that, in general, cleavage does not occur on the weakest plane, i.e. the θ^* angle (kink angle) is not the same as the Φ angle (rotation angle). However, as the value of the geometrical factor, a, is increased the fracture

path becomes closer to the weakest path. An increase in the value of a corresponds to a sharper drop of the surface energy near the weakest plane as well as an increase in the ratio of the maximum to the minimum energy values.

It is interesting to note that, for a given value of the minimum surface energy, γ_0 , the fracture toughness increases with an increase in a value. This result suggests that if a crack follows the weakest path, it does not necessarily consumes a lower energy, i.e. the increase in fracture energy due to a larger fraction of mode II component may be larger than the decrease in fracture resistance because fracture is occurring on a weaker path. It should be noted that the sharper change in $d\gamma_c(\theta)/d\theta$ as a function of θ is responsible for fracture to occur closer to the minimum surface energy plane. This phenomenon is demonstrated schematically in Figure 5. Consider two γ–plots, $\gamma^1(\theta)$ and $\gamma^2(\theta)$, where $d\gamma(\theta)/d\theta$ varies much faster for case 2. As shown in Figure 5, although in case 2 crack follows a path close to the minimum energy plane, it has a higher apparent fracture energy than case 1. Recent results [9] suggest that Si single crystals may fracture on a variety of crystallographic planes, however, all of these planes were determined to correspond to minimums (or cusps) associated with the γ-plot reported for this material [10]. The incorporation of surface energy cusps into the present model is expected to shift the fracture path toward rational crystallographic planes.

One interesting result of the approach presented here is that fracture path, and hence fracture energy depends on the crack propagation direction of the notch. For a give notch plane the crack propagation direction constitutes the [hkl] direction in Figure 1, and consequently, the fracture path. For example it has been shown [11,12] that the fracture path and fracture energy for Si crystals with a {110} notch plane depends on whether the crack is directed to grow in a <110> or in a <001> direction, which corresponds to the notch front orientation of <001> or <110>, respectively. The reported results indicate that when the crack front is parallel to a <110> direction the crack kinks into a {111} plane, however, when the crack front is parallel to a <100> direction it remains on this plane. Consistent with the predictions made here, the latter case shows a lower toughness, despite the fact that {111} planes in Si have a lower surface energy than {110} planes.

Experimental results indicate that in semi-brittle materials there are exclusive cleavage planes, e.g., bcc metals, such as iron, usually fracture on {100} planes and not on {110} planes, although the surface energy values of these two sets of planes are very close. Contrary to this experimental observation, elastic constant anisotropy is expected to drive the crack into high elastic modulus planes, and thus promote {110} cleavage planes in BCC type structures. On the other hand, recent results for NiAl [13], an ordered intermetallic with B2 crystal structure, indicate that for this material cleavage tends to occur on {110} planes rather than on {100} planes. These discrepancies are suggested to be related to plastic anisotropy. In semi-brittle materials, such as iron and NiAl, plastic deformation at the crack tip is essential to crack initiation and propagation, and consequently, the plastic anisotropy plays an important role in governing cleavage planes. In NiAl, owing to the strong ordering, the slip occurs on <100>{001} and <100>{011} slip systems rather than <111>{110} and <111>{112} slip systems which operate in BCC metals. This difference is expected to alter the plastic anisotropy which would affect the crack path. Plastic work can also be included in the γ-plot as part of the resistance to fracture, and therefore, the approach presented here is applicable to semi-brittle materials.

Summary

A two-dimensional analysis of crack propagation in anisotropic single crystal has revealed that the cleavage path depends on the shape of the γ-plot. Consequently, for a given notch plane the fracture path has been predicted to depend on the notch front orientation. The results of this study suggest that the fracture path depends not only on the level of resistance to fracture but also on the change of fracture energy with orientation. Furthermore, when a crack kinks into a minimum energy plane, it does not necessarily exhibit a lower fracture toughness than the case where crack follows a higher energy plane.

References

1.   N. H. Macmillan, in Atomistics of Fracture, R. M. Latanision and J. R. Pickens, Eds., P. 95, NATO Conference Series, Plenum Press (1983).

2.   J. H. Simmons, Materials Science and Engineering Department, University of Florida, unpublished results.

3.   K. Palaniswamy and W. G. Knauss, in Mechanics Today, S. Nemat-Nasser, Ed.,4, P. 87, Pergamon Press (1978).

4.   B. Cotterell and J. R. Rice, Int. J. of Fracture, 16(2), 155 (1980).

5.   K. Hayashi and S. Nemat-Nasser, Int. J. Solid Structures, 17, 107 (1981).

6.   G. C. Sih, Engng. Fracture Mech., 5, 365 (1973).

7.   F. Erdogan and G. C. Sih, J. Basic Eng., 85D, 519 (1963)

8.   W. W. Mullins, in Metal Surfaces: Structure, Energetics and Kinetics, P. 17, ASM publication, Ohio (1963).

9.   C. P. Chen and M. H. Leipold, Ceramic Bulletin, 59(4), 469 (1980).

10. Y. L. Tsai and J. J. Mecholsky, jr., J. Mater. Res., 6(6), 1248 (1991).

11. Lakshman Kalwani, Master of Science Thesis, Materials Science and Engineering Department, University of Florida (1993).

12. P. J. Hesketh, Chishein Ju, and s. Gowda, J. Electrochem. Soc., 140(4), 1080 (1993).

13. K.-M. Chang, R. Darolia, and H. A. Lipsitt, Acta Metall. Mater., 40, 2727 (1992).

Acknowlededements
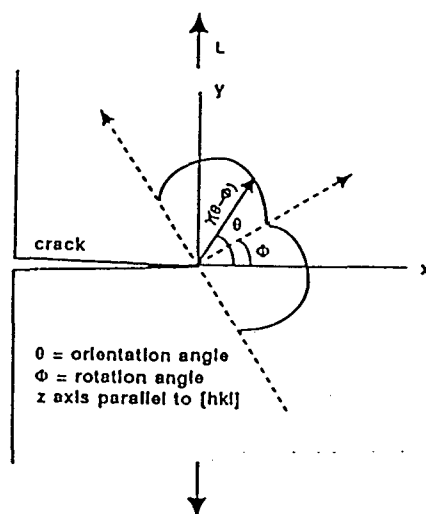
Figure 1. A schematic illustrating the orientation of the crystal relative to the crack.
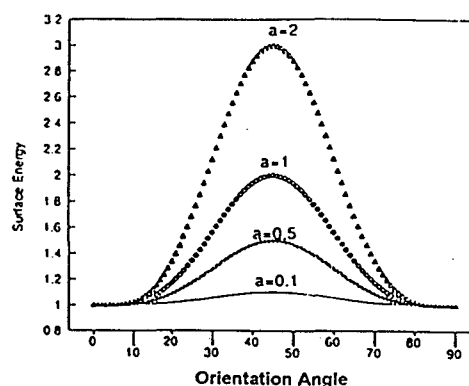
Figure 2. γ-plots for various values of the geometrical factor, a.
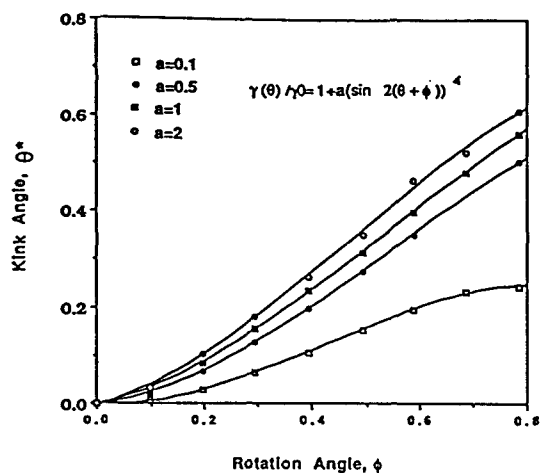
Figure 3. The carck kink angle as a function of the rotation anngle. Note that when $\theta = \Phi$, cleavage occurs on the weakest plane.
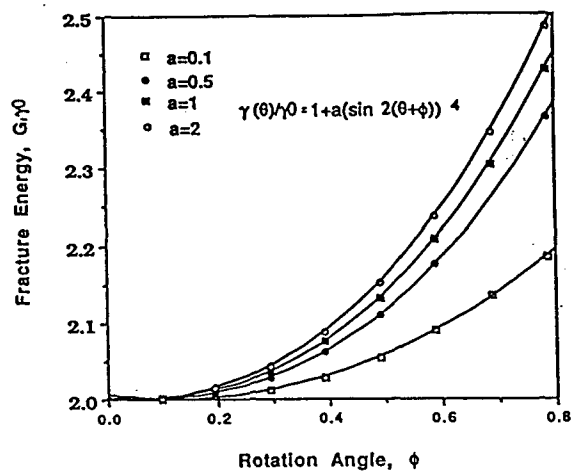
Figure 4. Fracture energy as a function of the rotation angle.
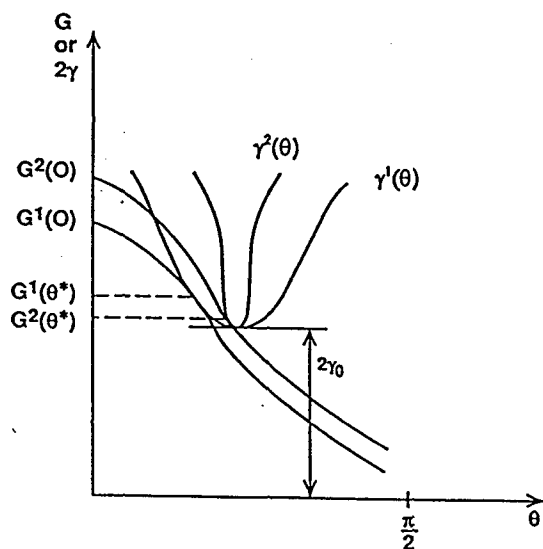
Figure 5. Schematic showing how the fracture energy depends on the shape of the $\gamma(\theta)$ curve.

ON EVALUATING THE FLOW STRESS IN NIOBIUM
OF COMMERCIAL PURITY

R. E. REED-HILL and M. J. KAUFMAN†

Department of Materials Science and Engineering, University of Florida, Gainesville, FL 32611, U.S.A.

Abstract—An analysis has been made of the CP niobium data presented in two papers by J. F. Fries, B. Houssin, G. Cizeron and P. Lacombe, *Jour. Less-Com. Met.* 33, 117 (1973) and J. F. Fries, C. Cizeron and P. Lacombe, *Rev. Phys. Appl.* 5, 371 (1970). This study involves a phenomenological procedure which assumes a rate controlling mechanism in which the force between a barrier and a mobile dislocation element varies inversely as the distance. The derived analytical curves obtained with this model are in very good agreement with all the experimental flow stress and strain-rate sensitivity data from 20 to about 600 K. This agreement supports the hypothesis that, in this particular CP niobium, the rate controlling mechanism might involve dislocation intersections where it is generally accepted that the force between an obstacle and a dislocation element varies inversely as the distance between them. An analysis of the effect of the interstitials on the shape of the flow stress–temperature curve was also made for specimens tested above 300 K. It was found that the unusual flow stress peak that appears in the plateau region at 570 K might be explained in terms of overlapping of the dynamic strain aging stresses of the three interstitials O, C and N near 570 K. That the phenomenological model is not in agreement with the experimental data above 600 K is possibly due to dynamic recovery of the metal's substructure.

INTRODUCTION

For many years, the large temperature dependence of the yield and flow stresses in b.c.c. metals at low temperatures has been a subject of considerable concern and disagreement. Historically, two basic views were evolved to explain this low temperature strengthening. One group [1–4] believed the rate controlling mechanism was overcoming Peierls–Nabarro potential barriers to dislocation motion. On the other hand, very strong evidence has also been presented [5–9] favoring a model in which strengthening was controlled by the thermal activation of dislocations past interstitial solute atom defects. This controversy apparently existed due to the fact that the b.c.c. metal deformation is complicated by interactions between solute atoms and, in particular, by those between interstitial and substitutional atoms. These interactions may lead to gettering or scavenging of interstitials and in turn to alloy softening. A complicating factor also occurs when the concentration of interstitials exceeds a limit, which depends on the alloy and the nature of the interstitials, resulting in a saturation effect [6] in which the temperature dependence of the flow stress does not change appreciably with interstitial concentration. In such cases, interstitial hardening may appear to be athermal [6]. Actually, either alloy softening or interstitial saturation would act to distort the temperature and compositional dependencies from those expected

in either model. The present paper adds additional information about the subject of alloy hardening in a b.c.c. metal which suggests that, while interstitial atoms may play an important role in the low temperature strengthening of b.c.c. metals, the rate controlling mechanism is probably not the thermal activation of mobile dislocations past interstitial solute atoms.

In a previous publication [10], a preliminary procedure was presented whose goal was to plot analytically the effects of dynamic strain aging, DSA, on the flow stress in a b.c.c. metal. This required the establishment of an analytical expression for the basic rate controlling mechanism. A study of the experimental commercial purity niobium flow stress and strain rate sensitivity data of Fries *et al.* [11, 12], made at temperatures well below those where DSA occurred, strongly suggested that the activation enthalpy of the basic rate controlling mechanism of this material conforms to

$$H = H^0 \ln \frac{\sigma_0^*}{\sigma^*} \qquad (1)$$

where H is the activation enthalpy, H^0 a material constant with units of energy, σ_0^* the effective stress at 0 K and σ^* the effective stress at any temperature. Three basic thermally activated dislocation mechanisms—(1) the Hartley [13] dislocation intersection mechanism, (2) the Schoeck and Seeger [14] thermally activated cross-slip mechanism, and (3) the Seeger [15] mechanism for overcoming the Peierls stress—all conform to this type of activation enthalpy.

---

†To whom all correspondence should be addressed.

Furthermore, as suggested by Hartley [13], this activation enthalpy may be expected if the stress exerted by a barrier on an element of a mobile dislocation line varies inversely as the distance between them. It is also true that equation (1) leads directly to a power law relationship between the effective stress and the strain rate.

Another assumption used in the procedure was that, in the absence of DSA, the flow stress consists of

$$\sigma = \sigma^* + \sigma_E \qquad (2)$$

where σ is the total flow stress, σ^* its thermally activated component and σ_E the athermal component. In temperature regimes where DSA exists, a dynamic strain aging component is added to the total flow stress

$$\sigma = \sigma^* + \sigma_E + \sigma_{DSA} \qquad (3)$$

where σ_{DSA} is the DSA component. In b.c.c. interstitial systems it has often been demonstrated experimentally that σ_{DSA} may consist of two additive parts so that

$$\sigma_{DSA} = \sigma_{Sn} + \sigma_{Cot} \qquad (4)$$

with σ_{Sn} the Snoek component and σ_{Cot} the Cottrell component. The various parts of the total flow stress will now be considered.

THE THERMALLY ACTIVATED STRESS

The thermally activated or effective component, σ^*, of the total stress is described by the power law

$$\sigma^* = \sigma_0^* \left(\frac{\dot{\epsilon}}{\dot{\epsilon}_0} \right)^{RT/H^0} \qquad (5)$$

where σ_0^* is a constant, $\dot{\epsilon}$ the strain-rate, R the international gas constant, T the absolute temperature and $\dot{\epsilon}_0$ another material constant with units s^{-1}. Equation (5) is often written

$$\sigma^* = \sigma_0^* \left(\frac{\dot{\epsilon}}{\dot{\epsilon}_0} \right)^n \qquad (6)$$

where $n = RT/H^0$ and is one form of strain-rate sensitivity parameter. Equation (6) accurately describes some of the b.c.c. and h.c.p. data in the literature obtained with relatively pure metals. Furthermore, it does not arbitrarily make the effective stress go to zero at the plateau of a constant strain-rate plot of σ vs T. If, in equation (6), $T = 0$ K the effective stress, σ^*, becomes σ_0^*, so that σ_0^* is the effective stress at 0 K. On the other hand, $\dot{\epsilon}_0$ corresponds to a strain rate that raises σ^* to σ_0^* at any temperature. For constant $\dot{\epsilon}$ data, equation (6) may also be written

$$\ln \sigma^* = \ln \sigma_0^* + BT \qquad (7)$$

where $B = (R/H^0) \times \ln(\dot{\epsilon}/\dot{\epsilon}_0)$ is a constant. If experimental flow stress data can be fitted by this linear equation, it is reasonable to assume they conform to

equation (5). Deviations will, of course, appear if the flow stress, σ, has a finite long range stress component, σ_E, or if DSA occurs. If there are no significant deviations then one may assume that $\sigma = \sigma^*$ and DSA is not a factor within the temperature range investigated. The power law will also not hold when the test temperature is high enough to allow dynamic recovery or dynamic recrystallization to alter the basic metallurgical structure. As stated earlier, the power law in equation (5) corresponds to an activation enthalpy, H, in the thermally activated strain-rate equation

$$\dot{\epsilon} = \dot{\epsilon}_0 \exp\left(-\frac{H}{RT} \right) \qquad (8)$$

equal to

$$H = H^0 \ln \frac{\sigma_0^*}{\sigma^*} \qquad (9)$$

where H is the activation enthalpy and H^0, σ^* and σ_0^* are defined in equation (5). In summary, the power law in equation (5) requires the use of the effective stress, σ^*, as opposed to the total stress, σ. The athermal component of the stress may be small enough to ignore if the specimens are annealed, undeformed, have a large grain size (or are single crystals) and are of high purity. On the other hand, if σ_E is finite, one must evaluate σ_E and subtract it from σ since $\sigma^* = \sigma - \sigma_E$. A procedure for doing this will be given later. This procedure [10] depends on the use of flow stress and strain-rate sensitivity data, obtained at low enough temperatures so that DSA does not occur, and a knowledge of the temperature dependence of the elastic modulus.

EVALUATING $\dot{\epsilon}_0$ AND H^0

Consider the alternative strain-rate sensitivity parameter S where

$$S = \frac{d\sigma}{d \ln \dot{\epsilon}}. \qquad (10)$$

Note that S has dimensions of stress and differs from the strain-rate sensitivity parameter n in equation (6). The defining equation for n is

$$n = \frac{d \ln \sigma^*}{d \ln \dot{\epsilon}} = \frac{d\sigma^*/\sigma^*}{d \ln \dot{\epsilon}} = \frac{d\sigma/\sigma^*}{d \ln \dot{\epsilon}}. \qquad (11)$$

S can be evaluated with the aid of constant temperature strain-rate change data and has the advantage that $d\sigma = d\sigma^*$ because the athermal flow stress component σ_E is independent of changes in $\dot{\epsilon}$. A typical S vs T plot is shown in Fig. 1. Note that S passes through a maximum at a temperature designated T_B. Assuming a power law relation between σ^* and $\dot{\epsilon}$, S can be shown to be

$$S = \frac{d\sigma}{d \ln \dot{\epsilon}} = \frac{RT}{H^0} \sigma_0^* \left(\frac{\dot{\epsilon}}{\dot{\epsilon}_0} \right)^{RT/H^0}. \qquad (12)$$
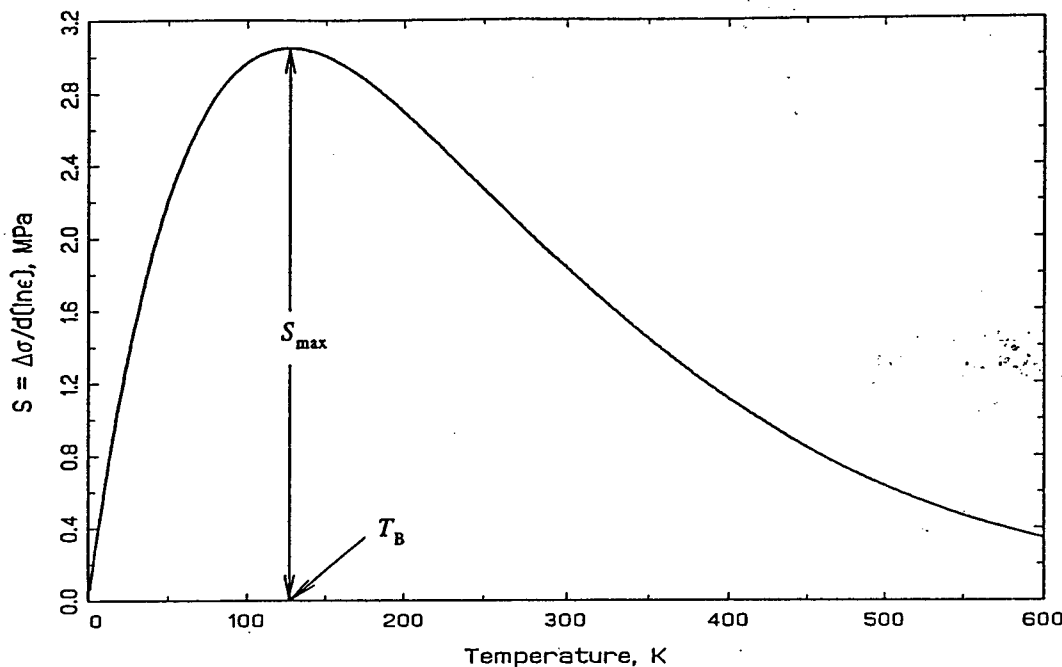
Fig. 1. If the enthalpy in the thermally activated strain rate equation, $\dot{\epsilon} = \dot{\epsilon}_0 \exp(-H/RT)$ is $H = H^0 \ln(\sigma_0^*/\sigma^*)$ and the strain rate sensitivity, $S = d\sigma/d \ln \dot{\epsilon}$, is plotted vs T, a curve with a maximum results. The temperature, T_B, and magnitude, S_{max}, of the maximum can be used to evaluate the material parameters H^0 and $\dot{\epsilon}_0$.

Taking the derivative of S with respect to T, setting it equal to zero and then solving for T, i.e. T_B, yields

$$T_B = -\frac{1}{\dfrac{R}{H^0}\ln(\dot{\epsilon}/\dot{\epsilon}_0)}. \qquad (13)$$

But, by equation (7), the slope of a linear plot of $\ln \sigma^*$ vs T was defined as $B = (R/H^0) \times \ln(\dot{\epsilon}/\dot{\epsilon}_0)$. Therefore

$$T_B = -\frac{1}{B}. \qquad (14)$$

This means that the temperature at the maximum on a S vs T plot equals the negative reciprocal of the slope of a $\ln \sigma^*$ vs T plot. Thus, if T_B can be identified, its reciprocal gives $-B$. Substituting T_B from equation (13) into equation (12) leads to

$$S_{max} = -\frac{\sigma_0^*}{e \times \ln(\dot{\epsilon}/\dot{\epsilon}_0)} \qquad (15)$$

where e is the base of the natural logarithms. This is an important result because equation (15) can be solved for $\dot{\epsilon}_0$ in equation (5) if experimental values of S_{max} and σ_0^* are available. Furthermore, solving

$$T_B = -\frac{1}{B} = -\frac{1}{(R/H^0)\ln(\dot{\epsilon}/\dot{\epsilon}_0)} \qquad (16)$$

for H^0 gives

$$H^0 = -T_B R \ln(\dot{\epsilon}/\dot{\epsilon}_0). \qquad (17)$$

Thus, measurements of T_B, S_{max} and σ_0^* can yield the material constants, H^0 and $\dot{\epsilon}_0$, in equation (5).

Figure 2 gives an example of an application of this statement. There are four plots in this diagram based on CP niobium data from a paper by Fries et al. [11] who used $\dot{\epsilon} = 1.1 \times 10^{-3} \text{s}^{-1}$ as the basic strain rate and a factor of 10 in their strain rate change tests. At the upper left in Fig. 2(A) is the plot of S vs T. In Fig. 2(B) to its right is the plot of σ vs T. Figure 2(C) gives $\ln \sigma^*$ vs T and, finally, Fig. 2(D) shows the dependence of n on T. Note that Fig. 2(A) is equivalent to Fig. 1. The maximum in Fig. 2(A) was estimated to occur at $T_B = 123$ K and $S_{max} = 16.4$ MPa while, as shown in the next section, $\sigma_0^* = 1072$ MPa. Substituting these values in equations (15) and (17) gave the values of H^0 and $\dot{\epsilon}_0$ shown in Table 1. All four diagrams in Fig. 2 were drawn analytically after substituting the data given in Table 1 into the power law [equations (5) and (7)] and strain-rate sensitivity [equations (10) and (11)] equations.

THE INTERNAL STRESS

It was demonstrated earlier [16], on the assumption of a zero entropy of activation, that the athermal component of the stress at 0 K can be determined by the equation

$$\sigma_{E_0} = \frac{\sigma_0 - e\,\sigma_{T_B}}{\left(1 - e\dfrac{E_{T_B}}{E_0}\right)} \qquad (18)$$

where σ_{E_0} is the athermal stress at 0 K, σ_0 the total stress at 0 K, e the base of the system of natural
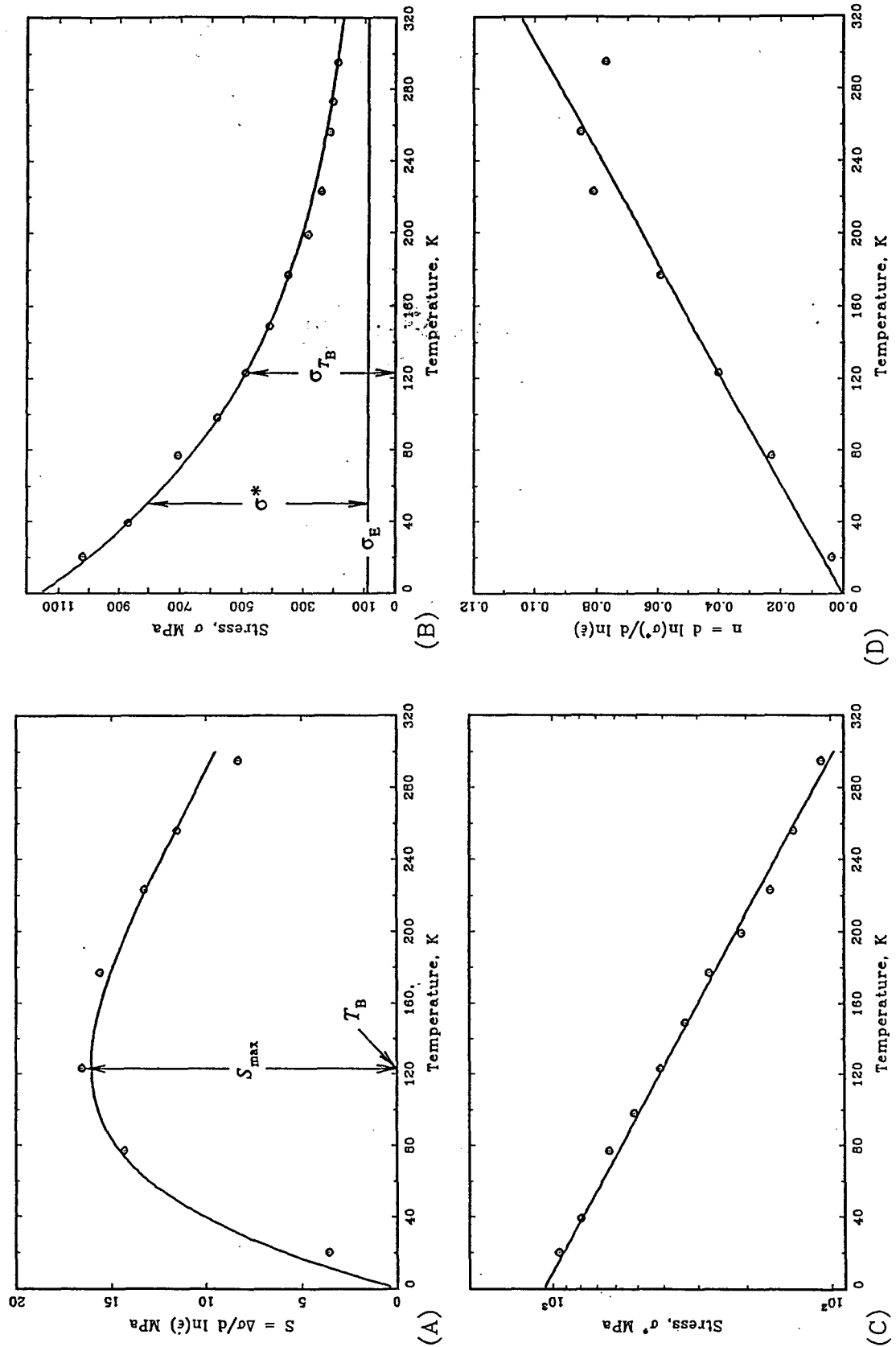
Fig. 2. The data points in these four figures show the temperature dependencies of S, σ, $\ln \sigma^*$ and n and are from the low temperature, 20–300 K, data in Ref. [11]. From the strain-rate sensitivity data in Fig. 2(A) it was deduced that $\sigma_E = 86$ MPa, $H^0 = 25,500$ J/mol and $\dot{\epsilon}_0 = 4.98 \times 10^7$ s^{-1} and from Fig. 2(B) it was estimated that $\sigma_0 = 1158$ MPa. All the analytical solid line curves were drawn by inserting these four parameters and the applied strain rate $\dot{\epsilon} = 1.1 \times 10^{-3}$ s^{-1} into the appropriate equations. Note the very good agreement between the analytical curves and the experimental data.

logarithms, σ_{T_B} the total stress at T_B, E_{T_B} the elastic modulus at T_B and E_0 the elastic modulus at 0 K. According to Fries et al. [11], the elastic modulus of niobium may be assumed temperature independent in the temperature range of the data in Fig. 2. Thus, equation (17) reduces to

$$\sigma_{E_0} = \frac{\sigma_0 - e\,\sigma_{T_B}}{(1 - e)}. \quad (19)$$

According to Fig. 2(B), $\sigma_0 = 1158$ MPa and $\sigma_{T_B} = 481$ MPa. When these values are substituted in equation (18), one obtains $\sigma_{E_0} = 86$ MPa making $\sigma_0^* = 1072$ MPa. The line near the bottom of the drawing in Fig. 2(B) represents σ_E; the difference between this line and the curve of the total stress, σ, gives σ^* as indicated on the drawing.

THE DSA STRESS

The commercial purity niobium specimens of Fries et al. [11, 12] were reported to contain in wt ppm: 300 O, 120 N and 70 C. In atomic percent this equals 0.19 O, 0.09 N and 0.05 C for a total of 0.33 at.%. Their CP niobium was also stated to have about 0.09 at.% total of seven different substitutional elements. This implies the ratio of interstitial to substitutional solute atoms was close to four. The interstitial element with the highest concentration was oxygen. The activation energy for the diffusion of oxygen in niobium is 110,000 J/mol, that for nitrogen 152,000 J/mol [17], and for carbon 138,000 J/mol [18]. The DSA phenomena in the Fries et al. specimens are consistent with the assumption that they are probably due to all three interstitial elements.

The three components of the DSA part of the stress will now be considered. All three are considered strain dependent. However, since the yield stress data was measured at a constant strain (0.2%) and a constant strain-rate (1.1×10^{-3} s^{-1}), the strain dependencies of the Snoek and Cottrell stresses of all three interstitials were ignored. First, consider the Snoek components which are due to the initial jumps of interstitial atoms into lower energy interstitial sites resulting from the presence of the strain fields of the dislocations. The kinetics of the Snoek aging component of a given interstitial can be determined [10] using the equation

$$\sigma_{Sn} = \sigma_{Sn_{max}}\left\{1 - \exp\left(-\frac{t_w}{\tau_{Sn}}\right)\right\} \quad (20)$$

where σ_{Sn} is the magnitude of the Snoek component of the stress, $\sigma_{Sn_{max}}$ is its maximum value that depends on the temperature and strain, t_w is the Sleeswyk [19]

waiting time for thermal activation of a dislocation at an obstacle and τ_{Sn} is the experimentally determined relaxation time for Snoek strain aging, which is about one-quarter of the relaxation time, τ_R, for the Snoek effect as measured with a torsion pendulum [10]. The Snoek oxygen strain aging relaxation time has an activation energy very close to that for the diffusion of oxygen in niobium. The Snoek strain aging relaxation times for the three interstial solutes in the CP niobium are

$$\tau_{Sn_O} = \frac{\tau_{R_O}}{4} = 7.77 \times 10^{-15} \exp\left(\frac{1.103 \times 10^5}{RT}\right) s \quad (21a)$$

$$\tau_{Sn_N} = \frac{\tau_{R_N}}{4} = 2.22 \times 10^{-16} \exp\left(\frac{1.52 \times 10^5}{RT}\right) s \quad (21b)$$

$$\tau_{Sn_C} = \frac{\tau_{R_C}}{4} = 1.425 \times 10^{-15} \exp\left(\frac{1.38 \times 10^5}{RT}\right) s \quad (21c)$$

where τ_{Sn_O}, τ_{Sn_N} and τ_{Sn_C} are the Snoek strain aging relaxation times while τ_{R_O}, τ_{R_N}, and τ_{R_C} are the corresponding relaxation times measured on a torsion pendulum. Cottrell aging involves the long range drift of interstitial atoms to lower energy positions near a dislocation and can be viewed as resulting in the formation of a dislocation atmosphere. It is accordingly a much slower process than Snoek aging. The kinetics of Cottrell aging can be followed using a modification of the Harper equation [10] given below

$$\sigma_{Cot} = \sigma_{Cot_{max}}\left\{1 - \exp\left[-\left(\frac{t_w}{\tau_{Cot}}\right)^{3/2}\right]\right\} \quad (22)$$

where σ_{Cot} is the Cottrell component of the DSA stress, $\sigma_{Cot_{max}}$ is its maximum value that also depends on the temperature and strain, t_w the dislocation waiting time, and τ_{Cot} the Cottrell relaxation time. The strain aging under stress experiments of Delobelle et al. [20] suggest that, in niobium, τ_{Cot_O} is approximately 5,000 times larger than τ_{Sn_O}. On the assumption that this ratio holds for all three interstitial elements one has

$$\tau_{Cot_O} = 3.89 \times 10^{-12} \exp\left(\frac{1.103 \times 10^5}{RT}\right) \quad (23a)$$

$$\tau_{Cot_N} = 1.11 \times 10^{-12} \exp\left(\frac{1.52 \times 10^5}{RT}\right) \quad (23b)$$

$$\tau_{Cot_C} = 7.10 \times 10^{-12} \exp\left(\frac{1.38 \times 10^5}{RT}\right). \quad (23c)$$

In a set of CP niobium strain aging experiments made under an applied stress and at four different constant temperatures between 344 and 418 K, it was observed [20, 21] that the oxygen Snoek and Cottrell strain aging stress amplitudes were temperature dependent and decreased in magnitude with increasing temperature at a rate equal to that of the thermal flow stress component, σ^*. In an aging under stress experiment, the specimen usually deforms as it is aged and it has

been demonstrated [20, 21] that it is reasonable to assume that the aging under stress strain aging kinetics follow those observed in static strain aging. Tests of this type are useful in relating static strain aging theory to dynamic strain aging. Therefore, it is assumed that the six amplitudes of the oxygen, nitrogen and carbon Snoek and Cottrell strain aging components have this same temperature dependence. Multiplying each amplitude by $\exp[B \times (T - 300)]$ will accomplish this, since

$$B = \frac{R}{H^0} \times \ln\left(\frac{\dot{\epsilon}}{\dot{\epsilon}_0}\right)$$

and

$$\exp[B \times (T - 300)] = \left(\frac{\dot{\epsilon}}{\dot{\epsilon}_0}\right)^{R(T-300)/H^0}. \quad (24)$$

Note that $\exp[B \times (T - 300)]$ normalizes the DSA amplitudes to 300 K (i.e. room temperature). Actually, the DSA stresses at a strain rate of $1.1 \times 10^{-3}\,\mathrm{s}^{-1}$ do not appear until well above 300 K. Finally, the total DSA stress component is as follows

$$\sigma_{DSA} = \left(\sigma_{Sn_{0max}}\left\{1 - \exp\left(-\frac{t_w}{\tau_{Sn_0}}\right)\right\}\right.$$
$$+ \sigma_{Cot_{0max}}\left\{1 - \exp\left(-\left(\frac{t_w}{\tau_{Cot_0}}\right)^{2/3}\right)\right\}$$
$$+ \sigma_{Sn_{Nmax}}\left\{\left(1 - \exp\left(-\frac{t_w}{\tau_{Sn_N}}\right)\right)\right\}$$
$$+ \sigma_{Cot_{Nmax}}\left\{1 - \exp\left(-\left(\frac{t_w}{\tau_{Cot_N}}\right)^{2/3}\right)\right\}$$
$$+ \sigma_{Sn_{Cmax}}\left\{1 - \exp\left(-\frac{t_w}{\tau_{Sn_C}}\right)\right\}$$
$$\left.+ \sigma_{Cot_{Cmax}}\left\{1 - \exp\left(-\left(\frac{t_w}{\tau_{Cot_C}}\right)^{2/3}\right)\right\}\right)$$
$$\times \exp(B \times (T - 300)). \quad (25)$$

The procedure used to evaluate the Snoek and Cottrell stress amplitudes $\sigma_{Sn_{max}}$ and $\sigma_{Cot_{max}}$ in equation (25) was as follows. The aging under stress experiments of Delobelle et al. [21] indicated that in niobium the oxygen Cottrell amplitude was about 4.3 times larger than the oxygen Snoek amplitude. This same ratio was assumed to hold for the ratio of the Cottrell to Snoek amplitudes of all three interstial elements. However, since all of the amplitudes were normalized to 300 K, the nitrogen amplitudes were also multiplied by a factor of 4 and the carbon amplitudes by a factor of two to obtain their amplitudes shown in Table 2. This was done in order to allow for the fact that both the nitrogen and carbon DSA occur at a higher temperature than does the oxygen DSA. The dynamic recovery factors fall by a factor of better than four between the temperatures where the oxygen and the nitrogen–carbon Snoek peaks occur. Also, the carbon amplitude was taken as

Table 2

$\sigma_{Sn_{max}O} = 30\,\mathrm{MPa}$	$\sigma_{Sn_{max}N} = 120\,\mathrm{MPa}$	$\sigma_{Sn_{max}C} = 60\,\mathrm{Max}$
$\sigma_{Cot_{max}O} = 145\,\mathrm{MPa}$	$\sigma_{Cot_{max}N} = 750\,\mathrm{MPa}$	$\sigma_{Cot_{max}C} = 750\,\mathrm{Max}$
	$t_w = 0.10\,\mathrm{s}$	

half that of nitrogen due to its lower ($\sim$50%) concentration. It should be noted that the amplitudes in Table 2 correspond to hypothetical stress amplitudes that would result when tests are made at 300 K. In practice, they were selected so that equation (27) would fit the observed magnitudes of the DSA data in the temperature range where DSA was observed.

The waiting time, t_w, on the other hand was chosen so as to make the start of the analytical plot of equation (25) coincide with the temperature at which the experimental evidence for DSA commences. This gave a waiting time of 0.10 s. Considering the relatively fast strain rate used in these tests, this value appears reasonable. However, it was decided to test it in terms of the mobile dislocation density using the Orowan equation

$$\dot{\epsilon} = \tfrac{1}{2}\rho_m b v \quad (26)$$

where ρ_m is the mobile dislocation density, b the Burgers vector, and v the dislocation velocity which may be assumed to be represented by

$$v = \frac{\bar{h}}{t_w} \quad (27)$$

where $\bar{h}$ is the average distance of advance of a mobile dislocation segment D where D is the average distance between obstacles (i.e. trees) along the dislocation, and t_w is the waiting time. The distance $\bar{h}$ was computed with the aid of Friedel's equation [22] for D

$$D = \left(\frac{2Eb\bar{l}^2}{\sigma^*}\right)^{1/3} \quad (28)$$

where E is the tensile modulus of niobium, $\bar{l}$ the average spacing between obstacles (trees) in the niobium lattice, and σ^* the thermal component of the flow stress. Friedel also points out that the area swept out by a dislocation on overcoming a barrier, A, should equal

$$A = 2D \times \bar{h}/2 = D \times \bar{h} \approx \bar{l}^2 \quad (29)$$

which leads to

$$\bar{h} = \frac{\bar{l}^2}{D}. \quad (30)$$

An evaluation of $\bar{h}$ at 300 K, assuming the rate controlling mechanism was overcoming forest dislocations and $\rho_f = 10^{10}\,\mathrm{m}^{-2}$ where ρ_f is the density of forest dislocations, gave a spacing of forest dislocations along a mobile dislocation of $D = 1.8 \times 10^{-6}\,\mathrm{m}$, $\bar{h} = 5.54 \times 10^{-5}\,\mathrm{m}$ and a mobile dislocation density $\rho_m = 1.44 \times 10^{10}\,\mathrm{m}^{-2}$. This dislocation density is very reasonable if the rate controlling mechanism is dislocation intersections.
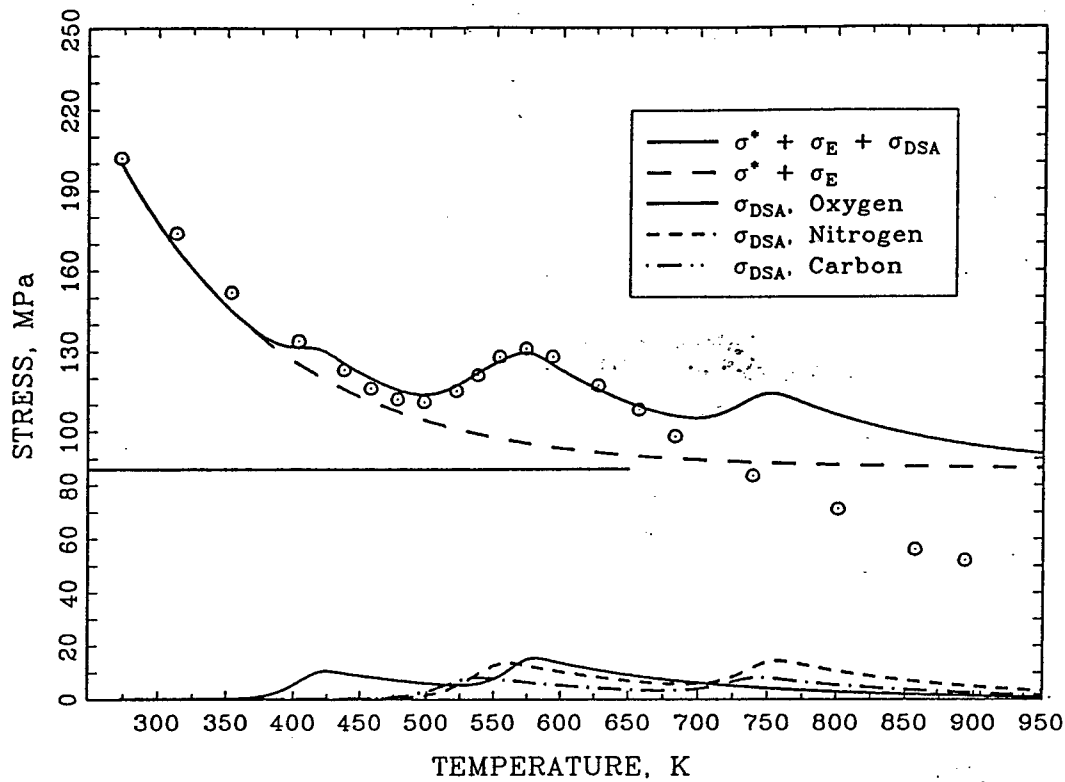
Fig. 3. This figure shows that the high temperature data above 300 K of Ref. [12] can be fitted to about 650 K by an analytical equation that assumes $\sigma = \sigma^* + \sigma_E + \sigma_{DSA}$ where σ^* and σ_E are extrapolated from the lower temperature data region and σ_{DSA} is the sum of the DSA stresses due to O, N and C. Note that the unusual stress peak in the plateau region at 570 K can be explained in this manner.
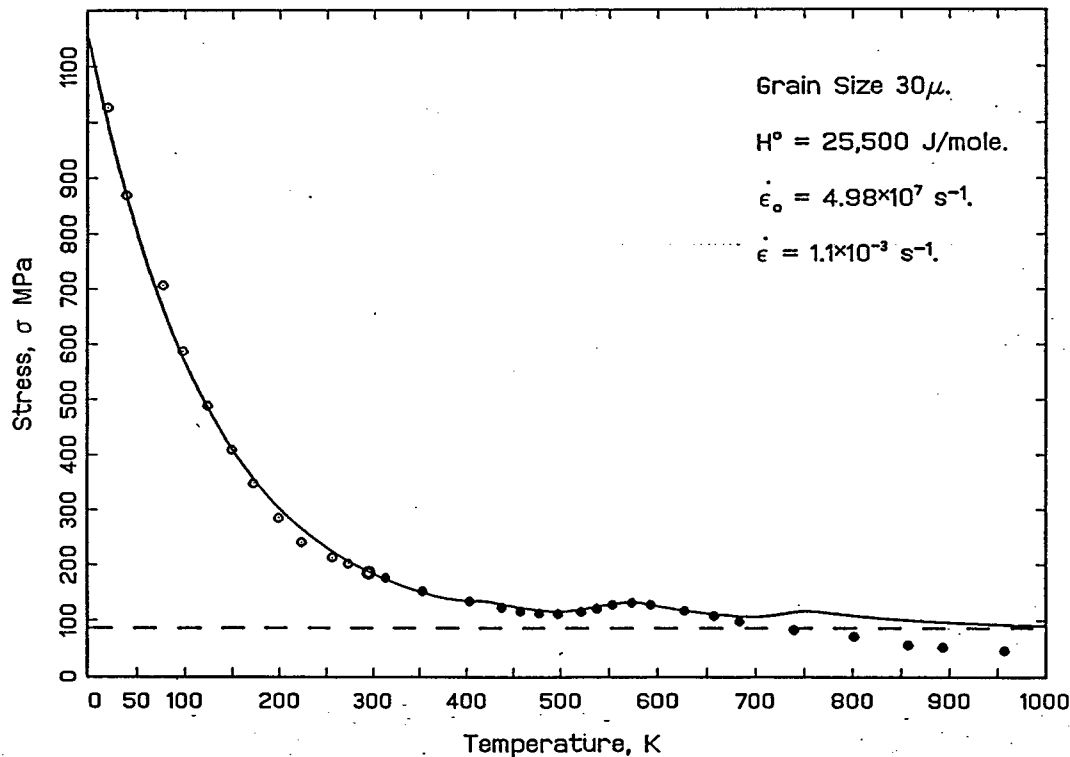
Fig. 4. In this figure the flow stress data from Refs [11, 12] as well as the analytical expressions for the flow stress are combined to cover the temperatures from 20 to 950 K.

The uppermost solid line curve in Fig. 3 was obtained by adding the total DSA stress to the effective and internal stresses. The DSA stress was obtained by inserting the values in Table 2 and the Snoek and Cottrell relaxation times, τ_{Sn} and τ_{Cot}, in equations (21) and (23) into equation (25). Also shown in this figure are curves for the internal stress σ_E and $\sigma^* + \sigma_E$ as extrapolated from the expressions for these components obtained using data from below 300 K (See Fig. 2). The three curves at the bottom of Fig. 3 correspond to the DSA stresses of the three individual interstitial elements O, N and C. Figure 4 compares all of the flow stress data points of Figs 2(B) and 3 with computed curves based on the low temperature power law parameters, $\dot{\epsilon}_0$ and H^0, and the DSA parameters discussed above.

DISCUSSION

As may be seen in Fig. 2, the assumption of the power law in equation (5) leads to analytical curves giving the temperature dependence of the flow stress, σ, the logarithm of the effective stress, σ^*, and the two strain-rate sensitivity parameters $S = d\sigma/d \ln \dot{\epsilon}$ and $n = d \ln \sigma^*/d \ln \dot{\epsilon}$ that are in very good agreement with the low temperature CP niobium data of Fries et al. [11]. Even if the power law procedure outlined in this paper is considered phenomenological, it clearly describes the data very well in this temperature range. Since, as Hartley [13] has pointed out, an activation energy of the form $H = H^0 \ln(\sigma_0^*/\sigma_0^*)$ is to be expected whenever the stress exerted on a mobile dislocation element varies inversely as the distance, this agreement cannot be considered consistent with the concept that the rate controlling mechanism in this grade of niobium is the overcoming of individual interstitial atom barriers. This is because the interaction force between a point defect and a dislocation has been calculated [23] to vary as $1/R^3$ and not as $1/R$ where R is the distance between them. On the other hand, there is strong evidence for the view that the interstitials are a factor in the plastic deformation strength of niobium. For example, the effective stress at 0 K, σ_0^*, increases with increasing interstitial concentration. Also the temperature dependence of the effective stress, σ^*, due to dynamic recovery, is the same as that shown earlier [20] for the DSA stress due to oxygen in the CP niobium specimens of Delobelle et al. [21] which were strain aged under stress at four different constant temperatures. In both cases, the dynamic recovery factor was $B = 8 \times 10^{-3} K^{-1}$. It would thus appear that the basic rate controlling mechanism, which may be dislocation intersections, controls the temperature and strain rate dependence of the effective flow stress while the interstitial concentration and its arrangement relative to the dislocations could possibly play a role in determining the level of the effective stress.

There remains the high temperature CP niobium data due to Fries, Cizeron and LaCombe covering temperatures from 20 to 850°C (293 to 1123 K). At a strain rate of $1.1 \times 10^{-3} s^{-1}$, serrated stress–strain curves were observed in these specimens between about 418 and 623 K. This implies that DSA occurred in this region. The Portevin–Le Chatelier effect, however, is only one of many aspects of DSA which include (1) an increase in the flow stress, (2) an abnormal and rate dependent work hardening peak, (3) the blue brittle effect, (4) a strain rate sensitivity minimum, and (5) a yield stress plateau. In general, it is believed that DSA can result in an increase in the net yield stress whether or not serrated yielding occurs. Only when the DSA is strong enough to make the strain-rate sensitivity become negative do serrations occur. What has been attempted here is to demonstrate that the yield stress plateau can be modeled by assuming that the DSA stress in this region can be added to the basic flow stress. The CP niobium specimens of Fries et al. [12] are interesting in this regard because their flow stress plateau is not temperature independent, as often observed, but contains a pronounced peak. These specimens were reported, however, to contain three interstitial elements in solution: O, N and C. When reasonable values for the Snoek and Cottrell amplitudes for the three interstitial elements are used in equation (25), a DSA stress peak is seen to occur analytically in the region where the peak is observed in the experimental data. This is because the maximum of the oxygen Cottrell DSA stress as well as the maxima of the Snoek DSA stresses due to nitrogen and carbon occur within the limits of the experimental peak. It should be noted that the fit between the analytical flow stress curve and experimental data points is, on the whole, very good in Figs 3 and 4 to about 650 K. Above this temperature, the experimental data points drop below the calculated flow stress curve with the deviation increasing with rising temperature. Note that they also fall below the extrapolated lower temperature athermal stress, σ_E, when the temperature exceeds about 700 K. This implies that, at these higher temperatures, dynamic recovery may alter the basic metallurgical substructure. Support for this conclusion is given by studies of static recovery in niobium summarized in a general review by English [24] on the properties of niobium.

CONCLUSIONS

1. It has been possible to derive analytical curves in very good agreement with the 20–300 K CP niobium experimental data of Fries, Cizeron, Houssin and Lacombe. These curves reproduce the temperature dependence of (1) the flow stress, σ, (2) the effective stress, σ^*, and (3) the strain-rate sensitivity parameters $S = d\sigma/d \ln \dot{\epsilon}$ and $n = d \ln \sigma^*/d \ln \dot{\epsilon}$.

2. The rate of dynamic recovery of the effective stress, σ^*, for data between 20 and 300 K was found to equal that previously reported for the oxygen DSA stress of the CP niobium specimens of Delobelle,

Oyatana and Varchon strain aged under stress at temperatures between 344 and 418 K.

3. The analytical curves based on the 20–300 K data assume an activation enthalpy of the form $H = H^0 \ln(\sigma_0^* / \sigma^*)$, which is characteristic of a mechanism in which the force between a barrier and a mobile dislocation element varies inversely as the distance. This suggests the rate controlling mechanism in the CP niobium specimens is not due to simple interactions between interstitial atoms and mobile dislocations since the force between a point defect and a dislocation element is not considered to vary inversely as their separation. Nevertheless, the low temperature dynamic recovery rate was found to equal that of the oxygen DSA stress at higher temperatures in specimens strain aged under stress. It is also true that the effective stress at 0 K, σ_0^*, increases with increasing interstitial concentration. This suggests that the interstitial concentration could be involved in a secondary role to the basic rate controlling mechanism. However, at the present time a mechanism relating the hardening effect of the interstitials on the basic rate controlling mechanism is not available.

4. That this CP niobium apparently conforms to the Ravi and Gibala interstitial concentration range where interstitial atoms control the low temperature strengthening of the flow stress is probably due to its large ratio of about four interstitial to substitutional solute atoms. This should result in a relatively small number of interstitial–solute atom pairs and reduce the importance of alloy softening. It is further felt that, although the concentration of interstitials is rather high, it is still not high enough to cause saturation which might make the temperature dependence of the flow stress and strain-rate sensitivity appear to be athermal.

5. The abnormal flow stress peak observed in the region of the plateau at 570 K is consistent with an assumption that it is due to DSA involving three different interstitials: O, N and C.

REFERENCES

1. J. F. Dorn, *Dislocation Dynamics*, p. 27. McGraw–Hill (1968).
2. H. Conrad, *The Relation Between The Structure and Mechanical Properties of Metals*, p. 475. H.M.S.O. (1963).
3. J. F. Dorn and S. Rajnak, *Trans. Am. Inst. Min. Engrs.* 14, 1052 (1964).
4. J. W. Christian and B. C. Marsters, *Proc. R. Soc.* A281, 223 (1964).
5. K. V. Ravi and R. Gibala, *Scripta metall.* 3, 547 (1969).
6. K. V. Ravi and R. Gibala, *Acta metall.* 18, 623 (1970).
7. R. L. Fleischer, *Acta metall.* 15, 1513 (1967).
8. D. F. Stein and J. R. Low Jr., *Acta metall.* 14, 1183 (1966).
9. W. Frank, *Physica status solidi (a)* 19, 239 (1967).
10. R. E. Reed-Hill and T. Zhu, *High Temp. Mater. Proc.* 6, 93 (1984).
11. J. F. Fries, B. Houssin, G. Cizeron and P. Lacombe, *Jour. Less-Com. Met.* 33, 117 (1973).
12. J. F. Fries, C. Cizeron and P. Lacombe, *Rev. Phys. Appl.* 5, 371 (1970).
13. C. S. Hartley, *2nd Int. Conf. Strength of Metals and Alloys*, p. 429, ASM, Metals Park, Ohio (1970).
14. G. Schoeck and A. Seeger, *Defects in Crystalline Solids*, p. 340. Physics Society, London (1955).
15. A. Seeger, *Phil. Mag.* 1, 651 (1956).
16. K. W. Qian and R. E. Reed-Hill, *Scripta metall.* 16, 807 (1982).
17. F. J. M. Boratto and R. E. Reed-Hill, *Metall. Trans. A* 8A, 1233 (1977).
18. R. W. Powers and Margaret V. Doyle, *J. appl. Phys.* 4, 514 (1959).
19. A. W. Sleeswyk, *Acta metall.* 6, 598 (1958).
20. R. E. Reed-Hill, S. C. Park and L. P. Beckerman, *Acta metall.* 31, 1715 (1983).
21. P. Delobelle, C. Oytana and D. Varchon, *Mater. Sci. Engng* 29, 261 (1977).
22. J. Friedel, *Dislocations*, p. 224. Pergamon Press, Oxford (1964).
23. R. W. Weeks, S. R. Pati, M. F. Ashby and P. Barrand, *Acta metall.* 17, 1403 (1969).
24. C. English, *Proc. Int. Symp. Niobium '81* (edited by H. Stuart). IMS, AIME, Pittsburgh, PA (1984).

The effects of interstitial content, heat treatment, and prestrain on the tensile properties of NiAl

M.L. Weaver[a], R.D. Noebe[b], J.J. Lewandowski[c], B.F. Oliver[d], M.J. Kaufman[a]

[a] University of Florida, Gainesville, FL 32611-2066, USA
[b] NASA Lewis Research Center, Cleveland, OH 44135, USA
[c] Case Western Reserve University, Cleveland, OH 44106, USA
[d] University of Tennessee, Knoxville, TN 37996, USA

Abstract

The tensile stress–strain response of polycrystalline NiAl was studied as a function of purity and pretest treatment (annealing and/or prestrain). After annealing at 1100 K for 7200 s (i.e. 2 h) followed by furnace cooling, high-purity and nitrogen-doped alloys exhibited continuous yielding, while conventional-purity or carbon-doped alloys exhibited a distinct yield point and Lüders strain. Prestrain by hydrostatic pressurization removed the yield point, but it could be reintroduced by further annealing treatments. Yield points could be reintroduced more rapidly if the specimens were prestrained uniaxially rather than hydrostatically, owing to the arrangement of dislocations into cell structures during uniaxial deformation. The time dependence of the strain aging events followed a $t^{2/3}$ relationship. In total, these results suggest that the yield points observed in polycrystalline NiAl result from the pinning of mobile dislocations by interstitials, specifically carbon, i.e. classic static strain aging.

Keywords: Heat treatment; Tensile properties; Nickel; Aluminium

1. Introduction

Several aspects of strain aging have been identified as playing a role in the deformation of polycrystalline and single-crystal NiAl. They are the occurrence of yield points and serrated stress–strain curves [1–6], strain rate sensitivity minima [7,8], yield stress plateaus as a function of temperature [9] and flow stress transients on changes in strain rate [8,10]. In addition, extensive work by Margevicius and co-workers [3,11–13] has shown that a sharp yield point can be formed in binary NiAl following annealing at 1100 K and furnace cooling. This yield point can be removed by subsequent prestraining of the material by hydrostatic pressurization prior to testing, and recovered by aging the prestrained material for 7200 s (i.e. 2 h) at 673 K. Similarly, Pascoe and Newey [7] observed the formation of room-temperature yield points in near-stoichiometric NiAl annealed for 3600 s (1 h) at 350 K following a uniaxial prestrain. Despite these observations, no complete investigation of classical strain aging has been conducted on ordered bcc intermetallic

alloys. The purpose of this document is to provide a preliminary description of the interrelated effects of interstitial content, heat treatment and prestrain on the tensile behavior of polycrystalline NiAl.

2. Experimental details

NiAl in the form of (a) a conventional-purity induction-melted casting (CP-NiAl), (b) a low-interstitial high-purity zone refined ingot (HP-NiAl), (c) a nitrogen-doped powder (NiAl-N), and (d) a zone-leveled carbon-doped ingot (NiAl-C) were the basic starting materials used in this investigation. All starting materials were extruded at 1200 K at either a 12:1 or 16:1 reduction ratio. Descriptions of the equipment and processes used to fabricate the high-purity and doped alloys are presented elsewhere [14–16].

Chemical analyses of the various extrusions were conducted at the NASA Lewis Research Center by the following techniques, deemed to be the most accurate for the particular elements. Ni and Al were determined

using analytical wet chemistry/titration techniques. Oxygen, nitrogen, carbon and sulfur contents were determined by combustion techniques using LECO oxygen/nitrogen and carbon/sulfur determinators.

Round button-head tensile specimens were ground from the extruded rods so that the gage lengths of the samples were parallel to the extrusion direction. Sample dimensions were 3.1 mm for the tensile gage diameters and 30.0 mm for the tensile gage lengths. Prior to testing, all samples were electropolished in a 10% perchloric acid-90% methanol solution that was cooled to 208 K. Tensile tests were performed on an Instron Model 1125 load frame at a constant cross-head velocity corresponding to an initial strain rate of 1.4×10^{-4} s^{-1}. All tests were performed in air at 300 K. True stress–strain data were calculated from the load–time plots, and yield stresses were determined by the 0.2%-offset method.

The tensile testing was accomplished in three steps. First, baseline mechanical properties were determined for all four alloys by testing them as follows: (a) as extruded, (b) as extruded + 1100 K/7200 s/furnace cooling (FC); and (c) as extruded + 1100 K/7200 s/FC + pressurized to 1.4 GPa. The heat treatment temperature and prestrain pressurization treatment were selected based on the observations of Marge-vicius and co-workers [3,11–13]. Second, a series of CP-NiAl specimens, having received treatment (c), were annealed at temperatures ranging from 500 K to 1100 K for up to 7200 s followed by FC, air cooling (AC) or water quenching (WQ) to room temperature to establish the optimum conditions for studying the kinetics of strain aging in NiAl. A more detailed accounting of the treatments employed will be provided in the Results and Discussion sections.

Finally, the kinetics of strain aging were investigated using the classic yield-point return technique whereby tensile specimens in the as-extruded condition were prestrained approximately 0.2%, unloaded, aged in situ on the load frame for aging times varying between 60 s and 113 000 s (30 h), and then tested in tension at room temperature. This test method allows specimen alignment to be maintained, and allows the stress level to be kept effectively constant during aging. After aging, the specimens were cooled by removing the furnace from the test frame and passing a forced stream of air over the specimen and the tensile grips. This method of cooling resulted in average temperature drops of 500 to 1000 K during the first minute of cooling.

The parameters used to evaluate the kinetics of strain aging are illustrated in Fig. 1. These include the upper yield stress increment $\Delta\sigma_u = \sigma_u - \sigma_a$, the lower yield stress increment $\Delta\sigma_L = \sigma_L - \sigma_a$, and the Lüders strain ε_L.

Fig. 1. Definition of strain-aging parameters.

Table 1
Compositions of extruded NiAl alloys (at.%)

Alloy (heat)	Ni	Al	O	N	C	S
CP-NiAl (L2971)	50.09	49.70	0.055	<0.0009	0.0147	<0.0007
HP-NiAl (L2987)	49.91	50.07	0.003	<0.0009	0.0043	<0.0007
NiAl-C (L2988)	50.18	49.77	0.003	<0.0009	0.0092	<0.0007
NiAl-N (P1810)	50.07	49.70	0.035	0.0904	0.0057	<0.0007

3. Experimental results

3.1. Composition and microstructure

Chemical analyses of the four alloys are shown in Table 1. Within experimental accuracy (± 0.2 at.% for Ni and Al), the Ni and Al contents of the four alloys are not significantly different from each other. The major differences between the materials are the carbon, oxygen and nitrogen contents.

Other than differences in grain size and the presence of semi-continuous stringers of nanometer-size nitride precipitates along prior particle boundaries in NiAl-N [16], all of the NiAl grain structures were similar as observed using optical microscopy. The micro-structures were fully dense, consisting of recrystallized and equiaxed grains with the average linear intercept grain sizes reported in Table 2. The grain sizes of the HP-NiAl and NiAl-C alloys, which were prepared by

extruding single crystals, are consistently larger than those of the cast and extruded CP-NiAl or the powder-processed NiAl-N.

3.2. Mechanical properties

Baseline mechanical properties were established by tensile-testing specimens of all four alloys in the as-extruded condition, following an anneal of 1100 K/7200 s/FC, and following an anneal of 1100 K/7200 s/FC plus pressurization to 1.4 GPa. These results are summarized in Table 3. Immediately obvious from Table 3 is that the yield stress of each

Table 2
Grain size of extruded NiAl alloys

Alloy	Reduction ratio[a]	Grain size (μm)
CP-NiAl (heat L2971)	16:1	18.7 ± 1.5
HP-NiAl (heat L2987)	12:1	51.5 ± 2.3
NiAl-C (heat L2988)	12:1	45.6 ± 4.0
NiAl-N (heat P1810)	16:1	4.0 ± 0.3

[a]All alloys extruded at 1200 K.

alloy generally decreased following the 1100 K/7200 s/FC anneal. In addition, it is obvious that further decreases in yield stress can be achieved in the CP-NiAl and NiAl-C alloys if the specimens are hydro-statically pressurized at 1.4 GPa, whereas no decrease is observed in the powder-processed NiAl-N alloy or the HP-NiAl material. Interestingly, even though the yield stress could be lowered by annealing and in some cases pressurizing, these treatments had no obvious influence on the tensile ductility.

Typical room-temperature true stress–plastic strain curves for the as-extruded alloys are shown in Fig. 2. The HP-NiAl, NiAl-C and NiAl-N alloys exhibited continuous yield behavior. The CP-NiAl alloy, however, exhibited discontinuous yield behavior. Similar discontinuous yield behavior has been previously reported for conventional-purity binary NiAl [3,11–13,16–19]. Following pressurization at 1.4 GPa, only continuous yielding was observed in the four alloys. However, if pressurized specimens were subsequently annealed at 1100 K/7200 s/FC, pronounced yield points and yield plateaus were observed in CP-NiAl and NiAl-C, whereas only continuous yielding was still observed in HP-NiAl or in NiAl-N. Typical true stress–strain curves for the pressurized plus annealed alloys are shown in Fig. 3.

Table 3
Baseline tensile properties of NiAl alloys

Material	Condition[a]	0.2% yield stress (MPa)	Fracture stress (MPa)	Ductility (%)	Observations[b]
CP-NiAl	As-extruded	269	379	2.11	YP
	As-extruded	275	368	1.83	YP
	Annealed/FC	184	301	2.08	UYP
	Annealed/FC	197	228	1.04	UYP
	Annealed/AC	154	309	2.26	Evidence of YP
	Annealed/WQ	143	228	1.13	CY
	Pressurized	154	288	1.86	CY
	Pressurized	159	317	1.81	CY
	Pressurized	154	322	2.16	CY
HP-NiAl	As-extruded	166	214	0.79	CY
	As-extruded	157	235	1.16	CY
	Annealed/FC	98	174	1.17	CY
	Pressurized	118	176	0.92	CY
NiAl-C	As-extruded	170	201	0.59	CY
	Annealed	113	157	0.68	YP
	Pressurized	96	171	0.98	CY
NiAl-N	As-extruded	298	409	1.32	CY
	As-extruded	297	476	2.20	CY
	Annealed/FC	265	468	2.45	CY
	Pressurized	266	434	2.16	CY
	Pressurized	274	352	1.03	CY

[a]Annealed/WQ = as-extruded + 1100 K/7200 s/WQ; annealed/AC = as-extruded + 1100 K/7200 s/AC; annealed/FC = as-extruded + 1100 K/7200 s/FC;pressurized = as-extruded + 1100 K/7200 s/FC + pressurize 1.4 GPa.
[b]UYP = discontinuous yielding, upper yield point, sharp yield drop; YP = discontinuous yielding, small yield drop or plateau; CY = continuous yielding.

Fig. 2. Typical room-temperature true stress–plastic strain curves for as-extruded NiAl alloys.

Fig. 4. $\ln \Delta \sigma_u$ vs. $\ln t$ for CP-NiAl specimens. Specimens were prestrained uniaxially in tension. The least-squares parameters are indicated on the figure.

Fig. 3. Typical room-temperature true stress–plastic strain curves for NiAl alloys following hydrostatic prestraining plus subsequent annealing at 1100 K/7200 s/FC.

mens were prestrained uniaxially, notable yield points formed readily after as little as 900 s (15 min) at 522 K and in as little as 60 s (1 min) at 700 K.

3.4. Kinetics of strain aging

In-situ static strain aging experiments were conducted, primarily on uniaxially prestrained samples. Single specimens were often aged several times to obtain a $\Delta \sigma_u$–time relationship. A specimen previously tested or prestrained uniaxially was given a recovery anneal, typically 1100 K/1800 s (30 min)/AC, prestrained approximately 0.2%, aged in situ and re-tested at room temperature. When this type of testing is adopted, the yield point exhibited in the undeformed material can be recovered, as can the yield point increment observed during the previous test. This means that it is possible to recover the dislocation structure and produce a reproducible $\Delta \sigma_u$ following the same strain aging (i.e. prestrain + annealing) treatment, justifying the use of multiple deformation experiments on single samples.

The time dependence of the flow stress increment $\Delta \sigma_u$ is shown in Fig. 4. The shapes of the aging curves up to the maximum value of $\Delta \sigma_u$ are comparable to similar curves reported for bcc metals [20]. Assuming $\Delta \sigma_u$ is proportional to the amount of solute segregating to dislocations, $\Delta \sigma_u$ will increase proportionally with $t^{2/3}$ during the early stages of aging. Later the dislocations will become saturated, leading to a leveling-out of $\Delta \sigma_u$ or to a decrease due to precipitation. The strain-aging time exponent, as determined by least-squares analysis of the data in Fig. 4, is in the range 0.57 to 0.67, which is close to the theoretical value of 2/3 predicted by Cottrell and Bilby [21]. In confirmation of this result, $\Delta \sigma_u$ is plotted versus $t^{2/3}$ in Fig. 5, demonstrating the satisfactory fit. Although experiments were

3.3. Influence of prestraining and annealing on baseline properties

In order to determine whether the observed yield points resulted from the hold at, or cooling from, the annealing temperature, specimens of CP-NiAl previously prestrained hydrostatically were annealed at 1100 K/7200 s followed by AC or WQ. After WQ, only continuous yielding was observed, while after AC there was some evidence of a yield plateau, which initially suggests that the yield points observed following FC are the result of the pinning of dislocations by mobile solute atoms during cooling through lower temperatures. As a result, annealing experiments were initiated at lower temperatures to determine the critical temperature for the migration of solute atoms to dislocations. It was observed that, following hydrostatic prestraining, yield plateaus formed in CP-NiAl following anneals of 700 K/7200 s/FC but not following anneals of 500 K/7200 s/FC. Conversely, if the speci-

Fig. 5. Plots of $\Delta\sigma_u$ vs. $t^{2/3}$ for CP-NiAl.

Fig. 6. Plot of $\Delta\sigma_u$ vs. ln t for CP-NiAl and NiAl-C at 616 K and 610 K respectively.

applying the Arrhenius equation. On this basis, an activation energy for the return of a lower yield point in CP-NiAl was determined to be approximately in the range 72 to 76 kJ mole⁻¹ (approximately 0.75 to 0.79 eV), which corresponds to the activation energies for the migration of interstitials in many bcc transition metals [22]. To check the Arrhenius calculation, the activation energy was also determined by the method used by Hartley [23]. This method entails taking the slopes S_1 of the plots of $\Delta\sigma_u/0.5(\sigma_u + \sigma_a)$ vs. $t^{2/3}$ and plotting $\ln(S_1 T^{2/3})$ vs. $2/(3RT)$. Using this method, an activation energy of 70 kJ mol⁻¹ (0.73 eV) was determined, which is in good agreement with the value determined using the Arrhenius method.

4. Discussion

4.1. Species responsible for strain aging in NiAl

Determination of the species responsible for strain-aging effects in NiAl can be made by examination of the aging behavior of all four alloys. Discontinuous yielding, in the form of yield points and yield plateaus, was observed in CP-NiAl and NiAl-C, while none was observed in HP-NiAl or NiAl-N following heat treatments known to produce yield points in conventional cast and extruded NiAl [11]. In NiAl-N, the oxygen and nitrogen contents are much higher than those observed in CP-NiAl, which suggests that nitrogen and oxygen are not the species responsible for the yield points observed in NiAl. In addition, no yield point phenomenon was observed in HP-NiAl. In NiAl-C, it was observed that longer aging times are required to achieve the same yield increment as observed in CP-NiAl. It is believed that this behavior is a result of the significant reduction in the concentrations of interstitials, particularly C. Since there is less carbon to pin dislocations in NiAl-C, the carbon present must, presumably, diffuse longer distances to cause pinning.

4.2. Influence of prestraining

As noted in Section 3, the return of a sharp yield point is much more rapid when the specimen has been prestrained uniaxially as opposed to hydrostatically. In uniaxially prestrained NiAl, dislocations can cross-slip easily, forming cell structures [16,24] that result in high work-hardening rates at room temperature compared to many metals. As a result, the dislocations are in essence pinned. In contrast, samples pressurized hydrostatically show an even distribution of dislocations which are not bound in a cell structure [13]. In uniaxially prestrained samples, since some of the dislocations are already locked up in cell structures,

only performed at 610 K for NiAl-C, a similar trend of higher $\Delta\sigma_u$ with increasing aging time was observed. In addition, the time exponent was found to be 0.59, in agreement with the observations for CP-NiAl.

The $\Delta\sigma_u$ vs. log time data for CP-NiAl and NiAl-C that were aged for various times at 616 and 610 K, respectively, are plotted together in Fig. 6 to illustrate the influence of carbon concentration on the yield-point return in NiAl. A significant difference in the magnitudes of the $\Delta\sigma_u$ values is evident, as is an increase in the time required for yield points to form in NiAl-C. In addition, the saturation stress increment is also a function of C content, as would be expected at low C levels.

In efforts to establish a mechanism for static strain aging in NiAl, apparent activation energies corresponding to specific time-dependent aging events (i.e. the activation energy for the return of the lower yield stress was determined where the logarithmic time dependence was exhibited for the times required to achieve a variety of stress increases) were deduced by

fewer mobile dislocations are available. Thus, less solute is required to pin the available mobile dislocations. In hydrostatically prestrained samples, however, since more mobile dislocations are available, more carbon must diffuse to these dislocations to cause pinning. As a result, longer aging times are required to achieve the same yield-point increments observed after uniaxial prestraining. A similar explanation has been applied to strain-aged steels prestrained in directions different to the original tensile direction [25].

4.3. Kinetics of strain aging

At least four different mechanisms have been postulated to explain strain-aging in metals and alloys. These include the formation of Cottrell atmospheres [21], Snoek ordering [26–28], Suzuki locking [29] and the precipitation of solute on dislocations [30].

During the early stages of Cottrell locking, the kinetics of yield-point return normally increase with time according to a $t^{2/3}$ power law. This relationship was originally deduced by Cottrell and Bilby [21] and has been confirmed for a number of systems involving interstitial atoms in transition metals, including Nb–O, Ni–H, Fe–C and Fe–N. The observed $\log t$ or approximate $t^{2/3}$ time dependence of $\Delta\sigma_u$ in NiAl due to carbon is consistent with the Cottrell–Bilby theory, which suggests that Cottrell locking is the mechanism responsible for the observed yield points.

Snoek ordering of impurity atoms within the stress field of a dislocation remains a possible mechanism. In this case, pinning is completed within the time interval of one atomic jump of the species responsible for pinning. The observations in this study certainly suggest that Snoek ordering does occur in NiAl. Nakada and Keh [31] have indicated that the apparent intercept of the $\Delta\sigma_u$ vs. $t^{2/3}$ curves is positive when Snoek ordering occurs prior to Cottrell atmosphere formation. As this is the case here, it can be concluded that some degree of Snoek ordering occurs in addition to the above-mentioned Cottrell locking.

Suzuki locking is considered to be inapplicable in the present investigation. This mechanism has its origin in a chemical interaction between solute atoms and stacking faults, and is only expected to be significant in metals of low stacking-fault energy in which the stacking-fault widths are large.

Precipitation on dislocations as a result of the segregation of solute would appear to be inappropriate, because precipitates were not observed in thin foils made from specimens of CP-NiAl and NiAl-C aged at 1100 K/7200 s/FC or 610 K/7200 s/AC. In addition, the shapes of the aging curves for CP-NiAl and NiAl-C for aging times up to 61 000 s at 700 K do not suggest the formation of precipitates due to overaging (satura-

tion of dislocations by solute). This is not to say that precipitation will not occur, but that it was not observed within the time–temperature range examined for alloys with the specific compositions studied. This does not preclude such a mechanism in alloys containing higher levels of substitutional contaminants [32–34].

Unfortunately, owing to the lack of diffusion data for NiAl, very little can be said about the derived activation energies, except that these activation energies lie below the self-diffusion energies for Ni and Al in NiAl, and that they lie below the activation energy for the creation and motion of vacancies [9], and that they are within the range for interstitial diffusion in bcc transition metals [22].

5. Conclusions

(1) The yield points observed in conventional-purity and carbon-doped NiAl are the result of strong dislocation pinning by interstitial carbon. Oxygen and nitrogen levels below 0.035 and 0.09 at.%, respectively, do not appear to pin dislocations in NiAl and therefore do not produce yield-point phenomena.

(2) The time dependence of strain aging appears to follow a $t^{2/3}$ relationship, which suggests Snoek aging and Cottrell locking as the cause for yield points in NiAl.

(3) Hydrostatic prestraining, as opposed to uniaxial prestraining, delays the kinetics of the yield-point return by forming random networks of free unpinned dislocations which require more diffusion time for strong locking to occur.

(4) Activation energies for yield-point return ranging from 70 to 76 kJ mol⁻¹ (0.73–0.79 eV per atom) have been calculated, which are within the range for the diffusion of interstitials in bcc transition metals.

References

[1] J.E. Hack, J.M. Brzeski, R. Darolia and R.D. Field, in I. Baker, R. Darolia, J.D. Whittenberger and M.H. Yoo (eds.),

High-Temperature Ordered Intermetallics V, Materials Research Society, Boston, MA, 1993, p. 1197.

[2] E.P. Lautenschlager, D.A. Kiewit and J.O. Brittain, *Trans. AIME, 233*, 1297 (1965).

[3] R.W. Margevicius and J.J. Lewandowski, *Scr. Mater., 25*, 2017 (1991).

[4] R.D. Field, D.F. Lahrman and R. Darolia, in I. Baker, R. Darolia, J.D. Whittenberger and M.H. Yoo (eds.), *High-Temperature Ordered Intermetallic Alloys V*, Materials Research Society, Boston, MA, 1993, p. 423.

[5] J.M. Brzeski, J.E. Hack, R. Darolia and R.D. Field, *Mater. Sci. Eng., A170* (1993) 11.

[6] C.T. Liu, E.H. Lee, E.P. George and A.J. Duncan, *Scr. Metall. Mater., 30* (1994) 387.

[7] R.T. Pascoe and C.W.A. Newey, *Metal Sci. J., 2* (1968) 138.

[8] R.T. Pascoe and C.W.A. Newey, *Metal Sci. J., 5* (1971) 50.

[9] R.D. Noebe, R.R. Bowman and M.V. Nathal, *Int. Mater. Rev., 38* (1993) 193.

[10] M.L. Weaver, University of Florida, unpublished research, 1993.

[11] R.W. Margevicius, J.J. Lewandowski, I.E. Locci and R.D. Noebe, *Scr. Metall. Mater., 29* (1993) 1309.

[12] R.W. Margevicius and J.J. Lewandowski, *Acta Metall. Mater., 41* (1993) 485.

[13] R.W. Margevicius, J.J. Lewandowski and I.E. Locci, in R. Darolia, J.J. Lewandowski, C.T. Liu, P.L. Martin, D.B. Miracle and M.V. Nathal (eds.), *Structural Intermetallics*, The Minerals, Metals and Materials Society, Warrendale, PA, 1993, p. 577.

[14] D.R. Johnson, S.M. Joslin, B.F. Oliver, R.D. Noebe and J.D. Whittenberger, in H. Henein and T. Oki (eds.), *First Int. Conf. on Processing Materials for Properties*, The Minerals, Metals and Materials Society, Warrendale, PA, 1993, p. 865.

[15] R.D. Reviere, B.F. Oliver and D.D. Bruns, *Mater. Manuf. Proc, 4* (1989) 103.

[16] R.D. Noebe and A. Garg, *Scr. Metall. Mater., 30* (1994) 815.

[17] R.D. Noebe and M.K. Behbehani, *Scr. Metall. Mater., 27* (1992) 1795.

[18] A.G. Rozner and R.J. Wasilewski, *J. Inst. Metals, 94* (1966) 169.

[19] K.H. Hahn and K. Vedula, *Scr. Metall., 23* (1989) 7.

[20] J.D. Baird, *Metall. Rev., 16* (1971) 1.

[21] A.H. Cottrell and B.A. Bilby, *Proc. Phys. Soc., Lond. A, 62* (1949) 49.

[22] H. Schultz, *Mater. Sci. Eng., 3* (1968/69) 189.

[23] S. Hartley, *Acta Metall., 14* (1966) 1237.

[24] R.R. Bowman, R.D. Noebe, S.V. Raj and I.E. Locci, *Metall. Trans., 23A* (1992) 1493.

[25] D.V. Wilson and G.R. Ogram, *J. Iron Steel Inst., 206* (1968) 911.

[26] J. Snoek, *Physica, 8* (1941) 711.

[27] J. Snoek, *Physica, 6* (1939) 591.

[28] G. Schoeck and A. Seeger, *Acta Metall., 7* (1959) 469.

[29] H. Suzuki, in *Dislocations and Mechanical Properties of Crystals*, Wiley, New York, NY, 1957.

[30] E.O. Hall, *Yield Point Phenomena in Metals and Alloys*, Plenum Press, New York, 1970.

[31] Y. Nakada and A.S. Keh, *Acta Metall., 15* (1967) 879.

[32] H.K. DeMarco, A.J. Ardell and R.D. Noebe, *ASM 3rd Int. Conf. on High Temperature Intermetallics*, San Diego, CA, ASM International, Materials Park, OH, 1995.

[33] A.J. Duncan, M.J. Kaufman and M.K. Miller, *Appl. Surf. Sci., 76/77* (1994) 160.

[34] R. Jayaram and M.K. Miller, *Acta Metall. Mater., 42* (1994) 1561.

MODELING FLOW STRESSES AND STRAIN RATE SENSITIVITIES USING LOW TEMPERATURE DEFORMATION DATA

Coimbatore V. Iswaran, Robert E. Reed-Hill, Vladimir I. Levit
and Michael J. Kaufman

Department of Materials Science and Engineering, University of Florida,
Gainesville Fl 32611

Introduction

Plastic deformation in metallic materials is now generally accepted as the result of the movement of dislocations through possible barriers to such motion in the crystal structure. The flow stress, i.e., the stress associated with a given value of the plastic strain, when viewed as a function of temperature, has been observed in many instances to decrease from a theoretical maximum at absolute zero to lower values, eventually leveling off at high temperatures.

Experimental data typically consist of stress-strain curves generated during deformation in tension or compression at a constant temperature and a constant strain rate for various temperatures. In addition, many researchers also report the change in stress during plastic flow that is associated with a finite change in the strain rate during deformation. Of importance in understanding the plastic deformation behavior are: (A) the value of the stress during plastic flow and (B) the strain rate sensitivity of this flow stress.

While the overall trend is for the flow stress to decrease with increasing temperature and the strain rate sensitivity increases, as the temperature is raised, one sometimes observes localized peaks in the flow stress versus temperature curve. These regimes correspond to dynamic strain aging (DSA) of the material due to mobile solute atoms. At even higher temperatures, recovery and recrystallization begin to take place. In order to obtain a better understanding of the strain aging, recovery and recrystallization phenomena under conditions where the material is undergoing plastic deformation, it is necessary to establish a base line for the flow-stress versus temperature curve, which can then be subtracted from the actual curve, thus isolating the effects of interest that are sought for study.

Over the years, various theories have been put forth to account for dislocation movement during plastic flow under an applied stress and in the presence of obstacles such as interstitial atoms. A common feature of all of these theories is that the flow stress is thought to be the sum of two components. The first of these is the effective stress which is thermally activated. The other component is the internal stress which depends on the elastic modulus of the material. The internal stress is athermal and depends on temperature only to the extent that the modulus varies with temperature.

941

Although the concept of the internal stress is accepted by most researchers, its value has been difficult to define and measure experimentally. It has been suggested that the value of this stress be taken as the value of the total flow stress as it reaches a plateau at higher temperatures (1). The problem with this idea is that in this temperature range, there may be other phenomena coming into prominence, such as DSA, due to the interaction of dislocations with solute atoms. In fact, this view has been the subject of considerable work by Reed-Hill and coworkers (2) where they account for the plateau by incorporating the DSA stress components into the total stress.

Ideally, the two components of the flow stress should be evaluated directly from measurements at low temperatures without resorting to the extrapolation of the higher temperature data where other factors influence the temperature dependence of the flow stress, thus complicating and possibly invalidating such an analysis. Qian and Reed-Hill (3) have proposed one method for accomplishing this objective using strain rate change data and a knowledge of the variation of the elastic modulus with tem-perature. What follows is a refinement of those ideas and a procedure for establishing the required baseline behavior of the flow stress with minimal experimental effort.

The Power Law Model

The model presented here is based on certain assumptions regarding the dependence of the effective part of the flow stress on the strain rate and of both the effective and the athermal components on temperature. Consider a system where the strain rate fits the thermally activated strain rate equation

$$\dot{\varepsilon} = \dot{\varepsilon}_0 . \exp\left(-\frac{H}{RT}\right) \tag{1}$$

where ε_0 is a material constant and H is the activation enthalpy. Hartley (4) suggested that if the force exerted by a barrier on a dislocation varied inversely as the distance between them, then one can show that the enthalpy in the above equation takes the form

$$H = H^0 . \ln\left(\frac{\sigma^*}{\sigma_0^*}\right) \tag{2}$$

Activation enthalpies similar in form to that in equation (2) form the basis of other dislocation interaction models for deformation phenomena (5-6). Combining equations (1) & (2) yields the power law:

$$\left(\frac{\sigma^*}{\sigma_0^*}\right) = \left(\frac{\dot{\varepsilon}}{\varepsilon_0}\right)^n \qquad \left[\text{with} \quad n = \frac{RT}{H^0}\right] \tag{3}$$

The parameter 'n', which increases linearly with temperature in this range in a variety of materials (7-11), is commonly reported as the strain rate sensitivity exponent and is independent of the flow stress and the applied strain rate. By contrast, the parameter 'S', defined below, depends both on the effective stress and on the strain rate, in addition to being explicitly temperature dependent. Precisely for this reason, a measurement of 'S' provides insight into the temperature dependence of the flow stress as demonstrated in the application of this model to experimental results, while the strain rate sensitivity exponent suppresses crucial information with regard to the variation of the flow stress with the applied strain rate.

By assuming typical values for the material parameters H^0 and $\dot{\varepsilon}_0$ as 44kJ and 10^8 s^{-1} respectively, we can generate an envelope of curves for the quantities of interest as they vary with temperature, for strain rates ranging from 10^{-1} down to 10^{-6} s^{-1}. Figures 1-4 were generated by this scheme. Figure 1 shows the variation of the enthalpy, H, while figure 2 depicts the variation of σ^*.

The Flow Stress

The measured flow stress is the sum of the effective stress σ^* and the internal stress σ_E.

$$\sigma(T) = \sigma^*(T) + \sigma_E(T) \tag{4}$$

This model assumes that the effective stress follows a power law when expressed in terms of the applied strain rate and the test temperature T, with a theoretical maximum of σ_0^* at absolute zero. It is also assumed that the internal stress varies directly as the elastic modulus at any temperature, with as the proportionality constant. Thus,

$$\sigma(T) = \sigma_0^* \cdot \left(\frac{\varepsilon}{\varepsilon_0}\right)^{\left(\frac{RT}{H^0}\right)} + \alpha \cdot E(T) \tag{5}$$

In order to extract the various quantities in the above equations, we need, in addition to the σ versus T data, information on the change in stress associated with a strain rate change during deformation at a constant temperature. This allows us to evaluate 'S' as described below.

The Parameter 'S' and the Temperature T_B

'S' is related to the more commonly used strain rate sensitivity parameter 'n' as follows:

$$S = \frac{d\sigma}{d \ln \varepsilon} = \frac{RT}{H^0} \cdot \sigma^* = \frac{RT}{H^0} \; \sigma_0^* \cdot \left(\frac{\varepsilon}{\varepsilon_0}\right)^{\left(\frac{RT}{H^0}\right)} \tag{6}$$

while

$$n = \frac{d \ln \sigma}{d \ln \varepsilon} = \frac{S}{\sigma^*} = \left(\frac{R}{H^0}\right) \cdot T \tag{7}$$

Figure 3 shows the dependence of 'S' on temperature. As already stated, 'S' depends on the value of the flow stress and hence on the applied strain rate, while 'n' contains only the material parameter H^0. The S versus T curve has a maximum at temperature T_B. For experiments performed at a given strain rate, at various temperatures, the introduction of this temperature T_B into the above equations greatly simplifies the algebra and allows for a straightforward analysis of the experimental data. T_B is obtained by setting the derivative of S in equation (4) equal to zero:

$$\left(\frac{dS}{dT}\right)_{T=T_B} = 0 \qquad \text{so that} \qquad \frac{RT_B}{H^0} = -\ln\left(\frac{\varepsilon}{\varepsilon_0}\right) \tag{8}$$

An inspection of equation (3) shows that T_B is also the negative reciprocal of the slope of the straight line representing the ln σ^* versus T curve. Thus, all of the pertinent equations can be recast in terms of T_B as follows:

$$S = \left(\frac{RT}{H_0}\right) \cdot \sigma_0^* \cdot \exp\left(-\frac{T}{T_B}\right) \tag{9}$$

and

$$\sigma(T) = \sigma_0^* . \exp\left(-\frac{T}{T_B}\right) + \alpha . E(T) \tag{10}$$

The temperature T_B is not a material constant and increases with as shown in figure 4.

Evaluation of T_B, H^0 and $\dot{\varepsilon}$ from Experimental Data

Equations (9) & (10) enable the calculation of the requisite material parameters from data at just two different temperatures. This is illustrated using contrived data from hypothetical tensile tests per-formed at room temperature (298K) and in a liquid nitrogen bath (77K). Let the values of the flow stress at 77 and 298K be 882 and 379 MPa respectively, for an applied strain rate of 2×10^{-3} s^{-1}. Further, when the strain rate is increased five fold to 10^{-2} s^{-1}, let the observed change in stress be 17.9 and 24.1 MPa, so that $S_{77} = 11.1$ and $S_{298} = 15.0$ MPa*. Also, let the elastic modulus at these temperatures be $E_{77} = 239.6$ GPa and $E_{298} = 226.3$ GPa.

If we write equation (9) for the two temperatures and divide: $S_1/S_2 = (T_1 / T_2) . \exp [- (T_1 - T_2)$ or $(11.1/15) = (77/298) . \exp [(298-77)/T_B]$ so that $T_B = 210 °$ K. Using this value of T_B, equation (10) can be solved simultaneously for σ^* and α, yielding 1110 MPa and 0.05 respectively. Plugging these values back into equation (9) gives $H^0 = 44$ kJ. Finally, from equation (8), the value ε_0 of for the experimental strain rate of 2×10^{-3} s^{-1} is 1.7×10^8 s^{-1}. Figure 5 shows the variation of S with T and figure 6 graphs the effective stress versus temperature for this material.

Note that this analysis provides the researcher with the necessary values of the key quantities from measurements at two temperatures, even though the complete picture, namely the variation of the flow stress and of the elastic modulus (and hence the internal stress), is not available. In principle, the experiments should be carried out at a number of temperatures and in this case, a complete characterization becomes possible using the analysis shown below.

Nonlinear Parametric Analysis

When the experiments are performed at more than two temperatures, the task of finding T_B, σ_0^*, H^0 σ_E and ε_0 from equations (9) and (10) becomes one of statistically evaluating the best fitting values rather than the exact solutions for these unknowns. The first step in this parametric analysis is to establish the value of T_B. This is done by recasting equation (9) in the form and finding the values of σ_0 and T_B that best fit the data.

The dependence of E on T must be available either as a discrete set of values at the appropriate test temperatures or in a functional form, $E(T) = f(T)$. The function f may have any number of parameters. For example, a straight line relationship would contain the slope and the intercept as the parameters. The function may also be defined piecewise for various temperature ranges (this is useful because it has often been observed that E increases linearly with decreasing T, eventually leveling off at temperatures close to absolute zero). In the former case, equation (10) can be used as is to find the statistical best fit for σ_0^* and

$$S = \beta . T . \exp\left(-\frac{T}{T_B}\right) \qquad \text{where} \qquad \beta = \left(\frac{R}{H^0}\right) . \sigma_0^* \tag{11}$$

---

* Actually an accurate rendition of 'S' when the strain rate change is finite would be:

$$S \underset{\Delta \ln(\varepsilon) \to 0}{=} \frac{\Delta \ln \sigma^*}{\Delta \ln (\varepsilon)} \underset{k \to 1}{=} \frac{k^{\left[\frac{RT}{H^0}\right]} - 1}{\ln k} . \sigma_0^* . \exp\left(-\frac{T}{T_B}\right)$$

The implications of values of k other than 1 on the value of 'S' are being explored at this writing.

α. In the latter case, since this model assumes that σ_E is proportional to E at all temperatures, the functional dependence of on T is a scalar multiple of that of E on T. Therefore, we only need to replace $\alpha E(T)$ in equation (10) with f(T) to obtain the necessary parameter values.

Finally, having established the values of σ_0^*, and T_B, H^0 is obtained from the slope of the straight line fit between the strain rate sensitivity n ($=S/\sigma_0^*$) and T {see equation (7)}. The value of ε_0 is ascertained from equation (8) by inserting the appropriate value of the applied strain rate.

The procedure outlined above is illustrated by analyzing the data of Fries et. al. (11,12) on commercially pure niobium. The model values for the pertinent parameters are:

$$H^0 = 24670 \pm 2320J; \ \dot{\varepsilon}_0 = 4.7 \times 10 s^{-1}; \ T_B = 121.2 \pm 8K; \ \sigma_0^* = 1112 \pm 17 \, Mpa \text{ and } \sigma_E = 85.3 \pm 7 \, Mpa$$

Figures (7) and (8) compare the calculated and experimental values of 'S' and as a function of T.

Acknowledgment

References

1. A. Seeger, *Dislocations and Mechanical Properties of Crystals*, (J.C. Fisher, W.G. Johnston, R. Thomson and T. Vreeland Jr. eds.), John Wiley, New York, 243 (1957).
2. R.E. Reed-Hill and T. Zhu, *High Temperature Materials and Processes*, 6, 93 (1984).
3. K.W. Qian and R.E. Reed-Hill, *Scripta Metallurgica*, 16, 807 (1982).
4. C.S. Hartley, *Second International Conference on the Strength of Metals and Alloys*, ASM, Metals Park, OH, 429 (1970).
5. A. Seeger, *Philosophical Magazine*, 1, 651 (1956).
6. G. Schoeck and A. Seegar, *Defects in Crystalline Solids*, Phys. Soc. London (1955).
7. D.H. Baldwin and R.E. Reed-Hill, *Transactions of TMS-AIME*, 242, 661 (1968).
8. M. Ahlers, *Metallurgical Transactions*, 1, 2415 (1970).
9. H.L. Prekel, A. Lawley and H. Conrad, Acta Metallurgica, 16, 337 (1968).
10. K.W. Qian and R.E. Reed-Hill, *Acta Metallurgica*, 31, 87, (1983).
11. J.F. Fries, B. Houssin, C. Cizeron and P. LaCombe, *Journal of the Less Common Metals*, 33, 117 (1973).

Pergamon

0956-716X(95)00152-2

A POWER LAW MODEL FOR THE FLOW STRESS AND STRAIN-RATE SENSITIVITY IN CP TITANIUM

R. E. Reed-Hill, C.V. Iswaran and M. J. Kaufman
Department of Materials Science and Engineering,
University of Florida, Gainesville FL 32611

Introduction

A recently revised model (1,2) for the tensile deformation of bcc CP niobium described very well both the temperature and strain-rate dependence of the flow stress in this grade of niobium. It was also able to rationalize the plateau in the flow stress-temperature diagram of this metal in terms of the dynamic strain aging stresses due to oxygen, carbon and nitrogen. The present paper deals with an application of this model to a hcp metal system using the A-70 CP titanium data of Okazaki and Conrad (3). The basic assumption of this model is that the effective stress, in the absence of dynamic strain aging, obeys the power law

$$\sigma^* = \sigma_o^* \left(\frac{\dot{\epsilon}}{\dot{\epsilon}_o} \right)^{\frac{RT}{H^o}} \tag{1}$$

where σ^* is the effective stress, σ_o^* the effective stress at 0 K, $\dot{\epsilon}$ the applied strain-rate, $\dot{\epsilon}_o$ a material constant equivalent to the strain-rate that makes $\sigma^* = \sigma_o^*$ at any temperature, R the international gas constant, T the Kelvin temperature, and H^o a constant with energy units. The effective stress is defined by $\sigma^* = \sigma - \sigma_L$, where σ is the applied stress and σ_L the long range internal or athermal stress whose temperature dependence follows that of the tensile modulus. It can easily be shown that if the effective stress obeys Eq. 1, the activation enthalpy, in the thermally activated strain rate equation, $\dot{\epsilon} = \dot{\epsilon}_o \exp(-H/RT)$, is $H = H^o \ln(\sigma_o^*/\sigma^*)$. If the power law controls the effective stress, it is also easily demonstrated that the strain-rate sensitivity parameter, S, is

$$S = \frac{d\sigma}{d \ln\left(\frac{\dot{\epsilon}}{\dot{\epsilon}_o}\right)} = (RT/H^o) \times \sigma^*, \tag{2}$$

Note that S can be evaluated empirically with the aid of constant temperature strain-rate change experiments. However, it should be noted that the data points thus obtained involve a finite change in strain-rate usually of the order of five or ten times whereas Eq. 2 is based on an infinitesimal change in $\dot{\epsilon}$. This means that the experimental data points require a small adjustment in order to be compared with Eq. 2. This has been done

157

in Fig. 1(A). There is an alternative strain rate sensitivity parameter $n = d \ln \sigma^*/d \ln \dot{\epsilon}$ so that $S = n\sigma^*$ and a linear plot of n versus T should yield a straight line whose slope is R/H^o.

It is also true that taking the logarithm of both sides of Eq. 1 yields

$$\sigma^* = \ln \sigma_o^* + \frac{RT}{H^o} \ln \left(\frac{\dot{\epsilon}}{\dot{\epsilon}_o} \right) \tag{3}$$

Thus, the power law predicts that a $\ln \sigma^*$ vs. T plot should yield a straight line with a slope of $(R/H^o)\ln (\dot{\epsilon}/\dot{\epsilon}_o)$. This slope is negative because $\dot{\epsilon}$ is smaller than $\dot{\epsilon}_o$. A useful tool for analyzing experimental data with respect to the power law in Eq. 1 is a plot of the strain-rate sensitivity parameter S with respect to temperature, T. The S vs. T plot shown in Fig. 1(A) is that for the Ti A-70 data. Note that S is zero at 0 K, rises rapidly to a maximum at an intermediate temperature, and then decreases with increasing temperature. Both the temperature and magnitude of the maximum in S are significant. It has been shown (4,5) that, if there is sufficient data, the magnitudes of these parameters can be estimated from an empirical plot of the S-T data as in Fig. 1(A). Assuming a zero entropy of activation, the experimental plot of the S vs. T data can also be used to evaluate the internal stress at 0 K (5) i.e. σ_{E_o}, using the relation (2)

$$\sigma_{E_o} = \frac{\sigma_o - e\,\sigma_{T_B}}{1 - e\,(E_{T_B}/E_o)} \tag{4}$$

where σ_{E_o} is the internal stress at 0 K, σ_o the applied stress at 0 K, determined by extrapolation, e the base of natural logarithms, σ_{T_B} the applied stress at the temperature of the strain-rate sensitivity maximum, E_{T_B} the elastic modulus at the temperature of the strain-rate sensitivity maximum and E_o the value of the elastic
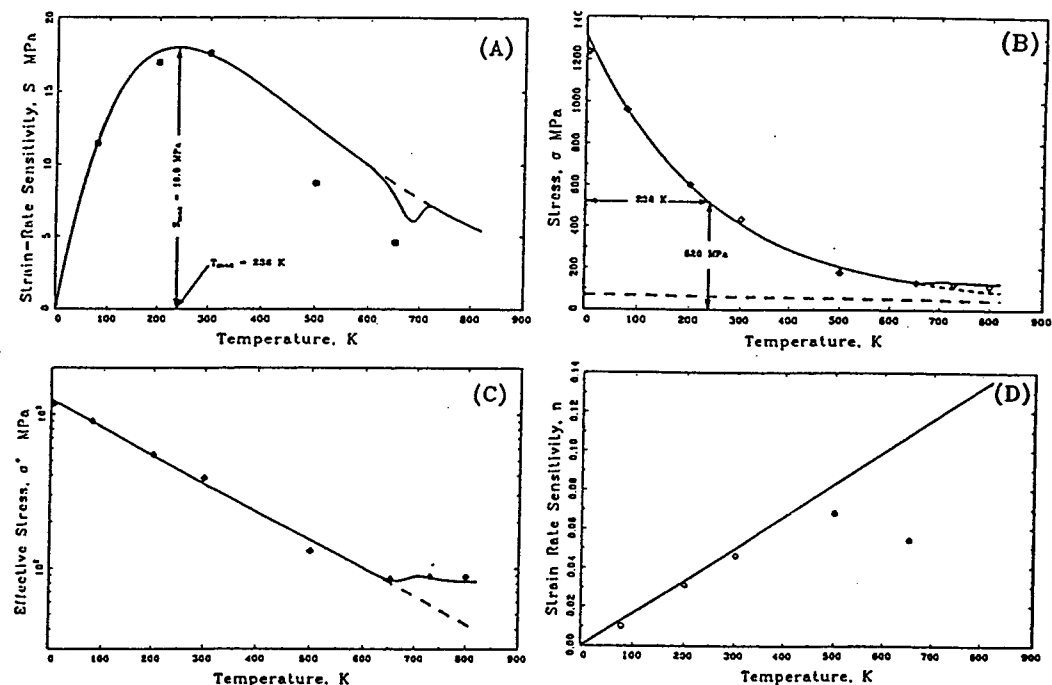
Figure 1. CP Titanium A-70. Grain Size 16μ. $\dot{\epsilon}= 3.34 \times 10^{-4}$. Data of K. Okazaki and H. Conrad, Acta Met., vol. 21, p. 1117 (1973). Plots for $H^o = 50,160$ J/mole and $\dot{\epsilon}_o = 3.41 \times 10^7$. (A) Strain Rate Sensitivity, S vs. T, (B) Flow Stress vs. T, (C) Log Effective Stress vs. T, (D) n vs. T.

modulus at 0 K. The flow stress at 0 K was estimated by extrapolation to be about 1,324 MPa. The 4.2 K flow stress data point would appear to be in disagreement with this extrapolation. However, at 4.2 K, plastic deformation involves serrated flow because, at this very low temperature, the flow stress falls rapidly with increasing temperature and the heat capacity of the metal is very low. Thus, as a metal starts to deform locally, the heat produced there causes a rapid drop in the flow stress which localizes the deformation. The excess plastic flow in this region causes work hardening which quickly stops the deformation. The entire sequence is then repeated over and over again. Thus, plastic flow at 4 K is discontinuous and difficult to relate to continuous flow so that flow stress measurements at 4 K are difficult to evaluate. The temperature dependence of the elastic modulus was assumed to be the same as that reported by de Meester, Doner, and Conrad (6) for Ti-6Al-4V an assumption consistent with the limited titanium modulus data in the literature. The Ti-6Al-4V modulus data covers the temperature range from 78 to 500 K and, within this region, Young's modulus varies nearly linearly with a slope $dE/dT = 0.0062$ GPa/K. In the following, this temperature dependence of the modulus was then assumed to hold between 0 and 800 K. With the aid of this information and Eq. 4, it was determined that $\sigma_{L_o} = 70$ MPa and that the internal stress between 0 and 800 K could be expressed by $\sigma_{L_o} = 70 - 0.0034\,T\,MPa$. The dashed line at the bottom of Fig. 1(B) shows the temperature variation of the internal stress as given by this latter equation.

Determination of the Power Law Parameters

It was mentioned earlier that the coordinates of the strain-rate sensitivity peak of the S vs. T diagram are important. This is because it has been demonstrated (1) that T_B is the negative reciprocal of the slope of the ln σ^* vs. T diagram. For these Ti A-70 data, as may be seen in Fig. 1(A), $T_B = 238$ K. Further,

$$T_B = -\frac{H^o}{R} \times \frac{1}{\ln\,(\dot{\epsilon}/\dot{\epsilon}_o)} \tag{5}$$

It can also be shown that if T_B is substituted into Eq. 2 one may obtain

$$S_{max} = \frac{\sigma_o^*}{e \times \ln\,(\dot{\epsilon}/\dot{\epsilon}_o)} \tag{6}$$

According to Fig. 1(A), $S_{max} = 18$ MPa and since $\dot{\epsilon}$, the applied strain-rate, was 3.34×10^{-4} s^{-1} and $\sigma_o^* = \sigma_o - \sigma_{L_o} = 1,324 - 70 = 1,254$ MPa the only unknowns in Eqs. 5 and 6 are H^o and $\dot{\epsilon}_o$. Solving Eqs. 5 and 6 simultaneously gives

$$H^o = 50,160 \text{ J/mol} \quad \text{and} \quad \dot{\epsilon}_o = 3.41 \times 10^7 \ s^{-1} \tag{7}$$

Discussion

The curves in Figs. 1(A) to 1(D) were drawn with a computer using the equations in this paper. The parameters involved in or determined by these equations are listed in Table 1. As may be seen in Fig. 1, the power law and its derived equations are in good agreement with the experimental A-70 titanium data up to about 500 K. Above this temperature there are deviations. However, at 500 K and a strain-rate of 3.34×10^{-4} s^{-1}, CP titanium begins to show evidence of dynamic strain aging and therefore a dynamic strain aging stress component, σ_{dsa}, should be added to the flow stress so that the total flow stress becomes $\sigma = \sigma^* + \sigma_L + \sigma_{dsa}$. Since titanium is a close packed hexagonal metal in which interstitial atoms are believed to occupy octahedral sites, the lattice strains that the interstitial atoms interstitial-subtitutional solute atom pairs that produce

TABLE 1

$\sigma_o = 1,324\,MPa$	$\dot{\varepsilon} = 3.34 \times 10^{-4}\,s^{-1}$
$\sigma_{g_o} = 70\,MPa$	$\dot{\varepsilon}_o = 3.41 \times 10^{7}\,s^{-1}$
$\sigma_g = 70 - 0.0033T\,MPa$	$H^o = 50,160\,J/mole$

ellipsoidal strain fields in the hcp crystal lattice (7,8) and stress induced reorientations of these i-s pairs are considered to involve the jumps of the interstitial atom. Furthermore, if it is assumed that the jump rate of the interstitial atoms are not significantly affected by the substitutional solute atom of the pairs, then it should be possible to use conventional volume diffusion data in the strain aging calculations (7). In this regard, the initial jump can be very rapid and analogous to the Snoek effect in bcc metals containing interstitials and therefore able to produce strain aging similar to Snoek strain aging in the bcc metals. On the other hand, the long range diffusion of interstitials to form pinning atmospheres around dislocations (i.e. Cottrell strain-aging in b.c.c. metals) is bound to be much slower as evidenced by the analogous case of strain aging in Nickel-200 containing interstitial carbon atoms (9). It is believed that in Ni-200 strain aging involves carbon atom-vacancy pairs and the long range strain aging has a time dependence of about $t^{1/7}$ as contrasted to the $t^{2/3}$ time dependence in Cottrell aging. Thus, it is believed that, in the present case, one should be able to ignore this latter form of strain aging and concentrate on the strain aging involving the initial reordering of the i-s pairs. The A-70 Ti used by Okazaki and Conrad had an average composition in ppm by weight of 2646 oxygen, 103 nitrogen, and 80 carbon. Because the oxygen concentration far exceeded that of the other two interstitials, it was decided to limit the strain aging calculations to a consideration of those due only to oxygen. The diffusion coefficient of oxygen in titanium is given by David, Beranger, and Garcia (10) as

$$D = D_o \exp\left(-Q/RT\right) \tag{8}$$

where D is the diffusion coefficient of oxygen in titanium, $D_o = 4.5 \times 10^{-5}\,m^2/s$, $Q = 201,000\,J/mol.$, $R = 8.415$ J/mol and T the Kelvin temperature. In a bcc. metal the internal friction or Snoek relaxation time of the interstitial atom can be related to its interstitial diffusion coefficient by the equation

$$D = \frac{\alpha\,a^2}{\tau_r} = \alpha\,a^2 v_r \tag{9}$$

where D is the interstitial atom diffusion coefficient, α a geometrical constant which for the bcc lattice is 1/36, a the bcc atom diameter, τ_r the Snoek torsion pendulum relaxation time and $v_r = 1/\tau_r$ the relaxation frequency. All interstitial atom jumps in the bcc lattice are equivalent. In the hcp lattice this is not true and one has to differentiate between jumps made in the basal plane and those occuring parallel to the c axis or normal to the basal plane (12,13,14,15). It is possible for interstitial atom of an interstitial-substitiutional atom pair to make both types of jumps. It has been demonstrated (15) that for data obtained with a torsion pendelum with a hcp metal wire the mean relaxation frequency for jumps of the interstitial atoms of i-s pair is given by

$$\overline{\lambda}_{i\text{-}s} = 3v_1 + v_2 \tag{10}$$

where $\overline{\lambda}_{i\text{-}s}$ is the mean relaxation frequency of a hcp metal as measured with a torsion pendulum while v_1 and v_2 are the jump frequencies of the interstitial atoms of i-s pairs in the basal plane and along the basal plane normal respectively. These jump frequencies are not the same but are probably related so that Moore (15) assumed

$$v_2 = \gamma v_1 \tag{11}$$

where γ is a constant which for oxygen jumps around substitutional impurities in several hcp metals was deduced empirically (15) to be close to 2.0. The basic problem now is to determine an equation relating the experimental diffusion coefficient for oxygen in titanium, D, to the mean relaxation frequency λ_{i-s} as determined using the vibration frequency at the internal friction maximum. This problem has been addressed by Moore (15) and involves the assumptions (1) that the relaxation is caused by the jumping of the interstitial atoms while the substitutional atoms remain immobile, (2) only interstitial atom jumps along the a and c directions are possible and, (3) all a jumps have the frequency, v_1, and all c jumps have the frequency, v_2. This led to the following equation

$$\overline{D} = \overline{\lambda}_{i-s} \; a^2 \; \frac{1 + \dfrac{\gamma}{12}\left(\dfrac{c}{a}\right)^2}{3 + \gamma} \tag{12}$$

where D is the oxygen diffusion coefficient, $\overline{\lambda}_{i-s}$ the mean interstitial atom relaxation frequency, a the distance between atom centers along a close packed direction in the basal plane, c the height of the hcp unit cell, and γ the constant defined in Eq. 11. When the values of the parameters $a = 2.950 \times 10^{-10}$ m, $c = 4.683 \times 10^{-10}$ m, $\gamma = 2.0$, $D_o = 4.5 \times 10^{-5}$ m^2/s and $Q = 2.01 \times 10^5$ $J/mole$ are inserted into Eq. 12, one obtains

$$\tau_{dsa_{i-s}} = 5.493 \times 10^{-16} \exp{(2.01 \times 10^5/RT)}\, s \tag{13}$$

The above relaxation time corresponds to that observed in a torsion pendulum. However, it has been found (16) that the relaxation time associated with bcc strain aging, τ_{dsa}, is normally about 1/4 that obtained with the torsion pendulum. This follows from the fact that the stress field near a dislocation is much higher than that normally existing in a torsion pendulum. Assuming that this ratio also applies to hcp strain aging one has

$$\tau_{dsa_{i-s}} = 1.373 \times 10^{-16} \exp{(2.01 \times 10^5/RT)}\, s \tag{14}$$

and in analogy with Snoek strain aging (1) we may write

$$\sigma_{dsa} = \sigma_{dsa_{max}} \times \exp\left(-\frac{(T-500)}{T_B}\right) \times \left(1 - \exp\left(-\frac{t_w}{\tau_{dsa_{i-s}}}\right)\right) \tag{15}$$

where t_w is the waiting time of the dislocation at an obstacle before thermal activation causes it to pass the obstacle, and $\tau_{dsa_{i-s}}$ the DSA mean relaxation time of an oxygen atom. There are two parameters in Eq. 13 that need to be evaluated t_w and $\sigma_{dsa_{max}}$. The former, t_w, was taken as 0.33 s so that the dynamic strain aging stress would conform to the fact that at a strain rate of 3.34×10^{-4} s^{-1} the oxygen dynamic strain aging component would become measurable at about 550 K in agreement with Santhanam's observations (17). It should also be pointed out that this waiting time compares well with the 0.1 s^{-1} value used in Ref. 1 which involved niobium specimens deformed at a strain rate of 1.1×10 s^{-1} since the ratio of the strain rates is the same as the ratio of the waiting times. The parameter $\sigma_{dsa_{max}}$ was taken as 11 MPa (normalized to 500 K, See Ref. (1)). When σ_{dsa} is added to the flow stress, one obtains the result shown in Figs. 1(B) and 1(C). In both figures note that adding the dynamic strain aging stress, σ_{dsa}, to $\sigma^* + \sigma_{\ell}$ accounts for the data points that lie above the $\sigma^* + \sigma_{\ell}$ curve in the plateau region. In this plateau region the value of $\sigma^* + \sigma_{\ell}$ is shown by a dashed line in each plot. It should also be pointed out that dynamic strain aging adds a component, S_{dsa}, to the strain-rate sensitivity. This may be determined by taking the derivative of σ_{dsa} with respect to $\ln \dot{\varepsilon}$ (See Eq. 15)

$$S_{dsa} = \frac{d\,\sigma_{dsa}}{d\,\ln\dot{\epsilon}} = -\,\sigma_{dsa_{max}} \times \exp\left(-\frac{(T-500)}{T_B}\right) \times \left(\frac{t_w}{\tau_{dsa_{ht}}}\right)$$
$$\times \exp\left(-\frac{t_w}{\tau_{dsa_{ht}}}\right) \tag{16}$$

Note that S_{dsa} is negative. The dip in Fig. 1(A) which shows the curve for the temperature dependence of the strain-rate sensitivity, S corresponds to the effect of oxygen DSA on the strain-rate sensitivity and helps to explain the low value of S at 650 K. The reason for the other low S data point at 500 K is unexplained at this time.

Summary

(1) Using the power law equation, $\sigma^* = \sigma_0^* \times (\dot{\epsilon}/\dot{\epsilon}_o)^{RT/H_o}$, the material parameters for a CP titanium system were evaluated with values $\sigma_0^* = 1,324\ MPa, \dot{\epsilon}_o = 4.01 \times 10^7\ s^{-1}$, and $H^\circ = 50,160\ J/mol$. The resulting power law equation was able to yield curves that followed the temperature dependence of the internal stress, the total flow stress and the strain-rate sensitivity S with considerable precision to approximately 500 K.

(2) It was also demonstrated that it is possible to explain quantitatively the plateau in the flow stress-temperature diagram above 500 K by assuming the flow stress in this region is the sum of three component stresses; the internal stress, the effective stress and a dynamic strain aging stress due to oxygen.

(3) It was further shown that a drop in the strain rate sensitivity parameter, S, at 650 K could be explained by the present treatment.

References

1. R. E. Reed-Hill and M. J. Kaufman, Accepted by *Acta metallurgica*.
2. R. E. Reed-Hill and Tuling Zhu, *High Temperature Materials*, 6, 93 (1984).
3. K. Okazaki and H. Conrad, *Acta metallurgica*, 21, 1117 (1973).
4. K. W. Qian and R. E. Reed-Hill, *Scripta metallurgica*, 16, 807 (1982).
5. C. V. Iswaran, R. E. Reed-Hill, V. Levit and M. J. Kaufman, *Scripta Metall.*, in press.
6. B. De Meester, M. Doner, and H. Conrad, *Met. Trans. A*, 6a, 65 (1975).
7. F. Povolo and E. A. Biscogni, *Acta Metall.*, 14, 711 (1966).
8. A. S. Nowick and B. S. Berry, *Anelastic Relaxation in Cryst. Solids*, p. 330, Acad. Press, Inc., New York (1972).
9. W. R. Cribb and R. E. Reed-Hill, *Met. Trans. A*, 8A, 71 (1977).
10. D. David, G. Beranger, and E. A. Garcia, *J. Electrochem. Soc.*, 130, 1423 (1983).
11. I. G. Ritchie and A. Atrens, *Jour. Nuclear Mats.*, 67, 254 (1977).
12. Y. A. Bertin, J. Parisot, and J. L. Gacougnolle, *Jour. Less Com. Mets.*, 69, 121 (1980).
13. I. G. Ritchie, H. E. Rossinger, and A. Atrens, *Jour. Nuclear Mats.*, 62, 1 (1976).
14. I. G. Ritchie and A. Atrens, *Jour. Nuclear Mats.*, 67, 254 (1977).
15. K. M. Browne, *Acta Met.*, 20, 507 (1972).
16. R. E. Reed-Hill, *Proc. Intl. Conf. Disloc. Modeling Phys. Systs.*, p. 163, Acta Metallurgica Inc, Oxford, (1981).
17. A. T. Santhanam, *University of Florida Thesis*, (1971).

THE INFLUENCE OF IRON ON THE PHYSICAL AND MECHANICAL PROPERTIES OF β-NiAl

Y.J. Lim, K.T. Hong, V. Levit and M.J. Kaufman
Dept. of Materials Science & Engineering. University of Florida. Gainesville, FL 32611

ABSTRACT

The influence of iron on the the microstructure and properties of B2 NiAl has been investigated using electrical resistivity, magnetic susceptibility, microhardness and transmission electron microscopy. The resistivity data suggest that quenched-in vacancies (1) enhance iron rearrangement at low temperatures (600-800 K) and (2) annihilate above 800 K. These effects depend strongly on Ni Al ratio and are greatest for Ni/Al=1. It is also shown that these data correlate directly with the results obtained using the other experimental techniques.

INTRODUCTION

The influence of iron on the mechanical properties (e.g., ductility) of NiAl has been the subject of considerable controversy over the past few years since Darolia[1] reported ductility enhancements in soft-oriented NiAl single crystals containing small additions of iron. gallium and molybdenum. This microalloying effect remains poorly understood in spite of the considerable amount of work aimed at elucidating it. Macroalloying with iron has also been investigated as a means of increasing ductility and toughness either by introducing a ductile second phase or by modifying the slip systems.[2,3]

In order to obtain a better understanding of the effects of iron on the properties of NiAl, a systematic study of its effects on both the physical and mechanical properties of NiAl has been undertaken. Of specific interest is the interaction of point defects (thermal and constitutional vacancies and anti-site atoms) with iron atoms and how point defect concentrations vary with iron content, substitution scheme (for Ni, for Al and for both Ni and Al) and temperature. Initially, the effects of thermal history on resistivity, magnetic properties and microhardness have been studied in an effort to provide insight as to how iron substitutes in the lattice and influences the overall defect behavior and mechanical properties

EXPERIMENTAL

The alloys used in this study (see Table 1) were prepared using 99.95% Ni shot, 99-99% Al pellets and 99.9% Fe all in weight percent by non-consumable arc melting and drop casting into a 12 mm diameter x 40 mm long copper chill mold. All castings were homogenized at 1473 K for 24 h in purified argon and then water quenched. Subsequently, each alloy was annealed for 20 min at successively increasing temperatures and then cooled to RT for the resistivity tests. The samples for resistivity measurements were cut into 1.1 mm thickness strips by electro-discharge machining (EDM). The resistance was measured by the four-point probe method at room temperature after the annealing treatments described above. Only changes in resistivity are reported since the absolute values depend not only on iron content but also on grain size and test temperature which varied around RT. For the magnetic susceptibility measurements. the vibrating sample method was used on cylindrical specimens 2 mm diameter by 6 mm long. Microstructural analysis was performed on selected samples using both optical and transmission electron microscopy (TEM). the latter using either a JEOL 4000FX or a JEOL 200CX microscope. The TEM samples were prepared by twin jet electropolishing in a solution of 10% perchloric acid-90% butoxyethanol solution at 0°C and 12 Volts. Finally, Vickers microhardness measurements were made using a Buehler Micromet II with a load of 0.5 kg.

Table I. Nominal composition of the alloys (atom %).

Alloy	Ni	Al	Fe
NiAl	50	50	
Ni 46Al	54	46	
Ni 54Al	46	54	
NiAl 0.5Fe	49.75	49.75	0.5
NiAl 3Fe	48.5	48.5	3
NiAl 6Fe	47	47	6
NiAl 12Fe	44	44	12
Ni 38Al 12Fe	50	38	12
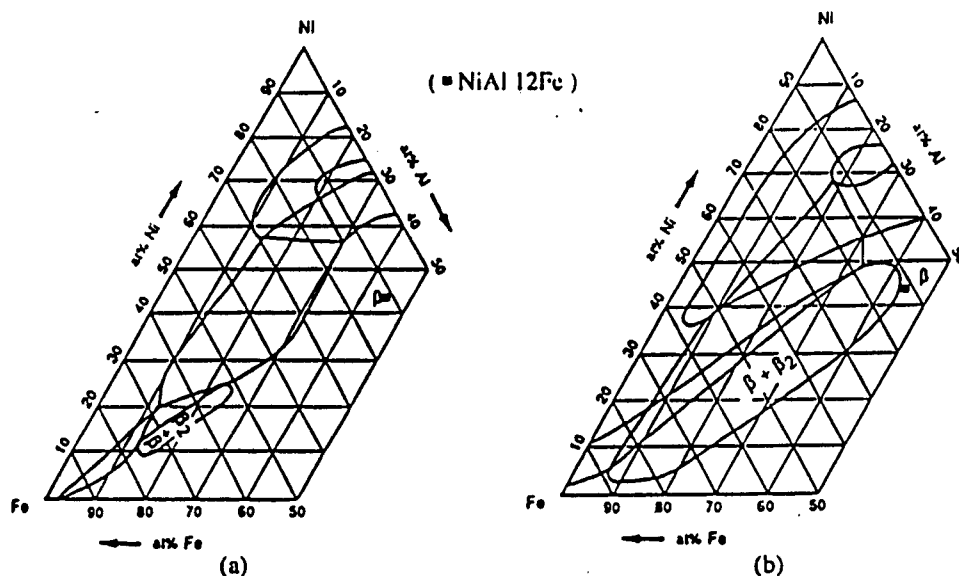
Fig. 1 Ni-Al-Fe ternary isotherms at 1223 K (a) and 1023 K (b). Note that NiAl-12Fe is located in the β single phase field at 1223 K and near the two phase $\beta + \beta_2$ phase field at 1023K[4].

RESULTS AND DISCUSSION

A plot of the RT resistivity vs. annealing temperature for the binary NiAl alloys is shown in Fig. 2. As can be seen, the resistivity decreased significantly starting at 800 K in the stoichiometric NiAl alloy upon annealing while the off-stoichiometry alloys showed little change except for a slight drop at considerably higher temperatures (~1050 K). Since NiAl is an intermetallic compound, it is anticipated that the electrical resistivity is determined primarily by the scattering of electrons by lattice defects. This suggests that the drop in resistivity in stoichiometric NiAl is probably related to vacancy annihilation. Likewise, the lack of a drop in the off-stoichiometric alloys suggests that the constitutional defects either hinder the formation of thermal vacancies or retard the annihilation process. Alternatively, this result may imply that the thermal vacancy concentration is negligible compared with the constitutional defects such that their annihilation during annealing has negligible effects on the overall resistivity. For example, if one assumes that the resistivity drop varies linearly with thermal vacancy concentration, then the Ni-

54Al alloy, which has approximately 8% constitutional vacancies, is not expected to display a significant change during annealing.

For the NiAl-12Fe alloy (Ni/Al = 1), the resistivity decreases rapidly at ~600K and reaches a minimum at 800K (Fig. 3). The other feature of interest is the relatively rapid increase in the resistivity above 800K which occurs at a considerably lower temperature than the less rapid increase observed above 1000 K in stoichiometric NiAl. TEM analysis of the 12Fe samples aged over this temperature range revealed the development of fine coherent precipitates which appeared to be disordered in nature (Fig. 4). This implies that the increase in resistivity at 800K in the NiAl-12Fe alloy correlates directly with the formation of disordered bcc precipitates in agreement with the phase diagrams in Fig. 1. However, a similar increase in the 6Fe alloy, which is believed to be within the single B2 phase field, makes this interpretation questionable. A more probable scenario involves the rearrangement of the iron atoms at the lower temperatures as suggested by Fu[5]. This rearrangement requires diffusion of vacancies and is probably enhanced by any quenched-in vacancies present as a result of the specific heat treatment employed. How this rearrangement leads to a drop in resistivity is unclear although it is possible that vacancy-iron binding occurs during the annealing treatment leading to the resistivity changes observed.
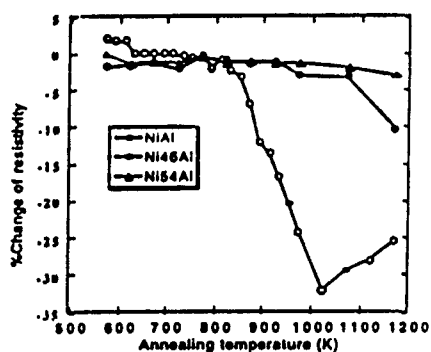
Fig. 2 Resistivity vs. annealing temperature   Fig. 3 Resistivity vs. annealing temperature
         in the binary NiAl alloys.   in the ternary Ni-Al-Fe alloys.
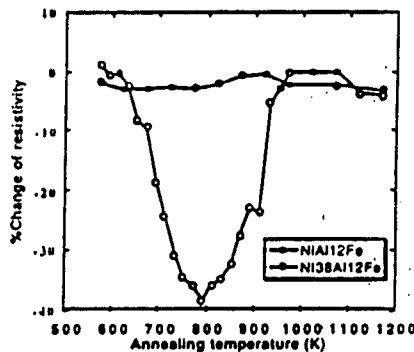
Consistent with the results in the off-stoichiometric binary alloys in which a similar drop in resistivity due to vacancy annihilation was not observed, the off-stoichiometric ternary alloys (e.g., Ni-38Al-12Fe in Fig. 3) also displayed no significant change in resistivity over the temperature range investigated (i.e., to 1200 K). This supports the contention that the thermal vacancies are a relatively small fraction of the total number of constitutional defects and/or that their annihilation has a negligible effect on resistivity. However, it is interesting to consider the effects of iron substitution scheme on site occupation and both thermal and constitutional defects. For example, the ternary substitutional atoms tend to favor one sublattice over the other in strongly ordered compounds such as NiAl. Previous studies indicated that iron prefers nickel sites due to the small difference in their atom sizes. More recently however, it was shown using the ALCHEMI technique[6] that, in alloys with Fe substituted for Ni, approximately 95% of the iron occupies Ni sites while in a Ni-40Al-10Fe alloy (iron substituted nominally for Al), 75% of the iron occupies Al sites. Furthermore, Fu[5] showed recently that the site occupation is a function of temperature which might explain some of the magnetic susceptibility measurements described below.

In an effort to further investigate these effects, alloys containing smaller iron additions (0.5, 3, and 6 atom percent) with Ni/Al = 1 were prepared and heat treated in a similar manner. Interestingly, the resistivity of the 0.5 Fe alloy decreased with annealing temperature although the effect was considerably less than in both the stoichiometric NiAl and NiAl-12Fe alloys (Fig.5).

The lack of a similar or intermediate change in the 3 Fe alloy was unexpected and the reason is unclear at this time. This may imply that the resistivity change in the iron-doped alloys depends on both the substitution scheme and the solute level in a complex manner.
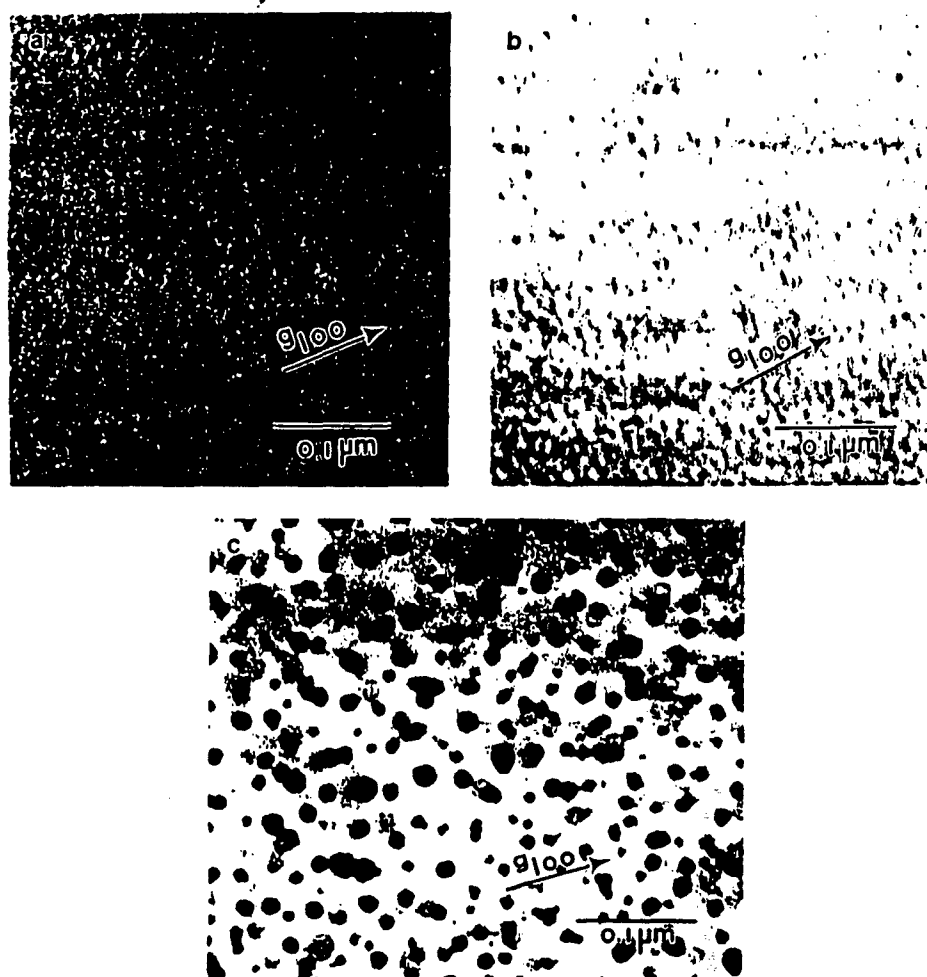
Fig. 4 Dark field transmission electron micrographs (g=100$_{NiAl}$) near B=[001] in the NiAl-12Fe alloy after (a) 1473 K, 24h/WQ ; (b) 1473 K, 24h/WQ + 873 K 20 min ; (c) 1473 K, 24h/WQ + 873 K 72h. The light regions are the B2 matrix and the dark regions correspond the disordered bcc precipitates

The results of the microhardness measurements are displayed in Fig. 6. For the three alloys investigated, the microhardnesses all appeared to show a peak in hardness after annealing at 873K although the small peak in the binary alloy is suspect and may be within the scatter of the experimental data. In addition, the iron-doped alloys were harder than binary stoichiometric NiAl consistent with the behavior expected based on previous studies. When the microhardness data are

plotted along with the resistivity data for the ternary Ni-Al-12Fe and Ni-38Al-12Fe alloys, it becomes clear that the hardness peak at 873 K in the "stoichiometric" iron-doped alloy is consistent with the increase in resistivity caused by the precipitation of the disordered β phase during annealing (see Fig. 7)
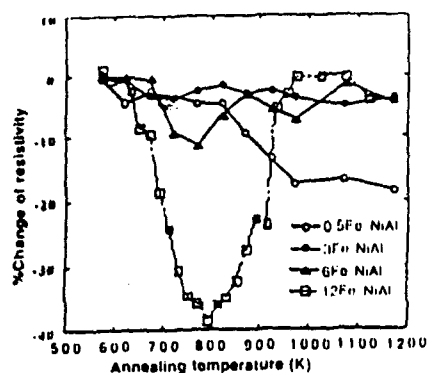
Fig. 5 Resistivity vs. annealing temperature for alloys with different Fe levels and Ni/Al-1
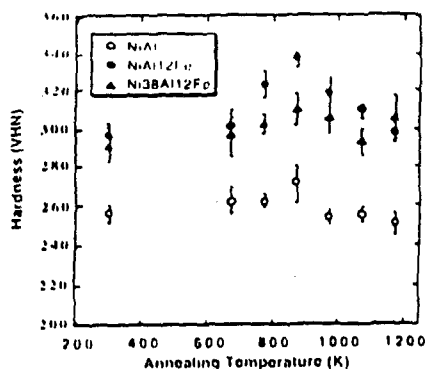
Fig. 6 Hardness of selected alloys vs. annealing temperature
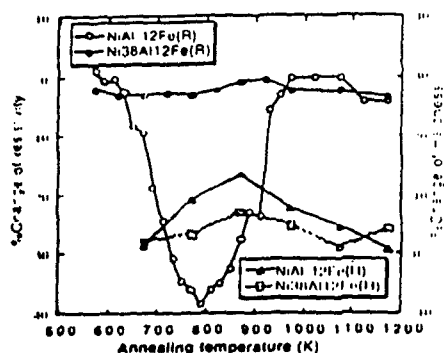
Fig. 7 Resistivity and hardness changes of NiAlFe alloys vs. annealing temperature
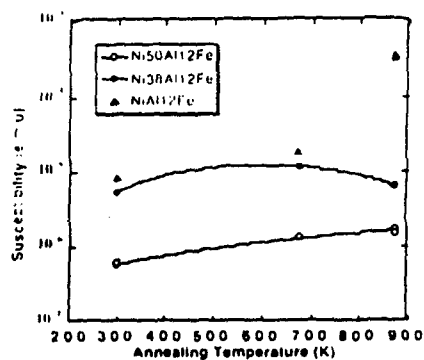
Fig. 8 Magnetic susceptibility of NiAlFe alloys vs. annealing temperature.

Finally, the magnetic susceptibility of the ternary alloys indicated that this technique is sensitive to minor changes in either precipitate formation or site occupation (i.e., Fe on Ni vs. Al sites). As seen in Fig. 8, the susceptibilities of the ternary NiAl-12Fe and Ni-38Al-12Fe alloys were about an order of magnitude higher than those of the Ni-50Al-12Fe (Fe for Ni) alloys. Furthermore, the NiAl-12Fe alloy becomes ferromagnetic above ~673 K while the other alloys' susceptibilities did not change significantly with annealing treatment. The reason for the change to ferromagnetic behavior is unknown although there are at least two plausible explanations. First of all, Kouvel[7] suggested that, in Fe-Al ordered compounds, the nearest neighbor site occupation influences the size of the magnetic domains than more distant sites. This probably explains the higher susceptibility of the Ni-38Al-12Fe alloy over that of the Ni-50Al-12Fe alloy since, in the former, it is more likely that the iron atoms will sit on Al sites and have Ni as their nearest neighbors and

thereby form more Fe-Ni bonds. The second possibility that may explain the increase in magnetic susceptibility involves the precipitation of a ferromagnetic second phase. Unfortunately, precipitates were not apparent after the 20 minute heat treatment at 873 K in spite of the change to ferromagnetic behavior. This may suggest that the precipitates are extremely fine and difficult to observe due to the small mismatch (a_{NiAl} = 0.2887 nm, a_{Fe}=0.2866 nm) and the similar crystal structure of the disordered and ordered phases. In either case, it is clear that further work is required to understand the behavior of this class of alloys.

SUMMARY

In binary NiAl alloys, only the stoichiometric alloy displays a significant drop in resistivity during annealing. This drop is believed to correspond to vacancy annihilation.

Iron leads to considerable resistivity changes when substituted for both elements (Ni/Al=1). It was speculated that this change is related to iron rearrangement and possble iron-vacancy binding in these alloys. For the other NiAlFe alloys, iron has little effect on resistivity and magnetic behavior.

The magnetic and microhardness properties of the iron-doped alloys displayed a similar effect to the resistivity indicating that iron has the greatest effect when Ni/Al = 1.

TEM analysis revealed the formation of bcc iron precipitates in the NiAl12Fe alloy when annealed at temperatures above 873K. These precipitates appear to account for the ferromagnetic properties and the changes in microhardness in this alloy.

ACKNOWLEDGEMENTS

REFERENCES

1. R. Darolia. D.F. Lahrman, and R.D. Field, Scripta. Metall. 26 1007-1012, 1992
2. A. Inoue, T. Masumoto, J. of Mater. Sci. 19, 3097-3106, 1984
3. S. Guha, P. Munroe, I. Baker, Scripta. Metall. 23, 897-900, 1989
4. A. J. Bradly and A. Taylor, Proc.Roy.Soc. London, 166, 1938, p. 353
5. J. Zou, C.L. Fu, presented at MRS Fall Meeting, Boston, MA, 1994 (this proceedings)
6. I. M. Anderson, A.J. Duncan, and J. Bentley, presented at MRS Fall Meeting, Boston, MA, 1994 (this proceedings)
7. J.S. Kouvel, Magnetism and Metallurgy edited by A.E.Berkowitz (Academic press N.Y and London 1969) pp. 523-575

THE INFLUENCE OF Mo ON THE PHYSICAL AND MECHANICAL PROPERTIES OF SINGLE CRYSTALLINE NiAl

J. Hu, V. Levit and M. J. Kaufman
Dept. of Materials Science and Engineering, University of Florida, Gainesville, FL 32611

ABSTRACT

The room and elevated temperature (300°C and 600°C) tensile properties of single crystalline NiAl with and without molybdenum additions have been investigated. It is shown that 0.2at% molybdenum has a considerable influence on the mechanical properties of NiAl and this influence is sensitive to heat treatment. At room temperature, the ductility of the Mo-doped alloy was higher than the binary NiAl after appropriate heat treatment. Furthermore, the elongations observed are highest at 300°C and are related to greater uniformity of deformation.

INTRODUCTION

NiAl alloys have drawn considerable attention in recent years owing to their potential application as high temperature materials. Unfortunately, stoichiometric NiAl and its alloys tend to be quite brittle at room temperature and weak at all temperatures; these deficiencies have prevented the application of these alloys. Many approaches have been attempted to increase the room temperature ductility. For example, the results reported by Darolia, et al. [1] suggest improvements in room temperature ductility in single crystalline NiAl microalloyed with Fe, Mo, and Ga. However, there is essentially no agreement concerning the role of these elements in spite of the considerable efforts to elucidate such behavior. Consequently, a further understanding of the mechanisms responsible for this increase should be beneficial to the development of NiAl alloys. Although the alloys microalloyed with iron have been studied to a significant extent [2,3], the Mo-doped NiAl alloys have been largely ignored due to the lesser ductility increase (1.9% vs. 5.9%) The purpose of the present work is to provide more insight into the effects of Mo on the physical and mechanical properties and microstructures of single crystalline NiAl. To accomplish this goal, the tensile properties of single crystalline stoichiometric NiAl and NiAl-0.2Mo (at%) after different heat treatments were measured. In addition, the fracture surfaces and microstructures were investigated by various methods.

EXPERIMENTAL

The feedstock materials used for growing single crystals were prepared from high purity elements by non-consumable arc melting under purified argon. Single crystals of stoichiometric NiAl and NiAl-0.2Mo were prepared by Bridgman growth in alumina crucibles and homogenized at 1300°C for 24 h followed by furnace cooling. The resulting crystals were oriented using the back reflection Laue method and tensile specimens were EDM cut with the tensile axis ~5° from <135>. These specimens were rectangular in cross section (1.4x2.2mm) with a gage length of approximately 12 mm. After EDM cutting, the specimens were heat treated in purified Ar. The heat treatment schedules were chosen based on the results of resistivity measurements made on high purity stoichiometric single crystalline NiAl and NiAl-0.2 Mo. All tensile specimens were electropolished in a 10% perchloric acid-90%methanol solution after heat treatment. Tensile tests were carried out on an Instron Model 1125 machine in

air at room temperature, 300°C and 600°C with a constant cross-head speed corresponding to an initial strain rate of $1 \times 10^{-4} \text{ s}^{-1}$.

TEM specimens were prepared by cutting 3.0 mm diameter rods by EDM from the bulk materials and then, after heat treatment, cutting into discs of 0.6 mm thickness using a low speed SiC saw before finally grinding to about 120 μm thick. The discs were then jet-polished with a solution of 70% ethanol, 14% distilled water, 10% butylcellusolve and 6% perchloric acid at 0°C. TEM analysis was conducted on a JEOL-200CX microscope and SEM analysis on a JSM-6400. The electrical resistivities were measured at 4.2K by standard potentiometric methods.

RESULTS

Tensile Behavior

The tensile properties and their dependence on heat treatment are summarized in Table 1. It is found that heat treatment has little effect on the tensile properties of stoichiometric NiAl at all three test temperatures. On the contrary, the properties of NiAl-0.2Mo appear to be sensitive to the heat treatment conditions when tested at room temperature and 300°C. When tested at room temperature, stoichiometric NiAl had a plastic elongation of about 2% and a yield stress of about 210 MPa regardless of the heat treatment procedures while NiAl-0.2Mo displayed smaller elongation and lower yield stress (~280 MPa) in the 1150°C quenched state and good ductility (~3.3%) and highest yield strength (~340 MPa) in the 600°C annealed state. Also worth noting is that NiAl-0.2Mo has the highest room temperature plastic elongation (~5.3%) and moderate yield stress (~180 MPa) in the 1300°C/FC state and appears to exhibit a yield point in the 300°C annealed state.

Upon testing at 300"C, stoichiometric NiAl exhibited large plastic elongations (~100%) with similar yield stresses while NiAl-0.2Mo also showed considerable elongation (50-70%) for

TABLE 1. Tensile test data on <135> oriented NiAl and NiAl-0.2Mo

Testing temperature	Alloy	Heat treatment*	0.2% Yield Strength, (MPa)	UTS (MPa)	Plastic Strain (%)
RT	NiAl	a	212	276	2.1
		b	219	285	2.1
		c	214	268	1.3
	NiAl-0.2Mo	a	273	280	0.6
		b	280	325	1.3
		c	339	459	3.3
		1300°C/FC	178	328	5.3
300°C	NiAl	a	109	291	110
		b	129	381	106
		c	96	298	100
	NiAl-0.2Mo	a	151	241	59
		b	142	324	66
		c	236	303	11
600°C	NiAl	a	43	61	40
		c	39	45	24
	NiAl-0.2Mo	a	190	216	24
		c	212	231	16

* (a) 1150°C/0.5h/WQ; (b) 1150°C/0.5h/WQ+300°C/1h/WQ; (c) 1150°C/0.5h/WQ+600°C/1h/WQ

samples after 1150°C/WQ(water quench) and after 1150°C/WQ+300°C/WQ. After 1150°C/WQ+600°C/WQ, the elongation of NiAl-0.2Mo dropped to about 10% and the yield strength increased by about 50% compared with the quenched samples. At 600°C, the heat treatment no longer had an effect on the mechanical properties of both NiAl and NiAl-0.2Mo. Both of them have limited elongation at about 20-40% but NiAl-0.2Mo has much higher yield strength (~200MPa) than stoichiometric NiAl (~40MPa).

Fracture Analysis

The fracture surfaces of the tensile specimens were investigated by SEM. The RT specimens showed typical cleavage features consisting of some flat areas and river patterns spreading out from the fracture origins (Fig. 1). It can be seen that the only apparent difference between the NiAl and NiAl-0.2Mo (after 1150°C/WQ+ 600°C/WQ) is that the latter has finer river patterns. At 300°C, the side surfaces of both alloys were quite "corrugated" consistent with

Fig. 1a. RT fracture surface of NiAl after
1150°C/0.5h/WQ+600°C/1h/WQ
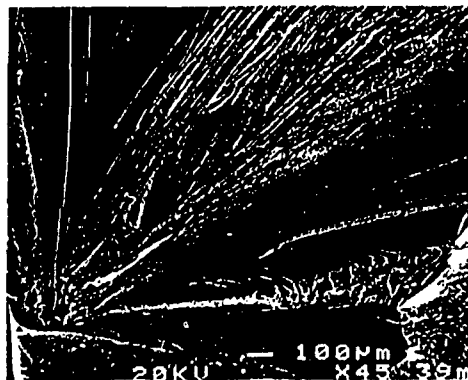
Fig. 1b. RT fracture surface of NiAl-0.2Mo after
1150°C/0.5h/WQ+600°C/1h/WQ
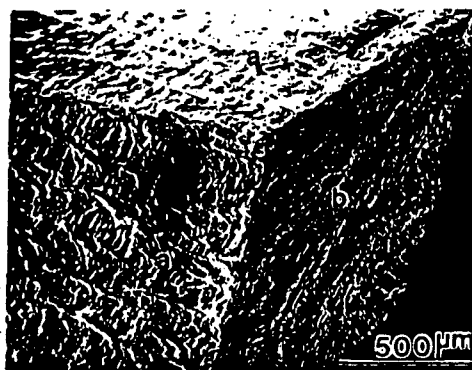
Fig. 2a. Side (a) and fracture (b) surface. NiAl-0.2Mo
(1150°C/0.5h/WQ+300°C/1h/WQ) at 300°C.
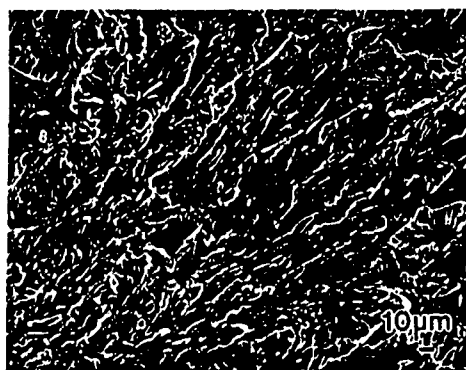
Fig. 2b. Fracture surface. NiAl-0.2Mo
(1150°C/0.5h/WQ+300°C/1h/WQ) at 300°C.

the large amount of non-uniform plasticity that occurred during plastic deformation (Fig. 2a). Higher magnification image of the fracture surfaces of these specimens revealed the fine

cleavage features indicating that the fractures were still cleavage-like on the microscale but the fracture was not via rapid crack growth. For the NiAl-0.2Mo alloy after 1150°C/WQ+ 600°C/WQ, which showed reduced elongation at 300°C, similar but less well developed deformation and fracture patterns were observed although part of the fracture surface consists of the river pattern more resembling those in the room temperature tested samples. The other characteristic of the 300°C test specimens was the uniform elongation prior to fracture. Specifically, it appeared that the whole gage length deformed uniformly prior to fracture (i.e., little necking) indicative of both a relatively high strain rate sensitivity factor and a large strain hardening coefficient. This was confirmed by the fact that the stress strain curve showed considerable resistance to localized necking. Finally, considerable necking was observed for both the binary and Mo-doped samples tested at 600°C indicating that the strain rate sensitivity was considerably lower; this is consistent with the recent measurements of Weaver, et al. [4].

Electrical Resistivity

The dependence of electrical resistivity on isochronal annealing is shown in Fig. 3 where it can be seen that both alloys display a substantial drop in resistivity presumably due to the annihilation of thermal vacancies [5,6]. Furthermore, the drop in the quenched-in resistivity value occurs about 150°C lower (peak occurred at 525°C) in NiAl-0.2Mo compared with the stoichiometric NiAl. While the reason for these enhanced kinetics is unclear, it may be related to the fact that α-Mo precipitates are observed in the quenched ternary alloys and that these precipitates coarsen during annealing (see following section) and act as sinks for the excess vacancies.
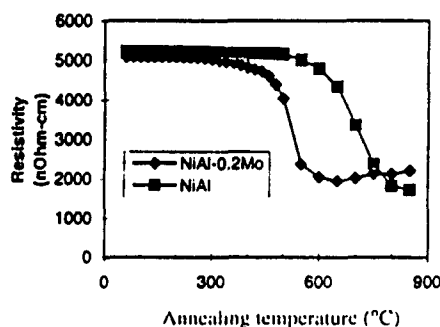
Fig. 3. Change of resistivity vs. annealing temperature after 1150°C quenching.

TEM Observations

Samples given similar heat treatments to the tensile specimens were examined by TEM. First of all, fine α-Mo precipitates were observed in essentially all NiAl-0.2Mo samples indicating the low solubility of Mo in NiAl. Quenching from 1150°C was insufficient to prevent this precipitation indicating that the room temperature solubility of Mo in NiAl is much less than 0.2at%, in agreement with [7,8]. It is also apparent from these micrographs that the α-Mo precipitates remain coherent with the NiAl matrix in spite of their considerable misfit. In addition, it appears that the α-Mo precipitates tend to form in rows parallel to <100> or in sheets parallel to {100}(Fig. 4a). While the reason for this alignment is unclear, it may be related to the large misfit and the fact that the NiAl matrix exhibits strong elastic anisotropy with the <100> being an elastically soft direction (i.e., coherency stress effect). Similar precipitate alignment has been reported in NiAl-Cr alloys by Cotton, et al. [9] although no explanation was provided.

While the 300°C annealing of the as-quenched sample did not appear to influence the microstructure, there was some apparent coarsening of the α-Mo precipitates at 600°C.

300

Furthermore, the coarsening speed depends on the quenching temperature as is apparent in Fig. 4b-4c. Similar heat treatments on the stoichiometric NiAl produced little apparent microstructural differences except that seemingly more dislocation debris, loops and voids were apparent after the 600°C anneal.

Fig. 4. α-Mo precipitates in NiAl-0.2Mo after (a) 1150°C/2h/WQ; (b) 1150°C/2h/WQ+600°C/2h/WQ and (c) 1300°C/2h/WQ+ 600°C/2h/WQ.

DISCUSSION

As noted above, the yield strength of the Mo-doped NiAl was higher than that of stoichiometric NiAl at all temperatures after similar heat treatments, in agreement with [1,10]. Furthermore, Mo appears to enhance the room temperature ductility after appropriate heat treatments (see Table 1) consistent with the report by Darolia, et al. [1]. One interesting observation made in the present study is that heat treatment effects both the strength and ductility of the Mo-doped material much more than in binary NiAl. Specifically, the Mo-doped material exhibited better room temperature ductility only after annealing at 600°C or after furnace cooling from high temperatures[*]. At room temperature, the Mo-doped alloy showed simultaneous increases in both yield strength and plastic elongation as the annealing temperature increased.

The resistivity measurements in Fig. 3 indicated that the quenched-in thermal vacancies started to anneal out at about 525°C and 675°C, respectively, for NiAl-0.2Mo and NiAl quenched from 1150°C. Thus, the Mo appears to accelerate the resistivity drop during annealing and hence the vacancy annihilation process. Likewise, the strengthening effect of Mo may be due to either solid solution strengthening by Mo or precipitation hardening. TEM observations indicated that the α-Mo precipitates were actually coarsening during the 600°C anneal indicating that the increase in yield stress at room temperature with annealing temperature for NiAl-0.2Mo is more likely a contribution of α-Mo precipitates as both the thermal vacancy and Mo concentrations in the NiAl matrix should decrease during annealing. The heat treatment carried out in this study seemed to have negligible effects on the mechanical properties of NiAl (see Table 1). This is in good agreement with the electrical resistivity measurements which indicated negligible vacancy annihilation below 675°C.

It has been suggested that the enhancement of room temperature ductility of Mo in NiAl could be due to the gettering of impurity atoms by Mo [1]. The results in this work suggest that it

---

(*) Due to the fact that specimens of rectangular cross section are more sensitive to surface defects than cylindrical specimens, premature fracture may occur leading to lower elongation values for some specimens. More work is underway to clarify this issue.

might also be possible that the enhancement is due to dislocation-particle or crack-particle interactions since the largest enhancement in the room temperature ductility was obtained after either the 600°C anneal or the furnace cool from 1300°C; both samples have a larger volume percentage of precipitates and less Mo in solution. Furthermore, the fracture surface displayed finer river patterns in the NiAl-0.2Mo with enhanced room temperature ductility. Apparently, more detailed work on the analysis of the aging and coarsening behavior of NiAl-0.2Mo as well as determination of Mo interactions with vacancies and impurity interstitials would be helpful in understanding what mechanism is responsible for the enhancement of ductility.

As seen in Table 1, stoichiometric NiAl exhibits very large elongations at 300°C. These results are in good agreement with those of Takasugi. et al. [11,12] obtained for soft oriented NiAl tested at similar temperatures. The Mo-doped materials also showed large elongations (50-70%) at 300°C although less than those of NiAl after similar heat treatments. The fracture surface analysis showed that, at 300°C, the cleavage features for NiAl-0.2Mo and NiAl are similar which suggests that, at this temperature, Mo addition does not change the mechanisms of deformation and fracture. The lower elongation of the Mo-doped sample may be related to its higher yield stress, a higher brittle-to-ductile transition temperature, and/or some effect due to the presence of the α-Mo precipitates.

SUMMARY

The influence of molybdenum on the mechanical properties of single crystalline NiAl has been studied by comparing the tensile behavior of single crystalline NiAl-0.2Mo with that of NiAl after various heat treatments. Unlike stoichiometric NiAl, the tensile behavior of NiAl-0.2Mo appears to be sensitive to the heat treatments used in the present study. After initially quenching from 1150°C, the yield stress of NiAl-0.2Mo increased with increasing annealing temperature for those samples tested at room temperature and 300°C. Mo also appears to enhance room temperature ductility after appropriate heat treatment although the mechanism for this enhancement remains unclear.

ACKNOWLEDGMENTS

REFERENCES

1. R. Darolia, D. F. Lahrman and R. D. Field, *Scripta Metall. Mater.* 26, 1007 (1992).
2. R. D. Field, D. F. Lahrman and R. Darolia, *MRS Symp. Proc.* 288, 423 (1993).
3. M. A. Morris, J. -F. Perez and R. Darolia, *Phil. Mag.* 69A, 485 (1994).
4. M. L. Weaver, V. Levit, M. J. Kaufman and R. D. Noebe, *MRS Symp. Proc.* (this proceedings).
5. J. E. Eibner, H. -J. Engell, H. Schultz, H. Jacobi and G. Schlatte. *Phil. Mag.* 31, 739 (1975).
6. Y. J. Lim, K. T. Hong and V. Levit and M. J. Kaufman, *MRS Symp. Proc.* (this proceedings).
7. P. Krishnan and M. J. Kaufman, *Metall. Trans.* 25A, 2111 (1994).
8. P. R. Subramanian, M. G. Mendiratta, D. B. Miracle and D. M. Dimiduk, *MRS Symp. P roc.* 194, 147 (1990).
9. J. D. Cotton, R. D. Noebe and M. J. Kaufman, *Intermetallics* 1, 3 (1993).
10. M. L. Weaver, M. J. Kaufman and R. D. Noebe, *Scripta Metall. Mater.* 29, 1113 (1993).
11. T. Takasugi, S. Watanabe and S. Hanada, *Mat. Sci. Eng.* A149, 183 (1992).
12. T. Takasugi, J. Kishino and S. Hanada, *Acta Metall. Mater.* 41, 1009 (1993).

The effects of interstitial content, heat treatment, and prestrain on the tensile properties of NiAl

M.L. Weaver[a], R.D. Noebe[b], J.J. Lewandowski[c], B.F. Oliver[d], M.J. Kaufman[a]

[a]*University of Florida, Gainesville, FL 32611-2066, USA*
[b]*NASA Lewis Research Center, Cleveland, OH 44135, USA*
[c]*Case Western Reserve University, Cleveland, OH 44106, USA*
[d]*University of Tennessee, Knoxville, TN 37996, USA*

Abstract

The tensile stress–strain response of polycrystalline NiAl was studied as a function of purity and pretest treatment (annealing and/or prestrain). After annealing at 1100 K for 7200 s (i.e. 2 h) followed by furnace cooling, high-purity and nitrogen-doped alloys exhibited continuous yielding, while conventional-purity or carbon-doped alloys exhibited a distinct yield point and Lüders strain. Prestrain by hydrostatic pressurization removed the yield point, but it could be reintroduced by further annealing treatments. Yield points could be reintroduced more rapidly if the specimens were prestrained uniaxially rather than hydrostatically, owing to the arrangement of dislocations into cell structures during uniaxial deformation. The time dependence of the strain aging events followed a $t^{2/3}$ relationship. In total, these results suggest that the yield points observed in polycrystalline NiAl result from the pinning of mobile dislocations by interstitials, specifically carbon, i.e. classic static strain aging.

Keywords: Heat treatment; Tensile properties; Nickel; Aluminium

1. Introduction

Several aspects of strain aging have been identified as playing a role in the deformation of polycrystalline and single-crystal NiAl. They are the occurrence of yield points and serrated stress–strain curves [1–6], strain rate sensitivity minima [7,8], yield stress plateaus as a function of temperature [9] and flow stress transients on changes in strain rate [8,10]. In addition, extensive work by Margevicius and co-workers [3,11–13] has shown that a sharp yield point can be formed in binary NiAl following annealing at 1100 K and furnace cooling. This yield point can be removed by subsequent prestraining of the material by hydrostatic pressurization prior to testing, and recovered by aging the prestrained material for 7200 s (i.e. 2 h) at 673 K. Similarly, Pascoe and Newey [7] observed the formation of room-temperature yield points in near-stoichiometric NiAl annealed for 3600 s (1 h) at 350 K following a uniaxial prestrain. Despite these observations, no complete investigation of classical strain aging has been conducted on ordered bcc intermetallic

alloys. The purpose of this document is to provide a preliminary description of the interrelated effects of interstitial content, heat treatment and prestrain on the tensile behavior of polycrystalline NiAl.

2. Experimental details

NiAl in the form of (a) a conventional-purity induction-melted casting (CP-NiAl), (b) a low-interstitial high-purity zone refined ingot (HP-NiAl), (c) a nitrogen-doped powder (NiAl-N), and (d) a zone-leveled carbon-doped ingot (NiAl-C) were the basic starting materials used in this investigation. All starting materials were extruded at 1200 K at either a 12:1 or 16:1 reduction ratio. Descriptions of the equipment and processes used to fabricate the high-purity and doped alloys are presented elsewhere [14–16].

Chemical analyses of the various extrusions were conducted at the NASA Lewis Research Center by the following techniques, deemed to be the most accurate for the particular elements. Ni and Al were determined

using analytical wet chemistry/titration techniques. Oxygen, nitrogen, carbon and sulfur contents were determined by combustion techniques using LECO oxygen/nitrogen and carbon/sulfur determinators.

Round button-head tensile specimens were ground from the extruded rods so that the gage lengths of the samples were parallel to the extrusion direction. Sample dimensions were 3.1 mm for the tensile gage diameters and 30.0 mm for the tensile gage lengths. Prior to testing, all samples were electropolished in a 10% perchloric acid–90% methanol solution that was cooled to 208 K. Tensile tests were performed on an Instron Model 1125 load frame at a constant cross-head velocity corresponding to an initial strain rate of 1.4×10^{-4} s^{-1}. All tests were performed in air at 300 K. True stress–strain data were calculated from the load–time plots, and yield stresses were determined by the 0.2%-offset method.

The tensile testing was accomplished in three steps. First, baseline mechanical properties were determined for all four alloys by testing them as follows: (a) as extruded, (b) as extruded + 1100 K/7200 s/furnace cooling (FC); and (c) as extruded + 1100 K/7200 s/FC + pressurized to 1.4 GPa. The heat treatment temperature and prestrain pressurization treatment were selected based on the observations of Marge-vicius and co-workers [3,11–13]. Second, a series of CP-NiAl specimens, having received treatment (c), were annealed at temperatures ranging from 500 K to 1100 K for up to 7200 s followed by FC, air cooling (AC) or water quenching (WQ) to room temperature to establish the optimum conditions for studying the kinetics of strain aging in NiAl. A more detailed accounting of the treatments employed will be provided in the Results and Discussion sections.

Finally, the kinetics of strain aging were investigated using the classic yield-point return technique whereby tensile specimens in the as-extruded condition were prestrained approximately 0.2%, unloaded, aged in situ on the load frame for aging times varying between 60 s and 113000 s (30 h), and then tested in tension at room temperature. This test method allows specimen alignment to be maintained, and allows the stress level to be kept effectively constant during aging. After aging, the specimens were cooled by removing the furnace from the test frame and passing a forced stream of air over the specimen and the tensile grips. This method of cooling resulted in average temperature drops of 500 to 1000 K during the first minute of cooling.

The parameters used to evaluate the kinetics of strain aging are illustrated in Fig. 1. These include the upper yield stress increment $\Delta\sigma_u = \sigma_u - \sigma_a$, the lower yield stress increment $\Delta\sigma_L = \sigma_L - \sigma_a$, and the Lüders strain ε_L.

Fig. 1. Definition of strain-aging parameters.

Table 1
Compositions of extruded NiAl alloys (at.%)

Alloy (heat)	Ni	Al	O	N	C	S
CP-NiAl (L2971)	50.09	49.70	0.055	<0.0009	0.0147	<0.0007
HP-NiAl (L2987)	49.91	50.07	0.003	<0.0009	0.0043	<0.0007
NiAl-C (L2988)	50.18	49.77	0.003	<0.0009	0.0092	<0.0007
NiAl-N (P1810)	50.07	49.70	0.035	0.0904	0.0057	<0.0007

3. Experimental results

3.1. Composition and microstructure

Chemical analyses of the four alloys are shown in Table 1. Within experimental accuracy (±0.2 at.% for Ni and Al), the Ni and Al contents of the four alloys are not significantly different from each other. The major differences between the materials are the carbon, oxygen and nitrogen contents.

Other than differences in grain size and the presence of semi-continuous stringers of nanometer-size nitride precipitates along prior particle boundaries in NiAl-N [16], all of the NiAl grain structures were similar as observed using optical microscopy. The microstructures were fully dense, consisting of recrystallized and equiaxed grains with the average linear intercept grain sizes reported in Table 2. The grain sizes of the HP-NiAl and NiAl-C alloys, which were prepared by

extruding single crystals, are consistently larger than those of the cast and extruded CP-NiAl or the powder-processed NiAl-N.

3.2. Mechanical properties

Baseline mechanical properties were established by tensile-testing specimens of all four alloys in the as-extruded condition, following an anneal of 1100 K/7200 s/FC, and following an anneal of 1100 K/7200 s/FC plus pressurization to 1.4 GPa. These results are summarized in Table 3. Immediately obvious from Table 3 is that the yield stress of each

alloy generally decreased following the 1100 K/7200 s/FC anneal. In addition, it is obvious that further decreases in yield stress can be achieved in the CP-NiAl and NiAl-C alloys if the specimens are hydro-statically pressurized at 1.4 GPa, whereas no decrease is observed in the powder-processed NiAl-N alloy or the HP-NiAl material. Interestingly, even though the yield stress could be lowered by annealing and in some cases pressurizing, these treatments had no obvious influence on the tensile ductility.

Typical room-temperature true stress–plastic strain curves for the as-extruded alloys are shown in Fig. 2. The HP-NiAl, NiAl-C and NiAl-N alloys exhibited continuous yield behavior. The CP-NiAl alloy, how-ever, exhibited discontinuous yield behavior. Similar discontinuous yield behavior has been previously reported for conventional-purity binary NiAl [3,11–13,16–19]. Following pressurization at 1.4 GPa, only continuous yielding was observed in the four alloys. However, if pressurized specimens were subsequently annealed at 1100 K/7200 s/FC, pronounced yield points and yield plateaus were observed in CP-NiAl and NiAl-C, whereas only con-tinuous yielding was still observed in HP-NiAl or in NiAl-N. Typical true stress–strain curves for the pressurized plus annealed alloys are shown in Fig. 3.

Table 2
Grain size of extruded NiAl alloys

Alloy	Reduction ratio[a]	Grain size (μm)
CP-NiAl (heat L2971)	16:1	18.7 ± 1.5
HP-NiAl (heat L2987)	12:1	51.5 ± 2.3
NiAl-C (heat L2988)	12:1	45.6 ± 4.0
NiAl-N (heat P1810)	16:1	4.0 ± 0.3

[a]All alloys extruded at 1200 K.

Table 3
Baseline tensile properties of NiAl alloys

Material	Condition[a]	0.2% yield stress (MPa)	Fracture stress (MPa)	Ductility (%)	Observations[b]
CP-NiAl	As-extruded	269	379	2.11	YP
	As-extruded	275	368	1.83	YP
	Annealed/FC	184	301	2.08	UYP
	Annealed/FC	197	228	1.04	UYP
	Annealed/AC	154	309	2.26	Evidence of YP
	Annealed/WQ	143	228	1.13	CY
	Pressurized	154	288	1.86	CY
	Pressurized	159	317	1.81	CY
	Pressurized	154	322	2.16	CY
HP-NiAl	As-extruded	166	214	0.79	CY
	As-extruded	157	235	1.16	CY
	Annealed/FC	98	174	1.17	CY
	Pressurized	118	176	0.92	CY
NiAl-C	As-extruded	170	201	0.59	CY
	Annealed	113	157	0.68	YP
	Pressurized	96	171	0.98	CY
NiAl-N	As-extruded	298	409	1.32	CY
	As-extruded	297	476	2.20	CY
	Annealed/FC	265	468	2.45	CY
	Pressurized	266	434	2.16	CY
	Pressurized	274	352	1.03	CY

[a]Annealed/WQ = as-extruded + 1100 K/7200 s/WQ; annealed/AC = as-extruded + 1100 K/7200 s/AC; annealed/FC = as-extruded + 1100 K/7200 s/FC; pressurized = as-extruded + 1100 K/7200 s/FC + pressurize 1.4 GPa.
[b]UYP = discontinuous yielding, upper yield point, sharp yield drop; YP = discontinuous yielding, small yield drop or plateau; CY = continuous yielding.

Fig. 2. Typical room-temperature true stress–plastic strain curves for as-extruded NiAl alloys.

Fig. 4. $\ln \Delta \sigma_u$ vs. $\ln t$ for CP-NiAl specimens. Specimens were prestrained uniaxially in tension. The least-squares parameters are indicated on the figure.

Fig. 3. Typical room-temperature true stress–plastic strain curves for NiAl alloys following hydrostatic prestraining plus subsequent annealing at 1100 K/7200 s/FC.

3.3. Influence of prestraining and annealing on baseline properties

In order to determine whether the observed yield points resulted from the hold at, or cooling from, the annealing temperature, specimens of CP-NiAl previously prestrained hydrostatically were annealed at 1100 K/7200 s followed by AC or WQ. After WQ, only continuous yielding was observed, while after AC there was some evidence of a yield plateau, which initially suggests that the yield points observed following FC are the result of the pinning of dislocations by mobile solute atoms during cooling through lower temperatures. As a result, annealing experiments were initiated at lower temperatures to determine the critical temperature for the migration of solute atoms to dislocations. It was observed that, following hydrostatic prestraining, yield plateaus formed in CP-NiAl following anneals of 700 K/7200 s/FC but not following anneals of 500 K/7200 s/FC. Conversely, if the speci-

mens were prestrained uniaxially, notable yield points formed readily after as little as 900 s (15 min) at 522 K and in as little as 60 s (1 min) at 700 K.

3.4. Kinetics of strain aging

In-situ static strain aging experiments were conducted, primarily on uniaxially prestrained samples. Single specimens were often aged several times to obtain a $\Delta\sigma_u$–time relationship. A specimen previously tested or prestrained uniaxially was given a recovery anneal, typically 1100 K/1800 s (30 min)/AC, prestrained approximately 0.2%, aged in situ and re-tested at room temperature. When this type of testing is adopted, the yield point exhibited in the undeformed material can be recovered, as can the yield point increment observed during the previous test. This means that it is possible to recover the dislocation structure and produce a reproducible $\Delta\sigma_u$ following the same strain aging (i.e. prestrain + annealing) treatment, justifying the use of multiple deformation experiments on single samples.

The time dependence of the flow stress increment $\Delta\sigma_u$ is shown in Fig. 4. The shapes of the aging curves up to the maximum value of $\Delta\sigma_u$ are comparable to similar curves reported for bcc metals [20]. Assuming $\Delta\sigma_u$ is proportional to the amount of solute segregating to dislocations, $\Delta\sigma_u$ will increase proportionally with $t^{2/3}$ during the early stages of aging. Later the dislocations will become saturated, leading to a leveling-out of $\Delta\sigma_u$ or to a decrease due to precipitation. The strain-aging time exponent, as determined by least-squares analysis of the data in Fig. 4, is in the range 0.57 to 0.67, which is close to the theoretical value of 2/3 predicted by Cottrell and Bilby [21]. In confirmation of this result, $\Delta\sigma_u$ is plotted versus $t^{2/3}$ in Fig. 5, demonstrating the satisfactory fit. Although experiments were

Fig. 5. Plots of $\Delta\sigma_u$ vs. $t^{2/3}$ for CP-NiAl.
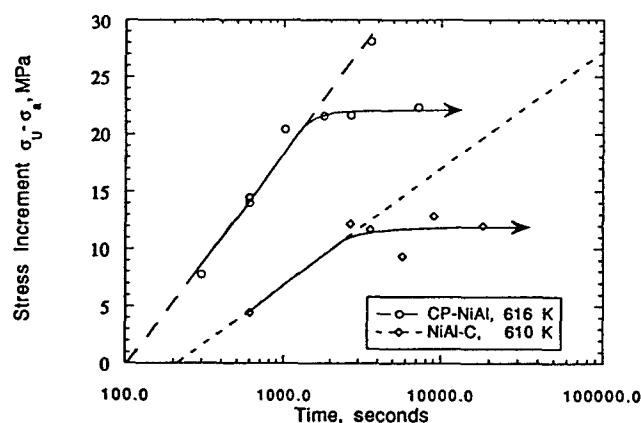
Fig. 6. Plot of $\Delta\sigma_u$ vs. $\ln t$ for CP-NiAl and NiAl-C at 616 K and 610 K respectively.

only performed at 610 K for NiAl-C, a similar trend of higher $\Delta\sigma_u$ with increasing aging time was observed. In addition, the time exponent was found to be 0.59, in agreement with the observations for CP-NiAl.

The $\Delta\sigma_u$ vs. log time data for CP-NiAl and NiAl-C that were aged for various times at 616 and 610 K, respectively, are plotted together in Fig. 6 to illustrate the influence of carbon concentration on the yield-point return in NiAl. A significant difference in the magnitudes of the $\Delta\sigma_u$ values is evident, as is an increase in the time required for yield points to form in NiAl-C. In addition, the saturation stress increment is also a function of C content, as would be expected at low C levels.

In efforts to establish a mechanism for static strain aging in NiAl, apparent activation energies corresponding to specific time-dependent aging events (i.e. the activation energy for the return of the lower yield stress was determined where the logarithmic time dependence was exhibited for the times required to achieve a variety of stress increases) were deduced by

applying the Arrhenius equation. On this basis, an activation energy for the return of a lower yield point in CP-NiAl was determined to be approximately in the range 72 to 76 kJ mole^{-1} (approximately 0.75 to 0.79 eV), which corresponds to the activation energies for the migration of interstitials in many bcc transition metals [22]. To check the Arrhenius calculation, the activation energy was also determined by the method used by Hartley [23]. This method entails taking the slopes S_1 of the plots of $\Delta\sigma_u/0.5(\sigma_u+\sigma_a)$ vs. $t^{2/3}$ and plotting $\ln(S_1 T^{2/3})$ vs. $2/(3RT)$. Using this method, an activation energy of 70 kJ mol^{-1} (0.73 eV) was determined, which is in good agreement with the value determined using the Arrhenius method.

4. Discussion

4.1. Species responsible for strain aging in NiAl

Determination of the species responsible for strain-aging effects in NiAl can be made by examination of the aging behavior of all four alloys. Discontinuous yielding, in the form of yield points and yield plateaus, was observed in CP-NiAl and NiAl-C, while none was observed in HP-NiAl or NiAl-N following heat treatments known to produce yield points in conventional cast and extruded NiAl [11]. In NiAl-N, the oxygen and nitrogen contents are much higher than those observed in CP-NiAl, which suggests that nitrogen and oxygen are not the species responsible for the yield points observed in NiAl. In addition, no yield point phenomenon was observed in HP-NiAl. In NiAl-C, it was observed that longer aging times are required to achieve the same yield increment as observed in CP-NiAl. It is believed that this behavior is a result of the significant reduction in the concentrations of interstitials, particularly C. Since there is less carbon to pin dislocations in NiAl-C, the carbon present must, presumably, diffuse longer distances to cause pinning.

4.2. Influence of prestraining

As noted in Section 3, the return of a sharp yield point is much more rapid when the specimen has been prestrained uniaxially as opposed to hydrostatically. In uniaxially prestrained NiAl, dislocations can cross-slip easily, forming cell structures [16,24] that result in high work-hardening rates at room temperature compared to many metals. As a result, the dislocations are in essence pinned. In contrast, samples pressurized hydrostatically show an even distribution of dislocations which are not bound in a cell structure [13]. In uniaxially prestrained samples, since some of the dislocations are already locked up in cell structures,

fewer mobile dislocations are available. Thus, less solute is required to pin the available mobile dislocations. In hydrostatically prestrained samples, however, since more mobile dislocations are available, more carbon must diffuse to these dislocations to cause pinning. As a result, longer aging times are required to achieve the same yield-point increments observed after uniaxial prestraining. A similar explanation has been applied to strain-aged steels prestrained in directions different to the original tensile direction [25].

4.3. Kinetics of strain aging

At least four different mechanisms have been postulated to explain strain-aging in metals and alloys. These include the formation of Cottrell atmospheres [21], Snoek ordering [26–28], Suzuki locking [29] and the precipitation of solute on dislocations [30].

During the early stages of Cottrell locking, the kinetics of yield-point return normally increase with time according to a $t^{2/3}$ power law. This relationship was originally deduced by Cottrell and Bilby [21] and has been confirmed for a number of systems involving interstitial atoms in transition metals, including Nb–O, Ni–H, Fe–C and Fe–N. The observed $\log t$ or approximate $t^{2/3}$ time dependence of $\Delta\sigma_u$ in NiAl due to carbon is consistent with the Cottrell–Bilby theory, which suggests that Cottrell locking is the mechanism responsible for the observed yield points.

Snoek ordering of impurity atoms within the stress field of a dislocation remains a possible mechanism. In this case, pinning is completed within the time interval of one atomic jump of the species responsible for pinning. The observations in this study certainly suggest that Snoek ordering does occur in NiAl. Nakada and Keh [31] have indicated that the apparent intercept of the $\Delta\sigma_u$ vs. $t^{2/3}$ curves is positive when Snoek ordering occurs prior to Cottrell atmosphere formation. As this is the case here, it can be concluded that some degree of Snoek ordering occurs in addition to the above-mentioned Cottrell locking.

Suzuki locking is considered to be inapplicable in the present investigation. This mechanism has its origin in a chemical interaction between solute atoms and stacking faults, and is only expected to be significant in metals of low stacking-fault energy in which the stacking-fault widths are large.

Precipitation on dislocations as a result of the segregation of solute would appear to be inappropriate, because precipitates were not observed in thin foils made from specimens of CP-NiAl and NiAl-C aged at 1100 K/7200 s/FC or 610 K/7200 s/AC. In addition, the shapes of the aging curves for CP-NiAl and NiAl-C for aging times up to 61 000 s at 700 K do not suggest the formation of precipitates due to overaging (satura-

tion of dislocations by solute). This is not to say that precipitation will not occur, but that it was not observed within the time–temperature range examined for alloys with the specific compositions studied. This does not preclude such a mechanism in alloys containing higher levels of substitutional contaminants [32–34].

Unfortunately, owing to the lack of diffusion data for NiAl, very little can be said about the derived activation energies, except that these activation energies lie below the self-diffusion energies for Ni and Al in NiAl, and that they lie below the activation energy for the creation and motion of vacancies [9], and that they are within the range for interstitial diffusion in bcc transition metals [22].

5. Conclusions

(1) The yield points observed in conventional-purity and carbon-doped NiAl are the result of strong dislocation pinning by interstitial carbon. Oxygen and nitrogen levels below 0.035 and 0.09 at.%, respectively, do not appear to pin dislocations in NiAl and therefore do not produce yield-point phenomena.

(2) The time dependence of strain aging appears to follow a $t^{2/3}$ relationship, which suggests Snoek aging and Cottrell locking as the cause for yield points in NiAl.

(3) Hydrostatic prestraining, as opposed to uniaxial prestraining, delays the kinetics of the yield-point return by forming random networks of free unpinned dislocations which require more diffusion time for strong locking to occur.

(4) Activation energies for yield-point return ranging from 70 to 76 kJ mol^{-1} (0.73–0.79 eV per atom) have been calculated, which are within the range for the diffusion of interstitials in bcc transition metals.

References

[1] J.E. Hack, J.M. Brzeski, R. Darolia and R.D. Field, in I. Baker, R. Darolia, J.D. Whittenberger and M.H. Yoo (eds.),

High-Temperature Ordered Intermetallics V, Materials Research Society, Boston, MA, 1993, p. 1197.

[2] E.P. Lautenschlager, D.A. Kiewit and J.O. Brittain, *Trans. AIME, 233*, 1297 (1965).

[3] R.W. Margevicius and J.J. Lewandowski, *Scr. Mater., 25*, 2017 (1991).

[4] R.D. Field, D.F. Lahrman and R. Darolia, in I. Baker, R. Darolia, J.D. Whittenberger and M.H. Yoo (eds.), *High-Temperature Ordered Intermetallic Alloys V*, Materials Research Society, Boston, MA, 1993, p. 423.

[5] J.M. Brzeski, J.E. Hack, R. Darolia and R.D. Field, *Mater. Sci. Eng., A170* (1993) 11.

[6] C.T. Liu, E.H. Lee, E.P. George and A.J. Duncan, *Scr. Metall. Mater., 30* (1994) 387.

[7] R.T. Pascoe and C.W.A. Newey, *Metal Sci. J., 2* (1968) 138.

[8] R.T. Pascoe and C.W.A. Newey, *Metal Sci. J., 5* (1971) 50.

[9] R.D. Noebe, R.R. Bowman and M.V. Nathal, *Int. Mater. Rev., 38* (1993) 193.

[10] M.L. Weaver, University of Florida, unpublished research, 1993.

[11] R.W. Margevicius, J.J. Lewandowski, I.E. Locci and R.D. Noebe, *Scr. Metall. Mater., 29* (1993) 1309.

[12] R.W. Margevicius and J.J. Lewandowski, *Acta Metall. Mater., 41* (1993) 485.

[13] R.W. Margevicius, J.J. Lewandowski and I.E. Locci, in R. Darolia, J.J. Lewandowski, C.T. Liu, P.L. Martin, D.B. Miracle and M.V. Nathal (eds.), *Structural Intermetallics*, The Minerals, Metals and Materials Society, Warrendale, PA, 1993, p. 577.

[14] D.R. Johnson, S.M. Joslin, B.F. Oliver, R.D. Noebe and J.D. Whittenberger, in H. Henein and T. Oki (eds.), *First Int. Conf. on Processing Materials for Properties*, The Minerals, Metals and Materials Society, Warrendale, PA, 1993, p. 865.

[15] R.D. Reviere, B.F. Oliver and D.D. Bruns, *Mater. Manuf. Proc, 4* (1989) 103.

[16] R.D. Noebe and A. Garg, *Scr. Metall. Mater., 30* (1994) 815.

[17] R.D. Noebe and M.K. Behbehani, *Scr. Metall. Mater., 27* (1992) 1795.

[18] A.G. Rozner and R.J. Wasilewski, *J. Inst. Metals, 94* (1966) 169.

[19] K.H. Hahn and K. Vedula, *Scr. Metall., 23* (1989) 7.

[20] J.D. Baird, *Metall. Rev., 16* (1971) 1.

[21] A.H. Cottrell and B.A. Bilby, *Proc. Phys. Soc., Lond. A, 62* (1949) 49.

[22] H. Schultz, *Mater. Sci. Eng., 3* (1968/69) 189.

[23] S. Hartley, *Acta Metall., 14* (1966) 1237.

[24] R.R. Bowman, R.D. Noebe, S.V. Raj and I.E. Locci, *Metall. Trans., 23A* (1992) 1493.

[25] D.V. Wilson and G.R. Ogram, *J. Iron Steel Inst., 206* (1968) 911.

[26] J. Snoek, *Physica, 8* (1941) 711.

[27] J. Snoek, *Physica, 6* (1939) 591.

[28] G. Schoeck and A. Seeger, *Acta Metall., 7* (1959) 469.

[29] H. Suzuki, in *Dislocations and Mechanical Properties of Crystals*, Wiley, New York, NY, 1957.

[30] E.O. Hall, *Yield Point Phenomena in Metals and Alloys*, Plenum Press, New York, 1970.

[31] Y. Nakada and A.S. Keh, *Acta Metall., 15* (1967) 879.

[32] H.K. DeMarco, A.J. Ardell and R.D. Noebe, *ASM 3rd Int. Conf. on High Temperature Intermetallics*, San Diego, CA, ASM International, Materials Park, OH, 1995.

[33] A.J. Duncan, M.J. Kaufman and M.K. Miller, *Appl. Surf. Sci., 76/77* (1994) 160.

[34] R. Jayaram and M.K. Miller, *Acta Metall. Mater., 42* (1994) 1561.

Kinetics of static strain aging in polycrystalline NiAl-based alloys

M. L. Weaver,[a] M. J. Kaufman[a] & R. D. Noebe[b]

[a]Department of Materials Science and Engineering, University of Florida, Gainesville, Fl 32611-2066, USA

[b]NASA Lewis Research Center, 21000 Brookpark Road, MS 49-3, Cleveland, OH 44135, USA

The kinetics of yield point return have been studied in two NiAl-based alloys as a function of aging time at temperatures between 300 and 700 K. The results indicate that the upper yield stress increment, $\Delta\sigma_u$ (i.e., stress difference between the upper yield point and the final flow stress achieved during prestraining), in conventional purity (CP-NiAl) and in high purity carbon-doped (NiAl-C) material first increased with a $t^{2/3}$ relationship before reaching a plateau. This behavior suggests that a Cottrell locking mechanism is the cause for yield points in NiAl. In addition, positive y-axis intercepts were observed in plots of $\Delta\sigma_u$ versus $t^{2/3}$ suggesting the operation of a Snoek mechanism. Analysis according to the Cottrell-Bilby model of atmosphere formation around dislocations yields an activation energy for yield point return in the range 70 to 76 kJ/mol which is comparable to the activation energy for diffusion of interstitial impurities in bcc metals. It is, thus, concluded that the kinetics of static strain aging in NiAl are controlled by the locking of dislocations by Cottrell atmospheres of carbon atoms around dislocations.

INTRODUCTION

It is generally accepted that bcc metals, in the presence of sufficient levels of interstitials, are subject to a strain aging phenomenon caused by elastic interactions between interstitial atoms and dislocations. The specific mechanisms by which this behavior occurs may involve Snoek ordering,[1,2] Cottrell aging,[3] Suzuki locking,[4] or precipitation on dislocations. In spite of the large number of papers dealing with strain aging, few discuss aspects of strain aging in ordered bcc alloys even though several manifestations of dynamic and static strain aging have been identified as playing a role in the deformation of polycrystalline and single crystal B2 intermetallic compounds. In the intermetallic compounds AgMg, FeCo, FeAl, and NiAl, for example, the occurrences of sharp yield points and serrated stress-strain curves,[5-16] strain rate sensitivity minima,[17-19] yield stress plateaus as a function of temperature[20] and flow stress transients on changes in

strain rate[18,21] have been reported. In addition, extensive work by Margevicius et al.[7,22-24] on NiAl has shown that a sharp yield point can be formed in binary NiAl following annealing at 1100 K and furnace cooling. This yield point can be removed by subsequent prestraining of the material by hydrostatic pressurization prior to testing and recovered by aging the prestrained material for 7200 s (i.e., 2 h) at 673 K. Similarly, Pascoe and Newey[17] observed the formation of room temperature yield points in near stoichiometric NiAl annealed for 3600s (1 h) at 350 K following a uniaxial prestrain. In addition, recent investigations of static[12,25] and dynamic[11] strain aging have shown that discontinuous yielding, in the form of yield points, yield plateaus and serrated yielding were observed in alloys containing high interstitial concentrations, particularly high carbon concentrations.[12,25] These phenomena were not observed in low interstitial high purity or in nitrogen doped material[11,12,25] suggesting that strain aging in NiAl is the result of strong dislocation pinning by

carbon atoms. Despite these observations, no complete investigation of classical strain aging has been conducted on ordered bcc intermetallic alloys. Consequently, the purpose of this paper is to describe the results of a detailed study on the kinetics of static strain aging in polycrystalline NiAl. Details of the influence of strain aging on the flow and fracture behavior of NiAl are provided in a previous document[12] and in a companion paper.[25]

EXPERIMENTAL

Materials

The alloys used in this study were prepared by extrusion of: (1) a nominally stoichiometric conventional purity induction melted ingot (CP-NiAl), and (2) a carbon-doped and zone-leveled ingot (NiAl-C). Both starting materials were extruded at 1200 K with the CP-NiAl and the NiAl-C ingots receiving 16:1 and 12:1 reduction ratios respectively. The as-extruded microstructures were fully dense consisting of recrystallized and equiaxed grains. The resulting compositions and as-extruded grain sizes are presented in Table 1.

Chemical analyses of the extruded materials were conducted at the NASA–Lewis Research Center by the following techniques deemed to be the most accurate for the particular elements. Ni and Al were determined using analytical wet chemistry/titration techniques and Si was determined by inductively coupled plasma atomic emission spectroscopy. Oxygen, nitrogen, carbon and sulfur contents were determined by combustion techniques using LECO oxygen/nitrogen and carbon/sulfur determinators. Additional details concerning materials processing and the chemical analysis techniques are presented elsewhere.[12,25]

Round button-head tensile specimens were ground from the extruded rods so that the gage lengths of the samples were parallel to the extrusion direction. Sample dimensions were 3·1 mm for the tensile gage diameters and 30·0 mm for the tensile gage lengths. Prior to testing, all samples were electropolished in a 10% perchloric acid–90% methanol solution that was cooled to 208 K.

Mechanical testing

Tensile tests were performed on an Instron Model 1125 load frame at a constant crosshead velocity corresponding to an initial strain rate of 1·4 × 10^{-4} s^{-1}. True stress–strain data were calculated from the load–time plots. All tests were performed in air at 300 K.

The kinetics of strain aging were investigated using the classic yield point return technique. Testing was conducted in two steps: (1) Initially, tensile specimens in the as-extruded condition were prestrained approximately 0·2% at room temperature, unloaded to a stress of approximately 2 MPa, aged *in situ* on the load frame at elevated temperatures for aging times varying between 60 and 113 000 s (30 h), and then tested in tension at room temperature. This test method allows specimen alignment to be maintained and the stress level to be kept effectively constant during aging. After aging, the specimens were cooled by removing the furnace from the test frame and passing a forced stream of ambient air over the specimen and the tensile grips. This method of cooling resulted in average temperature drops of 500 to 1000 K during the first minute of cooling. The parameters used to evaluate the kinetics of strain aging are illustrated in Fig. 1. These include the upper yield stress increment $\Delta\sigma_u$ = $\sigma_u-\sigma_a$, the lower yield stress increment $\Delta\sigma_L$ = $\sigma_L-\sigma_a$, and the Lüders strain ϵ_L. (2) Single speci-

Table 1. Compositions of extruded NiAl alloys (atomic percent)

Alloy (heat)	Grain size (μm)	Impurities						
		Ni[a]	Al[a]	Si[b]	C[c]	O[d]	N[d]	S[c]
CP-NiAl (L2971)	19 ± 2	50·0 ± 0·2	49·7 ± 0·2	0·15	0·0147	0·0070	<0·0009	<0·0007
NiAl-C (L2988)	45 ± 4	50·2 ± 0·2	49·8 ± 0·2	0·05	0·0092	0·0030	<0·0009	<0·0007

[a]Analysis performed using analytical wet chemistry/titration techniques, relative accuracy ±1%.
[b]Analysis performed on an ultraviolet/visible spectrophotometer, Shimadzu, Model UV-160, relative accuracy ±10%.
[c]Analysis performed on a simultaneous carbon/sulfur determinator, LECO Corp., Model CS-244, relative accuracy ±10%.
[d]Analysis performed on a simultaneous nitrogen/oxygen determinator, LECO Corp., Model TC-136 or Model TC-436, relative accuracy ±10%.

Fig. 1. Definition of strain-aging parameters.

L2971 #8
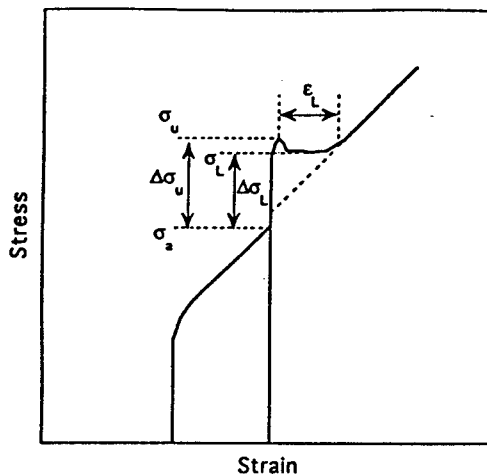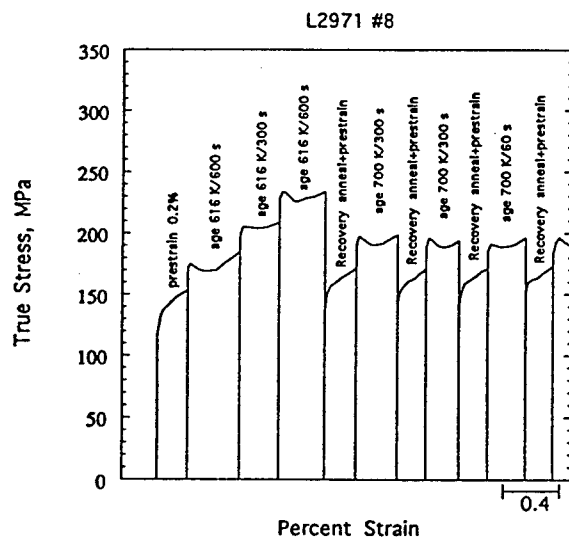
Fig. 2. Series of stress–strain curves illustrating the test method used to determine the strain aging kinetics in NiAl.
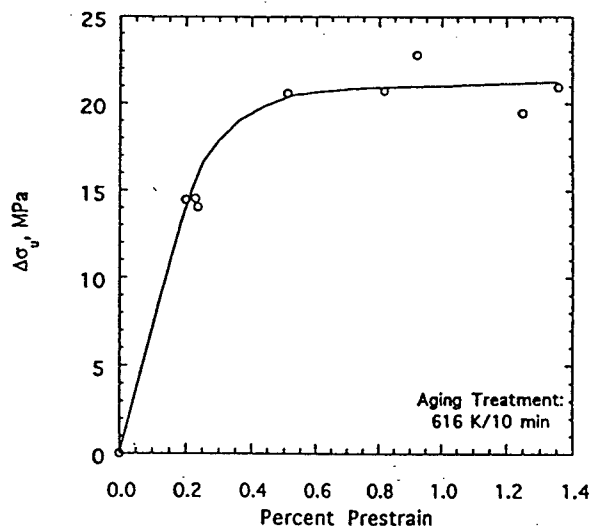
Fig. 3. Influence of % prestrain at room temperature followed by aging at 616 K/10 min on the subsequent yield stress increment measured at room-temperature.

mens were often aged several times to obtain a $\Delta\sigma_u$–time relationship. A specimen previously tested or prestrained uniaxially was given a recovery anneal, typically 1100 K/1800 s (30 min)/AC, prestrained approximately 0·2%, aged *in situ* and re-tested at room temperature. A typical series of stress–strain curves illustrating this procedure are shown in Fig. 2. When this type of testing is adopted, the yield point exhibited during the original deformation of the material can be recovered as can the yield point increment observed during the previous test. This means that it is possible to recover the dislocation structure and obtain a reproducible $\Delta\sigma_u$ following the same strain aging (i.e. prestrain + annealing) treatment, justifying the use of multiple deformation experiments on single samples.

RESULTS

Figure 3 shows the influence of prior strain on the resulting yield stress increment, $\Delta\sigma_u$, after aging of the CP-NiAl at 616 K. Increasing the amount of prior strain in samples aged at 616 K for 600 s, for example, leads initially to a rapid increase in $\Delta\sigma_u$ followed by an apparent plateau at prestrains exceeding 0·5%. Strain dependence of this type, which has been classified as type S by Kubin *et al.*,[26] is commonly observed in bcc alloys and is often associated with elastic interactions between dislocations and solute atoms.

The time dependence of $\Delta\sigma_u$ for the CP material is shown in Fig. 4. The data is summarized in
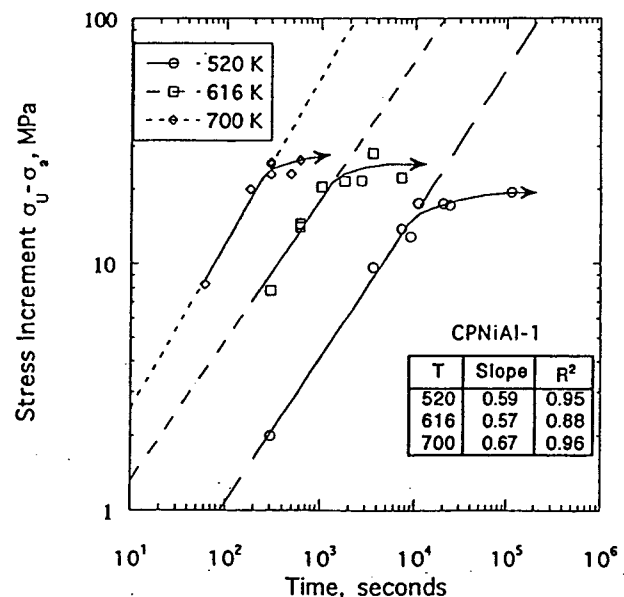
Fig. 4. ln $\Delta\sigma_u$ vs. ln *t* for CP-NiAl specimens. Specimens were prestrained uniaxially in tension to 0·2% prior to the strain aging treatments. The least squares parameters are indicated on the figure.

Table 2. The shapes of the aging curves up to the maximum value of $\Delta\sigma_u$ are comparable to similar curves reported for bcc metals.[27] Under type S conditions,[26] $\Delta\sigma_u$ will increase proportionally with $t^{2/3}$ during the early stages of aging, assuming $\Delta\sigma_u$ is proportional to the amount of solute segregating to dislocations. At longer times, the dislocations will become saturated with solute leading to a plateau in $\Delta\sigma_u$ or even to a decrease in $\Delta\sigma_u$ due to precipitation. The strain aging time exponent, as determined by least squares analysis of the data prior to saturation in Fig. 4, is in the range 0·57 to 0·67 which is close to the theoretical value of 2/3 predicted by Cottrell and Bilby.[3] In confirmation of this result, $\Delta\sigma_u$ is plotted versus $t^{2/3}$ in Fig. 5 demonstrating the satisfactory fit. Although experiments were only performed at 610 K for NiAl-C, a similar trend of higher $\Delta\sigma_u$ with increasing aging time was observed (Fig. 6 and Table 3). In addition, the time exponent was found to be 0·59 in agreement with the observations for CP-NiAl.

The $\Delta\sigma_u$ versus log time data for CP-NiAl and NiAl-C that were aged for various times at 616 and 610 K, respectively, are plotted together in
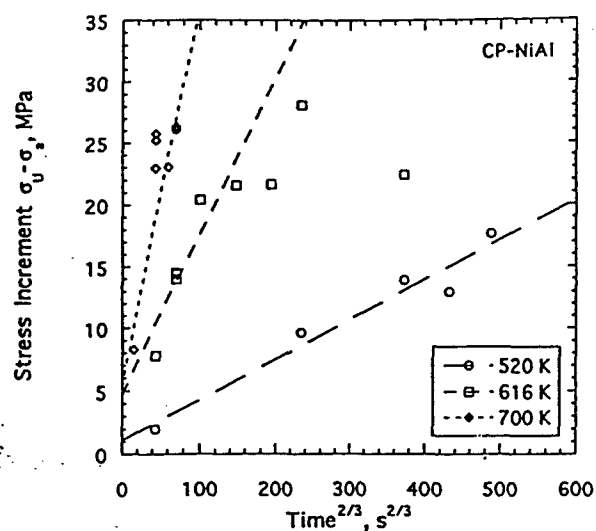
Fig. 5. Plots of $\Delta\sigma_u$ vs $t^{2/3}$ for CP-NiAl aged at 520, 616, and 700 K.

Fig. 6 to illustrate the influence of carbon concentration on the yield point return in NiAl. A significant difference in the magnitudes of the $\Delta\sigma_u$'s is evident as is an increase in the time required for yield points to form in NiAl-C. In addition, the saturation stress increment is lower

Table 2. The temperature dependence of the yield stress increment for CP-NiAl

Aging temperature, K	Aging time, s	Yield stress increment, MPa
520	300	2
520	3600	10
520	7200	14
520	9000	13
520	10800	18
520	19800	18
520	23400	17
520	113400	20
616	300	8
616	600	14
616	600	15
616	600	15
616	1020	20
616	1800	22
616	2700	22
616	3600	28
616	7200	22
616	11880	22
616	59820	25
700	60	8
700	180	20
700	300	23
700	300	26
700	300	25
700	480	23
700	600	26
700	600	26
700	7200	24
700	61200	23

Fig. 6. Plot of $\Delta\sigma_u$ vs natural log t for CP-NiAl and NiAl-C at 616 K and 610 K, respectively.

Table 3. Temperature dependence of yield stress increment for NiAl-C

Aging temperature, K	Aging time, s	Yield stress increment, MPa
610	600	5
610	1800	9
610	3600	12
610	4500	12
610	5760	9
610	9000	13
610	18360	12

in NiAl-C than in CP-NiAl. This behavior would be expected since NiAl-C has only about 2/3 the C level of CP-NiAl.

In an effort to establish a mechanism for static strain aging in NiAl, the activation energy for the return of the lower yield stress was determined by applying an Arrhenius equation which is derived from the expression of Cottrell and Bilby[3] for the number of atoms per length of dislocation line segregating into the vicinity of a dislocation in time t:

$$n(t) = aN_o \left(\frac{ADt}{kT}\right)^{2/3}$$ (1)

where, $\alpha \cong 3 \cdot 5$, N_o is the average volumetric concentration of defects in the lattice, D is the diffusivity of the defect at the aging temperature, T, k is Boltzmann's constant and A is a term corresponding to the binding energy between the defect and a dislocation. If prestraining and subsequent reloading are conducted at the same temperatures and if these temperatures are sufficiently low so that no aging occurs during testing, the number of defects required to pin a unit length of a dislocation line, $n(t^*)$, will be approximately constant. Thus, eqn (1) becomes:

$$C_1 = \left(\frac{n(t^*)}{N_o\alpha}\right)^{3/2}\left(\frac{k}{AD_o}\right) = \frac{t^*}{T}\exp\left(\frac{-Q}{RT}\right)$$ (2)

where D_o is the pre exponential factor for diffusivity of the defect and t^* represents the aging time for the reappearance of a yield point. Equation (2) can then be rewritten as:

$$\ln\left(\frac{T}{t^*}\right) = \ln\left(\frac{1}{C_1}\right) - \frac{Q}{RT}$$ (3)

The activation energy for diffusion of the pinning defect, Q, is determined from the slope of a plot of $\ln(T/t^*)$ versus $1/(RT)$. This method is illustrated in Fig. 7. On this basis, an activation energy for the return of a lower yield point in CP-NiAl was determined to be in the range 72 to 76 kJ/mole (approximately 0·75 to 0·79 eV/atom), which corresponds to the activation energies for the migration of interstitials in many bcc transition metals.[28]

As an alternative approach to the Arrhenius calculation, the activation energy was also determined by the method used by Hartley[29] who modified the Cottrell–Bilby relationship for the yield stress increment as follows:

$$\frac{\Delta\sigma_u}{\bar{\sigma}} = \frac{(\sigma_u - \sigma_a)}{\frac{1}{2}(\sigma_a + \sigma_u)} = K_1 + K_2\left(\frac{t}{T_a}\right)^{2/3}$$ (4)
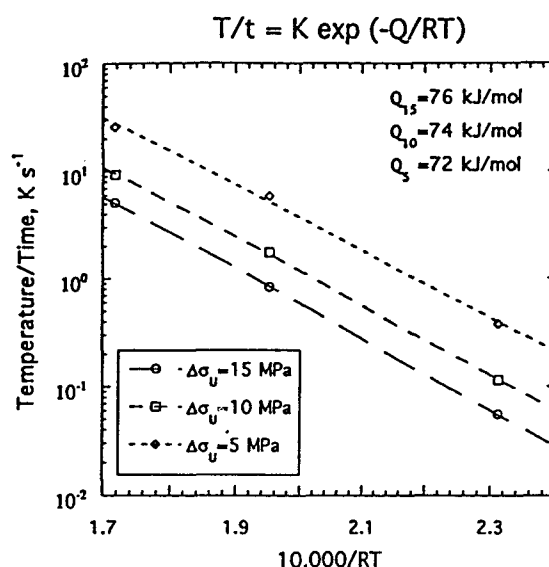
Fig. 7. Arrhenius representation of the strain aging data for CP-NiAl.

where K_1 is a constant, K_2 is a constant proportional to $D^{2/3}$, where D is the diffusivity, t is the aging time, and T_a is the aging temperature. Recalling that $D = D_o\exp(-Q/RT)$, activation energies are calculated by first determining the slope S_1 of a plot of $\Delta\sigma_u/\bar{\sigma}$ versus $t^{2/3}$ and then by plotting $\ln(S_1T^{2/3})$ versus $2/(3RT)$. This method is illustrated in Fig. 8. Using this approach, an activation energy of 70 kJ/mol (0·73 eV/atom) was determined which is in good agreement with the value established using the Arrhenius method.

Due to the lack of diffusion data for any type of interstitial solute in NiAl, little can be said about the activation energies derived in this investigation except that these values lie below the self diffusion energies for Ni and Al in NiAl and that they lie well below the activation energy for the creation and motion of vacancies.[20] However, the activation energies derived in this study are within the range for interstitial diffusion in bcc transition metals.[28]

DISCUSSION

Previously, it was shown that the discontinuous yielding observed in CP-NiAl and NiAl-C was the result of strong dislocation pinning by interstitial carbon,[12] whereas increased concentrations of oxygen and/or nitrogen had little or no influence on the properties of nominally stoichiometric NiAl.[12,30,31] Therefore, C has been identified as the major solute responsible for strain aging effects in NiAl.[12,25] In addition, it has been observed

$$\Delta\sigma_u/\bar{\sigma} = K_1 + K_2(t/T)^{2/3}$$

time, s

300 1200 2400 3600 5400 7200 9000

—o— ·520 K
— a- ·616 K
--♦--700 K

Time$^{2/3}$, s$^{2/3}$

Q≈70 kJ/mol

$10^4 \times 2/(3RT)$
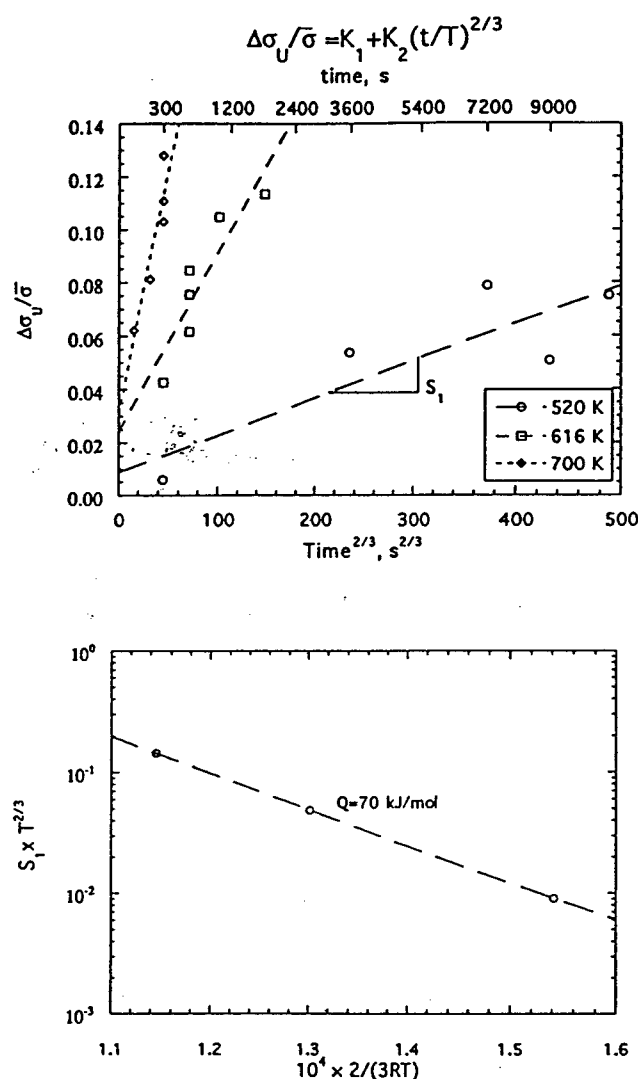
Fig. 8. Demonstration of the Hartley method[29] for determination of the activation energy for yield point return. (a) Strain aging parameters versus $t^{2/3}$ for CP-NiAl aged at 520, 616 and 700 K; (b) determination of the activation energy for yield point return using the Hartley method.

that longer aging times are required in NiAl-C to achieve the same yield stress increment as observed in CP-NiAl and that the yield increment after saturation is much greater in CP-NiAl than in NiAl-C. It is believed that this behavior is a result of the significant reduction in the concentration of interstitials, particularly C, in the NiAl-C alloy. Since there is less carbon to pin dislocations in NiAl-C, the carbon present must, presumably, diffuse longer distances to cause pinning.

At least four different mechanisms have been postulated to explain strain-aging in metals and alloys. These include: (1) the formation of Cottrell atmospheres,[3] (2) Snoek ordering,[1,2,32] (3) Suzuki locking,[4] and (4) the precipitation of solute on dislocations.[33]

Cottrell locking or aging involves the diffusion

of interstitial atoms to dislocations so as to form solute atmospheres around the dislocations. The driving force for this process is the reduction in strain energy of the system. Yield points form when the available dislocations are effectively locked by these solute atmospheres. The resulting increase in yield stress is due either to an increased stress required to move the locked dislocations or an increase in stress necessary to nucleate new dislocations permitting macroscopic plastic flow. The initial locking of dislocations requires long range diffusion of interstitials to the vicinity of dislocations and, as a result, requires many atom jumps. During the early stages of Cottrell locking, the kinetics of yield point return normally increase with time according to a $t^{2/3}$ power law. This relationship was originally deduced by Cottrell and Bilby[3] and has been confirmed for a number of systems involving interstitial atoms in transition metals including Nb–O, Ni–H, Fe–C and Fe–N.[27,32,34–38] The observed log t or approximate $t^{2/3}$ time dependence of $\Delta\sigma_u$ in NiAl due to carbon is consistent with the Cottrell–Bilby theory and suggests that Cottrell locking is the mechanism responsible for the observed yield points.

Snoek ordering of impurity atoms within the stress field of a dislocation remains a possible mechanism that may occur prior to the formation of a Cottrell atmosphere. This mechanism is best explained in terms of the Snoek effect as it occurs in bcc metals containing interstitial atoms in solution.[1,2,32] In the bcc lattice the tetrahedral sites are larger than the octrahedral sites. However, interstitial atoms typically occupy the smaller octahedral sites at the center of cube edges and cube faces because the lattice strain caused by octahedral occupancy can be more easily accommodated by the lattice than that caused by tetrahedral occupancy. For example, the insertion of an interstitial atom into the 1/2, 1/2, 0 position in Fig. 9 will cause atoms 1 and 2 to be displaced apart in the z direction resulting in a tetragonal distortion, whereas the insertion of an interstitial into the 1/2, 0, 0 position will cause a more uniform distortion of substitutional atoms 1–4. In the absence of an applied stress, a statistically equal number of interstitials will occupy sites parallel to each of the x, y and z axes. Thus, the unit cell remains cubic. The application of an external stress in the z direction, for example, causes the interstitial sites parallel to the z axis to enlarge while the openings perpendicular to the z axis decrease in size making it energetically more favorable for atoms at the 1/2, 1/2, 0 position, for example, to jump to the

1/2, 0, 1/2 position. This is known as the Snoek effect or Snoek ordering.[1,2] Since no long range diffusion is required, this process occurs very rapidly and is normally completed within the time interval of one atomic jump of the species responsible for pinning.

Similar behavior will be observed in B2 alloys. As in the case of bcc described above, an atom placed in an octahedral site results only in displacement of the two nearest atoms, whereas tetrahedral occupancy results in the distortion of the four neighboring atoms. Baker,[39] however, indicates that in the B2 crystal structure octahedral sites are not equivalent. Assuming that the A metal atoms represent Ni and the B metal atoms represent Al (i.e., $R_B > R_A$), the octahedral sites defined by Ni atoms will always be larger than those defined by Al atoms. In other words, an interstitial will prefer to occupy the octahedral position at 1/2, 1/2, 0 (face) in the B2 lattice illustrated in Fig. 9 as opposed to the 1/2, 0, 0 (edge) position because this site is larger than the edge position and allows for easier accommodation of an interstitial atom. However, even if the interstitials prefer only half of the total octahedral sites, the effect of stress on these remaining sites would still be the same as that described in the previous paragraph and Snoek ordering should still occur. Nakada and Keh[35] have indicated that the apparent intercept of the $\Delta\sigma_u$ versus $t^{2/3}$ curves is positive when Snoek ordering occurs prior to Cottrell

atmosphere formation. In Fig. 5, a positive intercept of the $\Delta\sigma_u$ versus $t^{2/3}$ curve is observed which suggests that some degree of Snoek ordering does occur in NiAl prior to the aforementioned Cottrell locking.

Suzuki locking is inapplicable to the present investigation. This mechanism has its origin in a chemical interaction between solute atoms and stacking faults and is only expected to be significant in metals of low stacking fault energy in which the stacking fault widths are large.

Precipitation on dislocations as a result of the segregation of solute would appear to be inappropriate because precipitates were not observed in thin foils made from specimens of CP-NiAl and NiAl-C aged at 1100 K 7200 s/FC or 610 K 7200 s/AC. In addition, the shapes of the aging curves for CP-NiAl and NiAl-C for aging times up to 61 000 s at 700 K (Fig. 4 and 6) do not suggest the formation of precipitates since a decrease in $\Delta\sigma_u$ that could be attributed to overaging and coarsening of any precipitates present was not observed at longer aging times. This does not preclude such a mechanism in alloys containing higher levels of substitutional contaminants as well as interstitial carbon.[40-42] However, precipitation was not observed within the time–temperature range examined for alloys with the specific compositions studied in this investigation.

Therefore, assuming a Cottrell type pinning mechanism does occur, additional kinetic information about C diffusion in NiAl can be obtained from the data generated during this study. Using the activation energies calculated above, it becomes possible to estimate the amount of enrichment at the dislocation core after strain aging. Assuming that the segregation of interstitials to a dislocation core is described by a Maxwellian distribution[43] where the solute concentration at the dislocation core, c, is determined according to:

$$c = c_o \exp\left(\frac{-W_m}{RT}\right) \tag{5}$$

where c_o represents the bulk solute concentration in the crystal, R is the universal gas constant, T is the absolute temperature and W_m is the dislocation–solute binding energy. Though W_m is currently unknown, a rough estimate can be obtained by substituting into eqn (5) the temperature above which yield point phenomena are not observed, T_{max} (which turns out to be approximately 900 K for CP-NiAl), and by setting c equal to unity. This results in an estimated W_m of 51 kJ/mol (0·5 eV/atom) which is a reasonable estimate when

□ octahedral interstices
○ tetrahedral interstices
● A metal atoms (Ni)
● B metal atoms (Al)
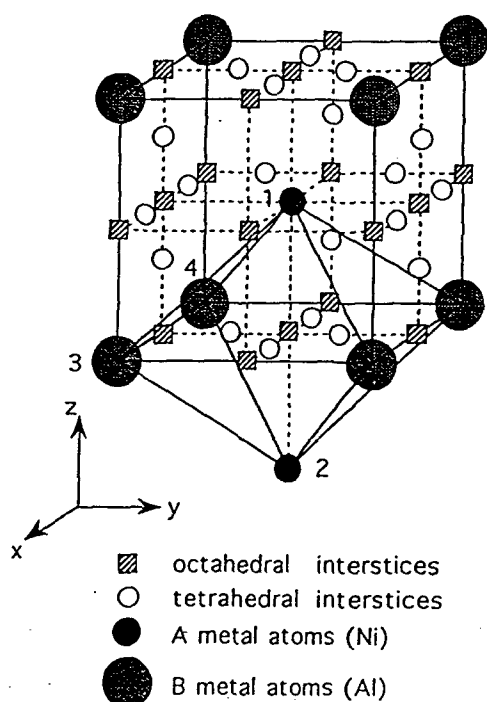
Fig. 9. Schematic illustration of the octahedral and tetrahedral interstitial sites in the bcc/B2 unit cell.

compared to similar numbers generated for bcc metals using the same assumptions.[28,43] Using this estimated value for W_m, an expression for the solute enrichment at the dislocation core after strain aging for time t_a at temperature T can be derived as follows:[43]

$$c - c_0 = \frac{\pi c_0}{b^2} \left[\frac{n(n+2)D|W_m|b^n t_a}{RT} \right]^{n/(n+2)} \quad (6)$$

where b represents the Burgers vector of the dislocations and n is a material parameter used to characterize the type of dislocation–solute interaction. For interactions due to size effects, as in this case, $n = 1$. The time required to saturate a dislocation at temperatures sufficiently low enough for stable saturation to occur is given by the condition $c = c_1 \gg c_0$ where c_1 is the critical solute concentration for saturation and is less than unity. Assuming that the carbon atoms (impurities) attract each other then $c_1 = 1/2$ and the saturation time, t_s, is related to the solute diffusivity as follows:[43]

$$t_s \cong \left(\frac{c_1}{\pi c_0} \right)^{\frac{n+2}{2}} \frac{RTb^2}{n(n+2)D|W_m|} \quad (7)$$

Assuming that t_s corresponds, to the minimum aging time required to induce yield point phenomena (i.e., sharp yield points or pronounced yield plateaus in the stress–strain curves), it becomes possible to calculate an upper bound for the diffusion coefficients for carbon in NiAl using the T and t_s values determined during this investigation and listed in Table 4. The resulting D values are also listed in Table 4. A linear least squares fit of ln D versus $1/(RT)$ using the values in Table 4 yields

$$D = (6 \times 10^{-9}) \exp \left(\frac{-Q}{RT} \right) \quad (8)$$

where the activation energy, Q, turn out to be 74 kJ/mol (0.77 eV/atom) which is equivalent to the values derived from the $\Delta\sigma_u$ vs t data in the results section. Furthermore, in the regime where static strain aging has been shown to occur in CP-NiAl, the calculated diffusivities of carbon in NiAl, are at least numerically equivalent to the diffusivities

Table 4. Calculated diffusion coefficients for C in NiAl

Temperature (K)	t_s, s	D cm^2 s^{-1}
522	3600	2×10^{-16}
616	300	3×10^{-15}
700	60	2×10^{-14}

of carbon in alpha iron within the strain aging regime (i.e., approximately 10^{-17} cm^2 s^{-1} at 298 K to approximately 10^{-10} cm^2 s^{-1} at 573 K.[44]

SUMMARY AND CONCLUSIONS

(1) The observed log t or approximate $t^{2/3}$ time dependence of $\Delta\sigma_u$ in NiAl due to carbon is consistent with the Cottrell–Bilby theory which suggests that Cottrell locking is the mechanism responsible for the observed yield points. In addition, positive intercepts on plots of $\Delta\sigma_u$ versus $t^{2/3}$ suggests that Snoek ordering also occurs prior to Cottrell train aging.

(2) Activation energies for yield point return ranging from 70 to 76 kJ/mol (0.73 to 0.79 eV atom^{-1}) have been calculated by two different techniques. These values are in the range for the diffusion of interstitials in bcc transition metals.

REFERENCES

1. Snoek, J., *Physica*, 6 (1939) 591.
2. Snoek, J., *Physica*, 8 (1941) 711.
3. Cottrell, A. H. & Bilby, B. A., *Proc. of the Physical Society, London*, A62 (1949) 49.
4. Suzuki, H., in *Dislocations and Mechanical properties of Crystals*. John Wiley and Sons, New York, 1957.
5. Hack, J. E., Brzeski, J. M., Darolia, R. & Field, R. D., *High-Temperature Ordered Intermetallics V*, eds I. Baker, R. Darolia, J. D. Whittenberger & M. H. Yoo. Materials Research Society, Boston, MA, 1993, p. 1197.
6. Lautenschlager, E. P., Kiewit, D. A. & Brittain, J. O., *Trans. AIME*, 233 (1965) 1297.
7. Margevicius, R. W. & Lewandowski, J. J., *Scripta. Metall. Mater.*, 25 (1991) 2017.
8. Field, R. D., Lahrman, D. F. & Darolia, R., *High-Temperature Ordered Intermetallic Alloys V*, eds I. Baker, R. Darolia, J. D. Whittenberger & M. H. Yoo. Materials Research Society, Boston, MA, 1993, p. 423.
9. Brzeski, J. M., Hack, J. E., Darolia, R. & Field, R. D., *Mater. Sci. Eng.*, A170 (1993) 11.

10. Liu, C. T., Lee, E. H., George, E. P. & Duncan, A. J., *Scripta Metall. Mater.*, **30** (1994) 387.

11. Hack, J. E., Brzeski, J. M. & Darolia, R., *Mater. Sci. Eng.*, **A192/193** (1995) 268.

12. Weaver, M. L., Noebe, R. D., Lewandowski, J. J., Oliver, B. F. & Kaufmann, M. J., *Mater. Sci. Eng.*, **A192/193** (1995) 179.

13. Gaydosh D. J., Draper, S. L., Noebe, R. D. & Nathal, M. V., *Mater. Sci. Eng.*, **A150** (1992) 7.

14. Morris, D. G., Joye, J. C. & Leboeuf, M., *Philos. Mag. A*, **69** (1994) 961.

15. Wood, D. L. & Westbrook, J. H., *Trans. Metall. Soc. AIME*, **224** (1962) 1024.

16. Dinhut, J. F., Lepinay, P. & Desoyer, J. C., *Phys. Stat. Sol. A*, **55** (1979) 621.

17. Pascoe, R. T. & Newey, C. W. A., *Metall. Sci. J.*, **2** (1968) 138.

18. Pascoe, R. T. & Newey, C. W. A., *Metall. Sci. J.*, **5** (1971) 50.

19. Kitano, K., Pollock, T. M. & Neobe, R. D., *Scripta Metall. Mater.*, **31** (1994) 397.

20. Noebe, R. D., Bowman, R. R. & Nathal, M. V., *Int. Mater. Rev.*, **38** (1993) 193.

21. Weaver, M. L., *The Effect of Molybdenum Additions on the Mechanical Behavior of NiAl*. University of Florida, Progress Report, August 1 to September 15, (1993).

22. Margevicius, R. W., Lewandowski, J. J., Locci, I. E. & Noebe, R. D., *Scripta Metall. Mater.*, **29** (1993) 1309.

23. Margevicius, R. W. & Lewandowski, J. J., *Acta Metall. Mater.*, **41** (1993) 485.

24. Margevicius, R. W., Lewandowski, J. J. & Locci, I. E., *Structural Intermetallics*, eds R. Darolia, J. J. Lewandowski, C. T. Liu, P. L. Martin, D. B. Miracle & M. V. Nathal. The Minerals, Metals and Materials Society, Seven Springs, PA, 1993, p. 577.

25. Weaver, M. L., Noebe. R. D., Lewandowski, J. J.,

Oliver, B. F. & Kaufman, M. J., submitted to *Intermetallics*.

26. Kubin, L. P., Estrin, Y. & Perrier, C., *Acta Metall. Mater.*, **40** (1992) 1037.

27. Baird, J. D., *Metall. Rev.*, **16** (1971) 1.

28. Schultz, H., *Mater. Sci. Eng.*, **3** (1968/69) 189.

29. Hartley, S., *Acta Metall.*, **14** (1966) 1237.

30. Noebe, R. D. & Garg, A., *Scripta Metall. Mater.*, **30** (1994) 815.

31. Cooper, R. M., Sikka, V. K. & Noebe, R. D., in *Advances in Powder Metallurgy and Particulate Materials 1994*. American Powder Metallurgy Institute, Princeton, NJ, 1994/5.

32. Schoeck, G. & Seeger, A., *Acta Metall.*, **7** (1959) 469.

33. Hall, E. O., *Yield Point. Phenomena in Metals and Alloys*. Plenum Press, New York, 1970.

34. Park, S. C., Beckerman, L. P. & Reed-Hill, R. E., *Metall. Trans. A*, **14A** (1983) 463.

35. Nakada, Y. & Keh, A. S., *Acta Metall.*, **15** (1967) 879.

36. Rosinger, H. E., Craig, G. B. & Bratina, W. J., *Mater. Sci. Eng.*, **5** (1969/70) 163.

37. Rosinger, H. E., *Metal. Sci.*, **9** (1975) 1.

38. Keh, A. S., Nakada, Y. & Leslie, W. C., in *Dislocation Dynamics*, eds. A. R. Rosenfield, G. T. Hahn, A. L. Bement & R. I. Jaffee. McGraw-Hill Book Company, New York, 1968, p. 381.

39. Baker, I., *J. Mater. Res.*, **8** (1993) 1203.

40. DeMarco, H. K., Ardell, A. J. & Noebe, R. D., *Mater. Sci. Eng.*, in press (1995).

41. Duncan, A. J., Kaufman, M. J. & Miller, M. K., *Appl. Surf. Sci.*, **76/77** (1994) 160.

42. Jayaram, R. & Miller, M. K., *Acta Metall. Mater.*, **42** (1994) 1561.

43. Friedel, J., *Dislocations*. Pergamon Press, Oxford, 1964.

44. Leslie, W. C., *The Physical Metallurgy of Steels*. McGraw-Hill, New York, 1981.

Manifestations of Dynamic Strain Aging in Soft-Oriented NiAl Single Crystals

M.L. WEAVER, M.J. KAUFMAN, and R.D. NOEBE

The tensile and compressive properties of six NiAl-base single-crystal alloys have been investigated at temperatures between 77 and 1200 K. The normalized critical resolved shear stresses (CRSS/E) and work-hardening rates (θ/E) for these alloys generally decreased with increasing temperature. However, anomalous peaks or plateaus for these properties were observed in conventional purity (CPNiAl), Si-doped (NiAl-Si), C-doped low Si (UF-NiAl1), and Mo-doped (NiAl-Mo) alloys at intermediate temperatures (600 to 1000 K). This anomalous behavior was not observed in high-purity, low interstitial material (HP-NiAl). Low or negative strain-rate sensitivities (SRS) also were observed in all six alloys in this intermediate temperature range. Coincident with the occurrence of negative strain-rate sensitivities was the observation of serrated stress-strain curves in the CPNiAl and NiAl-Si alloys. These phenomena have been attributed to dynamic strain aging (DSA). Chemical analysis of the alloys used in this study suggests that the main specie responsible for strain aging in NiAl is C but indicate that residual Si impurities can enhance the strain aging effects. The corresponding dislocation microstructures at low temperatures (300 to 600 K) were composed of well-defined cells. At intermediate temperatures (600 to 900 K), either poorly defined cells or coarse bands of localized slip, reminiscent of the vein structures observed in low-cycle fatigue specimens deformed in the DSA regime, were observed in conventional purity, Si-doped, and in Mo-doped alloys. In contrast, a well-defined cell structure persisted in the low interstitial, high-purity alloy. At elevated temperatures ($\geq$1000 K), more uniformly distributed dislocations and sub-boundaries were observed in all alloys. These observations are consistent with the occurrence of DSA in NiAl single-crystal alloys at intermediate temperatures.

I. INTRODUCTION

SEVERAL manifestations of strain aging have been identified as playing a role in the deformation of polycrystalline and single-crystal NiAl. They include the following: (1) the occurrence of yield points;[1-4] (2) serrated stress-strain curves;[1,5-10] (3) strain-rate sensitivity minima;[11,12] (4) yield stress plateaus as a function of temperature;[13] (5) the occurrence of local maxima or plateaus in plots of work-hardening rate (θ) as a function of temperature;[11,14] and (6) flow stress transients on changes in strain-rate.[12,15] Despite these observations, the significance of strain aging and its influence on the mechanical properties of NiAl have, until recently, been largely ignored. Lately, Hack and co-workers[5,6,9,16-18] have observed that the fracture toughness of soft-oriented single crystals is extremely sensitive to heat treatments in the 473 to 673 K range. For example, they observed that slow cooling through this temperature regime resulted in brittle specimens with low fracture toughness ($\approx$4 MPa$\sqrt{m}$), whereas fast cooling resulted in an increased fracture toughness ($\approx$16 MPa$\sqrt{m}$) and more ductile behavior. They attributed the reduction in ductility

during slow cooling to static strain aging (SSA), which is a time-dependent process that results when solute atoms segregate to the strain fields around dislocations causing pinning. Similar observations have been made for polycrystalline NiAl. For example, Margevicius et al.[2] observed that sharp upper yield points can be induced in conventional-purity binary NiAl by furnace cooling a cast and extruded or prestrained alloy from 1100 K to room temperature. Furthermore, Weaver et al.[14,15,19-21] showed that the magnitude of the yield point increased with aging time according to a $t^{2/3}$ relationship in conventional purity and carbon-doped NiAl, and reported the occurrence of serrated flow. Further evidence supporting the occurrence of strain aging was provided by the observations of serrated flow in these same conventional purity NiAl polycrystals and single crystals at elevated temperatures (>700 K) and the lack of such serrations in high-purity materials.[5,6,9,15-18,22]

The purpose of this article is to thoroughly describe the dynamic strain aging (DSA) behavior observed in NiAl single crystals and to identify the species responsible. To accomplish these objectives, nominally stoichiometric NiAl single crystals with differing interstitial contents were studied. Since dilute additions of reactive elements have been reported to retard the strain-aging behavior in body-centered cubic (bcc) metals, an alloy intentionally doped with Mo also was investigated to analyze the role of a strong gettering agent on the strain-aging behavior of NiAl single crystals. Because Si is a common impurity in conventional-purity NiAl single crystals due to interaction with alumina-silicate shell molds during directional solidification, an alloy containing an intentional addition of Si also was investigated to ascertain the role of this substitutional impurity on the deformation behavior of NiAl.

M.L. WEAVER, formerly Graduate Student, Department of Materials Science and Engineering, University of Florida, is Research Associate, Center for Nonlinear and Nonequilibrium Aeroscience, Florida A & M University, Tallahassee, FL 323306, and the Center for Materials Research and Technology, Florida State University, Tallahassee, FL 32310. M.J. KAUFMAN, Associate Professor, is with the Department of Materials Science and Engineering, University of Florida, Gainesville, FL 32611. R.D. NOEBE, Materials Research Engineer, Materials Division NASA-Lewis Research Center, Cleveland, OH 44135.
Manuscript submitted August 7, 1995.

Alloy Ingot	[*hkl*]	At. Pct				Interstitials (At. Ppm)			
		Ni	Al	Mo	Si	C	O	N	S
HP-NiAl UT-HP2	[123]	50.2 ± 0.2	49.8 ± 0.2	—	0.04	76	40	24	<10
CPNiAl-1 D5-553	[123]	50.6 ± 0.2	49.2 ± 0.2	—	0.17	112	87	<6	<10
CPNiAl-2 D5-1273	[110]	50.4 ± 0.2	49.4 ± 0.2	—	0.15	209	612	<6	<10
UF-NiAl1 UF-001	[123]	50.3 ± 0.2	49.3 ± 0.2	—	0.01	136	132	15	<10
NiAl-Mo D52-783	[123]	50.0 ± 0.2	49.8 ± 0.2	0.11	0.23	558	316	25	<10
NiAl-Si UF-003	[110]	50.4 ± 0.2	49.3 ± 0.2	—	0.29	220	95	12	<10

Ni and Al Analysis performed using wet chemistry/titration techniques, relative accuracy ± 1 pct.

Mo Analysis performed on a flame atomic absorption emission spectrophotometer, Perkin-Elmer model 5000 (Perkin-Elmer Physical Electronics, Eden Prairie, MN), relative accuracy ± 5 pct.

C and S Analysis performed on a simultaneous carbon/sulfur determinator, LECO Corporation (St. Joseph, MI), model CS-244, relative accuracy ± 10 pct.

N and O Analysis performed on a simultaneous nitrogen/oxygen determinator, LECO Corp., model TC-136 or model TC-436, relative accuracy ± 10 pct.

Si Analysis performed on an ultraviolet/visible spectrophotometer, Shimadzu, Columbia, MD, model UV-160, relative accuracy ± 10 pct.

II. EXPERIMENTAL

One Mo-doped (NiAl-Mo), one Si-doped (NiAl-Si), and three nominally stoichiometric NiAl (CPNiAl-1, CPNiAl-2, and UF-NiAl1) single-crystal slabs were grown under an argon atmosphere by a Bridgman procedure. Slabs CPNiAl-1, CPNiAl-2, and NiAl-Mo were produced at General Electric Aircraft Engines (Cincinnati, OH), using alumina-silicate shell molds and measured 25 × 32 × 100 mm. Slabs UF-NiAl1 and NiAl-Si were produced at the University of Florida (Gainesville, FL) using high-purity alumina crucibles and measured 25-mm diameter × 60-mm length. A low interstitial, high-purity ingot of stoichiometric NiAl (HP-NiAl), 25-mm diameter × 50-mm length, was produced *via* a containerless electromagnetic levitating zone process at the University of Tennessee (Knoxville, TN). All slabs were homogenized at 1589 K for at least 1 hour in argon, followed by furnace cooling to room-temperature prior to machining into test specimens.

Postprocessing chemical analyses were conducted using the techniques deemed the most accurate for the particular elements. The results of these analyses are listed in Table I. The crystals were oriented using the back-reflection Laue technique and either ground into round button-head tensile specimens parallel to the ⟨123⟩ axis or (EDM) wire cut into cylindrical compression specimens parallel to the ⟨123⟩ or ⟨110⟩ axis. Specimen dimensions were (1) 3.1 and 30.0 mm for the tensile gage diameter and gage length and (2) 3.0 mm and 6.4 mm for the compression sample diameter and height, respectively. All tensile specimens were electropolished prior to testing in a 10 pct perchloric acid-90 pct methanol solution that was cooled to 208 K.

All mechanical tests were performed on an Instron Model 1125 load frame at constant crosshead velocities corresponding to initial strain rates ranging from 2.8×10^{-5} s^{-1} to 2.8×10^{-4} s^{-1}. Tests between 300 and 1100 K were run in air by heating the samples in a clamshell-type resistance furnace. Testing below room temperature was accomplished in compression by cooling in liquid baths. True stress-strain data were calculated from the load-time plots and yield stresses were determined by the 0.2 pct offset method. During some of the elevated-temperature compression tests, strain was measured using a clip-on strain gage extensometer attached to a compression cage. The strain-rate sensitivity (SRS) was determined by increasing the strain rate by a factor of ten from the base strain rate at fixed plastic strain intervals. The quantity extracted from these experiments was the SRS, $s = \Delta\sigma/\Delta \ln \dot{\varepsilon}$.

Samples for transmission electron microscopy (TEM) were cut from the tested tensile or compression specimens with a low-speed diamond saw and twin-jet electropolished in a solution of 70 pct ethanol, 14 pct distilled water, 10 pct butylcellusolve, and 6 pct perchloric acid at 273 K, 25V, and 0.15 mA. The TEM examinations were conducted in a modified JEOL* 100C microscope operating at an ac-

---

*JEOL is a trademark of Japan Electron Optics Limited, Tokyo.

---

celerating voltage of 120 kV.

III. RESULTS

A. *Composition and Microstructure*

The results of the chemical analyses indicated that within experimental accuracy, the Ni and Al contents of the six alloys are not significantly different from one another. The major differences between the materials are the residual Si, C, O, and N contents and the addition of 0.1 at. pct Mo to NiAl-Mo, which resulted in the formation of coarse precipitates (Figure 1). The results of energy-dispersive spectroscopic analysis and TEM microdiffraction indicated that these particles were Mo_2C. The presence of silicon in NiAl-Mo, CPNiAl-1, and CPNiAl-2 has been attributed to reaction between the melt and the ceramic shell molds during processing. The lack of Si in UF-NiAl1 has been attributed to the use of arc-melted as opposed to vacuum-induction-melted feed stock and the use of higher purity crucibles during directional solidification.

B. *Mechanical Properties*

The temperature-dependent properties (*i.e.*, critical resolved shear stress at 0.2 pct strain (CRSS), work-hardening rate evaluated over the range 0.2 to 1.8 pct plastic strain, and SRS evaluated at 1.8 and 5.0 pct plastic strain have been determined for all six alloys and are summarized in Figures 2 and 3. Work-hardening and SRS parameters were
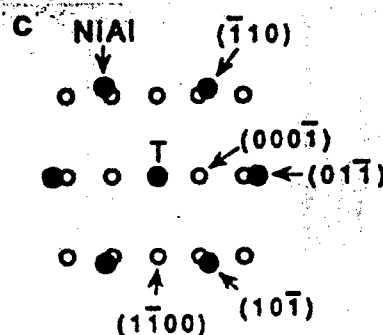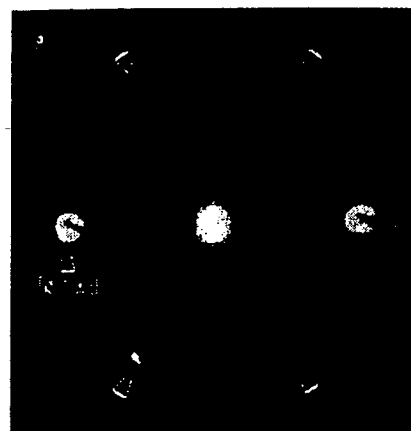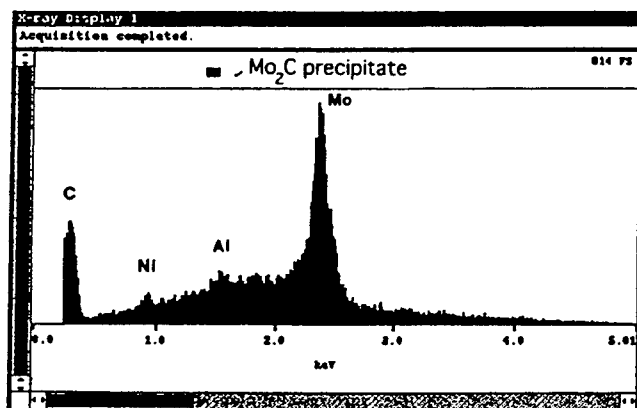
Fig. 1—Precipitates observed in NiAl-Mo: (a) bright-field TEM micrograph of Mo_2C precipitates in NiAl-Mo; (b) TEM microdiffraction pattern illustrating an orientation relationship of $[111]_{NiAl}//[1120]_{Mo_2C}$ and $(01\bar{1})_{NiAl}//(000\bar{1})_{Mo_2C}$ between the precipitate and NiAl matrix; (c) a schematic representation of (b); and (d) SEM EDS spectra for one of the precipitates indicating that they contain Mo and C.

not measured at higher strains due to limited tensile ductility at lower temperatures and due to pronounced barreling after approximately 5.0 pct deformation in compression. Figure 2 shows the temperature dependence of the CRSS at 0.2 pct plastic strain and the work-hardening characteristics for all six alloys. The work-hardening characteristics of these materials have been evaluated from the average work-hardening rate ($\theta = \Delta\sigma/\Delta\varepsilon$). As noted by Kocks,[23] in most materials, flow stress and θ decrease in a monotonic fashion with increasing temperature, in part because the shear and elastic moduli also decrease with increasing temperature and contribute negatively to the flow stress. Consequently, in cases where the temperature dependence of the elastic modulus, for example, is sufficiently negative, relatively slight positive contributions from DSA can be masked by modulus effects. As a result, the work-hardening and CRSS results presented in Figure 2 have been normalized with respect to the elastic modulus E. Since no estimates of E for $\langle123\rangle$-oriented single crystals (E_{123}) were available, it was assumed that E_{123} was equivalent to E for $\langle111\rangle$-oriented single crystals (E_{111}), as determined by Wasilewski[24] (i.e., $E_{123} \cong E_{111}$).

In agreement with prior investigations on single-crystal and polycrystalline NiAl as reviewed in References 13, 25, and 26, both the CRSS/E and the θ/E generally decreased with increasing temperature. However, in CPNiAl-1, CPNiAl-2, UF-NiAl1, NiAl-Mo, and NiAl-Si, apparent plateaus or peaks were observed in the temperature range of 650 to 1000 K. In HP-NiAl, however, no such plateau was observed, in agreement with the previous observations on a similarly processed material.[15,27] Figures 4 and 5 show portions of load-elongation curves for NiAl-Si, HP-NiAl, and UF-NiAl1 following uniaxial deformation and strain-rate change tests performed at various temperatures. In NiAl-Si (Figure 4), serrated flow was observed in the load-elongation curves at temperatures below those associated with the apparent plateaus or peaks in CRSS. Similar observations were made in CPNiAl-1 and CPNiAl-2, while no serrated flow was observed in UF-NiAl11, NiAl-Mo, or in HP-NiAl. The occurrence of serrated flow has been previously reported in NiAl.[5-7,9,17] Since serrated flow can be associated with DSA and the Portevin–Le Chatelier (PLC) effect, the SRS has been deduced from strain-rate change tests. The temperature dependence of the strain-rate sensi-
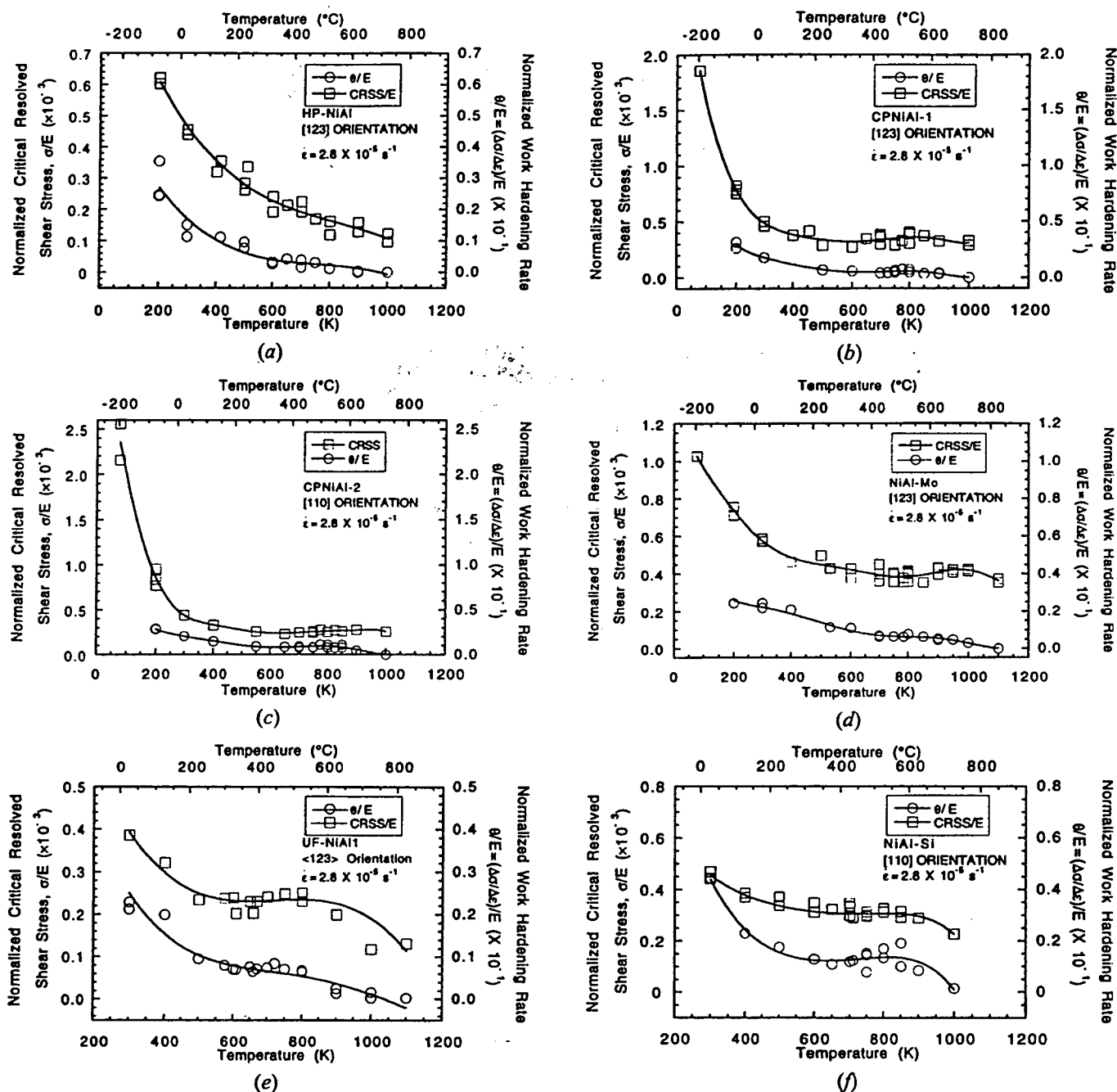
Fig. 2—Temperature dependence of the normalized CRSS at 0.2 pct strain and work hardening rate, θ/E, for NiAl single crystals: (a) HP-NiAl; (b) CPNiAl-1; (c) CPNiAl-2; (d) NiAl-Mo; (e) UF-NiAl1; and (f) NiAl-Si.

tivity is presented in Figure 3. For all six alloys, SRS exhibits distinct local minimums in the temperature ranges 300 to 400 K (low temperature) and 600 to 800 K (intermediate temperature), with s actually becoming negative for CPNiAl-1, CPNiAl-2, and NiAl-Si at 1.8 pct and at ~5.0 pct strain in the intermediate temperature range. Coincident with those temperatures where a negative SRS was observed was the occurrence of the aforementioned serrated yielding. In addition to the studies mentioned previously, recent independent analyses of conventional-purity NiAl[16,18] and NiAl-Si[28,29] have confirmed the occurrence of serrated flow at intermediate temperatures. In addition, Winton et al.,[28,29] who have performed strain-rate change experiments on NiAl-Si at higher strains, have confirmed the existence

of a pronounced SRS minimum at intermediate temperatures where SRS approached zero but tended to remain slightly positive. In UF-NiAl1 and NiAl-Mo, where SRS remained positive, flow stress transients in the form of sharp upper yield points were observed, whereas no such transients were observed in HP-NiAl in this temperature regime. In the low-temperature interval, however, diffuse flow-stress transients were consistently observed in HP-NiAl and in UF-NiAl1 with the later exhibiting the most pronounced effects (Figures 5(b) and (c)). No low temperature transients were exhibited by CPNiAl-1, CPNiAl-2, NiAl-Mo, or NiAl-Si.

Serrated yielding typically occurred after a small critical plastic strain ε_c. The temperature T and strain-rate $\dot{\varepsilon}$ de-

300 K

Type C

800 K

600 K

50 kg

Type B

700 K

Type B+C

750 K

900 K

0.5% strain

(a)

$\dot{\varepsilon}_1$

~ 300 K

$\dot{\varepsilon}_2$

$\dot{\varepsilon}_1$

1.0% strain

$\dot{\varepsilon}_2$

800 K
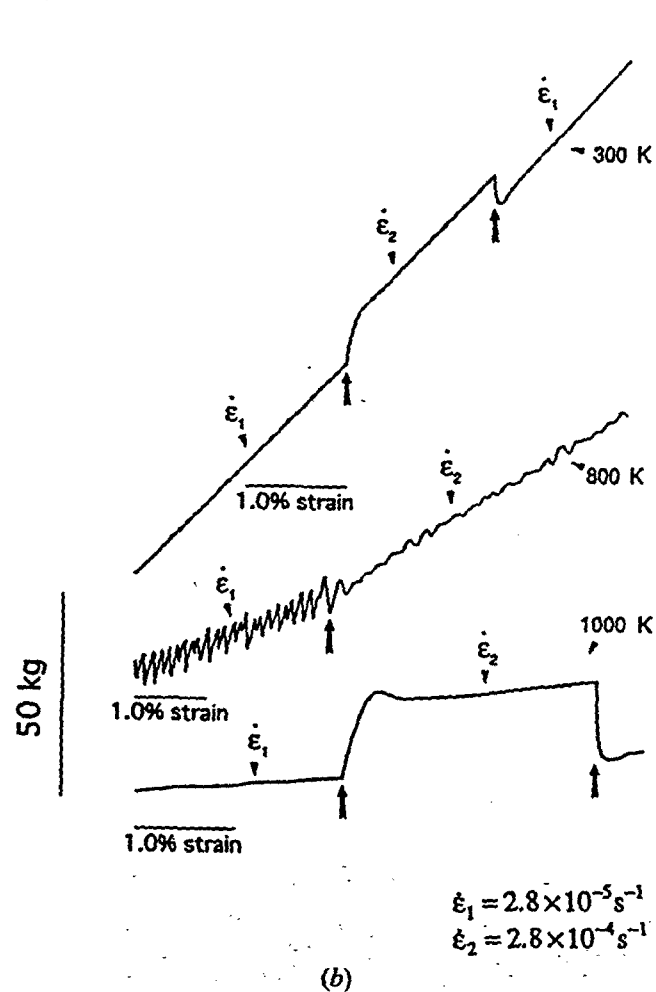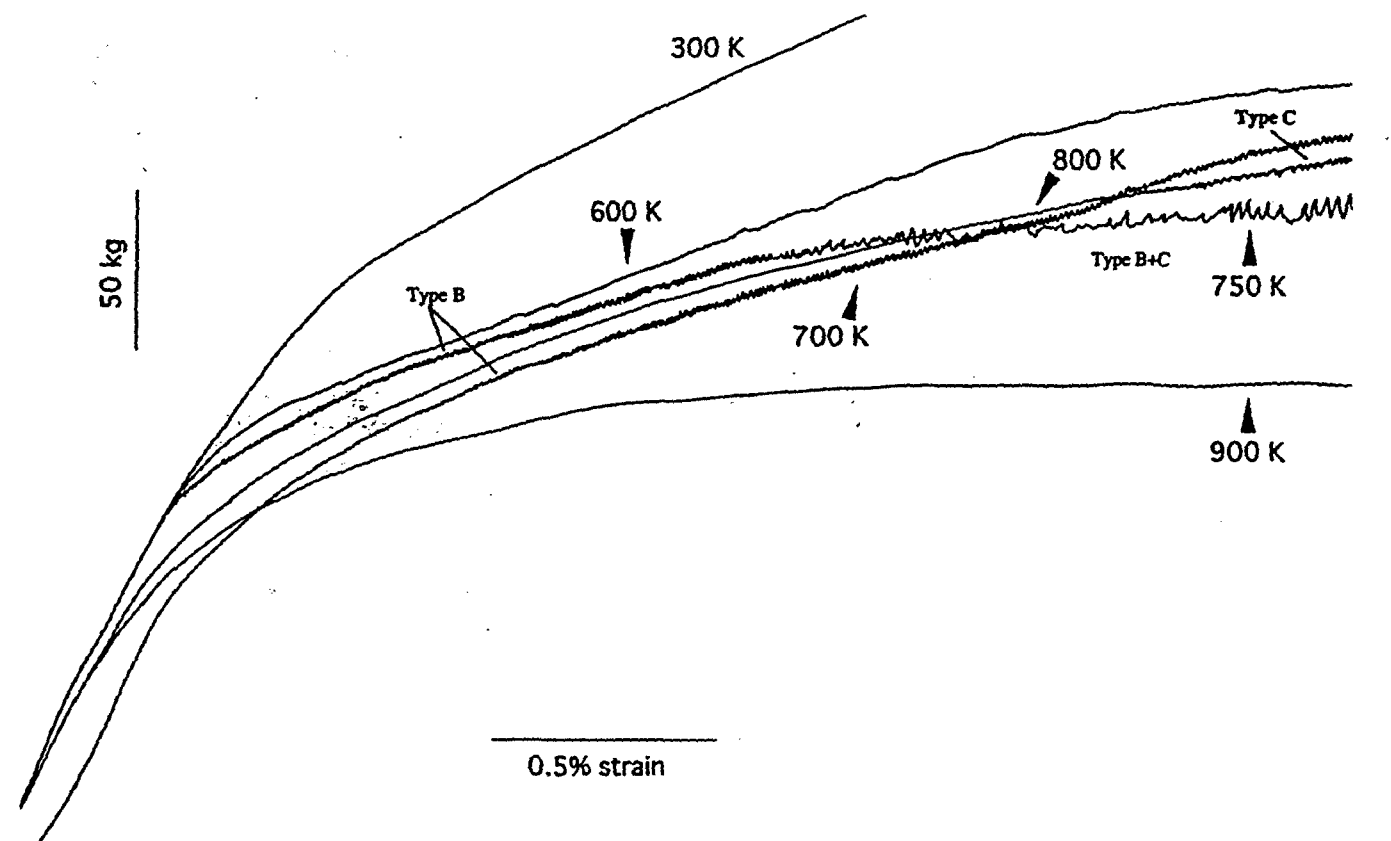
Fig. 4—The effect of temperature on the shape of the flow curves in Si-doped NiAl deformed at $\dot{\varepsilon} = 2.8 \times 10^{-3}$ s⁻¹. (a) and (b) NiAl-Si following uniaxial deformation and strain-rate change experiments conducted near 5 pct plastic strain. Note the transition from type-B serrations at lower temperatures to type-C serrations at higher temperatures and strains. Similar flow curves were observed for CPNiAl-1 and CPNiAl-2.

$\dot{\varepsilon}_1$

1000 K

50 kg

$\dot{\varepsilon}_2$

1.0% strain

$\dot{\varepsilon}_1$

$\dot{\varepsilon}_1$

1.0% strain

$\dot{\varepsilon}_1 = 2.8 \times 10^{-5}$ s⁻¹

$\dot{\varepsilon}_2 = 2.8 \times 10^{-4}$ s⁻¹

(b)

types of serrations are characteristic of unlocking of pinned dislocations and are associated with discontinuous deformation band propagation.

In this investigation the activation energy Q for serrated flow was ascertained *via* three distinct methods. In the first method, the critical plastic strain was related to $\dot{\epsilon}$ and T by the following equation:[30,31]

$$\epsilon_c^{(m+\beta)} = K\dot{\epsilon}\ \exp\ (Q/RT) \qquad [1]$$

where m and β are exponents related to the variation in vacancy concentration C_v and mobile dislocation density ρ_m (*i.e.*, $C_v \propto \epsilon^m$ and $\rho_m \propto \epsilon^\beta$), K is a constant, and R and T have their usual meanings. The exponent $(m + \beta)$, determined from the slope of the plot of $\ln\dot{\epsilon}$ *vs* $\ln\epsilon_c$ at a constant temperature (Figure 6(a)), was in the range 0.93 to 1.27 for CPNiAl-1, CPNiAl-2, and NiAl-Si. The activation energy is then determined from a plot of $\ln\epsilon_c$ *vs* $1/RT$ (Figure 6(b))[32,33] (*i.e.*, Q = slope $\times$ $(m + \beta)$). This method produces activation energies in the range 71 to 94 kJ/mol for the onset of serrated flow over the temperature range where ϵ_c decreases with increasing temperature.

In the second method, Q can be determined from the slope of an Arrhenius plot of $\ln\dot{\epsilon}$ *vs* $1/RT$ for conditions where serrated yielding occurs. In this case, the onset lines marking the beginning of serrated flow in Figure 7 for CPNiAl-1, CPNiAl-2, and NiAl-Si were used.[33] This method yields an activation energy ranging from 66 to 75 kJ/mol.

Finally, the activation energy for serrated flow can be determined from the stress-drop technique.[33,34] For this method, the magnitude of the stress drop $\Delta\sigma$ accompanying serrated flow is measured at a given strain for a range of $\dot{\epsilon}$ and T and plotted as indicated in Figure 8(a). A constant value for $\Delta\sigma$ is then selected from which the $\dot{\epsilon}$ corresponding to this $\Delta\sigma$ is determined for each temperature. The resulting $\dot{\epsilon}$ is then plotted as a function of $1/T$ and Q is determined from its slope (*i.e.*, $Q = -(\ln\dot{\epsilon}RT)$). Detailed descriptions of this method are provided in References 33 and 34. Figures 8(a) through (c) show the $\Delta\sigma$ *vs* $\dot{\epsilon}$ and $\dot{\epsilon}$ *vs* $1/T$ plots for CPNiAl-1, CPNiAl-2, and NiAl-Si. Activation energies in the range 86 to 102 kJ/mol were ascertained for all three alloys by this technique.

Activation energies determined by all three methods are summarized in Table II and are in very good agreement with the activation energies determined for SSA in polycrystalline NiAl (70 to 76 kJ/mol)[15,19,20] and are only marginally less than the activation energy for serrated flow in single-crystal NiAl reported by Brzeski and co-workers (115 and 134 kJ/mol).[5,16]

C. *Optical Microscopy and TEM Observations of Deformed Samples*

Representative TEM bright-field images of the dislocation structures after deformation at room temperature, in the DSA regime, and above the DSA regime for the various alloys are shown in Figures 9 through 13. Diffraction contrast analysis revealed that deformation occurred by the motion of $\langle 001 \rangle$-type dislocations at all temperatures. Figure 9 shows the deformation microstructures in CPNiAl-2 samples deformed at room temperature to two different strain levels. In agreement with previous observations,[15,35–38] the
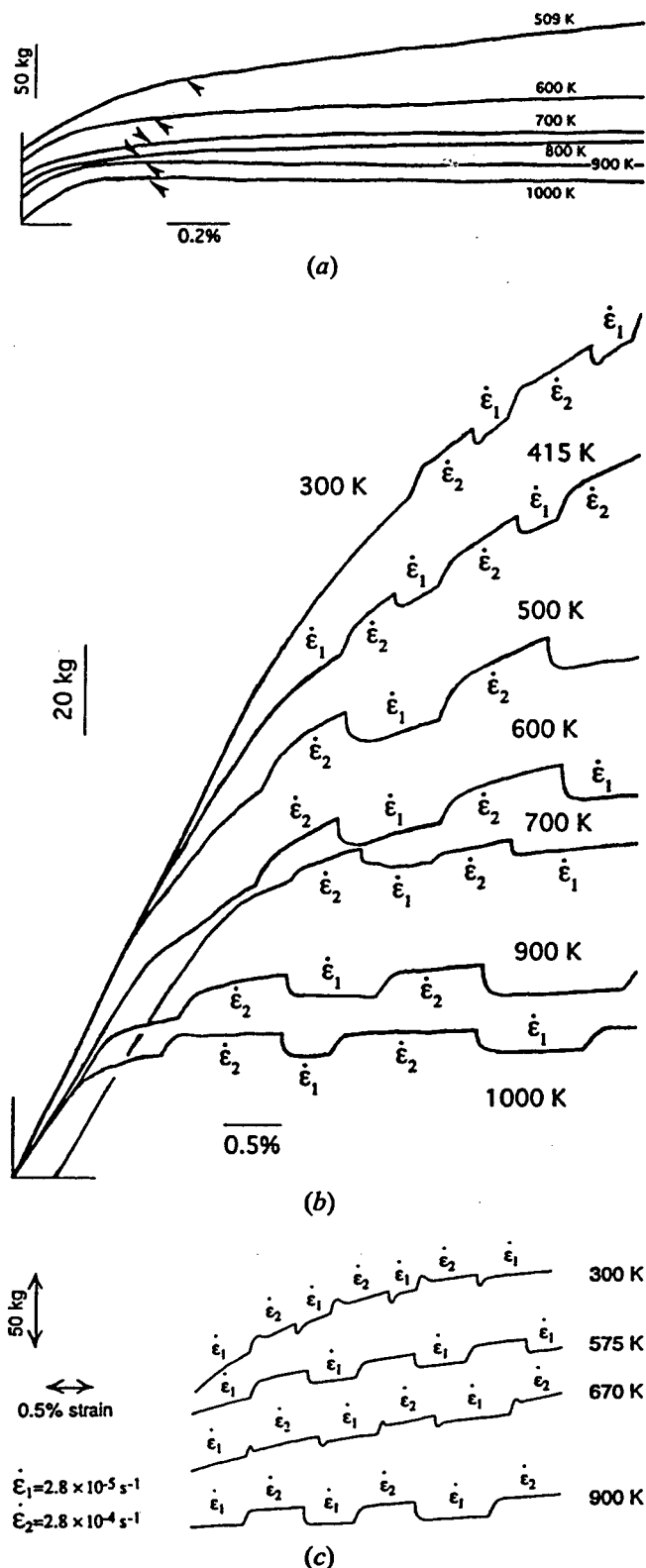
Fig. 5—The effect of temperature on the shape of the flow curves of HP-NiAl and UF-NiAll deformed at $\dot{\epsilon} = 2.8 \times 10^{-5}$ s^{-1}. (a) and (b) HP-NiAl following unixial deformation and strain-rate change experiments. (c) UF-NiAll following strain rate change experiments near 5 pct plastic strain. The arrows in (a) denote the location of the 0.2 pct offset yield stress.

microstructure consists of jogged and curved dislocation segments and dislocation debris in the form of elongated
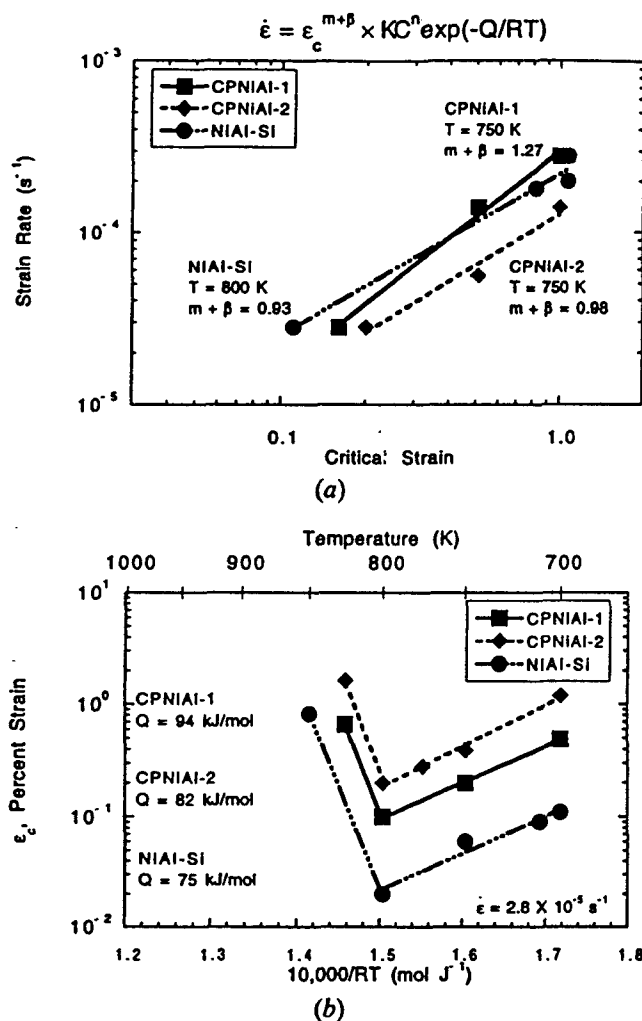
$$\dot{\varepsilon} = \varepsilon_c^{m+\beta} \times KC^n \exp(-Q/RT)$$

(a)

(b)

Fig. 6—The influence of $\dot{\varepsilon}$ and T on the critical strain for the onset of serrated flow, ε_c, for CPNiAl-1, CPNiAl-2, and NiAl-Si: (a) ln $\dot{\varepsilon}$ vs ln ε_c and (b) ln ε_c vs 1/T.

(a)

(b)

(c)

Fig. 7—Plots of ln $\dot{\varepsilon}$ vs 1/T for CPNiAl-1, CPNiAl-2, and NiAl-Si illustrating the T-$\dot{\varepsilon}$ regimes for the occurrence of serrated flow. (a) CPNiAl-1, (b) CPNiAl-2, and (c) NiAl-Si.

loops. At high strains (Figure 9(b)), the dislocations arrange themselves into cellular networks containing a low volume fraction of intercellular dislocations or debris. Such structures are attributed to the easy cross-slip of screw dislocations during room-temperature deformation.[35–38]

Figure 10(a) shows the deformation microstructure of a CPNiAl-1 sample deformed at 700 K in the DSA regime. The microstructure of CPNiAl-1 consists of poorly defined cells or the beginning of a vein structure with the densest cell walls oriented parallel to the $\langle 110 \rangle$ crystallographic direction. Coincident with this deformation structure was a relatively high density of dislocations within the cell walls Figure 10(a). Cell walls in non-$\langle 110 \rangle$ directions were particularly poorly defined indicating some sort of localized or planar deformation process in this temperature regime. This structure is reminiscent of the ones developed during low-cycle fatigue testing of ferritic Fe-24Cr-4Al[39] and polycrystalline NiAl in the DSA regime.[40] Similar deformation microstructures were observed in $\langle 110 \rangle$-oriented CPNiAl-2 and NiAl-Si. An example of the structure that evolved in the NiAl-Si alloy following deformation at its SRS minimum is shown in Figure 10(b). In this case, the cell walls oriented parallel to the $\langle 100 \rangle$ direction. Similar observations

have been reported previously for $\langle 110 \rangle$-oriented conventional purity NiAl single crystals.[41,42,43]

Figure 11 shows the deformation substructure observed in CPNiAl-1 following deformation at 1000 K. This structure was characterized by a much lower dislocation density
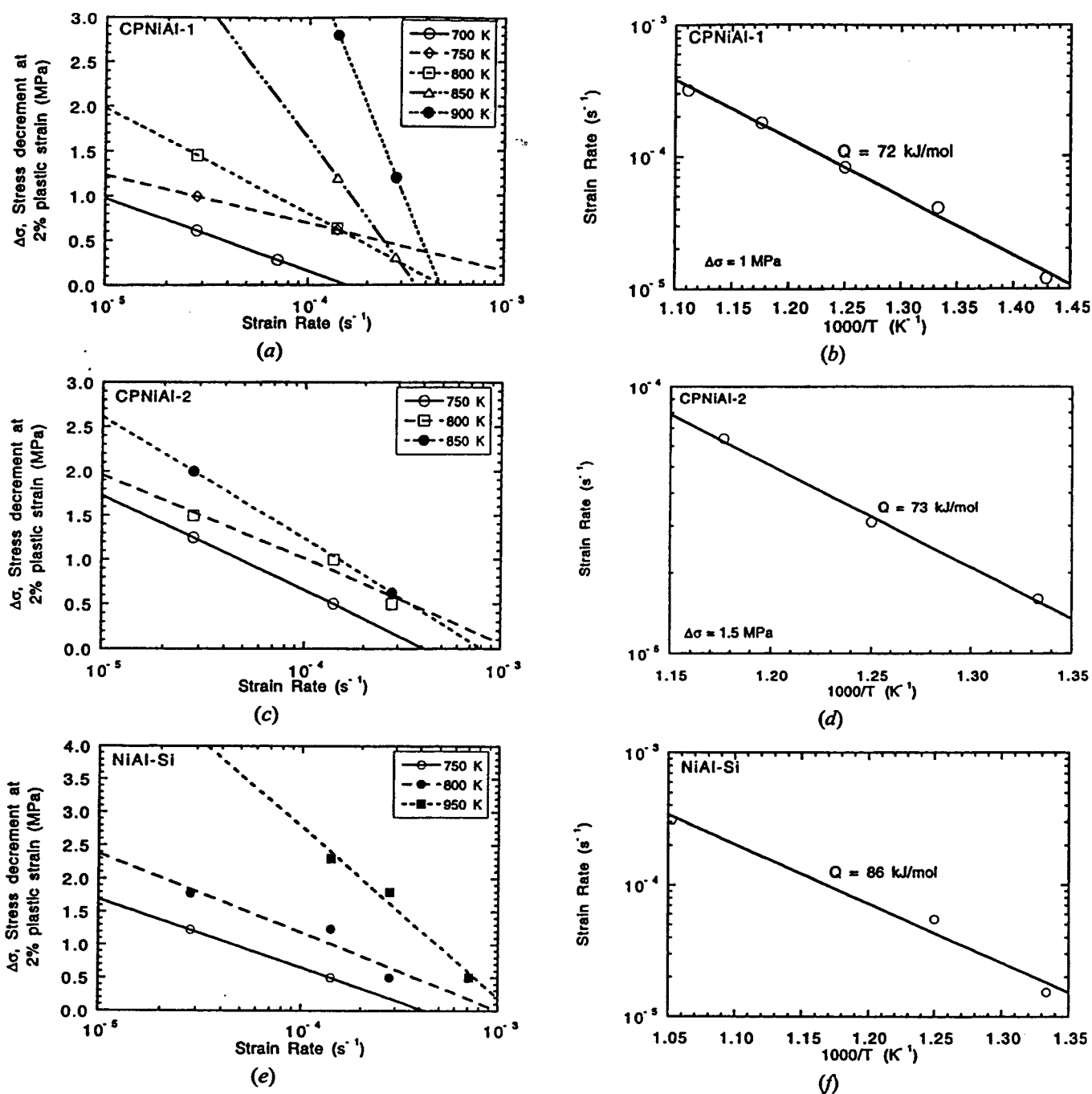
Fig. 8—Plots of the stress drop at 2 pct plastic strain vs $\dot{\varepsilon}$ at constant T and $\dot{\varepsilon}$ vs $1/T$ for CPNiAl-1, CPNiAl-2, and NiAl-Si illustrating use of the stress drop method for determining activation energy.[13] (a) and (b) CPNiAl-1; (c) and (d) CPNiAl-2; and (e) and (f) NiAl-Si.

Table II. Summary of the Activation Energies for Serrated Flow Evaluated Using Different Methods for Conventional Purity and Si-Doped NiAl Single Crystals

Method Employed to Evaluate Q	Activation Energy, Q (kJ/mol)				
	CPNiAl-1 <123>	CPNiAl-2 <110>	NiAl-Si <110>	CP-NiAl <110>	CP-NiAl <110>
(1) From log $\dot{\varepsilon}_c$ vs $1/T$ plots	94	82	71	—	—
(2) From onset of log $\dot{\varepsilon}$ vs $1/T$ map	66	77	68	115[5]	134[16]
(3) Stress drop method	102	88	86	—	—
Average Q for the onset of serrations using methods 1 through 3	87 ± 19	82 ± 7	75 ± 10	—	—

(a)
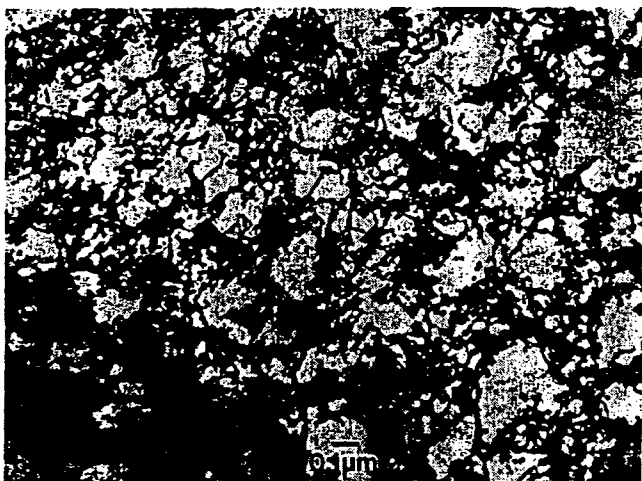
(b)

Fig. 9—Room-temperature deformation structure observed in CPNiAl-2: (a) after ~0.2 pct plastic deformation and (b) after ~2 pct plastic deformation.

(a)

(b)

Fig. 10—Deformation structures observed in CPNiAl-1 and NiAl-Si after ~17 pct plastic deformation. (a) CPNiAl-1 at 700 K and (b) NiAl-Si at 700 K.

than that observed at 300 K or at the SRS minimum and the general lack of a cell structure. This is attributed to the greater relaxation and recovery effects which become important at this temperature.

In NiAl-Mo following deformation at the SRS minimum (Figure 12), structures consisting of poorly defined cells and dislocation tangles were observed. However, the vein structures observed in CPNiAl-1 were not as evident, though the densest cell walls were again those aligned along ⟨110⟩. In addition, a lower density of intercellular debris and dislocations was observed even after levels of deformation equivalent to those in CPNiAl-1. In HP-NiAl (Figure 13(a)), cellular structures characterized by large, loosely packed cell walls with very little intercellular debris were observed, indicating a much greater ease of cross-slip in this alloy compared to either CPNiAl-1, NiAl-Si, or NiAl-Mo at comparable intermediate temperatures. On occasion, single slip bands were observed propagating across the sample (Figure 13(b)), indicating some localized slip processes but not to the same degree as in the other alloys.

Fig. 11—Dislocation morphology observed in CPNiAl-1 after 11 pct deformation at 1000 K.

Fig. 12—Deformation structure observed in NiAl-Mo after 9 pct plastic deformation at 700 K.

(a)

(b)

Fig. 13—Deformation structure observed in HP-NiAl after 9 pct plastic deformation at 725 K. (a) Cellular morphology typical of most samples and (b) a single deformation band observed in one of the foils.

Additional evidence for planar slip processes in the DSA regime was revealed in the optical morphology of slip traces on the various specimen surfaces (Figures 14 and 15). Slip bands were observed throughout the gage of all specimens and at all test temperatures similar to the behavior shown in Figure 14 for CPNiAl-1. In CPNiAl-1, for example, indistinct slip traces were observed on specimens tested at room temperature (Figure 14(a)). However, as the test temperature was increased towards the SRS minimum, the slip traces became more distinct and more coarsely spaced (Figures 14(b) through (d)). At temperatures well above the SRS minimum, more indistinct, finely spaced, and diffuse traces were again observed (Figure 14(e)). In the ⟨123⟩-oriented specimens, single slip traces were predominantly observed, whereas in ⟨110⟩-oriented specimens intersecting slip traces from multiple slip systems were common. An example of this is illustrated in Figure 15. In agreement with prior studies,[18,35,44] slip trace analysis confirmed that slip occurred on {110} or {100} planes with the actual slip plane being dependent upon specimen orientation. In ⟨110⟩-oriented specimens, traces consistent with {100} slip planes were typically observed, while traces consistent with {110} slip planes were observed in ⟨123⟩-oriented specimens. The DSA and serrated flow behavior were observed to the same extent regardless of the operative slip plane.

IV. DISCUSSION

A. Manifestations of Dynamic Strain Aging

The temperature-dependent properties (i.e., CRSS/E, SRS, and θ/E) and the deformation substructures exhibit several features that can be associated with the occurrence of strain aging. First, the temperature dependencies of the CRSS/E and θ/E should decrease with increasing temperature. In the cases of the CPNiAl-1, CPNiAl-2, UF-NiAl1, NiAl-Mo, and NiAl-Si alloys, however, anomalous regions in the form of local peaks or plateaus were observed in the
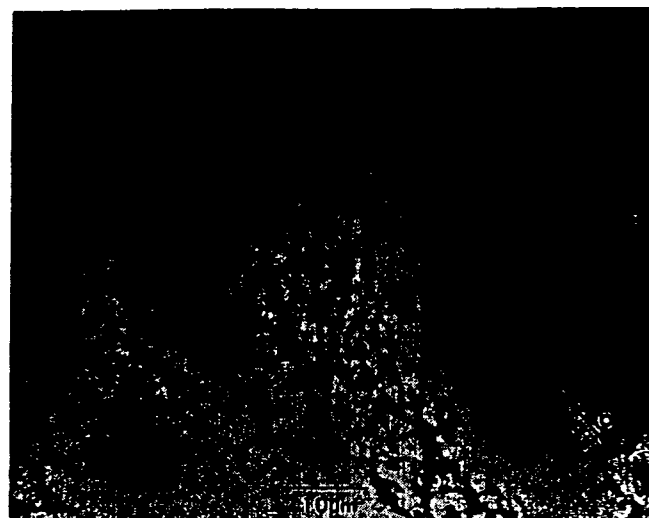
temperature range of 650 to 1000 K. No similar features were observed for HP-NiAl.

Second, the temperature dependence of the SRS exhibited distinct minimums for all six alloys in low and intermediate temperature ranges, with SRS actually becoming negative for CPNiAl-1, CPNiAl-2, and NiAl-Si in the intermediate temperature range. Coincident with this region of negative SRS was the observation of serrated flow during mechanical testing, which directly supports the premise that DSA occurs in this intermediate temperature range in NiAl. In HP-NiAl, NiAl-Mo, and in UF-NiAl1, SRS always remained positive and serrated flow was not observed. However, flow-stress transients on changes in strain rate in the form of sharp upper yield points were consistently observed during testing near the SRS minimum in UF-NiAl1 and NiAl-Mo, which are again indicative of DSA. No flow-stress transients were observed at intermediate temperatures during the testing of HP-NiAl. Additionally, SRS minima were observed to occur at lower temperatures than the CRSS/E or θ/E maxima. Such observations support the no-

(a)

(b)

(c)

(d)

(e)
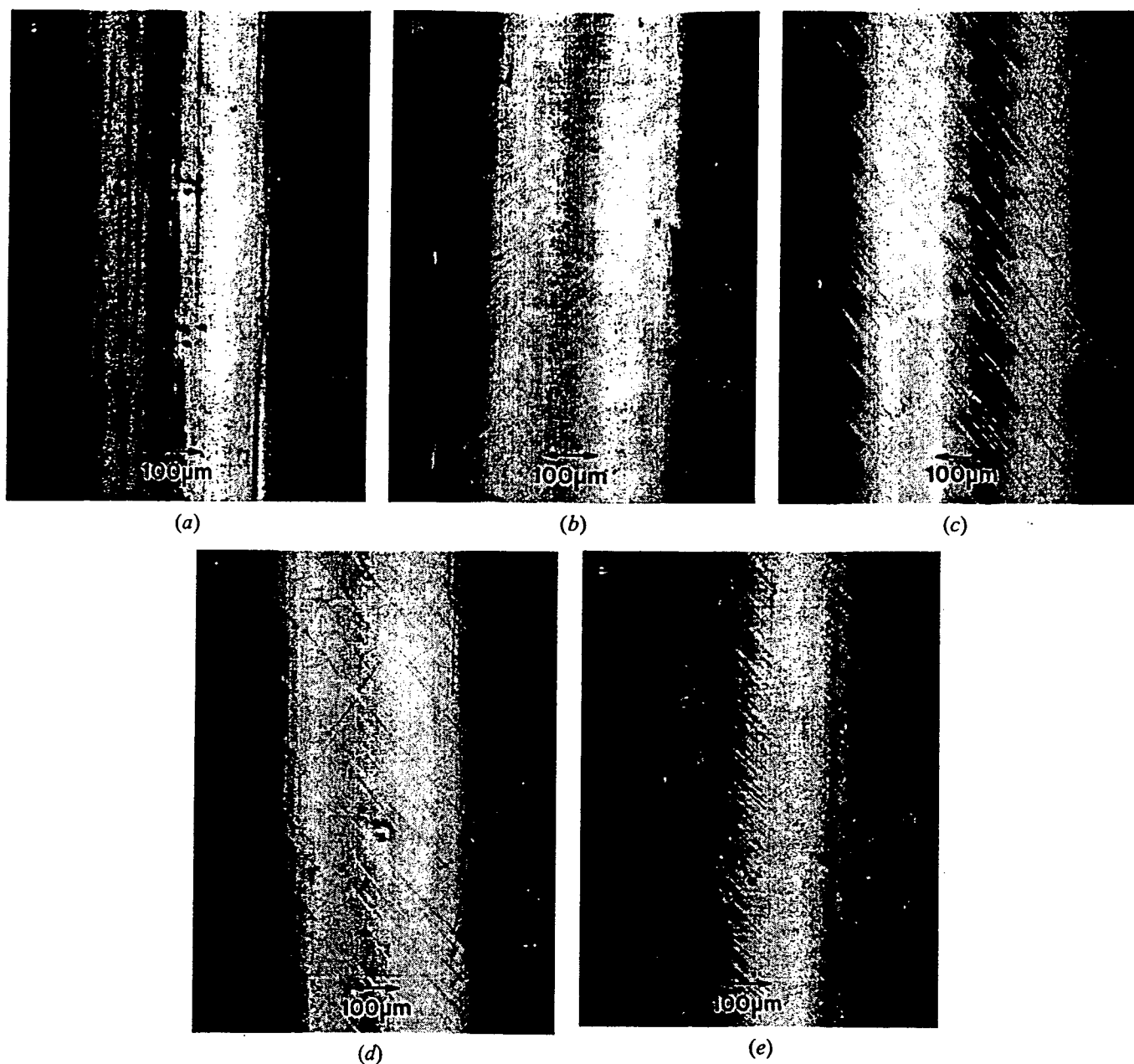
Fig. 14—Optical micrographs of the gage section CPNiAl-1 samples deformed in tension over the temperature range 300 to 1000 K. (a) 300 K, (b) 500 K, (c) 600 K, (d) 750 K, and (e) 1000 K. Note the presence of coarse slip traces at 600 and 750 K.

tion of a DSA effect.[30,31,45] Classical theory[31,45] indicates that during the occurrence of DSA, dislocation motion is characterized by a waiting time t_w during which dislocations are temporarily arrested at obstacles in the slip path. During this waiting time the dislocations can be further pinned by diffusing solutes. This causes the obstacles to dislocation motion to become stronger with increased waiting time and results in an enhanced resistance to plastic deformation. The SRS is said to become minimum when the time required to pin a dislocation t_a becomes equal to the waiting time. Thus, when t_w is fixed by fixing the strain rate, strengthening will become maximum when the temperature becomes high enough that $t_a << t_w$, i.e., maximum strengthening will occur at higher temperatures than the SRS minimum.

Third, distinctively coarse slip traces were observed on the surfaces of specimens deformed in the intermediate temperature range, while finer traces persisted outside of this temperature regime. Slip-trace analysis confirmed that these traces were preferentially oriented along specific crystallographic directions based upon the initial orientation of the crystal. More detailed analysis of the dislocation substructures formed during deformation at temperatures both below and above the regime where serrated flow occurs were characterized by cell structures and dense tangles. These structures are characteristic of intense cross-slip at low temperatures or dislocation climb at high temperatures. In contrast, the substructure formed in the DSA regime was typified by a coarse dislocation vein structure. An important additional feature in samples exhibiting serrated flow is that the regions between the dislocation walls often contain a rather uniform dislocation distribution. It is proposed that
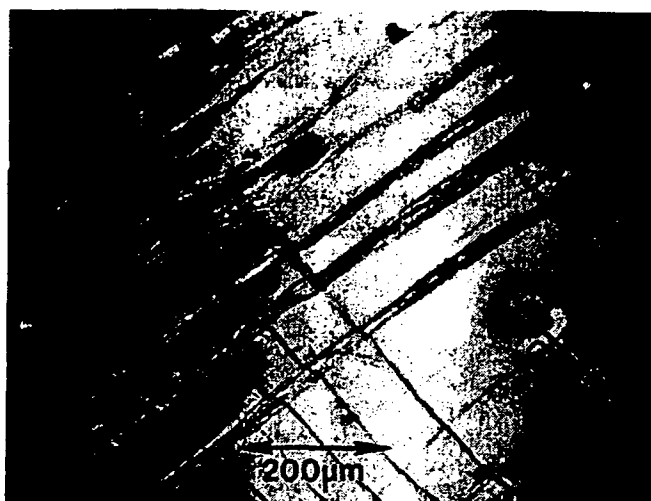
Fig. 15—Optical micrograph of NiAl-Si deformed in compression at 800 K illustrating interesecting ⟨100⟩ slip traces.

Alloy/ Metal	Element/Point Defect*					
	H	C	N	O	Vacancy	subst. solutes
V	—	114	143	121	—	—
Nb	—	138	146	113	—	—
Ta	25[46]	161	158	107	—	—
Cr	—	—	102	—	—	—
Fe	8.4 12 to 13	80 to 84	73 to 78	—	—	—
W	—	169	—	—	—	—
NiAl	—	—	—	—	~300[13]	~225[13]

Data taken from Ref. [47] unless otherwise noted.

these interwall dislocations result from solute locking of slow-moving dislocations between slip bands. Inhomogeneous deformation occurs as a result of differential movement of dislocations within and between the dislocation walls.

Based on the results described here, it is possible to attribute the anomalous mechanical behaviors observed in this study to DSA or the migration of solutes to mobile dislocations during deformation. Additional confirmation of this phenomenon is provided by SSA and DSA studies performed on soft-oriented single crystals[5,6,9,16–18] and on polycrystalline NiAl,[14,15,19,20] wherein serrated yielding, flow stress transients, and a $t^{2/3}$ time dependence of the yield point return have been observed in conventional purity and in carbon doped NiAl alloys.

B. The Diffusing Species

It is possible to ascertain the species responsible for strain aging by examining the data generated in this study. In Section III, it was noted that the values for the exponent $(m + \beta)$ were within the range 0.9 to 1.3. Typically when $(m + \beta)$ is between 2 and 3, the specie resulting in serrated yielding is a substitutional element, whereas when $(m + \beta)$ is in the range 0.5 and 1, an interstitial specie is responsible.[30] Additional inferences can be made by comparing the calculated activation energies for strain aging with the limited diffusion data available for NiAl. Independent of composition, the average activation energy for the diffusion of substitutional elements in NiAl is in the neighborhood of 225 ± 39 kJ/mol, which is somewhat inconsistent with the activation energy for the formation and migration of vacancies in NiAl which is closer to 300 kJ/mol.[13] Nonetheless, as indicated Section III, the experimentally determined activation energies for strain aging lie within the range 70 to 100 kJ/mol, which are far lower than those required to move substitutional solutes or point defects and which are within the range for the diffusion of interstitial solutes in bcc metals (Table III).

The specific interstitial species responsible for DSA can be identified by comparison of the deformation behavior for the six single-crystal alloys vs their composition and the

results from previous studies.[14,15,19,20] In these previous studies, O and N were ruled out as the cause of SSA effects in polycrystalline alloys. In this study, serrated flow was observed in CPNiAl-1, CPNiAl-2, and NiAl-Si, but, not in HP-NiAl, UF-NiAl1, or NiAl-Mo. In HP-NiAl, the C and Si concentrations were much lower than those observed in CPNiAl-1, CPNiAl-2, or NiAl-Si (i.e., 76 at. ppm C vs >150 at. ppm C and 500 at. ppm Si vs >1500 at. ppm Si), which suggests that the lack of serrated flow in HP-NiAl is related to reductions in the C and/or Si contents. That both elements are important for the observation of DSA is supported by the results of Weaver[15] and the results of Hack and co-workers[5,6,9,16,17] and Brzeski.[18] Weaver showed that yield-point formation is enhanced and that serrated flow is observed in conventional-purity polycrystalline alloys containing >1500 at. ppm Si in addition to normal levels of C (approximately 150 at. ppm). Similarly, Hack and co-workers and Brzeski observed dramatic increases in fracture toughness following intermediate temperature annealing and serrated flow in soft-oriented single crystals containing between 145 and 470 at. ppm C and between 1300 and 2500 at. ppm Si. When C is maintained at levels comparable to the conventional-purity single-crystal alloys but Si is reduced to less than 100 at. ppm, as in the case of UF-NiAl1, serrated flow is not observed but yield stress transients upon an increase in strain rate and a yield-stress plateau are still observed between 600 and 900 K. This indicates that C still causes some strain-aging behaviors but that Si somehow enhances the effect. Finally, in NiAl-Mo, the bulk Si levels were nearly equivalent to those in NiAl-Si (i.e., 0.23 vs 0.29 at. pct Si) while the bulk interstitial levels were higher than those observed in CPNiAl-1, CPNiAl-2, and NiAl-Si, the three alloys that exhibited serrated flow. However, no serrated flow was observed in NiAl-Mo. The microstructural analysis presented in this article showed that this alloy contains a distribution of coarse Mo_2C precipitates and suggests that the lack of serrated flow in NiAl-Mo is due to the gettering of C from the NiAl matrix. Were Si the cause for the serrated yielding instead of C, it is expected that serrated yielding would also be observed in NiAl-Mo since it contains nearly as much Si as the NiAl-Si alloy. In addition, if C alone were the cause, then it is expected that serrated yielding would be observed in UF-NiAl1, which contains more C than CPNiAl-2 but only 69 at. ppm Si. Therefore, these results strongly suggest that the serrated yielding in NiAl is a result of interactions

between dislocations and solute atoms, namely C and Si, but that C is the main cause for the manifestations of DSA observed in the NiAl single crystals investigated in this study.

In Section III, it was noted that two SRS minima were observed for each alloy: one at low temperatures and the other at intermediate temperatures. Though it is tempting to attribute the low and intermediate temperature minima to C and Si, respectively, a conclusive statement cannot be made at this time. Were the low-temperature SRS minima the result of C, it is expected that the conventional-purity and Si-doped alloys also would exhibit flow-stress transients or serrated flow at low temperatures. Prior investigations have illustrated, both experimentally and theoretically, that two SRS minima due to Snoek ordering and Cottrell atmosphere formation are often observed in bcc and in bcc-like (e.g., B2) systems when DSA is caused by an interstitial specie[48-53] and other systems where interstitial-vacancy clusters are known to cause DSA.[54] Thus, it is possible that both minima are caused by the same specie, however, more complete investigations of the low temperature regime are warranted before a definitive conclusion can be formulated.

Furthermore, while it is impossible to devise a definitive mechanism by which Si and C can synergistically cause serrated flow, it is possible to speculate. First, it is possible that Si simply modifies the activity coefficient of C in NiAl. It has been observed in austenitic Fe-Mn-C alloys[55,56] that the addition of aluminum raised the activation energy for the onset of serrated flow by reducing the carbon activity, and thus its diffusivity, in these alloys. The opposite effect could occur in the case of NiAl, where Si increases the activity and diffusivity of C in NiAl and thus decreases the activation energy for the onset of serrated flow. The results collected in this study indicate that the activation energies for the onset of serrated flow in CPNiAl-1 (0.17 at. pct Si), CPNiAl-2 (0.15 at. pct Si), and in NiAl-Si (0.25 at. pct Si) are similar. Unfortunately, no activation energy could be calculated for NiAl containing lower Si concentrations, since serrated flow was not observed.

Second, DSA could be the result of an interaction solid solution hardening (ISSH) effect as described in References 57 through 61. This process is attributed to the strengthening that arises from the simultaneous presence in solid solution of substitutional and interstitial atoms that exhibit an affinity for each other. The exact reasons for ISSH are unknown but depend upon how these solute atoms interact with each other and with moving dislocations.[59] For example, when interstitials bind strongly to dislocations, strain-aging effects are caused by the reduced mobility of the dislocations which must now drag interstitial atmospheres along with them. However, if interstitials also bind strongly with substitutional solutes, strain aging can be extended to higher temperatures due to the reduced mobility of the interstitial caused by interaction with the substitutional solute (i.e., dislocations must now drag interstitial-substitutional clusters rather than individual interstitials). Diffusion-couple studies between NiAl, Ni₃Al, and SiC[62,63] have suggested that Si may diffuse as fast as or faster than C in NiAl and may result in the formation of complex Ni-Al-Si-C phases. This suggests that some clustering of C

with Si, Ni, and Al may occur resulting in an expansion of the DSA regime and stronger pinning.

A third possibility is that substitution of a smaller Si atom can result in an increased tetragonal distortion in the NiAl lattice. Recent theoretical results suggest that Si will only occupy Al lattice positions,[64] whereas other substitutional elements such as Fe or Ga will tend to occupy the site of the stoichiometrically deficient host element.[64,65] Assuming that C atoms occupy octahedral sites, it is theorized that the substitution of smaller Si atoms for Al will result not only in a reduction in the size of the octahedral interstices but also into more localized distortions of the lattice. Similarly, in the cases of Fe or Ga, which occupy the stoichiometrically deficient host element sites, the overall distortions in the lattice will be minimized because the tetragonal distortions created by interstitial atoms can be partially accomodated, resulting in reduced strain-aging effects. Recently, serrated yielding has been reported to occur over a smaller temperature range in both Fe-doped and in Ga-doped single-crystal alloys,[66] which suggests that there might be some validity to this potential mechanism though more work is needed.

Determination of the actual mechanism behind the synergistic effect of C plus Si on DSA in NiAl will require further study. In light of the fact that Si is frequently present in conventional-purity NiAl single crystals grown by the Bridgman method due to contamination from alumina-silicate shell molds, this topic deserves additional attention.

V. SUMMARY AND CONCLUSIONS

Five of the six alloys examined in the present study exhibit yield stress and work-hardening plateaus or small peaks in the temperature range 650 to 1000 K, indicative of DSA. In HP-NiAl, anomalous behavior was not evident.

Pronounced regions of negative SRS have been observed in conventional-purity (CPNiAl-1 and CPNiAl-2) and Si-doped (NiAl-Si) alloys in the temperature range 600 to 800 K. Coincident with this temperature regime was the occurrence of serrated flow (i.e., the PLC effect).

In the temperature range where serrated flow occurs, the dislocation distribution consists mainly of thick dislocation walls or the beginning of a vein structure indicating localized slip. In HP-NiAl and NiAl-Mo, the dislocations maintain cellular networks indicating more abundant and, therefore, easier cross slip. At temperatures above or below the regime of serrated flow, well-developed cell structures dominate for all alloys.

Average activation energies for serrated flow have been calculated using three methods: 84 ± 10 kJ/mol (ε_c vs T), 73 ± 1 kJ/mol (stress-drop method), and 78 ± 7 kJ/mol (Arrhenius method). All values are reasonable order of magnitude estimates for interstitial diffusion in bcc lattices and agree with prior observations in polycrystalline NiAl and with Hack and co-workers.[5,6,9,16,17]

Overall, these results suggest that a combination of interstitial and substitutional solutes, namely, C and Si, cause serrated flow in soft-oriented NiAl. Small additions of Mo to NiAl caused a dramatic increase in yield stress but eliminated the serrated yielding. This latter effect is attributed to the gettering of C by Mo.

REFERENCES

1. R.W. Margevicius and J.J. Lewandowski: *Scripta Metall. Mater.*, 1991, vol. 25, pp. 2017-22.
2. R.W. Margevicius, J.J. Lewandowski, I.E. Locci, and R.D. Noebe: *Scripta Metall. Mater.*, 1993, vol. 29, pp. 1309-12.
3. R.W. Margevicius and J.J. Lewandowski: *Acta Metall. Mater.*, 1993, vol. 41, pp. 485-96.
4. R.W. Margevicius, J.J. Lewandowski, and I.E. Locci: in *Structural Intermetallics*, R. Darolia, J.J. Lewandowski, C.T. Liu, P.L. Martin, D.B. Miracle, and M.V. Nathal, eds., TMS, Warrendale, PA, 1993, pp. 577-84.
5. J.E. Hack, J.M. Brzeski, and R. Darolia: *Mater. Sci. Eng.*, 1995, vols. A192–A193, pp. 268-76.
6. J.E. Hack, J.M. Brzeski, R. Darolia, and R.D. Field: in *High-Temperature Ordered Intermetallics V*, I. Baker, R. Darolia, J.D. Whittenberger, and M.H. Yoo, eds., Materials Research Society, Pittsburgh, PA, 1993, vol. 288, pp. 1197-1202.
7. E.P. Lautenschlager, D.A. Kiewit, and J.O. Brittain: *Trans. TMS-AIME*, 1965, vol. 233, pp. 1297-1302.
8. R.D. Field, D.F. Lahrman, and R. Darolia: in *High-Temperature Ordered Intermetallic Alloys V*, I. Baker, R. Darolia, J.D. Whittenberger, and M.H. Yoo, eds., Materials Research Society, Pittsburgh, PA, 1993, vol. 288, pp. 423-28.
9. J.M. Brzeski, J.E. Hack, R. Darolia, and R.D. Field: *Mater. Sci. Eng.*, 1993, vol. A170, pp. 11-18.
10. C.T. Liu, E.H. Lee, E.P. George, and A.J. Duncan: *Scripta Metall. Mater.*, 1994, vol. 30, pp. 387-92.
11. R.T. Pascoe and C.W.A. Newey: *Metall. Sci. J.*, 1968, vol. 2, pp. 138-43.
12. R.T. Pascoe and C.W.A. Newey: *Metall. Sci. J.*, 1971, vol. 5, pp. 50-55.
13. R.D. Noebe, R.R. Bowman, and M.V. Nathal: *Int. Mater. Rev.*, 1993, vol. 38, pp. 193-232.
14. M.L. Weaver, V. Levit, M.J. Kaufman, and R.D. Noebe: in *High-Temperature Ordered Intermetallic Alloys VI*, J.A. Horton, I. Baker, S. Hanada, R.D. Noebe, and D.S. Schwartz, eds., Materials Research Society, Pittsburgh, PA, 1995, vol. 364, pp. 425-30.
15. M.L. Weaver: Ph.D. Dissertation, University of Florida, Gainesville, FL, 1995.
16. J.M. Brzeski, J.E. Hack, and R. Darolia: in *High-Temperature Ordered Intermetallic Alloys VI*, J.A. Horton, I. Baker, S. Hanada, R.D. Noebe, and D.S. Schwartz, eds., Materials Research Society, Pittsburgh, PA, 1995, vol. 364, pp. 419-24.
17. J.E. Hack, J.M. Brzeski, and R. Darolia: *Scripta Metall. Mater.*, 1992, vol. 27, pp. 1259-63.
18. J.M. Brzeski: Ph.D. Dissertation, Yale University, New Haven, CT, 1995.
19. M.L. Weaver, M.J. Kaufman, and R.D. Noebe: *Intermetallics*, 1996, vol. 4, pp. 121-29.
20. M.L. Weaver, R.D. Noebe, J.J. Lewandowski, B.F. Oliver, and M.J. Kaufman: *Mater. Sci. Eng.*, 1995, vols. A192–A193, pp. 179-85.
21. M.L. Weaver, R.D. Noebe, J.J. Lewandowski, B.F. Oliver, and M.J. Kaufman: *Intermetallics*, 1996, accepted for publication.
22. M.L. Weaver, R.D. Noebe, and M.J. Kaufman: *Scripta Mater.*, 1996, vol. 34, pp. 941-48.
23. U.F. Kocks: *Metall. Trans. A*, 1985, vol. 16A, pp. 2109-29.
24. R.J. Wasilewski: *Trans. TMS-AIME*, 1966, vol. 36, pp. 455-57.
25. R.D. Noebe, R.R. Bowman, and M.V. Nathal: in *Physical Metallurgy and Processing of Intermetallic Compounds*, N.S. Stoloff and V.K. Sikka, eds., Chapman and Hall, New York, NY, 1995, pp. 212-50.
26. D.B. Miracle: *Acta Metall. Mater.*, 1993, vol. 41, pp. 649-84.
27. M.L. Weaver, M.J. Kaufman, and R.D. Noebe: *Scripta Metall. Mater.*, 1993, vol. 29, pp. 1113-18.
28. J.S. Winton, A.A. Morrone, V.I. Levit, and M.J. Kaufman: Paper presented at the TMS Fall Meeting, Cleveland, OH, 1995.
29. J.S. Winton, V.I. Levit, and M.J. Kaufman: University of Florida, Gainesville, FL, unpublished research, 1995.
30. P. Rodriquez: *Bull. Mater. Sci. (India)*, 1984, vol. 6, pp. 653-63.
31. P.G. McCormick: *Acta Metall.*, 1972, vol. 20, pp. 351-54.
32. S. Venkadesan, C. Phaniraj, P.V. Sivaprasad, and P. Rodriguez: *Acta Metall. Mater.*, 1992, vol. 40, pp. 569-80.
33. E. Pink: *Scripta Metall.*, 1983, vol. 17, pp. 847-52.
34. R.W. Hayes and W.C. Hayes: *Acta Metall.*, 1982, vol. 30, pp. 1295-1301.
35. J.T. Kim: Ph.D. Dissertation, The University of Michigan, Ann Arbor, MI, 1990.
36. P. Nagpal, I. Baker, and J.A. Horton: *Intermetallics*, 1994, vol. 2, pp. 23-29.
37. P. Nagpal and I. Baker: *J. Mater. Lett.*, 1992, vol. 11, pp. 1209-10.
38. J.T. Kim, R.D. Noebe, and R. Gibala: *Proc. Int. Symp. of Intermetallic Compounds—Structural and Mechanical Properties*, O. Izumi, ed., Japan Institute of Metals, Sendai, 1991, pp. 591-95.
39. S.C. Tjong and J.S. Zhang: *Scripta Metall. Mater.*, 1995, vol. 32, pp. 1589-93.
40. C.L. Cullers, S.D. Antolovich, and R.D. Noebe: in *High-Temperature Ordered Intermetallic Alloys V*, I. Baker, R. Darolia, J.D. Whittenberger, and M.H. Yoo, eds., Materials Research Society, Pittsburgh, PA, 1993, vol. 288, pp. 531-36.
41. T. Takasugi, J. Kishino, and S. Hanada: *Acta Metall. Mater.*, 1993, vol. 41, pp. 1009-20.
42. M.A. Crimp, S.C. Tonn, and Y. Zhang: *Mater. Sci. Eng.*, 1993, vol. A170, pp. 95-102.
43. Y. Zhang, S.C. Tonn, and M.A. Crimp: in *High-Temperature Ordered Intermetallic Alloys V*, I. Baker, R. Darolia, J.D. Whittenberger, and M.H. Yoo, eds., Materials Research Society, Pittsburgh, PA, 1993, vol. 288, pp. 379-84.
44. R.D. Field, D.F. Lahrman, and R. Darolia: in *High-Temperature Ordered Intermetallic Alloys IV*, L.A. Johnson, D.P. Pope, and J.O. Stiegler, eds., Materials Research Society, Pittsburgh, PA, 1991, vol. 213, pp. 255-60.
45. L.P. Kubin and Y. Estrin: *J. Phys. III*, 1991, vol. 1, pp. 929-43.
46. C.R. Brooks: in *ASM Metals Handbook Desk Edition*, H.E. Boyer and T.L. Gall, eds., ASM, Metals Park, OH, 1985, pp. 28.66.
47. E.T. Stephenson: *Trans. TMS-AIME*, 1965, vol. 233, pp. 1183-84.
48. M. Koiwa: *Phil. Mag.*, 1971, vol. 24, pp. 81-106.
49. M. Koiwa: *Phil. Mag.*, 1971, vol. 24, pp. 799-814.
50. M. Koiwa: *Phil. Mag.*, 1971, vol. 24, pp. 539-54.
51. M. Koiwa: *Phil. Mag.*, 1971, vol. 24, pp. 107-22.
52. R.E. Reed-Hill and T. Zhu: *High Temp. Mater. Proc.*, 1984, vol. 6, pp. 93-117.
53. R.E. Reed-Hill and M.J. Kaufman: *Acta Metall. Mater.*, 1995, vol. 43, pp. 1731-39.
54. K.S.B. Rose and S.G. Glover: *Acta Metall.*, 1966, vol. 14, pp. 1505-16.
55. B.K. Zuidema, D.K. Subramanyam, and W.C. Leslie: *Metall. Trans. A*, 1987, vol. 18A, pp. 1629-39.
56. T. Shun, C.M. Wan, and J.G. Byrne: *Acta Metall. Mater.*, 1992, vol. 40, pp. 3407-12.
57. J.D. Baird and C.R. MacKenzie: *J. Iron Steel Inst.*, 1964, vol. 202, pp. 427-36.
58. J.D. Baird and A. Jamieson: *J. Iron Steel Inst.*, 1966, vol. 204, pp. 793-803.
59. J.D. Baird and A. Jamieson: *J. Iron Steel Inst.*, 1972, vol. 210, pp. 841-46.
60. R.L. Klueh and R.E. Oakes, Jr.: *J. Eng. Mater. Technol.*, 1976, vol. 98, pp. 361-68.
61. R.L. Klueh: *J. Nucl. Mater.*, 1977, vol. 68, pp. 294-307.
62. T.C. Chou and T.G. Nieh: *Scripta Metall. Mater.*, 1991, vol. 25, pp. 2059-64.
63. T.C. Chou and T.G. Nieh: in *High-Temperature Ordered Intermetallic Alloys IV*, L.A. Johnson, D.P. Pope, and J.O. Stiegler, eds., Materials Research Society, Pittsburgh, PA, 1991, vol. 213, pp. 1045-50.
64. H. Hosoda, K. Inoue, and Y. Mishima: in *High-Temperature Ordered Intermetallic Alloys VI*, J. Horton, I. Baker, S. Hanada, R.D. Noebe, and D.S. Schwartz, eds., Materials Research Society, Pittsburgh, PA, 1995, vol. 364, pp. 437-42.

65. I.M. Anderson, A.J. Duncan, and J. Bentley: in *High-Temperature Ordered Intermetallic Alloys VI*, J. Horton, I. Baker, S. Hanada, R.D. Noebe, and D.S. Schwartz, eds., Materials Research Society, Pittsburgh, PA, 1995, vol. 364, pp. 443-48.

66. R. Darolia, R.D. Field, R.D. Noebe, A. Garg, and W.S. Walston: *A Mechanistic Study of Microalloying Effects in NiAl*, GE Aircraft Engines/Air Force Office of Scientific Research, Final Report, July 1, 1991–Mar. 31, 1995.

Observations of static strain-aging in polycrystalline NiAl

M. L. Weaver,[a] R. D. Noebe,[b] J. J. Lewandowski,[c] B. F. Oliver[d] & M. J. Kaufman[e]

[a]Center for Nonlinear and Nonequilibrium Aeroscience, Florida A&M University, Tallahassee, Florida 32310, USA and Department of Mechanical Engineering, FAMU/FSU College of Engineering, Florida A&M University/Florida State University, Tallahassee, Florida 32310, USA
[b]NASA Lewis Research Center, Cleveland, Ohio 44135, USA
[c]Department of Materials Science & Engineering, Case Western Reserve University, Cleveland, Ohio 44106, USA
[d]Department of Materials Science & Engineering, University of Tennessee, Knoxville, Tennessee 37996, USA
[e]Department of Materials Science & Engineering, University of Florida, Gainesville, Florida 32611, USA

Static strain-aging has been investigated in eight polycrystalline NiAl alloys. After annealing at 1100 K for 7200 s followed by furnace cooling, high-purity, nitrogen-doped, and titanium-doped alloys exhibited continuous yielding, while conventional-purity and carbon-doped alloys exhibited distinct upper yield points and Lüders strains. Either water quenching from 1100 K or prestraining via hydrostatic pressurization suppressed the yield points in the latter alloys, but they could be reintroduced by further annealing treatments. Yield points could be re-introduced more rapidly if the specimens were prestrained uniaxially rather than hydrostatically, owing to the arrangement of dislocations into cell structures during uniaxial deformation. Chemical analysis suggests that the species responsible for strain-aging is interstitial carbon. Copyright © 1996 Elsevier Science Limited

Key words: A. nickel aluminides, based on TiAl B. mechanical properties at ambient temperature, microalloying, strain-aging, yield stress.

INTRODUCTION

Body-centered cubic (BCC) metals and alloys exhibit an extreme sensitivity to minute additions of interstitials which can lead to strain-aging phenomena. Not surprisingly, several aspects of strain-aging have also been identified as playing a role in the deformation of polycrystalline and single crystal B2 NiAl. They are the occurrence of yield stress plateaus as a function of temperature, yield points, strain-rate sensitivity minima, serrated stress–strain curves, and flow stress transients after changes in strain-rate.[1-21] Extensive work by Margevicius et al.[6,19-21] has shown that a sharp yield point can occur in binary NiAl following annealing at 1100 K and furnace cooling. This yield point can be suppressed by subsequent prestraining of the material by hydrostatic pressurization prior to testing, and it can be recovered by aging the prestrained material for 7200 s, (i.e. 2 h) at 673 K. Similarly, Pascoe and Newey[10] observed the formation of room temperature yield points in near stoichiometric NiAl annealed for 3600 s (1 h) at 350 K following a uniaxial prestrain. In addition, preliminary investiga-

tions by Weaver et al.[13] have shown that these yield points can be suppressed by water quenching from high temperature as opposed to furnace cooling. Despite these observations, no complete investigation of the interrelated effects of interstitial content, annealing and prestrain on mechanical behavior has been conducted on NiAl. Consequently, the purpose of this document is to provide a more thorough description of the combined effects of interstitial content, annealing and prestrain on the tensile flow and fracture behavior of polycrystalline NiAl.

EXPERIMENTAL DETAILS

Material

NiAl alloys in the form of: (1) one titanium doped vacuum induction melted (VIM) ingot (NiAl–Ti); (2) two conventional purity (CPNiAl-1, CPNiAl-2) ingots; (3) two carbon doped castings with varying carbon and oxygen concentrations (NiAl–100C and NiAl–300C); (4) two low interstitial

high-purity zone refined ingots, one of which was subsequently zone leveled with carbon (HP-NiAl and HPNiAl–C respectively); and (5) a nitrogen-atomized powder (NiAl–N) were the basic starting materials used in this investigation. All were extruded at 1200 K at either a 12:1 or 16:1 reduction ratio. Descriptions of the equipment and processes used to fabricate the high purity, zone leveled and nitrogen doped alloys are presented elsewhere.[22-24]

Material characterization

Chemical analyses of the eight extrusions were conducted using the techniques deemed to be the most accurate for the particular elements. The results of these analyses are presented in Table 1 along with the post extrusion grain sizes obtained using the linear intercept method.

Optical microscopy, scanning electron microscopy (SEM) and transmission electron microscopy (TEM) were used to assess the microstructure of the materials. Polished optical microscopy specimens were etched by swabbing with a mixture of 0·10 kg MoO_3, 50 ml HF and 150 ml H_2O.

Samples for transmission electron microscopy (TEM) were cut from the gages of tested tensile specimens with a low-speed diamond saw and twin jet-electropolished in a solution of 70% ethanol, 14% distilled water, 10% butylcellusolve and 6%

perchloric acid at 273 K, 20–25 V and 0·15 mA. TEM examinations were conducted in either a JEOL 100CX or a Philips EM420 microscope operating at accelerating voltage of 120 kV.

Fracture surfaces of selected tensile samples were examined using a Cambridge 200 scanning electron microscope. Quantitative fractography was performed to determine the percentage of intergranular fracture for most alloys. This was accomplished by taking at least five random micrographs of appropriate magnification relative to the grain size from each test specimen and using a point counting technique.

Mechanical testing

Round button-head tensile specimens were ground from the extruded rods so that the gage lengths of the samples were parallel to the extrusion direction. Sample dimensions were 3·1 mm for the tensile gage diameters and 30·0 mm for the tensile gage lengths. Prior to testing, all samples were electropolished in a 10% perchloric acid–90% methanol solution that was cooled to 208 K. Tensile tests were performed on an Instron Model 1125 load frame at a constant crosshead velocity corresponding to an initial strain-rate, $\dot{\varepsilon}$, of 1·4 × 10⁻⁴ s⁻¹. All tests were performed in air at 300 K. True stress–strain data were calculated from the load–time plots and

Table 1. Compositions and grain sizes of the polycrystalline NiAl alloys investigated

| Alloy (heat) | Grain size (μm) | At% | | | | Atppm | | | |
		Ni	Al	Ti	Si	C	O	N	S
CPNiAl-1 (L2971)	18·7±1·5	50·1±0·2	49·7±0·2	—	0·15	147	70*	<9	<7
CPNiAl-2 (L3199)	18·0±2·0	50·1±0·2	49·8±0·2	—	0·02	186	94	<9	<7
HP-NiAl (L2987)	51·4±2·3	49·9±0·2	50·1±0·2	—	0·02	43	32	<9	<7
HPNiAl–C (L2988)	44·6±4·0	50·2±0·2	49·8±0·2	—	0·05	92	30	<9	<7
NiAl–N (P1810)	4·0±0·3	50·1±0·2	49·7±0·2	—	0·02	57	347	904	<7
NiAl–100C (L3218)	20·0±2·0	49·9±0·2	50·0±0·2	—	0·02	490	183	<9	<13
NiAl–300C (L3217)	20·0±2·0	49·9±0·2	50·0±0·2	—	0·01	1153	131	<9	<12
NiAl–Ti (L3215)	20·0±2·0	49·9±0·2	50·0±0·2	0·03	0·00	214	113	15	<7

Ni and Al: Analysis performed using wet chemistry/titration techniques, relative accuracy ± 1%.
C and S: Analysis performed on a simultaneous carbon/sulfur determinator, LECO Corp., Model CS-244, relative accuracy ± 10%.
N and O: Analysis performed on a simultaneous nitrogen/oxygen determinator, LECO Corp., Model TC-136 or Model TC-436, relative accuracy ± 10%.
Ti: Analysis performed using inductively-coupled plasma emission spectroscopy, relative accuracy ± 5%.
Si: Analysis performed on an ultraviolet/visible spectrophotometer, Shimadzu, Model UV-160, relative accuracy ± 10%.
*: The figure of 550 atppm quoted in earlier papers was in error.

yield stresses were determined by the 0·2% offset method.

The tensile testing was accomplished in three steps:

First, baseline mechanical properties were determined for all eight alloys by testing them as follows: (1) as-extruded and (2) as-extruded + 1100 K/7200 s/furnace cool (FC). (3) Four alloys (CPNiAl-1, HP-NiAl, HPNiAl–C, and NiAl–N), having received treatment (2), were prestrained via hydrostatic pressurization to 1·4 GPa. The prestrain pressurization treatment was selected based on the observations of Margeviċius *et al.*[6,19–21]

Second, the temperature regime resulting in the maximum recovery of the yield point was determined for a series of CP-NiAl specimens, having received treatment (3). Specimens were annealed at temperatures ranging from 500 to 1100 K for times ranging between 60 s and 604800 s (168 h) followed by FC, air cooling (AC), or water quenching (WQ).

Third, some specimens were statically strain aged as follows: specimens were prestrained approximately 0·2% in tension at room temperature, unloaded, aged *in situ* on the load frame for aging times varying between 50 s and 113000 s (30 h), and then restrained at room temperature to approximately 0·2%. Aging temperatures were selected based on the results from the test sequences described above. On several occasions, specimens were subjected to recovery anneals of 1100 K/1800 s (30 min.)/AC following an aging cycle. These procedures were repeated several times until fracture occurred in an effort to elucidate the influence of strain-aging on flow and fracture behavior of NiAl. The results of one such experiment are presented in Fig. 1, which shows the stress–strain curves for an alloy following multiple strain-aging cycles. A more detailed accounting of the test method used to study static strain-aging in NiAl is provided in refs 12,13 and 15.
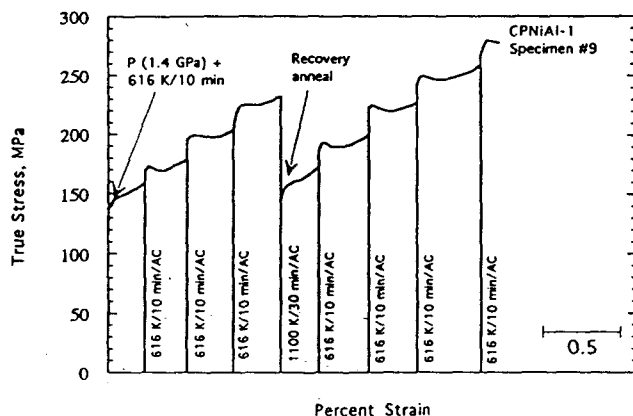
Fig. 1. Series of true stress–strain curves for CP-NiAl after multiple strain-aging cycles.

EXPERIMENTAL RESULTS

Composition and microstructure

Within experimental accuracy (±0·2 at% for Ni and Al), the Ni and Al contents of the eight alloys are not significantly different from each other. The major differences between the materials are the residual Si, C, O and N contents and the presence of Ti as an alloying addition to NiAl–Ti.

The microstructures of all the NiAl alloys were similar as observed by optical microscopy and TEM, and consisted of fully dense, recrystallized and equiaxed grains. The only differences were the observation of semi-continuous distributions of nanometer-size precipitates in the NiAl–N (see ref. 24) and NiAl–Ti alloys, (Fig. 2). In the case of NiAl–N, previous studies have revealed that the precipitates are AlN.[24] Energy dispersive spectroscopic (EDS)
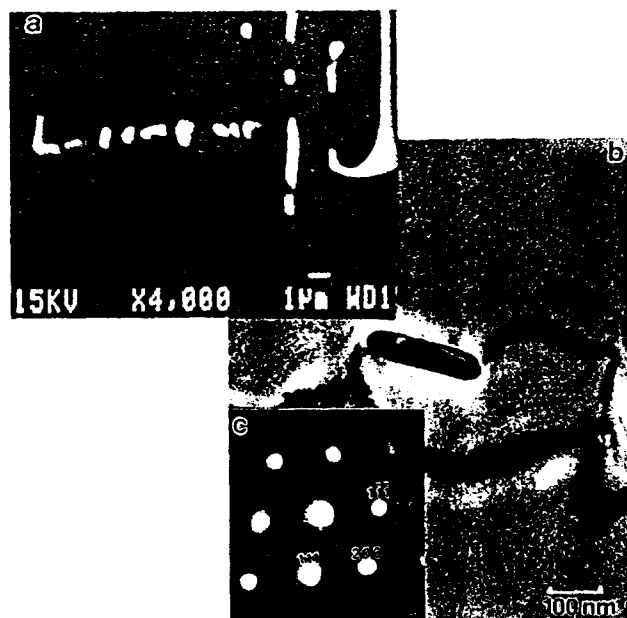
Fig. 2. Precipitates observed in NiAl–Ti: (a) backscattered scanning electron micrograph of TiC precipitates in NiAl–Ti; (b) BFTEM micrograph of a large TiC precipitate; (c) TEM microdiffraction pattern from the TiC precipitate ([001] TiC zone axis); and (d) EDS spectra for the particle in (c) indicating the presence of Ti.

analysis in the TEM indicated that the precipitates in NiAl–Ti were rich in Ti. The individual precipitates were, in general, too fine for analysis. On occasion, however, larger precipitates were observed within individual grains or along grain boundaries. These precipitates were typically elongated in shape as indicated in Fig. 2. Low-intensity EDS peaks corresponding to carbon were detected for some of these precipitates in addition to the distinct Ti peaks. Careful analysis of TEM microdiffraction patterns taken from these larger particles indicated that they were crystallographically consistent with TiC.

Mechanical properties

The baseline mechanical properties are summarized in Table 2. Typical room-temperature stress–strain curves for each alloy are shown in Figs 3–7. From this data it is observed that the yield stress of each alloy decreased following the 1100 K/7200 s/FC anneal. In addition, a tendency for discontinuous yielding was apparent in the CPNiAl-1, CPNiAl-2, HPNiAl-C, NiAl–100C and NiAl–300C alloys but not in HP-NiAl, NiAl–N or in NiAl–Ti. Further decreases in yield stress and elimination of the tendency for discontinuous yielding were achieved

Table 2. Baseline tensile properties of NiAl alloys

Material	Condition*	0·2% yield stress (MPa)	Fracture stress (MPa)	Ductility (%)	Intergranular fracture (%)	Observations[†]
CPNiAl-1	As-extruded	269	379	2·11	na	DY, YP
	As-extruded	275	368	1·83	36·0	DY, YP
	Annealed/FC	184	301	2·08	36·1	DY, sharp YP
	Annealed/FC	197	228	1·04	na	DY, sharp YP
	Annealed/AC	154	309	2·26	na	DY, plateau
	Annealed/WQ	143	228	1·13	46·2	CY
	Pressurized	154	288	1·86	na	CY
	Pressurized	159	317	1·81	37·5	CY
	Pressurised	154	322	2·16	37·4	CY
CPNiAl-2	As-extruded	164	241	1·05	30·8	CY
	As-extruded	172	306	1·70	37·9	CY
	Annealed	117	257	2·05	35·2	DY, sharp YP
	Annealed	116	336	3·34	40·2	DY, sharp YP
HP-NiAl	As-extruded	166	214	0·79	57·5	CY
	As-extruded	157	235	1·16	60·4	CY
	Annealed/FC	98	174	1·17	63·2	CY
	Pressurized	118	176	0·92	58·2	CY
HPNiAl-C	As-extruded	170	201	0·59	43·4	CY
	Annealed	113	157	0·68	na	YP
	Pressurized	96	171	0·98	39·4	CY
NiAl–100C	As-extruded	155	255	1·35	37·5	DY, plateau
	As-extruded	151	319	2·25	33·0	DY, plateau
	Annealed	113	342	3·29	41·9	DY, sharp YP
	Annealed	115	285	2·35	40·1	DY, sharp YP
NiAl–300C	As-extruded	180	322	2·02	32·4	CY
	As-extruded	162	297	1·84	28·6	DY, plateau
	Annealed	109	343	3·29	42·8	DY, plateau
	Annealed	108	352	3·38	48·4	DY, plateau
NiAl–N	As-extruded	298	409	1·32	na	CY
	As-extruded	297	476	2·20	34·1	CY
	Annealed/FC	265	468	2·45	31·9	CY
	Pressurized	266	434	2·16	na	CY
	Pressurized	274	352	1·03	33·5	CY
NiAl–Ti	As-extruded	170	235	0·86	57·5	CY
	As-extruded	176	176	0·20	56·2	CY
	Annealed	123	256	1·76	64·7	CY
	Annealed	124	265	1·81	64·3	CY

*Annealed/FC or annealed = as-extruded + 1100 K/7200 s/FC; Annealed/AC = as-extruded + 1100 K/7200 s/AC; Annealed/WQ = as-extruded + 1100 K/7200 s/WQ; Pressurized = as-extruded + 1100 K/7200 s/FC + pressurize 1·4 GPa.
[†]DY = discontinuous yielding, upper yield point, sharp yield drop; YP = yield point; CY = continuous yielding; na = not available. Intergranular fracture: accuracy = ± 10%.
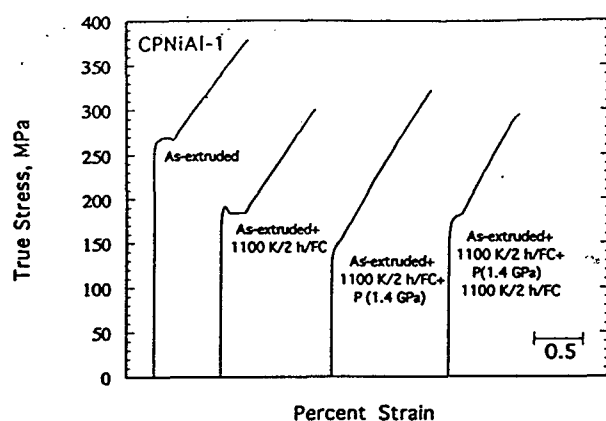
Fig. 3. Room-temperature tensile stress–strain curves for CPNiAl-1 in the as-extruded, annealed, pressurized and pressurized+annealed conditions.

Fig. 6. Room-temperature tensile stress–strain curves for NiAl–N in the as-extruded, annealed, and pressurized conditions.

Fig. 4. Room-temperature tensile stress–strain curves for HPNiAl–C in the as-extruded, annealed, and pressurized conditions.
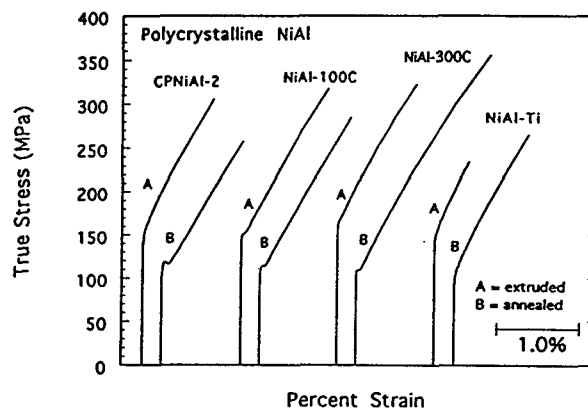
Fig. 7. Representative room-temperature tensile stress–strain curves for CPNiAl-2, NiAl–100C, NiAl–300C and NiAl–Ti.

Fig. 5. Room-temperature tensile stress–strain curves for HP-NiAl in the as-extruded, annealed, and pressurized conditions.

in the CPNiAl-1 and HPNiAl–C alloys if the specimens were subsequently hydrostatically pressurized at 1·4 GPa, whereas no additional decreases in yield stress or other apparent changes in flow behavior were observed in the powder processed NiAl–N alloy or in the HP-NiAl material after hydrostatic pressurization (Figs 3–6). Pressurization treatments were not conducted on the remaining alloys.

Recovery of the discontinuous yield behavior (in those alloys where such behavior was observed) following pressurization could be accomplished by re-annealing pressurized specimens at 1100 K/2 h followed by furnace cooling (Fig. 4). Interestingly, even though the yield stress could be reduced by annealing and in some cases by hydrostatic pressurization, these treatments had no obvious influence on the tensile ductility or fracture behavior of the various alloys (Table 2). Similar observations have been recently reported by Margevicius and Lewandowski for single crystal and polycrystalline NiAl alloys.[25] Representative scanning electron micrographs of the typical fracture surfaces observed in this study are exhibited in Fig. 8 and the percentage of intergranular fracture for all materials is summarized in Table 2. For all specimens, failure was always by a combination of intergranular separation and transgranular cleavage. Surprisingly, the HP-NiAl and NiAl–Ti exhibited a greater tendency for intergranular failure and lower tensile ductility than the other alloys.

Influence of prestraining and annealing on baseline properties

To determine whether the observed yield points resulted from the hold at temperature or during cooling from the annealing temperature, specimens of CPNiAl-1 previously prestrained hydrostatically, were annealed at 1100 K/7200 s followed by AC or WQ. The resulting properties are summarized in Fig. 9 and in Table 2. After WQ, only continuous yielding was observed while after AC, there was some evidence of a yield plateau which initially suggests that the yield points observed following FC are the result of the pinning of dislocations by mobile solute atoms during cooling through lower temperatures. As a result, annealing experiments were initiated at lower temperatures to determine the critical temperature for the migration of solute atoms to dislocations. The results of these experiments are summarized in Fig. 10. It was observed that yield plateaus formed in CP-NiAl after hydrostatic prestraining followed by annealing
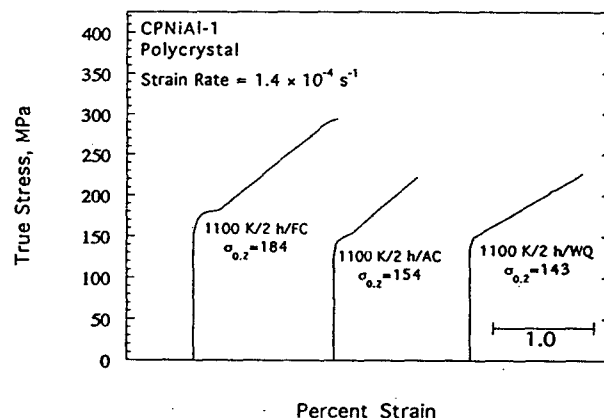
Fig. 9. Room-temperature stress–strain curves illustrating the influence of cooling rate on the tensile flow behaviour of CP-NiAl.

Fig. 8. Representative fracture surfaces of CPNiAl-1 samples tensile tested at room temperature: (a) as-extruded; (b) after annealing at 1100 K for 2 h followed by furnace cooling; (c) after annealing followed by subsequent pressurization. Similar fracture surfaces were observed in the other alloys tested in this study.
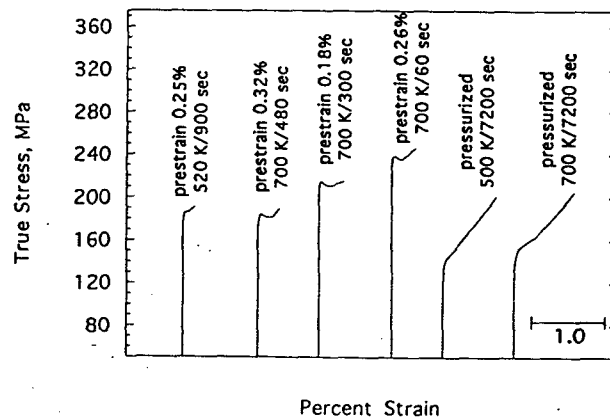
Fig. 10. Room-temperature stress–strain curves illustrating the influence of various prestraining and annealing treatments on the tensile flow behavior of CP-NiAl.

treatments of 700 K/7200 s FC but not following anneals of 500 K/7200 s/FC. Conversely. if the specimens were prestrained uniaxially. notable yield points formed readily after as little as 900 s (15 min) at 522 K and in as little as 60 s (1 min) at 700 K. Additionally. no yield points were observed when annealing temperatures exceeded 900 K.
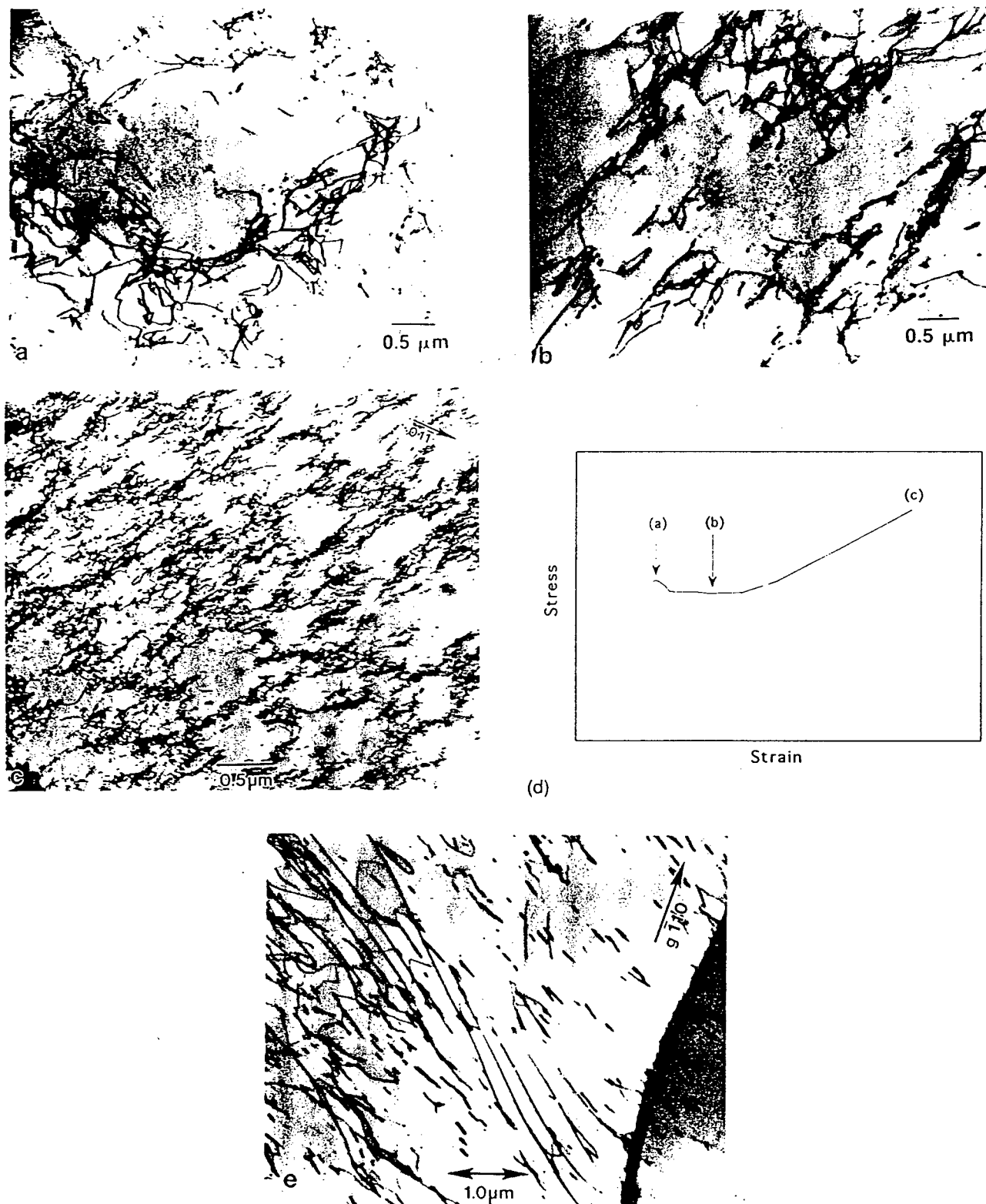
Fig. 11. Transmission electron micrographs of CPNiAl-1 after uniaxial and hydrostatic prestraining at 300 K: (a) CPNiAl-1 prestrained uniaxially 0·05%; (b) CPNiAl-1 prestrained uniaxially 0·40%; (c) CPNiAl-1 prestrained uniaxially 2·04%; (d) schematic stress–strain curve showing stress–strain levels where specimens in (a)-(c) were taken from; (e) prestrained hydrostatically to 1·4 GPa.

TEM observations of deformed specimens

Figure 11 shows a series of TEM bright field images of CPNiAl-1 that was deformed at room-temperature following anneals of 1100 K/2 h/FC. Tensile tests were interrupted at plastic strains of 0·05, 0·31 and 2·04% corresponding to the yield stress peak, the Lüders region and after fracture respectively. At 0·05 and 0·31% strain (Figs 11(a) and (b)), the dislocation structure consisted of a low density of inhomogeneously distributed dislocations arranged into poorly defined cells and dense tangles. Some intercellular/inter-tangle dislocation debris was observed although the cell interiors remained largely dislocation free. As the strain was increased to 2·04% (Fig. 11), the dislocation density increased and the cells were well defined. The dislocations observed were predominantly <100> dislocations of mixed character. The predominant slip plane was {011} although some dislocation debris lying on {001} slip planes was occasionally detected.

Figure 11(e) shows the dislocation substructure observed in CPNiAl-1 following hydrostatic pre-straining to 1·4 GPa. In agreement with the reports of Margevicius and co-workers[20, 21] for conventional purity cast and extruded NiAl, the dislocation sub-structures consisted of a more uniform distribution of long, straight dislocations generated from grain boundaries. Diffraction contrast analysis revealed that all of the dislocations were of <100> type.

In agreement with the many prior studies of extruded near-stoichiometric NiAl in bulk form[26–28] and during *in situ* TEM observations,[29] the deformation substructure following straining at room-temperature consisted of a network of poorly defined dislocation cells, dense tangles and intercellular debris. Well defined deformation bands were not observed by TEM nor was there evidence of coarse slip bands intersecting the specimen surfaces.

DISCUSSION

Species responsible for strain-aging in NiAl

A preliminary determination of the species most likely responsible for the strain-aging effects in NiAl can be made by examination of the aging behaviors of all eight alloys. Discontinuous yielding, in the form of yield points and yield plateaus, was observed in CPNiAl-1, CPNiAl-2, NiAl–100C, NiAl–300C and HPNiAl–C, while continuous yielding was observed in HP-NiAl, NiAl–Ti or NiAl–N following heat treatments known to produce yield points

in conventional cast and extruded NiAl.[19] In NiAl–N, the oxygen and nitrogen contents were much higher than those observed in CPNiAl-1 or CPNiAl-2 while the C-content was much lower, which suggests that nitrogen and oxygen are not the species responsible for the observed yield points. When all excess interstitials were reduced sufficiently, as in the case of HP-NiAl, no yield points were observed; however, doubling the carbon concentration (HPNiAl–C) resulted in a well-defined yield point. These observations are supported by the prior investigations of Noebe and Garg[24] who observed sharp yield points in powder processed conventional purity NiAl (C=143 appm, O=227 appm, and N=6 appm) but no yield points in powder processed nitrogen-doped NiAl (C=57 appm, O=347 appm, and N=904 appm). Also, in HPNiAl–C, it was observed[12,13] that longer aging times are required to achieve the same yield increment as observed in CPNiAl-1 and CPNiAl-2. It is believed that this behavior is a result of the significant reduction in the concentrations of interstitials, particularly C. Since there is less carbon to pin dislocations in NiAl–C, the carbon present must, presumably, diffuse longer distances to cause pinning. Finally, in NiAl–Ti, the bulk interstitial levels were equivalent to those observed in CP-NiAl-2 which exhibited yield point behavior. However, no yield points were observed in NiAl–Ti which was shown to contain TiC precipitates; this suggests that the lack of a yield point in NiAl–Ti is due to the gettering of sufficient carbon from the NiAl matrix and that carbon is the species responsible for the observed yield points.

Influence of prestraining

As noted in the Results, the return of a sharp yield point is much more rapid when the specimen has been prestrained uniaxially as opposed to hydrostatically. During uniaxial deformation of NiAl, dislocations cross-slip easily forming cell structures[24,26,28–30] that result in high work hardening rates at room temperature. As a result, the dislocations are in essence pinned. In contrast, samples pressurized hydrostatically show a more even distribution of dislocations which are not bound in cells (Fig. 11 and ref. 21). In uniaxially prestrained samples, since some of the dislocations are already locked up in cell structures, fewer mobile dislocations are available. Thus, less solute is required to pin the available mobile dislocations. Since more mobile dislocations are available in hydrostatically prestrained samples, more carbon

is required to cause pinning. As a result, longer aging times are required to achieve the same yield point increments observed after uniaxial prestraining. A similar explanation has been applied to train-aged steels prestrained in directions non-parallel to the original tensile direction.[31]

The results of this study also revealed a further reduction in the yield stress of CPNiAl-1, HP-NiAl, and HPNiAl–C following pressurization to 1·4 GPa. However, no such effect was observed in NiAl–N. Prior investigations by Margevicius *et al.*[21] on pressurized NiAl alloys have shown that dislocation generation is enhanced by compositional differences between neighboring grains. This suggests that higher dislocation densities will be induced in CPNiAl-l, HP-NiAl, and HPNiAl–C over NiAl–N due to the larger compositional variations between the neighboring grains as a result of the casting process.

Despite its influence on the tensile flow behavior of NiAl alloys, prestraining, whether uniaxial or hydrostatic, had no observable influence on the tensile ductility and fracture behavior of NiAl. In CP-NiAl, for example, the fracture surfaces were approximately 37% intergranular regardless of how the specimens were prestrained or strain aged prior to testing. In HP-NiAl, however, there was an apparently higher propensity for intergranular fracture over transgranular failure. Interestingly, this alloy, although apparently closer to stoichiometry and free from high interstitial levels, exhibited lower tensile ductilities than the CP-NiAl and the NiAl–N alloys. This observation contradicts the observations in single crystals where soft-oriented specimens having low interstitial levels and high purity were shown to exhibit nearly 5% tensile ductility at room temperature, regardless of pretest treatments.[22] Although some of these observations can be related to the differences in grain size between the alloys,[32] a more thorough investigation of these issues are required.

CONCLUSIONS

The yield points observed in conventional purity and carbon-doped NiAl are the result of strong dislocation pinning by interstitial carbon. Oxygen and nitrogen levels as high as 0·035 and 0·09 at%, respectively, do not appear to pin dislocations in NiAl and, therefore, do not produce yield point phenomena.

Hydrostatic prestraining as opposed to uniaxial prestraining delays the kinetics of the yield point return by forming random networks of free unpinned

dislocations which require more diffusion time for strong locking to occur.

Yield point phenomena can be removed by microalloying with sufficient levels of reactive elements such as Ti, which getters carbon from the matrix by forming precipitates of TiC.

Despite their influence on the flow behavior of NiAl, prestraining and/or strain-aging have no observable impact on the room-temperature fracture characteristics of NiAl alloys. In fact, fracture always occurs by a mixture of intergranular failure and transgranular cleavage and tensile ductility was unaffected by the various prestrain and annealing treatments performed.

REFERENCES

1. Noebe, R. D., Bowman, R. R. & Nathal, M. V., *Int. Mater. Rev.*, 38 (1993) 193.
2. Pascoe, R. T. & Newey, C. W. A., *Metall. Sci. J.*, 5 (1971) 50.
3. Hack, J. E., Brzeski, J. M. & Darolia, R., *Mater. Sci. Eng.*, A192/193 (1995) 268.
4. Hack, J. E., Brzeski, J. M., Darolia, R. & Field, R. D., *High-Temperature Ordered Intermetallics V*, Eds I. Baker, R. Darolia, J. D. Whittenberger & M. H. Yoo, Materials Research Society, vol. 288, Pittsburgh, PA, 1993, p. 1197.
5. Lautenschlager, E. P., Kiewit, D. A. & Brittain, J. O. *Trans. Metall. Soc. AIME*, 233 (1965) 1297.
6. Margevicius, R. W. & Lewandowski, J. J., *Scripta Metall. Mater.*, 25 (1991) 2017.
7. Field, R. D., Lahrman, D. F. & Darolia, R., *High-Temperature Ordered Intermetallic Alloys V*, Eds I. Baker, R. Darolia, J. D. Whittenberger & M. H. Yoo, Materials Research Society, vol. 288, Pittsburgh, PA, 1993, p. 423.
8. Brzeski, J. M., Hack, J. E., Darolia, R. & Field, R. D., *Mater. Sci. Eng.*, A170 (1993) 11.
9. Liu, C. T., Lee, E. H., George, E. P. & Duncan, A. J., *Scripta Metall. Mater.*, 30 (1994) 387.
10. Pascoe, R. T. & Newey, C. W. A., *Metall. Sci. J.*, 2 (1968) 138.
11. Brzeski, J. M., Hack, J. E. & Darolia, R., *High-Temperature Ordered Intermetallic Alloys VI*, Eds J. A. Horton, I. Baker, S. Hanada, R. D. Noebe and D. S. Schwartz, Materials Research Society, vol. 364, Pittsburgh, PA, 1995, p. 419.
12. Weaver, M. L., Kaufman, M. J. & Noebe, R. D., *Intermetallics*, 4 (1996) 121.

13. Weaver, M. L., Noebe, R. D., Lewandowski, J. J., Oliver, B. F., & Kaufman, M. J., *Mater. Sci. Eng.*, **A192/193**, (1995) 179.

14. Weaver, M. L., Levit, V. Kaufman, M. J. & Noebe, R. D., *High-Temperature Ordered Intermetallic Alloys VI.* Eds. J. A. Horton, I. Baker, S. Hanada, R. D. Noebe & D. S. Schwartz, Materials Research Society, vol. 364, Pittsburgh, PA, 1995, p. 425.

15. Weaver, M. L., Investigation of Strain Aging in the Ordered Intermetallic Compound β-NiAl, Ph.D. Dissertation, University of Florida, 1995.

16. Weaver, M. L., Noebe, R. D. & Kaufman, M. J., *Metall. Mater. Trans. A* (1996 in press).

17. Kitano, K. & Pollock, T. M., *Structural Intermetallics,* Eds R. Darolia, J. J. Lewandowski, C. T. Liu, P. L. Martin, D. B. Miracle and M. V. Nathal, The Minerals, Metals and Materials Society, Warrendale, PA, 1993, p. 591.

18. Kitano, K., Pollock, T. M. & Noebe, R. D., *Scripta Metall. Mater.*, **31** (1994) 397.

19. Margevicius, R. W., Lewandowski, J. J., Locci, I. E. & Noebe, R. D., *Scripta Metall. Mater.*, **29** (1993) 1309.

20. Margevicius, R. W. & Lewandowski, J. J., *Acta Metall. Mater.*, **41** (1993) 485.

21. Margevicius, R. W., Lewandowski, J. J. & Locci, I. E., *Structural Intermetallics*, Eds R. Darolia, J. J. Lewandowski, C. T. Liu, P. L. Martin, D. B. Miracle & M. V. Nathal, The Minerals. Metals and Materials Society, Warrendale, PA, 1993, p. 577.

22. Johnson, D. R., Joslin, S. M., Oliver, B. F., Noebe, R. D. & Whittenberger, J. D., *First International Conference on Processing Materials for Properties*, Eds H. Henein & T. Oki, TMS, Warrendale, PA, 1993 p. 865.

23. Reviere, R. D., Oliver, B. F. & Bruns, D. D., *Mater. Manuf. Proc.*, **4** (1989) 103.

24. Noebe, R. D. & Garg, A., *Scripta Metall. Mater.*, **30** (1994) 815.

25. Margevicius, R. W. & Lewandowski, J. J., *Metall. Mater. Trans. A*, **25A** (1994) 1457.

26. Kim, J. T., Noebe, R. D. & Gibala, R., *Proceedings of the International Symposium of Intermetallic Compounds — Structural and Mechanical Properties*, Ed, O. Izumi, Japan Institute of Metals, Sendai, Japan, 1991, p. 591.

27. Bowman, R. R. & Noebe. R. D., *Superalloys 1992*, Eds S. D. Antolovich, R. W. Stusrud, R. A. MacKay, D. L. Anton, T. Khan, R. D. Kissinger & D. L. Klarstrom, The Minerals, Metals & Materials Society, Warrendale, PA, 1992 p. 341.

28. Nagpal, P. & Baker, I., *J. Mater. Let.*, **11** (1992) 1209.

29. Nagpal, P., Baker, I. & Horton. J. A., *Intermetallics*, **2** (1994) 23.

30. Bowman, R. R., Noebe, R. D., Raj, S. V. & Locci, I. E., *Metall. Trans.*, **23A** (1992) 1493.

31. Wilson, D. V. & Ogram, G. R., *JISI*, **206** (1968) 911.

32. Weaver, M. L., unpublished research, University of Florida/NASA-Lewis Research Center, 1995.

S

HIGH TENSILE ELONGATION OF
β-NiAl SINGLE CRYSTALS AT 293 K

V.I. Levit, I.A. Bul, J. Hu and M.J. Kaufman
Department of Materials Science and Engineering,
University of Florida, Gainesville, FL 32611-6400

Introduction

It is well established that both polycrystals and ("hard") <001> oriented single crystals of NiAl show practically no ductility at room temperature (1–3). For "soft" (non-<001>) oriented single crystals, the elongations at room temperature typically do not exceed 1–2% (4,5). Higher room temperature ductilities have been achieved using various schemes such as heat treatment, microalloying, etc. (1–10). In one of the more controversial papers, Darolia et al. (1) presented single crystal data suggesting that small (< 1%) additions of iron, gallium or molybdenum enhance the room temperature tensile ductility of <110> single crystals to 5–6%; this spurned a large amount of work around the world aimed at elucidating the mechanism(s) responsible for this effect. While there has been no apparent independent confirmation of this unexpected ductilization effect, various investigators have suggested and, in some cases, shown that the following factors are of extreme importance to the mechanical behavior of this compound: impurity content, heat treatment (thermal vacancies), constitutional defects (due to deviations from stoichiometry), orientation, prestraining and surface condition (1–12). For example, prestraining at temperatures ranging from RT to 1000K has been reported to increase the fracture toughness (6,11), tensile ductility and yield stress (8) while pressurization led to a decreased yield stress (12) presumably by introducing new mobile dislocations and/or by unpinning existing ones. In a recent study, Noebe et al. (7) noted that, out of six specimens from a stoichiometric crystal, one exhibited 12.9% elongation whereas the other five had elongations between 1 and 2.4%.

The purpose of this note is to illustrate that it is possible to achieve high (~ 25%) RT tensile elongations by optimizing these factors and to shed further light on the overall behavior of NiAl single crystals in soft orientations.

Experimental Procedure

A NiAl single crystal (28 mm diameter by 75 mm length) was grown in a high purity alumina crucible by the Bridgman technique in an atmosphere of purified argon. The starting charge was in the form of small ingots prepared by non-consumable arc melting. Care was taken to use high purity starting materials (99.98 Ni and 99.999 Al) and the chemical analysis of the crystal indicated that the purity was high and that the Ni/Al ratio was near the stoichiometric composition (Table 1). After growth, the crystal was annealed at 1573 K for 3 h and cooled inside the furnace at ~ 0.1 K/s. The orientation of the single crystal

TABLE 1

Chemical Composition of the NiAl Single Crystals Used in This and Previous Studies

Ni, at.%	Al, at.%	Si, at.%	C, appm	O, appm	N, appm	S, appm	Source
49.4	50.55	0.017	50	80	<10	<10	Present
50.2	49.75	0.060	<36	<27	<31	<13	Ref. 9
48.5	51.35	0.200	250	180	<20	N/R	Ref. 11
50.1	49.80	N/R	N/R	120	<15	N/R	Ref. 14

was determined to be approximately [213] using the back reflection Laue method. After heat treatment, the crystal was cut into two cylindrical sections with the cylinder axes parallel to the growth direction using an electrodischarge machine (EDM). One of the cylinders was wrapped in Fiberfax insulation, placed in a carbon steel pipe, heated to 1273 K in a muffle furnace and then deformed radially in compression using an Instron 1125 testing machine at a strain rate of $\sim 10^{-3}$ s^{-1}. A total strain of $\sim 10\%$ was calculated from the ratio of the initial and final heights of the sample.

After compression, both deformed and undeformed crystals were reheated to 1273 K, held for 0.5h, and then cooled inside the furnace as before. Tensile specimens were cut from both prestrained and undeformed sections of the single crystal with their tensile axes nearly parallel to [213] (Fig. 1). The specimens had rectangular gage sections (1.6 × 2.4 mm), 10 mm gage lengths and 25 mm total lengths (Fig. 1). Significantly, the orientations of the faces and sides of the specimens are as shown in Fig. 1 where it is noted that the narrow sides of the prestrained specimens and the flat faces of the unprestrained specimens are nearly parallel to (111), i.e., there is an approximate 90° rotation between the gage sections. While this rotation was unintentional, it revealed some intriguing results as will become apparent below. After cutting, the tensile specimens were electropolished in a 10% perchloric acid–90% methanol solution at temperatures slightly below ambient. Tensile tests were performed under ambient conditions using an Instron 1125 testing machine at a strain rate of 10^{-4} s^{-1}. Tensile elongation, e, true strain, ε, and 0.2% offset yield stress, $\sigma_{0.2}$, were calculated using routine methods. Both shear stress, $\tau = \sigma_{0.2} \cdot f_s$, and shear strain, $\gamma = \varepsilon / f_s$, where f_s is the instantaneous Schmid factor assuming the operation of a single slip system, namely, [001]/(110), were calculated. The value of f_s was calculated for the initial and final orientations, as determined from back reflection Laue patterns, and was estimated for some of the intermediate orientations.

After testing the specimens to failure, the fracture surfaces were examined using JEOL 35C scanning electron microscope at accelerating voltages of 10 kV. For the dislocation substructure examination, thin foils were prepared from undeformed material and the deformed gage sections using standard methods and examined in a JEOL 200CX transmission electron microscope. For the deformed material, the foils were cut parallel to the faces of the gage sections which, as mentioned above, were at $\sim 90°$ to each other. Standard diffraction contrast (g · b) analyses were performed to determine the nature of slip after deformation.
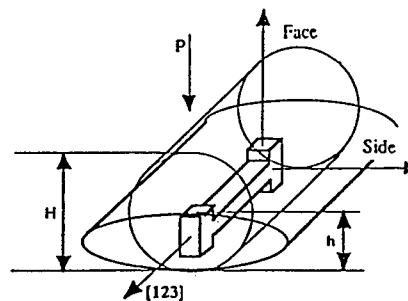
Figure 1. Schematic of the single crystal geometry before and after prestraining as well as the orientation of the tensile specimens.
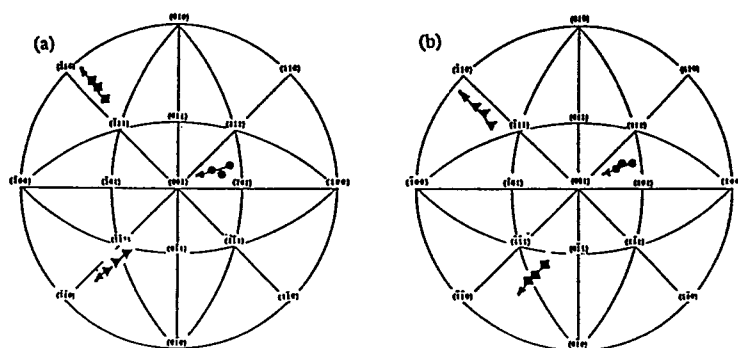
Figure 2. Stereograms showing initial and final orientations of (a) prestrained specimens and (b) control specimens after testing in tension at room temperature. ■-face, ▼-side, ●-tensile axis (see text). The arrows indicate the nature of the rotation during the tensile deformation.

Results

Prestraining the crystals prior to testing produced a substructure consisting of ~50 μm subgrains, containing a low dislocation density, separated by low angle subboundaries. Standard diffraction contrast (g · b) experiments revealed that essentially all of the dislocations in both the subboundaries and the subgrains had <100> Burger's vectors. Misorientations, $\Delta\phi$, across typical dislocation walls were of the order of $\Delta\phi = b/h = 10^{-2}$ rad, where b = 0.28 nm and h = 20 nm is the average distance between adjacent dislocations in the subboundary. No other significant differences between the prestrained and unprestrained (control) specimens were apparent.

The tensile properties of these crystals are presented in Table 2 and compared in Fig. 3. Significantly, the $\sigma_{0.2}$ and τ values are slightly below those typically reported for NiAl crystals in this orientation whereas the elongations are considerably higher (1–5). It is also apparent that the prestrained samples had higher elongations and shear strains, while both $\sigma_{0.2}$ and τ decreased somewhat relative to the unprestrained material. The basis for this difference will be discussed further below.

TEM analysis of the dislocation substructure in the gage length after tensile testing revealed that the subboundaries in the prestrained material were still present although, as expected, the material contained a higher dislocation density than before testing. Furthermore, the dislocation distribution in the unprestrained and prestrained samples were observed to be radically different when observed in the foils cut parallel to the faces of the gage sections. Specifically, the dislocations formed cells in the unprestrained

TABLE 2

The Mechanical Properties of the NiAl Single Crystals at 293K

Sample description	$\sigma_{0.2}$, MPa	ε,%	CRSS, MPa	Θ_σ, MPa	$\Theta\tau$, MPa
Control #1	115	15.3	54	599	91
Control#2	105	13.6	49	586	114
Control #3	103	17.6	48	648	103
Control #4	112	16.2	53	540	100
Prestrained #1	107	28	48	389	46
Prestrained #2	98	24.4	44	362	46
Prestrained #3	95	11.4	43	537	88
Prestrained #4	100	23.9	45	393	50
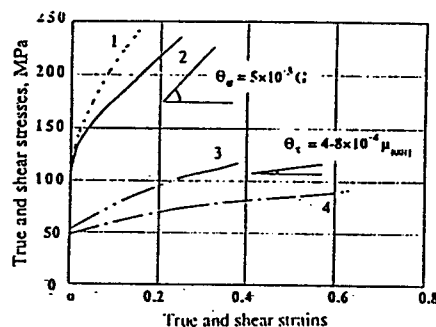
Figure 3. True stress-true strain (1,2) and shear stress-shear strain (3,4) curves. 1,3—control; 2,4—prestrained specimens.

Figure 4. TEM bright-field images of the dislocation substructure of the prestrained specimen after 23.9% deformation at RT (a,b), and of the control specimen after 15.3% deformation at RT (c).

specimens and bands in the prestrained specimens (Fig. 4). Diffraction contrast experiments (Fig. 4 a and b) revealed that essentially all of the dislocations in the bands were edge in nature with $b = [001]$ as expected based on the initial orientation. However, in the samples cut from the unprestrained material, the dislocation distribution in the cell walls was considerably more complex (Fig. 4 c) indicating the more complex slip behavior. In both cases, the overall dislocation density was quite low considering the significant amount of plastic strain ($e = 0.2$) imparted; this implies that the material primarily underwent single slip prior to fracture.

Back reflection Laue patterns obtained from the fracture surfaces after more than 20% elongation were almost as sharp as those before testing suggesting low residual stress levels (i.e., low accumulated strains) at the fracture surface as a result of the large deformation. Laue patterns obtained from the gage sides, however, exhibited much higher distortions implying that the strain in the material near the sides was considerably higher. Finally, it was noted from the Laue analysis that the orientation parallel to the tensile axis rotated during the deformation from the initial [213] towards the [001] corner of the triangle although not directly towards [001]. The final orientation was near the [215] (Fig. 2) and the angular path is that expected for the operation of the [001](110) system, i.e., since the tensile axis, slip plane and slip direction are non-coplanar, the rotation of the stress axis is not exactly towards the slip direction but, rather, is towards the 001-110 symmetry line which contains both the slip direction and the slip plane normal.

Another check as to whether single slip is the dominant deformation mechanism is to correlate the angular rotation with the predicted shear strain. Using the standard notation of Ref. (13) where λ_0 and λ_1 are the angles between the axis and the slip direction before and after deformation, respectively, and χ_0 and χ_1 are the angles between the axis and the slip plane before and after deformation, respectively, then the shear strain is given by

$$\gamma = \frac{\cos \lambda_1}{\sin \chi_1} - \frac{\cos \lambda_0}{\sin \chi_0}.$$

When the measured angles are input, the calculated value of ε is 0.55 for the prestrained specimen that displayed 28% elongation. The calculated shear strain using the empirical data and the appropriate Schmid factor for [001](110) slip is 0.63 and is well within the experimental errors of the measurements. This provides strong evidence that the deformation indeed occurs by the operation of a single slip system.

The fracture surfaces appeared brittle macroscopically (Fig. 5) and tended to be oriented at angles of between 35° and 55° to the tensile axis; this is consistent with the reports of other authors (4). In addition, there was no evidence of strain localization in the form of necking in the gage length or load drop in the load-elongation curves. In essentially all cases, single cracks were nucleated, at or near the sample surface, and propagated at or across the whole cross section. The only apparent difference between the samples fractured after 11% elongation and those after 28% was the larger distortion of the gage cross section in the latter (Fig. 5). It should be noted that this distortion also appears to be reasonably consistent with the
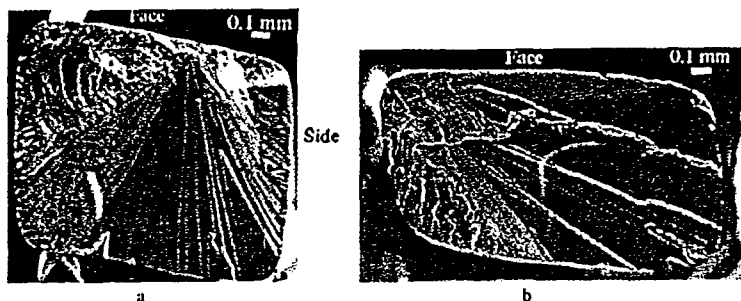
Figure 5. Fracture surfaces of the tensile specimens tested at room temperature: (a) prestrained, 28% elongation; (b) control, 16.2% elongation.

operation of a single slip system as noted above and suggested by the different shape changes corresponding to the different initial orientations. Finally, there was no apparent surface or near-surface defects associated with the nucleation of the cracks even though the fractures almost always nucleated at or near the surface.

Discussion

The high tensile elongations achieved in the present study indicate clearly that NiAl is not as intrinsically brittle as previously believed. In fact, RT elongations of over 20% are remarkably higher than anything published previously suggesting that important issues concerning the deformation and fracture of NiAl remain poorly understood. Since the highest reported tensile elongation prior to these results was less than 13% (approximately one-half of the current maximum elongation), it is important to discuss these results accordingly.

As pointed out above, the dislocation substructure after deformation and fracture as well as the shape change of the cross section are strong indications that the material primarily underwent single slip in these experiments. In addition, the rotation of the stress axis towards the [001] part of the stereographic triangle is consistent with the operative slip system being [001](110) which has a slightly higher Schmid factor (0.455 vs. 0.429) than the alternative [001](010) system. Likewise, if [001](100) were operative, the [100](001) system would also be expected (same Schmid factor) and the overall rotation would be towards the 101 corner of the stereographic triangle. It should be mentioned that the slip plane may not be well defined in this system, i.e., it might be of the type {hk0} as suggested by Takasugi (14); however, as noted above, the observed rotation is consistent with the (011) slip plane as suggested above and in the calculation of shear strain using the initial and final orientations.

By taking this into account and assuming the slip system to be [001](110), it is possible to calculate the CRSS values and draw shear stress-shear strain (τ vs. γ) curves based on the true stress-true strain (σ vs. ε) curves and noting the initial and final orientations of the crystal. These results are shown in Fig. 3 where it is clear that the work hardening rate, θ (= $d\tau/d\gamma$), is ~ 46–88 MPa (Table 2). This value is~ 4–8 × 10^{-4} times the shear modulus of NiAl along the elastically softest <001> direction (μ_{001} = 112 GPa) (15). For comparison purposes, it is interesting to note that the work hardening rate in hcp crystals (Zn, Mg and Cd) undergoing single slip is typically of the order of 10^{-4} times the shear modulus and these crystals are able to undergo over 100% elongation at room temperature via the operation of a single slip system. Therefore, even though the B2 structure appears more like a bcc cell, the strong tendency for cube lip accounts for its tendency to behave more like an hcp metal when oriented for single slip. Another feature consistent with this comparison is the tendency for the material to undergo kinking in both compression (2,3) and tension (16), the latter under the special circumstances of misalignment away from the hard orientation and misalignment of the sample in the grips. All of these issues will be addressed in detail in a forthcoming paper.

Conclusions

NiAl single crystals oriented along [213] exhibit tensile elongations of up to 28% at room temperature under certain conditions. Based on the analysis of these crystals, it appears that the majority of the deformation is by the single slip system [001](110); this leads to a rotation of the tensile axis towards the 001-110 symmetry line. Furthermore, the work hardening rate is found to be quite low (about 0.1% of the shear modulus) when the crystal rotation (decreasing Schmid factor) is taken into account; this is consistent with single slip as noted in HCP crystals.

The CRSS is quite low (45–55 MPa) for the crystals tested and is ~ 10% lower after prestraining at 1273K. Prestraining also leads to an increase in the tensile elongation from an average value of 16% to 26%. While this effect is not completely understood, it was noted that the high temperature prestraining resulted in the production of dislocation-free subgrain volumes, separated by low energy dislocation boundaries; these may act as sources for mobile dislocations and lead to more uniform strain throughout the gage length. Alternatively, the different orientations of the gage sections may account for the variations in elongation.

The fractures typically occurred by the nucleation of single cracks from the sides/corners of the gage sections. The back reflection Laue patterns taken from the fracture surface indicated low residual stress levels near the fracture consistent with the operation of a single slip system with negligible work hardening. In addition, there was no apparent "preferred" cleavage plane as the fracture surfaces tended to occur on macroscopic planes that were between 35° and 55° from the tensile axis consistent with previous reports.

Acknowledgments

References

1. R. Darolia, D. Larman and R.D. Field *Scripta Metall. Mater.*, **26**, 1007 (1992).
2. D.B. Miracle, *Acta Metall. Mater.*, **41**, 649 (1993).
3. R.D. Noebe, R.R. Bowman and M.V. Nathal, *Inter. Mater. Rev.*, **38**, 193 (1993).
4. J.H. Schneibel, R. Darolia, D.F. Lahrman and S. Schmauder, *Met. Trans. A*, **24A**, 1363 (1993).
5. T. Takasugi, J. Kishino and S. Hanada, *Acta Metall. Mater.*, **41**, 1009 (1993).
6. J.E. Hack, J.M. Brzeski and R. Darolia, *Scripta Metall.Mater.*, **27**,1259 (1992).
7. R.D. Noebe, A. Garg, and P. Dickerson, *Private Communication* (1995).
8. M.A. Morris, J.-F. Perez and R. Darolia, *Phil. Mag.*, **69**, 507 (1994).
9. M.L. Weaver, M.J. Kaufman and R.N. Noebe, *Scripta Metall. Mater.*, **29**, 1113 (1993).
10. R.D. Noebe and R. Gibala, *Scripta Metall. Mater.*, **20**, 1635 (1986).
11. J.E. Hack, J.M. Brzeski and R. Darolia, *Mater. Sci. Eng.*, **A192/193**, 268 (1995).
12. R.W. Margevicius, J.J. Lewandowski, and I. Locci, *Scripta Metall. Mater.*, **26**, 1733 (1992).
13. R.W.K. Honeycombe, *The Plastic Deformation of Metals*, E. Arnold (Publishers) Ltd, London (1968).
14. T. Takasugi, J. Kishino and S. Hanada, *Acta Metall. Mater.*, **41**, 1021 (1993).
15. R.J. Wasilewski, *Trans. Metall. Soc. AIME*, **236**, 455 (1966).
16. J.S. Winton, V.I. Levit and M.J. Kaufman, to be published.

THE INFLUENCE OF C AND Si ON THE FLOW BEHAVIOR OF NiAl SINGLE CRYSTALS

M.L. Weaver*, R.D. Noebe**, and M.J. Kaufman***

*Center for Nonlinear and Nonequilibrium Aeroscience, Florida A&M University,
Tallahassee, FL 32310
*and Department of Mechanical Engineering, FAMU/FSU College of Engineering
Florida A&M University/Florida State University, Tallahassee, FL 32316
**NASA Lewis Research Center, MS 49-3, Cleveland, OH 44135
***Department of Materials Science and Engineering, University of Florida,
Gainesville, FL 32611

Introduction

Alloys based on the intermetallic compound NiAl are considered potential replacements for Ni and Co-based superalloys in high temperature structural applications due to their excellent oxidation resistance, low densities, high thermal conductivities, and increased melting points. Unfortunately, NiAl exhibits low tensile ductility at room temperature and low strengths at elevated temperatures which have combined to hinder its development. Recent efforts, have revealed that NiAl in the presence of sufficient solute levels, is subject to the phenomenon of strain aging [1-13] which manifests itself as: sharp yield points, abnormally low strain rate sensitivities (SRS), plateaus or peaks in yield stress and work hardening rate as a function of temperature, flow stress transients upon an upward change in strain rate, reduced tensile elongations at elevated temperatures, and serrated stress-strain curves. Though recent efforts via either alloying or the removal of interstitial impurities [14,15], have resulted in consistent room-temperature tensile elongations exceeding 5% and the elimination of serrated flow, the effects of particular substitutional and interstitial elements and the mechanisms by which they might enhance or hinder the mechanical properties remain unknown. Consequently, the purpose of the present paper is to provide a preliminary assessment of the influence of common substitutional and interstitial impurities on the deformation behavior of NiAl. To accomplish this goal a series of NiAl single crystal alloys containing various interstitial solutes were prepared and their mechanical properties were evaluated between 77 and 1100 K. Because Si is a common impurity in conventional purity single crystals grown by the Bridgman method, Si concentrations were also varied in order to determine the influence of this element.

Experimental Procedure

Four nominally stoichiometric NiAl single crystals were grown in argon using a modified Bridgman procedure. One conventional purity crystal (CPNiAl-1) was produced at General Electric Aircraft Engines

TABLE 1
Chemical Compositions and Crystallographic Orientations of Materials Used

Alloy	Orientation	at.%			at. ppm			
		Ni	Al	Si	C	O	N	S
CPNiAl-1	[123]	50.6±0.2	49.2±0.2	0.17	112	87	<6	<10
UF-NiAll	[123]	50.3±0.2	49.3±0.2	0.01	136	132	15	<10
NiAl-Si	[110]	50.4±0.2	49.3±0.2	0.29	220	95	12	<10
HP-NiAl	[123]	50.2±0.2	49.8±0.2	0.04	76	40	24	24

Ni & Al   Analysis performed using analytical wet chemistry/titration techniques, relative accuracy ±1%
Si   Analysis performed on an Ultraviolet/Visible Spectrophotometer, Shimadzu, Model UV-160, relative
          accuracy ±10%
C & S   Analysis performed on a Simultaneous Carbon/Sulfur Determinator, LECO Corp., Model CS-244, relative
          accuracy ±10%
N & O   Analysis performed on a Simultaneous Nitrogen/Oxygen Determinator, LECO Corp., Model TC-136 or
          Model TC-436, relative accuracy ±10%

and measured 25 mm × 32 mm × 100 mm. Ingots of C-doped low Si (UF-NiAll) and Si-doped NiAl were produced at the University of Florida using arc melted and vacuum induction melted feed stock respectively. These ingots measured 25 mm diameter × 60 mm length. A fourth low interstitial high purity ingot (HP-NiAl), 25 mm diameter × 50 mm length, was produced via a containerless electromagnetic levitating zone process at the University of Tennessee. All slabs were homogenized at 1589 K for a minimum of 1 hour in argon followed by furnace cooling to room-temperature prior to machining into test specimens.

Post-processing chemical analyses were conducted using the techniques deemed the most accurate for the particular elements. The results of these analyses are listed in Table 1. The crystals were oriented using the back reflection Laue technique and either centerless ground as round button-head tensile specimens parallel to the <123> axis or EDM wire cut into cylindrical compression specimens parallel to the <110> or <123> axes. Specimen dimensions were: (1) 3.1 mm and 30 mm for the tensile gage diameter and gage length; and (2) 3.0 mm and 6.4 mm or (3) 4.0 mm and 10 mm for the compression sample diameter and height, respectively. All tensile specimens were electropolished prior to testing in a 10% perchloric acid-90% methanol solution that was cooled to 208 K. All mechanical tests were performed on an Instron Model 1125 load frame at constant crosshead velocities corresponding to initial strain rates in the range 2.8×10^{-5} s^{-1} to 2.8×10^{-4} s^{-1}. Tests were run in air between 300 and 1100 K by heating the samples in a clamshell type resistance furnace. Testing below room temperature was accomplished in compression by cooling the specimens in liquid baths. True stress-strain data were calculated from the load-time plots and yield stresses were determined by the 0.2% offset method. During some of the elevated temperature tests, particularly in the temperature range where DSA was evident, strain was measured and controlled using a clip on strain gage extensometer attached to the compression cage. The strain rate sensitivity (SRS) was determined by increasing the strain rate by a factor of ten from the base strain rate at plastic strains of 1.8 and 5.0%. The quantity extracted from these experiments was the SRS, $s = \Delta\sigma/\Delta\ln\dot{\varepsilon}$. The flow stress difference was measured using the extrapolation technique. When serrated flow was observed, the extrapolations were drawn tangent to the stress peaks.
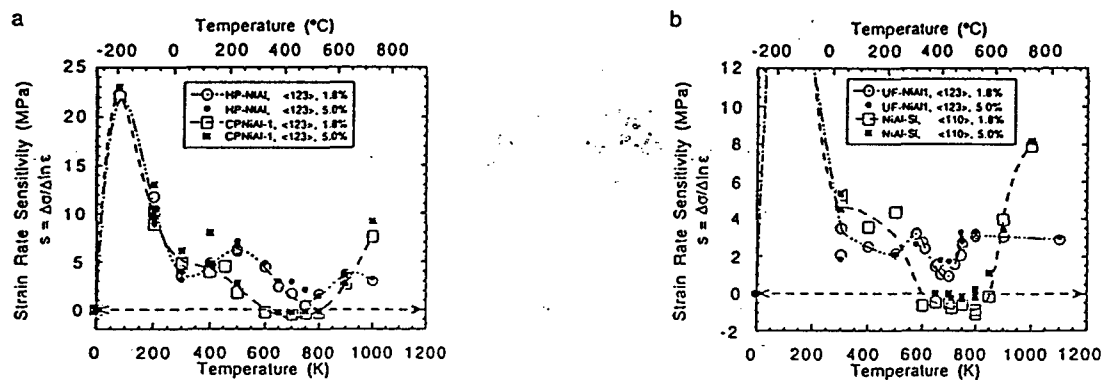
Figure 1. The temperature dependence of the strain rate sensitivity, $s = \Delta\sigma/\Delta \ln \dot{\varepsilon}$, at 1.8% and 5.0% plastic strain. (a) HP-NiAl and CPNiAl-1, and (b) UF-NiAll and NiAl-Si. Base strain rate = 2.8×10^{-5} s^{-1}.

Results

The results of the chemical analyses indicated that within experimental accuracy, the Ni and Al contents of the four alloys were not significantly different from each other. The major differences between the materials are the residual Si, C, O, and N contents. The presence of residual Si in CPNiAl-1 has been attributed to interaction between the molten NiAl and alumina-silicate mold during processing. The lower concentrations of Si in UF-NiAll and HP-NiAl have been attributed to the use of higher purity feed stock and, in the case of UF-NiAll, to directional solidification in higher purity ceramic molds, and in HP-NiAl, use of a containerless processing technique.

The temperature dependence of the SRS is presented in Fig. 1. For all four alloys, distinct SRS minima were observed in the temperature ranges 300 to 400 K (low temperature) and 600 to 800 K (intermediate temperature) with SRS actually becoming slightly negative in the intermediate temperature range for CPNiAl-1 and NiAl-Si at 1.8% and at ~5% plastic strain (e.g., in NiAl-Si at 5% plastic strain, $s = -0.8 \pm 0.5$ at 800 K). Coincident with the intermediate temperature SRS minima were the occurrence of flow stress transients in the form of sharp upper yield points in UF-NiAll and serrated flow in CPNiAl-1 and
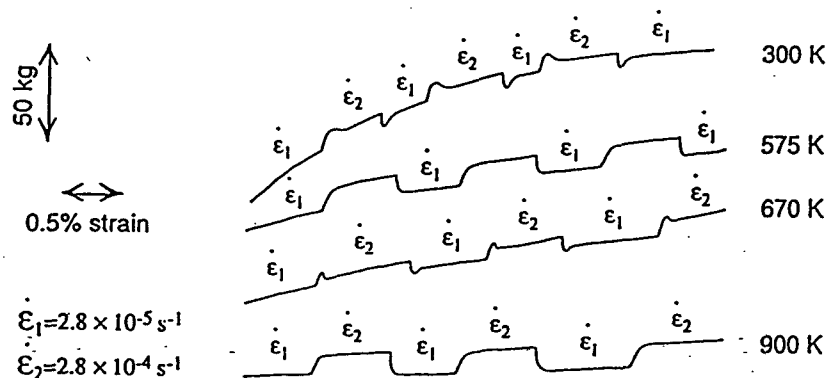
Figure 2. Portions of load-elongation curves for UF-NiAll following strain rate change experiments at 300, 575, 670, and 900 K. ($\dot{\varepsilon}_2/\dot{\varepsilon}_1 = 10$).
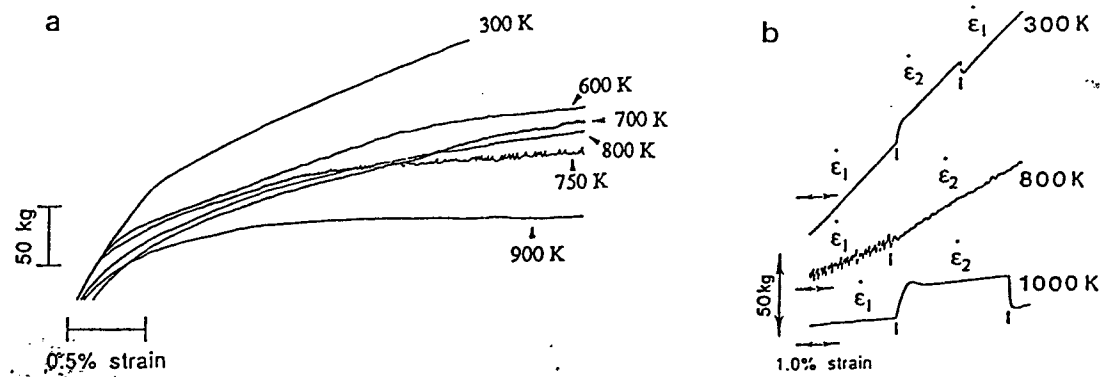
Figure 3. The effect of temperature on the shape of the flow curves in NiAl-Si. (a) Typical flow curves following deformation at $\dot{\epsilon}$ =2.8 x 10^{-5} s^{-1}. (b) Typical flow curves following strain rate change experiments near 5% plastic strain at 300, 800, and 1000 K ($\dot{\epsilon}_2/\dot{\epsilon}_1$ = 10). Note the negative SRS at 800 K.

NiAl-Si. Recently, independent analyses of conventional purity NiAl [10] and NiAl-Si [15] have confirmed the occurrence of serrated flow at intermediate temperatures. In addition, Winton *et al.* [15], who performed strain rate change experiments on NiAl-Si at higher strains, have confirmed the existence ьf a pronounced SRS minimum at intermediate temperatures where SRS approached zero but tended to remain slightly positive. More detailed investigations of this aspect are in progress [15]. No serrated flow or flow stress transients were observed near the intermediate temperature SRS minimum in HP-NiAl. At low temperatures, diffuse flow stress transients were observed in HP-NiAl and UF-NiAl1 with UF-NiAl1 exhibiting more pronounced effects. However, no such behavior was exhibited by CPNiAl-1 or NiAl-Si. Examples of the effects of test temperature on the flow behavior of UF-NiAl1 and NiAl-Si are illustrated in Figs. 2 and 3 respectively. In UF-NiAl1, flow curves were always smooth and positive SRS values were always observed. However, sharp upper yield points (Fig. 2) were consistently observed upon an upward change in strain rate in the temperature interval ~670 to 750 K as were more diffuse upper yield points at low temperatures. No such behavior was observed outside of these temperature regimes. In NiAl-Si, flow curves were smooth when test temperatures were maintained below 600 K or above 900 K. At
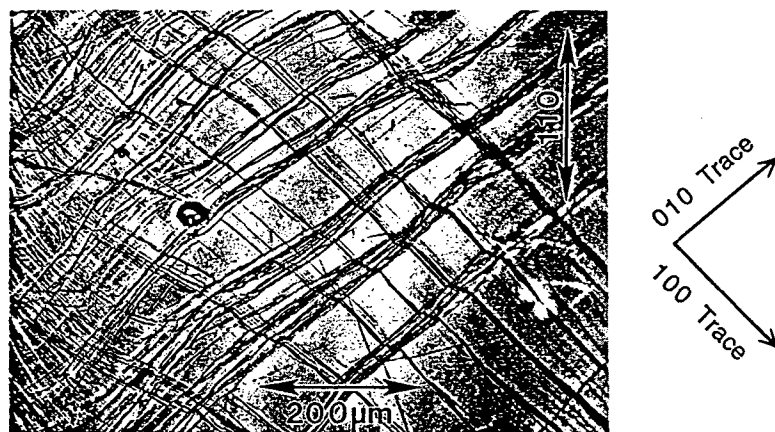
Figure 4. Examples of slip bands observed at 800 K in NiAl-Si. Similar bands were observed in CPNiAl-1.
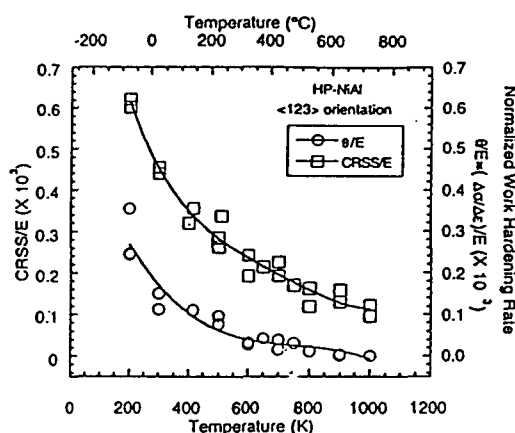
Figure 5. Temperature dependence of CRSS/E and θ/E for HP-NiAl.
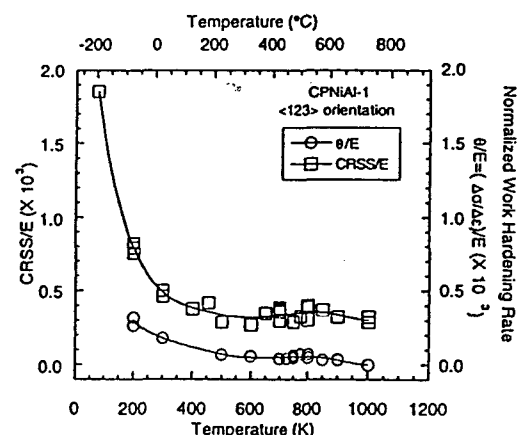
Figure 6. Temperature dependence of CRSS/E and θ/E for CPNiAl-1.

temperatures between 650 and 850 K, however, SRS became negative (Fig. 2a) and serrated yielding was observed. Analogous flow behavior was observed in CPNiAl-1, the other alloy that exhibited a negative SRS. During strain rate change tests run in the serrated flow regime, two other features were observed: (1) the flow stress either decreased or remained constant when the strain rate was increased with the magnitude of the shift being dependent upon strain; and (2) critical strains for the onset of serrations were observed with their magnitudes being dependent upon test temperature (see [1,5] for more details).

Analysis of the specimens after testing in the serrated flow regime revealed coarse slip bands. An example of such bands in NiAl-Si deformed at 800 K is shown in Fig. 4. Detailed investigations [16] have shown that the number of serrations on each load-elongation curve is proportional to the number of slip bands (i.e., each serration is associated with the formation of a localized slip band). Analysis of the dislocation substructures [1,5] revealed that these bands were composed of [100] type dislocations and were oriented parallel to either the [100] or [110] crystallographic directions.

Figs. 5-8 show the temperature dependence of the critical resolved shear stress (CRSS) and the work hardening rate, $\theta = \Delta\sigma/\Delta\epsilon$, normalized with respect to the elastic modulus, E. Since no estimates of E for <123> oriented crystals (E_{123}) were available it was assumed that E_{123} was equivalent to E for <111> oriented single crystals (E_{111}) as determined by Wasilewski [17] (i.e., $E_{123} = E_{111}$). In agreement with prior investigations on single crystal and polycrystalline NiAl [1,5,18-21], both the flow stress and the WHR generally decreased with increasing temperature. In CPNiAl-1, UF-NiAl, and NiAl-Si, however, apparent plateaus or peaks were observed in the temperature range 600 to 900 K while no such peaks or plateaus were observed in HP-NiAl. The CRSS and work hardening plateaus/peaks were observed to occur at higher temperatures than the minimums in SRS.

Discussion

Several important features were observed in the four NiAl alloys used in this study. (1) In CPNiAl-1, NiAl-Si and UF-NiAl1 tested at intermediate temperatures (i.e., ~600 to 1000 K), both CRSS/E and θ/E increase anomalously or remain constant within increasing temperature. Such behavior is not observed in HP-NiAl. (2) All four alloys exhibit distinct SRS minima in the temperature ranges 300 to 400 K and 600 to 800 K with SRS actually becoming negative between 600 and 800 K for CPNiAl-1 and NiAl-Si. Coincident with the occurrence of negative SRS values was the occurrence of serrated flow. (3) SRS
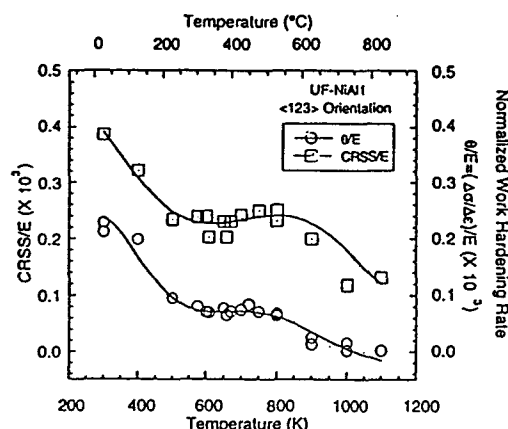
Figure 7. Temperature dependence of CRSS/E and θ/E for UF-NiAl1.
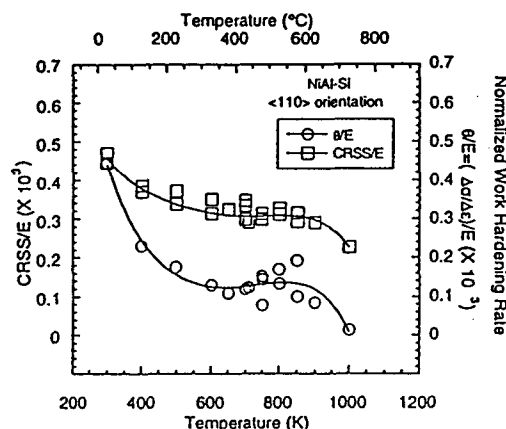
Figure 8. Temperature dependence of CRSS/E and θ/E for NiAl-Si.

minima occur at lower temperatures than CRSS or WHR maxima. Such observations are indicative of the occurrence of DSA [22-24]. Classical theory [22,23] indicates that during DSA, dislocation motion is characterized by a waiting time, t_w, during which dislocations are temporarily arrested at obstacles in the slip path. During this waiting time the dislocations can be further pinned by diffusing solute atoms which causes the obstacles to dislocation motion to become stronger with increasing waiting time. This results in an enhanced resistance to plastic deformation. SRS is said to become minimum when the time required to pin a dislocation, t_a, becomes equal to the waiting time. Thus, at any fixed strain rate (which fixes t_w), strengthening will become maximum when the temperature becomes high enough that $t_a \ll t_w$ (i.e., maximum strengthening occurs above the SRS minimum).

Serrated flow was observed in CPNiAl-1 and NiAl-Si, but not in UF-NiAl1 or HP-NiAl. However, some interesting observations in UF-NiAl1 and HP-NiAl were: (1) the lack of a flow stress plateau or anomalous work hardening region in HP-NiAl and the presence of such anomalies in UF-NiAl1; (2) the presence of a very pronounced SRS minimum in HP-NiAl and a less pronounced minimum in UF-NiAl1; and (3) the occurrence of diffuse flow stress transients at low temperatures in both alloys and the appearance of sharp flow stress transients at intermediate temperatures in UF-NiAl1 upon a change in strain rate. It is suggested that these peculiar observations are composition related. Independent analyses of NiAl single crystals and polycrystals has shown that the propensity for the occurrence of serrated flow is independent of O concentration [1,5,18]. In this study, dramatic flow stress serrations were observed in CPNiAl-1 and NiAl-Si whose C and Si contents are significantly higher than HP-NiAl which suggests that the lack of serrated flow is related to reductions in the C and Si concentrations. If C is maintained at levels comparable to the conventional purity alloys but Si is reduced to less than 100 at. ppm, as in the case of UF-NiAl1, serrated flow is not observed but flow stress transients upon an increase in strain rate are observed as is a yield stress plateau and a SRS minimum. This suggests that C still causes some strain aging behavior but that it's influence is enhanced by the presence of Si. Above, it was noted that two SRS minima were observed for each alloy: one near room temperature and the other at intermediate temperatures. Though it is tempting in this case to attribute the low and intermediate temperature SRS minima to C and Si respectively, it is more likely that both SRS minima are caused by the same specie. Classical investigations have shown that two SRS minima due to Snoek ordering and Cottrell atmosphere formation are often observed in BCC systems where DSA is caused by an interstitial specie [25,26] or in other alloy systems when DSA is caused by interstitial-substitutional or interstitial-vacancy clusters [27].

More rigorous analyses of the results obtained here (see references [1] and [5]) suggests that C and Si act in a synergistic fashion via a possible modification of the diffusion kinetics or an interactive solid solution hardening effect. More complete descriptions of the possible synergistic effects of C and Si in NiAl are presented elsewhere [1,5] and more detailed investigations of the influence of Si on the mechanical behavior of NiAl are in progress.

Conclusions

Three of the four alloys examined in the present study exhibit anomalous work hardening and flow stress plateaus/peaks in the temperature range 600 to 900 K which are indicative of DSA. Such regions were not as obvious in low interstitial-high purity NiAl, however.

Pronounced regions of negative SRS have been observed in conventional purity (CPNiAl-1) and in Si-doped NiAl at strains of 1.8% and 5.0% in the temperature range 600 to 800 K. Coincident with this temperature regime was the occurrence of serrated flow. In addition, coarse bands of localized slip were observed in this temperature range while no such bands were observed at higher or lower temperatures.

Compositional analyses suggest that a combination of interstitial and substitutional solutes, namely C and Si, cause strain aging in NiAl.

Acknowledgments

References

1. M.L. Weaver, Investigation of Strain Aging in the Ordered Intermetallic Compound β-NiAl, Ph.D. Dissertation, University of Florida (1995).
2. M.L. Weaver, R.D. Noebe, J.J. Lewandowski, B.F. Oliver and M.J. Kaufman, *Mater. Sci. Eng.* A192/193, 179 (1995).
3. M.L. Weaver, V. Levit, M.J. Kaufman and R.D. Noebe, in High-Temperature Ordered Intermetallic Alloys VI, J. A. Horton, I. Baker, S. Hanada, R.D. Noebe and D.S. Schwartz, Eds., Materials Research Society, vol. 364, Pittsburgh, PA, p. 425 (1995).
4. M.L. Weaver, M.J. Kaufman and R.D. Noebe, *Intermetallics*, in press (1995).
5. M.L. Weaver, R.D. Noebe and M.J. Kaufman, submitted to *Metallurgical Transactions A* (1995).
6. J.E. Hack, J.M. Brzeski and R. Darolia, *Scripta Metall. Mater.* 27, 1259 (1992).
7. J.E. Hack, J.M. Brzeski, R. Darolia and R.D. Field, in High-Temperature Ordered Intermetallics V, I. Baker, R. Darolia, J. D. Whittenberger and M.H. Yoo, Eds., Materials Research Society, vol. 288, Pittsburgh, PA, p. 1197 (1993).
8. J.E. Hack, J.M. Brzeski and R. Darolia, *Mater. Sci. Eng.* A192/193, 268 (1995).
9. J.M. Brzeski, J.E. Hack, R. Darolia and R.D. Field, *Mater. Sci. Eng.* A170, 11 (1993).
10. J.M. Brzeski, J.E. Hack and R.Darolia, in High-Temperature Ordered Intermetallic Alloys VI, J.A. Horton, I. Baker, S. Hanada, R.D. Noebe and D.S. Schwartz, Eds., Materials Research Society, vol. 364, Pittsburgh, PA, p. 419 (1995).
11. K. Kitano, T.M. Pollock and R.D. Noebe, *Scripta Metall. Mater.* 31, 397 (1994).
12. K. Kitano and T.M. Pollock, in Structural Intermetallics, R. Darolia, J.J. Lewandowski, C.T. Liu, P.L. Martin, D.B. Miracle and M.V. Nathal, Eds., The Minerals, Metals and Materials Society, Warrendale, PA, p. 591 (1993).
13. C.T. Liu, E. H. Lee, E.P. George and A. J. Duncan, *Scripta Metall. Mater.* 30, 387 (1994).
14. R. Darolia, D. Lahrman and R. Field, *Scripta Metall. Mater.* 26, 1007 (1992).
15. J.S. Winton, V.I. Levit and M.J. Kaufman, unpublished research, University of Florida (1995).
16. M.L. Weaver, unpublished research, University of Florida/NASA-Lewis Research Center (1995).
17. R.J. Wasilewski, *Trans. AIME* 36, 455 (1966).
18. M.L. Weaver, R.D. Noebe, J.J. Lewandowski, B.F. Oliver and M.J. Kaufman, submitted to *Intermetallics* (1995).
19. D.B. Miracle, *Acta Metall. Mater.* 41, 649 (1993).
20. R.D. Noebe, R.R. Bowman and M.V. Nathal, *Int. Mater. Rev.* 38, 193 (1993).

21. R.D. Noebe, R.R. Bowman and M.V. Nathal, Physical and Mechanical Metallurgy of NiAl, N. S. Stoloff and V. K. Sikka, Eds., Physical Metallurgy and Processing of Intermetallic Compounds, Chapman & Hall, New York, NY, (1995).
22. L.P. Kubin and Y. Estrin, *J. Phys. III* 1, 929 (1991).
23. P.G. McCormick, *Acta Metall.* 20, 351 (1972).
24. P. Rodriquez, *Bull. Mat. Sci.* 6, 653 (1984).
25. R.E. Reed-Hill and T. Zhu, *High Temp. Mater. Proc.* 6, 93 (1984).
26. R.E. Reed-Hill and M.J. Kaufman, *Acta Metall. Mater.* 43, 1731 (1995).
27. K.S.B. Rose and S.G. Glover, *Acta Metall.* 14, 1505 (1966).

NATURE OF SLIP DURING KNOOP INDENTATION
ON {100} SURFACE OF NiAl

F. Ebrahimi, A. Gomez, and T. G. Hicks
Materials Science and Engineering Department
University of Florida, Gainesville, FL 32611
e-mail: febra@mse.ufl.edu

(1

(....... August 22, 1995)

Introduction

The intermetallic NiAl, because of its excellent thermal conductivity, high temperature oxidation resistance, and low density, is a candidate material for high temperature applications in jet engines. Stoichiometric NiAl single crystal is a semibrittle material, in which plasticity always precedes fracture. When compared to a semibrittle bcc metal such as Mo, NiAl has a comparable fracture toughness (5–15 MPam$^{1/2}$ [1]) but its ductile-to-brittle transition temperature (DBTT) is much higher (Mo$_{[100]}$: DBTT/T_m = 0.05–0.07 [2], NiAl$_{[110]}$: DBTT/T_m = 0.26 [3]). This difference in DBTT can not be attributed to a difference in yield strength, since NiAl seems to be a softer material than Mo (σ_{ys} of Mo$_{[100]}$ = 160 MPa at T/T_m = 0.07 [2], σ_{ys} of NiAl$_{[110]}$ = 100 MPa at T/T_m = 0.26 [3]). Perhaps the most important difference between NiAl, which has an ordered B2 structure, and bcc metals is the nature and number of slip systems. Slip in NiAl has been reported to occur mainly on {110} or {100} planes in <001> directions, which provide only three independent systems [4]. The lack of enough number of slip systems in the highly ordered NiAl crystal is predicted to create very high local stresses in the plastic zone of cracks [5]. Furthermore, the limited number of slip systems promotes a highly anisotropic stress distribution at the crack tip and cause toughness of NiAl single crystals to depend on crystallographic orientation [1].

When NiAl crystals are tested in tension along <100> directions, initially the resolved shear stresses on {110}<001> and {100}<001> slip systems will be zero, and activation of {110}<110> and {112} <111> slip systems has been reported [6]. Inhomogeneous deformation situations, such as shear band formation during tensile testing or plastic zone development at a crack tip, can also produce high shear stresses on planes other than {100} and {110}. Contrary to tensile testing, during hardness indentation on a {100} face, because of the triaxiality of stress state, the resolved shear stresses on {110}<001> and {100}<001> slip systems may not be zero everywhere. For a given indentation plane, the variation in hardness with indentation direction has been shown to reflect the anisotropy in slip and the nature of dislocation interactions [7, 8]. One method to study slip is by analysis of slip lines. The purpose of this study was to investigate the nature of slip and the anisotropy of plastic deformation during Knoop microhardness indentation of a {100} face in NiAl single crystals using slip trace analysis.

TABLE 1
Knoop Hardness Data for {100} Indentation Plane.

Indentation Angle		0	22.5	35.	45	60	90	120	135	150	180
#1*	KHN, Kg/mm²	276	253	257	261	247	277	296	268	253	245
	σ**	2.8	2.5	7.3	2.9	7.2	1.4	0	0	3.5	1.8
#2*	KHN, Kg/mm²	210	—	—	—	219	203	191	—	—	228
	σ**	6.2	—	—	—	3.4	5.9	2.4	—	—	7

* Specimen Number
**Standard Deviation

Materials and Experimental Procedures

Single crystals of NiAl were provided by General Electric, Aircraft Division in Cincinnati, Ohio. The as-received crystals had been homogenized in an argon filled vacuum furnace at 1350°C for 50 hours. The orientation of crystals were determined using Laue back-scattered x-ray diffraction technique. Two specimens were prepared to confirm the observations reported. In each specimen parallel {100} faces were cut and the surface of a {100} face (here we refer to it as (010) face) was mechanically polished and subsequently electropolished using a perchloric solution. The orientation of the samples were checked after electropolishing. The hardness measurements were made with a microhardness machine using a Knoop indentor with an indentation time of 12 seconds. Five measurements were performed per orientation. The slip lines were studied using optical microscopy technique.

Results and Discussion

Table 1 presents the results of Knoop hardness measurements for 500 g applied load. The average hardness values for both specimens are plotted in Figure 1. The standard deviation values calculated indicate that variation in hardness with indentation orientation is significant. Surprisingly the hardness did not show the expected four-fold symmetry. The hardness values on equivalent crystallographic orientations were not the same and consistently, for both specimens, one side was softer than the other side.

Optical observation of indents provided at 7000 g load revealed formation of slip lines around the indents. At this load level the hardness behavior was the same as that at 500 g applied load. The slip lines were consistently observed only for the indents applied at 120° ([10$\bar{3}$], minimum hardness orientation) and 90° ([10$\bar{1}$]) angles. Figure 2 shows the slip lines for these two orientations. It was interesting to note that the slip lines were observed only on one side of the indents. This behavior persisted for all indentations applied in these two orientations. The trace of slip lines were found to be [101], [301], and [$\bar{1}$0$\bar{3}$] directions as identified on the micrographs shown in Figure 2. These slip traces can not be explained by motion of a<110> dislocations, however, they can be associated with two slip scenarios. One possibility is that a<111> dislocations are activated and [101], [301] and [$\bar{1}$0$\bar{3}$] slip traces represent activation of ($\bar{1}$21)[$\bar{1}$11] or ($\bar{1}$21)[11$\bar{1}$], (12$\bar{3}$)[111], or ($\bar{1}$23)[1$\bar{1}$1], and (32$\bar{1}$)[1$\bar{1}$1] or ($\bar{3}$21)[111] slip systems, respectively. The slip traces shown in Figure 2a indicate that the slip changes from [101] to [301] direction suggesting the cross slip of dislocations. However, there is no <111> direction shared by the possible slip
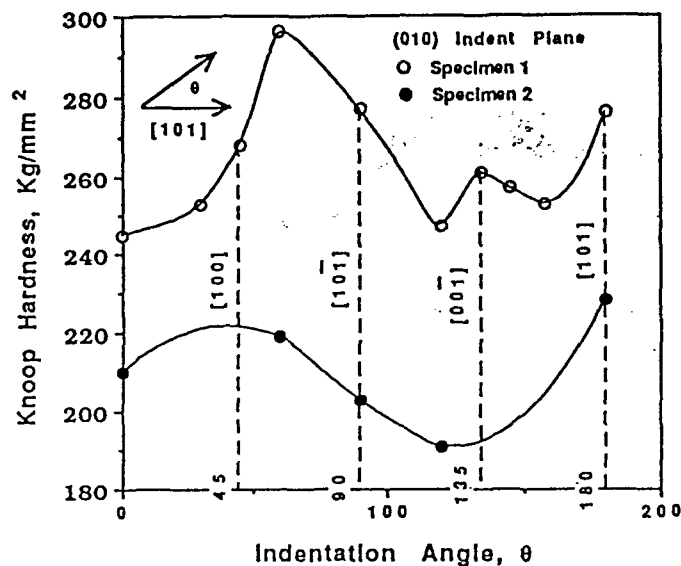
Figure 1. Averge Knoop microhardness numbers as a function of indentation angle.

systems for these two traces, and hence the a<111> dislocations could not have been activated. The other possiblity is the activation of a<100> dislocations. Slip along [100] and [001] directions, which are parallel to the indent plane, does not produce slip traces on (010) indent plane. Assuming that [010] dislocations can cross slip to $\{h0l\}$ planes, the [101], [301], and [$\bar{1}03$] traces can be attributed to the activation of ($\bar{1}01$) ($\bar{1}03$), and (30$\bar{1}$) slip planes. This slip scenario allows the cross slip of [010] dislocations consistent with the slip line analysis.

Formation of slip bands consistent with $\{103\}<010>$ slip has been observed during creep testing of NiAl single crystals at elevated temperatures [9]. It has been suggested that these slip bands develop by microscopic pencil glide on $\{100\}$ and $\{110\}$ planes. However, in this study we did not observe any slip trace that corresponded to slip of a[010] dislocations on (100) or (001) planes. Furthermore, as can be seen
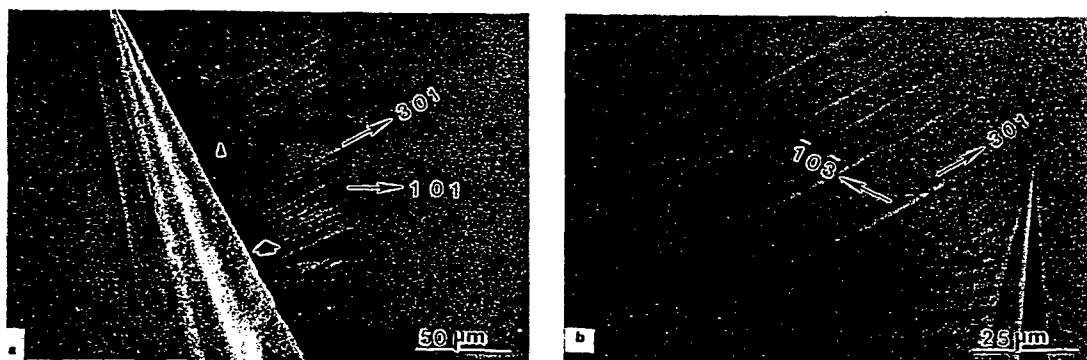
Figure 2. Optical micrographs showing the slip traces for (a) 120° and (b) 90° indentation angles. Arrows mark slip traces that indicate cross slip.

in Figure 2, the slip traces are very straight and are not wavy as would have been expected for repeated cross slip of screw dislocations between ($\overline{1}$01) and (100) or (001) planes. Therefore, it is concluded that indeed slip occurs on {301} planes. Slip on {301}<010> provides 12 physically distinct slip systems, of which three are independent. The number of independent slip systems, however, does not increase when pencil glide with {101}<010> and {100}<010> slip systems occur. An increase in the possibility of cross slip is expected to enhance recovery processes and hence play an important role in the ductile-to-brittle transition in NiAl. Recent observations made during *in-situ* straining in TEM have also suggested extensive cross slip to occur in stoichiometric NiAl [10].

It is interesting that slip occurred on the {301} planes and not the {201} planes. As shown in Figure 3, in NiAl, because of its B2 structure, the {402} planes, which consist of either Ni or Al atoms, rather than the {201} planes should be considered. The {301} planes consist of both Ni and Al atoms and have a larger spacing than the {402} planes, hence the Peierls stress is expected to be smaller for the former planes. Note that the motion of a[010] dislocations on either of these planes does not create antiphase boundary. The of lack four-fold symmetry in hardness data (see Table 1) and the associated formation of slip traces only in one corner of the indents can be explained by considering the resolved shear stress for the observed slip systems. The stress field produced by a Knoop indenter may be approximated as a flat punch [7, 8] and is given by [11]:

$$\sigma_{xx} = -(P/2\pi)[2(\Phi_1 - \Phi_2) + \sin 2\Phi_1 - \sin 2\Phi_2],$$

$$\sigma_{zz} = -(P/2\pi)[2(\Phi_1 - \Phi_2) + \sin 2\Phi_1 - \sin 2\Phi_2],$$

$$\sigma_{xz} = -(P/2\pi)[\cos 2\Phi_1 - \cos 2\Phi_2],$$

$$\sigma_{yy} = \nu(\sigma_{xx} + \sigma_{zz})$$

$$\tan \Phi_1 = z/x, \text{ and } \tan \Phi_2 = z/(x + w/2)$$

Here, w is the width of the punch, Φ_1 and Φ_2 are the angles made with the surface by lines connecting each indenter edge to the point at which the stresses are to be calculated, P is the load applied, and x, y, and z are directions normal to and along the indenter edges, and normal to the surface respectively. Figure 4a presents the coordinate system for the stress field. For regions outside the indenter edge and near the surface (x >> z), where slip traces are observed, the Φ_1 and Φ_2 angles are small and consequently all stress components except for σ_{xx} and σ_{yy} are zero. In these regions the resolved shear stress on any plane parallel to the [010] direction (z axis) will be zero, and when the loading axis is a few degree off the [010] direction, then slip on {h0l} planes becomes possible. This misorientation destroys the symmetry and hence
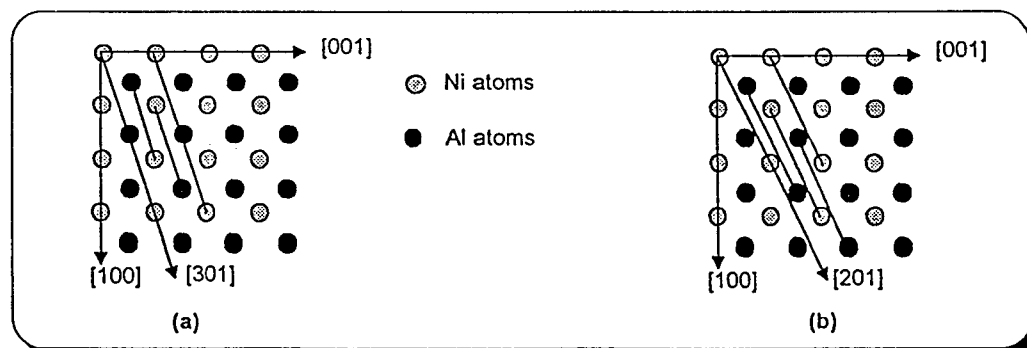
Figure 3. Schematics showing the traces of (a) ($\overline{1}$03) and (b) ($\overline{2}$04) planes on (010) projection.
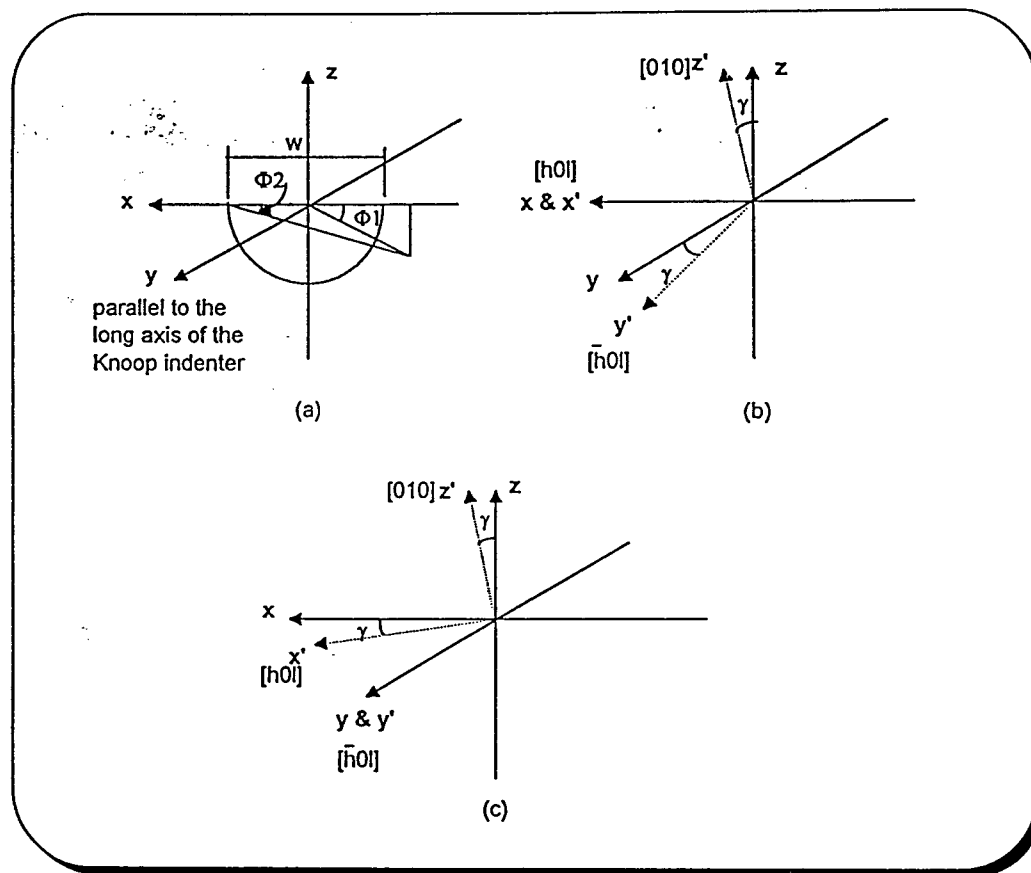
Figure 4. (a) Coordinate system for the stress field of a long flat punch subject to a uniform pressure. (b) Rotation of the z-axis in the yz plane (resolved shear stress near the surface and outside the punch = σ'_{yz} = cos γ sin γ σ'_{yy}). (c) Rotation of the z-axis in the zx plane (resolved shear stress near the surface and outside the punch = σ'_{yz} = 0).

slip occurs preferentially in one corner. Recent tensile data for <100> loading axis also indicate that a small misorientation (<5 degree) results in a much lower measured strength and preferential activation of one slip system [12]. Owing to the two-fold symmetry of the Knoop indenter the direction of misorientation of the loading axis relative to the long axis of the indenter affects the magnitudes of the resolved shear stress. Therefore, the crystal appears to be softer in one quadrant and the ($h0l$):($\bar{h}0l$) asymmetry is observed. This is demonstrated for a simple case in Figure 4. When the z-axis is rotated in the yz plane (Figure 4b) the resolved shear stress on the ($\bar{h}0l$) plane, σ'_{yz}, will be non-zero. However, when the z-axis is rotated in the zx plane (Figure 4c) the resolved shear stress on the [$\bar{h}0l$] plane will remain zero. Consequently, the rotation of the specimen by 90 degree may result in a situation that outside the indenter slip cannot be activated and the hardness will be high. Note that in regions under the punch and away from the surface the resolved shear stress values on slip planes are not insignificant and the general hardness level depends on the interaction of dislocations in these regions. Although the x-ray analysis revealed that the specimens had the z-axis within one degree from the [010] orientation, during hardness testing the whole system cannot be aligned with such accuracy and a few degree misalignment is inevitable. Other parameters that can contribute to the lack of symmetry in hardness data are asymmetry of dislocation core

structure and the preferential existence of dislocations with similar signs. However, the results of this investigation are insufficient for evaluation of such parameters. As far as the inconsistency in hardness values between the two specimens is concerned, since they were cut from the same crystal, the difference in hardness between the two specimens may be associated with an inhomogeneous distribution of defects in the crystal as well as a difference in their misalignment.

Summary

The Knoop hardness variation with crystallographic orientation on a {100} face of an NiAl single crystal was evaluated. The absence of four-fold symmetry in hardness was attributed to a slight crystallographic misorientation of the specimens relative to the loading axis. Analysis of the slip traces indicate that a<100> dislocations slip on {301} planes and cross slip between {301} and {101} planes. This mode of slip is expected to occur at elevated temperatures and/or under triaxial stress state.

Acknowledgments

References

1. S. Shrivastava and F. Ebrahimi, MRS Symposium Proceedings, Vol. 364, Part I, 431 (1995).
2. H. Haung and W. W. Gerberich, Acta metall. mater. 42, 639, (1994).
3. R. D. Noebe, R. R. Bowman, and M. V. Nathal, Inter. Mater. Rev. 38, 193 (1993).
4. J. D. Cotton, M. J. Kaufman, and R. D. Noebe, Scripta metall. mater. 25, 2395 (1991).
5. M. Saeedvafa and J. R. Rice, Modelling Simul. Mater. Sci. Eng. 1, 53 (1992).
6. D. B. Miracle, Acta metall. mater. 41, 649 (1993).
7. P. B. Hirsch, P. Pirouz, S. G. Roberts, and P. D. Warren, Phil. Mag. 52(3), 759 (1985).
8. S. G. Roberts, P. D. Warren, and P. B. Hirsch, J. Mater. Res. 1(1), 162 (1986).
9. A. Nadia, Plasticity, p. 247, McGraw-Hill, New York (1931).
10. W. R. Kanne Jr., P. R. Strutt, and R. A. Dodd, Trans. Metall. Soc. AIME 245, 1259 (1969).
11. P. Nagpal, I. Baker, and J. A. Horton, Intermetallics 1, 23 (1994).
12. J. Winton, L. Levit, and M. J. Kaufman, To be published.

BRITTLE-TO-DUCTILE TRANSITION IN POLYCRYSTALLINE NiAl

F. EBRAHIMI and T. G. HOYLE

Materials Science and Engineering Department, University of Florida, Gainesville, FL 32611, U.S.A.

Abstract—The brittle-to-ductile transition (BDT) of stoichiometric NiAl and Ni–49Al–1Ti alloys was investigated using tensile and fracture toughness testing methods. The BDT in these alloys was found to be associated with a sharp drop in strain hardening rate, which causes the general yielding and plastic instability (necking) to precede unstable fracture in notched and tensile specimens, respectively. The addition of Ti increases the strength, low temperature toughness, and BDT temperature of NiAl significantly. The occurrence of intergranular fracture in NiAl alloys has been correlated with the development of localized internal stresses near grain boundaries owing to a lack of sufficient slip systems. The results of this study suggest that the vacancy concentration in NiAl depends significantly on the stress state and the amount of deformation. This phenomenon may be responsible for the microvoid coalescence fracture mechanism observed in tensile specimens, and the enhancement of dislocation climb at moderate temperatures. © *1997 Acta Metallurgica Inc.*

1. INTRODUCTION

There has been an interest in developing alloys based on NiAl for high temperature structural applications in aircraft engines [1]. NiAl is an ordered intermetallic with a B2 (CsCl) crystal structure. Because of its high ordering energy, slip in this material is limited to $a\langle 100 \rangle$ Burgers vectors [2], except in the case of single crystals oriented in the hard $\langle 100 \rangle$ direction [3–5]. The $a\langle 100 \rangle$ slip occurs preferentially on $\{110\}$ and $\{100\}$ planes, respectively; however, $\{hk0\}$ slip planes can also become activated [6–8]. The $a\langle 100 \rangle$ deformation mode results in only three independent slip systems, and hence strain compatibility between grains in a polycrystalline material cannot be achieved and consequently the room temperature (RT) tensile ductility of NiAl is almost nil [9].

The BDT of nominally stoichiometric polycrystalline NiAl has been evaluated based on the tensile ductility [10–14]. The BDT temperature has been reported to be around 300°C at a nominal strain rate of $10^{-4}\,\text{s}^{-1}$ and to increase at higher applied strain rates [12]. The increase in tensile ductility is suggested to be associated with a change in fracture morphology from predominantly intergranular to predominantly transgranular fracture [12], which upon further increase in the test temperature to 600°C changes to a microvoid coalescence fracture mechanism [10]. The BDT has been attributed to the onset of dislocation climb [11], which allows the strain compatibility problem to be overcome and hence changes the crack nucleation mechanism from an intergranular to a transgranular mechanism [12]. However, in another study [13] the fracture mechanism has been reported to remain predomi-

nantly intergranular throughout the BDT regime and change to a microvoid coalescence mechanism at temperatures above 525°C.

The tensile ductility of NiAl has been shown to be independent of grain size at grains larger than about 20 μm and to increase with a further decrease in grain size [14]. The fracture morphology has been shown to change from predominantly transgranular in specimens with large grain size (125 μm) to predominantly intergranular in a fine grain size (14 μm) microstructure. However, a further decrease in grain size (8 μm) has been reported to reverse the fracture morphology to a predominantly transgranular fracture [14].

The intergranular fracture of NiAl has been attributed to the low cohesive strength of the grain boundaries and boron has been added to improve the grain boundary fracture energy of NiAl [15]. Although the B-doped NiAl shows predominantly transgranular fracture, the change in fracture behavior is believed to be a result of an increase in yield strength and limited plasticity preceding fracture [12]. The addition of Zr has also been shown to enhance the transgranular fracture mode and increase the strength and BDT temperature of NiAl [13].

The limited number of reported fracture toughness studies using notched four-point bend specimens with 50 mm × 6 mm × 4 mm dimensions and a 2-mm deep notch at a displacement rate of 2×10^{-4} mm/s [16, 17] suggest that the BDT, similar to the tensile data, occurs at around 300°C. No detailed fractographic results have been reported in these studies.

The purpose of this study was to evaluate the BDT behavior of nominally stoichiometric NiAl using

fracture toughness and tensile testing methods. In particular we were interested in the occurrence of various fracture morphologies and their correlation with mechanical properties. It has been reported that addition of Ti provides excellent high temperature strengthening [1]. Therefore, we wanted to know the effect of Ti addition on the BDT temperature of NiAl. Furthermore, the effect of plastic constraint and displacement rate on BDT behavior was evaluated.

2. MATERIALS AND EXPERIMENTAL PROCEDURE

The stoichiometric NiAl and NiAl + 1 at.%Ti alloys for this study were cast and extruded at NASA Lewis Research Center in Cleveland, Ohio. The alloys were induction melted in an inert atmosphere and cast into copper chill molds. The ingots were sealed in a 2-in outside diameter mild steel can and were then extruded at a 12:1 reduction ratio. The NiAl and NiAl + Ti alloys were extruded at 875°C and 900°C, respectively. The microstructure of the as-extruded alloys was recrystallized and showed a wide range of grain size distribution with average grain sizes of 9 μm and 12 μm for NiAl and NiAl + Ti alloys, respectively.

Tensile specimens with a 12 mm gauge length and a square cross-section (approximately 1.7 mm × 1.7 mm) were cut by electric discharge machine (EDM). The cut tensile specimens were heat treated at 1000°C for one hour and cooled in flowing argon to room temperature. The specimens were subsequently electropolished to remove the surface damage produced by the cutting process and heat treatment. The heat treatment at 1000°C resulted in a narrower grain size distribution with average grain sizes of 84 μm and 27 μm for NiAl and NiAl + Ti alloys, respectively.

The single-edge notched-bend fracture specimens (thickness = 3.5 mm, width = 7.0 mm) were cut by EDM. The notch (crack length = 3.5 mm) was made using a slow speed diamond saw. In order to investigate the effect of specimen thickness on BDT temperature, a few NiAl + Ti specimens were prepared with a larger thickness (7.0 mm). After the notches were cut, the specimens were heat treated similar to the tensile specimens. Before testing, the sides of the fracture specimens were electropolished in order to remove the damaged surface layer, which could modify the stress state and hence the constraint at the notch tip.

Both the as-extruded and heat treated mechanical properties were evaluated at room temperature. The properties of the heat treated alloys were characterized at elevated temperatures up to 600°C. Mechanical testing was conducted in an oxygen-gettered argon atmosphere using a closed-loop hydraulic system. Heating was achieved by a tungsten mesh (5 in hot zone) which surrounded the sample inside the furnace chamber. The specimen temperature

was monitored with a thermocouple close to the specimen. Once the temperature was reached, at least 15 min was given for the system to attain thermal equilibrium. Tensile testing was conducted at a nominal strain rate of 6.7 × 10⁻⁵ s⁻¹. The fracture toughness testing was performed at a displacement rate of 10⁻³ mm/s. A few NiAl fracture specimens were tested at a displacement rate of 10⁻⁴ mm/s. A fully articulated four-point bend fixture [span(1) = 20 mm, span(2) = 40 mm] was used for fracture testing of the single-edge notched specimens. The fracture toughness was calculated as the critical stress intensity factor at the point of crack instability (sudden load drop) using the relationship given in Ref. [18].

The fracture surfaces were characterized using a scanning electron microscope. A four-point bend specimen of the stoichiometric NiAl was partially loaded at 500°C and subsequently sectioned and analyzed for determining the crack initiation mechanism.

3. RESULTS

3.1. Tensile testing

The results of tensile testing are summarized in Table 1. Heat treatment at 1000°C resulted in a decrease in yield strength, strain hardening rate, and fracture strength, as well as a decrease in ductility of the alloys investigated.

True tensile stress–strain curves for NiAl specimens tested at various temperatures are shown in Fig. 1. The NiAl specimens broke without necking up to 300°C test temperature; however, the specimen tested at 400°C showed extensive necking before fracture. Figure 2 is a plot of engineering fracture strain as a function of test temperature for NiAl. The plot indicates a small increase in tensile ductility up to 300°C, followed by a dramatic increase at 400°C. The yield strength of NiAl varied moderately with test temperature; however, the average strain hardening rate was decreased significantly with an increase in temperature (see Fig. 1 and refer to Table 1).

The NiAl + Ti alloy showed much lower ductility than the NiAl alloy. At ambient and 200°C test temperatures the heat treated specimens broke in the elastic regime with no apparent plasticity. At 300°C and above, yielding preceded fracture; however, no necking was observed in these specimens, even at 600°C test temperature. In the test temperature regime studied the yield strength of the NiAl + Ti alloy was less temperature dependent and was much higher than for the NiAl alloy (see Table 1). The strain hardening rate values obtained above 300°C were also much less temperature dependent and higher than those observed for NiAl.

The true tensile strength values reported in Table 1 also represent the fracture stress, except for the NiAl specimen tested at 400°C. For both NiAl and

EFFECT OF PRESTRAINING ON THE BRITTLE-TO-DUCTILE TRANSITION OF NiAl SINGLE CRYSTALS

S. Shrivastava and F. Ebrahimi
Department of Materials Science and Engineering
University of Florida, Gainesville, FL 32611

ABSTRACT

The brittle-to-ductile transition (BDT) has been established for NiAl single crystals as evaluated by fracture toughness testing and also the effects of prestraining on the brittle-to-ductile transition temperature (BDTT) have been investigated. Specimens were prestrained to a 10% plastic strain level at 200^0C under tension prior to toughness testing. The BDT of the prestrained specimens was compared to that of the as homogenized specimens. The results have revealed the occurrence of two competing effects upon prestraining: (1) an increase in dislocation sources causing a difficulty in micro-crack initiation and resulting in an increase in toughness at low temperatures, and (2) an increase in the flow stress resulting in an increase in BDT temperature. The crack initiation and propagation mechanisms were also analyzed and have been discussed.

INTRODUCTION

Intermetallic compound NiAl possesses a high melting temperature. high thermal conductivity, relatively low density and good high temperature oxidation resistance. These properties make it a potential candidate for high temperature structural applications. However, it suffers from low room temperature ductility and fracture toughness. Few studies have been published in the literature regarding the BDT in NiAl single crystals[1]. The room temperature fracture toughness of NiAl has been reported to be in the range of 4 to 11 $MPam^{1/2}$ depending on the orientation. impurity concentration and heat treatment[2-4]. The fracture toughness of single-crystalline materials is very sensitive to the dislocation activity in the notch tip. This scenario is different from polycrystalline materials where grain boundaries are present that act as additional sinks/sources of dislocations. Similar to other B2 ordered compounds such as FeAl. the dislocation density of annealed NiAl single crystals is rather low[5]. One way of enhancing the dislocation density is by prestraining the material at elevated temperatures. Few studies have reported an influence of prestraining on the BDTT of single crystalline materials such as Si and MgO[6,7]. The objective of the present study has been to understand the effect of prestraining on the room temperature fracture toughness and also on the BDT of NiAl single crystals.

MATERIALS AND EXPERIMENTAL PROCEDURES

Single crystals of stoichiometric NiAl grown at the University of Florida were used in this study. The homogenization treatment for these crystals was performed at 1300^0C for 3 hours followed by cooling at a rate of $2.4^0C/min$. The orientations of crystals were determined using Laue back-scattered x-ray diffraction technique.

· Fracture toughness testing was conducted using double-notched tensile specimens which were cut using an electric discharge machine (EDM). The geometry and orientation of these specimens are shown in Figure 1. The specimens were electropolished using a solution containing 10 volume% perchloric acid and 90 volume% methanol to remove the
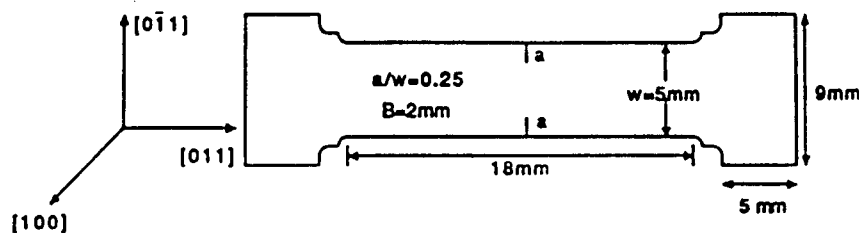
Figure 1: Geometry and orientation of the double-notched tensile specimens.

damaged zone created during the electric discharge cutting. After electropolishing, selected specimens were prestrained under tension at 200°C using a closed loop hydraulic mechanical testing system at a nominal strain rate of $5 \times 10^{-4} \text{sec}^{-1}$. The 200°C temperature was found to be an optimum temperature for prestraining. The tensile data show that above 200°C the localized deformation (necking) starts at relatively low strain values and below 200°C the material fails with small ductility. Prestraining was conducted at 1%, 5%, 10%, and 15% plastic strain. Following the prestraining to the desired strain level, the specimens were unloaded and cooled under flowing argon. Notches were introduced after prestraining the specimens. A 300 μm thick diamond saw was used to cut notches in all the specimens. Fracture toughness tests were carried out in a displacement control mode at a displacement rate of 10^{-2} mm/sec. The fracture toughness, K_Q, was estimated using the following formula[8]:

$$K_Q = Y\sigma a^{1/2} \tag{1}$$

$$Y = 1.99 + 0.76\,(a/w) - 8.48\,(a/w)^2 + 27.32\,(a/w)^3 \tag{2}$$

where σ is the stress applied, a is the initial crack size, w is the width of the specimen, and Y is the geometric factor. At elevated temperatures, where the load-displacement curve was non-linear, the fracture toughness was calculated as K_{JC} using the equation (3).

$$K_{JC} = K_Q + (J_p E)^{1/2} \tag{3}$$

J_p was calculated from the area under the plastic regime of the load-displacement curves[9] and E is the modulus of elasticity. Fracture surfaces were analyzed using a JEOL 200CX scanning electron microscope.

RESULTS

A tensile test was performed at 200°C to study the slip behavior prior to selecting the prestraining levels. The engineering stress-strain curve is shown in Figure 2. The curve shows the four prestrain levels chosen for toughness measurements. Figure 3 shows the fracture toughness values as a function of the level of prestraining. In general the fracture toughness of NiAl single crystal was increased upon prestraining. Initially, the fracture toughness increased significantly from 5.8 MPam$^{1/2}$ to 8.4 MPam$^{1/2}$, however, the rate of increase in fracture toughness decreased upon further prestraining.

A symmetrical tilt grain boundary was introduced by a mirror reflection operation with the grain boundary plane being perpendicular to the y axis and thus coinciding with the crack front. We chose a $\Sigma = 5$ grain boundary, which has been widely studied in the past. We studied three possible structures of this boundary corresponding to different local chemical compositions in the boundary region. For all the cases studied this plane was the (120) plane and the crack front was the (001)tilt axis. The equilibrium grain boundary structure involves a certain rigid body translation of one of the two crystals relative to the other. This translation was studied in simulations without the crack and the equilibrium values were used in the fracture simulations.

For each case, the value of K_{IC} was calculated as follows:

$$K_{IC}^{est} = (2\mu^{eff}\gamma_{coh})^{1/2}$$

where μ^{eff} is the shear modulus. If anisotropic elasticity is used μ^{eff} is calculated for the particular orientation of the crack plane and if isotropic elasticity is used, μ^{eff} is taken as the Voigt average. γ_{coh} is the cohesive energy of the crack plane (twice the grain boundary energy minus the grain boundary energy). The values of the surface energy γ_s used in this study are tabulated in Table I along with the values of the K_{IC} which were calculated using the above procedure. The comparison of the anisotropic and isotropic calculations gives an idea of the approximations involved in treating the problem with isotropic theory, as done below for the grain boundary simulations.

Table I: Values of critical stress intensity factors predicted for the bulk in anisotropic and isotropic formulations

Crack-Plane	Crack-front	$2\gamma_s in J/m^2$	K_{IC} (MPa $m^{1/2}$)	isotropic K_{IC} (MPa $m^{1/2}$)
{100}	{100}	3.95(average)	0.82	0.95
	{110}	3.95(average)	0.88	0.95
{110}	{100}	3.40	1.09	0.88
	{110}	3.40	0.93	0.88

Simulations were carried out at various external loads, both below and above the computed values of K_{IC}, for each of the four orientations. The atomistic blocks used in the simulations include 10,000 to 60,000 atoms.

Grain Boundary Structure in NiAl

Petton and Farkas [4] studied the multiplicity of possible grain boundary structures for $\Sigma = 5$ symmetrical tilt boundary in ordered B2 Ni aluminide. These boundaries were investigated considering possible variations of the local chemical composition and environment. More recently Mishin and Farkas [5] have also studied grain boundary structure in this compound, using a more correct scheme for the calculations of the energies of off-stoichiometric boundaries [6]. Using the correct method for the calculation of the energies of the chemical potentials in the alloy, one can calculate the correct grain boundary energies for off-stoichiometric boundaries. The most important consequence of this calculation is that the grain boundary energies will be different in different bulk stoichiometries. The Al-rich boundaries present lower energies for Al-rich bulk and the Ni-rich boundaries present lower energies for Ni-rich bulk. The results of this more recent investigation agree with the initial

results of Petton an Farkas [4] for structures and the cohesive energies of the boundaries. The observed trends indicate that the Al-rich boundaries present lower cohesive energies. The role of Al content in the boundary energetics is therefore particularly important. In that work it was also concluded that there is a variety of possible structures with similar energies that may actually play a role in the real crystal. For the present investigation we chose three structures, corresponding to the lowest possible energy for stoichiometric, Ni-rich, and Al-rich, respectively. The three structures are shown in Figure 1.

Table II gives the grain boundary energies and equilibrium rigid body displacements(Δx, Δz) for the three structures. Δy gives the expansion of the boundary.

Table II: Grain boundary energies(J/m^2), equilibrium rigid body displacements(Δx, Δz) and expansions Δy. Δx, Δy and Δz are expressed in terms of the lattice parameter a

Boundary	Cohesive Energy	Energy in a Ni-rich bulk	Energy in a Al-rich bulk	Δx	Δy	Δz
Stoichiometric	3.09	0.77	0.77	$a/2\sqrt5$	0.186 a	a/2
Ni-rich	3.40	0.75	1.64	0	0.166 a	0
Al-rich	2.67	1.04	0.15	$a/2\sqrt5$	0.274 a	0

Figure 1: $\Sigma = 5$ (210) Grain Boundary Structures in NiAl. a)Stoichiometric boundary where the lower crystal is shifted by a/2 along the tilt axis. b)Ni-rich boundary. c)Al-rich boundary.
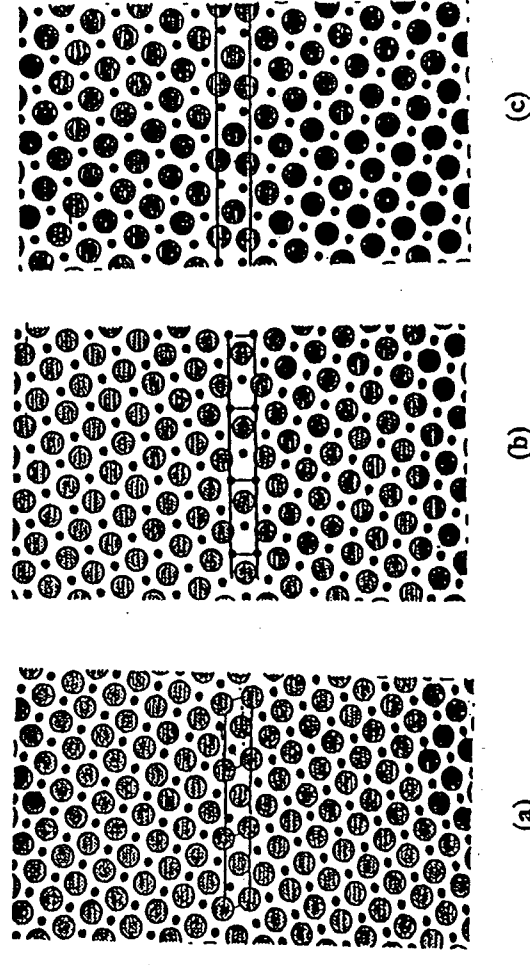
Energetics of Grain Boundary Fracture

We consider the energetics of grain boundary fracture first in a Griffith framework. The calculation of the Griffith condition for crack propagation along the grain boundary can

Figure 2: Fracture along a stoichiometric $\Sigma = 5$ (210) Grain Boundary in NiAl a) 0.96 MPa $m^{1/2}$ b) 1.44 MPa $m^{1/2}$ c) 4.80 MPa $m^{1/2}$
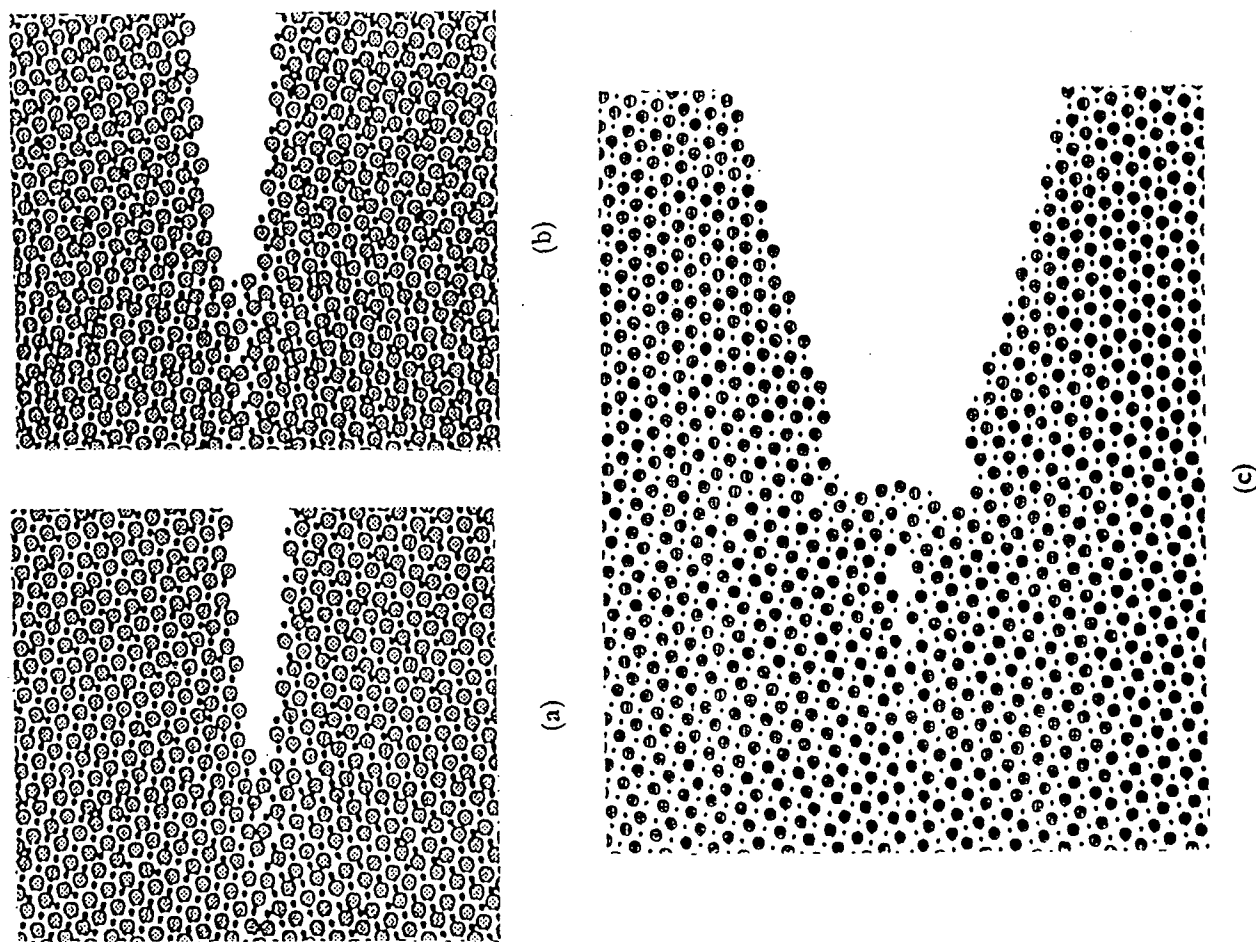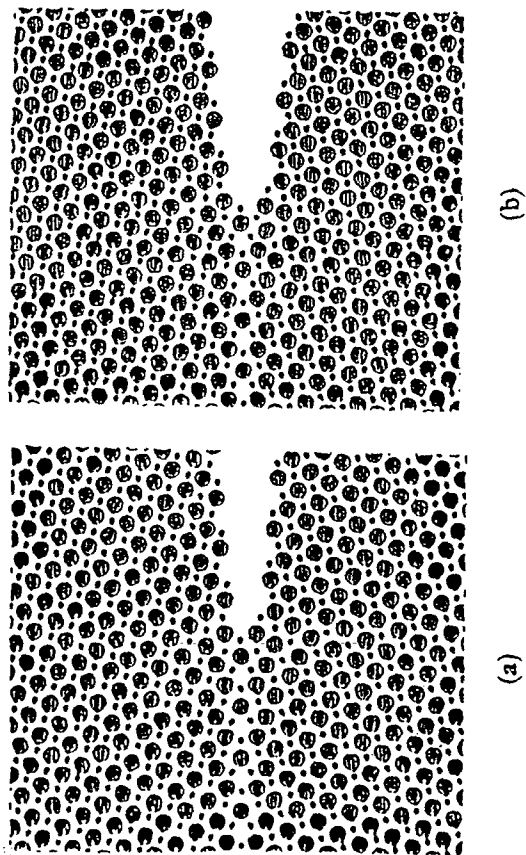
(a)

(b)

(c)

be done by using the cohesive energy of the boundary instead of twice the surface energy. The cohesive energy of the boundary is defined as twice the surface energy minus the grain boundary energy. Table III shows the results of such a calculation given by the potentials used here and a Voigt average shear modulus.

Table III: Griffith condition calculated using the cohesive energies of the boundaries

Crack type	$K_{Ic}(MPa\sqrt{m})$
Bulk{110}plane	0.88
Stoichiometric $\Sigma = 5$ Boundary	0.82
Al-Rich $\Sigma = 5$ Boundary	0.78
Ni-rich $\Sigma = 5$ Boundary	0.88

These results show that the Ni-rich boundary is actually as strong as the bulk. The stoichiometric boundary is only marginally weaker than the bulk. The Al-rich boundary studied is significantly weaker than the bulk.

Results for a Stoichiometric Boundary

The atomistic configuration of the crack tip region found for this boundary under varying stress intensities is depicted in Figure 2. The crack does not advance in a brittle manner, but rather it remains in a similar configuration up to stress intensities that are significantly higher than the Griffith critical value. For a stress intensity that is about 50% higher than the Griffith value, the configuration at the crack tip changes and the crack still does not advance. The change in tip configuration further stabilizes the crack that still does not grow at this level of stress intensity. Crack growth was observed at much higher stresses, with significant blunting of the crack tip.

Results for a Ni-rich Boundary

A similar result was obtained for the Ni-rich boundary. This is shown in Figure 3. For this boundary, we found extensive blunting of the crack tip. The blunted crack does not grow in an unstable fashion at stresses that are higher than three times the Griffith value. The present results suggest ductility in the Ni-rich boundaries.

Results for an Al-rich Boundary

The results for the Al-rich boundary are different, with the crack advancing at a stress about 50% higher than the Griffith value. However, at higher stresses some blunting is also observed in this boundary, as shown in Figure 4d. The blunting observed at this higher stresses is much less than that observed for the Ni-rich boundary. Nevertheless, there is an indication of limited ductility even in the Al-rich boundary.
This is shown in Figure 4.

Discussion: Inter vs. Intragranular fracture in NiAl

The Griffith loads for the grain boundaries investigated here are the same or lower than those of the bulk along the 110 plane. This indicates that under the geometry investigated

Figure 4: Fracture along Al-rich Σ= 5 (210) Grain Boundary in NiAl a) 0.96 MPa m^1/2 b) 1.44 MPa m^1/2 c) 4.80 MPa m^1/2

Figure 3: Fracture along a Ni-rich Σ= 5 (210) Grain Boundary in NiAl a) 0.96 MPa m^1/2 b) 1.44 MPa m^1/2 c) 4.80 MPa m^1/2

405

404
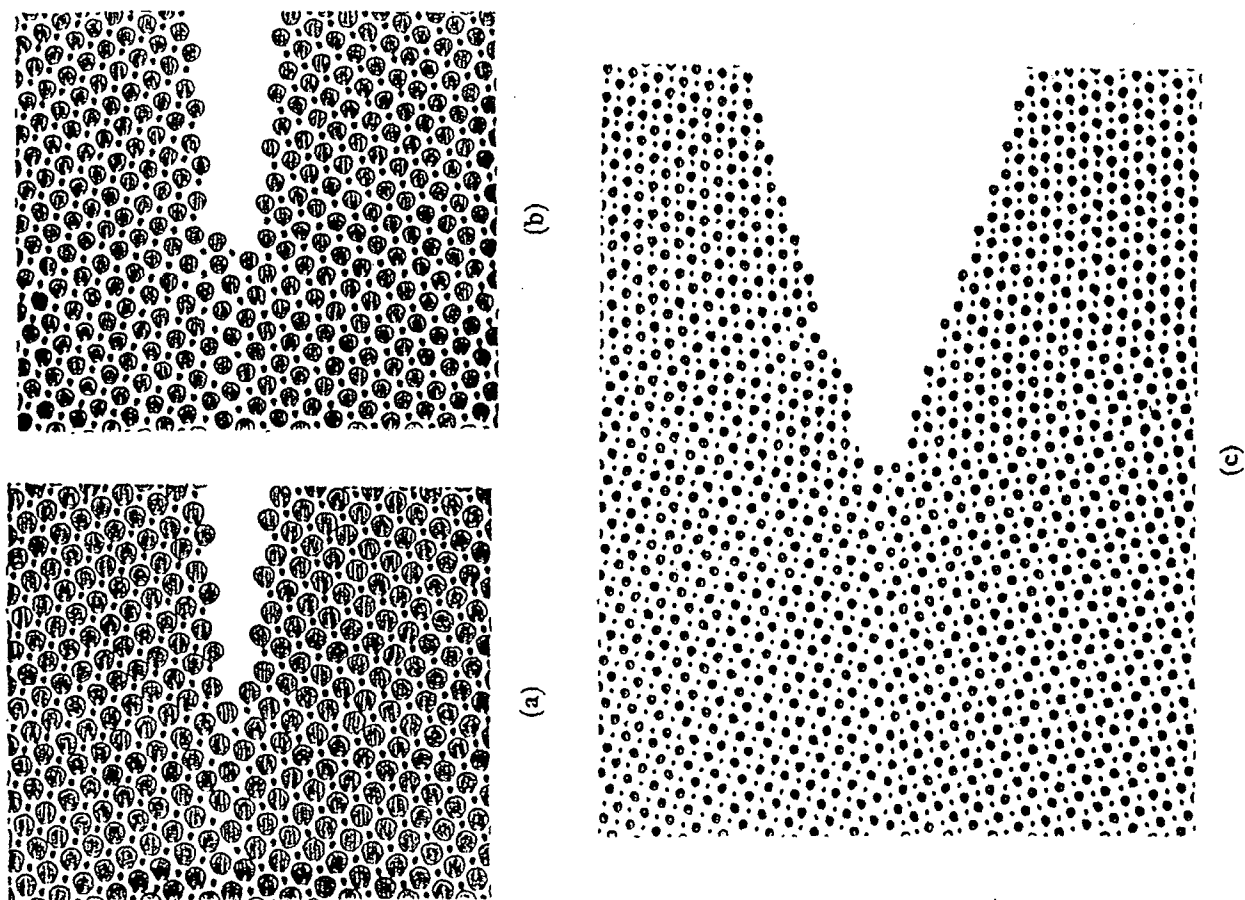
here one would expect intergranular fracture. Indeed we observed crack extension along the grain boundary but this extension is accompanied by blunting of the crack. Blunting of the crack tip enables the crack to be stable at loads up to three times the Griffith load. The results suggest that the grain boundaries in this compound are not intrinsically brittle. This agrees with the conclusions of recent experimental work in This materials as well as other intermetallics indicating that the grain boundary brittleness observed in these materials is related to environmental effects, particularly interstitial impurities such as hydrogen [7, 8].

Conclusions

We have carried out atomistic simulations of fracture of grain boundaries in NiAl. The first important point to be noted is that lattice trapping for the case of a grain boundary is much more important than it is for the bulk. The cases we have investigated show lattice trapping of about 50%, as opposed to around 10% typically observed in the bulk. We have seen evidence of blunting of the cracks running along the high angle grain boundaries investigated. The Ni-rich boundary studied showed more blunting than the Al-rich boundary. The boundaries that are more prone to failure are the Al-rich ones, because of a lower Griffith critical loading and because they present less blunting of the crack tip.

REFERENCES

1. G. C. Sih and H. Liebowitz, Mathematical theories of brittle fracture. in *Fracture - An Advanced Treatise*, edited by H. Liebowitz, volume II, pages 69–189. Academic Press, New York, 1968.

2. V. Shastry and D. Farkas, (1996), to appear.

3. D. Farkas, B. Mutasa, C. Vailhé, and K. Ternes, Modelling and Simulation in Materials Science and Engineering 3, 201 (1994).

4. G. Petton and D. Farkas, Scripta Metallurgica et Materialia 25, 55 (1991).

5. Y. Mishin and D. Farkas, Phil. Mag.. (1996).

6. M. Hagen and M. W. Finnis, Materials Science Forum 207-209, 245 (1996).

7. E. George and C. Liu. Journal of Materials Research 5, 754 (1990).

8. C. Liu, Moisture–induced environmental embrittlement of ordered intermetallic alloy at ambient temperatures. in *Ordered Intermetallics - Physical Metallurgy and Mechanical Behaviour*, edited by C. Liu, R. Cahn, and G. Sauthoff, volume 213 of *NATO ASI Series*, pages 321–334. Kluwer Academic Publishers, 1992.

Crack initiation and propagation in brittle-to-ductile transition regime of NiAl single crystals

F. Ebrahimi *, S. Shrivastava

Materials Science and Engineering Department, University of Florida, Gainesville, FL 32611, USA

Abstract

The mechanisms of crack initiation and propagation in the brittle-to-ductile transition (BDT) regime were evaluated in double-notched tensile specimens of a stoichiometric NiAl single crystal. The crack initiation was found to occur by formation of stable microcracks in the localized slip bands that form in the vicinity of the notch. A study of the crack path revealed that the unstable crack prefers to propagate along the {511} planes. The results of this study suggest that the BDT in NiAl correlates with the onset of net-section yielding. Decreasing the displacement rate resulted in a reduction in BDT temperature to below room temperature. The effect of displacement rate on BDT temperature has been attributed to the higher probability of cross-slip at low strain rates. © 1997 Elsevier Science S.A.

Keywords: NiAl; Single crystal; Fracture toughness; Brittle-to-ductile transition; Crack initiation; Crack propagation

1. Introduction

In comparison with other cleavagable crystals, NiAl has a relatively high brittle-to-ductile transition temperature (BDTT). For example, Mo single crystal has BDTT/Tm = 0.05–0.07 [1], while for similar a displacement rate NiAl has been reported to have BDTT/Tm = 0.25 [2,3]. This difference in BDT behavior cannot be attributed to a difference in yield strength, since NiAl seems to be a softer material than Mo (at BDTT σ_{ys}(Mo) = 160 MPA [1], and σ_{ys}(NiAl) = 60 MPa [3]). One important difference between NiAl and Mo is their number of independent slip systems. The intermetallic NiAl has a B2 crystal structure. Because of its very high ordering energy, the slip vector in this material is $a\langle 100 \rangle$, except when it is deformed along $\langle 100 \rangle$ directions [4]. The preferred slip planes are {001} and {011} planes; however, {013} slip planes have been reported at elevated deformation temperatures [5] and upon micro-indentation at room temperature [6]. The $a\langle 100 \rangle$ slip directions result in only three independent slip systems. A lack of enough slip systems to accommodate the strain incompatibility between the grains results in formation of intergranular microcracks [7] and development of very high internal hydrostatic stress compo-

nents in polycrystalline materials [8]. These high elastic internal stresses provide the driving force for crack propagation and cause the high BDTT observed in polycrystalline NiAl [9].

The BDTT is commonly defined as the temperature at which notch toughness increases rapidly with temperature. This temperature depends on the size and geometry of the specimen, as well as the applied displacement rate [10]. The objectives of this research were to establish the BDT behavior in a NiAl single crystal loaded along a $\langle 110 \rangle$ direction for various displacement rates and to study the processes of crack initiation and propagation in the BDT temperature regime.

2. Materials and experimental procedures

The NiAl single crystal used in this study was grown at the University of Florida by Dr M.J. Kaufman's group. The crystal was homogenized at 1300°C for 3 h in a controlled atmosphere furnace and was cooled to room temperature at a rate of 2.4°C min⁻¹. The orientation of the crystal was determined using the Laue back-scattered X-ray diffraction technique.

Double-notched tensile specimens with the geometry and orientation shown in Fig. 1 were cut using an electric discharge machine (EDM). The specimens were

* Corresponding author.
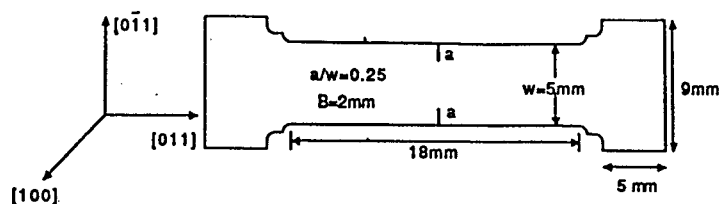
Fig. 1. Schematic showing the geometry and crystallographic orientation of the double-notched tensile specimens used for fracture toughness testing.

electropolished using a solution of 10% perchloric acid and 90% methanol to remove the surface damage produced during cutting. The notches were introduced after electropolishing using a 300 μm thick diamond saw.

Fracture toughness testing was conducted using a closed loop hydraulic mechanical testing system equipped with a controlled atmosphere furnace. The elevated temperature tests were performed under flowing argon. The specimens were slowly heated to the test temperature and soaked for 1 h prior to testing. The thermocouples were located close to the specimens. Tests were conducted in the temperature range of room temperature to 350°C. Three displacement rates viz. 10^{-2}, 2×10^{-4} and 2×10^{-5} mm s^{-1} were used for investigating the effect of strain rate on the BDT behavior. Two specimens were tested at selected conditions.

The apparent fracture toughness, K_{JC}, was calculated using the following equations [11,12]:

$$K_{JC} = (YP_f a^{1/2})/BW + (J_p E)^{1/2}$$

$$Y = 1.99 + 0.76(a/W) - 8.48(a/W)^2 + 27.32(a/W)^3$$

$$J_p = 2A_p/B(W - a)$$

where P_f is the load at the point of unstable fracture, a is the crack length, B is the thickness, W is the width, and A_p is the area under the plastic regime of the load-displacement curve [11]. It is acknowledged that the above equations apply to sharp cracks, however a small variation in the room temperature toughness was found as a function of notch radius [13].

3. Results

3.1. Fracture toughness testing

The results of fracture toughness testing are given in Table 1 and plotted in Fig. 2. At the displacement rate of 10^{-2} mm s^{-1} the toughness remained constant at approximately 5 MPa m$^{1/2}$ up to 100°C (lower shelf regime) and increased drastically to 26 MPa m$^{1/2}$ at 200°C test temperature. Fig. 3 presents the load displacement curves for the 10^{-2} mm s^{-1} displacement rate tests. The increase in toughness at 200°C coincides

with the net section yielding of the specimen as indicated by the non-linear behavior of the curve. The sharp increase in apparent toughness above this temperature correlates with a decrease in the net-section yield load (limit load) and extensive plasticity preceding fracture. A decrease in the displacement rate did not affect the lower shelf toughness value, however, it reduced the BDTT such that, at the 2×10^{-5} mm s^{-1} displacement rate, the BDTT was below room temperature. Fig. 4 presents load-displacement curves at different displacement rates at 100°C test temperature. Similar to the temperature effect, a decrease in the displacement rate reduced the limit load and increased the extent of plasticity that preceded unstable fracture.

3.2. Fractography and slip line analysis

A study of the fracture surfaces revealed that all specimens fractured by cleavage and no microvoid coalescence was observed. In all specimens, the unstable crack was invariably initiated from one of the two notches and near the sides of the specimen as shown in Fig. 5(a) for a specimen tested at room temperature. The analysis of the crack profiles indicated that the intersection of the large initial cleavage facet with the (100) side plane was always at approximately 34° from the [01̄1] direction as shown in Fig. 5(b). The angles between [06̄1] the [05̄1] directions with [1̄10] are 35.5 and 33.7°, respectively. These directions suggest that the cleavage plane is one of the {x16} or {x15} planes. Since {511} planes have been previously reported [14,15] as cleavage facets in NiAl, it may be concluded that in this case also the cleavage plane is the (115) plane. The main cleavage crack was eventually diverted back to the other notch. The distance that the unstable crack propagated before it was diverted decreased with an increase in temperature and a decrease in the displacement rate.

Fig. 6(a) shows the crack initiation site in a specimen tested at 350°C temperature. Note the Poisson's effect and extensive plasticity that has occurred in the plastic zone adjacent to the side of the specimen as a result of plane stress condition. The river marks observed on the fracture surface confirmed that the crack started ahead of the notch and propagated back to the notch tip. Fig.

Table 1
Fracture toughness results

Temperature (°C)	Displacement rate					
	10^{-2} mm s^{-1}		2×10^{-4} mm s^{-1}		2×10^{-5} mm s^{-1}	
	K_{JC} (MPa m$^{1/2}$)	Behavior	K_{JC} (MPa m$^{1/2}$)	Behavior	K_{JC} (MPa m$^{1/2}$)	Behavior
20	5.0	Linear	5.4	Linear	18.3	Non-linear
100	4.6, 5.0	Linear	24.3	Non-Linear	58.2	Non-Linear
200	25.9	Non-linear	24.3	Non-linear	242.3	Non-linear
250			203.0 230.9	Non-linear		
300	142.0 138.1	Non-linear	461.8	Non-linear		
350	191.6, 186.2	Non-linear				

6(b) presents a higher magnification scanning electron microscopy (SEM) fractograph revealing the formation of stable microcracks on the slip bands. The formation of slip bands are better shown in the optical micrograph of the region near the notch tip in a partially loaded specimen given in Fig. 7(a). The slip bands are along the [001] and [010] slip directions. Ideally these slip vectors lie in the side planes, which are parallel to the (100) plane, and they should not be observed. However, slight misorientations are inevitable during specimen preparation and for large strain values the amount of displacement is apparently sufficient for revealing the slip traces. Note that some rotation of the crystal has occurred in the vicinity of the notch. The position of the intense deformation zone near the notch tip (point A) correlates with the distance at which crack initiation was observed on the fracture surface. Small microcracks along the slip bands were also found at the notch tip as shown in the micrograph given in Fig. 7(b).

At low toughness levels (low temperatures and high displacement rates) the crack initiation occurred from the notch tip as shown in Fig. 8(a) for a specimen tested at 200°C at 10^{-2} mm s^{-1} displacement rate. A study of the sides of this specimen revealed formation of stable microcracks at the notch tip as shown in Fig. 8(b).

Note the presence of a stable sharp microcrack that has initially started from a slip band.

The observation of the duplex slip traces on the (100) side plane of the fracture specimens suggest the operation of the ⟨100⟩ slip vectors, but it does not provide information regarding the slip planes. Fig. 9 presents the slip trace analysis performed on a smooth tensile specimen loaded to 25% plastic strain at 200°C. Similar to the area near the notch of the fracture specimens, slip traces along [100] and [010] directions were found in this specimen as shown in Fig. 9(a). It must be noted that (010), and all {hk0} planes intersect with the (100) plane along the [001] direction and similarly (001), and all {h0l} planes intersect with the (100) plane along the [010] direction. The slip planes can be determined unambiguously by studying the slip traces on the (0Ī1) face, which is perpendicular to the (100) plane. As shown in Fig. 9(b) the slip traces are wavy in nature which indicates that extensive cross slip of screw dislocations has occurred (pencil glide). Owing to the waviness of the slip traces, it is not possible to determine all

Fig. 2. Fracture toughness as a function of test temperature for the three applied displacement rates used in this study.
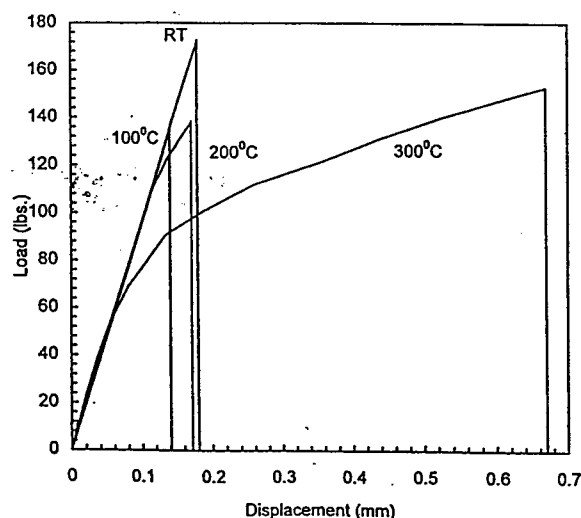
Fig. 3. Load-displacement curves at various test temperatures for an applied displacement rate of 10^{-2} mm s^{-1}.
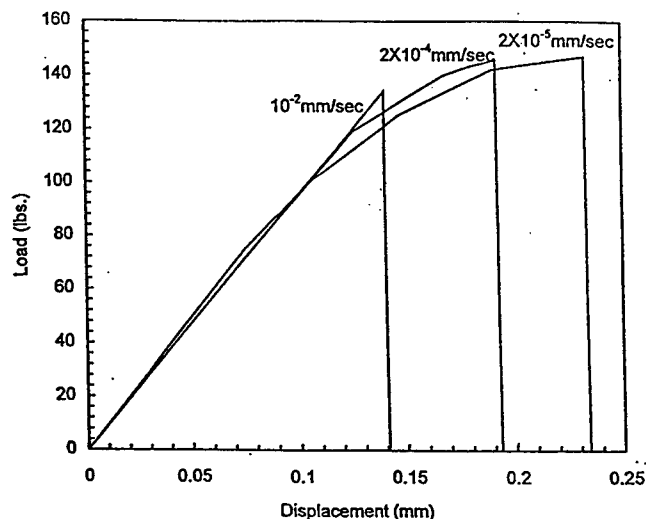
Fig. 4. Load-displacement curves at various displacement rates at 100°C test temperature.

of the activated slip planes. However, the analysis of the straight segments suggest that many {h0l} and {0kl} planes have been operative. The most interesting slip traces, are [511] and [5$\bar{1}\bar{1}$] directions (see Fig. 9(b)), which indicate that slip has occurred on ($\bar{1}$05) and (150) planes. The fact that these traces start straight from the corner of the sample suggests that slip started on these planes and then the screw dislocations cross slipped to the other possible slip planes.

4. Discussion

The combination of microcrack and stress distributions in the plastic zone governs the point of crack instability in a notched specimen. The results of this investigation indicate that crack initiation in the NiAl single crystal specimens studied occurs along the slip bands. The microcracks develop at the intersection of the slip bands with the notch tip at low strain levels, and as the plastic zone extends, they form at the intersection of slip bands ahead of the notch. At low test temperatures the distribution of the microcracks developed at the crack tip is sufficient for the onset of crack instability. However, at elevated temperatures microcracking ahead of the notch leads to unstable fracture. The crack initiation site was always found to be near the sides of the specimen, where the stress state is close to a plane stress condition. Strain localization occurs easier under plane stress condition, and therefore, can lead to microcracking. Apparently the higher probability of forming stable microcracks near the sides overrides the higher stress levels that develop in the midsection of the specimen, where the stress state is in plane strain condition.

The main cleavage facet by which the initial crack propagation occurred in the double-notched NiAl specimens was concluded to be a {511} plane. Fracture path depends on the complex interaction of properties such as interplanar spacing, elastic constants, surface energy, and applied stress distribution as a function of orientation [16]. Assuming that the theoretical fracture stress can be estimated as $(E\gamma/a)^{1/2}$, where E is the elastic constant perpendicular to the cleavage plane, γ is the surface energy, and a is the lattice parameter, it is anticipated for cleavage to occur on a plane that maximizes a and minimizes E and γ. In bcc crystals, depending on the relative values of E and γ, {100} and {110}
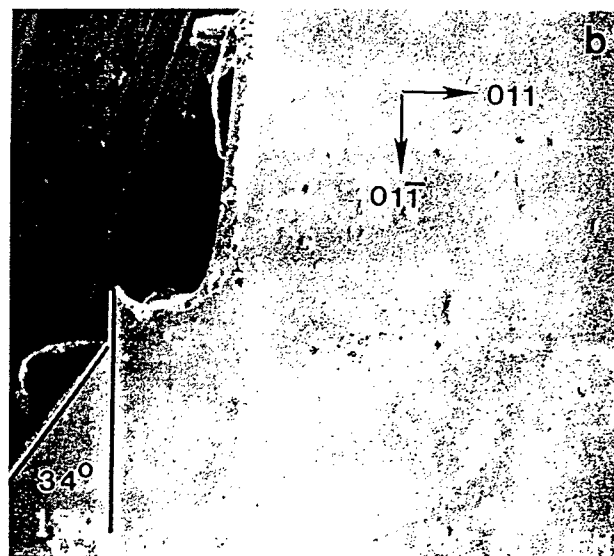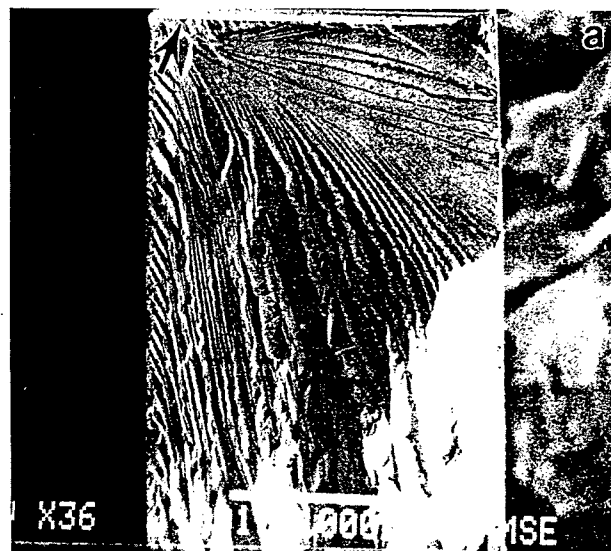
Fig. 5. (a) SEM fractograph showing the off-center crack initiation site in a specimen tested at room temperature at a displacement rate of 10^{-2} mm s^{-1}. The crack initiation site is marked by an arrow. (b) The crack profile of the specimen given in (a) showing that the crack profile makes a 34° angle with the [01$\bar{1}$] direction.
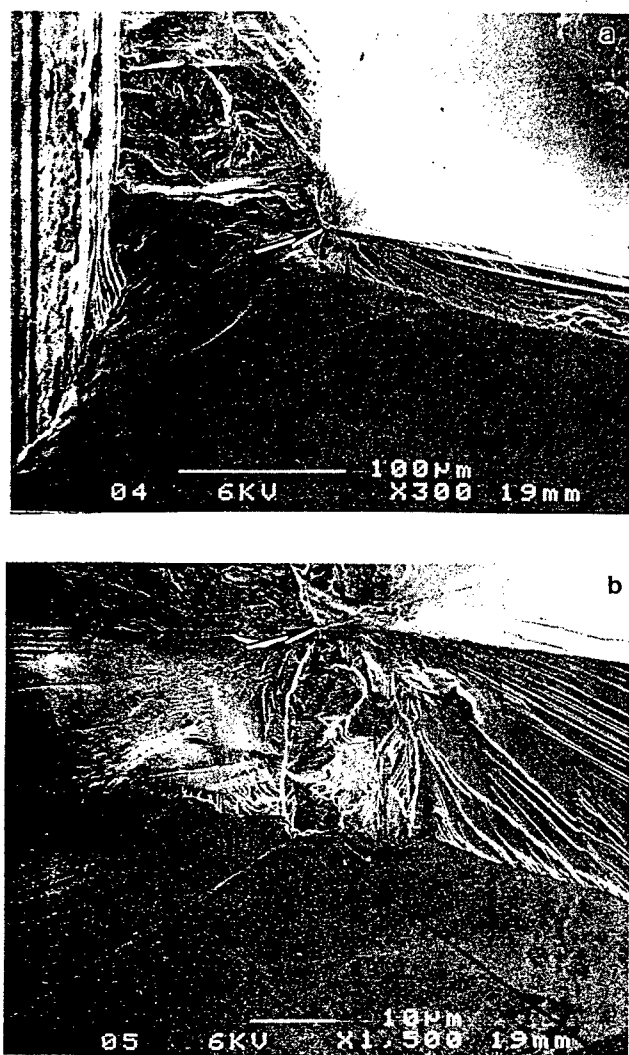
Fig. 6. SEM fractograph showing (a) the crack initiation site near the edge, and (b) the existence of the stable microcracks along slip bands. in a specimen tested at 350°C at 10^{-2} mm s^{-1} displacement rate.

thermore, the lower the strain hardening of the material, the lower the rate of increase in local stresses; hence, the extent of plastic deformation prior to crack instability will be increased. The results of this study indicate that increasing the test temperature and decreasing the displacement rate result in a reduction in the limit load. The question is which thermally activated processes result in a reduction in net-section yielding. While the yield strength of the NiAl single crystal is reduced significantly with test temperature (the tensile yield strength drops from 110 Mpa at 20°C to 69 Mpa at 200°C at the applied strain rate of 5×10^{-3} s^{-1} [13]), its value is insensitive to the applied strain rate within the BDT range [13]. Therefore, reduction in yield strength cannot explain the decrease in the limit load observed with the applied displacement rate. The net-section yielding load is governed by the strain hardening rate of a material as well as its yield strength
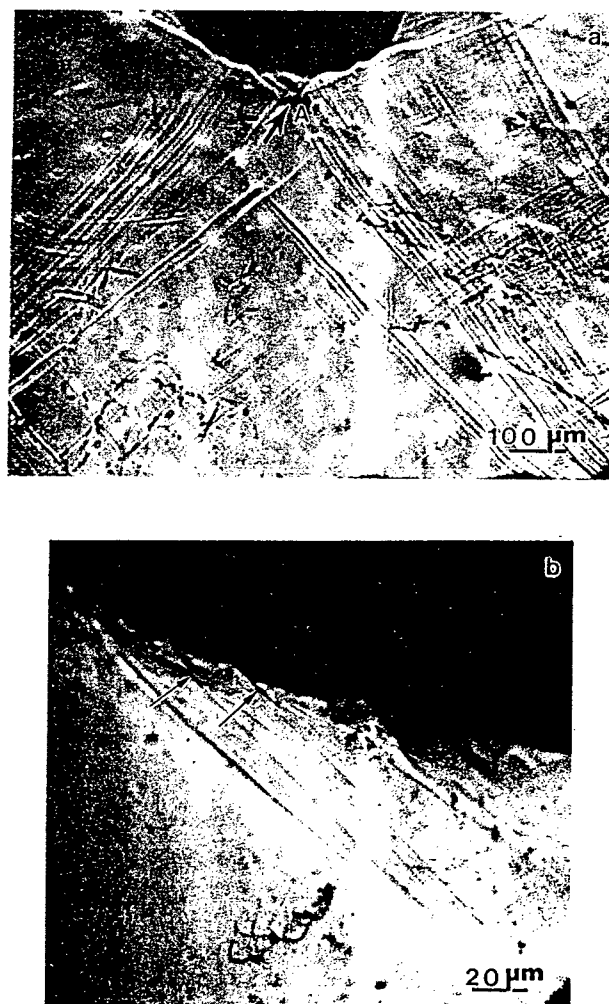
Fig. 7. (a) Optical micrographs showing (a) the slip traces near the notch, and (b) formation of microcracks along the slip bands of a specimen partially loaded at 350°C at 10^{-2} mm s^{-1} displacement rate.

planes are the candidate cleavage planes and indeed these planes have been observed on the fracture surface of single-edge notched-bend specimens of NiAl [14,15,17]. Therefore, it is suggested that the occurrence of {511} cleavage planes may be associated with the distribution of local stresses owing to the slip pattern and the relative orientation of the directional Ni–Al bonds to these stresses.

The BDT in NiAl single crystals, similar to the polycrystalline NiAl [9], is associated with the onset of net-section yielding in the specimens. At the point of net-section yielding the slip bands traverse the whole ligament between the two notches of a double-notched tensile specimen. This connectivity of the plastic region results in a loss of plastic constraint and stresses can be increased further only through strain hardening [18]. This leads to an increase in the extent of plastic deformation needed for the onset of crack instability. Fur-

Fig. 8. (a) SEM fractograph showing the crack instability starting from the notch in a specimen tested at 200°C. (b) SEM micrograph showing the slip traces and the formation of a stable microcrack from the notch. The initial segment of the crack. which is along a slip line, is marked by an arrow.

[19]. Tensile testing of the NiAl single crystal oriented along ⟨110⟩ direction has revealed that in contrast to yield strength, strain hardening rate is dependent on the applied strain rate (strain hardening exponent decreases from 0.52 to 0.28 with an increase in strain rate from 5×10^{-3} to 5×10^{-6} s^{-1} at 20°C [13]). The slip line analysis presented in this study suggests that cross-slip is a viable mechanism that controls the strain hardening of the ⟨110⟩ oriented NiAl single crystal. The analysis of fracture toughness results has revealed an activation energy of about 50 kJ mol^{-1} for BDT [13]. Further work is needed to evaluate whether this value is close to the activation energy for cross slip in NiAl. It should be noted that although cross slip reduces the local build-up of dislocations, it does not increase the number of

independent slip systems. Hence, even at elevated temperatures and low strain rates, hydrostatic internal stresses that develop because of strain incompatability lead to cleavage fracture.

5. Conclusions

The fracture behavior of NiAl double-notched tensile specimens with loading and notch directions parallel to ⟨110⟩ and ⟨001⟩ crystallographic directions, respectively, were characterized in the BDT regime using fracture toughness testing, fractography, and slip trace analysis. Based on the results of this investigation the following conclusions may be drawn:
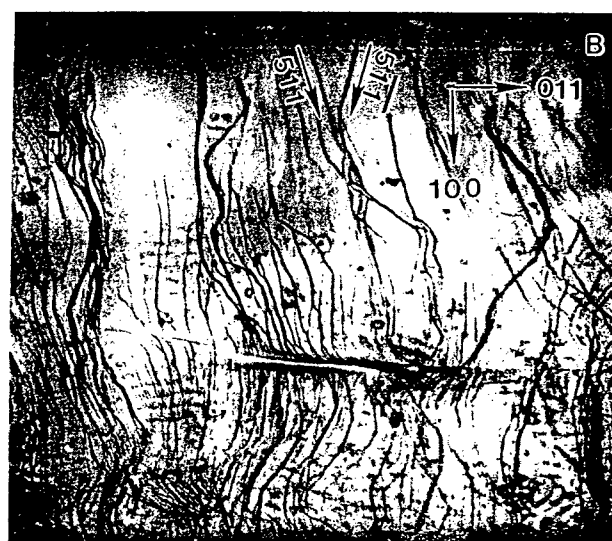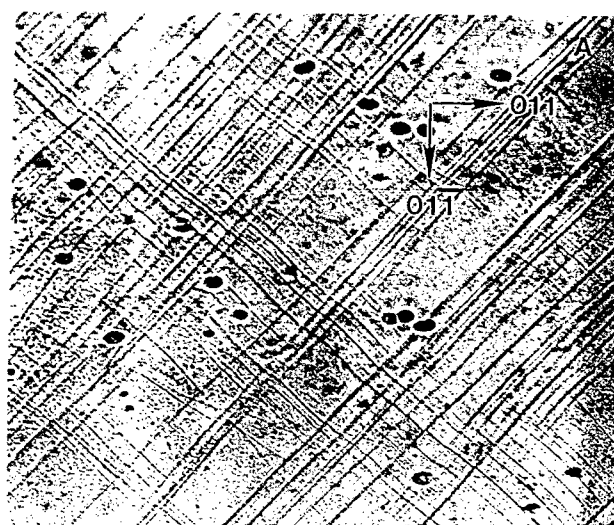
Fig. 9. Optical micrographs showing slip traces on a tensile specimen partially loaded at 200°C. (a) (100) face. (b) (0ī1) face.

(i) Microcracks formed on localized slip bands at the notch tip and at the intersection of slip bands ahead of the notch.

(ii) The plane stress condition near the sides of the fracture specimens promoted slip localization, and hence, more microcracking occurred in these regions. As a result, the unstable crack always started near the side of the specimens.

(iii) The first main cleavage facet formed on a {511} plane.

(iv) Slip trace anaysis revealed that in addition to {001} planes, $a\langle 100\rangle$ dislocations slip on many {0kl} planes, including the {051} planes.

(v) The BDTT decreased with the applied displacement rate, however, the lower shelf toughness was not affected.

(vi) The BDT was found to be associated with the net-section yielding of the notched specimens and was correlated with the occurrence of cross slip of $a\langle 100\rangle$ dislocations to {0kl} planes.

Acknowledgements

References

[1] H. Haung, W.W. Gerbrich, Acta Metall. Mater. 42 (1994) 639.

[2] G. Bergmann, H. Vehoff, Scr. Metall. Mater. 30 (1994) 969.

[3] S. Shrivastava, F. Ebrahimi, MRS Proc., vol. 460, Mater. Res. Soc., Pittsburgh, PA, 1997, p. 393.

[4] R.D. Noebe, R.R. Bowman, M. Nathal, Inter. Mater. Rev. 38 (1993) 193.

[5] W.R. Kanne Jr., P.R. Strutt, R.A. Dodd, Trans. Metall. Soc. AIME 245 (1969) 1259.

[6] F. Ebrahimi, A. Gomez, G.T. Hicks, Scr. Mater. 34 (1996) 337.

[7] F. Ebrahimi, J.R. Catillo-Gomez, Acta Metall. Mater. 40 (1992) 1409.

[8] B.K. Kad, M. Dao, R.J. Asaro, Philos. Mag. 71 (1995) 367.

[9] F. Ebrahimi, T.G. Hoyle, Acta Mater. 45 (1997) 4193.

[10] F. Ebrahimi, in: D.T. Read, R.P. Read (Eds.), Fracture Mechanics Engineering Symp., ASTM STP 945, American Society for Testing Materials, Philadelphia, 1988, p. 555.

[11] ASTM Standard E813-87, Standard Test Method for J_{IC}, A Measure of Facture Toughness, Annual Book of ASTM, Vol. 03.01, 1989, p. 738.

[12] D. Broek, Elementary Engineering Fracture Mechanics, 3rd edn., Martinus Nijhoff, Boston, 1982, p. 76.

[13] S. Shrivastava, Brittle-to-ductile transition in NiAl single crystals, Ph.D. Dissertation, Materials Science and Engineering Department, University of Florida, 1997.

[14] K.M. Chang, R. Darolia, H.A. Lipsitt, Acta Matter. Mater. 40 (1992) 2727.

[15] J.H. Schneibel, R. Darolia, D.F. Lahrman, S. Schmoauder, Met. Trans. A 24 (1993) 1363.

[16] F. Ebrahimi, Scr. Metall. Mater. 32 (1995) 1507.

[17] S. Shrivastava, F. Ebrahimi, Proc. Mater. Res. Soc. 36 (1995) 431.

[18] F.A. McClintock, in: H. Liebowitz (Ed.), Fracture, An Advanced Teatise, Vol III, Academic Press, New York, 1972, p. 48.

[19] C.E. Turner, in: D.G.H. Latzko (Ed.), Post-Yield Fracture Mechanics, Applied Science, London, 1979, p. 23.

Table 1. Summary of tensile testing results for the NiAl alloys

Temperature (C°)	Proportional limit (MPa)	0.2% Yield strength (MPa)	True tensile strength (MPa)	Average strain hardening rate (MPa)†	Engineering fracture strain (%)‡
As-extruded Ni–Al					
RT	Yield point Phenomenon	172	327	5536	2.8
Heat treated NiAl					
RT	120	141	227	9727	1.1
RT	99	130	195	12,000	0.8
200	72	85	192	6000	2.0
300	50	61	191	2275	6.2
300	52	69	194	2491	5.7
400	32	41	164	528	61.0
As-extruded NiAl + Ti					
RT	340	452	458	53,636	0.22
Heat treated NiAl + Ti					
RT	—	—	265	—	—
RT	—	—	305	—	—
200	—	—	242	—	—
300	192	231	243	18,214	0.28
400	190	—	234	33,846	0.13
400	204	—	222	18,000	0.10
500	180	220	230	17,241	0.29
600	150	190	210	8333	0.72

†These values were calculated as: $\dfrac{\text{true tensile strength} - \text{proportional limit}}{\text{true maximum uniform strain}}$

‡In order to eliminate the contribution from the compliance of the testing system, the strain values are calculated based on the plastic deformation. These values also represent the maximum uniform strain, except for the NiAl specimen tested at 400°C.

NiAl + Ti alloys the fracture stress did not depend on temperature, except that it seemed to be slightly higher in specimens that showed no apparent plasticity. At all temperatures the NiAl + Ti alloy showed a higher fracture stress than the NiAl alloy did.

3.2. Fracture toughness testing

Tables 2 and 3 summarize the fracture toughness results for NiAl and NiAl + Ti alloys, respectively. The heat treatment improved the toughness of NiAl + Ti alloy significantly; however, the toughness of the stoichiometric NiAl was decreased slightly.

The fracture toughness values as a function of test temperature are plotted in Figs 3 and 4. Within the temperature range investigated both alloys showed the BDT as defined by a sharp increase in the

toughness. At a given displacement rate and an equivalent thickness, the low temperature toughness values were higher for the NiAl + Ti alloy and they decreased with specimen thickness as demonstrated in Fig. 3. The effect of an order of magnitude decrease in displacement rate on the low temperature toughness of NiAl was insignificant; however, it modified the shape of the toughness vs temperature curve and shifted the BDT temperature to a lower temperature. The NiAl alloy showed a lower BDT temperature than the NiAl + Ti alloy did.

As shown in Fig. 5 the load–displacement curve obtained during fracture toughness testing of NiAl changed from linear to nonlinear behavior as the test temperature was raised. For specimens tested at and above 500°C at 10^{-3} mm/s and those tested at and above 400°C at 10^{-4} mm/s the load–displacement
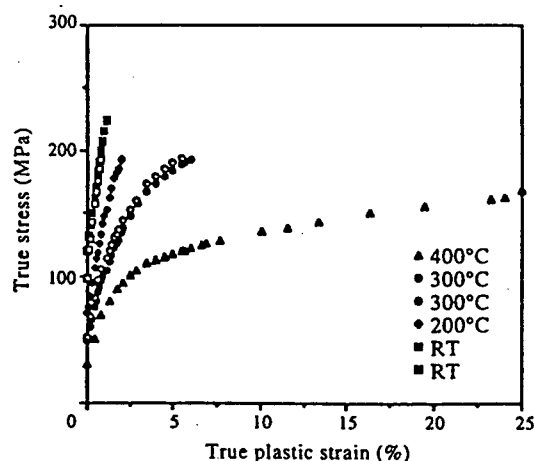
Fig. 1. Tensile stress–strain curves of the heat treated NiAl alloy tested at various temperatures.
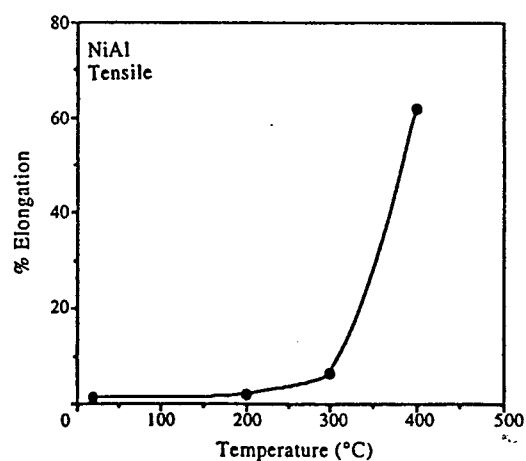
Fig. 2. Tensile ductility of NiAl as a function of test temperature.

Table 2. Summary of fracture toughness testing results for NiAl alloy; the thickness of the specimens was 3.5 mm

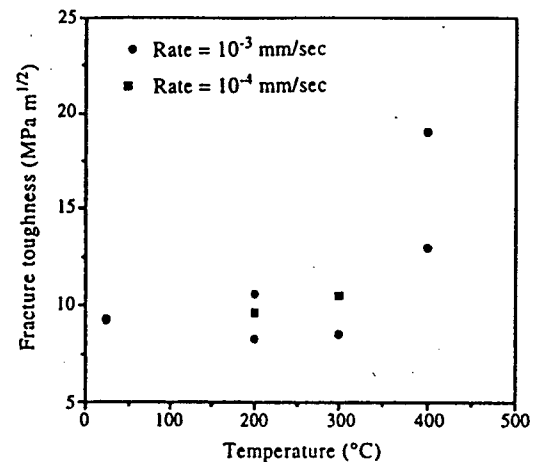| Displacement rate (mm/s)	Temperature (°C)	K_c (MPa m$^{1/2}$)	Behavior
As-extruded			
10^{-3}	RT	11.6	Linear, unstable
Heat treated			
10^{-3}	RT	9.2	Linear, unstable
		9.3	Linear, unstable
	200	8.3	Linear, unstable
		10.6	Nonlinear, unstable
	300	8.5	Nonlinear, unstable
	400	13.0	Nonlinear, unstable
		19.0	Nonlinear, unstable
	500 & 600	—	Nonlinear, stable
10^{-4}	200	9.6	Linear, unstable
	300	10.5	Linear, unstable
	400	—	Nonlinear, stable

Fig. 3. Fracture toughness, K_c, of the heat treated NiAl alloy as a function of test temperature. Note that the specimen tested at the lower displacement rate did not show crack instability at 400°C.

curves showed local instabilities, which were observed as small load drops; however, the specimens as a whole remained stable.

3.3. Fractography

3.3.1. Tensile specimens. The fracture surface of NiAl specimens that showed no necking was predominantly intergranular as shown in Fig. 6. The as-extruded NiAl specimen which had a much smaller grain size showed a slightly higher percent of transgranular fracture than the heat treated specimen did. The specimen tested at 400°C showed extensive necking as shown in Fig. 7(a), where significant elongation of the grains in the neck region can be observed. This specimen fractured by a microvoid coalescence mechanism as shown in Fig. 7(b). The microvoids were very deep and associated with extensive plasticity. Figure 8 presents micrographs showing the slip lines on the surface of the NiAl tensile specimen deformed at 400°C. The slip traces were predominantly straight; however, some grains showed wavy slip lines. The slip lines seemed to lie along two preferential directions.

The as-extruded NiAl + Ti alloy fractured in a predominantly transgranular mode The fracture surface of heat treated NiAl + Ti specimens tested at lower temperatures showed some intergranular fracture (11% at RT to 14% at 400°C); however, it increased to 27.5% at 600°C as demonstrated in fractographs presented in Fig. 9.

3.3.2. Fracture toughness specimens. The fracture surfaces of the fracture toughness specimens were similar to those of tensile specimens; however, in general, the bend specimens showed more transgranular fracture than did the tensile specimens. Similar to tensile specimens, as shown in Fig. 10, the as-extruded specimens showed less intergranular fracture than did the heat treated specimens. One important difference between the as-extruded and heat treated specimens was the presence of large cavities in the vicinity of the notches as shown in Fig. 11. These cavities were not observed away from the notch tip region.

Table 3. Summary of fracture toughness testing results for NiAl + Ti alloy; the displacement rate for fracture toughness testing was 10^{-3} mm/s

Specimen thickness (mm)	Temperature (°C)	K_D (MPa m$^{1/2}$)	Behavior
As-extruded			
3.5	RT	6.0	Linear, unstable
Heat treated			
3.5	RT	15.0	Linear, unstable
	200	15.6	Linear, unstable
	300	11.6	Linear, unstable
		16.2	Linear, unstable
	400	18.4	Linear, unstable
	600	24.4	Nonlinear, unstable
7.0	RT	10.9	Linear, pop-in
	200	11.5	Linear, unstable
	300	12.4	Linear, unstable
	400	14.0	Linear, unstable
	600	27.5	Nonlinear, unstable
		28.7	Nonlinear, unstable

Fig. 4. Fracture toughness, K_c, of the heat treated NiAl + Ti alloy as a function of test temperature.
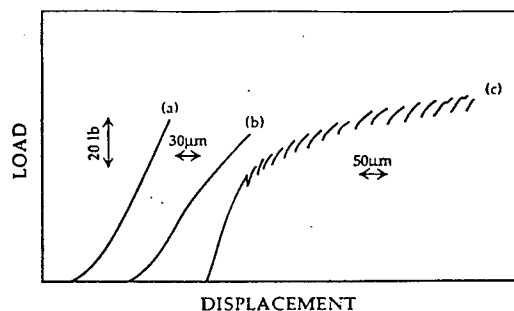
Fig. 5. Traces of load–displacement curves obtained during fracture toughness testing of the heat treated NiAl at (a) room temperature. (b) 300°C, and (c) 500°C.
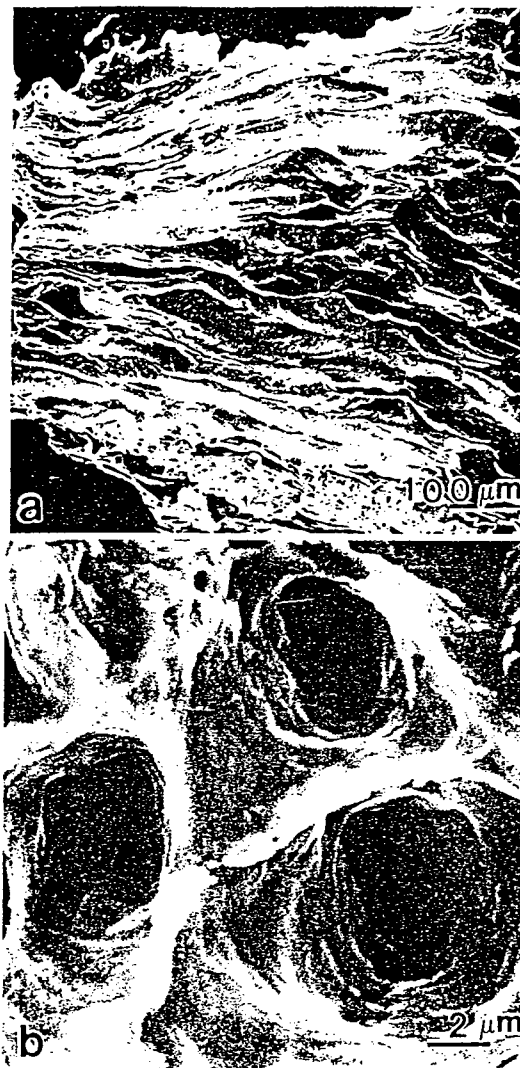

Fig. 7. SEM fractographs of the heat treated NiAl alloy tested in tension at 400°C showing (a) extensive elongation of grains in the neck region. and (b) microvoid coalescence mechanism.

The NiAl + Ti alloy showed predominantly transgranular fracture except at the tearing ridges, where the fracture morphology was predominantly intergranular as shown in Fig. 12. Tearing ridges develop when the ligament between two unstable cracks formed on different levels is torn in model III (plane stress). No noticeable difference in the amount of intergranular fracture between areas near and away from the notch was detected.

In order to investigate the mechanism responsible for the load–displacement behavior observed for NiAl specimens tested at high temperatures. an NiAl fracture specimen was partially loaded at 500°C, sectioned in mid-thickness, and then the area near the notch was investigated. Figure 13 shows the existence of small and large stable microcracks in the vicinity of the notch. The microcracks were intergranular in nature and the small microcracks were found to form predominantly at triple points.

Fig. 6. SEM fractograph showing the predominantly intergranular fracture in the heat treated NiAl alloy tested in tension at room temperature.

4. DISCUSSION

The results of this study indicate that the propensity for intergranular cracking in NiAl alloys depends on the yield strength and the stress state. The amount of intergranular fracture decreased with an increase in the yield strength of the alloy as achieved by addition of titanium or lowering the test temperature. In the absence of a triaxial stress state and hence plastic constraint. such as the stress state in the tearing ridges, a higher percent of intergranular fracture was observed. Based on these observations it is concluded that the occurrence of intergranular fracture in NiAl alloys is associated with plastic deformation and it is not related to a low cohesive energy of grain boundaries. It should be noted that in contrast to the observations made in this study, the classical grain boundary embrittlement. which occurs due to a low cohesive energy of the grain boundaries,

is enhanced by a high strength level and a triaxial stress state [19].

Plasticity in ordered structures, such as some intermetallics and ceramics, has been shown to result in intergranular fracture [20, 21]. The slip–grain boundary interaction results in intergranular microcracking when the boundary is stressed in tension owing to a geometrical incompatibility, which is achieved by impingement of two slip bands on both sides of a boundary or a slip band on a grain boundary triple point [21]. While the crack initiation occurs intergranularly the question arises as to why the crack continues to propagate intergranularly. In an intrinsically brittle material the proportion of intergranular fracture depends on the symmetry of the crystal (e.g. the possible number of cleavage planes and the anisotropy of elastic constants) as well as the ratio of the grain boundary energy to surface energy of the cleavage planes [22]. In the case

Fig. 9. SEM fractographs showing the increase in the amount of intergranular fracture with test temperature in NiAl – Ti tensile specimens (a) 300°C. (b) 600°C.
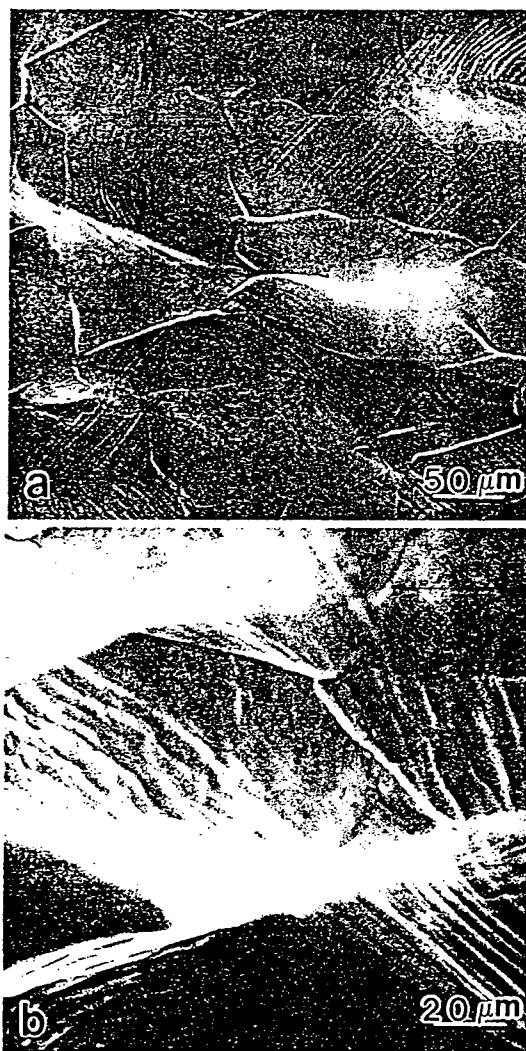
Fig. 8. (a) SEM micrograph showing the deformation in the uniformly deformed region of the specimen shown in Fig. 7. (b) High SEM micrograph showing straight and wavy slip lines.

of ductile materials, in addition, the probability of intergranular fracture depends on the nature of plastic deformation. Recent finite element analysis of a polycrystalline microstructure which has three allowed slip systems has revealed that levels of deformation and stress can be orders of magnitude higher close to grain boundaries, and the degree of deformation inhomogeneity increases with an increase in the applied plastic strain [23]. Therefore, it is suggested that the very high elastic internal stresses that develop near the grain boundaries because of strain incompatibility provide a preferential intergranular crack path in materials with limited slip systems. Increases in tensile yield strength and triaxiality of the stress state elevate the stress levels in the plastic zone of fracture specimens, and hence cause crack instability to be achieved at lower levels of applied strain. In these cases, because of insufficient stress localization near the grain bound-

aries at the point of crack instability, the probability that the crack may follow the intergranular path is decreased.

No direct correlation between grain size and the relative amount of intergranular fracture existed in these alloys. For example the NiAl + Ti alloy in the heat treated condition has a larger grain size than does the as-extruded NiAl; however, the latter showed more intergranular fracture. In contrast, the as-extruded NiAl specimen with a finer grain size than the heat treated specimen showed a lower percent of intergranular fracture. Grain size is expected to affect the crack instability and fracture morphology in many ways. An increase in grain size increases the probability of finding large microcracks and hence fracture strain will be reduced, which results in less propensity for intergranular crack propagation. On the other hand, the strain gradient is smaller in large grains, which results in less probability of crack initiation and lower strain hardening rates. Consequently, crack instability will occur at larger deformations, and hence the probability of intergranular fracture is increased.

Fig. 10. SEM fractographs of (a) as-extruded and (b) heat treated NiAl specimens.

These opposite effects may explain why the percent of intergranular fracture is maximum at an intermediate grain size range as presented in the Introduction.

As a single-phase material, polycrystalline NiAl shows a gradual transition from elastic to plastic behavior and extremely high strain hardening rates. For example silver, a low stacking fault energy metal, at $T/T_m = 0.06$ has an average strain hardening rate of 1000 MPa ($\sim E/70$) [24] and NiAl at $T/T_m = 0.16$ has an average strain hardening rate of 10,000 MPa ($\sim E/20$); the latter value is more typical of composite materials. The high strain hardening rate of polycrystalline NiAl can also be attributed to the strain incompatibility between the grains owing to a lack of enough slip systems. The incompatibility results in generation/accumulation of dislocations near the boundaries, as well as the build-up of elastic internal stresses. The latter stresses, similar to two-phase materials, arise because initially only some grains deform plastically and this behavior leads to development of long range image stresses [25] and initially large slopes of stress–strain curves [26].

The results of this study show that the strain hardening rate decreases with temperature and the change becomes drastic above 300°C. The slip lines observed on the surface of the tensile specimen tested at 400°C indicate that some cross-slip has occurred, but the slip has remained predominantly planar. The cross-slip of $a\langle 100 \rangle$ Burgers vectors to $\{0kl\}$ planes has been observed in NiAl at elevated temperatures [6, 7] and under a triaxial stress state at room temperature [8]. While the activation of $\{0kl\}$ planes enhances the recovery of dislocation substructure, it does not increase the number of independent slip systems in NiAl and hence the climb of dislocations is necessary to accommodate the strain compatibility between grains [11]. Considering that the activation energy for interdiffusion in stoichiometric NiAl is about 200 kJ/mol [27] the question has been raised as to whether 300°C ($T/T_m = 0.3$) is a high enough temperature to allow extensive diffusion to occur in NiAl. It has been suggested [12] that short circuit diffusion processes, such as grain boundary diffusion, are responsible for climb of dislocations near grain boundaries.

The observation of large cavities near the notch of fracture specimens upon heat treatment at 1000°C is very interesting. Since these cavities were not observed in the as-extruded specimens and were found only near the notch of the heat treated specimens it is concluded that they form as a result of the cutting process and subsequent heat treatment. It has been shown that vacancy clusters and very fine voids form in NiAl upon annealing in the temperature range of $0.3–0.5T_m$ [28, 29]. When a notch is cut using a diamond blade plasticity occurs around the notch, and similar to an indentation process it leaves residual stresses after unloading. One method by which excess concentration of vacancies can be generated is the plastic deformation caused by
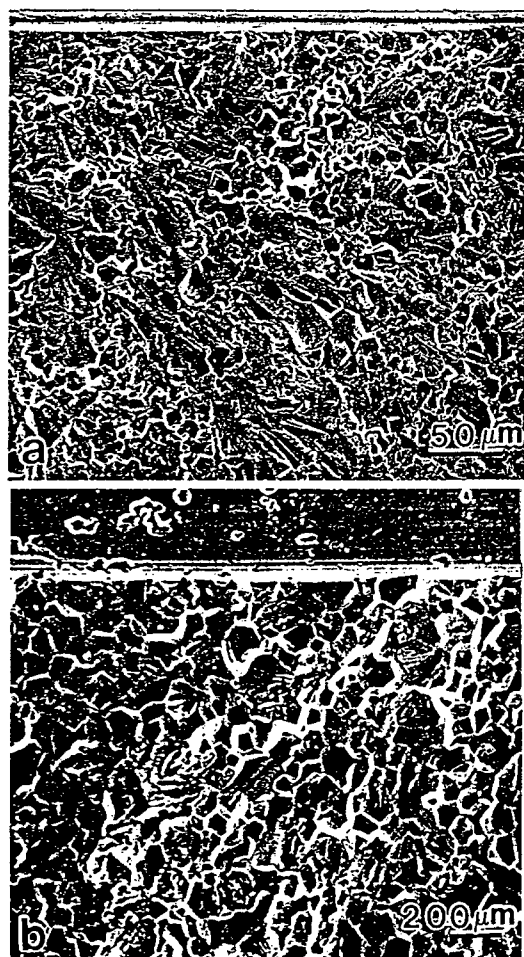
Fig. 11. SEM fractographs showing the presence of cavities near the notch in heat treated fracture specimens of a) NiAl and (b) NiAl + Ti alloy.

the cutting process. Upon annealing, similar to diffusional creep, the residual stress gradient near the notch is expected to establish a flux of vacancies. The very large size of the voids implies that the vacancy concentration gradient in the notch region must have been large. It should be noted that the diffusion distance, (diffusion coefficient × time)$^{1/2}$, at 1000 C for one hour is considerable, and is approximately 0.1 μm using the pre-exponential term, D, for Ni diffusion in stoichiometric NiAl (4.461 × 10^{-4} m^2 s [27]). Assuming that the vacancy concentration in

NiAl is very sensitive to the stress state, it may be speculated that at a microscopic level the extreme inhomogeneities in the hydrostatic stress distribution, which result from the strain incompatibility between grains [23], may also establish a vacancy concentration gradient. The enhanced vacancy flow owing to the vacancy concentration gradient would increase the velocity of climb of dislocations in NiAl.

Fracture in the tensile specimen of stoichiometric NiAl tested at 400 C occurred by microvoid coalescence. Considering that there are no second-

Fig. 12. SEM micrograph showing the preferential intergranular fracture path in a tearing ridge on the fracture surface of the as-extruded NiAl + Ti alloy.

phase particles in the NiAl alloy studied, the origin of the microvoid coalescence mechanism observed on the fracture surface of a single-phase polycrystalline material can be attributed to (i) microcracks formed at grain boundary triple points, (ii) microcracks formed at slip band intersection points, (iii) decohesion of dislocation cell boundaries, and (iv) formation of voids by vacancy coalescence or growth of existing vacancy clusters. As can be seen in Fig. 7 the spacing between microvoids is too small for them

to be nucleated at grain boundaries considering that the average grain size of this material is 83 μm. No microcracks were found at the intersection of the slip bands, and hence this mechanism could not be operative. The voids that form by dislocation cell boundary decohesion are usually ultrafine and relatively shallow. Owing to the size of the voids and their depth, this mechanism is probably not responsible for void nucleation in this material. It is, therefore, concluded that microvoids observed on the fracture surface of NiAl specimen were formed by coalescence of vacancies. The further growth of these voids by plasticity resulted in the microvoid coalescence fracture. It is acknowledged that the diffusivity in NiAl at 400°C is very limited. However, the size of voids needed for initiation of microvoids can be very small and does not require a long diffusion distance. Furthermore, after the specimens were heat treated at 1000°C, they were cooled under flowing argon gas, which is a relatively fast cooling rate, and hence some vacancies are expected to be trapped in the crystal. It should be noted that the stoichiometric NiAl has been reported to have 0.5–1% thermal vacancies after quenching from moderate temperatures [30]. Vacancy condensation has recently been suggested as a possible mechanism for ductile fracture in f.c.c. single crystals at elevated temperatures [31].

The addition of 1 at.% Ti, which is within the solubility of Ti in NiAl [32], increased the yield strength of NiAl considerably (see Table 1). The higher yield strength of NiAl + Ti alloy can be

Fig. 13. SEM micrograph showing microcracking near the notch of a heat treated NiAl specimen partially loaded at 500°C. The arrows mark the presence of very fine microcracks formed at grain boundary triple points.

Table 4. Comparison of theoretical general yield point with the load at the limit of linear elastic behavior, P_{limit}, and the fracture load, P_F, which were obtained from the load–displacement curves

Test temperature (°C)	P_{Gy}/L (lb)	P_{limit} (lb)	P_F (lb)
NiAl			
200	41.0	52.0 (L = 1.3)	60.0
300	29.4	42.0 (L = 1.4)	68.4
400	19.8	28 (L = 1.4)	93.2
NiAl + Ti			
600†	61	120 (L = 2)	176
		280 (L = 1.4)	392
600‡	193	276 (L = 1.4)	408

†Specimen thickness = 3.5 mm.
‡Specimen thickness = 7.00 mm.

$$P_{Gy}/L = \frac{\sigma_y B(W - a)^2}{S_1 - S_2}$$

where σ_y = yield strength, B = thickness, W = width, a = crack length, S_1 and S_2 = spans, L = constraint factor, P_{Gy} = load at general yielding.

attributed to point defect hardening, which includes the conventional solid solution hardening mechanism. The strength of NiAl is known to be very sensitive to deviations from stoichiometry and the defect structure [27]. The persistence of high work hardening rates at high temperatures in NiAl + Ti alloy suggests that the modification of the point defect structure, which may affect both the number and mobility of vacancies, must have made the climb of dislocations more difficult in this alloy. Consistently the tensile ductility of the NiAl + Ti alloy remained negligible up to 600°C test temperature.

In agreement with previously reported studies, the BDT of polycrystalline stoichiometric NiAl occurred in the 300–400°C temperature range. The BDT in NiAl can be correlated with a loss of strain hardening rate as temperature is increased. The BDT in notched bend specimens of this alloy was associated with a non-linearity in the load–displacement curve. This non-linearity can arise from general yielding and/or slow crack growth. Table 4 compares the predicted general yield loads with the load values observed for specimens that showed non-linear behavior. It is obvious from these results that general yielding preceded fracture in these specimens. The existence of microcracks ahead of the notch in the NiAl specimen, which was partially loaded at 500°C, suggests that extensive microcracking occurs in the plastic zone ahead of the notch before crack growth and instability proceed. Assuming pre-existing intergranular microcracks of the order of the grain size in tensile specimens, the toughness can be estimated using the relationship for a penny-shape crack [$K = \sigma(d/\pi)^{1/2}$, where d is the grain size and σ is the measured fracture stress in tension]. The estimated values for NiAl and NiAl + Ti in the as-extruded and heat treated conditions, respectively, are 0.903,

1.55, 1.09, and 1.81 Mpa m$^{1/2}$, which are much smaller than the measured room temperature values. This comparison supports the notion that in notched specimens crack propagation rather than initiation controls the toughness. Therefore, fracture in polycrystalline NiAl occurs by development of (i) a plastic zone ahead of the notch, (ii) formation of intergranular microcracks in the plastic zone, and (iii) unstable fracture which depends on the number and size distribution of microcracks and the level of stresses in the plastic zone. The increase in toughness becomes drastic, and hence it is called a BDT, when the strain hardening rate is decreased significantly. The loss of strain hardening rate is associated with a smaller probability of intergranular microcrack formation and a lower stress distribution in the plastic zone at a given applied stress intensity factor. Hence, the probability of unstable fracture is decreased and general yielding precedes unstable fracture. At temperatures below BDT temperature, the fracture process in stoichiometric NiAl is similar to the fracture of low carbon steels [33], except that in the latter material microcracking is transgranular. In low carbon steels there is competition between brittle and ductile fracture and the BDT occurs when the fracture mechanism changes from cleavage to microvoid coalescence [34]. In NiAl, however, no stable slow crack growth was observed, and consequently the BDT temperature coincides with the general yielding of the specimen. A decrease in displacement rate did not affect the low temperature toughness of NiAl. However, it reduced the BDT temperature and made the transition sharper. This observation suggests that strain rate, similar to test temperature, affects the driving force for unstable crack propagation by modifying the development of the internal stresses owing to strain incompatibility, which drive the crack propagation. Relaxation of these stresses at low strain rates or high temperatures reduces the net applied driving force, and hence instability is not achieved and the deformation proceeds to the point of general yielding. After general yielding owing to a loss of plastic constraint the stresses in the plastic region can be intensified only through strain hardening and very large applied strains are needed for the onset of crack instability.

The BDT temperature for NiAl + Ti alloy, similar to the NiAl alloy coincided with the general yielding of the fracture specimens. An increase in the specimen thickness reduced the low temperature toughness. The effect of specimen thickness on toughness has been attributed to a change in the stress state as well as an increase in the probability of finding large microcracks that can cause crack instability [35]. However, since the BDT temperature is not affected considerably by a change in the specimen thickness, it may be concluded that thickness did not affect the plastic constraint and the reduction in toughness can be attributed to the higher number of defects, including the voids formed upon heat treatment.

For stoichiometric NiAl, the BDT temperature as evaluated by tensile testing was similar to that obtained by testing notched specimens. Interestingly, the NiAl + Ti alloy did not show a BDT upon tensile testing up to 600°C; however, the testing of notched fracture specimens indicated the BDT to be around 400–500°C. These observations are in contrast to those in b.c.c. metals and alloys, for example in steels, where the BDT temperature, as evaluated by testing notched specimens, is usually much higher than that obtained by testing smooth specimens [34]. This difference in behavior may suggest the localization of strain in tensile specimens, for example in the form of shear bands. Further work is needed to investigate this phenomenon.

Considering that fracture in tensile specimens is initiation controlled, the reduction in tensile ductility and fracture strength with heat treatment (see Table 1) can be attributed to an increase in the grain size [14]. The larger the grain size, the larger the size of intergranular microcracks and hence the higher the probability of fracture. The effect of heat treatment on fracture toughness cannot be evaluated directly, because in addition to a change in grain size, heat treatment introduced two other effects in notched specimens: the relaxation of residual stresses near the notch, which should increase the toughness, and formation of cavities, which is expected to sharpen and lengthen the crack, and hence reduce the apparent toughness.

5. CONCLUSIONS

The BDT of polycrystalline NiAl and NiAl + 1 at.% Ti alloys was evaluated using tensile and fracture toughness testing. The results of this study have led to the following conclusions:

(a) The BDT in these alloys is associated with the loss of strain hardening rate, which results in general yielding and plastic instability (necking) preceding unstable fracture in bend and tensile specimens, respectively. The loss of strain hardening is attributed to cross-slip of $\langle 100 \rangle$ dislocations to $\{0kl\}$ planes and climb of dislocations.

(b) The brittle crack nucleation occurs intergranulary in these alloys. The crack propagates intergranularly when sufficient internal stresses are developed preferentially at grain boundaries. The propensity to intergranular fracture decreases with increases in yield strength and plastic constraint because the condition for crack instability is achieved before sufficient stresses are built up preferentially adjacent to the grain boundaries.

(c) The BDT is not associated with a change in fracture mode from intergranular to transgranular in these alloys. However, for tensile specimens the BDT is associated with a change

in fracture mode to a microvoid coalescence mechanism.

(d) The lack of enough independent slip systems in these alloys creates very high localized elastic stresses, which are suggested to be responsible for high strain hardening, intergranular fracture, and enhanced diffusivity.

(e) The addition of Ti increases yield strength and BDT temperature; however, it may result in an increase in the apparent low temperature toughness.

(f) A decrease in the applied displacement rate allows the relaxation of internal stresses and decreases the BDT temperature, but does not affect the low temperature toughness level significantly. In contrast, an increase in the specimen thickness provides a larger number of possible crack initiation sites and decreases the low temperature toughness, but does not affect BDT temperature significantly.

REFERENCES

1. *Structural Intermetallics*. Darolia, R., Lewandowski, J. J., Liu, C. T., Martin, P. L., Miracle, D. B. Nathal, M. V. (eds) The Minerals, Metals, and Materials Society, Warrendale, Pennsylvania, U.S.A. 1993.
2. Ball, A. and Smallman, R. E., *Acta metall.*, 1966, 14, 1517.
3. Pascoe, R. T. and Newey, C. W., *Phys. stat. solidi*, 1968, 29, 357.
4. Loretto, M. H. and Wasilewski, R. J., *Phil. Mag.*, 1971, 23, 1311.
5. Field, R. D., Lahrman, D. F. and Darolia, R., *Acta metall. mater.*, 1991, 39, 2951.
6. Kanne, W. R. Jr, Strutt, P. R. and Dodd, R. A., *Trans. Metall. Soc. AIME*, 1969, 245, 1259.
7. Nagal, P., Baker, I. and Horton, J. A., *Intermetallics*, 1994, 1, 23.
8. Ebrahimi, F., Gomez, A. and Hicks, T. G., *Scripta matte.*, 1996, 34, 337.
9. Ball, A. and Smallman, R. E., *Acta metall.*, 1996, 14, 1349.
10. Hahn, K. H. and Vedula, K., *Scripta metall.*, 1989, 23, 7.
11. Noebe, R. D., Bowman, R. R., Cullers, C. L. and Raj, S. V., *Mater. Res. Symp. Proc.*, 1991, 213, 589.
12. Noebe, R. D., Cullers, C. L. and Bowman, R. R., *J. Mater. Res.*, 1992, 7, 605.
13. Bowman, R. R., Noebe, R. D., Raj, S. V. and Locci, I. E., *Metall. Trans.*, 1992, 23A, 1493.
14. Schulson, E. M. and Barker, D. R., *Scripta metall.*, 1983, 17, 519.
15. George, E. P. and Liu, C. T., *J. Mater. Res.*, 1990, 5, 754.
16. Ruess, S. and Vehoff, H. *Scripta metall.*, 1990, 24, 1021.
17. Bergman, G. and Vehoff, H., *Mater. Sci. Engng*, 1995, 192/193, 309.
18. Towers, O. L., Stress intensity factors, compliances and elasticy factors for six test geometries. NBS Report 7709.0181/249.1, Boulder, Colorado, U.S.A. 1980.
19. Losch, W., in *Chemistry and Physics of Fracture*, ed.

R. M. Latanision and R. H. Jones, NATO ASI Series. Martinus Nijhoff Publishers, Boston, MA, U.S.A. 1987, p. 461.

20. Gandhi, C. and Ashby, M. F., *Acta metall.*, 1979, 27, 1565.

21. Ebrahimi, F. and Castillo-Gomez, J. R., *Acta metall. mater.*, 1992, 40, 1409.

22. Ebrahimi, F., *Scripta metall. mater.*, 1991, 25, 1737.

23. Kad, B. K., Dao, M. and Asaro, J., *Phil Mag.*, 1995, 71, 367.

24. Carreker, R. P. Jr, *Trans AIME*, 1957, 209, 112.

25. Mori, T. and Tanaka, T., *Acta metall.*, 1973, 21, 571.

26. Tomota, Y., Kuroki, K., Mori, T. and Tamura, *Mater. Sci. Engng*, 1976, 24, 85.

27. Miracle, D. B., *Acta metall mater.*, 1993, 41, 649.

28. Epperson, J. E., Gerstenberg, K. W. and Berner, D., *Phil. Mag.*, 1978, 38, 529.

29. Yang, W., Dodd, R. A. and Strutt, P. R., *Metall. Trans. A*, 1972, 3, 2049.

30. Noebe, R. D., Bowman, R. R. and Nathal, M. V., *Int. Mater. Rev.*, 1993, 38, 193.

31. Cuitino, A. M. and Oritz, M., *Acta mater.*, 1996, 44, 427.

32. Field, R. D., Darolia, R. and Lahrman, D. F., *Scripta metall.*, 1989, 23, 1469.

33. Cottrell, A. H., *Trans. Metall. Soc. AIME*, 1958, 192.

34. Ebrahimi, F. and Seo, H. K., *Acta mater.*, 1996, 44, 831.

35. Wallin, K., *Engng Fract. Mech.*, 1985, 22, 149.

BRITTLE-TO-DUCTILE TRANSITION IN NiAl SINGLE CRYSTAL

F. EBRAHIMI and S. SHRIVASTAVA

Materials Science and Engineering Department, University of Florida, Gainesville, FL 32611, U.S.A.

Abstract—The brittle-to-ductile transition (BDT) of NiAl single crystals was studied as a function of displacement rate and prestraining using double-notched tensile specimens loaded along a (110) orientation with the crack front parallel to a (001) direction. The tensile properties were also evaluated as a function of strain rate and test temperature. For specimens tested, the BDT coincided with the onset of net-section yielding. It has been found that decreasing the applied displacement rate reduced the BDT temperature and strain hardening rate without affecting the low temperature toughness and yield strength significantly. Prestraining improved the low temperature toughness level but increased the BDT temperature. It has been shown that fracture in NiAl single crystal occurs by development of microcracks on slip bands and their subsequent instability. The effects of displacement rate and prestraining are discussed in terms of the plastic flow mechanisms and their effects on crack initiation and propagation processes. It has been suggested that the cross-slip of screw dislocations at elevated temperatures and low strain rates retards plastic strain localization, and hence, toughness is improved. © *1998 Acta Metallurgica Inc.*

1. INTRODUCTION

Crystalline materials that cleave show a brittle-to-ductile transition (BDT) upon an increase in the test temperature. The BDT is conventionally defined as a sharp increase in the material's toughness which is evaluated at the point of crack instability. This sudden increase in toughness is usually a result of non-linearity in the load–displacement curve which is initiated by either slow crack growth or gross yielding (non-contained yielding) followed by unstable fracture. However, BDT can also be achieved within the linear-elastic fracture mechanics frame as long as the specimen size is increased with an elevation in the test temperature. In this case the BDT is more gradual in nature.

The brittleness of a material can be viewed as either a low, lower-shelf toughness or a high, brittle-to-ductile transition temperature (BDTT) as depicted schematically in Fig. 1. In semi-brittle materials, local plasticity always precedes unstable fracture, even at low test temperatures [1, 2]. Because of the blunting of the original crack tip, microcracking usually precedes unstable fracture, i.e. sharp microcracks form at or ahead of the blunted crack tip. In single phase materials intergranular microcracking, shear decohesion, and cleavage microcracking owing to the intersection of twins or slip bands are examples of crack initiation processes. These microcracks have to reach a critical length (or velocity) in order to cause the global instability of the specimen. The gradual increase in toughness as a function of temperature within the lower shelf region is usually due to a decrease of

the yield strength which reduces the probabilities of microcracking and its subsequent instability. Any factor that affects these probabilities will also change the variation of toughness with temperature in this regime. The BDT arises from the intervention of either ductile fracture or gross yielding. The BDT has been studied extensively in steels, in which case it is often associated with the development of slow crack growth prior to unstable fracture [3, 4]. The slow crack grows by microvoid coalescence mechanism in steels; however, the mechanism of unstable crack propagation can be cleavage, quasi-cleavage or microvoid coalescence, depending on the microstructure and deformation behavior of the steel. An increase in the crack tip opening displacement for ductile crack initiation indeed results in a higher BDT temperature in steels [4]. In single-phase materials, where microvoid initiation occurs by mechanisms such as decohesion at dislocation cell boundaries or intersection of slip bands [4, 5], the toughness at the point of ductile crack initiation can be relatively high. Hence, gross yielding is expected to precede the initiation of slow crack growth in the absence of environmental effects.

The brittle-to-ductile transition of materials has been found to be dependent on displacement rate, specimen geometry, and prestraining. It is well known that BDTT of steels increases with an increase in the displacement rate [6]. This effect has been recently investigated in other materials [7–10]. In general, the effect of displacement rate is explained in terms of local plastic yielding which is controlled by the number and velocity of dislocations near the crack tip. A reduction in the speci-
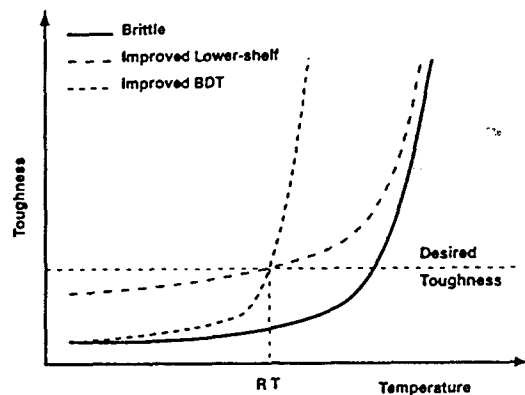
Fig. 1. A schematic showing how the room temperature (*RT*) toughness can be improved by shifting the BDTT below *RT* and/or increasing the lower-shelf toughness level.

men dimensions decreases the total number of the microcracks near the crack tip, as well as allowing gross yielding to precede unstable cracking at lower test temperatures, thus decreasing BDTT [3]. Increasing the notch root radius modifies the stress distribution ahead of the notch and may lead to a lower BDTT [11]. The effect of prestraining depends on the nature of the material. If the introduction of dislocations increases the yield strength of the material considerably, then the BDTT will be increased. For example a cold worked steel shows a higher BDTT than it does in the annealed condition. However, in materials with a low density of mobile dislocations, prestraining may result in a reduction of yield strength and hence, in improvement of the toughness [12]. For example, prestraining silicon has been shown to reduce hardness and increase room temperature toughness [13], as well as decreasing the BDTT by changing the shape of the toughness vs temperature curve [14].

The intermetallic NiAl has been considered to have a poor room temperature fracture toughness which makes it unsuitable for high temperature structural applications [15]. In polycrystalline form NiAl has a lower-shelf toughness of $10-15$ MPa·m$^{1/2}$ and a BDT temperature around $400°C$ [16]. NiAl has a B2 crystal structure and its slip vector is $a\langle 100\rangle$ [17], except when it is loaded uniaxially along a $\langle 100\rangle$ direction [18]. The preferred slip planes are $\{001\}$ and $\{011\}$ planes; however, $\{013\}$ and $\{015\}$ slip planes have also been observed [19,20]. The a $\langle 100\rangle$ slip directions result in only three independent slip systems. The multiplicity of slip planes does not increase the number of independent slip systems, however, it facilitates cross-slip by so-called "pencil" glide [21]. A lack of enough slip systems to accommodate the strain incompatibility between the grains leads to formation of intergranular microcracks and development of high internal hydrostatic stress components that provide the driving force for intergranular crack propagation [16]. This material fractures by

microvoid coalescence at high temperatures, where stress-assisted diffusion can cause coalescence of vacancies [16]. However, the BDT in polycrystalline NiAl was found to be associated with gross yielding, which occurred at a lower temperature than that at which cracking by microvoid coalescence was possible. The low lower-shelf toughness and the high BDT temperature of the polycrystalline NiAl has been attributed to the plasticity-induced intergranular microcracking and the existence of high internal stresses arising from incompatibility between grains [16].

The lower-shelf fracture toughness of single-crystalline NiAl depends on the crystallographic orientation and heat treatment, and its value varies between 4 and 15 MPa·m$^{1/2}$ [22]. This range of toughness is comparable to the lower shelf of b.c.c. single crystals such as molybdenum [9]. The limited work on BDT of NiAl single crystal indicates a $BDTT/T_m$ ratio of 0.22 to 0.35 (transition temperature range of $150°C-400°C$ [22,23]), which is much higher than the ratio for metallic single crystals such as Mo ($BDTT/T_m = 0.05-0.07$ [9]) but much lower than covalently bonded single crystals such as Si ($BDTT/T_m = 0.46-0.58$ [7]). The BDT in silicon is strongly strain-rate dependent, and it corresponds with non-linearity in load–displacement curve owing to gross plasticity [7]. Models based on dislocation nucleation [25] as well as dislocation motion [26] have been proposed to explain the shielding and blunting of the crack tip in Si which drop the stress intensity factor at the crack tip below that necessary for breaking atomic bonds. In contrast to Si, the yield strength of Mo does not drop very fast with temperature and it is less temperature sensitive within the BDT regime. Accordingly, the BDTT of Mo is not strongly dependent on the applied displacement rate [9]. The BDT in this material has been explained by plasticity-enhanced microcleavage [2,9]. The purpose of this paper is to understand the mechanism(s) of BDT in NiAl single crystals oriented along a $\langle 110\rangle$ orientation.

2. MATERIALS AND EXPERIMENTAL PROCEDURES

Stoichiometric NiAl single crystals studied in this investigation were grown using a modified Bridgeman technique. The as-grown crystals were homogenized in an argon atmosphere at $1300°C$ for three hours and were cooled to room temperature at a rate of $2.4°C/min$ to eliminate the thermal vacancies generated at high temperatures. The crystal orientation was determined using the Laue back-scattered X-ray technique.

Tensile and fracture toughness tests were performed using a closed loop hydraulic testing system. The high temperature tests were conducted in a closed furnace, with tungsten mesh as heating el-
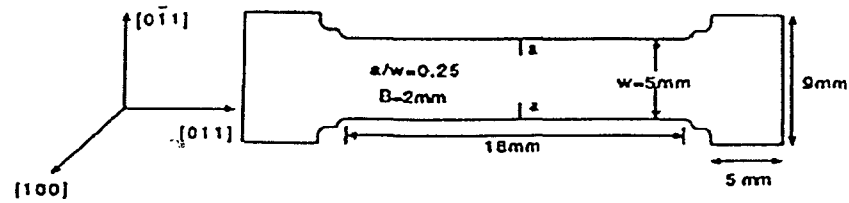
Fig. 2. Schematic showing the geometry and crystallographic orientation of the specimens used for tensile and fracture toughness testings.
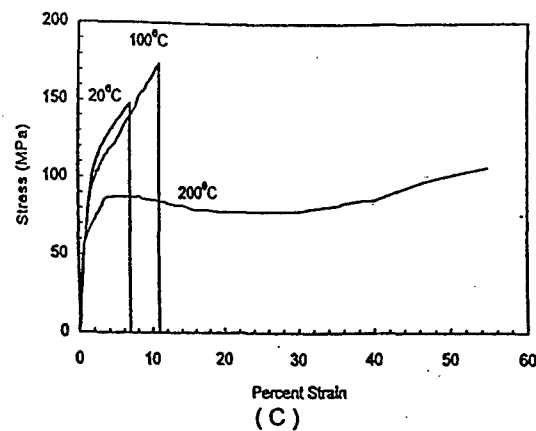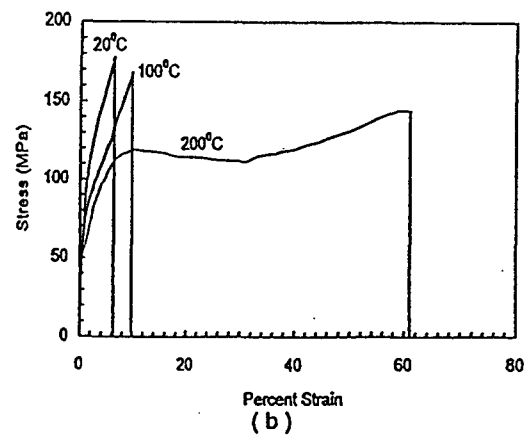

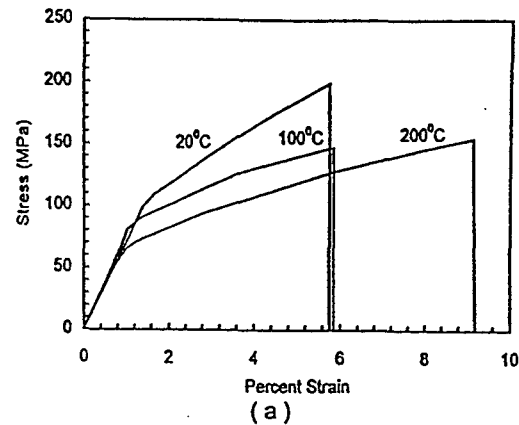Fig. 3. Tensile engineering stress–strain curves at a strain rate of (a) 5×10^{-3}/s, (b) 5×10^{-5}/s, and (c) 5×10^{-6}/s.

Table 1. Tensile properties of NiAl single crystal

Strain rate (s^{-1})	Temperature $(^\circ C)$	Yield strength (MPa)	Fracture stress (MPa)	Ductility (%)
5×10^{-3}	20	110	211	5.8
	100	83	151	5.8
	200	69	168	9.1
5×10^{-5}	20	98	189	6.3
	100	75.5	186	10.0
	200	56	—	61
	300	28	—	>63
5×10^{-6}	20	94	163.5	6.9
	100	84	192	11.0
	200	56	—	>56

ement, under a constant flow of oxygen-gettered argon gas. The specimens were soaked at the test temperature for an hour before testing. Tensile tests were conducted in the temperature range of room temperature to 300°C at approximate strain rates of 5×10^{-3}/s, 5×10^{-5}/s, and 5×10^{-6}/s. Three displacement rates viz, 10^{-2} mm/s, 2×10^{-4} mm/s, and 2×10^{-5} mm/s were used for establishing the BDT.

A double-notched tension specimen was used for characterizing the BDT as shown in Fig. 2. This geometry was adopted primarily because it allows a uniform prestraining to be performed prior to making notches. The notches were introduced using a slow speed saw with a diamond wafering blade of 300 μm thickness. Specimens with the same geometry and dimensions as shown in Fig. 2, but in an "un-notched" form, were used for tensile testing.

Prestraining was performed at a strain rate of 5×10^{-4}/s at 200°C to a level of 10% strain. At these conditions the specimen showed adequate maximum uniform strain [23]. The specimens were cooled to room temperature under flowing argon after unloading. The specimens were notched after prestraining. Fracture toughness testing of prestrained specimens were conducted at the displacement rate of 10^{-3} mm/s.

The apparent fracture toughness, K_{JC}, was calculated using the following equations [27,28]:

$$K_{JC} = (YP_f a^{1/2})/BW + (J_p E)^{1/2}$$

$$Y = 1.99 + 0.76(a/W) - 8.48(a/W)^2 + 27.32(a/W)^3$$

$$J_p = 2A_p/B(W - a)$$

where P_f is the load at the point of unstable fracture, a is the crack length, B is the thickness, W is the width, and A_p is the area under the plastic regime of the load–displacement curve.

3. RESULTS

3.1. Tensile testing

Engineering stress–strain curves for the three strain rates tested are shown in Fig. 3, and the tensile properties are summarized in Table 1. The yield strength decreased considerably with test tempera-
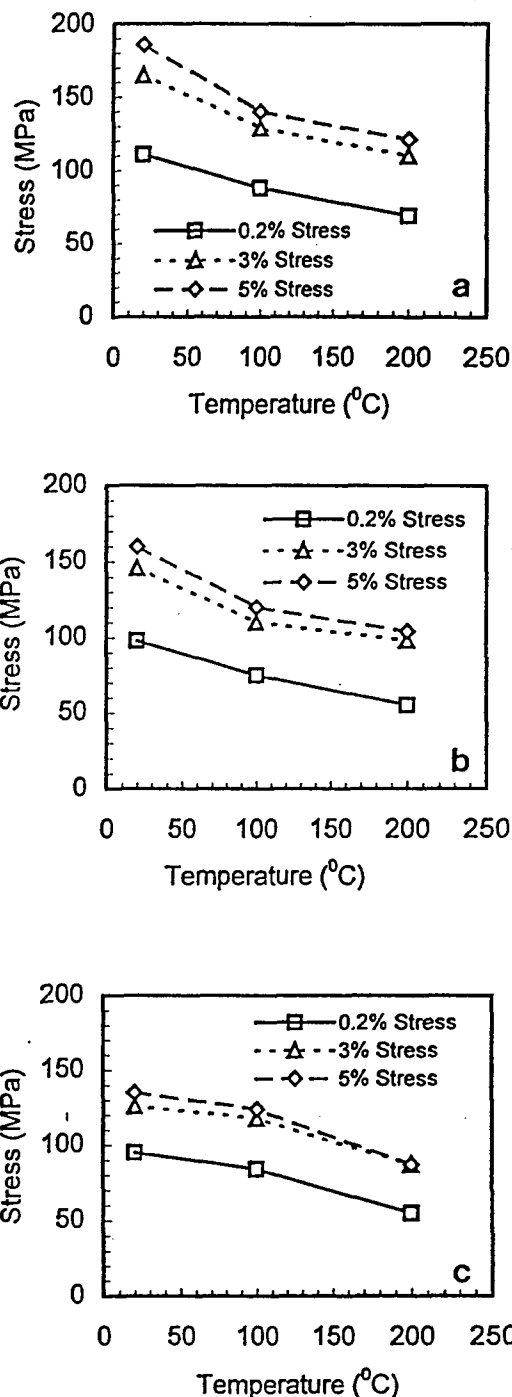
Fig. 4. Effect of temperature on flow stress at a strain rate of (a) 5×10^{-3}/s, (b) 5×10^{-5}/s, and (c) 5×10^{-6}/s.

ture; however, the effect of strain rate was not as significant. Figure 4 presents flow stress as a function of temperature at various strain rates. These curves show that initially the strain hardening rate is very high, as reflected in the large difference in the flow stress values at 0.2% and 3% strain levels. However, the strain hardening rate decreased significantly at higher strain levels as indicated by the small difference in the flow stress at 2% and 3%

Table 2. Strain hardening rate† (MPa) as a function of temperature and strain rate

	20°C	100°C	200°C
$5 \times 10^{-3}\,s^{-1}$	1546	1172	1056
$5 \times 10^{-5}\,s^{-1}$	1240	900	1026
$5 \times 10^{-6}\,s^{-1}$	604	784	686

†Strain hardening rate was defined as: $(\sigma_{5\%}-\sigma_{0.2\%})/0.048$, where $\sigma_{5\%}$ and $\sigma_{0.2\%}$ are the flow stress at 5% and 0.2% strain, respectively.

Table 3. Strain rate sensitivity. m†. as a function of temperature

Temperature °C	Strain rate sensitivity	
	high strain rates	low strain rates
20	0.024	0.014
100	0.022	−0.045
200	0.047	0

†$m = \ln(\sigma_2/\sigma_1)\,/\ln(\dot{\varepsilon}_2/\dot{\varepsilon}_1)$, where σ is the yield strength, $\dot{\varepsilon}$ is the strain rate. and subscripts 1 and 2 refer to the two levels of strain rate.

strain levels. Table 2 presents an estimate of the initial strain hardening rate for various temperatures and strain rates tested. The strain hardening rate decreased significantly with a reduction in the strain rate. The effect of temperature on strain hardening rate was not as significant and the strain hardening rate remained almost constant at the lowest strain rate tested.

Figure 5 presents yield stress as a function of the applied strain rate. The strain rate sensitivity values calculated from these curves are given in Table 3. The negative strain rate sensitivity observed at 100°C and low strain rates suggests the occurrence of dynamic strain aging at this temperature. The activation energy for yielding was estimated based on the data at room temperature and 200°C test temperatures. The 100°C temperature results were excluded because of the occurrence of dynamic strain aging. The activation energy, Q, was calculated from:

$$Q = [-R \log(\dot{\varepsilon}_2/\dot{\varepsilon}_1)/(1/T_2 - 1/T_1)]_\sigma$$

where $\dot{\varepsilon}$ is strain rate, T is temperature, σ is the flow stress, and R gas constant. The subscripts 1 and 2 refer to 25°C and 200°C test temperatures. Within the stress range of 70 to 90 MPa, the activation energy was found to be 97 kJ/mol and independent of the stress level.

The specimens that did not show plastic instability (necking) broke near the shoulder where the cross-section area changed drastically. At 200°C,

where the specimens necked before fracture, the maximum uniform strain was reduced considerably with a decrease in the applied strain rate from 5×10^{-5} to 5×10^{-6}. The tensile ductility in specimens fractured in the specimen's shoulder was in the range of 5–11% but it increased drastically (>60%) in specimens that did not break in the shoulder area. This transition was not observed in the specimens tested at 5×10^{-3}/s, suggesting that the transition temperature should be above 200°C.

Analysis of the slip traces on both sides of specimens that showed significant ductility has revealed that {100} and {110} slip planes as well as various {hk0} planes were activated [20]. The wavy nature of the slip lines as shown in Fig. 6 indicated extensive cross-slip of dislocations between the slip planes.

3.2. Fracture toughness testing

The effect of displacement rate on the BDT is shown in Fig. 7. All specimens tested, except for the specimen tested at 250°C at the displacement rate of 2×10^{-5} mm/s, broke in an unstable manner

Fig. 5. Effect of strain rate on yield strength at different test temperatures.

Fig. 6. SEM micrograph showing the relationship between the slip traces on faces of a tensile specimen loaded to a strain of 25% at 200°C.
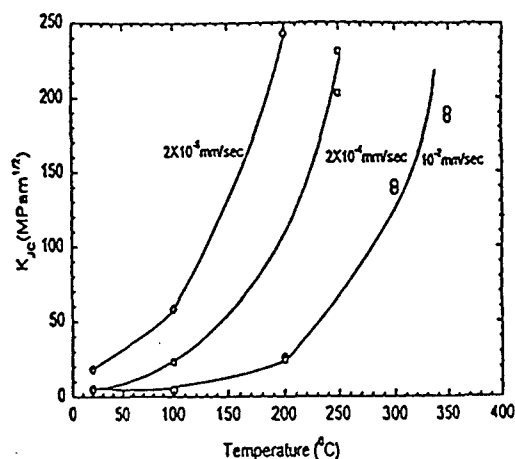
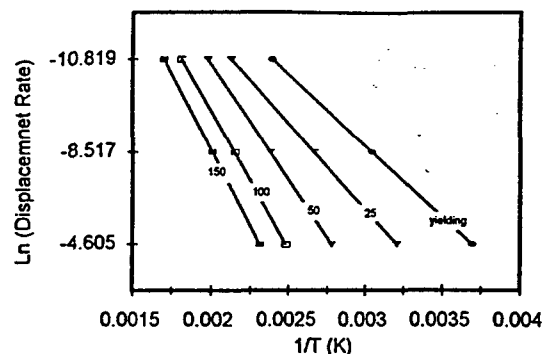Fig. 7. Fracture toughness as a function of test temperature at different applied displacement rate [21].

Fig. 8. Ln displacement rate vs reciprocal of absolute temperature at various stress intensity factor, K, levels.

without a noticeable slow crack growth. The BDT temperature, as defined by the temperature at which toughness increases drastically with temperature, coincided with the onset of nonlinearity in the load–displacement curve [20]. This nonlinearity is due to the net-section yielding of the specimen. Table 4 compares the actual load at the onset of nonlinearity, P_y, with that predicted based on the net-section area, A_{net}. The results indicate that the constraint factor, $L = P_y/\sigma_y A_{net}$, is about 1.4–1.5 in specimens tested. Decreasing the displacement rate reduced the BDTT without improving the low temperature toughness level (lower-shelf toughness) noticeably.

The activation energy for BDTT was estimated by plotting the displacement rate as a function of the inverse of temperature at the point where unstable fracture correspond with net-section yielding as shown in Fig. 8. For comparison the curves at $K_{JC} = 25$, 50, 100 and 150 MPa·m$^{1/2}$ are also included. The activation energy values calculated are presented in Table 5. The activation energy values increased with an increase in the apparent K value. Note that the activation energy corresponding to BDT is significantly smaller than the value for yielding (48 kJ/mol for BDT vs 97 kJ/mol for tensile yielding).

The effect of prestraining on BDT behavior is shown in Fig. 9. The average lower-shelf toughness was increased from 4.9 MPa·m$^{1/2}$ to 8.5 MPa·m$^{1/2}$;

however, the BDTT was shifted to a higher temperature upon prestraining. Similar to the as-homogenized specimens, the BDTT corresponded to the onset of net-section yielding.

3.3. Fractography

Unstable fracture occurred by cleavage fracture in all notched and un-notched specimens and no microvoid coalescence mechanism was observed. The processes of crack initiation and propagation have been presented in detail elsewhere [20] and here only salient features are presented. At all conditions crack nucleation occurred by shear decohesion along concentrated slip bands. Figure 10 presents three examples of microcracking: at the notch tip (low temperature, below net-section yielding), ahead but near the notch (intermediate temperature, above net-section yielding but below general yielding), and in the mid-section of a specimen (high temperature, above general yielding). The crack initiation and propagation was found to start invariably near the sides of the specimens as shown in Fig. 11. As demonstrated in Fig. 12, the plane stress condition near the surface enhanced localized plastic deformation which is the pre-curser to crack initiation and propagation in NiAl single crystals.

4. DISCUSSION

Based on the fractographic analysis, cleavage microcracks are produced by slip decohesion on the slip planes in NiAl single crystals. It should be noted that {100} and {110} planes act as both slip and cleavage planes in this material. The microcracks formed preferentially near the sides of the

Table 4. A comparison of load at the onset of non-linearity. $P_y(N)$, with $P = \sigma_y A_{net}(N)$. The values in the parenthesis are the plastic constraint factor, L

	5×10^{-3} s^{-1}	5×10^{-5} s^{-1}	5×10^{-6} s^{-1}
20°C	a	a	$P_y = 623$, $P = 480$ (1.3)
100°C	a	$P_y = 534$, $P = 383$ (1.4)	$P_y = 445$, $P = 414$ (1.1)
200°C	$P_y = 489$, $P = 351$ (1.4)	$P_y = 427$, $P = 285$ (1.5)	$P_y = 423$, $P = 285$ (1.5)

a Fracture occurred within the linear portion of the load–displacement curve.

Table 5. Activation energy calculated at various K_{JC} values

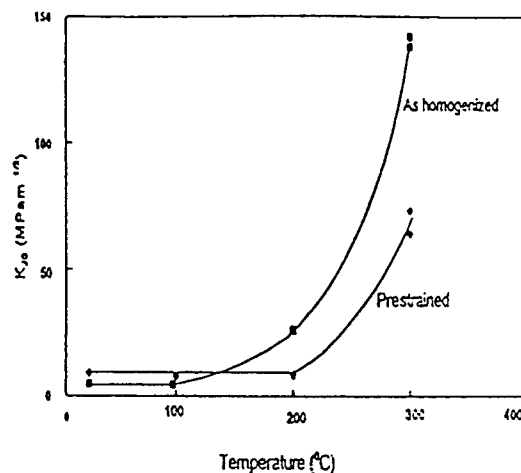| K Level (MPa·m$^{1/2}$)	Activation energy (kJ/mol)
Net section yielding	48
25	52
50	66
100	79
150	84

Fig. 9. Brittle-to-ductile transition in as-homogenized and prestrained conditions [24].

specimens tested, where the stress state is close to the plane stress condition. This stress state enhances shear localization and thus microcracking. The fact that unstable cracks always started from the sides of the specimens suggests that microcrack formation is the main mechanism that controls the apparent fracture toughness of the NiAl specimens tested. Consistently, the abrupt decrease in tensile ductility with a reduction in temperature is attributed to the localization of plastic strain near the tensile specimen shoulders which causes crack initiation and leads to a premature fracture.

In contrast to the observations made for silicon single crystals [14], the BDT temperature was increased with prestraining of the NiAl single crystal tested in this study. This contradiction may be related to the difference in the prestraining procedures. In the case of silicon, prestraining was conducted after a sharp crack has been introduced by microindentation [14]. Since silicon single crystals have a very low dislocation density, dislocations formed upon prestraining are expected to be generated from the crack tip. These dislocations reduce the stress intensity factor at the crack tip during low temperature fracture toughness testing by blunting the originally sharp crack tip and acting as shielding dislocations. In this study prestraining was conducted prior to the introduction of the notches. The random distribution of the dislocations and the absence of a change in the notch tip geometry may reflect why the BDTT was not improved in the case of NiAl single crystal studied here. Furthermore, our recent results indicate that the toughness of silicon can also be improved by high temperature prestraining performed prior to the introduction of cracks [13]. We have also found that room temperature hardness of silicon is reduced by prestraining. This result suggests that the improvement of toughness and the reduction of BDTT in silicon are associated with introduction of dislocation sources

Fig. 10. SEM micrographs showing microcracking in NiAl single crystals. (a) Microcracks at the notch tip. (b) Microcracks within the heavily deformed region ahead of the notch. (c) Microcracks in the middle of a specimen.

upon prestraining. The increase in the BDTT of NiAl with prestraining suggests that dislocation generation is not the mechanism that controls the toughness of NiAl single crystals. Indeed, TEM studies have revealed that homogenized NiAl single crystals show small angle boundaries indicating that a reasonable number of dislocation sources exist in this material [29]. Therefore, lack of enough dislocations is not a reason for the brittleness of NiAl single crystals. The effect of prestraining on BDT behavior of NiAl is depicted in Fig. 13(a). The increase in the BDTT with prestraining can be attributed to the increase in the flow stress which
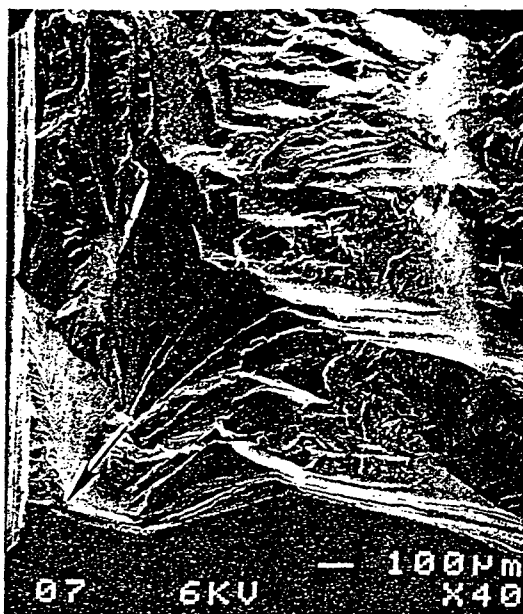
Fig. 11. SEM micrograph showing crack initiation site in a specimen fractured at 350 C at 10^{-2} mm s. The arrow indicates the crack initiation site.

raises the load level. and hence the applied K (or J) value at which net-section yielding occurs. Therefore. the intervention of gross yielding is postponed to higher temperatures. In addition. the increase in the stress distribution level in the plastic zone increases the probability that microcracks may lead to instability. The improvement of the room temperature toughness with prestraining can be attributed to the uniformity of deformation in the

Fig. 12. SEM micrograph showing the extensive plastic deformation and the Poisson's effect near the side of a specimen fractured at 350 C at 10^{-2} mm·s [21]. The arrow indicates the crack initiation site.
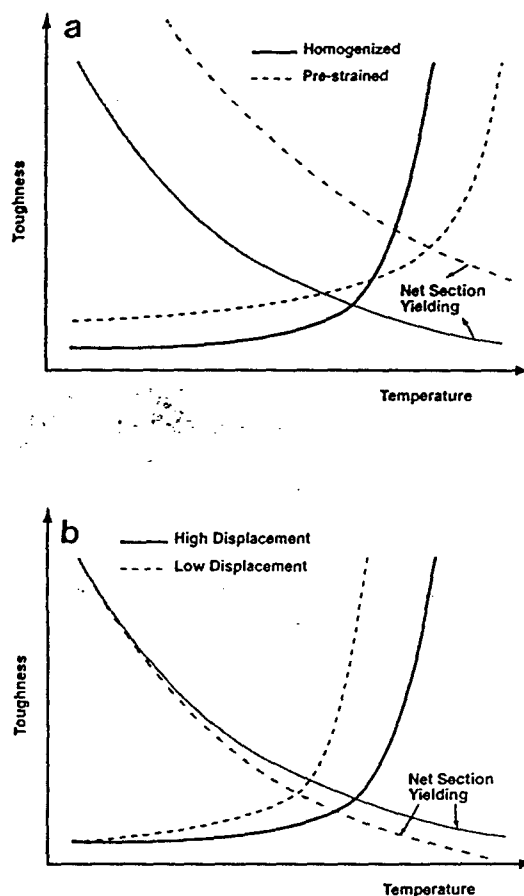
Fig. 13. Schematics depicting the effects of (a) prestraining and (b) displacement rate on BDT of NiAl single crystal

plastic zone. At low temperatures the toughness is strongly dependent on the resistance to crack initiation. The uniformity of deformation resulted from prestraining retards plastic strain localization and consequently for microcracking to occur larger plastic strains are required. Apparently this effect offsets the adverse effect of the high flow stress, and thus toughness is improved.

The results presented here indicated that BDT temperature is reduced significantly with decreasing the applied displacement rate. This observation is similar to the results reported for silicon. However, in contrast to the behavior of silicon, within the temperature range studied here. the yield strength of NiAl is insensitive to the applied strain rate. Therefore, models that explain the displacement rate dependency of BDTT based on the variation of the yield strength are not applicable. Consistently, the estimated activation energy for yielding was found to be much higher than the activation energy associated with BDT.

Although the yield strength was found to be independent of the applied strain rate, the strain hardening rate was influenced considerably (see Table 2). Slip trace analysis of NiAl tensile specimens loaded in a ⟨110⟩ direction has revealed that double cross-

Influence of Interstitials on the Mechanical Properties of Metallic Materials

R.E. REED-HILL, C.V. ISWARAN, and M.J. KAUFMAN

The role of interstitials on the mechanical properties of metals has become more clearly understood as the result of investigations of systems whose interstitial solute concentrations in solid solution are effectively constant over a wide temperature range (from 0 K to well into the plateau of the flow stress *vs* temperature diagram). These studies strongly imply that both solid solution hardening and dynamic strain aging are due to pinning of dislocations by interstitial solute atoms. Furthermore, the strain rate is controlled by a mechanism whose activation enthalpy is a function of the effective stress, as suggested by Yokobori.

I. INTRODUCTION

INTERSTITIAL atoms in solid solution are able to produce two very significant effects on the mechanical properties of metallic materials; at lower temperatures, where the interstitial atom diffusion rates are insignificant, they produce solid solution hardening, and at higher temperatures, where diffusion rates become appreciable, they cause dynamic strain aging (DSA). Both phenomena involve pinning of dislocations by interstitial atoms. In solid solution hardening, the pinning occurs by *in situ* interstitials that are effectively stationary. This is illustrated in Figure 1, which is based on a figure in Hirth and Lothe's *Theory of Dislocations*.[1] These authors point out that at low temperatures, because the interaction force between a dislocation and a solute atom has a very short range, "a dislocation becomes wiggly, adjusting its configuration to conform to the internal stresses of the immobile solute atoms." In Figure 1(a), the dislocation is assumed to be unstressed, while in Fig. 1(b), the dislocation is under stress. At DSA temperatures, the interstitials are mobile and thus able to increase the level of pinning by either forming solute atom atmospheres at the dislocations (Cottrell–Bilby aging[2]) or by jumping into lower energy interstitial sites lying within the stress fields of the dislocations (Snoek aging[3]).

II. OUTLINE OF THE ANALYSIS

The effects of these pinning phenomena on the mechanical properties are capable of being rationalized over an extensive temperature range, but it is first necessary to find an alloy whose interstitial solute concentrations and metallurgical structure are basically temperature independent within this range and whose internal stress can also be properly evaluated in this interval.

The analysis for doing this uses the following universally accepted metallurgical relations.

(1) The flow stress σ:

$$\sigma = \sigma_\mu + \sigma^*$$

where σ_μ is the internal stress and σ^* the effective stress.

(2) The thermally activated strain rate equation:

$$\dot{\varepsilon} = \dot{\varepsilon}_0 \exp\left(-\frac{H}{RT}\right)$$

where $\dot{\varepsilon}$ is the strain rate, $\dot{\varepsilon}_0$ a constant, H the activation enthalpy, R the gas constant, and T the Kelvin temperature.

(3) The activation volume v:

$$v = -\left(\frac{\partial H}{\partial \sigma^*}\right)_T$$

(4) The Conrad–Wiedersich equation:[4]

$$H = -Tv\left(\frac{\partial \sigma^*}{\partial T}\right)_{\dot{\varepsilon}}$$

where $(\partial \sigma^*/\partial T)_{\dot{\varepsilon}}$ is the slope of a σ^* *vs* T plot obtained at a constant strain rate.

(5) The dimensionless strain rate sensitivity n:

$$n = \frac{d \ln (\sigma^*)}{d \ln (\dot{\varepsilon})}$$

(6) The alternative strain rate sensitivity S:

$$S = \frac{d\sigma^*}{d \ln (\dot{\varepsilon})}$$

III. THE YOKOBORI ACTIVATION ENTHALPY

The present procedure differs from the traditional technique of analyzing stress strain data because of its use of the Yokobori[5] activation enthalpy:

$$H = H^0 \ln\left(\frac{\sigma_0^*}{\sigma^*}\right)$$

where H^0 is a material constant, σ_0^* the effective stress at 0 K, and σ^* the effective stress at a given temperature. Substituting this enthalpy into the thermally activated strain rate equation makes it possible to develop the following simple analytical expressions which completely describe the stress strain behavior.

R.E. REED-HILL, Professor Emeritus, C.V. ISWARAN, Postdoctoral Associate, and M.J. KAUFMAN, Professor, are with the Department of Materials Science and Engineering, University of Florida, Gainesville, FL 32611.
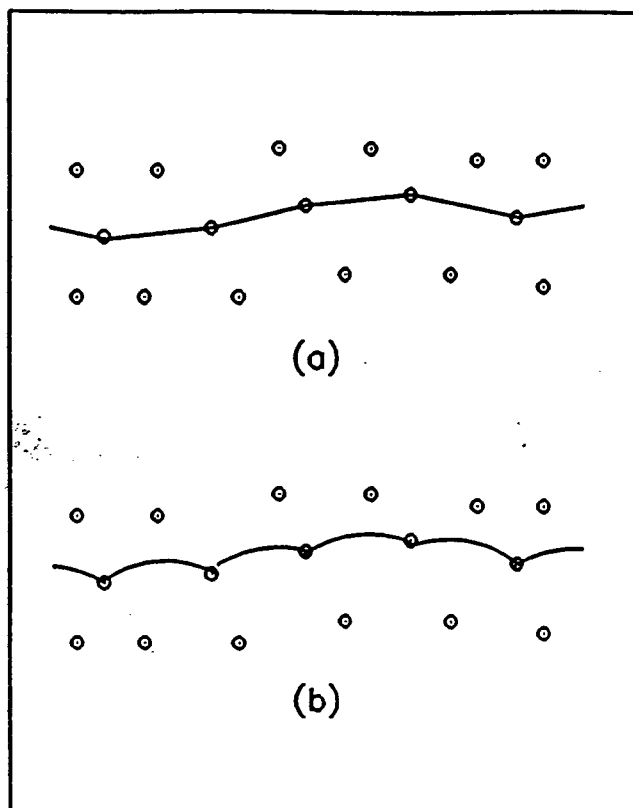
Fig. 1—Interstitials in solid solution have short range stress fields and, at low temperatures, they are effectively stationary. Thus, an unstressed and a stressed dislocation are assumed to look schematically like (a) and (b).[1]

(1) A simple power-law formulation describing the temperature dependence of the effective stress σ^*:

$$\sigma^* = \sigma_0^* \left(\frac{\dot{\varepsilon}}{\dot{\varepsilon}_0}\right)^{\frac{RT}{H^\circ}}$$

(2) A linear relationship between $\ln \sigma^*$ and temperature T:

$$\ln \sigma^* = \ln \sigma_0^* + \frac{R}{H^\circ} \ln \left(\frac{\dot{\varepsilon}}{\dot{\varepsilon}_0}\right) \times T$$

whose slope is $(R/H^\circ) \times \ln (\dot{\varepsilon}/\dot{\varepsilon}_0)$.

(3) The dimensionless strain rate sensitivity n:

$$n = \frac{RT}{H^\circ}$$

(4) The alternate strain rate sensitivity S:

$$S = n\sigma^*$$

(5) The activation volume v:

$$v = \frac{H^\circ}{\sigma^*}$$

(6) The material constant H°:

$$H^\circ = v\sigma^*$$

This signifies that H° is the work done per mole of thermally activated events by the effective stress.

When the preceding relations are substituted into the
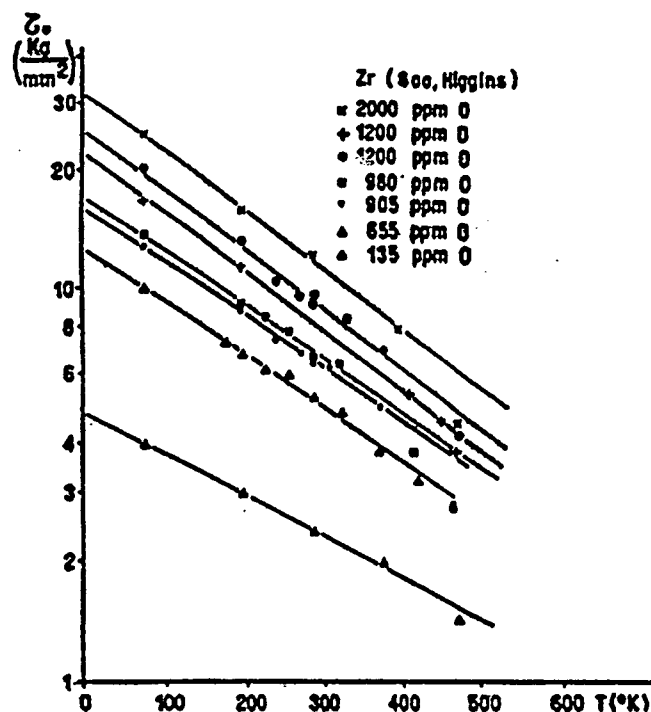
Fig. 2—The logarithm of the critical resolved shear stress vs temperature for zirconium single crystals doped with six levels of oxygen. Data of Soo and Higgins[6] as plotted by Ahlers.[7]

Conrad–Wiedersich equation, the latter reduces to the Yokobori activation enthalpy:

$$H = H^\circ \ln \left(\frac{\sigma_0^*}{\sigma^*}\right)$$

It should be emphasized that the Yokobori enthalpy requires the use of the effective stress, σ^*. However, if σ_μ is negligible, the previous relations based on the Yokobori enthalpy should still be valid, if the flow stress, σ, is introduced into the Yokobori enthalpy. An example of this is shown in Figure 2, where the logarithms of the critical resolved shear stresses of high purity single crystals of zirconium[6] doped with six levels of oxygen are plotted vs the temperature. This figure is due to Ahlers[7] who used the data of Soo and Higgins.[6] These linear plots not only imply that the data are consistent with the Yokobori activation enthalpy but also that the internal stress was negligible in these single crystals. This small σ_μ is consistent with the absence of grain boundaries, a low immobile dislocation density at the critical resolved shear stress (CRSS), and a base metal of high purity. However, it should be noted that when σ_μ is significant, the use of the flow stress in the Yokobori enthalpy is invalid.

IV. THE INTERNAL STRESS

A strong point of the present analysis is that it provides reliable techniques for determining σ_μ, one of which is based on S strain rate sensitivity data.[8] This allows σ_μ to be determined at 0 K and, if the temperature dependence of the shear modulus is known, σ_μ can be evaluated as a function of T. Subtracting this internal stress from the corresponding flow stress gives the desired values of σ^* at any temperature.

Traditionally, σ_μ has been evaluated by the back extrapolation (BE) technique, which assumes that the plateau region, in a constant $\dot\varepsilon$ plot of σ vs T, is a region of athermal deformation where σ^* is zero and $\sigma = \sigma_\mu$. However, these plateau regions are normally found to be intervals where dynamic strain aging occurs and the apparent independence of σ on temperature and strain rate is due to changes in the flow stress caused by DSA.

A proper evaluation of σ_μ is required in order to obtain a valid σ^* and power-law parameters H^0 and $\dot\varepsilon_0$, since they are ultimately dependent on the choice of σ_μ. In general, the BE technique overestimates σ_μ and thus underestimates σ^*.

V. EXAMPLES OF ANALYSES

Figure 3 shows[8] the results of an analysis, based on the Yokobori activation enthalpy, of the tensile stress strain data of a (bcc) commercial purity (CP) niobium published by Fries et al.[9] Note the excellent fit between the empirical data and the analytical equations, given previously, for the

temperature dependence of the S and n strain rate sensitivities, the flow stress σ, and the logarithm of the effective stress, ln σ^*. Similar analyses[10,11] have been made for a (hcp) CP titanium[12] and a two-phase (hcp + bcc) Ti-6Al-4V alloy.[13]

VI. THE DSA STRESS

Since DSA involves an increase in the level of the pinning of a dislocation by the interstitial solute atoms, it is reasonable to assume the DSA component of the stress may be directly added to that due to solid solution hardening caused by the in situ interstitial solute atoms. The procedures for evaluating the DSA component of the stress have been described in some detail elsewhere.[8,11] In brief, they are based on Sleeswyk's[14] proposal that while a dislocation waits at a barrier for thermal activation, it is subject to strain aging by mobile solute atoms. This waiting time is inversely proportional to the applied strain rate. With the aid of Sleeswyk's concept and the theories of static strain aging, one is able to compute meaningful DSA stresses pro-
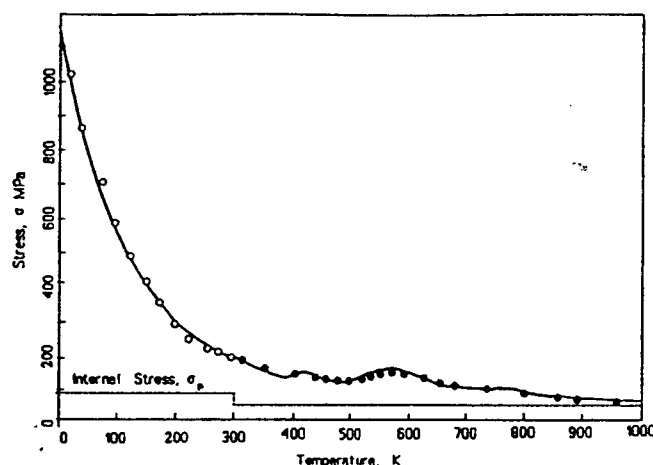
Fig. 4—CP Nb data[9] from below 300 K are plotted above with data[15] from 300 to 1000 K. The solid line is the flow stress ($\sigma = \sigma^* + \sigma_\mu + \sigma_{DSA}$), and the dashed lines represents σ_μ. Note that σ_μ is smaller above 300 K than below it because the flow stresses were measured at a smaller strain above this temperature (discussed in text).
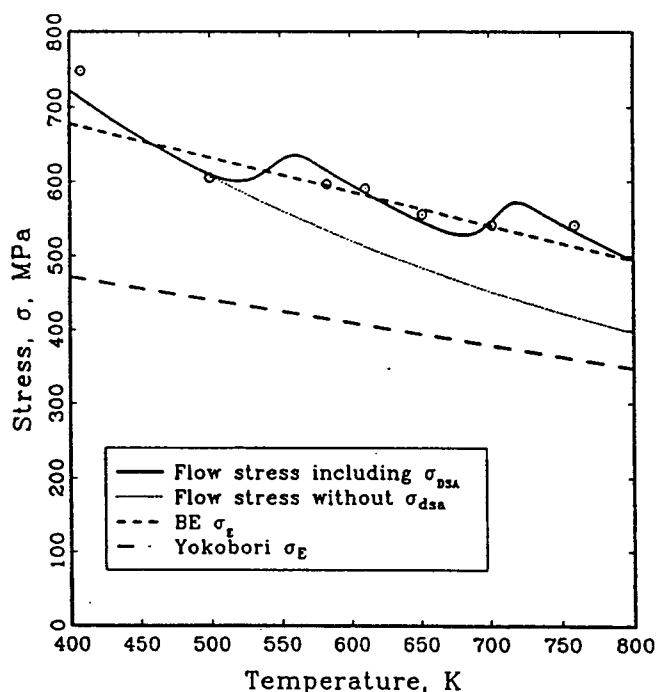
Fig. 5—Expanded view of the flow stress plateau of a Ti-6Al-4V alloy. Note the differences between the back extrapolated and Yokobori enthalpy versions of the internal stress.

vided the diffusion coefficients of the interstitial solutes in the metal under study are known. This DSA stress can then be added to the sum of the solid solution hardening stress component and the internal stress. An example of the application of this procedure is shown in Figure 4, where CP niobium data[15] from above 300 K are combined with those from below this temperature. It should be noted that below 300 K, lower yield stresses (2 pct strain) were recorded, while above this temperature, upper yield stresses (0.2 pct strain) were used. This difference in strain, at which the two sets of data were obtained, should correspond to a smaller internal stress above 300 K than below this temperature, since the internal stress should be smaller at the

smaller strain. The size of this decrease was estimated to be at least equal to the difference between the upper and lower yield stresses for their 300 K specimen. As a result, the internal stress above 300 K in Figure 4 is plotted at 43 MPa instead of at 86 MPa as below 300 K. Note the good fit of the analytical curve to the empirical data to approximately 1000 K.

An enlarged view of the plateau region of a Ti-6Al-4V alloy[13] is shown in Figure 5. This alloy was originally analyzed[13] by the BE technique which yielded a σ_μ that varies with temperature, as shown by the upper line (small dashes). Note that it makes a good fit with the data points and was thus a reasonable approach for defining the internal stress before the significance of the DSA phenomenon was understood. The lower line (long dashes) represents σ_μ, as determined by an analysis by the Yokobori enthalpy. In the plateau region, this internal stress is about 30 pct smaller than that based on the BE technique and gives the solid line for the total flow stress when the DSA contribution is included. As may be seen, it makes a better fit with the data points in the plateau region than does the BE σ_μ line.

VII. CONCERNING THE BACK EXTRAPOLATED INTERNAL STRESS

A number of "independent methods" for measuring the internal stress have been invoked in support of the BE approach. In our opinion, these determinations are unreliable. For example, consider the use of stress relaxation in Reference 13, where a Ti-6Al-4V specimen was strained to its 0.2 pct yield stress, the testing machine stopped, and the stress was allowed to relax for 1 day. In this period, the stress fell to 767 MPa, which was taken as an upper limit for the fully relaxed σ_μ at 300 K. This latter was determined by BE to be 726 MPa. The results of the 24-hour stress relaxation test are confirmed within the experimental error in Figure 6, where an analytical stress relaxation curve, based on an analysis using the Yokobori enthalpy, is shown for this same period. However, 1 day is hardly sufficient time to determine the fully relaxed stress for a function that relaxes exponentially. In this regard, Figure 7 shows the relaxation curve between 1 day and 100 years, with time plotted logarithmically. Note that the relaxed stress drops below the BE internal stress in a few days and reaches about 650 MPa at the end of 100 years. Even after a million years, it only falls to about 600 MPa.

VIII. DISCUSSION

There are basic difficulties when one attempts to apply a mechanistic interpretation to the analysis of these data. This results from the fact that the Yokobori activation enthalpy is associated with a force-distance relationship between a dislocation segment and an obstacle that varies as $1/r$, where r is the dislocation-obstacle distance. This type of interaction is long range. On the other hand, the force-distance relation between a point obstacle, such as an interstitial atom, and a dislocation segment varies as $1/r^3$ and, consequently, as mentioned earlier, has a very short range. From this, it can be concluded that the basic long range rate controlling mechanism is not overcoming solute atoms. It may be either (1) dislocation intersections, (2) thermally
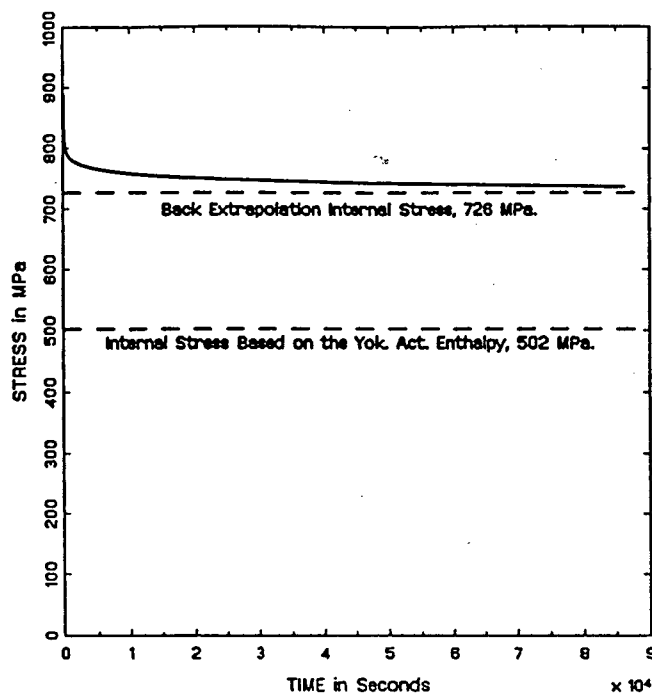
Fig. 6—Plot of stress relaxation *vs* time for a Ti-6Al-4V specimen at 300 K using an equation based on the Yokobori activation enthalpy. Note that the stress drops to about the BE internal stress in 1 day. However, as shown in Fig. 7, 1 day is hardly sufficient time to determine the completely relaxed stress (σ_u) of a system that relaxes exponentially.
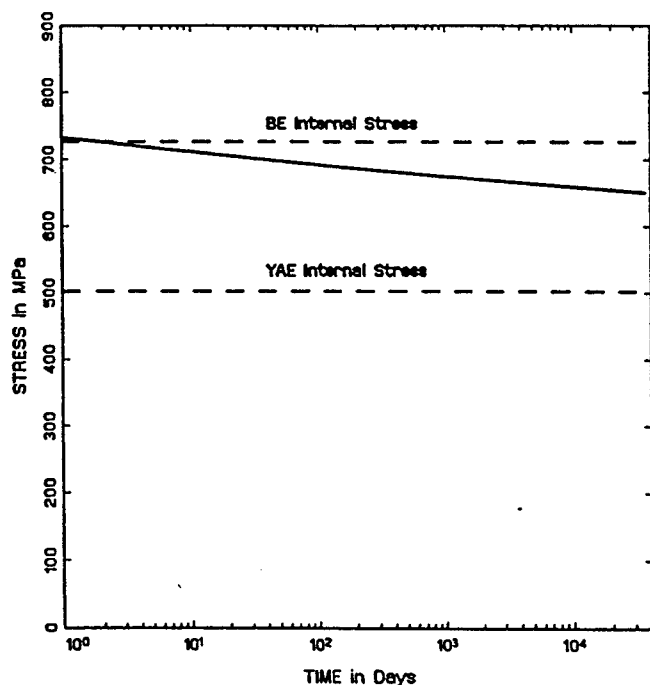

Fig. 7—The stress relaxation curve for a Ti-6Al-4V between 1 day and 100 years. Note that in several days the relaxed stress falls below the BE internal stress.

activated cross-slip, or (3) overcoming the Peierls stress or some other mechanism conforming to a 1/*r* force-distance relationship.

It is also significant that in Figure 2, the slopes of the ln σ^* *vs* *T* curves are parallel within the experimental error, implying that the rate controlling mechanism is similar for
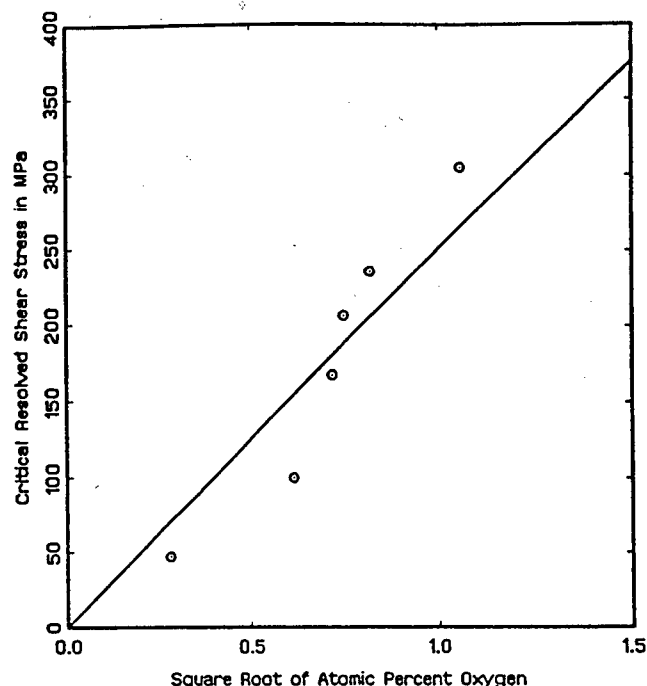
Fig. 8—A plot of the CRSS at 0 K of the Soo and Higgins zirconium single crystals as a function of the square root of their oxygen concentrations. This shows that the stress level depends markedly on the interstitial concentration.

a wide range of oxygen concentration levels. Furthermore, the oxygen level has a strong effect on the overall stress level, as illustrated in Figure 8, where σ_0^* is plotted against the square root of the oxygen concentration of the zirconium single crystals of Figure 2. This suggests that the pinning by the interstitial solute atoms might produce a basic friction stress so that the net effective stress could possibly be the sum of that required by the long range basic rate controlling mechanism and that needed to overcome the short range pinning of solute atoms lying along activated dislocation segments. This assumption needs to be further investigated carefully and in depth.

ACKNOWLEDGMENTS

REFERENCES

1. J.P. Hirth and J. Lothe: *Theory of Dislocations*, McGraw-Hill Book Company, New York, NY, 1968, pp. 623-26.
2. A.H. Cottrell and B.A. Bilby: *Proc. Phys. Soc.*, 1949, vol. A62, p. 49.
3. G. Schoeck and A. Seeger: *Acta Metall.*, 1959, vol. 7, pp. 469-77.
4. H. Conrad and H. Wiedersich: *Acta Metall.*, 1960, vol. 8, p. 128.
5. T. Yokobori: *Phys. Rev.*, 1952, vol. 88, p. 1423.
6. P. Soo and G.T. Higgins: *Acta Metall.*, 1968, vol. 16, p. 177.
7. M. Ahlers: *Metall. Trans.*, 1970, vol. 1, p. 2415.
8. R.E. Reed-Hill and M.J. Kaufman: *Acta Metall. Mater.*, 1995, vol. 43, pp. 1731-39.
9. J.F. Fries, B. Houssin, C. Cizeron, and P. Lacombe: *J. Less-Common Met.*, 1973, vol. 33, p. 373.

10. R.E. Reed-Hill, C.V. Iswaran, and M.J. Kaufman: *Scripta Metall. Mater.*, 1995, vol. 33, pp. 157-62.
11. R.E. Reed-Hill, C.V. Iswaran, and M.J. Kaufman: University of Florida, Gainesville, FL, unpublished research, 1996.
12. K. Okazaki and H. Conrad: *Acta Metall.*, 1973, vol. 21, p. 1117.
13. B. de Meester, M. Döner, and H. Conrad: *Metall. Trans. A*, 1975, vol. 6A, pp. 65-74.
14. A.W. Sleeswyk: *Acta Metall.*, 1958, vol. 6, p. 598.
15. J.F. Fries, C. Cizeron, and P. Lacombe: *Rev. Phys. Appl.*, 1970, vol. 5, p. 371.

An Analysis of the Flow Stress of a Two-Phase Alloy System, Ti-6Al-4V

R.E. REED-HILL, C.V. ISWARAN, and M.J. KAUFMAN

An analysis of the tensile deformation behavior of a two-phase body-centered cubic (bcc)-hexagonal close-packed (hcp) alloy, Ti-6Al-4V, has been made. This has shown that the temperature dependence of the flow stress, the logarithm of the effective stress, and the strain-rate sensitivities can be described by simple analytical equations if the thermally activated strain-rate equation contains the Yokobori activation enthalpy $H = H^0 \ln (\sigma_0^*/\sigma^*)$, where H^0 is a constant, σ^* the effective stress, and σ_0^* its 0 K value. The flow stress-temperature plateau region (500 to 600 K) also can be rationalized analytically in terms of oxygen dynamic strain aging in the alpha phase

I. INTRODUCTION

A power law was used in several recent articles, based on the Yokobori[1] activation enthalpy

$$H = H^0 \ln \left(\frac{\sigma_0^*}{\sigma^*} \right) \qquad [1]$$

where H^0 is a constant related to the work done by the applied stress during an activated event,[2] σ^* the effective stress, and σ_0^* its 0 K value. In these articles, it was shown that it is possible to model the tensile deformation behavior of body-centered cubic (bcc) commercial-purity niobium[3] and hexagonal close-packed (hcp) commercial-purity titanium.[4] It will now be demonstrated that this power-law model is also capable of rationalizing the two-phase (hcp-bcc) Ti-6Al-4V stress-strain data of De Meester et al.[5] Basically, the model assumes the effective stress σ^* is a function of the strain rate

$$\sigma^* = \sigma_0^* \left(\frac{\dot{\varepsilon}}{\dot{\varepsilon}_0} \right)^{\frac{RT}{H^0}} \qquad [2]$$

where $\dot{\varepsilon}$ is the strain rate, $\dot{\varepsilon}_0$ a material constant equal to the strain rate that makes σ^* equal to σ_0^* at any temperature, R the universal gas constant, and T the Kelvin temperature. At a constant $\dot{\varepsilon}$, Eq. [1] may be expressed as

$$\ln \sigma^* = \ln \sigma_0^* + \beta T \qquad [3]$$

whose slope is $\beta = (R/H^0) \ln (\dot{\varepsilon}/\dot{\varepsilon}_0)$. Note that β has dimensions T^{-1} and is a function of both $\dot{\varepsilon}_0$ and H^0. This latter is important because, to properly identify the slope for a given material, one needs to determine both $\dot{\varepsilon}_0$ and H^0.

An important parameter in empirical stress-strain analysis is the strain-rate sensitivity

$$S = \frac{d\sigma^*}{d \ln \dot{\varepsilon}} = \frac{d\sigma}{d \ln \dot{\varepsilon}} \qquad [4]$$

where it is assumed that $d\sigma = d\sigma^*$ since σ_μ, the internal

stress, by definition[3] does not vary during an isothermal change in strain rate. In terms of the power law, Eq. [4] may be written

$$S = \frac{RT}{H^0} \cdot \sigma^* \qquad [5]$$

In practice, S is determined experimentally using

$$S_m = \frac{\Delta \sigma}{\Delta \ln \dot{\varepsilon}} \qquad [6]$$

where S_m is the measured strain-rate sensitivity and $\Delta \sigma$ the incremental change in flow stress for a finite change in strain rate. Equation [4] assumes infinitesimal changes in $\ln \dot{\varepsilon}$ and σ^*, whereas experimentally, finite increments are used. It is possible to correct for this difference[6] with the following equation:

$$S = \frac{[k^{(RT/H^0)} - 1]}{\ln k} \cdot \sigma^* \qquad [7]$$

where k is the strain-rate change factor ($k = 5$ for the de Meester et al.[5] data). Equation [7] reduces to Eq. [3] in the limit as $k \rightarrow 1$. Finally, the exponent in Eq. [2] is also considered a strain-rate sensitivity factor, normally written as n, so that

$$n = \frac{RT}{H^0} \qquad [8]$$

Experimentally, n is determined by

$$n = \frac{d \ln \sigma^*}{d \ln (\dot{\varepsilon})} \qquad [9]$$

With the aid of the procedures in References 3, 4, and 6, the internal stress σ_μ for the de Meester et al. data was determined to be

$$\sigma_\mu = \sigma_{\mu_0} - 0.309T, \text{ MPa} \qquad [10]$$

where $\sigma_{\mu_0} = 595$ MPa. In Eq. [10], σ_μ has the temperature dependence of the Ti-6Al-4V shear modulus as given by de Meester et al.[5] In addition to σ_μ, it was determined that the material parameters in Eqs. [2] and [3] could be represented by their values in Table I, where σ_0 is the value of the flow stress at 0 K.

The parameters in Table I, which define the stress-strain

R.E. REED-HILL, Professor Emeritus, C.V. ISWARAN, OPS Professional, and M.J. KAUFMAN, Professor, are with the Department of Materials Science and Engineering, University of Florida, Gainesville, FL 32611.
Manuscript submitted February 27, 1996.

Table I. Parameters

$$\sigma_0 = 1890 \text{ MPa}$$
$$\sigma_{\mu_0} = 595 \text{ MPa}$$
$$\sigma_0^* = 1295 \text{ MPa}$$
$$H^\circ = 66000 \text{ J/mole}$$
$$\dot{\varepsilon}_0 = 4.56 \times 10^{10} \text{ s}^{-1}$$
$$\beta = 0.0041 \text{ K}^{-1}$$

behavior in the low-temperature regime (<500 K), were used to generate the model curves for the flow stress σ, the internal stress σ_μ, the effective stress σ^*, as well as the strain-rate sensitivities S and n (where $S = d(\sigma)/d \ln (\dot{\varepsilon})$ and $n = d \ln (\sigma^*)/d \ln (\dot{\varepsilon})$), all as functions of temperature in Figures 1(a) through (d), respectively. Above 500 K, a dynamic strain aging (DSA) component needs to be added to this baseline value, as is discussed subsequently.

II. DYNAMIC STRAIN AGING

The DSA is presumed to be due to the interaction of the interstitial atoms with the mobile dislocations. In this regard, the composition of the Ti-6Al-4V in wt pct was C = 0.022, O = 0.14, N = 0.010, H = 0.006, Al = 6.3, V = 4.2 or, in at. pct of interstitials, C = 0.08, O = 0.40, N = 0.03, and H = 0.028. Given the temperature range of the DSA phenomena and that the oxygen concentration was much higher than that of the other interstitials, it is reasonable to assume oxygen to be the primary source of DSA. In the two-phase structure of the Ti-6Al-4V alloy, DSA might occur in either the alpha or the beta phases or in both. Since the volume fractions of these phases were 77 and 23 pct, respectively,[5] one might expect that the DSA occurred primarily in the more abundant hcp alpha phase, making it analogous to that in the previously analyzed[4] hcp CP Ti of Okazaki and Conrad.[7] In that analysis, it was shown that a phenomenon similar to the Snoek effect was involved in the DSA that is due to jumps of interstitial atoms around the substitutional atoms of interstitial-substitutional atom pairs. Only a single DSA component was found in the CP Ti data below 800 K, the upper temperature of the data. However, for the Ti-6Al-4V data, a visual inspection of Figure 1(a) suggests that there may be two DSA peaks below this temperature. The additional DSA component is probably due to Cottrell strain aging, which is supported by an earlier alpha CP titanium static strain-aging investigation.[8] The DSA stress in Figures 1(a) and (b) was modeled along these lines of reasoning and assumed to be given by

$$\sigma_{DSA} = \left\{ \sigma_{i-s_{max}} \left[1 - \exp \left(-\frac{t_w}{\tau_{i-s}} \right) \right] \right.$$
$$\left. + \sigma_{cot_{max}} \left[1 - \exp \left(-\frac{t_w^{2/3}}{\tau_{cot}} \right) \right] \right\} \exp (\beta(T - 450)) \quad [11]$$

where σ_{dsa} is the DSA stress, $\sigma_{i-s_{max}}$ the maximum stress due to the i-s pair type of strain aging, $\sigma_{cot_{max}}$ the maximum stress for the Cottrell form of strain aging, t_w the waiting time of a dislocation at an obstacle for thermal activation, τ_{i-s} the relaxation time for i-s pair reordering, τ_{cot} the Cottrell relaxation time, and β is defined in Eq. [3]. The last term

in Eq. [11] normalizes the DSA stress to 450 K and gives it the same temperature dependence as the effective stress (see Reference 3). The values of the parameters used in Eq. [11] were $\sigma_{i-s_{max}} = 150$ MPa, $\sigma_{cot_{max}} = 380$ MPa, and $t_w = 0.33$ s, while the relaxation times were computed with

$$\tau_{i-s} = 5.49 \times 10^{-16} \exp \left(-\frac{1.60 \times 10^5}{RT} \right) \quad [12]$$

$$\tau_{cot} = 1.65 \times 10^{-12} \exp \left(-\frac{1.60 \times 10^5}{RT} \right)$$

where the pre-exponential term in τ_{i-s} is the same as in the CP Ti analysis[4] and τ_{cot} is taken as $3300 \times \tau_{i-s}$. In the bcc niobium analysis,[3] this factor was 5000. The waiting time t_w is the same as that for the CP Ti[4] analysis since the strain rate for Ti-6Al-4V was the same as that for the CP Ti. Equation [12] assumes an activation energy for the diffusion of oxygen in Ti-6Al-4V of 1.51×10^5 J/mole. This activation energy is somewhat smaller than Miller's torsion pendulum values[9] of 1.82×10^5 J/mole for oxygen diffusion in a Ti-10 at. pct Al alloy and 1.71×10^5 J/mole in a Ti-10 at. pct Zr alloy, both of which are alpha phase alloys.

The total flow stress in the oxygen DSA interval was accordingly

$$\sigma = \sigma^* + \sigma_\mu + \sigma_{DSA} \quad [13]$$

Note that the agreement between the analytical curve and the flow stress data of de Meester et al.[5] is very good. The plot in Figure 1(b) shows the variation of $\ln \sigma^*$ with T. Here again, the fit between the analytical curve and the data is good.

III. THE STRAIN-RATE SENSITIVITIES

With respect to the strain-rate sensitivities that are functions of the stress increments produced by strain-rate changes, it was noted by the authors[5] that "significant 'positive' yield points for strain-rate increases and 'negative' yield points for strain-rate decreases were observed between 210 and 700 K." Because of these yield points, two values of $\Delta\sigma$ were recorded: (1) the "peak" or maximum value of the stress increase observed on a rate increase and (2) the "extrapolated" value obtained by extrapolating the subsequent flow stress curve back through the yield point. These two sets of $\Delta\sigma$ data are shown in Figure 2, which is copied from the authors' article.[5] Peak values are represented as open circles and extrapolated values as crosses. In Figures 1(c) and (d) analytical curves based on Eqs. [7] and [9] are plotted that show the strain-rate sensitivities S and n as functions of temperature and compares them with the empirical S and n data points based on the peak $\Delta\sigma$ values in Figure 2. Except for the 78 K data point, the agreement of both analytical curves with the data is excellent up to 500 K. Above 500 K, pronounced DSA occurs, which explains abberations in both the S and n plots. With regard to the S data point at 78 K, which falls well above the analytical S curve, it should be noted that the accuracy of measuring a small increase in a large flow stress resulting from a strain-rate change of only a factor of 5 is not large at 78 K. Furthermore, the authors' plotted
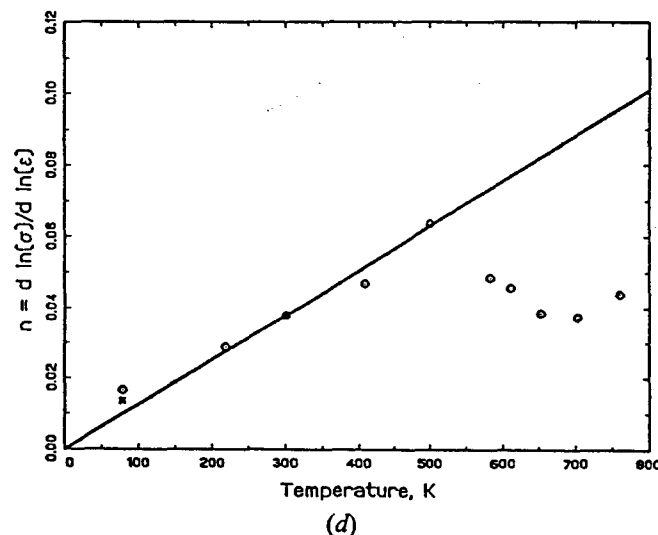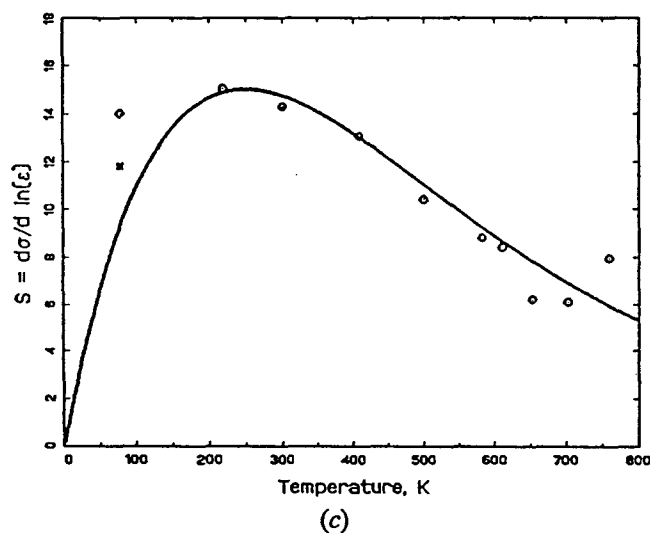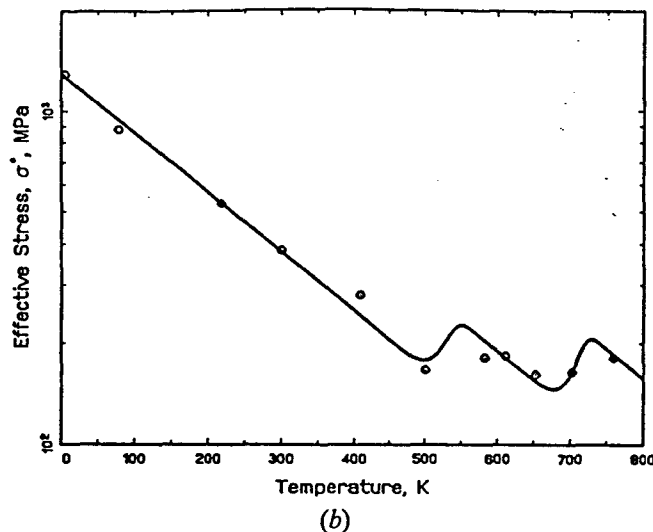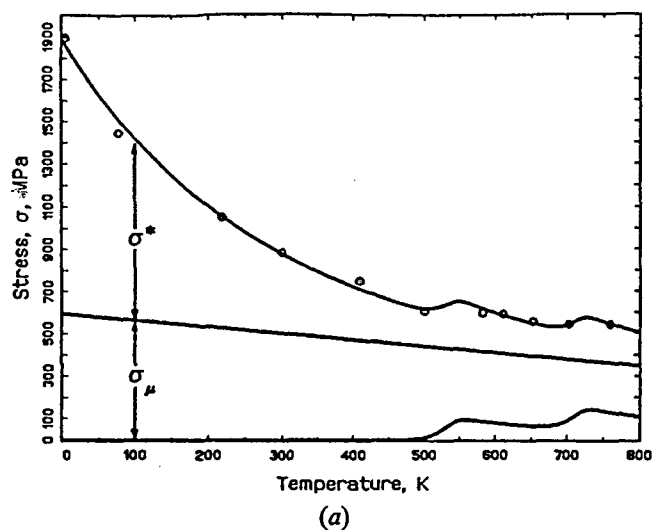
Fig. 1—Analytical curves based on the Yokobori power law plotted with the de Meester *et al.* empirical data[5] obtained from Ti-6Al-4V specimens of 5-μ grain size: (a) σ vs T, (b) ln σ* vs T, (c) S vs T, and (d) n vs T.
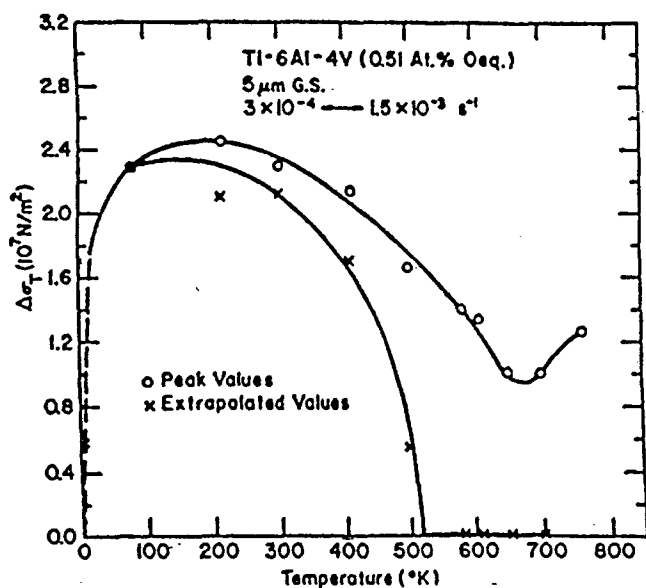

Fig. 2—De Meester *et al.*'s[5] Fig. 5, showing the two types of Δσ stress increments obtained using a factor of 5 increase in the strain rate.

78 K stress-strain curve suggests that the size of the 78 K Δσ may have been overestimated by about 20 pct. Accounting for this would lower the 78 K point to the position marked by a ★ in Figure 1(c). This change would also have an effect on the position of the 78 K n data point, as shown in Figure 1(d).

IV. THE ACTIVATION ENTHALPY

The temperature dependence of the activation energy was determined by the authors with the aid of the Conrad–Wiedersich equation

$$Q^* = - Tv \left(\frac{d\sigma^*}{dT} \right)_{\dot{\varepsilon}} \qquad [14]$$

where T is the absolute temperature, v the activation volume ($v = RT \, (\partial \ln \dot{\varepsilon}/\partial \, \sigma)_T$), and $(d\sigma^*/dT)_{\dot{\varepsilon}}$ the slope of the constant strain rate σ^* vs T curve. Equation [14] was evaluated by the authors in terms of a back extrapolated (BE) internal stress designated here as $\sigma_{\mu_{bc}}$. As may be seen in Figure 3(a), $\sigma_{\mu_{bc}}^0$ was equated to the flow stress σ at 538 K,
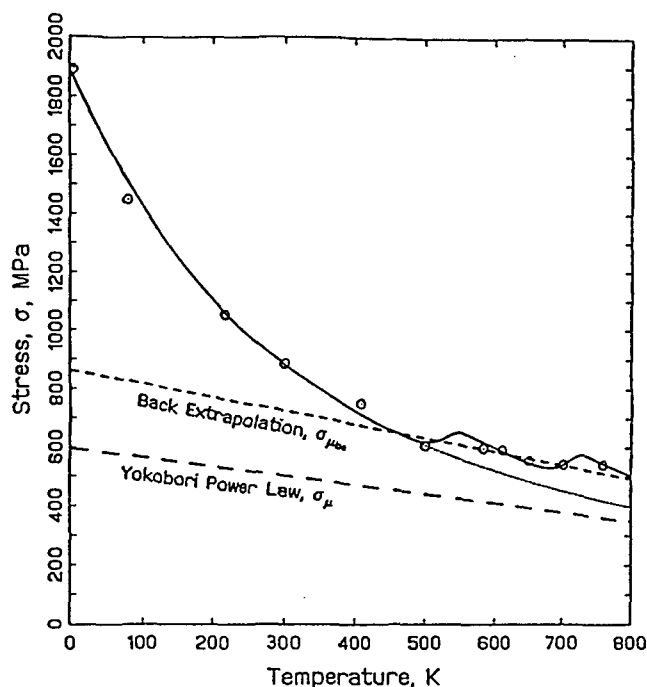
Fig. 3—Plot of σ vs T, illustrating the difference between the back extrapolated internal stress and the Yokobori power-law formalism internal stress.
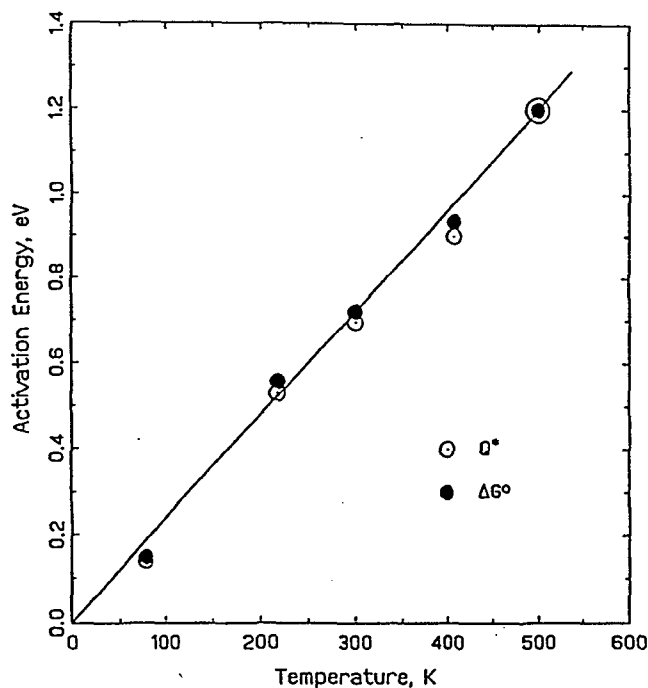
Fig. 4—Replica of the de Meester et al.[5] plot of Q^* and ΔG^0, where Q^* is the Conrad–Wiedersich activation enthalpy and $\Delta G^0 = Q^0 + 1/2\ \alpha v \sigma^*_{be}$.

at the start of the σ vs T flow stress plateau, and then $\sigma_{\mu_{be}}$ at any other temperature was given the temperature dependence of the shear modulus μ. The following relation gives the temperature dependence of $\sigma_{\mu_{be}}$:

$$\sigma_{\mu_{be}} = 858 - 0.460T \qquad [15]$$

A basic feature of this BE technique is that σ^* is assumed to be zero at and above 538 K. The relation of $\sigma_{\mu_{be}}$ in Eq.

[15] to the experimental data is shown in Figure 3, where it may also be compared to the internal stress σ_μ based on the Yokobori formalism in Eq. [10]. Note that $\sigma_{\mu_{be}}$ is just over 40 pct larger than σ_μ. The effective stress between 0 and 500 K was next evaluated with the aid of the following equation:

$$\sigma^*_{be} = \sigma - \sigma_{\mu_{be}} \qquad [16]$$

at the five temperatures between 0 and 538 K, where flow stress measurements had been made. The results were then plotted in a σ^*_{be} vs T curve whose slope was used in the Conrad–Wiedersich equation. Next, the extrapolated $\Delta\sigma$ measurements of Figure 2 were used to determine the activation volume at these five temperatures. The extrapolated $\Delta\sigma$ values were used because they were zero between 540 and 700 K, a fact interpreted by de Meester et al. as confirming the alloy was strain-rate insensitive in the flow stress plateau region. This is now recognized as inconsistent with the existence of DSA in this region. Values of Q^* calculated on the preceding assumptions are plotted against the temperature in Figure 4. Here the Q^* data are open circles, while the filled circles represent a function $\Delta G^0 = Q^* + \frac{1}{2}\alpha v \sigma^*$, where $\alpha = (T/\mu)d\mu/dT$. The $\frac{1}{2}\alpha v \sigma^*$ term was stated by the authors to be a correction "for the changes in dislocation segment length l which occur during the temperature and stress changes made to obtain the deformation partials $\partial\sigma^*/\partial T|_{\dot\varepsilon}$ and $\partial \ln \dot\varepsilon/\partial\sigma|_T$ of the Conrad–Wiedersich equation."[5] It was also noted by de Meester et al. that this correction was small, as may be seen in Figure 4. The slope of the line drawn through these data was then used in conjunction with the thermally activated strain-rate equation

$$\dot\varepsilon = \dot\varepsilon_0 \exp\left(-\frac{H}{RT}\right) \qquad [17]$$

to determine $\dot\varepsilon_0$, which yielded $\dot\varepsilon_0 = 4.5 \times 10^8$ s^{-1}. This differs significantly from the $\dot\varepsilon_0 = 4.56 \times 10^{10}$ s^{-1} value in Table I. It should be noted that by Eq. [3], if one couples $\dot\varepsilon_0 = 4.5 \times 10^8$ s^{-1} with $H^0 = 56,650$ J/mole, it is possible to obtain the slope $\beta = 0.0041$ for the ln σ^*_{be} vs T diagram so that it is possible to fit analytical σ vs T and ln σ^*_{be} vs T curves to the empirical data, as may be seen in Figures 5(a) and (b). On the other hand, note that in Figures 5(c) and (d), where analytical S and n curves based on extrapolated values of $\Delta\sigma$ of Figure 2 are shown, the fit is very poor.

A comparison between the de Meester et al.[5] activation energy and that predicted by the Yokobori activation analysis is shown in Figure 6. In this figure, the upper solid straight line is a plot of Eq. [1], $H = H^0 \ln (\sigma^*_0/\sigma^*)$ vs T. The lower dashed line is the de Meester et al. $G^0 - Q^*$ line of Figure 4.

V. DISLOCATION KINETICS

The ln σ^* vs T plot in Figure 1(b) shows that the ln σ^* data plots linearly to just above 500 K. This strongly suggests that (1) the low-temperature rate-controlling mechanism corresponds to one with a Yokobori activation enthalpy, and (2) the internal stress σ_μ of Eq. [10] is correct. The Yokobori activation enthalpy (Eq. [1]) is associated[2] with a mechanism in which the force between a dislocation
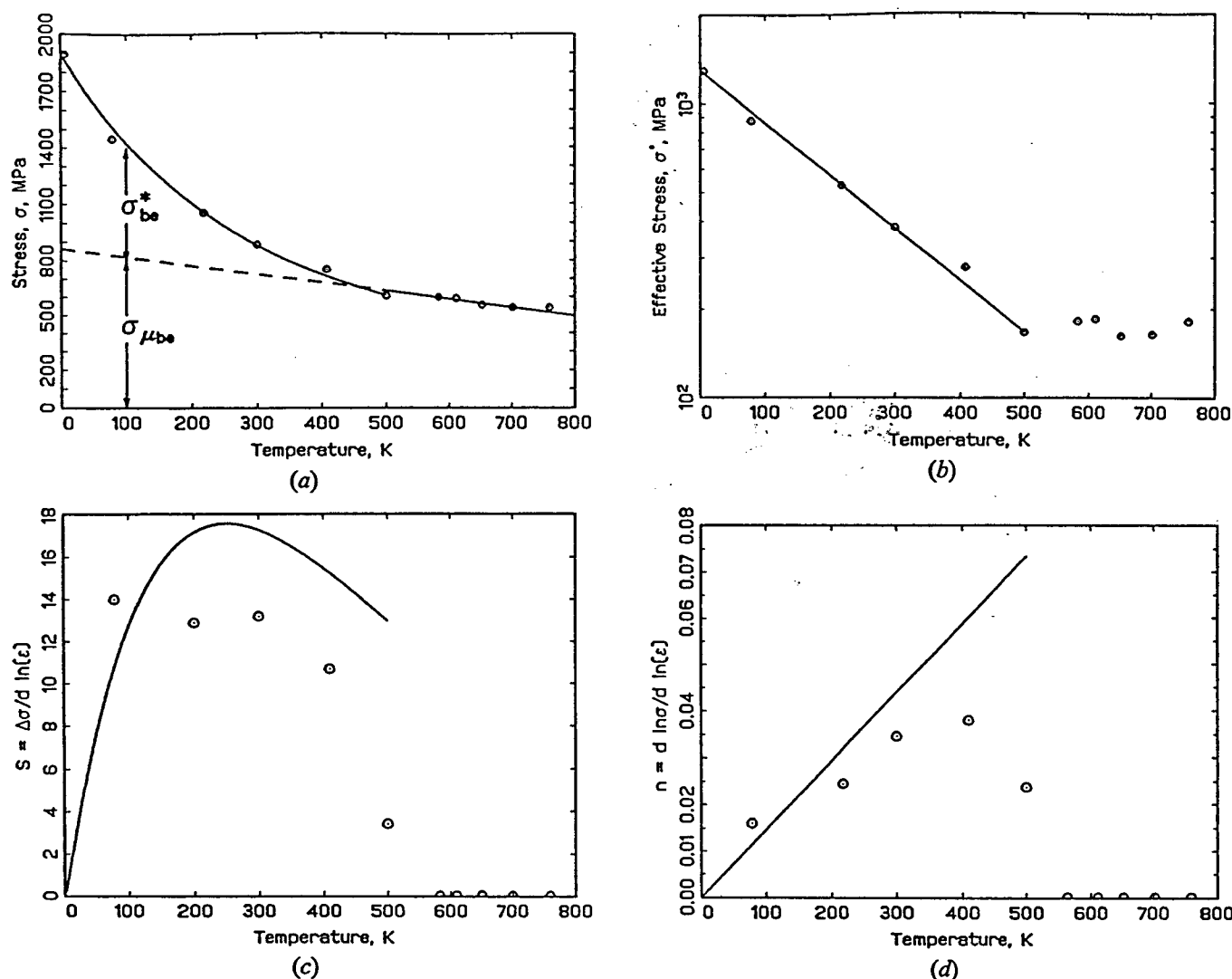
Fig. 5—(a) through (d) The curves in Fig. 1 replotted assuming that the internal stress, $\sigma_{\mu_{be}}$, is obtained by the back extrapolation technique.

segment and a barrier to its motion varies inversely as the distance r between them (*i.e.*, as $1/r$). As a result, one may conclude that the basic rate-controlling mechanism cannot be overcoming interstitial atom barriers since the force between a point defect and a dislocation segment is predicted to vary as $1/r^3$[10] and not as $1/r$. Theory does show that there are at least three types of barriers consistent with a $1/r$ force-distance relationship. These are (1) dislocation intersections,[11] (2) thermally activated cross-slip,[12,13] and (3) overcoming the Peierl's barrier.[14] As a result, it is proposed that solute atoms work in conjunction with a barrier of the $1/r$ type. An important factor in this regard is that the $1/r^3$ force-distance relation between an interstitial atom and a dislocation segment should be short range and should only involve solute atoms lying very close to the dislocation. As pointed out by Hirth and Lothe,[10] "at temperatures so low that diffusion is neglible, a dislocation becomes wiggly, adjusting its configuration to conform to the internal stresses of the immobile solute atoms." This can be interpreted as meaning a dislocation at rest should be effectively pinned by the solute atoms with which it is in contact. Thus, a mobile dislocation halted before forest

dislocations will have to overcome the pinning action of the solute atoms before it can cut through a tree and move ahead. The total stress required to move a dislocation segment should then equal that to cut the tree plus that required to unpin it from the solute atoms. Alternatively, a dislocation segment that either undergoes a cross-slip event or overcomes a Peierl's force barrier should also have to tear itself away from the pinning solute atoms along its length.

The preceding proposal for the dual nature of the activation enthalpy relation of Eq. [16] implies that the temperature dependence of the effective stress is primarily determined by the basic rate-controlling mechanism (dislocation intersections, *etc.*), whereas at a given temperature, σ^* is determined by the solute concentration. This is supported by Figure 12 of the de Meester *et al.* article,[5] which shows that at both 4.2 and 300 K, the effective stress varies approximately as the square root of the interstitial solute concentration in a number of titanium alloys with solute concentrations of the order of 1 wt pct or less. Furthermore, this square-root dependence of σ^* on solute concentration has also been predicted theoretically for dilute-solute concentrations.[10]
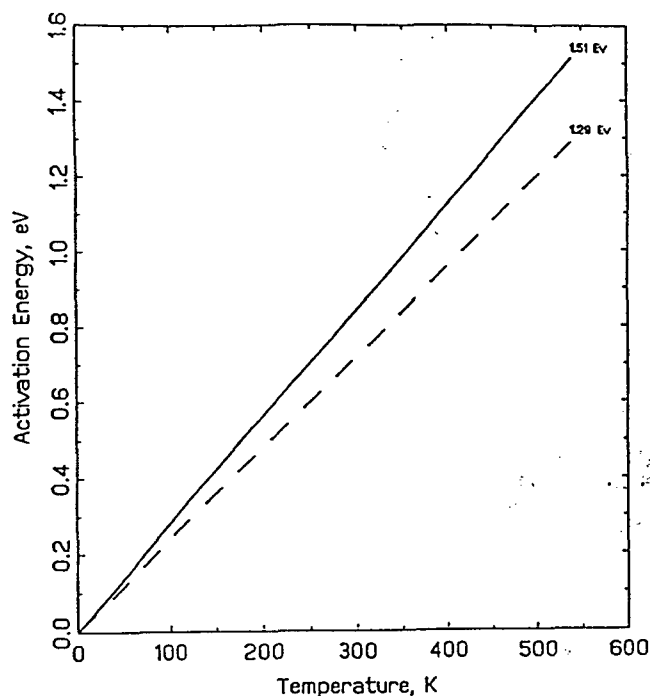
Fig. 6—Comparison of the temperature dependence of the activation energy determined by the Yokobori activation enthalpy (solid line) and the de Meester et al.[5] Q^* (dashed line).

VI. CONCLUSIONS

1. If the Yokobori activation enthalpy is substituted for the enthalpy of the thermally activated strain-rate equation, a set of mathematical relationships can be formulated capable of accurately describing the mechanical properties of not only a bcc and a hcp metal of commercial purity but also a two-phase bcc-hcp alloy, Ti-6Al-4V.
2. With these equations, it is not only possible to describe the mechanical behavior below those temperatures in which DSA is significant but also well into the DSA interval commonly designated as the flow stress plateau.
3. De Meester et al.[5] determined the internal stress by the back extrapolation technique. This resulted in an internal stress slightly over 40 pct larger than that found by the present formalism based on the Yokobori activation enthalpy. There are several inherent problems with using the back extrapolation method. First, it overestimates the size of the internal stress, which leads to an underestimation of the magnitude of the effective stress, and, second, it requires the effective stress to become zero in the DSA plateau. These two factors make it impossible to describe the temperature and strain-rate dependence of the effective stress with simple mathematical equations capable of predicting the stress-strain behavior. Consequently, it is concluded that the back extrapolation technique should be used with extreme caution, if at all.

4. The flow stress data in the DSA interval above 500 K in Ti-6Al-4V can be modeled on the assumption that they correspond to DSA that occurs in the alpha phase.
5. The Yokobori activation enthalpy requires a $1/r$ long-range force-distance relationship between a dislocation segment and an obstacle to its motion while a point defect, such as an interstitial atom, has a $1/r^3$ short-range force-distance relationship. It is, therefore, proposed that the mechanism controlling the strain rate is one with a $1/r$ relationship such as dislocation intersections. The short-range nature of the interaction between a dislocation and an interstitial atom suggests that a dislocation segment, whose motion is thermally activated, is pinned by interstitials. Thus, the net effective force required to move the dislocation segments should equal the sum of that needed to cut through a forest dislocation plus that required to free the segments from the pinning action of the interstitial atoms. As pointed out previously,[2] it appears that the temperature dependence of the effective stress is a function of the rate-controlling mechanism (dislocation intersections, etc.), whereas at a given temperature, σ^* is determined by the solute concentration. However, this matter needs to be further investigated both carefully and in depth.

ACKNOWLEDGMENT

REFERENCES

1. T. Yokobori: Phys. Rev., 1952, vol. 88, p. 1423.
2. R.E. Reed-Hill, C.V. Iswaran, and M.J. Kaufman: Metall. Mater. Trans. A, 1996, vol. 27A, pp. 0000-00.
3. R.E. Reed-Hill and M.J. Kaufman: Acta Metall. Mater., 1995, vol. 43, pp. 1731-39.
4. R.E. Reed-Hill, C.V. Iswaran, and M.J. Kaufman: Scripta Metall. Mater., 1995, vol. 33, pp. 1157-62.
5. B. de Meester, M. Döner, and H. Conrad: Metall. Trans. A, 1975, vol. 6A, pp. 65-75.
6. C.V. Iswaran, R.E. Reed-Hill, V.I. Levit, and M.J. Kaufman: Scripta Metall. Mater., 1995, vol. 32, pp. 941-47.
7. K. Okazaki and H. Conrad: Acta Metall., 1979, vol. 21, pp. 1117-29.
8. J.R. Donoso and R.E. Reed-Hill: Metall. Trans. A, 1977, vol. 8A, pp. 945-48.
9. D.R. Miller: TMS-AIME, 1962, vol. 224, pp. 275-81.
10. J.P. Hirth and J. Lothe: Theory of Dislocations, McGraw-Hill Book Company, New York, NY, 1968, pp. 623-26.
11. C.S. Hartley: 2nd Int. Conf. on Str. Metals and Alloys, ASM, Metals Park, OH, 1970, pp. 429-33.
12. G. Schoeck and A. Seeger: Defects in Crystalline Solids, Physics Society, London, 1955, p. 340.
13. H. Wolf: Z. Natur forsch., 1960, vol. 15a, p. 180.
14. A. Seeger: Phil. Mag., 1956, vol. 1, p. 651.

CHALLENGES IN THE DEVELOPMENT AND APPLICATION OF β-NiAl AS A

STRUCTURAL MATERIAL

V.I. Levit, J. Hu, I.A. Bul, J.S. Winton and M.J. Kaufman

Dept. of Materials Science and Engineering
University of Florida
Gainesville, Florida 32611

Abstract

High purity single crytals of stoichiometric NiAl have been deformed in tension over a range of temperatures and strain rates. Elongations approaching 35% are possible at room temperature when the sample geometry is controlled properly whereas elongations as high as 200% have been achieved at intermediate temperatures (e.g., 600K). Subsequent analysis of the dislocation substructure, the macroscopic shape change and the nature of the fracture indicate that deformation in the soft-oriented crystals is dominated by slip of <001> dislocations and that the material remains brittle even when the elongations are as high as 200%. Finally, the implications of these results on the applicability of NiAl as a structural material are discussed in some detail.

P.

The

185

Introduction

In the past decade, there has been a resurgence of interest in developing β-NiAl as a structural material. This is largely a consequence of its high melting temperature, reasonably low density and excellent oxidation resistance. As with many other intermetallics, however, NiAl has low toughness at low temperatures and low strength at all temperatures. Clearly, the challenge has been to enhance both the strength and toughness of this compound although most studies have tended to address one deficiency while largely ignoring the other.

There have been several excellent reviews on the subject of NiAl (1, 2). Based on these reviews as well as more recent publications, a number of things that influence the mechanical properties of NiAl have been identified as summarized below:

a. deviations from stoichiometry;
b. concentration of thermal vacancies as influenced by heat treatment (3, 4);
c. substitutional and interstitial impurities (4, 5, 6, 7, 8);
d. surface condition (9);
e. orientation (single crystals) (10, 11);
f. texture (polycrystals) (12); and
g. prestraining to produce mobile dislocations (13, 14, 15);

The purpose of this paper is to discuss some of these issues along with some new experimental data that will allow us to make some definitive statements concerning the viability of NiAl as a potential engineering material.

Low Temperature Properties

It is well established that the critical resolved shear stress (CRSS) for <100> slip in NiAl is quite low although there is considerable controversy as to the actual values, slip planes, etc. Clearly, the various published data mentioned above indicate that the CRSS is strongly dependent on such parameters as purity, thermal history, deviations from stoichiometry, prestrain, etc. It is also widely accepted that the number of active slip systems in NiAl is insufficient to allow for the "general" deformation of a random polycrystalline body according to the von Mises criterion. What has not been addressed adequately in our view is the rather low tensile ductility in single crystals oriented in soft (non-<100>) directions. Specifically, the question of why high purity NiAl, which has a very low CRSS (~60 MPa) when oriented for single (e.g., tensile axis (TA) parallel to <112>) or double (e.g., TA parallel to <011>) slip, fractures after elongations typically below 5% remains unanswered. In addition, it is also unclear why NiAl single crystals microalloyed with Fe, Mo and Ga displayed higher elongations when tested parallel to <110> (double slip) than the single slip orientations in the study by Darolia, et al. (16).

In this study, the initial tensile specimens were cut with an EDM to have rectangular (nominally 1.6 x 2.4 mm prior to electropolishing) cross sections, 10-15 mm gage lengths and 25-30 mm total lengths instead of the cylindrical button-head geometry (produced by centerless grinding) used in the majority of the previous studies to date. In the preliminary tests with [2̄13] (tensile specimens, elongations above 25% were achieved at room temperature. Furthermore, it became clear that the elongation was strongly dependent on the orientation of the slip plane and direction relative to the face and side of the specimen; i.e., the highest elongations were obtained

with the slip plane orthogonal to the 2.4 mm "face" of the specimen (see Fig. 1). Furtherm it was noted that (1) the change in the geometry and dimensions of the gage cross section the rotation of the tensile axis during the deformation, and (3) the measured work hardening were all consistent with the deformation occurring mostly by single slip on the [001](system and that the slip plane is not (hk0) where h≠k as was suggested as a possibilit Takasugi, et al. (11). TEM analysis of these samples after different elongations reveale presence of pile-ups of edge dislocations with b=[001] on (1̄10) planes. These were sp approximately 1 mm apart depending on the deformation level. No pure screw disloca were observed consistent with their elastic instability as pointed out by Loretto (17).

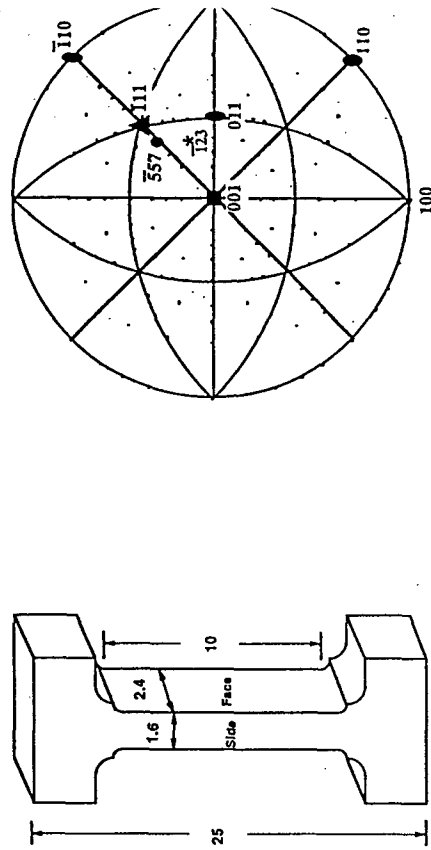Figure 2 - Stereographic projection with relevant directions indicated.

Figure 1 - Geometry of tensile specimens used in the current study. All dimensions in mm.

In order to examine this phenomenon more thoroughly, tensile specimens were intentior oriented for single slip with their TA parallel to either [5̄57] or [111] (Schmid factors of and 0.47, respectively) (see Fig. 2). For these orientations, the specimen rotation due to slip the [001]/(1̄10) system is about the orthogonal [110] axis. Thus, the specimens were cut either the (110) plane parallel to the face or side in Fig. 1 in order to provide insight into specimen constraint and geometry issue. The results of these tests are summarized in Tat where it is apparent that (1) the strengths are indicative of high purity material and (2) samples with their faces cut approximately parallel to (110) exhibit considerably la elongations (9-34%) compared with the samples cut with their sides parallel to (110) (15%). In all cases, the ensuing fracture was brittle cleavage in spite of the single slip natur the deformation which usually does not lead to brittle fracture. Finally, the measured v hardening rates were also consistent with single slip being approximately 5×10^{-4} times the s modulus, μ, in the [001] direction where μ_{001} = 112.1 GPa according to Wasilewski (18) order to determine what factors led to the higher elongations in the "Face (110)" specim such things as specimen cross section, constraints in the grips, and gage length were va systematically. The results indicate clearly that constraints in the grip are important at plastic strains and become less important at the higher elongations (above ~3%). This app to be the reason that the cylindrical, button-head specimens exhibit higher elongations w tested parallel to <110> as it is this orientation in which there is no rotation as described ab However, for the purer crystals that undergo higher elongations, it appears that it is

single crystals of compounds that have fewer than five independent slip systems yet where Von-Mises criterion is only applicable to polycrystalline deformation or to complex loadin single crystals. This work suggests that multiple systems are required for uniaxial te: deformation of single crystals oriented for easy glide if the sample is constrained whereas removal of the constraints allows the sample to deform to larger strains before the stres: some sort of stress concentration(s) reaches the fracture stress. In other words, materials : as NiAl that have low CRSS values are still likely to be brittle in single crystal form wher. other slip systems have much higher CRSS values. Such behavior has been observed in cer: oxides such as MgO which is also both soft and brittle. In both materials, the st: concentrations that develop during deformation can not be relieved by activating other systems.

Influence of Temperature on Deformation Behavior

Based on the realization of the importance of specimen geometry on tensile elongation, sim samples of binary NiAl were tested over a range of temperature. The results for [111] crys (Fig. 4) clearly indicate that the CRSS is a strong function of temperature as is characteristic BCC and HCP metals and alloys. Significantly, finite elongations were also measurable at s ambient temperatures (Fig. 5).

As the testing temperature is increased above room temperature, the tensile elongation incre: to high values (above 200% in some cases) at intermediate temperatures (e.g., 600K) and t decreases again much like in the reports of Takasugi, et al. (20) and Lahrman, et al. (21) (F 5). It is also clear that the present specimen geometries were superior for achieving hig elongations at all temperatures and that the temperature range of the high elongations in the specimens was considerably larger than in the previous investigations. Typical load-elongation curves for the samples undergoing the highest elongations are shown in Fig. 6a where it is clear that the load decreases after yielding before increasing again. This drop in load is quite gradual and is not characteristic of typical Lüders behavior where the drop is much more rapid. In an effort to analyze this behavior more completely, the crosshead was stopped at different points on the stress-strain curve, the sample was then cooled to room temperature and the specimen photographed. This examination allowed us to note that the sample begins to neck immediately after yielding; this neck continues to localize and then stops as the work hardening increases the flow stress locally. Based on these intermediate observations, it is possible to draw approximate shear stress-shear strain curves; the results (Fig. 6b) imply that the shear stress doesn't drop and that the work hardening rate is quite low except at the localized region of the neck. It should be mention that similar results have been observed in Cu-In single crystals (22) and Mg crystals (2:

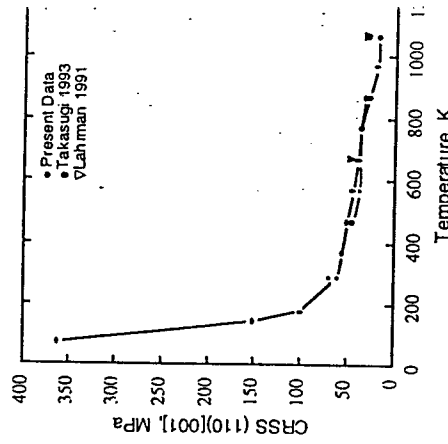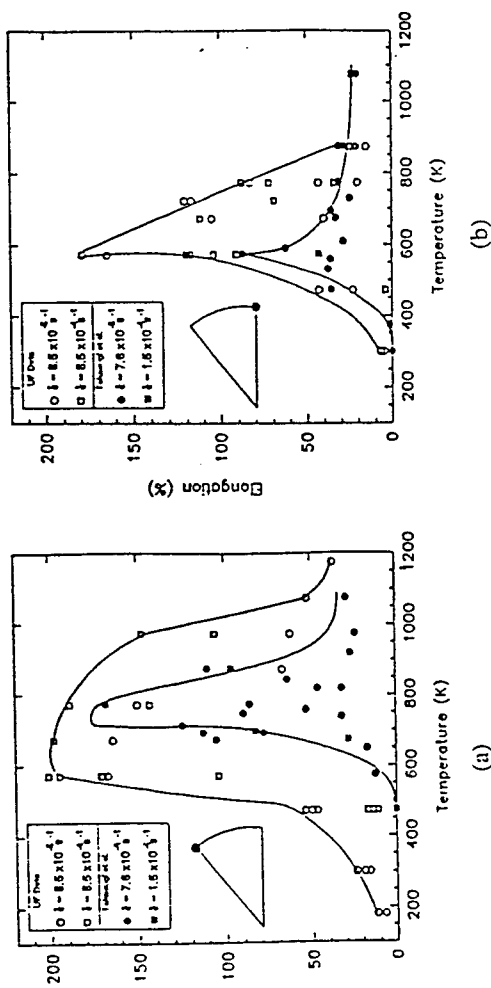Figure 4 - CRSS vs. temperature for t [001](1̄10) slip system take from tests on [111] specimens.

specimen geometry (the aspect ratio) which is more important for achieving the higher strains. In fact, when single slip causes the cross section to change from rectangular to square, the elongations are typically greater than those where the aspect ratio deviates further from square. This clearly had a greater effect than changes in the gage length or whether the face or side was parallel to the slip direction. Typical shear stress - shear strain curves depicting this behavior are shown in Fig. 3. These variations and their effects on properties will be covered in greater detail in a separate paper. TEM analysis of the deformation substructure in these specimens revealed again that the dislocations present after deformation were similar to those observed in the [123] specimens (19).

As mentioned above, specimens oriented for double slip with their TA along [011] were also investigated. Unlike the single slip samples, however, this orientation is stable with respect to rotation during straining due to the offsetting nature of the two active slip systems, namely [001](010) and [010](001) which are at right angles to each other. The results of this comparison indicated that (1) this orientation is indeed stable with respect to rotation, (2) the tensile elongations are lower than in the single slip samples, (3) the CRSS for slip of b=<001> dislocations on cube planes is similar to that on (011) planes, and (4) the work hardening rate is about an order of magnitude higher than for the single slip case. For the comparison of CRSS values, specimens taken from the same crystals indicate that, indeed, the CRSS values are similar (60 ± 5 MPa).

The dislocations observed in the samples tested in this orientation were also primarily edge in nature and again were distributed as pile-ups parallel to the cube slip planes. As anticipated, there were approximately equal amounts of dislocations corresponding to the two slip. The unusual geometry of double slip in NiAl and the manner in which dislocation intersections might occur is quite interesting and will be addressed further in a subsequent paper.

In light of these high tensile elongations at room temperature, it is of interest to reconsider the issue of low elongation in

Sample Description	$\sigma_{0.2\%}$ MPa	Elong. %	σ_f MPa
Side (110) 15 mm gage	140	6.2	205
	132	4.5	184
	127	10.3	196
	137	15.0	239
	134	12.6	221
	141	2.5	183
Face (110) 15 mm gage	101	16.6	196
	98	9.4	158
	100	22.0	195
	97	12.1	215
	94	26.0	203
	105	13.9	188
Face (110) 10 mm gage	115	17.9	218
	114	33.9	266
	109	16.2	190

Table 1 Mechanical properties of NiAl crystals tested parallel to <5̄57> at room temperature.

Figure 3 - Shear stress vs. shear strain for [5̄57] crystals tested at room temperature illustrating the importance of the specimen geometry on elongation.

The drop-off in the elongation at elevated temperatures (Fig. 6a) can be correlated with increased tendency for the material to neck prior to fracture (Fig. 7). When the strain rate sensitivity and work hardening rates were examined as a function of temperature, it became obvious that the strain rate sensitivity increases with increasing temperature whereas the work hardening rate drops off presumably due to dynamic recovery effects. However, the drop in work hardening rate outweighs the increase in SRS resulting in the increase tendency for the necks to localize the deformation and lead to fracture at shorter total elongations.

Implications of Deformation Behavior

Taken collectively, the present result indicate that high elongations are achievable in high purity NiAl when both orientation and specimen geometry are controlled properly. As expected for "unconstrained" deformation, the highest elongations are observed in the samples oriented for single slip due to the lower work hardening rate associated with Stage I deformation. Even though the CRSS for slip on {011} and {001} planes is similar, a direct comparison of the deformation response is difficult since slip on cube planes is always duplex whereas slip on the {011} planes is rarely duplex (e.g., for [uvw] between [$\bar{1}$11] and [$\bar{1}$22]). This behavior is rather unique for metals and intermetallics and is of academic interest for this reason.

Figure 7 - Scanning electron micrographs of [$\bar{1}$11] samples tested at (a) 573K (strain rate = 10^{-3} s^{-1}) and (b) 873K (strain rate = 10^{-4} s^{-1}) showing the greater necking at the higher temperatures.

It should be mentioned that the behavior after some plastic deformation may change from single to multiple slip depending on the initial orientation and the amount of strain.

In spite of the high elongations at both room and elevated temperature, it is clear from the present results that the possibility of producing tough, damage tolerant, monolithic NiAl is low. As already stated, this is due to the lack of a sufficient number of operative deformation mechanisms which, in turn, is related to the disparity between the CRSS values of dislocation with b=<001> vs. those with b=<011> and b=<111>. This realization combined with the fact that the fracture of NiAl is brittle even after large 100-200% elongations implies that the transition from negligible to high elongation cannot be correlated directly with the BDTT. In fact, it appears that the true BDTT must actually occur at temperatures above that where the highest elongations are observed, since the latter still exhibit brittle cleavage fracture. This indicates that the correlation of the BDTT with high tensile elongation may be nebulous in intermetallic compounds of this type. Likewise, this may explain why investigators have moved away from using Chevron-notch specimens to more traditional impact experiments.
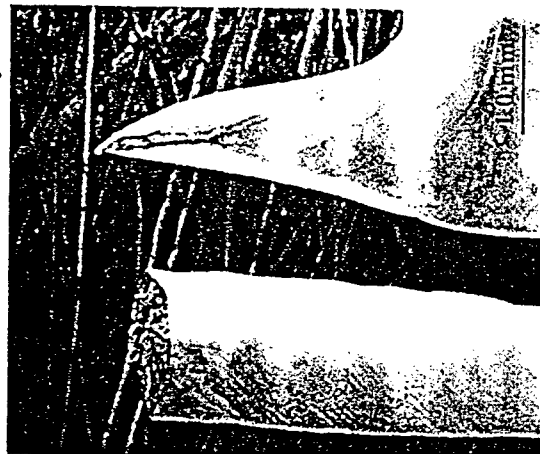

Figure 5 - Tensile elongation vs. temperature for (a) <111> and (b) <110> samples comparing the present data with that of Takasugi, et al. (20) and Lahrman, et al. (21).

Figure 6 - (a) Load vs. elongation for <111> crystal tested at 573K. (b) Shear stress vs. shear strain of same taking into account both Lüders band propagation (actual area) and specimen rotation during elongation. Strain rate = 10^{-3} s^{-1}.

Comparable results were also obtained on the [011] specimens although the range of temperatures over which the high elongations were observed was considerably narrower.

After the Lüders band propagates along the total length of the specimen, the material then begins to demonstrate a fairly typical work hardening response as is clear in Fig. 6. During this deformation, the material is relatively resistant to necking and tends to undergo extensive elongations. These observations are consistent with the recent theoretical work by Hähner (24, 25) who used a dynamic dislocation model to predict the behavior of Lüders bands in both single crystals and polycrystals. In spite of these large elongations, the ensuing fracture is still brittle in appearance.

Based on these results, it is important to reconsider the mechanism of the high elongations in greater detail. This issue has been somewhat controversial with some groups promoting the idea that climb of <001> edge dislocations (1) is responsible for the transition to high elongations while others suggest that it is related to the operation of secondary slip systems (26). It would appear from the present results that the former mechanism is more likely due to both the nature of the dislocation substructures as well as the macroscopic shape changes that occur at the high strains. In fact, the latter can only be accounted for by the operation of <001> edge dislocations. Significantly, Takasugi found that the high elongations observed at intermediate temperatures displayed a strong strain rate dependence consistent with the climb mechanism. Thus, it appears that the high elongations are possible whenever the stresses at stress concentrations can be relieved by the combination of glide and climb of the cube dislocations. Clearly, such factors as interstitial and substitutional solute content, deviations from stoichiometry, vacancy concentration, strain rate, dislocation density (prestraining effects), etc., are important and need to be considered when studying the behavior of this compound.

Summary and Conclusions

The present results indicate that it is possible to achieve fairly high elongations in NiAl at temperatures well below the so-called BDTT by careful control of the sample geometry and purity. Unfortunately, high elongations don't necessarily equate to high toughness and ductility. Based on these results, it is possible to draw the following conclusions:

1. High elongations (approaching 35% at room temperature) are possible in single crystals of NiAl at both sub-ambient and ambient temperatures when the specimen geometry and purity are controlled.

2. At intermediate temperatures, the elongations frequently exceed 200%. This has been correlated with lower initial flow stress, decreasing work hardening rates and increasing strain rate sensitivities with increasing temperature. The fracture surfaces after such high elongations are still brittle in nature.

3. Above the temperature of maximum elongation, localized necking occurs due to the decreased work hardening rate. Even so, the fractures are still brittle except for the samples that neck to a chisel point.

4. The soft, brittle nature of NiAl appears to be reasonably well understood at this point. Unfortunately, it is our belief that it will not be possible to enhance both the strength and toughness of monolithic NiAl due to the fact that the toughness of the high purity NiAl is negligible and that elements added to enhance the strength will reduce the toughness.

Acknowledgements

References

1. R. D. Noebe, R. R. Bowman, M. V. Nathal, in *Physical Metallurgy and Processing Intermetallic Compounds, Chapter 9* N. S. Stoloff, V. K. Sikka, Eds. New York, N 1994).

2. D. B. Miracle, *Acta. metall. mater.* 41, 649-684 (1993).

3. J. E. Hack, J. M. Brzeski, R. Darolia, *Scripta Met. et Mat.* 27, 1259-1263 (1992).

4. M. L. Weaver, R. D. Noebe, J. J. Lewandowski, B. F. Oliver, M. J. Kaufman, M *Sci. & Engr.* A192, 179-185 (1995).

5. E. P. George, C. T. Liu, *J. Mater. Res.* 5, 754-762 (1990).

6. D. Goldberg, G. Sauthoff, *Intermetallics* 4, 143-158 (1995).

7. J. M. Brzeski, J. E. Hack, R. Darolia, R. D. Field, *Mats. Sci. & Engr.* A170, 11 (1993).

8. J. M. Brzeski, J. E. Hack, R. Darolia, *Mat. Res. Soc. Symp. Proc.* 364, 419 (1995).

9. J. H. Schneibel, S. R. Agnew, C. A. Carmichael, *Met. Trans. A* 24A, 2593-2 (1993).

10. D. F. Lahrman, R. D. Field, R. Darolia, *Mats. Res. Soc. Symp. Proc.* 288, 679 (199

11. T. Takasugi, S. Watanabe, S. Hanada, *Mats. Sci. & Engr.* A149, 183-193 (1992).

12. T. R. Bieler, R. D. Noebe, M. Hebsur, R. Saminathan, The effects of extrus parameters on recrystallization kinetics, texture, and corresponding fracture toughness NiAl, J. J. Jonas, T. R. Bieler, K. J. Bowmans, Eds., Advances in Hot Deformat Textures and Microstructures; The Minerials, Metals & Materials Society 1994).

13. R. W. Margevicius, J. J. Lewandowski, *Metall. and Mat. Trans. A* 25A, 1457-14 (1994).

14. Margevicius, Lewandowski, Locci, *Scripta Metallurgica et Materialia* 26, 1733-1 (1992).

15. M. A. Morris, J.-F. Perez, R. Darolia, *Phil. Mag. A* 69, 507-526 (1993).

16. R. Darolia, D. F. Lahrman, R. D. Field, A. J. Freeman, in *High Temperature Orde Intermetallic Alloys III* . C. T. Liu, A. I. Taub, N. S. Stoloff, C. C. Koch, E (Materials Research Society, Boston, 1989).

17. M. H. Loretto, R. J. Wasilewski, *Phil. Mag.* 23, 1311-1328 (1971).

18. R. J. Wasilewski, *Trans. Metall. Soc. AIME* 36, 455-457 (1966).

MECHANISMS OF HIGH TENSILE ELONGATION IN NiAl SINGLE CRYSTALS AT INTERMEDIATE TEMPERATURES

V. I. Levit, J.S. Winton, Yu. N. Gornostyrev* and M. J. Kaufman

Department of Materials Science and Engineering, University of Florida
202 Rhines Hall, Gainesville, FL 32611-6400; vlevi@eng.ufl.edu
*Institute of Metal Physics, Urals Branch Russian Acad. Sci., 18 Kovalevskaya St.
Ekaterinburg, 620219, Russia

ABSTRACT

NiAl single crystals oriented parallel to [557], [110] and [111] were tested in tension over a range of temperatures and strain rates. Under certain conditions, high tensile elongations (100 - 350%) were observed and the load-elongation curves displayed a load maximum followed by a minimum and then a linear increase in load until fracture. Detailed analysis of the deformation behavior revealed that the load drop was associated with non-uniform deformation and, when both specimen cross section and rotation were taken into account, it was noted that there were no peaks in the shear stress-shear strain diagrams. For these conditions the resolved shear stress depends on both temperature and strain rate according to a power law with an exponent, n, of 8.4 ± 2 and an apparent activation energy, ΔH, of 147 ± 20 kJ/mol.

INTRODUCTION

Dynamic recrystallization (DR) is common in single crystals of copper [1], silver [2], nickel [3], and certain nickel-based superalloys [e.g., 4] and its initiation during tensile tests is characterized by a peak in load-elongation (and shear stress-shear strain) curves followed by softening. DR also occurs in polycrystals and this peak is reached at 2-3 times lower strains due to the faster rate of strain accumulation [4-5]. Somewhat similar load-elongation curves have been reported in NiAl single crystals at temperature/strain rate combinations that result in elongations of 100-350% [6]. The peak in these curves typically occurs after 10-30% elongation; post-mortem examination of the deformed microstructures revealed no evidence of DR. The purpose of this article is to provide further insight into this peak in the load-elongation curves by describing the microstructural development that occurs as the deformation progresses.

EXPERIMENTAL PROCEDURE

A NiAl single crystal (28 mm diameter by 75 mm length) was grown in a high purity alumina crucible by the Bridgman technique in an atmosphere of purified argon. Heat treatment and sample preparation procedures were described elsewhere [7]. The crystal was then oriented using back reflection Laue methods and tensile specimens were cut parallel to [557] and [111] (for single slip) and [011] (for symmetrical double slip). The tensile specimens were cut with rectangular cross sections with their thicknesses (xx mm) being thicker than their widths (xx mm) in contrast to typical flat tensile specimens cut from sheet material (Fig. 1a). For the [557] and [011] specimens, the plane containing the Burgers vector, slip plane normal, and tensile axis (TA) was placed either parallel or perpendicular to the thickness (wide side) of the sample cross section while the orientation of this plane was random in the [111] specimens. In the case of the [557] specimens, this plane is (110) whereas for the [011] specimens, it is (100) (Fig. 1b); this is the plane for which plane strain conditions hold. For the case where this plane is oriented parallel to the thickness (wide side), the condition will be referred to as PW (parallel to the wide side), when parallel to the narrow side, this plane will be called PN (parallel to the narrow side). For the [557] orientation, the axis of rotation of the slip plane during deformation is the normal to this plane, i.e., [1̄10]. In the double slip orientation, the specimen is "stable" with respect to rotation since the slip systems are offsetting in nature; however, any localized rotations will occur about the orthogonal to this particular plane, namely [100].

The tensile tests were performed in air using an Instron 1125 machine at temperatures from 473 to 1273 K and strain rates from 10^{-1} to 10^{-4} s^{-1}. In order to construct accurate stress-strain curves, the tensile tests were interrupted at intermediate strains and the samples were removed, measured, and photographed. The samples were then returned to the fixture and the tests were continued. In addition, one [557] and one [011] sample were marked with Vickers indents (2.5 N load) along their gage length at 0.5 mm intervals prior to testing at 673K and $\dot{\varepsilon}=10^{-3}$ s^{-1}. The samples were annealed for 0.5 h at 750 K in order to remove and residual stresses resulting from the indentations.
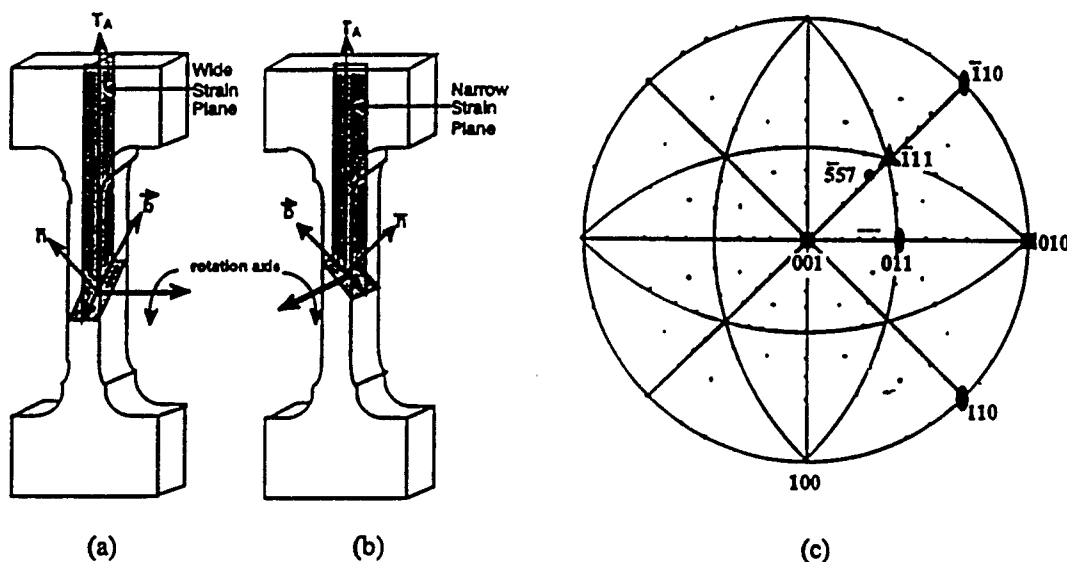
Figure 1. Schematics of tensile specimens used in this study: (a) PW orientation and (b) PN orientation. (c) Stereogram with tensile orientations and slip systems indicated.

The tests for these samples were interrupted six to eight times in order to measure the change in spacing between these markings and the current cross-section. Shear stresses at each interruption were calculated after noting the current minimum cross-section, load, and orientation [8]. Immediately after testing, the samples were removed from the furnace and cooled to room temperature on a cold metallic surface.

RESULTS AND DISCUSSION

Fig. 2 displays the elongation vs. temperature behavior for the double slip (TA=[011]) and single slip (TA=[557]) orientations. From these curves, it is apparent that, for a given strain rate, the elongation increases to high levels and then decreases again. In addition, it is also clear that the PW geometry exhibits higher elongations than the PN geometry. Fig. 3. displays the behavior of the <111> specimens with random geometries tested at a variety of temperatures and strain rates along with the data from the Takasugi, et al. study [6]. As is evident, the elongations are lower when the geometry is not controlled (compare with Fig. 3) and the temperature of the peak in elongation increases with increasing strain rate implying that thermal activation is important in the deformation behavior observed.

(a)   (b)
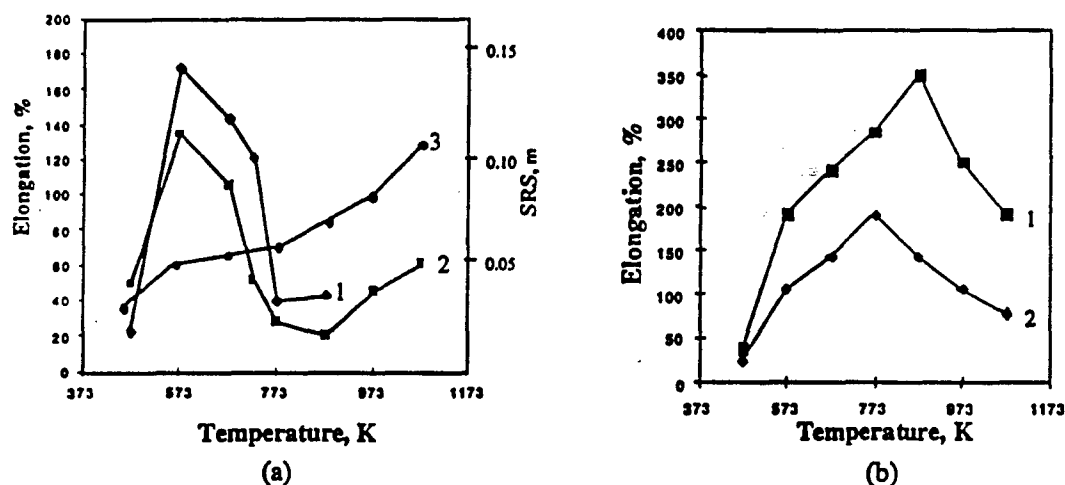
Figure 2. Elongation vs. temperature curves (strain rate = $10^{-3}s^{-1}$) for the [011] (a) and [557] (b) crystals showing the importance of both specimen orientation and geometry (1-PW and 2-PN). The strain rate sensitivity is also shown for the [011] samples.

For the samples tested at temperatures at and below those corresponding to the peak elongation, the fracture surfaces were brittle in appearance with little evidence of strain localization near the fracture surface. At the higher temperatures corresponding to the drop in elongation, the samples necked locally near the fracture, ultimately to a chisel point at the highest temperatures. For the [011] specimens, the strain rate sensitivity (SRS) $m=dln\sigma/dln\dot{\varepsilon}$ was measured by changing the strain rate from 10^{-2} to $10^{-4}s^{-1}$ during the tests and the results indicated that, regardless of the geometry, the SRS increased with increasing temperature from 0.03 at 473 K to 0.12 at 1073 K (Curve 3, Fig. 2a). Since the value of m in the range of temperatures where the maxima in elongation are observed is about an order of magnitude lower than that typical of superplastic materials, then the mechanism responsible for the high elongations in these crystals has a different origin as will be discussed further below.

639
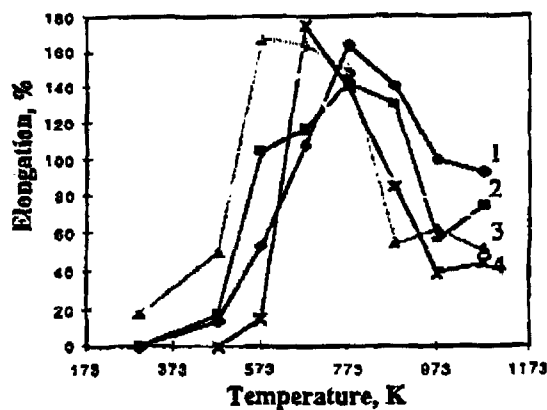
Figure 3. Elongation vs. temperature for the [111] specimens with more random geometries (i.e., neither PW or PN) at a variety of strain rates: 1: 10^{-2} s^{-1}, 2: 10^{-3} s^{-1}, 3: 10^{-4} s^{-1} and 4: 10^{-4} s^{-1} data from Takasugi et al. [6].
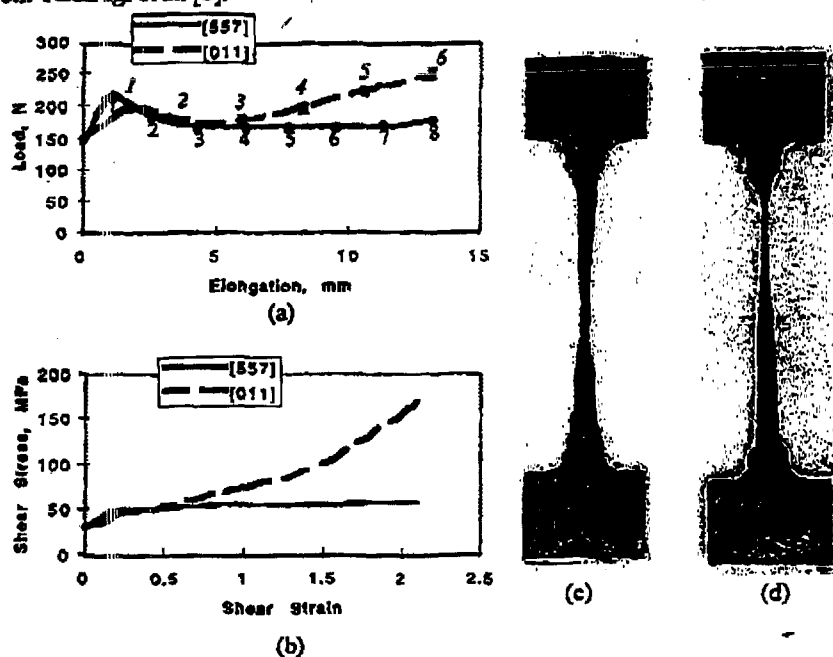

Figure 4. (a) Load-elongation curves with numbers indicating the interruptions; (b) corresponding shear stress vs. shear strain curves. (c) [011] and (d) [557] specimens photographed prior to fracture at 673K and $10^{-3}s^{-1}$ showing the non-uniform nature of the deformation process.

640

Typical load-elongation curves corresponding to the maximum elongations for both orientations are shown in Fig. 4. As can be seen, the load increases to a maximum and then decreases gradually to a minimum before increasing again. Significantly, this drop in load occurs over much larger strains than typical Luder's bands (LB's) indicating a different mechanism. When the tests were interrupted, it became clear that the drop in load in the present tests corresponds to strain localization on a much coarser scale than that typical of LB behavior. By observing the displacement of the marks during the interrupted tests, it was possible to quantify the nature of the strain localization. Furthermore, as will be reported elsewhere, the rotation that accompanied the deformation of the [557] specimens was measured independently using electron back scattering methods [10] and these data were used to estimate the Schmid factor in the regions of minimum cross sectional area. Taking into account both of these factors, it was possible to estimate the shear stress - shear strain curves (Fig. 4b) where it can be seen that there is no peak that corresponds to the load peak. In addition, there is little or no apparent work hardening for the single slip orientation and moderate hardening for the double slip orientation consistent with the greater dislocation interactions expected in the latter.

The interrupted tests on the samples marked with indents were used to determine whether one or more bands propagated along the gage length as well as the curvature of the band front. For the double slip orientation (Fig. 5a), multiple necks formed whereas the single slip orientation had only one neck which initiated near one fillet and propagated as a band along the gage length. Significantly, the amount of elongation corresponding to this band propagation stage was greater than 100% in contrast to typical Luder's band behavior where the propagation stage occurs over elongations of 1-2%. Figs. 4c and 4d display the structure of typical samples where the nature of the diffuse bands during this stage of non-uniform deformation is apparent.
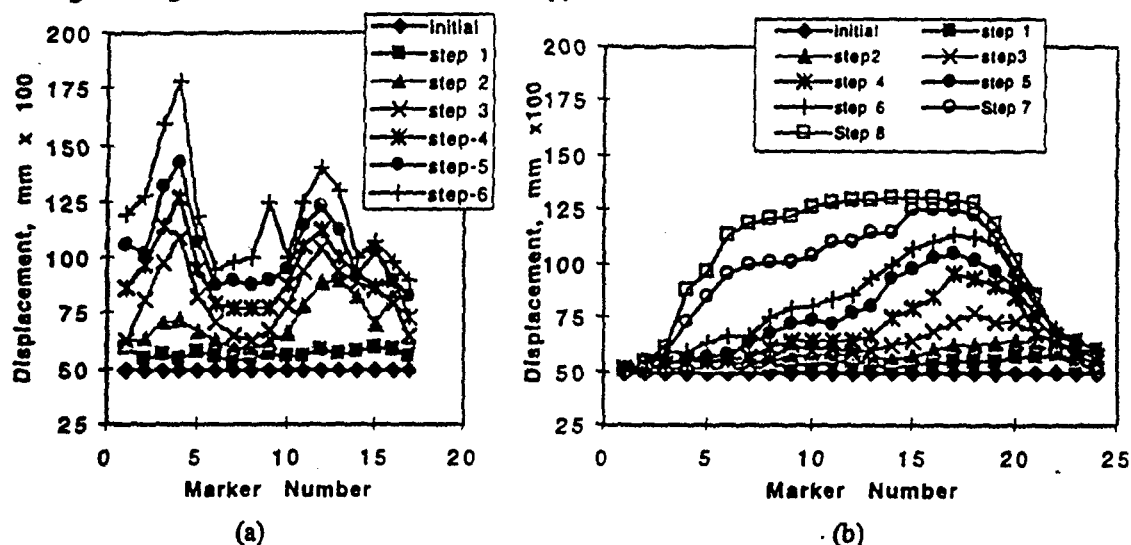
Figure 5. Marker displacement at different steps used to follow the strain distribution in [011] (a) and [557] (b) specimens at 673 K and 10^{-3} s^{-1}. The difference in the number of markers is not due to gage length or spacing differences but, rather, relates to the inititial misplacement of the first few marks in the [011] specimens.

The resolved shear stresses τ_p corresponding to the peak load for the [557] crystals were determined as a function of temperature and strain rate according to the relationship $Z = \tau_p^n$, where $Z = \dot{\varepsilon}^{\Delta H/RT}$ the

Hollomon-Zener parameter, $\Delta H=147\pm20$ kJ/mol the apparent activation energy, and exponent $n=8.7\pm2$ (as determined using standard thermal activation analysis [8])

The data from Takasugi's [111] crystals are included on this plot for comparison purposes and it is apparent that the value of n for both sets of data is approximately 8.7 which is close to the value published by Takasugi. Since $n=1/m$, this analysis is consistent with the SRS measurements described above. Also included in Fig. 6 are vertical dashed lines bracketing the temperatures and strain rates corresponding to the high tensile elongations where the band propagation was observed. For the data corresponding to ln Z >25 (low temperature and/or high strain rate), the samples exhibited lower elongations and uniform deformation. For the regime where the Hollomon-Zener relationship holds, the value of ΔH is approximately half that measured by Forbes and Nix [10] in their creep studies of NiAl single crystals; this implies that the mechanism of deformation in this regime is not controlled by diffusion only, however involves both conservative (slip) and non-conservative (climb) mechanisms. This is in good agreement with subgrain structure formation reported by Takasugi [6] after TEM study. No dynamic recrystallization was observed after structure examination of our single crystals.
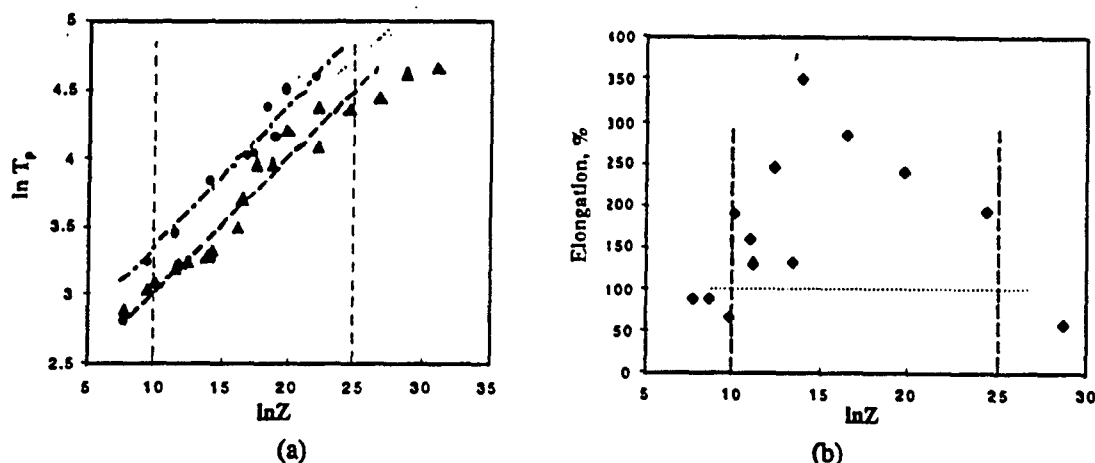
Figure 6. Hollomon-Zener plot of peak stresses (including Takasugi, et al. [6] data indicated by •) (a) and tensile elongations (b).

GEOMETRIC EFFECT ON FLOW INSTABILITY

There are two physical explanations for the flow instability that leads to shape instabilities (necking, band propagation, etc.) during plastic deformation [8]. Cottrell [11] and Brindley et al. [12] suggested that these instabilities are connected with dislocation pinning/unpinning by impurities while Gilman and Johnston argued that they are related to peculiarities in the dislocation ensemble kinetics [13]. Based on the later model, Haehner presented a model of LB's involving solitary plastic wave propagation [14], where the LB's propagate at low dislocation density and small strains (<2%). In the present case, the geometrical bands propagate at strains one to two orders of magnitude higher. The load peaks involve h-type instabilities [15], where the work hardening rate, θ, is insufficient for stable flow ($\theta > \theta$). For this case, "geometrical softening" due to changes in the specimen cross section are important as is "orientation softening" which results in changes in the Schmid factor for those "unstable" orientations that involve single slip (e.g. [557]). Let us consider the "stable" double slip [011] orientation. The stress tensor components σ_{bn} in two-dimensional space can be presented as [16]:

$$\sigma_{bn} = \frac{1}{2}\sigma_{xx}^0 \left(1 + \varepsilon + (h_0^2 - \frac{3}{2}y^2)\varepsilon''\right) \tag{1}$$

where σ_{xx} is the uniaxially applied tensile stress, $\varepsilon = \varepsilon_{xx}$ the true strain, $\varepsilon'' = d^2\varepsilon(x)/dx^2$, h_0 the sample half-thickness in the y direction and x the tensile direction.

The term $1+\varepsilon$ represents the strain and is responsible for the "geometrical softening" which leads to strain localization. The second term $(h_0^2...)$ in parentheses represents the *biaxial stresses* which depend on cross section curvature ε'' and lead to a decrease in the strain localization.

By averaging of the stresses σ_{bn} across the cross section of the plate from $-h_0$ to $+h_0$ gives:

$$\overline{\sigma}_{bn} = \frac{1}{2}\sigma_{xx}^0 \left(1 + \varepsilon + h_0^2\varepsilon'\right) \tag{2}$$

which is quite different from Haehner's results [14] for small strains. After routine stability analysis, we have:

$$\sigma_{xx}^0 > \frac{\theta}{1 - 0.5(h_0/\lambda)^2} \tag{3}$$

where λ is the instability scale, which depends on the mesoscopical dislocation inhomogeneity and is independent of h_0. Significantly, the value of h_0 is larger for the PW geometry than the PN geometry. Hence, higher stresses are required to develop the instability for the PW case consistent with the higher elongations characteristic of the PW samples. Furthermore, $h_0/\lambda << 1$ represents common instability conditions corresponding to $\sigma_{xx}^0 > \theta$.

The stress distribution in the [557] samples oriented for single slip is given by:

$$\sigma_{bn} = \frac{1}{2}\sigma_{xx}^0 \left(1 + \varepsilon - \frac{1}{2}y^2\varepsilon'' - 2y\varepsilon'\right) \tag{4}$$

and is quite different from Eqn. (2) for the [011] orientation. When single slip is dominant, the *bending stresses* become very important. In particular, these stresses lead to asymmetries in the stress distribution which cause one band to dominate and spread from one end of the sample to the other. This is in good agreement with our experimental observations and the schematic given in Reference 14. An additional effect concerning the stability of the [557] crystals is due to "orientation hardening" since the Schmid factor decreases with strain due to the rotation mentioned above; this provides for stable geometrical band spreading along the sample under constant shear stresses.

CONCLUSIONS

1. High purity NiAl single crystals exhibit an abnormal dependence of tensile elongation on temperature over the range 500-1300K for strain rates of 10^{-1}-10^{-4} s^{-1}. For the crystals oriented for single slip (e.g. [557]), elongations of 100-350% between 500 and 1300 K are common and are sensitive to strain rate where higher strain rates are required at the higher temperatures.

2. The [011] crystals, on the other hand, display a much narrower temperature interval where high tensile elongations (550-650 K) are observed. The highest tensile elongations were obtained at the conditions where the Burgers vector, normal to the slip plane and tensile direction were coplanar and parallel with the widest side of the sample.

3. Peaks were observed on load-elongation curves as previously reported in other research. No peaks on shear stress-shear strain diagrams were observed after normalizing to cross-sectional area and current orientation. Accordingly no dynamic recrystallization was observed after structure examination.

4. Unusual geometrical band propagation was the dominating strain mechanism in samples with the highest elongations. Bands propagate over large strains (e.g. 100%) at stresses considerably higher than the CRSS.

5. When bands are observed, the resolved shear stress depends on both temperature and strain rate according to the power law with an exponent, n, of 8.4 ± 2 and apparent activation energy ΔH, of 147 ± 20 kJ/mol.

REFERENCES

1. P. Karduck, G. Gottstein, and H. Mecking: Acta metall. 31, 1983, p.1525
2. P. J. T Stuije and G. Gottstein: Z. Metallk. 71, 1980, p. 279
3. G. Gottstein and U.F. Kocks: Acta Metall. 31, 1983, p.175
4. N. D. Bakhteyeva, V.I. Levit et al: Phys. Metals and Metallography. 51. 1982, p. 149
5. T. Sakai and J. J. Jonas: Acta Metall. 32, 1984, p. 189
6. T. Takasugi, J. Kishino, and S. Hanada: Acta Metall. 41, 1993, p. 1009
7. V. I. Levit, I. A. Bul, J. Hu and M. J. Kaufman: Scripta Materialia. 34, 1996, p. 1925
8. R. W. K. Honeycombe: The Plastic Deformation of Metals, *E.Arnold* (Publ.) London, 1968
9. K.R. Forbes, U. Glatzel, R. Darolia and W.D. Nix : Met. Transactions, 27 A, 1996, p.1229
10. V.I. Levit, J.Hu, J. Fischer-Buehner, G.G.Gottstein and M.J.Kaufman to be published
11. A. H. Cottrell: Phil. Mag. 43, 1952, p. 645
12. B. J. Brindley, D. J. Corderoy, and R. W. K. Honeycombe: Acta met. 10, 1962, p. 1043
13. W. G. Jonston and J. J. Gillman: Appl. Phys. 30, 1959. p. 129
14. P. Haehner: Appl. Phys. (Solids and Surfaces) A 58. 1994, p. 49
15. Y. Estrin, L.P.Kubin: Res. Mech. 23, 1988, p.197
16. Yu. N. Gomostyrev, V.I. Levit and M.J. Kaufman to be published.

ACKNOWLEDGMENTS

SIMULATION OF GRAIN BOUNDARY INSTABILITIES DURING HOT STRAINING

A. V. Kaptsan*, Yu. N. Gornostyrev**, V. I. Levit and M. J. Kaufman

Materials Science and Engineering Dept. University of Florida
202 Rhines Hall, Gainesville, FL 32611-6400; *vlevi@eng.ufl.edu*
*Iron and Steel Works, 93 Kirova Str. Magnitogorsk, 455002, Russia
**Institute of Metal Physics, Urals Branch Russian Acad. Sci., 18 Kovalevskaya St.
Ekaterinburg, 620219, Russia

ABSTRACT

A model describing the appearance and development of periodic grain boundary shape irregularities during hot straining of single phase materials is presented. The dislocations entering into the grain boundary and interacting inside bring the grain boundary into an unstable, high energy condition, which could be characterized by induced anisotropy of surface energy. Predicted periodic serrations or waves at grain boundaries could not be produced in the framework of existing models.

INTRODUCTION

Grain boundary shape irregularities are important during the high temperature deformation of single phase solid solutions. Both the period and the amplitude of the irregularities are known to increase with increasing temperature and/or decreasing strain rate [1]. During this process, the irregularities may develop into a smooth sinusoidal shape; these "bumps" become the nuclei for the necklace of fine grains that form along the grain boundaries (GB) during dynamic recrystallization (Fig.1) [1-3].

The model by Bailey and Hirsch [4] for the formation of recrystallization nuclei by strain induced grain boundary migration was modified for dynamic recrystallization conditions by Derby and Ashby [5]. Both models adequately describe the formation of single bulges at the GB where the bulge has an orientation similar to the parent grain it grows from. However, neither model considers any periodic irregularities or necklace formation during dynamic recrystallization. In this paper, we present a model of grain boundary instability development based on the analysis of extrinsic grain boundary dislocations (EGBDs) produced during hot straining.

EVOLUTION OF EGBD ENSEMBLE

During plastic deformation of polycrystals, dislocations are known to glide through the grains and enter into grain boundaries. Because the dislocations sliding in two misoriented grains are usually non-coplanar, the grain boundaries tend to accumulate EGBD's as geometrically necessary

571

dislocations (Fig.2). We will not consider the real structure of the grain boundaries or the GB dislocations which depend on lattice type and misorientation. Instead, we will assume that the grain boundaries contain EGBDs which can be characterized by a density vector, ξ (where the direction of ξ is related to the sum effect of the dislocations that exist locally). Specifically, ξ is a vector that describes how the sum of the dislocations' Burgers vectors, δB, at any given point along the GB line (in 2-D) changes when one moves to an adjacent point along the GB line by an amount δl. Furthermore, ξ is a function of both coordinate l and t (during plastic deformation) and is given by

$$\xi(l,t) = \frac{\delta B}{\delta l} \tag{1}$$

a

b

c
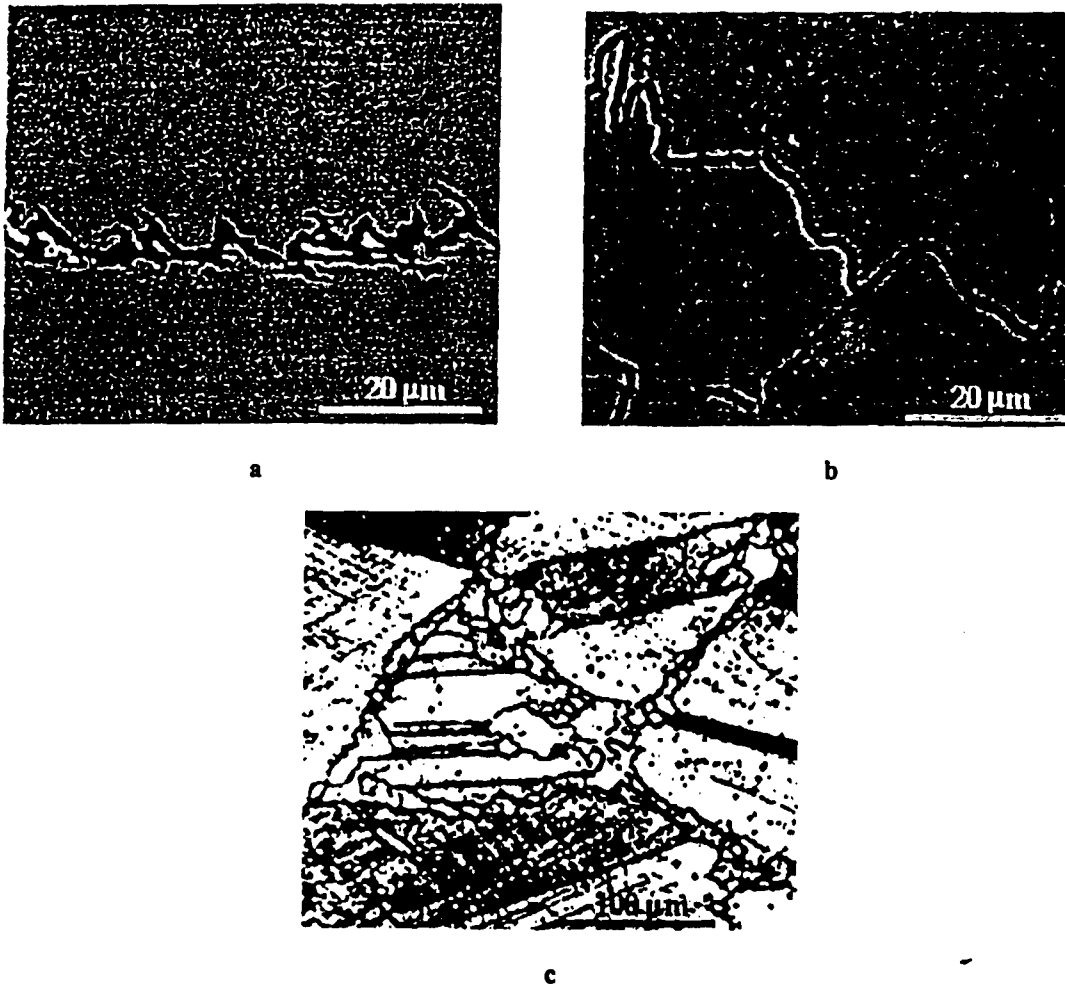
Figure 1. Grain boundary shape after hot straining. (a) Carbide precipitation along a serrated GB in Ni-Cr austenitic steel, T= 1400 K, Strain rate= 10 s^{-1}. (b) Ni-10%Al, T=1073K, Strain rate=10^{-3}s^{-1}. (c) "Necklace" of DRX grains in nimonic 80A alloy. T=1473K, Strain rate=10^{-3}s^{-1}.

It should be noted that both the EGBD density and velocity vary in time. Also, ξ is composed of component parts which correspond to different elementary processes. First of all, we consider dislocations gliding in adjacent grains entering the GB region (Fig. 2). The Burgers vector of the glide dislocations in grain 1 is described as b_{g1} and in grain 2 as b_{g2}. These glide dislocations lead to component density vectors, ξ_{g1} and ξ_{g2}, whose rate of change is given by

$$\dot{\xi}_{gi} = \dot{\varepsilon}\, b_{gi} \frac{b_{gi} N}{b_{gi} b_{gi}} \qquad (2)$$

where $i = 1,2$ for grains 1 and 2, $\dot{\varepsilon}$ is the strain rate which is assumed to be the same in grains 1 and 2 and N is the normal to the GB line. Physically, this says that ξ_{gi} depends on strain rate, the Burgers vectors of the dislocations and on the position of the grain boundary plane relative to the glide planes of the dislocations.

The second component of ξ is ξ_r and is due to the reaction between dislocations b_{g1} and b_{g2} entering into the GB from grains 1 and 2 to produce dislocations with Burgers vector $b_r = b_{g1} + b_{g2}$. The rate of change of the density vector due to these dislocations depends on both the time required for the dislocations to climb to meet one another and on dislocation density and is given by

$$\dot{\xi}_r = -M_d G \xi_{g1} \xi_{g2} (\xi_{g1} + \xi_{g2}) \qquad (3)$$

where M_d is the dislocation mobility and G is the shear modulus.
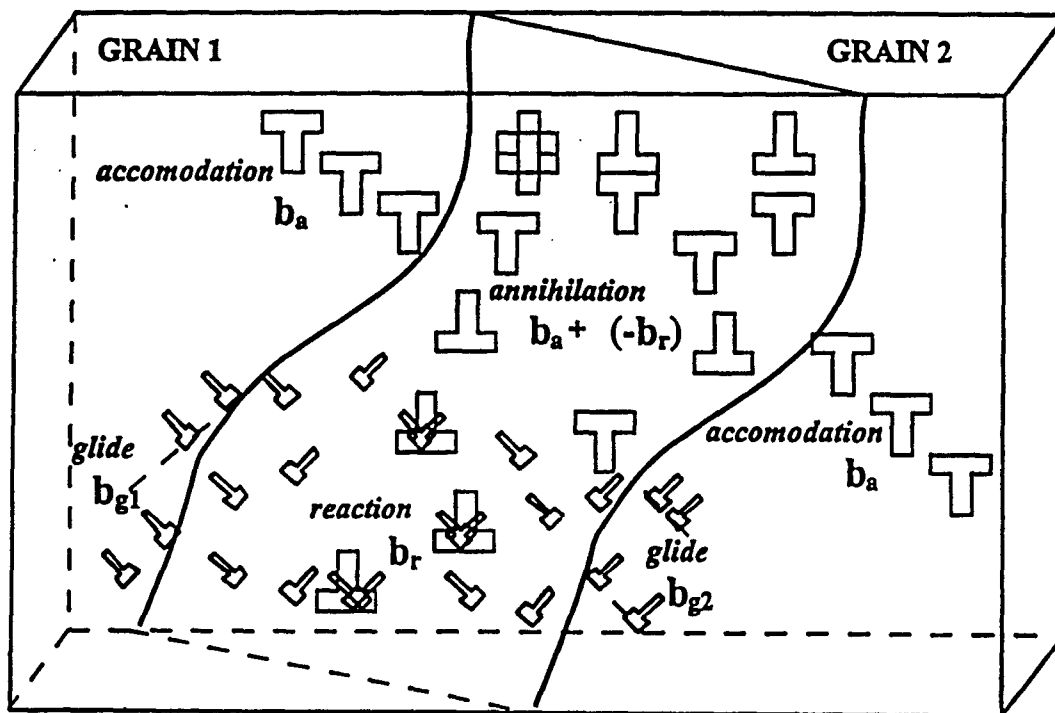
Figure 2. Accumulation and redistribution of EGBD at grain boundry.

During plastic deformation, the interaction and accumulation of dislocations in the grain boundaries leads to stress concentrations and "accomodation" strain to relieve these stresses. The resulting dislocations, with Burgers vector b_a and density vector, ξ_a can reenter the GB and interact with the other dislocations just described. If we assume that the dislocations due to accommodation shear are limited by some maximum in EGBD density, ξ_{max}, the rate of change of the accommodation dislocation density is given by:

$$\dot{\xi}_a^i = -(\dot{\xi}_{b1} + \dot{\xi}_{b2} + \dot{\xi}_r)\theta(|\xi_t| - \xi_{max}) \tag{4}$$

were $\xi_t = \xi_{b1} + \xi_{b2} + \xi_r + \xi_a$ and θ is the Heaviside function.

The stress required for accommodation shear is approximately the flow stress, σ_f, and, therefore, the maximum EGBD density $\xi_{max} = \sigma_f / G$. For simplicity, assume $b_a = -b_r$ so that dislocations with Burgers vectors b_a and b_r could mutually annihilate with rates of change similar to that described in Eqn. (3) and given by

$$\dot{\xi}_a^r = -M_d G \xi_a (\xi_a \xi_r) \text{ and } \dot{\xi}_r^r = -M_d G \xi_r (\xi_a \xi_r) \tag{5}$$

It is assumed that each EGBD with Burgers vector b experiences some average stress $\hat{\sigma}$ due to all of the dislocations in the grain boundary. As a result, the dislocation moves along the GB with a velocity

$$V_d = M_d [(b\,\hat{\sigma}) \times [L \times N]] L \tag{6}$$

where L - is unit vector tangent to the GB line. Accordingly, the EGBD density changes with a speed

$$\dot{\xi}^c = \frac{\partial}{\partial l}(\xi V_d) \tag{7}$$

BOUNDARY STABILITY VERSUS SMALL IRREGULARITIES

During hot straining, portions of the GB may deflect slightly from their initial positions, e.g. due to stresses from coarse slip bands stopped at GB. These deflections vary in sign along the GB containing the EGBDs and can result in a sinusoidal (for simplicity) boundary shape given by

$$y = h\sin(2\pi x / a) \tag{8}$$

where the amplitude h is much smaller than the period a (Fig.3).

These periodic deflections cause elastic interactions of EGBDs. The driving force, F_d, favoring the development of the sinusoidal GB structure is related to the maximum EGBD density, ξ_{max}, where the Burgers vectors are aligned along 0X, and is given by

$$F_d = \frac{h\pi G \xi_{max}^2}{2a(1-v)} \tag{9}$$

where v is the Poisson coefficient

574
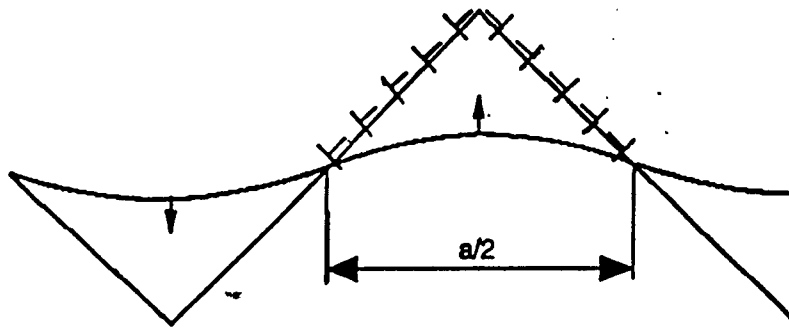
Figure 3. Evolution of the grain-boundary shape during deformation at a high strain rate (1 s⁻¹).

As the GB increases in area during this process, the surface tension attempts to restrain the continued growth in the amplitude, h, with the "restraining" force F_b given by

$$F_b = 2\gamma_b \left(\frac{\pi}{a}\right)^2 h \qquad (10)$$

where γ_b is the grain boundary surface energy.

The GB is unstable to small shape deviations when $F_d > F_b$, or, following (9) and (10), when the period of deviation $a > a_c$; where

$$a_c = \frac{4\pi\gamma_b(1-\nu)}{G\xi_{max}} = \frac{4\pi\gamma_b(1-\nu)}{\sigma_f} \qquad (11)$$

From (11), it follows that increases in the flow stress, σ_f (i.e. by increasing the strain rate $\dot{\varepsilon}$ and/or decreasing the temperature T) lead to growth in the period of the sinusoidal deviations in agreement with experimental data.

NUMERICAL SIMULATION OF BOUNDARY SHAPE EVOLUTION

The development of small deviations during hot straining leads to macroscopical changes in the GB shape. This can be analyzed by numerical simulation. The grain boundary migration occurs in response to the following forces:

(a) the recrystallization driving force:

$$F_\rho = Gb^2 \Delta\rho \qquad (12)$$

where $\Delta\rho$ is the dislocation density difference in neighboring grains;

(b) the force due to elastic interaction of the EGBDs inside the GB, according to (6):

$$F_d = [(\xi, \hat{\sigma}) \times [L \times N]]N \qquad (13)$$

the stress applied to each piece of GB could be found by integration of the elastic stress fields produced by all of the EGBDs on the GB; and

(c) the surface tension force

$$F_b = -\gamma_b / R \qquad (14)$$

where $R(l)$ is the local radius of GB curvature.

The velocity of GB migration, V, depends on the balance of these driving forces as follows

$$V = M_b(F_\rho + F_d + F_b) \qquad (15)$$

The calculation of V requires that the EGBD distribution along the grain boundary be known at each period of time. This distribution can be calculated by the solution of the density vector change equations described above.

For the calculations, we assumed that the initial period, a, of the GB irregularities was approximately 20 μm (Fig.3) which exists after the very beginning of deformation. This value corresponds to clearance between coarse slip lines stopped at grain boundaries during the initial period of hot straining [6]. The GB mobility coefficient $M_b = 10^{-12}$ m^3/(N·s) was taken according to [6]. Parameters $\xi_{max} = \sigma_e/G = 0.001$ and $M_d = 10^{-12}$ m^2/(N·s) have reasonable values which are typical for hot straining conditions.

The rate of EGBD rearrangement inside the GB is negligible if the strain rate is sufficiently high and/or the temperature sufficiently low. The simulation carried out for $\dot{\varepsilon} = 1$ s^{-1} and $\Delta\rho = 0$ demonstrates that a GB will bend until it acquires a serrated shape with right angles at the tips (Fig.3). This serrated configuration has low energy and is dynamically stable during the deformation because the EGBD Burgers vectors are placed perpendicularly to the boundary line along the length of the boundary.

In case of lower strain rates and/or higher temperatures, EGBD migration along the GB plays an important role in EGBD rearrangement. Serrated GB shapes become energetically unfavorable in comparison with sinusoidal ones (Fig 4).
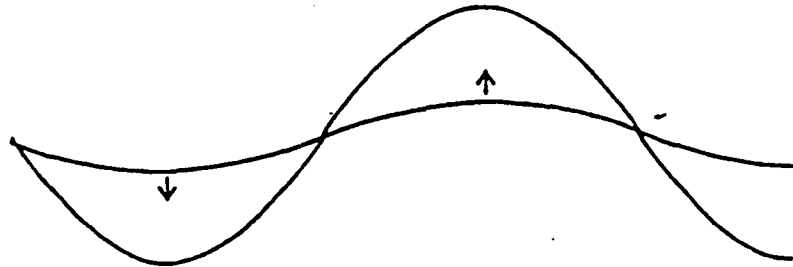
Figure 4. Evolution of the grain boundary shape during deformation at a low strain rate (10^{-2} s^{-1})

NUCLEATION OF DYNAMIC RECRYSTALLIZATION

Dynamically stable serrated or sinusoidal GB shapes could be produced with an assumption that $\Delta\rho=0$, i.e. the dislocation density on both side of the GB is about the same. When continuing deformation could not compensate the dislocation density behind and ahead of a moving part of the GB, Δr starts to grow and GB irregularities are no longer restricted by a stable configuration. They can then grow turning into "protuberances" which become nuclei of dynamic recrystallization.

Simulations with $\Delta\rho=10^{14}$ m^{-2} show how the irregularities could be developed into a necklace of new dynamically recrystallized grains along the existing GB (Fig.5).
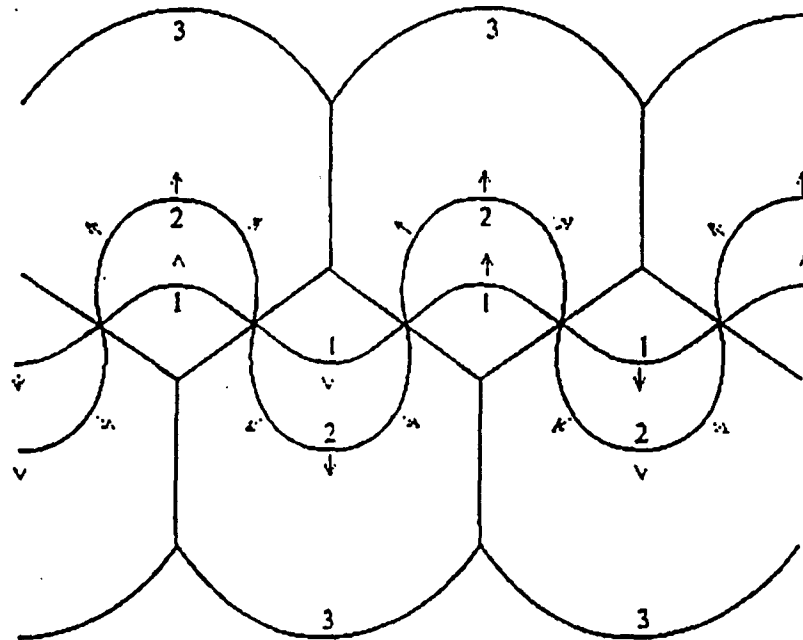
Figure 5. Evolution of the grain boundary shape at $\Delta\rho=10^{14}$ m^{-2}. Lines 1,2 and 3 denote successive positions of the grain boundary at the moment 0.1, 0.3 and 0.5 s, respectively.

According to this model, the dynamically recrystallized grains should be oriented periodically close to the first or second initial grains. This could be checked experimentally using an SEM equipped with electron channeling capabilities.

CONCLUSIONS

A model describing the appearance and development of periodic grain boundary shape irregularities during hot straining of single phase materials is presented. The dislocations entering into the grain boundary and interacting inside bring the grain boundary into an unstable, high energy condition, which could be characterized by induced anisotropy of surface energy. Taking into account these circumstances allows one to understand and predict periodic serrations or waves at grain boundaries, which could not be produced in the framework of existing models [4-6].

577

According to the model presented, small irregularities in grain boundary shape increase their period with increasing temperature and/or decreasing strain rate. Computer simulations predicted simultaneous changes in grain boundary shape from serrated to sinusoidal when the temperature is raised or the strain rate lowered.

By considering the large dislocation density differences that can exist behind and in front of the GB irregularities, it is shown that the irregularities can grow and become the nuclei for the necklace of dynamic recrystallized grains along the existing grain boundary. Following from the model, the effect of strain rate and deformation temperature on the shape and period of the grain boundary irregularities are in good agreement with published experimental data. Finally, the periodic change in dynamically recrystallized grain orientation in the necklace structures is in need of experimental verification.

REFERENCES

1. E. N. Sokolkov and V. D. Sadovskiy: Phys. Met and Metallogr. 19, 1965, p. 226.
2. V. I. Syutkina and E. S. Yakovleva: Phys. Met. and Metallogr. 12, 1961, p. 740.
3. T. Sakai and J. J. Jonas: Acta Met. 32, 1984, p. 189.
4. J. E. Bailey and P. B. Hirsch: Proc. Roy. Soc. A267, 1962, p. 11.
5. B. Derby and M. F. Ashby: Scr. Metall. 21, 1987, p. 879.
6. R. Sandstrom and R. Lagneborg: Acta Metall. 23, 1975, p. 387.

ACKNOWLEDGEMENTS

ON DETERMINING THE INTERNAL STRESS USING HALL-PETCH DATA

R.E. Reed-Hill, C.V. Iswaran and M.J. Kaufman
Department of Materials Science and Engineering,
University of Florida, Gainesville, FL 32611

Abstract

Accurate evaluation of σ_μ, the internal stress, is essential for determining σ^*, the effective stress, because experimental yield stress data yield only the sum of σ^* and σ_μ. In the past, the most popular method of determining σ_μ has been the back extrapolation technique which assumes that $\sigma^* = 0$ at the flow stress plateau of a constant strain rate σ vs. T plot, so that in this region $\sigma = \sigma_\mu$. Back extrapolating this σ_μ to absolute zero while giving it the temperature dependence of the shear modulus was then assumed to determine σ_μ at temperatures below the plateau. This technique has been shown to seriously overestimate σ_μ and underestimate σ^* and it has been shown that σ_μ may be measured more accurately [1,2,3] using strain rate sensitivity data. However, strain rate sensitivity data at sub-ambient temperatures are very difficult to obtain accurately. This paper discusses another possible method for measuring σ_μ based on Hall-Petch data, which appears to be much easier to use and of still greater accuracy.

Introduction

It was recently demonstrated [1] that the Okazaki and Conrad [4] commercial purity titanium Ti A-70 stress strain data could be modeled by a power law based on the Yokobori [5] activation enthalphy, $H = H^o(\sigma_o^*/\sigma^*)$ where H^o is a material constant with units of energy, σ^* the effective stress with σ_o^* its value at 0 K. When this H is used in the thermally activated strain rate equation [1], one is able to obtain the following power law for the effective stress σ^*

$$\sigma^* = \sigma_o^* \left(\frac{\dot{\epsilon}}{\dot{\epsilon}_o} \right)^{\frac{RT}{H^o}}$$

(1)

where $\dot{\epsilon}$ is the strain rate and $\dot{\epsilon}_o$ a material constant with units of strain rate. In order to evaluate σ^* using flow stress data, one must first determine the internal stress σ_μ and subtract it from the experimentally measured flow stress σ. Techniques designed for determining σ_μ using strain rate sensitivity data are recorded elsewhere [1,6,7].

Table 1 lists parameters determined in [1], which when used in Eq. 1, make it possible to model the temperature dependence of the $\sigma_{0.2}$ yield stress of the Okazaki and Conrad [4] 16 μm grain size Ti A-70 tensile specimens.

TABLE 1

$H^p = 50, 150\ J/mol$	$\dot{\epsilon}_o = 3.41 \times 10^7\ s^{-1}$	$\dot{\epsilon} = 3.34 \times 10^{-4}\ s^{-1}$
$\epsilon = 0.2\%$	$\sigma_o^* = 1,254\ MPa$	$\sigma_\mu = 70 - 0.0034 \times T\ MPa$

When H^o, $\dot{\epsilon}$, $\dot{\epsilon}_o$, σ_o^* and σ_μ from Table 1 are inserted in Eq. 1, one obtains the yield stress equation

$$\sigma_{0.2} = \sigma^* + \sigma_\mu = 1,254\,(9.82 \times 10^{-12})^{1.66 \times 10^{-4} T} + (70 - 0.034 \times T) \tag{2}$$

In addition to their tensile yield stress data, Okazaki and Conrad also included extensive Ti A-70 Hall-Petch data with an important analysis of their significance. Two of their 300 K and $\dot{\epsilon} = 3.34 \times 10^{-4} s^{-1}$ Hall-Petch plots are reproduced in Fig. 1. Note that they correspond to flow stresses involving different prestrains, $\epsilon = 0.2\%$ and 10.0%. Both are plotted against $d^{-1/2}$ where d is the grain diameter determined by the linear intercept technique. In both cases, four specimens with grain sizes 16, 6, 2.5 and 1.5 μm were tested. Hall-Petch plots are normally assumed to follow an equation of the form

$$\sigma = \sigma_i + kd^{-1/2} \tag{3}$$

where σ is the flow stress, σ_i the flow stress at the intercept of the Hall-Petch plot with the ordinate axis and corresponds to a stress for an infinite grain size, i.e. $1/d^{1/2} = 0$. In practice, one may assume σ_i to be the flow stress for a single crystal with the same composition and "texture" as the polycrystalline specimens. A significant feature of Fig. 1 is that σ_i is about 45 percent larger for the Hall-Petch plot at $\epsilon = 10\%$ than at $\epsilon = 0.2\%$. This suggests that σ_i depends strongly on a specimen's prestrain. Okazaki and Conrad also investigated the relationship between σ_i, ϵ and T as shown in Fig. 2 copied from their paper. Note that in Figs. 1 and 2 the stress is expressed in Kg/mm^2 which can be converted to MPa by multiplying by 9.81. Also note that in Fig. 2 Okazaki and Conrad were able to draw straight lines through their σ_i vs. $\epsilon^{1/2}$ data at each of the five temperatures investigated; 4.2, 77, 200, 300, 500 and 650 K.

At this point, consider the significance of the isothermal lines in Fig. 2. First, each data point on these lines is a σ_i or a stress with a zero contribution from the grain size. Second, the intercepts of these lines with the y-axis occur at $h_i\epsilon^{1/2} = 0$ signifying the strain contribution to the stress is also zero. Therefore, assuming the primary sources of the internal stress in A-70 are the grain size and the strain, it is reasonable to conclude that the intercept of an isothermal line with the y-axis in Fig. 2 should equal the effective
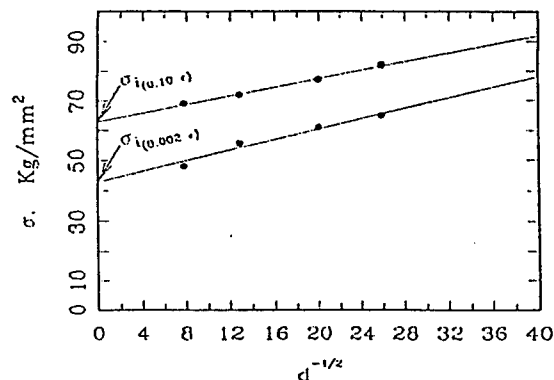
Figure 1. Two of the Okazaki and Conrad 300 K Hall-Petch plots involving different flow stress prestrains $\epsilon = 0.002$ and 0.10.
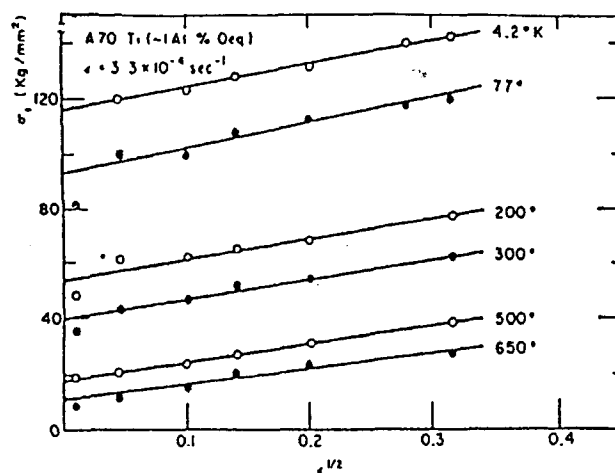
Figure 2. The effects of strain and temperature on the Hall-Petch intercept, σ_i. Data of Okazaki and Conrad [2].

stress, σ^*, at the temperature of the line. It is significant that Okazaki and Conrad concluded that as a result of the data in Figs. 1 and 2 the Hall-Petch equation could be written in the following form

$$\sigma = \sigma^o(\dot{\epsilon}, T, C_i) + h_i(\mu, C_i) \times \epsilon^{1/2} + kd^{-1/2} \tag{4}$$

where σ_o is a function of $\dot{\epsilon}$(the strain rate), T (the temperature) and C_i (the interstitial concentration). These are actually the charcteristics of σ^*. Okazaki and Conrad did not comment on this fact probably because of σ^o did not equal their back extrapolation σ^*. The present paper demonstrates that independent calculations of σ^* and σ_μ based on the use of Eq. 2, support the Okazaki and Conrad conclusions about the Hall-Petch relationship in Eq. 4. First, however, it must be pointed out that the data in Table 1 correspond to Ti A-70 specimens with a 16 μm grain size deformed to $\epsilon = 0.2\%$. Furthermore, both σ_μ and σ^* were evaluated using strain rate sensitivity data. It now appears that the evaluation of these parameters can be made more accurately using the Hall-Petch analysis of Okazaki and Conrad. Thus, according to the Hall-Petch data, the Ti A-70 specimens should have a σ_{μ_s} component due to the 16 μm grain size of 56 MPa and a 36 MPa component due to the 0.2% prestrain for a total $\sigma_{\mu_s} = 92\ MPa$. This is still well below the back extrapolation value of Okazaki and Conrad which was $\sigma_{\mu_s} = 198\ MPa$. It was also found necessary to re-evaluate σ_o^* in terms of the Hall-Petch analysis. The result was $\sigma_o^* = 1,315\ MPa$ versus 1,254 MPa as previously estimated [1]. In terms of these Hall-Petch parameters the variation of σ^* with T now becomes

$$\sigma^* - 1,315 \times (9.82 \times 10^{-12})^{1.66 \times 10^{-4}T}. \tag{5}$$

Equation 5 now makes it possible to test whether the Fig. 2 y-axis intercepts correspond to values of σ^*. In this regard the stresses at the Fig. 2 intercepts were plotted on the σ^* vs. T diagram in Fig. 3 together with an analytical curve obtained using Eq. 5. Note the good agreement between the analytical σ^* curve and the Fig. 2 intercepts except possibly at the lowest temperatures. The data in Fig. 2 are replotted in Fig. 4 as five σ_i vs. T diagrams each corresponding to one of the prestrains involved in the data. The analytical curves in these plots were obtained by adding to the temperature dependence of the effective stress, expressed by Eq. 5, an internal stress consistent with the prestrains given the specimens. These internal stresses were evaluated as follows. It was first assumed that 4.2 K was sufficiently close to absolute zero
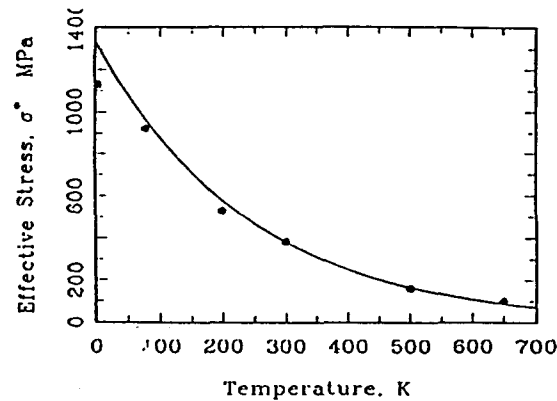
Figure 3. The variation of σ^* with T according to Eq. 5 is shown by the solid line curve while the data points represent the intercepts of the isothermal lines in Fig. 2 with the $\epsilon^{1/2} = 0$ ordinate axis in Fig. 2.

that the internal stress could be considered equivalent to σ_{μ_e}. The internal stresses at temperatures above 0 K were then obtained by subtracting a factor to give σ_μ the temperature dependence of the shear modulus. The uppermost isothermal line in Fig. 2 contains the 4.2 K σ_i data points so that by Eq. 7 one may express this line as

$$\sigma_i = \sigma^* + \sigma_{\mu_e} = \sigma^* + h_i \epsilon^{1/2} \quad MPa \tag{6}$$

where $h_i = 807\ MPa$ and $\sigma_{\mu_{e_e}} = 807 \times \epsilon^{1/2}\ MPa$. The following expression was used to give the strain component of the internal stress the temperature dependence of the shear modulus, μ, with $\mu_o = 49,000$ MPa.

$$\sigma_{\mu_e} = \sigma_{\mu_{e_e}} - \frac{\sigma_{\mu_{e_e}}}{\mu_o} \times (26.1T) = 807 \times \epsilon^{1/2} - 0.43 \times \epsilon^{1/2} \times T \tag{7}$$

Thus, with the aid of Eqs. 5 and 7 the total expression for $\sigma_i = \sigma^* + \sigma_{\mu_e}$ becomes

$$\sigma_i = \{1,315 \times (9.82 \times 10^{-12})^{1.66 \times 10^{-4}T}\} + \{807 \times \epsilon^{1/2} - 0.43 \times \epsilon^{1/2} \times T\} \tag{8}$$

Each of the five analytical curves in Fig. 4 was drawn using Eq. 8. The agreement of these curves with the experimental σ_i data is very good except at 4.2 K. This probably results from the fact that at 4.2 K the stress strain curves were severely serrated because, at this temperature twinning deformation becomes particularly important, the specific heat of a metal becomes vanishingly small, and the heat released by rapid plastic deformation produces sharp localized increases in temperature. Because the flow stress drops rapidly with increasing temperature in this range, this results in plastic instability or serrated flow due to localized heating causing local softening. The deviation in the 4.2 K flow stress data can therefore be explained by the localized deformations in the specimen that occur at a higher temperature than that of the bath and thus at a lower stress than if the deformation was uniform throughout the gage section.

Discussion

Although the Hall-Petch equation has been an important empirical relation for many years, there still remain questions about the significance of its components. Historically, three basic theoretical approaches were developed to rationalize the Hall-Petch equation. These were based on (a) dislocation pileup models, (b) work hardening models and (c) grain boundary source models. The earliest and most popular was
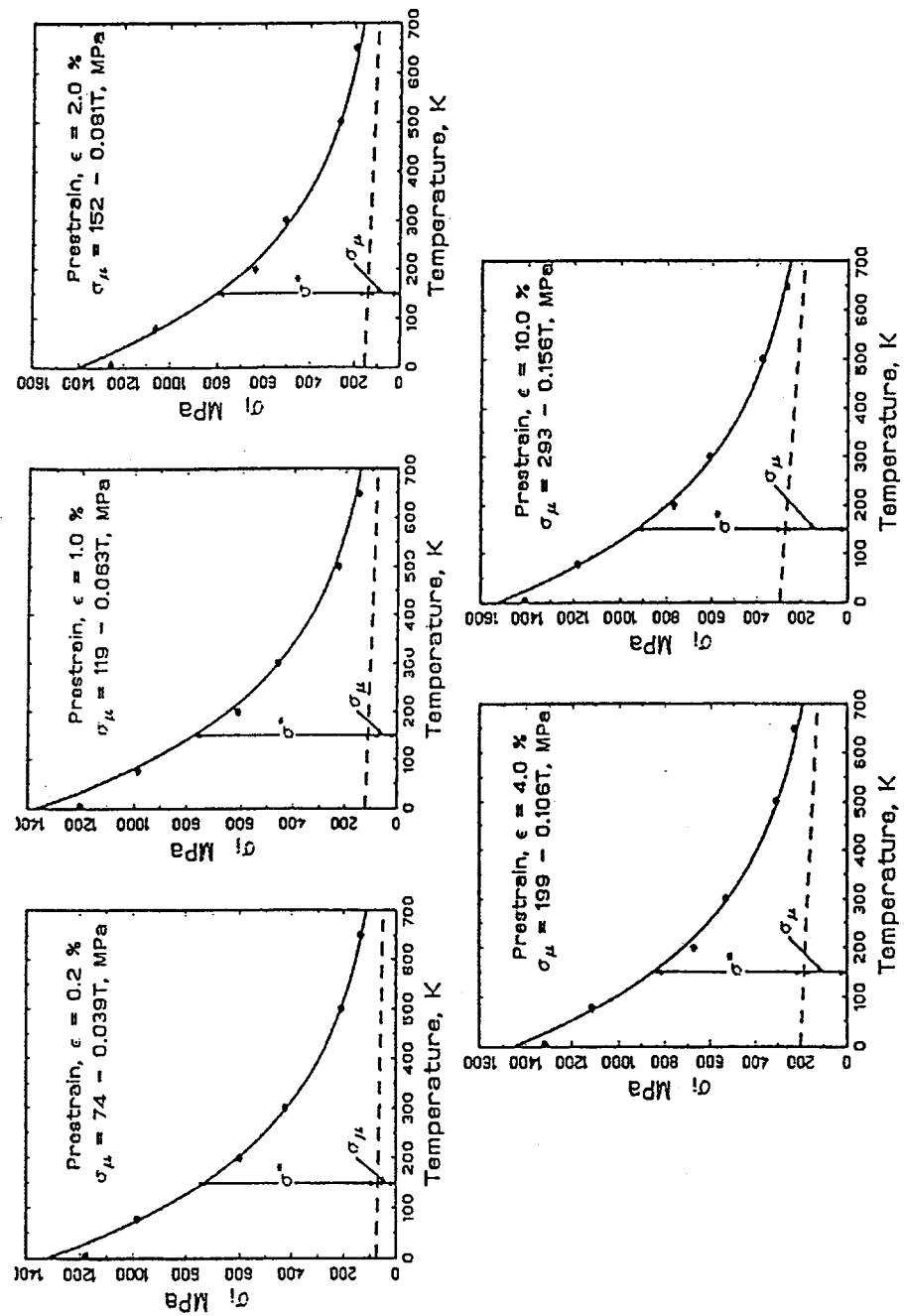
Figure 4. The above five diagrams show the variation of σ_i for all five prestrains used with the Ti A-70 specimens. The solid line curves in the figures were obtained with the aid of Eq. 8. Note that σ_μ in the five plots was assumed to be due only to the prestrain.

based on the dislocation pileup concept. According to this theory, pileups of dislocations on a slip plane at a grain boundary activate dislocation sources at or on the other side of the boundary [8,9]. Attention later turned to work hardening and grain-boundary source models. In this regard, the work hardening models make more assumptions than the pileup model, for example: (a) a linear relation between the flow stress and the square root of the dislocation density, (b) the average slip distance is proportional to the grain size d, and (c) the total dislocation density may be obtained by assuming all dislocations remain in the system. On the other hand, in grain boundary source theories, the grain boundaries are considered to be the sources of dislocations with the total length of dislocation emitted per unit area of boundary assumed to be a constant, m. It is significant that Li and Chou [9] mention that both of the latter theories suggest that at low temperatures $kd^{-1/2}$ is in the athermal part of the flow stress due to dislocations. The other part, σ_i, consists of the thermal part σ^* and an athermal part σ_s of other origin such as precipitates. Okazaki and Conrad have clearly shown that there is also an athermal component of σ_i related to the strain. We believe that the present work based on the use of the Yokobori activation enthalpy gives quantitative support to the Okazaki and Conrad conclusions. This strongly suggests that, with the aid of a Hall-Petch analysis, it should be possible to measure quantitatively the two primary components of the internal stress in a single phase alloy namely that due to grain size and that due to strain. This conclusion is in reference to Ti A-70 which is a single phase interstitial solid solution alloy. There is a good possibility, however, that this analysis can be expanded to the realm of alloys with more than one phase where there may be additional components of the internal stress, e.g. in alloys containing precipitates.

Summary

Calculations of σ^* based on the Yokobori activation enthalpy support the Okazaki and Conrad proposal that σ_i of the Hall-Petch equation, $\sigma = \sigma_i + kd^{-1/2}$, contains two components $\sigma^\circ(\dot{\varepsilon}, T, C_i)$ and $h_i(\mu, C_i) \times \varepsilon^{1/2}$ and indicate that the first term is the effective stress σ^* and that the second $h_i\varepsilon^{1/2}$ is the athermal component resulting from strain given the specimens prior to a flow stress measurement. This implies that the internal stress in Ti A-70 contains two components ($h_i\varepsilon^{1/2}$ and $kd^{-1/2}$). If it is possible to determine σ_μ quantitatively then, since $\sigma^* = \sigma - \sigma_\mu$, the effective stress should also be capable of being evaluated accurately. The present analysis demonstrates that $h_i\varepsilon^{1/2}$ can be quantitatively measured. It also indicates that it is probable that $kd^{-1/2}$ is also capable of being measured quantitatively. Additional data are necessary above and beyond those in the Okazaki and Conrad paper [2] in order to prove this. Although Ti A-70 is a single phase interstitial solid solution alloy, it is probable that other components of the internal stress may be capable of being evaluated in materials with more than one phase, i.e. those containing precipitates.

Acknowledgments

References

1. R.E. Reed-Hill, C.V. Iswaran and M.J. Kaufman, Scripta metall. mater., 33, 157 (1995).
2. R.E. Reed-Hill, C.V. Iswaran and M.J. Kaufman, Metall. Mater. Trans. A 27, 3524 (1996).
3. R.E. Reed-Hill, C.V. Iswaran and M.J. Kaufman, Metall. Mater. Trans. A 27, 3957 (1996).
4. K. Okazaki and H. Conrad, Acta Metallurgica, 21, 1117 (1973).
5. T. Yokobori, Phys. Rev., 88, 1423 (1952).
6. C.V. Iswaran, R.E. Reed-Hill, Vladimir I. Levit and M.J. Kaufman, Scripta metall. mater., 32, 941 (1995).
7. R.E. Reed-Hill, and M.J. Kaufman, Acta metall. mater., 43, 1731 (1995).
8. J.P. Hirth and J. Lothe, Theory of Dislocations, p. 716, McGraw-Hill Book Company, New York (1968).
9. J.C.M. Li and Y.T. Chou, Met. Trans. A, 1, 1145 (1970).

DEVELOPMENT OF NiAl SINGLE CRYSTALS AND THEIR MECHANICAL PROPERTIES

V.I. Levit, J. Hu, I.A. Bul, J.S. Winton and M.J. Kaufman
Dept. of Materials Science and Engineering
University of Florida
Gainesville, Florida 32611

Abstract

Single crystals of stoichiometric NiAl and NiAl alloys have been produced by Bridgman growth in high purity, high density alumina crucibles. The stoichiometric crystals contain lower silicon and higher carbon levels compared with the zone melted, high purity crystals produced in Oliver's laboratory and are considerably purer than the "commercial purity" (CP) crystals produced by General Electric. The compositional analyses are readily confirmed by simple mechanical property measurements where it has been found that the critical resolved shear stress (CRSS) for cube slip on either the {011} or {001} planes of high-purity, stoichiometric NiAl is about 55 MPa, approximately half that of the CP crystals. It is shown that the mechanical properties of NiAl crystals depend on such things as purity, stoichiometry, specimen and grip geometry; when these are optimized, elongations as high as 35% are possible at room temperature whereas elongations as high as 300% may be achieved at intermediate temperatures and strain rates (e.g., 800K, $10^{-3}s^{-1}$). In fact, the properties of NiAl are a strong function of strain rate and test temperature and, when considered over a wide range of conditions, it is shown that NiAl is a reasonably well-behaved material. It is also concluded that the limited number of independent deformation mechanisms may be a "show stopper" for this material since, no matter what is done to address the property deficiencies, NiAl will always be brittle due to this particular characteristic. More generally, this implies that any compound that does not have a sufficient number of deformation mechanisms (independent slip systems) to satisfy the von-Mises criterion, even though the dislocations can move readily, will be brittle in both the single and polycrystalline form.

RECENT RESURGENCE IN INTEREST IN developing β-NiAl as a structural material has led to many advances in our understanding of its structure and properties. While NiAl has the potential of being a low density, high temperature and oxidation resistant structural material, it suffers from the same problems as many other intermetallics, namely, low strength and toughness. Although the strength can be readily enhanced using typical metallurgical approaches (see papers by Noebe, et al. and Darolia, et al. in this proceedings), any benefits in this area tend to be offset by reductions in toughness and this dichotomy has not been resolved as yet in this or any other system to our knowledge. This is in spite of the fact that relatively high elongations (5-10%) have been achieved in single crystal NiAl via both composition — stoichiometry, purity and microalloying — and heat treatment control (1-5). More recently, we have shown that even higher elongations (approaching 35%) can be achieved by controlling both the specimen and grip geometries in addition to the previously mentioned variables [6]. Unfortunately, these elongations in single crystals cannot be equated with increased toughnesses as will be discussed further below. The purpose of this paper is to highlight some of the recent advances in our understanding of the deformation and fracture behavior of high purity NiAl over a range of temperatures and strain rates. A more complete analysis of these issues will be published elsewhere.

Single Crystal Development

The lack of five independent slip systems is believed to preclude the attainment of significant ductility in polycrystalline NiAl (1,2). This, combined with the fact that single crystals tend to have better high temperature properties and are better for fundamental studies of deformation behavior have led investigators in more recent years to concentrate on single crystal development. Many of the single crystals studied by investigators around the world

in the recent past have been prepared and supplied by Darolia and co-workers at General Electric. These "commercial purity (CP)" crystals were processed by simply extending the technology developed for cast nickel-base superalloys, namely, by using investment-cast molds produced using alumina-silica slurries. Unfortunately, the higher temperatures required for melting/processing NiAl combined with its higher aluminum activity leads to silicon contamination. In terms of interstitials, the levels are similar to those in superalloys although, as shown by Hack et al. (3), Weaver et al. (4), NiAl is very sensitive to interstitial contamination indicating that this conventional commercial approaches are probably unsuitable for this material. Specifically, carbon has been shown to cause both static and dynamic strain aging in NiAl, much like in steels, and silicon appears to exacerbate the problem by some unknown mechanism (4).

In this study, high purity (HP) NiAl crystals of various orientations have been made by Bridgman growth in high-purity, high-density alumina crucibles using prealloyed material that was either arc melted or vacuum induction melted using high purity elemental constituents, the latter in high-purity, low-density alumina crucibles. The resulting crystals exhibited higher purities than the CP crystals in terms of both interstitial levels and silicon contamination and had lower silicon and slightly higher carbon than the high purity, zone melted crystals produced by Oliver, et al. using his containerless zone melting system (e.g., 4). The melting point of our high purity NiAl was measured to be 1955±5 K which is close to that reported by Walston and Darolia (5) and about 50 K higher than published phase diagrams indicate (e.g., (1,2). The higher purity of the Bridgman crystals was confirmed in the mechanical property studies as described below. For the latter, tensile specimens with rectangular cross sections were cut from these crystals by electro-discharge machining (EDM) as described elsewhere (Fig. 1a) (6).

Slip Behavior and Work Hardening

It is well established that <100> slip is dominant in NiAl under almost all testing conditions (Fig.1); the other slip vectors (110 and 111) become important only under special conditions such as when testing in the <100> hard orientation where the resolved shear stress (RSS) for <100> slip is negligible. The CRSS for cube slip on both {110} and {001} planes is about 55 MPa for the HP NiAl at room temperature vs. about 100 MPa for CP NiAl (6-8). However, unlike pure metals which tend to have low CRSS values and high ductilities, single crystal NiAl has low CRSS and low ductility. The reasons for the latter has been somewhat unclear in view of the relatively high ductilities exhibited by other intermetallics in single crystal form. This issue of low elongations will be addressed further below.

Although the CRSS values for slip on either {110} or {100} appear to be similar, slip on the {011} planes can, and frequently does occur by single slip (i.e., for tensile axes parallel to <uuw> where u>0 and w>1 such as [557] in Fig. 1c) whereas slip on {001} (e.g., for tensile axes parallel to [011] in Fig. 1c) is always duplex in nature due to the fact that the Schmid factor is the same for slip on both the [001](010) and [010](001) systems (Fig. 1c). Consequently, the crystals undergoing duplex slip tend to exhibit considerably higher work hardening rates than the single slip geometries as expected for normal deformation behavior.
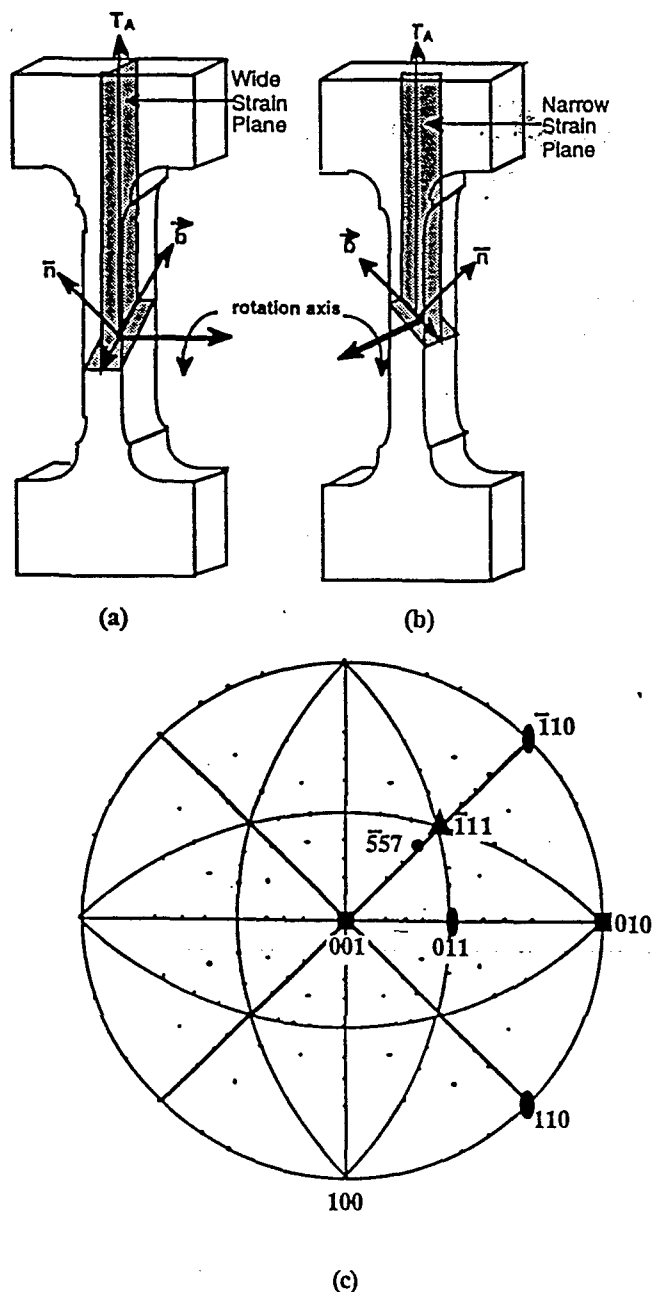

(a)   (b)

(c)

Fig. 1. Schematics of tensile specimens used in this study: (a) Wide strain plane (WSP) - optimum for high elongation, (b) Narrow strain plane (NSP), and (c) Stereogram with tensile orientations and slip systems indicated.

Recent investigations of the deformation substructures have revealed that, for both systems, the dislocations are mostly edge in nature — in the case of cube slip on cube planes, the dislocation line direction tends to be along the third <100> whereas for slip on {110}, the line direction is parallel to the <110> that lies in this slip plane. Furthermore, it has been recently shown that these dislocations are in the form of slip bands after deformation at room temperature and are more uniformly distributed after deformation at sub-ambient temperatures (~180K).

Tensile Properties

Ambient and Sub-ambient Behavior. As mentioned above, the CRSS for cube slip is quite low in high purity NiAl and increases with increasing solute concentration in a manner similar to that for metals. Furthermore the CRSS for cube slip exhibits a temperature dependence similar to that of many bcc metals (Fig. 2) which makes it tempting to compare their behavior with classical Peierls stress arguments (7-9). However, such comparisons may not be applicable in view of the different slip vector in NiAl. The observations (6) that the deformation substructures consist primarily of edge dislocations suggest that the screw components are much more mobile at room temperature consistent with the behavior in bcc metals. Unfortunately, the behavior at lower temperatures, where long pure screw components are commonly observed in bcc metals, has not been examined to date and, therefore, nothing can be concluded concerning the mechanism of increasing CRSS with decreasing temperature.

(a)

(b)
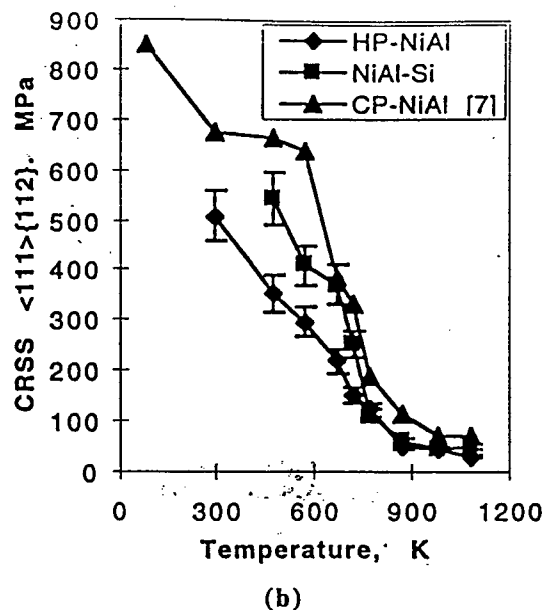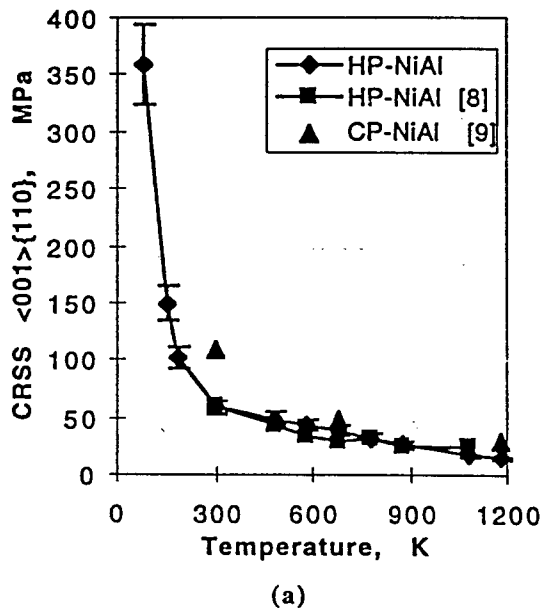
Fig. 2. Temperature dependence of "critical" resolved shear stress for both HP and CP NiAl single crystals calculated at 0.2% strain for both [111] "soft" (a) and [001] "hard" (b) orientations. For the "hard" crystals, the <111>{112} system was used for the RSS calculations.

The CRSS for <111> slip has been determined using <001>-oriented crystals and was found to decrease with increasing temperature (Fig. 2b) in agreement with the results of Bowman et.al. (7). As expected, the values were somewhat lower than those reported for CP crystals consistent with their higher purity. It is interesting to note that, in the HP crystals, there is no plateau in the CRSS vs. temperature curve, while this plateau in the CP crystals was correlated with a change in the slip vector from <111> to <110> (2). Its absence in the HP crystals indicates that there may not be a "sharp" transition from <111> to <110> slip as suggested in some recent experiments in our laboratory.

As alluded to above, the elongation depends on purity and geometry of the specimens. A comparison of the HP-NiAl (in tension) and the CP-NiAl (in compression) behavior for different orientations is shown in Fig. 3a. As can be seen, the yield stresses are lower for the HP material and the elongations are considerably higher. Furthermore, the work hardening rates for the HP-NiAl is lower than for the CP-NiAl with the single slip orientation (TA//[111]) displaying a lower WHR than the double slip geometry (TA//[011]). Furthermore, the elongation corresponding to the single slip geometry is consistently higher presumably due to the lower stresses that develop at stress concentrations during plastic deformation.

It is important to note that the surface preparation plays a critical role in the achievment of high tensile elongations in the HP-NiAl as well as in the CP material as pointed out by Walston and Darolia (10). However, the influence of

surface oxidation in the HP-NiAl is detrimental to the elongation behavior in contrast to the behavior reported by Kim, et al. (12) for their CP-Ni-48Al (Fig. 3b). Furthermore, there appears to be no softening associated with the surface oxidation for the HP-NiAl indicating that the oxide is not necessary for acting as a source of dislocations.
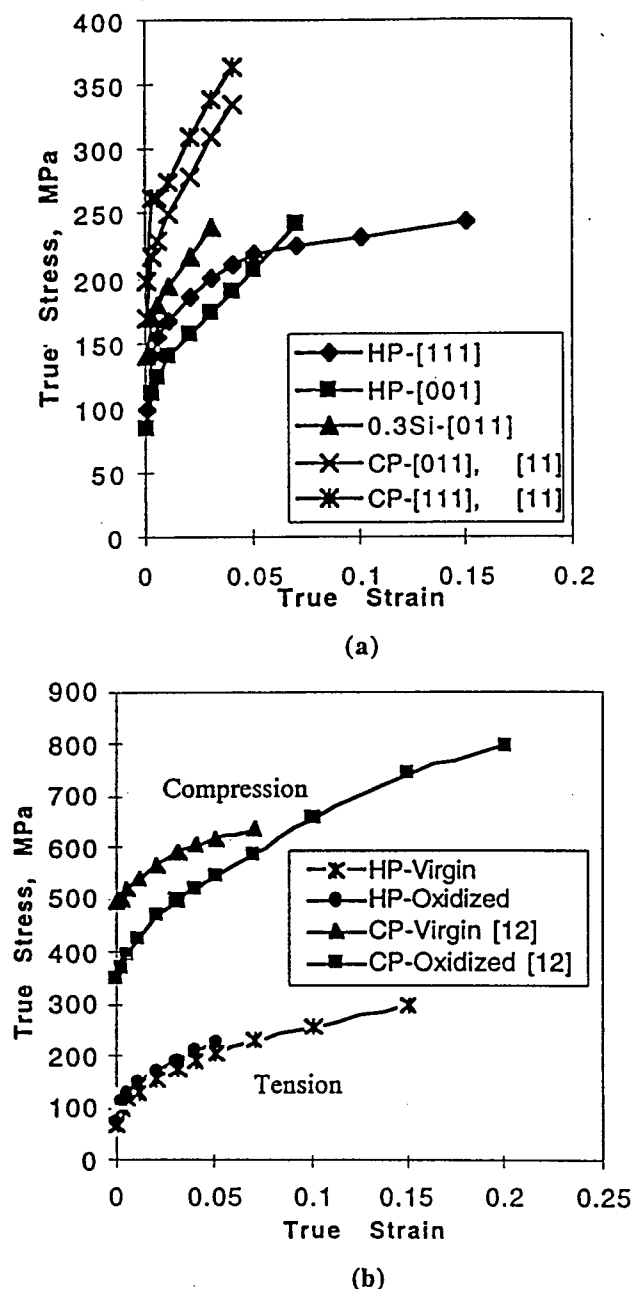

(a)

(b)

Fig. 3. Orientation and purity (a) and surface oxidation (b) effects on mechanical behavior of NiAl single crystals at room temperature. Tensile tests for HP crystals and compression for CP crystals

Elevated Temperature Behavior. Based on the above description of the deformation and fracture behavior, it is interesting to discuss the properties of NiAl at

elevated temperatures. As noted Takasugi et al (13), the elongation in the high purity NiAl crystals increases with increasing temperature up to a maximum before dropping off at even higher temperatures. In the present study, this behavior was confirmed and extended to higher elongations and wider temperature intervals (~350%) by controlling the orientation and geometry of the crystals and by varying the strain rate (Fig. 4).

For the highest elongations, the load-elongation curves displayed somewhat unusual behavior similar to that surmised from the stress-strain data reported by Takasugi, et al.(13) By performing interrupted tensile tests, it was shown that the drop in the load at low strains corresponded to strain localization in the form of a diffuse neck (or necks for the duplex slip orientation) which spread along the gage length. This was followed by more general deformation of the gage section until the material underwent a brittle fracture.

For the [357] orientation, the single slip deformation leads to the rotation of the tensile axis towards the [001] slip vector (Fig. 1) which, in turn, leads to a decreasing Schmid factor with increasing strain. Electron backscattering patterns from a sample containing a diffuse neck were obtained and confirmed the nature of the rotation and its variation across the neck. This decreasing Schmid factor leads to effective hardening in the "necked" region which help to initiate a "geometrical" band. This band spreads along the gage length during continued deformation. By accounting for both the rotation and the cross section changes, the shear stress-shear strain curves were plotted (Fig.5) and indicated that the work hardening in the single slip orientation was very low.

For the [011] orientation, the duplex nature of the slip stabilizes the specimen against macroscopic lattice rotation and the Schmid factor is approximately constant (0.5) during deformation. However, the work hardening rate is about an order of magnitude higher than the single slip case which leads to hardening in the necked region and spreading of the neck along the gage length. Furthermore, because of the more stable geometry due to the offsetting, duplex nature of the slip, multiple necks are commonly observed in contrast to the single slip case where a single neck is most common.

The elongation behavior as a function of test temperature is shown in Fig. 4 for a range of orientations, geometries and strain rates and it is clear that the peak in elongation depends on both geometry and strain rate. For a given orientation and geometry, it is clear that the peak in elongation shifts to higher temperatures with increasing strain rates. This behavior is normal for thermally activated plastic flow; although the specific rate controlling process has not been identified, the apparent activation energy is approximately 150 kJ/mol, in good agreement with the Takasugi et al. data (13).

The present results indicate that the behavior of NiAl is between metals and ceramic. Specifically, the

dislocations move readily in the HP material and their mobility is hindered, as in metals, by introducing solute and/or precipitates. For orientations where only one slip
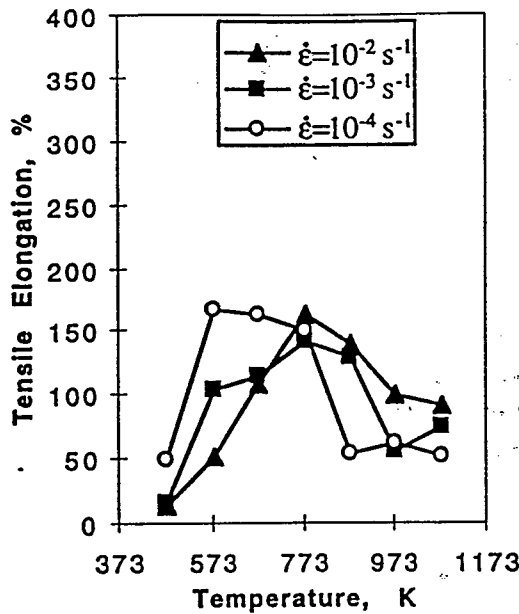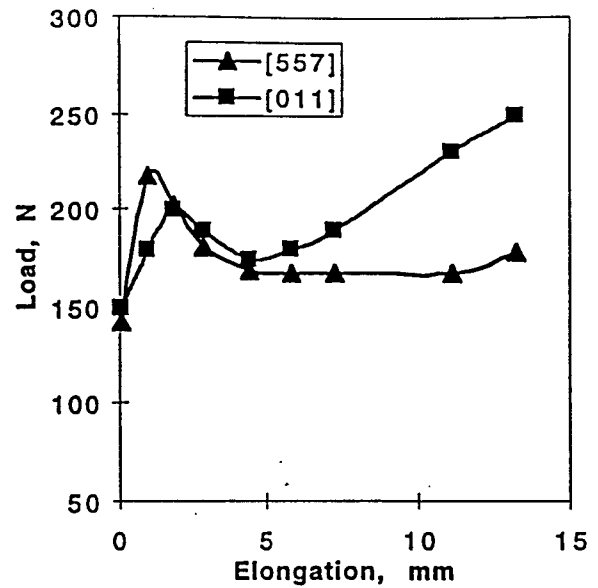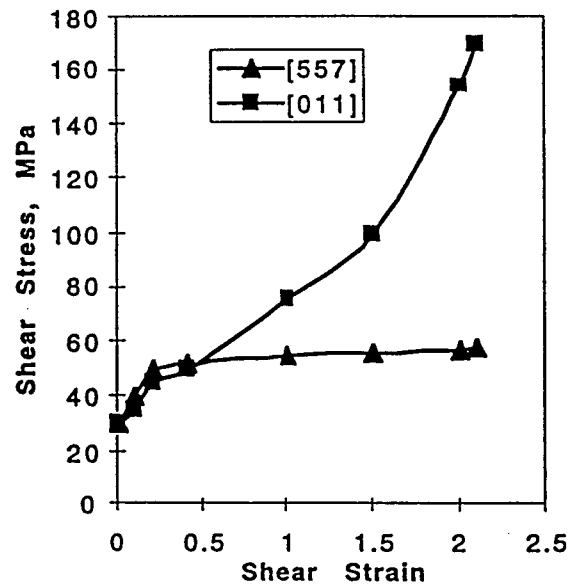

(a)
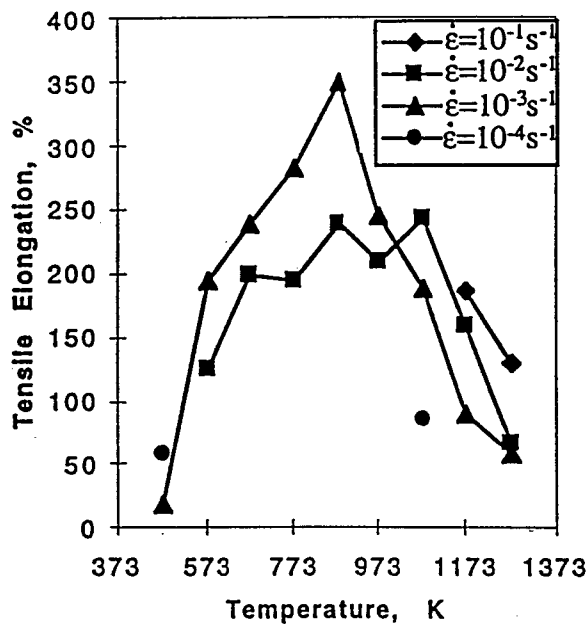
(b)

Fig. 4. Orientation and geometry effects on the tensile elongation of NiAl single crystals oriented for single slip: (a) [111] TA with random geometry; (b) [557] specimens with the geometry optimized.

(a)

(b)

Fig. 5. (a) Load elongation and (b) shear stress-shear strain diagrams of NiAl crystals tested at 673K and $\varepsilon=10^{-3}s^{-1}$.

system is operative, the lattice rotates during deformation leading to a change in the Schmid factor. While this rotation leads to macroscopic hardening, it is clear that microscopically, little hardening occurs during deformation. For the duplex slip geometry, no lattice rotation occurs (other than localized rotation across slip bands) and the work hardening rate is considerably higher than the single slip case.

Whereas NiAl deforms much like a metal, the problem arises when stresses develop at stress concentrations. Since these stresses cannot be relieved by

activating other deformation mechanisms, the stress eventually exceeds the fracture stress and brittle fracture occurs. Like ceramics, the macroscopic stress and elongation vary considerably due to the statistical nature of brittle fracture. Thus, careful control of such variables as purity, surface finish, specimen geometry and prestrain leads to higher elongations prior to brittle fracture. Likewise, the temperature and strain rate also are important since the temperature (I) leads to a lower CRSS and (II) allows for thermally activated mechanisms to become operative to lower the stress at stress concentrations. Likewise, the strain rate is also important for the same reason in the temperature regime where thermally activated deformation is possible. Unfortunately, these arguments imply that the material will be very sensitive to high strain rate impacts at elevated temperatures.

Finally, this data strongly suggests that any intermetallic (or any material for that matter) which undergoes slip deformation at low resolved shear stresses will be brittle in both single and polycrystalline form if there are insufficient deformation mechanisms available to avoid the high stresses that will inevitably develop at stress concentrations.

Summary

It has been shown that the plastic deformation of β-NiAl single crystals occurs in a manner quite similar to that in many metals and alloys as indicated by the following statements. Unfortunately, the lack of five independent deformation mechanisms leads to premature fracture in single crystals due to the stresses that develop at stress concentrations; this, in turn gives rise to the brittle, ceramic-like behavior of NiAl.

1. NiAl is softest in the highest purity state and undergoes both solid solution and precipitation hardening when alloying additions and/or impurities are present.

2. Surface oxidation has a negligible softening effect on HP-NiAl and a detrimental effect on elongation behavior.

3. High elongations are possible in NiAl by optimizing the purity, geometry and surface finish. The temperature dependence of elongation has been explained as being due to the development and propagation of a "geometrical" band for the samples oriented for single slip and multiple diffuse necks when symmetrical double slip is operative.

4. The temperature dependence of the CRSS in NiAl appears quite similar to that observed for typical bcc metals. While the observations after deformation at room temperature are consistent with a higher mobility of screw dislocations, the behavior at liquid nitrogen temperatures is still under investigation.

References

1. Noebe, R.D., R.R. Bowman and M.V. Nathal, in Physical Metallurgy and Processing of Intermetallic Compounds, Chapter 9 N. S. Stoloff, V. K. Sikka, Eds. New York, NY, (1994)

2. Miracle, D.B., Acta. Metall. Mater. 41, 649-684 (1993)

3. Hack, J.E., J.M. Brzeski and R. Darolia, Scripta Metall. Mater. 27, 1259-1263 (1992)

4. Weaver, M.L., R.D. Noebe, J.J. Lewandowski, B.F. Oliver, M.J. Kaufman, Mater. Sci. & Engr. A192, 179-185 (1995)

5. Walston, W.S., and R. Darolia, MRS Symp. Proc., 288, 237-242 (1993)

6. Levit, V.I., I.A. Bul, J. Hu and M.J. Kaufman, Scripta Mater. 34, 1925-1930 (1996).

7. Bowman, R.R., R.D. Noebe and R.Darolia, NASA CP-10104, 38-1 -38-15 (1989)

8. Takasugi, T., S. Watanabe and S. Hanada, Mater. Sci. & Engr. A149, 183-193 (1992)

9. Lahrman, D.F., R.D. Field and R. Darolia, MRS Symp. Proc., 213, 603-607 (1991)

10. Darolia, R. and W.S. Walston, Intermetallics, 4, 505-516 (1996)

11. Kim, J.T., R.D. Noebe and R. Gibala, Intermetallic Compounds: Structure and Mechanical Properties (ed. by O. Izumi), 591-595 (1991)

12. Field, R.D., D.F. Lahrman and R. Darolia, MRS Symp. Proc., 213, 255-260 (1991)

13. Takasugi, T., J. Kishino and S. Hanada, Acta. Metall. Mater. 41, 1009-1020 (1993)

TENSILE BEHAVIOR OF β-NiAl: INTRINSIC VS. EXTRINSIC PROPERTIES

V.I. Levit and M.J. Kaufman

Department of Materials Science and Engineering
University of Florida
Gainesville, FL 32611

Abstract

The influences of such variables as specimen geometry (cylindrical vs. rectangular), orientation, purity, stoichiometry, thermal history, surface oxidation, surface damage and prestrain on the room temperature tensile properties of β-NiAl single crystals are described. The results indicate that $<001>\{110\}$ and $<001>\{100\}$ slip in high purity, stoichiometric NiAl occurs at similar, low stresses (CRSS ~ 50 MPa) consistent with slip in pure metals. Furthermore, prestrain, surface oxides, alloying additions, impurities and thermal vacancies all harden NiAl in a manner similar to their effects in pure metals. Finally, it is shown that NiAl fractures by brittle cleavage even after elongations of up to 34% due to the lack of a sufficient number of slip systems. The implications of these results are described with respect to the potential of using this or other intermetallics with a limited number of slip systems in structural applications.

Introduction

Although the compound β-NiAl has been promoted as one of the more promising potential structural intermetallics because of its high melting point, wide solubility range and oxidation resistance, its transition into application has been delayed by the fact that it is both soft and brittle in the unalloyed condition (1). While both of these properties can be enhanced somewhat via composition control, the enhancements tend to be offsetting in nature (2), i.e., alloying additions that enhance strength tend to increase brittleness whereas high purity crystals that are somewhat less brittle exhibit low strengths (3,4). In addition, the discrepancies in the literature concerning the effects of such extrinsic variables as surface films (5), impurities (6-10), thermal vacancies (6,9), prestrain (10-12), microalloying additions (13), surface finish (14,15), specimen and grip geometries (4,16,17), etc. have led to considerable confusion such that there has developed a definite need for a systematic study aimed at clarifying some or all of these issues. The AFOSR-sponsored University Research Initiative (URI) at the University of Florida and the Johns Hopkins University was aimed at generating the necessary understanding of the microstructure-property-processing relationships in this compound. The purpose of this paper is to describe some of the more recent results, mostly at room temperature, and their relationship to previous reports.

Experimental

Oriented single crystals of nominally stoichiometric NiAl and one silicon-doped alloy were prepared by Bridgman growth as described elsewhere [4], homogenized at 1573 K for 3h and furnace cooled (HFC). The compositions of the crystals used in the present study were measured using standard methods and are summarized in Table I. After homogenization, tensile specimens were cut using an electrical discharge machine (EDM). These specimens had rectangular cross sections with dimensions 1.6 mm wide (W) x 2.4 mm thick (T)[1] (approximately 1.3mm x 2.1mm after electropolishing to remove the recast layer and any surface roughness) and nominal gage lengths of 10 mm. The tests were performed in an Instron Model 1125 at a nominal strain rate of $10^{-4}s^{-1}$. For the non-$<001>$ specimens, the orientations of the sides of the rectangular sections were either random with respect to the preferred $<001>$ slip vector(s) or non-random, i.e., for tensile axes parallel to $<557>$ (single slip with Schmid factor, f_s, of 0.5) or $<011>$ (double slip with $f_s = 0.5$), one of the sides was cut parallel to the plane containing the tensile axis, the Burgers vector(s), $\mathbf{b}$, and the slip plane normal(s), $\mathbf{n}$. Specifically, for the $<557>$ specimens, this was the parallel $\{011\}$ plane while for the $<011>$ specimens, it was the parallel $\{001\}$ plane (Fig. 1). Since the specimens are rectangular, the gage faces were cut such that this plane was parallel to either the thickness or the width of the specimens in order to determine the influence of the initial geometry, shape change and degree of constraint on the deformation and fracture behavior. Because of the nature of gripping such samples in the button-head grips, when the plane containing the tensile axis, $\mathbf{b}$, and $\mathbf{n}$ is parallel to the width (Fig. 1a), there is greater constraint than when

---

[1] these dimensions were varied in one portion of the study in order to determine their influence on tensile properties.

parallel to the thickness (Fig. 1b). Consequently, these will be referred to as "constrained (C)" and "less constrained (LC)" geometries, respectively. It is noted that these special geometries correspond to plane strain conditions in the sense that the dimension orthogonal to this special plane does not change during plastic deformation whereas any dimension parallel to this plane does. For example, there is a change in the dimensions as shown in Fig. 1a where the plane OABC changes to OA'B'C' whereas the thickness, CD, does not change.

After spark cutting, the specimens were electropolished and, in some cases, given subsequent heat treatments in order to vary the vacancy concentration and/or the oxide thickness. These samples were cooled in one of the following ways: furnace cool (FC), air cool (AC) or water quench (WQ). A set of specimens were also notched to different depths in order to determine the notch sensitivity of the rectangular specimens. Most of the tests described here were performed at room temperature; the elevated temperature tests are described elsewhere [16].

Table I. Compositions of the NiAl single crystals used in this study.

Crystal ID	Ni at. %	Al at. %	Si ppm	Fe ppm	Cu ppm	C ppm	S ppm	O ppm	N ppm
SC-18	49.7	50.2	260	110	20	14	-	-	-
SC-64	50.6	49.3	240	-	-	180	n/d	81	<15
SC-36	49.7	50.2	300	50	-	53	-	-	-
SC-34	50.4	49.5	n/d	-	-	82	<5	106	<15
SC-31B*	50.0	49.9	136	-	-	50	7	90	12
SC-31T*	50.0	49.9	n/d	-	-	70	5	80	12
SC-60B*	49.2	50.7	170	27	-	18	-	-	-
SC-60T*	49.6	50.3	160	n/d	-	42	-	-	-
SC-76	50.1	49.8	107	-	-	93	-	73	-
SC-40	50.0	49.9	100	-	-	110	13	100	9
SC-93**	50.0	49.6	3400	-	-	180	<10	124	<15

* B represents the bottom and T the top part of the crystal relative to the growth direction.
** average composition of initial VIM rods used as feedstock for SC 93.

Constrained (C)

a

Less Constrained (LC)

b
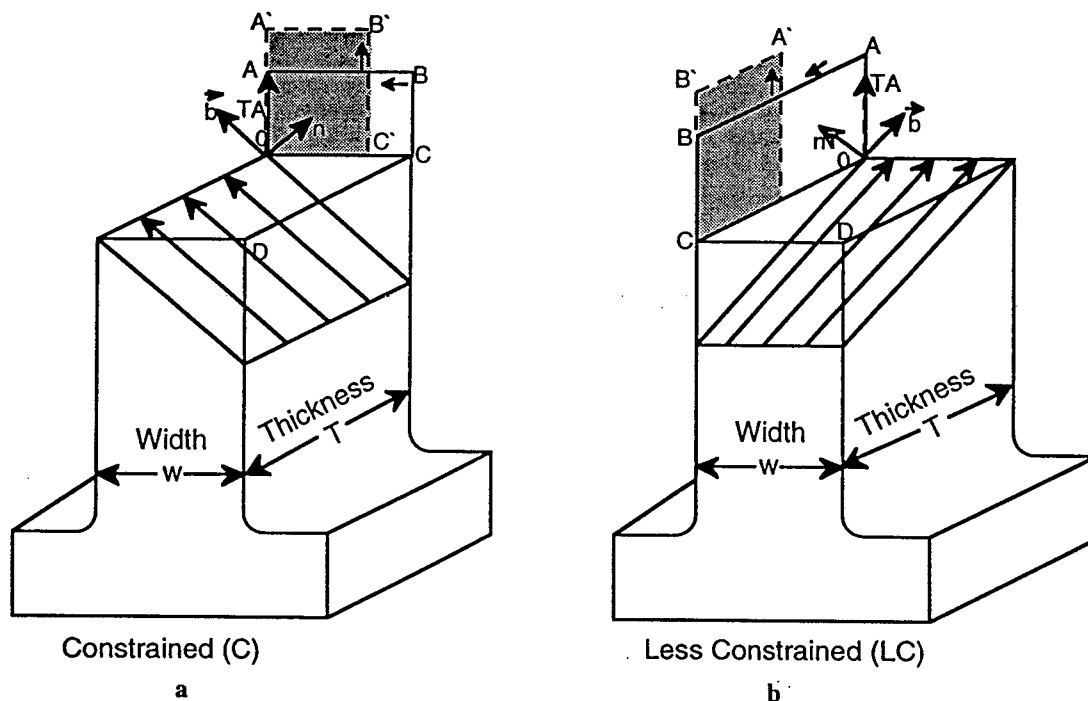
Figure 1. Schematics of the rectangular tensile specimens before and after deformation. Note the shape change (shaded) is consistent with "plane strain" in that there is no change in the thickness (T) in the constrained (C) specimens or the width (W) in the less constrained (LC) specimens.

Results

The results are subdivided into sections that address such issues as the influence of purity, prestrain, thermal vacancies, surface oxidation and surface finish on the mechanical properties of NiAl. The first section addresses the importance of specimen geometry and constraints in the grips and justifies why the majority of the tests were performed on rectangular instead of the more commonly used cylindrical specimens.

Specimen Geometry

When the literature concerning the tensile properties of NiAl is examined, it becomes apparent that the majority of the data were generated using cylindrical, button-head specimens whose gage sections were prepared by centerless grinding followed by electropolishing to a "shiny" surface finish. However, the present results generated using cylindrical and rectangular specimens cut from the same single crystal (SC-76) (Table II) provide important insight into the influence of geometry on tensile properties. While the CRSS values are not affected significantly by the specimen geometry and surface finish as might be expected, the elongations and fracture stresses depend strongly on these parameters. Clearly, the elongations are highest for the rectangular specimens, lowest for the cylindrical specimens that were lightly polished, and intermediate in the cylindrical specimens that were repolished after observing the low elongations characteristic of the samples given the light polish. This implies that the damage zone from centerless grinding exceeded the thickness of the material removed during the standard light polishing. These results are in agreement with the recent reports by Darolia and Walston (15). Considering the soft nature of the high purity NiAl crystals, it is not surprising that the extent of the damage that results from grinding may be considerably greater than that observed in stronger multiphase crystals or polycrystals.

The other important factor realized after these tests was that the rectangular geometry is superior to the cylindrical geometry in terms of achieving the highest elongations. This is presumably related to the greater constraints that exist when gripping cylindrical button-head specimens as described elsewhere (17). Consequently, the remaining tests were performed using rectangular specimens.

"Plane Strain" Tests

As will be shown below, the highest elongations were achieved using the LC geometry sketched in Figure 1. In this part of the study, it was of interest to determine whether or not the high tensile elongations were related to the small specimen sizes which might allow the dislocations to slip out of the crystal more readily, thereby increasing the extent of Stage 1 deformation as happens in fcc metals such as copper (18). Small specimen sizes might also lead to higher elongations since the probability of the sample containing critical flaws decreases with decreasing cross-sectional area. Therefore, both LC and C specimens were tested with different cross-sectional areas. The results indicate that the elongation is not a strong function of specimen size. In fact, it appears that the elongation does not increase with decreasing cross-sectional

Table II. Tensile data for [135] specimens cut from SC-76 illustrating the influence of specimen geometry (R-rectangular, C-cylindrical) and surface finish (SP-standard polish, LP-lightly polished, RP-repolished).

Orient. Shape	Surface Finish	$\sigma_{0.2}$ MPa	σ_f MPa	El. %
[135]R	SP	132	217	7.8
[135]R	SP	135	206	5.3
[135]C	LP	-	145	<0.1
[135]C	LP	-	142	<0.1
[135]C	RP	142	230	3.4
[135]C	RP	145	221	2.8

area; this may be related to the fact that the thinner specimens are more sensitive to surface damage or defects. It is noted that, for the single slip specimens, the rotation of the slip vector towards the tensile axis does not lead to conjugate slip as in fcc metals and, therefore, the slip can continue as long as the stress does not reach the fracture stress at some stress concentration. Consequently, the onset of Stage 2 deformation is not realized in these samples prior to fracture at room temperature.

It should be emphasized that the amount of scatter in the CRSS values for a given set of specimens is quite low whereas the scatter in the elongations and fracture stresses is high. This implies that the deformation of NiAl is similar to that of metals and is reasonably reproducible whereas the fracture stress and elongation vary considerably, consistent with the statistical nature of brittle fracture. As noted in ([1,2,4,17), this is related to an insufficient number of slip systems to satisfy the von-Mises criterion and avoid the high stresses that develop at stress concentrations in the material.

Table III. Tensile properties (TA=[557]) of rectangular (C and LC) specimens cut from SC-34 with slightly different dimensions. The higher $\sigma_{0.2}$ values for the 34T specimens are due to compositional differences.

ID	Geom.	Dimensions (W x T) mm	CSA* mm²	$\sigma_{0.2}$ MPa	σ_f MPa	El. %
34B	LC	1.3 x 2.1	2.13	108	190	16
34B	"	1.2 x 1.3	1.56	137	317	13
34B	"	1.3 x 1.3	1.69	103	164	4
34B	"	1.3 x 0.8	1.04	100	206	10
34B	"	1.3 x 0.8	1.04	116	220	13
34B	"	1.1 x 1.0	1.10	87	225	8
34T	C	1.3 x 2.2	2.86	148	255	16
34T	"	1.4 x 1.0	1.40	142	242	15
34T	"	1.4 x 0.8	1.12	142	201	5
34T	"	1.3 x 0.8	1.04	155	249	15

*CSA = cross-sectional area

Notch Effects

In view of the higher elongations achieved in the rectangular specimens, an attempt was made to determine the effects of notches when the constraints were less than in the cylindrical (constrained) specimens where, as already shown,

any surface damage leads to negligible elongation. Consequently, standard rectangular specimens of both the LC and C geometries were notched using the wire EDM to different depths ranging from 50 to 1000 μm on one of the faces. It is clear from Table IV that the specimens cut from the top of the crystal were stronger than those from the bottom as already described. More importantly, the influence of the notches resulted in a decrease in elongation. In all cases, the fracture originated at the notch as expected. It should be noted, however, that the elongations were still significant and considerably higher than those achieved with cylindrical specimens where the notch sensitivity appears to be enhanced presumably due to the constraining effects mentioned above.

Table IV. Effects of notch depth on the properties of [557] crystals of NiAl.

ID	Geom.	Notch Depth	$\sigma_{0.2}$ MPa	σ_f MPa	El. %
34B	LC	Unnotched	108	190	16
"	"	1 mm	-	168	0
"	"	500 μm	-	136	<0.1
"	"	250 μm	110	117	0.2
"	"	100 μm	122	142	0.5
"	"	50 μm	111	156	3.4
"	"	75 μm	120	157	2
"	"	"	112	131	1.4
"	"	"	111	152	2.7
"	"	"	109	114	0.4
34T	C	Unnotched	148	255	16
"	"	75 μm	158	161	0.7
"	"	"	152	157	0.4
"	"	"	126	147	0.9
"	"	"	144	181	2.9
"	"	"	142	169	2.1

Orientation Effects

It is clear from Table V, that the samples tested along the hard <001> orientation are considerably stronger than those tested along the softer orientations due to the negligible Schmid factor for cube slip. This leads to elastic deformation with no elongation and considerable scatter in the fracture stress as expected based on the above discussion.

For the soft orientations, it is important to realize the need to exercise caution when defining the CRSS based on a 0.2% offset value. Specifically, while easy glide (Stage 1) in fcc crystals assures that the CRSS at 0.2% strain is similar to that at the proportional limit, σ_p, where the dislocations first start to move, this is not necessarily the case in NiAl in spite of the fact that most reports of the CRSS in NiAl are calculated at 0.2% strain [1-3]. This is especially a concern in the higher purity crystals where there is no plateau in true stress - true strain curves as frequently observed for lower purity NiAl (see Fig. 2 and Table V).

In addition, it is necessary to distinguish between the behavior of specimens oriented for single slip (e.g., <557>)

and those oriented for double slip (e.g., <011>). When a large sampling of test results from these samples are examined, the following conclusions become apparent. First of all, the CRSS for cube slip on {001} planes is essentially equal to that on {011} planes at room temperature and falls typically between 40 and 60 MPa. This variation is due mostly to purity or Ni/Al ratio as confirmed by noting that the CRSS for samples cut from the same region of the same crystal (e.g., the [011] and [557] specimens from 34T as well as the [233] and [557] specimens from 34B) exhibit similar τ_p and $\tau_{0.2}$ values.
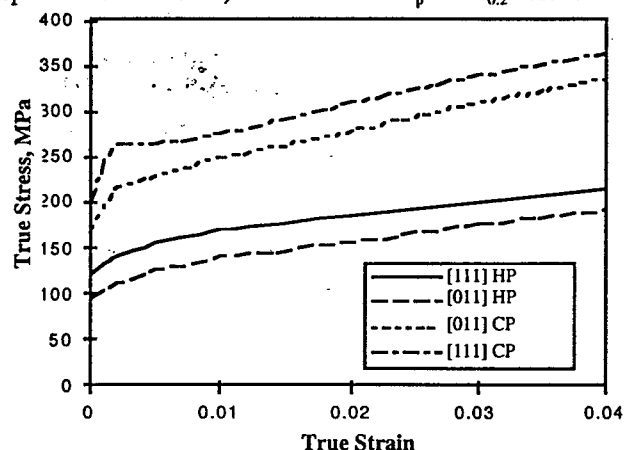

Figure 2. True stress vs. true strain for both high purity (HP) and commercial purity (CP) (19) NiAl along the [111] (single slip) and [011] (double slip) orientations.

In spite of their similar CRSS values, it is apparent that the work hardening rates (WHR) for the double slip orientations are considerably higher than those for single slip whereas the elongations tend to be lower. Clearly, this latter result is expected since the higher WHR, calculated from the shear stress - shear strain curves (Fig. 3) and compared with the <001> shear modulus where μ_{001}=112 GPa (20), leads to higher stresses for a given amount of elongation; these stresses, in turn, lead to fracture at lower total elongations.
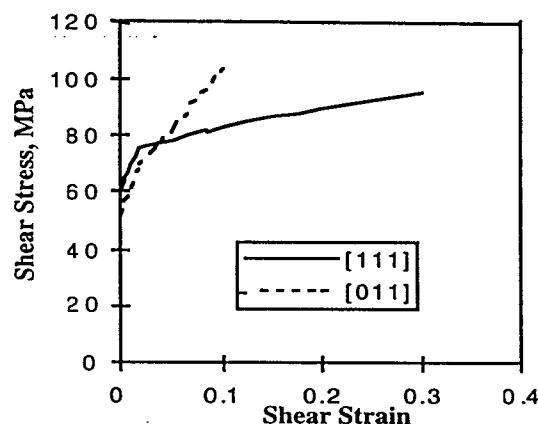

Figure 3. Shear stress vs. shear strain for high purity crystals tested along [111] (single slip) and [011] (double slip). Note the higher work hardening rate for the [011] as well as the comparable proportional limit.

Table V. Summary of tensile data for rectangular single crystal specimens of NiAl along different crystallographic directions.

Crystal ID	Orient.	f_s	σ_p MPa	τ_p MPa	$\sigma_{0.2}$ MPa	$\tau_{0.2}$ MPa	WHR (θ=dτ/dγ) MPa	σ_f MPa	El. %
18	[100]	.5	1040	520	-	-	-	1040	0
18	[100]	.5	890	495	-	-	-	890	0
122	[100]	.5	1121	560	-	-	-	1121	0
122	[100]	.5	1120	560	1167	583	-	1167	0.2
36	[111]	.485	122	59	140	68		244	15
36	[111]	.485	134	65	156	76		213	6
36	[111]	.485	106	51.5	130	63		187	4
34B	[557]T	.5	104	52	114	57	62	266	34
34B	[557]T	.5	96	48	115	57.5		218	18
34B	[557]T	.5	98	49	109	54.5		190	16
34B	[233]	.485	98	47.5	117	56.5		186	5
34B	[233]	.485	97	47	119	57.5		202	4
34B	[233]	.485	110	53.5	127	61.5		169	3
34 T	[557]W	.5	114	57	137	68.5	102	239	15
34 T	[557]W	.5	121	60.5	134	67		221	13
34 T	[557]W	.5	107	53.5	127	63.5		196	10
34 T	[011]	.5	135	67.5	147	73.5		205	3
34 T	[011]	.5	95	47.5	133	66.5		180	3
34 T	[011]	.5	123	61.5	139	69.5		192	2
64	[011]T	.5	96	48	111	55.5	468	242	7
64	[011]T	.5	104	52	117	58.5	563	237	6
64	[011]T	.5	93	46.5	102	51		230	5
64	[011]W	.5	97	48.5	111	55.5	448	235	6
64	[011]W	.5	89	44.5	102	51	476	212	5
40	[123]	.454	98	44.5	116	52.5	110	306	19
40	[123]	.454	86	40	110	50	114	304	15
40	[123]	.454	102	46	124	56.5	109	318	14
60	[135]	.41	78	32	103	42	103	272	18
60	[135]	.41	98	40	112	46	100	241	16
60	[135]	.41	96	39.5	115	47	91	266	15

It has been noted that the [011] orientation is "stable" with respect to lattice rotation during deformation due to the offsetting nature of the equivalent slip systems ([001]/(010) and [010]/(001)). As pointed out previously [17], this appears to be the reason that the highest elongations in cylindrical specimens are achieved using <011> specimens where there is little or no torque generated during deformation in contrast to the single slip orientations (e.g., TA=[557]; in this case, the crystal rotates in the classical sense with the slip plane normal rotating away from the tensile axis (i.e., the TA rotating toward the Burger's vector on the stereographic projection as shown in Fig. 4).

For the rectangular cross sections, higher elongations can be achieved due to (1) the lesser constraint in the grips and (2) the lower WHR associated with single slip. When these parameters were optimized, it was possible, using <557>T specimens, to achieve elongations as high as 10% at 180K, 34% at room temperature (Table V) and 350% at 600K (17). The cross-sections of these samples reveal the change in geometry and the fracture surfaces indicates that the fractures occur by brittle cleavage (Fig. 5a and 5b). Considering that the thin dimension gets thinner in the C samples as well as

their greater constraints in the grips, then it is not surprising that they experience lower elongations. It should also be noted that, for random specimens where the sides were not oriented parallel to the Burgers vector and the tensile axis was not coplanar with b and n, the shape change was more arbitrary (Fig. 5c) and the elongations
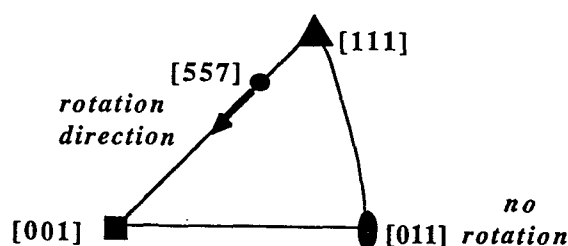

Figure 4. Orientations and nature of rotation during single (TA=[557]) and double (TA=[011]) slip. Note that no rotation is expected for the double slip geometry and that rotation in the single slip geometry which results in a drop in the Schmid factor.

687

tended to be somewhat lower. This may be due to the development of bending stresses and/or stress concentrations at the specimen corners during plastic deformation.
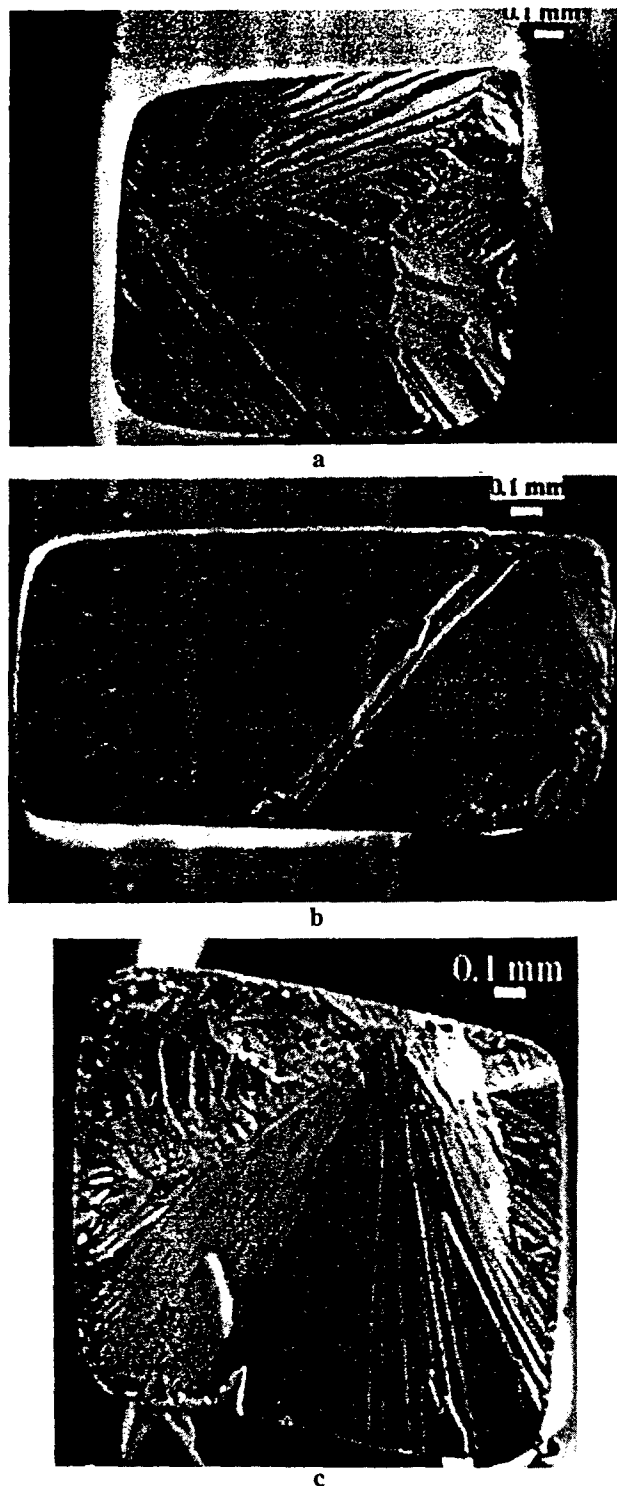
a

b

c

Figure 5. Scanning electron micrographs of the fracture surfaces of single crystal specimens after RT testing in tension. (a) LC geometry, TA=<557>; (b) C geometry; (c) random geometry.

Effects of Prestrain, Surface Oxides and Cooling Rate (Thermal Vacancies)

It has been proposed in the literature that the ductility and fracture toughness of NiAl can be enhanced by prestraining or by producing an appropriate surface film since both of these may produce mobile dislocations in a material that might normally have few such dislocations and few sources. In contrast, the influence of thermal vacancies has been reported to result in considerable hardening of NiAl which, in turn, leads to a decrease in elongation. Of interest in the present study was the examination of these effects as a function of specimen purity. Thus, both stoichiometric NiAl and NiAl doped with silicon were examined after various treatments designed to investigate these effects. As is apparent in Table VI, air cooling from 1000K leads to a slight reduction in ductility although there was little effect on the yield stress/CRSS. By prestraining 9% at 1000K and then air cooling, the specimen exhibited higher CRSS and elongations similar to those that were not prestrained. This suggests that the prestrain leads to hardening in NiAl much like in traditional metals and that NiAl does not suffer from a lack of dislocation sources.

For the silicon-doped crystal (SC-93), the properties depended somewhat on the thermal treatment and quench rate as indicated in Table VI. Although the elongation was not a strong function of these treatments and hovered around 2%, it appears that the 1000K treatment followed by WQ results in a decrease in yield stress suggesting that the silicon and/or interstitials may not have had time to segregate to dislocations and cause pinning.

As apparent in Table VII, water quenching from 1273 K results in a doubling of the yield stress and essentially eliminates the elongation compared to NiAl that was furnace cooled from 1273 K or given the original HFC treatment. It is noted that the fracture stress is not significantly different for the FC and WQ specimens consistent with the normal stress reaching some "critical" value in the material at which point a crack somewhere in the specimen becomes unstable. In addition, these results indicate that the vacancy concentration is considerably higher at 1273 K compared with that at 1000K and that the resulting thermal vacancies increase the CRSS considerably in high-purity NiAl. It should also be noted that the elongations are comparable to those achieved in commercial purity NiAl specimens tested after the HFC treatment.

The influence of surface oxides on tensile properties was established by comparing samples that had been heat treated in air with samples given equivalent heat treatments in argon. In addition, some of the specimens were repolished after the heat treatment in air in order to remove the surface oxide. The results are summarized in Table VIII where it is clear that the surface oxide results in higher $\sigma_{0.2}$ values and considerably lower elongations. Furthermore, the data indicate that it is possible to reclaim the elongation levels somewhat by removing the oxide via repolishing. Again, this implies that high purity NiAl has sufficient mobile dislocations and, therefore, surface oxides may only enhance the "ductility" of lower purity NiAl. While it could be argued that the surface oxide was non-adherent in these studies, the heat treatment temperature used was sufficiently low to insure an adherent scale.

Table VI. Effect of prestraining and cooling rate on tensile properties of NiAl and NiAl-Si single crystals at room temperature. AC = air cool; FC = furnace cool; HFC = homogenized and furnace cooled.

ID	T.A.	Heat Treatment	σ_p MPa	$\sigma_{0.2}$ MPa	σ_f MPa	El. %
40	[123]	HFC	98	116	306	18.8
"	"	HFC	102	124	318	14.0
"	"	HFC	86	110	304	15.4
"	"	1000K, 0.5h, AC	95	103	188	4.3
"	"	1000K, 0.5h, AC	80	105	149	3.1
"	"	1000K, 0.5h, e=9%, AC	126	148	253	3.8
"	"	1000K, 0.5h, e=1.5%, AC	114	132	228	2.7
"	"	1000K, 0.5h, FC	79	116	237	6.5
"	"	1000K, 0.5h, e=1.5%, FC	82	117	229	3.4
93Si	[135]	HFC	168	187	232	1.6
"	"	HFC	144	211	240	1.1
"	"	1000K, 0.5h, FAC	127	161	231	2.4
"	"	1000K, 0.5h, e=1.5%, FAC	144	168	239	1.2
"	"	1000K, 0.5h, FC	174	206	259	2.4
"	"	1000K, 0.5h, e=1.5%, FC	189	220	278	2.6

Table VII. Influence of thermal treatment on the tensile properties of NiAl. All tests on SC-109 using the standard <557>LC geometry. FC = furnace cool; WQ = water quench.

Heat Treatment	$\sigma_{0.2}$ MPa	σ_f MPa	El. %
HFC	118	183	9
HFC	126	212	12
1273K, FC	117	185	10
1273K, FC	112	173	7
1273K, FC	120	191	10
1273K, WQ	225	244	1.5
1273K, WQ	243	273	1
1273K, WQ	-	178	<0.1

Table VIII. Effect of surface oxidation on the tensile properties of NiAl. FC = furnace cool; AC = air cool; WQ = water quench.

ID	Heat Treatment	Surface condition	$\sigma_{0.2}$ MPa	σ_f MPa	El. %
76	HFC	polished	128	211	7.5
76	HFC	polished	122	216	8.3
76	1273K, air, FC	oxidized	132	208	7
76	1273K, air, AC	oxidized	135	209	4.7
76	1273K, air, WQ	repolished*	141	207	2
76	1273K, AC	polished	149	252	11.8
76	1273K, AC	polished	142	237	6.7
60	HFC	polished	115	226	10.5
60	HFC	repolished	117	289	16
60	HFC	repolished	108	272	16.2
60	1273K, AC	oxidized	167	193	0.5
60	1273K, AC	oxidized	173	205	1
60	1273K, FC	oxidized	127	191	0.7
60	1273K, FC	oxidized	134	167	1.2

*this sample although repolished, retained some surface cavities

Discussion

The results of this study indicate that NiAl is a relatively well-behaved material and that much of the confusion in previous studies presumably stems from various extrinsic effects. For high purity NiAl, the results of this study and those of previous studies (6-10) indicate that (1) prestrain, (2) surface oxides, (3) interstitials, (4) substitutional solutes, (5) thermal vacancies and (6) deviations from stoichiometry (constitutional defects) all lead to increases in the CRSS of the cube dislocations from a very low value (~50 MPa) in "virgin" NiAl. This implies that the CRSS for cube slip in NiAl is similar to that in conventional metals and alloys in terms of its response to such extrinsic variables.

On the other hand, the fracture resistance of NiAl is quite different from typical metals and alloys. In fact, it is clear from these and other studies that fracture in NiAl tends to occur by brittle cleavage in spite of the ease of dislocation flow at room and elevated temperature. This implies that certain intermetallics (or other compounds for that matter) may exhibit the characteristics of being both soft and brittle. This, in turn, seems to imply that NiAl is representative of a class of materials where the dislocations can move readily yet where the material fails in a brittle manner due to the simple fact that there is an insufficient number of active slip systems to satisfy the von-Mises criterion for general deformation and relieve the stress concentrations that develop during deformation. Whereas one might argue that this problem might not be as significant in single crystals, the present results suggest otherwise although it is clear that one can extend the elongation by careful selection of tensile axis and specimen geometry. Bearing this in mind, it is concluded that any

compound with fewer than five independent <u>active</u> deformation mechanisms will undergo brittle fracture regardless of the ease at which dislocations can move. It seems logical to extend this statement further and note that the significant amount of work on increasing the symmetry of a compound by alloying is only viable if the dislocations are mobile and the symmetry increase results in at least five independent slip systems.

Conclusions

It has been shown that many of the properties of pure NiAl respond to extrinsic variables in a manner very similar to those of pure metals. However, unlike pure metals, the fracture of NiAl single crystals tends to occur by brittle cleavage regardless the amount of tensile elongation. The effects of alloying additions, impurities, prestrain, surface films, etc. all tend to increase strength and decrease ductility much like in pure metals. Consequently, although NiAl can be strengthened using standard metallurgical approaches, it is not possible to overcome the brittleness problem without modifying the slip systems and this has not been possible to date. The implications are that all compounds that do not possess enough independent deformation mechanisms to satisfy the von-Mises criterion will be brittle in both the single and polycrystalline form, even when the dislocations can move readily.

References

1. D.B. Miracle, *Acta Metall. Mater.*, **41**, 649 (1993).

2. R.D. Noebe, R.R. Bowman, and M.V. Nathal, Physical and Mechanical Metallurgy of NiAl, NASA Technical Paper 3398 (1994).

3. T. Takasugi, J. Kishino, and S. Hanada, *Acta Metall. Mater.*, **41**, 1009 (1993).

4. V.I. Levit, I.A. Bul, J. Hu and M.J. Kaufman, *Scripta Mater.* **34**, 1925 (1996).

5. R.D. Noebe and R. Gibala, *Scripta Metall.*, **20**, 1635 (1986).

6. J.E. Hack, J.M. Brzeski, and R. Darolia, *Scripta Metall.*, **27**, 1259 (1992).

7. M.L. Weaver, M.J. Kaufman, and R.N. Noebe, *Scripta Metall.*, **29**, 1113 (1993).

8. J.E. Hack, J.M. Brzeski, and R. Darolia, *Mater. Sci. Eng.*, **A170**, 11 (1993).

9. M.L. Weaver, R.D. Noebe, J.J. Lewandowski, B.F. Oliver and M.J. Kaufman, *Mater. Sci. Eng.*, **A192/193**, 179 (1995).

10. J.E. Hack, J.M. Brzeski, and R. Darolia, *Mater. Sci. Eng.*, **A192/193**, 268 (1995).

11. M.A. Morris, J.-F. Perez, and R. Darolia, *Phil. Mag.*, **69**, 507 (1994).

12. R.W. Margevicius, J.J. Lewandowski, and I. Locci, *Scripta Metall.*, **26**, 1733 (1992).

13. R. Darolia, D. Lahrman, and R.D. Field, *Scripta Metall. Mater.*, **26**, 1007 (1992).

14. J.H. Schneibel, S.R. Agnew, and C.A. Carmichael, *Met. Trans. A*, **24A**, 2593 (1993).

15. R. Darolia and W.S. Walston, *Intermetallics*, **4**, 505 (1996).

16. J.S. Winton, J. Hu, Yu.N. Gornostyrev, V.I. Levit and M.J. Kaufman,, *Proceedings of the International Conference REX-96*, Monterey, CA, in press.

17. V.I. Levit, J. Hu, I.A. Bul, J.S. Winton and M.J. Kaufman, "Challenges in the Development and Application of β-NiAl as an Engineering Material" (Paper presented at the Engineering Foundation Meeting, Davos, Switzerland, May 19-24, 1996).

18. R.W.K. Honeycombe, *The Plastic Deformation of Metals*, E. Arnold (Publishers) Ltd, London 1968).

19. R.D. Field, D.F. Lahrman, and R. Darolia, in *High-Temperature Ordered Intermetallic Alloys IV*, Materials Research Society Symposium Proceedings, editors L. Johnson et al, MRS, Pittsburgh, PA, **213**, 255 (1991)

20. R.J. Wasilewski, *Trans. Metall. Soc. AIME*, **236**, 455 (1966).

SIMULATION OF DEFORMATION IN NIAL SINGLE CRYSTALS

Chulho Yang and Ashok V. Kumar
Department of Mechanical Engineering
University of Florida
Gainesville, FL 32611, USA

Date: May, 1997

To be submitted to:

SIMULATION OF DEFORMATION IN NIAL SINGLE CRYSTALS

Chulho Yang and Ashok V. Kumar

Department of Mechanical Engineering
University of Florida
Gainesville, FL 32611, USA

ABSTRACT

Deformation of NiAl single crystals during tensile testing was simulated using finite element analysis to investigate the modes of localized deformation. The effect of varying the loading direction with respect to lattice was studied to understand the deformation mechanism. Three-dimensional finite element models of tensile testing were created to study the effect of latent hardening when multiple slip systems are active. In particular, necking, neck diffusion and kink band formation were studied and the material and geometric characteristics that influence the deformation mode were investigated.

1. INTRODUCTION

NiAl has gained much attention as a potential structural material due to its desirable material characteristics such as high melting point, low density, good oxidation resistance and excellent mechanical properties at high temperatures including hardness, toughness, thermal stability and ductility. It has been considered a possible alternative to Nickel-based super alloys for building turbine blades where due to lower weight and higher operating temperatures it is expected to provide increased engine thermodynamic efficiency. To find application as a commercial structural material, it should have desirable structural properties over a range of working temperature. However, NiAl has low ductility and poor fracture toughness at ambient temperatures. The tensile plastic strain before fracture at room temperature is typically 0.5-2.5% (Lahrman, 1991 and Miracle, 1993). To understand its low ductility, it is desirable to understand the deformation mechanism responsible for its mechanical behavior over a broad range of temperatures. Many modes of non-uniform deformation such as necking, localized shear, kinking etc. have been observed in NiAl single crystals. These localized deformations contribute significantly to the total plastic strain and eventual failure (Miracle, 1993). Significant tensile ductility is obtained only at and above 473 K (Wasilewski, 1967, Lahrman, 1991, etc.). Therefore, many approaches to improve the ambient temperature material properties of NiAl have been investigated (Darolia, 1991 and Darolia, et. al. 1992). A detailed survey of literature and a critical review of the physical and mechanical properties of NiAl has been presented by Miracle (1993).

NiAl has a B2 type ordered crystal structure (see Fig. 1) similar to body centered cubic (bcc) crystals. Mechanical properties of NiAl single crystals vary with respect to the orientation of crystal lattice. Plastic deformation in NiAl occurs predominantly due to slip in the <001> directions along either {110} or {100} planes when loaded along non-<001> direction (or soft orientations). NiAl crystal subjected to loading along the <001> direction (hard orientation) shows high flow stress at low temperatures and enhanced creep strength at elevated temperatures. In this orientation, deformation
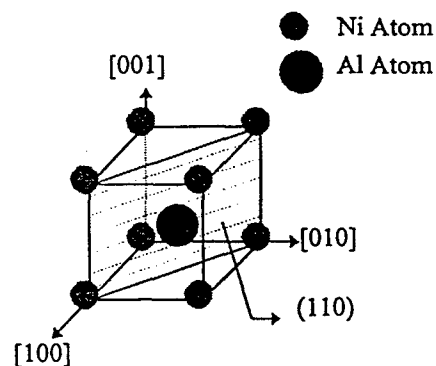

Figure 1. NiAl crystal structure

occurs by non-<001> dislocation.

Most ductile single crystals (Chang and Asaro, 1981, Pierce et al 1982) exhibit localized deformation modes when subjected to large plastic deformation process. Understanding the causes of localized deformation is of great importance because such non-uniform deformation creates voids or damages on the surface that eventually lead to initiation of fracture. In single crystals of NiAl, significant lattice rotation is observed especially when deformation occurs by slip

in a single slip system. These lattice rotations can result in orientation or geometric softening that promotes various forms of localized eformation. Common forms of localization observed in single crystals are necking, shear localization and kink bands. Macroscopic shear bands have not been observed experimentally in NiAl, however it is possible that microscopic shear localizations may be responsible for stress concentrations and crack initiation. Kink bands have been observed in NiAl single crystals subjected to compressive loads along the orientations very close to the hard-orientation.

In this paper, we have investigated various modes of localized and diffused deformation observed in NiAl and studied the role of various parameters such as lattice orientation, rate sensitivity, latent hardening ratio etc. in promoting these modes of deformation. A rate-dependent constitutive model for single crystals was implemented into ABAQUS [1], a commercial finite element code that is capable of modeling large deformation and large strains. The rate dependent constitutive equation was integrated using forward gradient method which has been found to be effective (Pierce et al 1983 and Wenner, 1993) provided sufficiently small time-steps are used for the time integration. For the simulation of localizations (shear band and kink band) we used incompatible elements (Simo and Rifai, 1990) available in ABAQUS. These elements have been found to be particularly suitable for modeling incompressible behavior and for modeling strain localizations (Simo and Armero, 1992).

2. CONSTITUTIVE MODELING

In this section, we present a constitutive model for the elastic-plastic mechanical behavior of NiAl single crystals. The formulation used here is based on the well established rate dependent model for single crystals (Pierce et al, 1983 and Asaro, 1983).

The Jaumann rate of Kirchoff stress of single crystal can be related to the elastic rate of stretching by Hooke's law, $\sigma^{\nabla*} = L:D^*$. Here L is the 4th order tensor of elastic moduli. Jaumann stress rate of Kirchoff stress $\sigma^{\nabla*}$ with respect to a coordinate that spins with the lattice is defined as

$$\sigma^{\nabla*} = \dot{\sigma} - \Omega^* \cdot \sigma + \sigma \cdot \Omega^* \qquad (2.1)$$

$\dot{\sigma}$ is material rate of Kirchoff stress and Ω^* is the the rate of spin tensor. The Jaumann stress rate of Kirchoff stress that spins with the material is given by

$$\sigma^{\nabla} = \dot{\sigma} - \Omega \cdot \sigma + \sigma \cdot \Omega \qquad (2.2)$$

The difference between these two expressions is:

$$\sigma^{\nabla*} - \sigma^{\nabla} = \sum \beta^{(\alpha)} \cdot \dot{\gamma}^{(\alpha)} \qquad (2.3)$$

where, $\beta^{(\alpha)} = W^{(\alpha)} \cdot \sigma - \sigma \cdot W^{(\alpha)}$

Finally, the constitutive equation may be stated as:

$$\sigma^{\nabla} = L:D - \sum_{\alpha=1}^{n} \dot{\gamma}^{(\alpha)} R^{(\alpha)} \qquad (2.4)$$

where, $R^{(\alpha)} = L:P^{(\alpha)} + \beta^{(\alpha)}$, $P^{(\alpha)} = \frac{1}{2}(s^{(\alpha)} \cdot m^{(\alpha)} + m^{(\alpha)} \cdot s^{(\alpha)})$.

$s^{(\alpha)}$ is the slip direction vector and $m^{(\alpha)}$ is the slip plane normal vector.

For a strain rate dependent material of the single crystal, the slip rate of the α-th slip system is assumed to be related to the resolved shear stress by power law (Pan and Rice, 1983)

$$\dot{\gamma}^{(\alpha)} = \dot{a}^{(\alpha)} \left[\frac{\tau^{(\alpha)}}{\tau_c^{(\alpha)}} \right] \left[\left| \frac{\tau^{(\alpha)}}{\tau_c^{(\alpha)}} \right| \right]^{(1/m)-1} \qquad (2.5)$$

where, m is the rate sensitivity parameter, $\tau_c^{(\alpha)}$ is the critical resolved shear stress for the slip system α, $\dot{a}^{(\alpha)}$ is a reference strain rate on each slip systems. The shear rate $\dot{\gamma}$ in each slip system is uniquely determined by power law Eq. (2.5). For a rate dependent model, the rate of increase of the function $\tau_c^{(\alpha)}$ has therefore been specified as (Pierce et al, 1982),

$$\dot{\tau}_c^{(\alpha)} = \sum_{\beta=1}^{n} h_{\alpha\beta} |\dot{\gamma}^{(\beta)}| \qquad (2.6)$$

The form of hardening moduli $h_{\alpha\beta}$ matrix commonly used is (Hutchinson, 1970),

$$h_{\alpha\beta} = qh + (1-q)h\delta_{\alpha\beta} \qquad (2.7)$$

where, q is the latent hardening ratio. The hardening rate, h is the rate of change of critical resolved shear stress with shear strain. The hardening curve $\tau_c(\gamma)$ and hardening rate $h(\gamma)$ for single slip in such materials is often represented using the following equations

$$\tau_c(\gamma) = \tau_0 + (\tau_s - \tau_0) \tanh\left(\frac{h_0 \gamma}{\tau_s - \tau_0} \right) \quad \text{and}$$

$$h(\gamma) = h_0 \sec h^2 \left(\frac{h_0 \gamma}{\tau_s - \tau_0} \right) \qquad (2.8)$$

3. NECK DIFFUSION IN NIAL

Finite element simulation of the deformation of the tensile specimen along various orientations were performed and compared with experimental data (Levit et al. 1996, Winton, 1995). The factors that most significantly affect the deformation mode include the rate sensitivity parameter (m), the latent hardening ratio (q) and the hardening curve (τ_c vs γ) of the material.

Depending on the orientation of the tensile load with respect to the lattice of the crystal, different slip systems are activated. NiAl exhibits low ductility and low fracture toughness near room temperature. Significant ductility is obtained only above 200°C. Tensile test in two orientation [$\bar{5}57$] and [110] were simulated for temperatures above 200°C and compared with experimental results. Very large strains were obtained with some diffused necking for both orientations. Detailed experimental study by Levit (1996) indicates that necks that form initially spread or diffuse at larger strains. Finite element simulation of these tensile tests are described in the next two sub-sections.
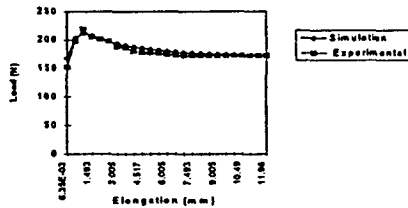
Figure 2 (a) Load vs. Elongation in the [$\bar{5}57$] orientation
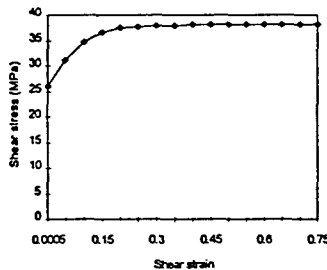
Figure 2 (b) Shear stress vs shear strain for the simulation

3.1 Orientation Hardening

Loading along <557> orientation activates {110}<001> slip system resulting in single slip. Several numerical simulations of deformation along [$\bar{5}57$] direction were performed using the hardening curve in Eq. (2.8) while varying the values of the parameters τ_0, τ_s, h_0. Figure 2 (a) shows the close match between the load vs. elongation curve obtained experimentally and numerically. Figure 2 (b) shows the hardening curve that was used for the numerical simulation where $\tau_s = 38$ MPa, $\tau_0 = 26$ MPa, $h_0 = 110$ Mpa.

The load versus elongation curve obtained for [$\bar{5}57$] orientation increases to a peak and then decreases gradually to a minimum before increasing again (see Fig. 2 a). The drop in load after the peak load is due to localized deformation that results in a neck. However, the neck spreads after the initial localization. This behavior has been experimentally observed (Levit et al 1996) and explained in terms of the orientation hardening that results from the large amount of lattice
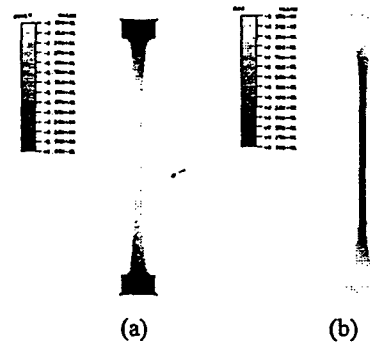
Figure 3. (a) Contour plot of crystal lattice rotation (b) Contour plot of strain in Y-direction (at 64 % nominal strain , [$\bar{5}57$] orientation)

rotation that occurs during single slip. Numerical simulation based on our finite element model confirms this phenomenon. The load versus deformation curve obtained numerically has identical shape. Figure 3 (a) shows the deformed specimen with contour plot of lattice rotation. The direction of the lattice rotation is such that the Schmid factor decreases. As a result, a higher tensile load is required to produce the resolved shear stress necessary for slip on the active slip plane. The resulting increase in yield stress along the tensile direction (referred to as "orientation hardening") prevents further deformation at the neck causing the neck to spread. Figure 3 (b) shows the contour plots of strain in y direction. It can be seen that the deformation is more or less uniform within the gauge length.

3.2 Work Hardening

Tensile elongation along the [110] direction activates the {100}<001> slip system. However, unlike in the previous case, elongation in this direction produces double slip. Both the (100) and (010) planes become active simultaneously since the Schmid factor for both these planes are identical. Furthermore, no lattice rotation occurs because these planes are located symmetrically about the tensile axes
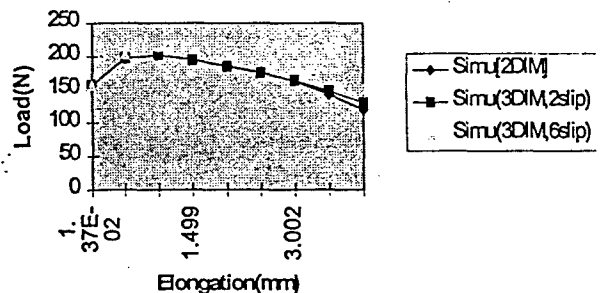

Figure 4. Load vs. elongation for loading along [110] orientation

and identical amount of slip occurs in both slip planes. The load

versus elongation curve obtained experimentally (Levit et al) seems to suggest considerable work hardening. Simulation of the elongation long [110] using the hardening curve used earlier (Fig. 2b) and q = 1 yielded poor results at large strains as seen in Fig. 4.
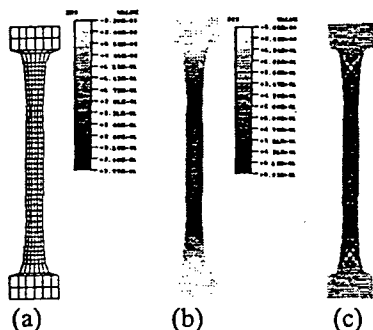

Figure 5. (a)deformed mesh (b) strain in Y-dir (c) stress in Y-dir (q=1.0, at 20% nominal strain)

The numerically obtained load-elongation curve predicts the initial peak followed by a load drop. However, the load increases at higher strains for the experimental specimen, while it drops due to a sharp neck for the numerical simulation. Increasing the latent hardening parameter moves the load versus elongation curve upwards but does not result in the desired increase in load at large deformation. This suggests that there is considerable work hardening for the {100}<001> slip system The initial drop in load seen in the experimental curve was due to neck formation. The subsequent increase in load at large deformation was accompanied by spreading of the neck. This requires an unusually high rate of hardening at large strains. It is possible that this increased hardening is associated with activation of {110}<001> slip planes at large deformation. Since activation of {110} planes result in non-planar deformation, a 3-dimensional finite element model of the single crystal is required to simulate the deformation and confirm this hypothesis. Figure 5, shows the results of 2D simulation of deformation along [110] direction.

4. 3D SIMULATION OF TENSILE TEST

For NiAl crystal loaded along [110] direction, there are four {110}<001> type slip systems that can become active in addition to the two {100}<001> slip systems. If all the six slip systems are activated simultaneously, the resultant deformation is 3 dimensional requiring a 3D finite element model. In addition, the work hardening model becomes complicated since we need to account for the latent hardening of {110}<001> slip systems when <100><001> slip system is activated and vice versa. We use the notation q_{aa}, q_{ab}, q_{ba} and q_{bb} to denote the four possible latent hardening ratios, where q_{ab} is the ratio of hardening in slip system 'a' when slip system 'b' is active etc. We denote slip systems {110}<001> using 'a' and slip systems {100}<001> using 'b'.

Figure 4 shows the load vs. elongation curves obtained using 2D model and 3D models. When only the two {100}<001> slip systems are modeled, the load elongation curve for both 2D and 3D models are almost identical. However, when all six slip systems are allowed to be
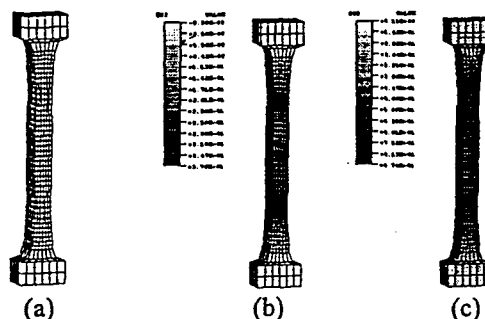

Figure 6. (a) deformed mesh (b) strain in Y-dir (c) stress in Y-dir. at 20% nominal strain

active, the {110}<001> slip system becomes active after a significant amount of deformation. This causes significant latent hardening on the {100}<001> slip systems resulting in a overall higher work hardening as can be seen in Fig. 4. It is hypothesized that this enhanced work hardening due to activation of {110}<001> slip systems is responsible of spreading of the neck and rising of the load elongation curve at large deformations as seen experimentally. To obtain a good match between experimental curve and simulation curve, appropriate values for the four latent hardening ratios need to be determined. Further
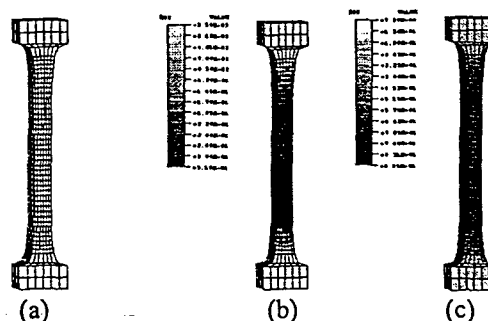

Figure7 (a) deformed mesh (b) strain in Y dir (c) stress in Y dir at 20% nominal strain ($q_{aa} = q_{ba} = 1.0$, $q_{bb} = 1.4$, $q_{ab} = 0.6$)

research is required to fully understand their effect in the mode of deformation.

Figure 6 and 7 shows the results of 3D simulation of tensile test along [110] direction. Figure 6 shows the deformation when only the {100}<001> slip systems are active. With only primary slip systems {100}<010> active, both 2D (Fig. 5) and 3D (Fig. 6) models, predict necking at the top and bottom of the gauge length at 20% elongation. However, when the secondary slip systems {110}<001> are activated more hardening occurs and that resists neck formation as can be seen in Fig. 7.

5. DEFORMATION ALONG HARD ORIENTATION

Kinking is a highly localized form of deformation that has been observed in NiAl during compression near the hard orientation (<100> direction) (Frasier et al, 1973a,b). When compressed along the hard orientation, the resolved shear stress along <001> directions is zero. As a result glide occurs along other directions such as <111> or <110> (Miracle, 1993). However, if the direction of compression is misaligned slightly from the <001> direction, either {110}<001> or {100}<001> systems can get activated depending on the direction of misalignment. Such misalignment has been observed to favor kinking. Experimental studies by Fraser et al (1973), shows that deformation in the kink band occurs on {110} planes due to slip along the <100> direction parallel to the compression axes. However, all three <100> dislocations have been observed experimentally (Miracle, 1993).

(a)   (b)   (c)

Figure 8. Deformed mesh with 10°off from compression axes (a) 0.4 % nominal strain (b) 2.76 % nominal strain (c) 7.5 % nominal strain

Kinking can be explained in terms of orientation softening that occurs due to large lattice rotation. Once a slip system is activated, the lattice rotation increases the resolved shear stress in that system, making it softer so that activation of the other possible systems are unlikely. When non-uniform deformation is induced due to specimen geometry or imperfections, the region where more lattice rotation occurs due to higher strains becomes softer than the rest of the specimen causing further deformation to localize in this region. The exact location of the formation of the band depends on the applied imperfection.

When a {110}<001> slip system is activated, single slip occurs while double slip occurs when {100}<001> systems are activated. Significant lattice rotation occurs in both cases. Numerical simulation were performed for both these situations with compressive load applied along directions misaligned by 5-10° from the [001] direction. Figure 8 shows stages of kink band formation due to single slip along (110)<001>, when the compression direction is misaligned 10° from [001] direction.

Kink bands were obtained during simulation of both single slip or double slip situations. More lattice rotation occurs during single slip than in the double slip case. Figure 9 shows lattice rotation that occurred during the deformation. More than 60° of lattice rotation has occurred along the band during single slip. This agrees well with the experimental observation of Fraser et al (1973) where they have reported slip along {110}<001> slip system and ~60° lattice rotation in the kink band.

5. SUMMARY AND CONCLUSION

(a)   (b)

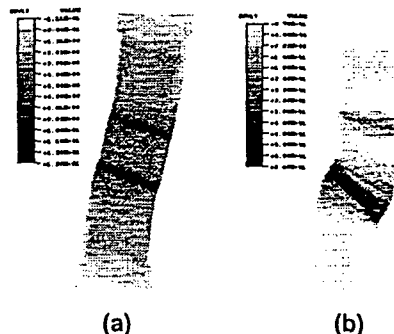**Figure 9. Contour plot of crystal lattice rotation at 2.265% nominal strain (a) double slip (θ=80°, 170°) (b) single slip (θ=85°)**

Deformation of NiAl single crystals were studied using finite element simulations. Tensile loading of NiAl single crystals along [557] and [110] crystal orientations were simulated. The numerically simulated load vs. elongation curve matched well with experiment for elongation along the [557] direction. Simulation of elongation in the [110] direction, with the assumption that only {100}<001> slip systems are activated, did not agree with experimental data. The increase in load at large deformation observed experimentally requires unusually large work hardening at large deformation. Three-dimensional simulation of the specimen suggests that activation of {110}<001> systems results in more hardening at large deformation due to latent hardening effect.

Simulation of kinking during compression along directions close to the hard-orientation of the crystal revealed that kink bands may form due to either single slip along {110}<001> slip system or due to double slip in {100}<001> slip system. In both cases, the direction of lattice rotation is such that orientation softening occurs which leads to deformation localization. Low rate sensitivity and low hardening were found to promote kink band formation.

6. ACKNOWLEDGMENTS

7. REFERENCES

ABAQUS, 1994, Manual version 5.4,

R. J. Asaro, 1979, "Geometrical Effects in the Inhomogeneous Deformation of Ductile Single Crystals", *Acta metall.*, vol. 27, pp. 445-453

R. J. Asaro, 1983, "Micromechanics of Crystals and Polycrystals", *Advances in appl. Mech.,* vol. 23, pp. 1-115, eds. J. W. Hutchinson, T. Y. Wu, N. Y. Academic Press

Y. W. Chang and R. J Asaro, 1981, "Lattice Rotations and Localized Shearing in Single Crystals", *Acta metall.,* vol. 29, pp. 241.

R. Darolia, 1991, "NiAl alloys for high-temperature structural applications", *J. Metals,* vol. 43, no. 3, pp. 44-49

R. Darolia, D. F. Lahrman, R. D. Field, F. R. Dobbs, K. M. Chang, E. H. Goldman and D. G. Konitzer, 1992, Ordered intermetallics - physical metallurgy and mechanical behaviour, (edited by C. T. Lui, R. Cahn and G. Sauthoff), NATO ASI Series E: Applied sciences, vol. 213, pp. 229.

H. Deve, S. Harren, C. McCullough and R. J. Asaro, 1988, "Micro and Macroscopic Aspects of Shear Band Formation in Internally Nitried Single Crystal of Fe-Ti-Mn Alloys", *Acta metall.,* vol 36, no.2, pp. 341-365

H. L. Fraser, R. E. Smallman and M. H. Loretto, 1973a, "The plastic deformation if NiAl single crystals between 300°K and 1050°K - I. Experimental evidence on the role of kinking and uniform deformation in crystals compressed along <001> ", *Phil. Mag.,* vol. 28, p. 651.

H. L. Fraser, M. H. Loretto and R. E. Smallman, 1973b, "The plastic deformation if NiAl single crystals between 300°K and 1050°K - II. The mechanism of kinking and uniform deformation", *Phil. Mag.,* vol. 28, p. 667.

R. Hill and J. R. Hutchinson, 1975, "Bifurcation Phenomena in the Plane Tension test", *J. Mech. Phys. Solids,* vol. 23, pp. 239.

J. W. Hutchinson, 1970, "Elastic-Plastic Behavior of Polycrystalline Metals and Composites", *Proc. R. Soc.,* Lond A319, pp. 247-272

F. Lahrman, R. D. Field and R. Darolia, 1991, High Temperature Ordered Intermetallic Alloys IV, MRS Proc., vol. 213, pp. 603.

E. H. Lee, 1969, "Elastic-Plastic Deformation at Finite Strains", *J. appl. Mech.,* vol. 36, pp. 1

V.I. Levit, J.S. Winton, Yu Gornostyrev, M. J. Kaufman, 1996, "Mechanism of high tensile elongation in NiAl single crystals at intermediate temperatures", To be published

D. B. Miracle, 1993, "The Physical and Mechanical Properties of NiAl", *Acta metall.,* vol.41, No.3, pp. 649-684.

J. Pan and J. R. Rice, 1983, "Rate Sensitivity of Plastic Flow and Implications for Yield-Surface Vertices", *Int. J. Solid Struct,* vol. 19, pp. 973-987.

D. Pierce, R. J. Asaro and A. Needleman, 1982, "An Analysis of Nonuniform and Localized Deformation in Ductile Single Crystal", *Acta metall.,* vol. 30, pp. 1087-1119.

D. Pierce, R. J. Asaro and A. Needleman, 1983, "Material Rate Dependence and Localized Deformation in Crystalline Solids", *Acta metall.* vol. 31, no.12, pp. 1951-1976.

J. C. Simo and F. Armero, 1992, " Geometrically non-linear enhanced strain mixed methods and the method of incompatible modes", *Int. J. for Num. Meth. in Engineering,* Vol. 33, pp. 1413-1449.

J. C. Simo and M.S. Rifai, 1990, "A class of mixed assumed strain methods and the method of incompatible modes", *Int. J. for Num. Meth. in Engineering,* Vol. 29, pp. 1595-1638.

V. Tvergaard et al., 1981, "Flow Localization in the Plane Strain Tensile Test", *J. Mech. Phys. Solids,* vol. 29, pp. 115-142.

R. J. Wasilewski, S. R. Butler and J. E. Hanlon, 1967, *Trans. Metall. Soc. AIME,* vol. 239, pp. 1357.

M. L. Wenner, 1993, "A Generalized Forward Gradient Procedure for Rate Sensitive Constitutive Equations", *Int. J. for Num. Meth. in Engineering,* vol. 36, pp. 985-995.

J. S. Winton, 1995, "The Effect of Orientation, Temperature, and Strain Rate on the Mechanical Properties of NiAl Single Crystals", MS thesis, Univ. of Florida.

TENSILE PROPERTIES OF NiAl BICRYSTALS

J.B. LeBleu, Jr., P.R. Mei, V.I. Levit[1] and M.J. Kaufman
Department of Materials Science and Engineering, University of Florida,
Gainesville, FL 32611-6400

Introduction

The intermetallic compound β-NiAl continues to receive considerable attention in spite of its lack of room temperature toughness and high temperature strength. Although the dislocations are mobile at room temperature (1–2), the lack of a sufficient number of slip systems precludes significant elongation in single and polycrystalline NiAl except in single crystals under special conditions (1). In the case of polycrystals of stoichiometric NiAl, the room temperature fracture tends to be mostly intergranular; this has been related to the stresses that build up at the grain boundaries during plastic deformation due to the lack of active independent deformation mechanisms or the possibility that the grain boundaries are intrinsically weak. According to Vitek and Yan (3), the proposed intrinsic brittleness of NiAl boundaries has yet to be unambiguously explained. The present study was designed to establish the condition of grain boundary fracture by performing tensile tests at different temperatures and strain rates on bicrystals of NiAl containing natural boundaries produced by Bridgman growth. This approach was selected based on the previous work on NiAl bicrystals produced by diffusion bonding/brazing (4–6) and Bridgman growth (7). In some cases, these boundaries were reportedly enriched in nickel although it is unclear, based on the limited atomistic modeling efforts to date (4), whether this is a result of sample processing or is a characteristic of this compound. Furthermore, the previous studies of slip behavior were performed in compression which is less suitable for examining the relative strength of the grain boundaries (5).

Experimental Procedure

All bicrystals and their seeds were grown using stoichiometric NiAl feedstock that had been produced initially by vacuum induction melting. Hemi-cylindrical single crystal seed halves were cut from oriented single crystals of the desired orientation. All orientations were measured using standard back-reflection Laue methods. After unsuccessful attempts to weld the two seeds together prior to growth, the seed halves were simply set in a cylindrical, pure alumina crucible of 28 mm internal diameter. The seeds welded together upon melting of the overlying charge material and the bicrystals were then Bridgman grown in purified argon. This produced a bicrystal containing a "natural" boundary as shown in Figure 1. The withdrawal rate was varied in order to determine its influence on boundary declination (see Table 1). Two orientations of tensile samples were cut with the desired orientation from

---

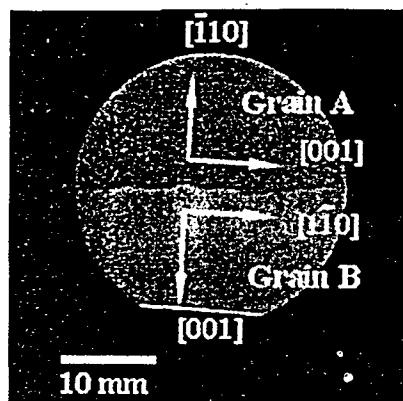[1]Now at Analytical Services and Materials Inc., 107 Research Dr., Hampton, VA 23666.

Figure 1. Top view of bicrystal ingot BI-5 where both grains were grown along [110]. The flat region corresponds to a cut made approximately parallel to (001).

sample BI-5 with the grain boundary approximately perpendicular to the tensile axis (see Figures 1 and 2). After heat treating at 1300°C for three hours and furnace cooling, tensile samples with rectangular sections were cut from BI-5 with a wire electro-discharge machine (EDM) as shown in Figure 2. The other bicyrstals (BI-1 to BI-4) were not tested due to the boundary declination. Samples were electropolished in a 90% methanol, 10% perchloric acid solution to remove at least 0.1 mm from the entire sample surface.

The samples were tested in an Instron Model 1125 unit from room temperature up to 1000°C in air and at nominal strain rates of $\sim 10^{-3}$ to $\sim 10^{-5}$ s^{-1}. Since no plastic strain was observed in the [001] grain, all calculations assume an effective gage length of 5 mm. For comparison, $\langle 001 \rangle$ and $\langle 110 \rangle$ single

(a)   (b)
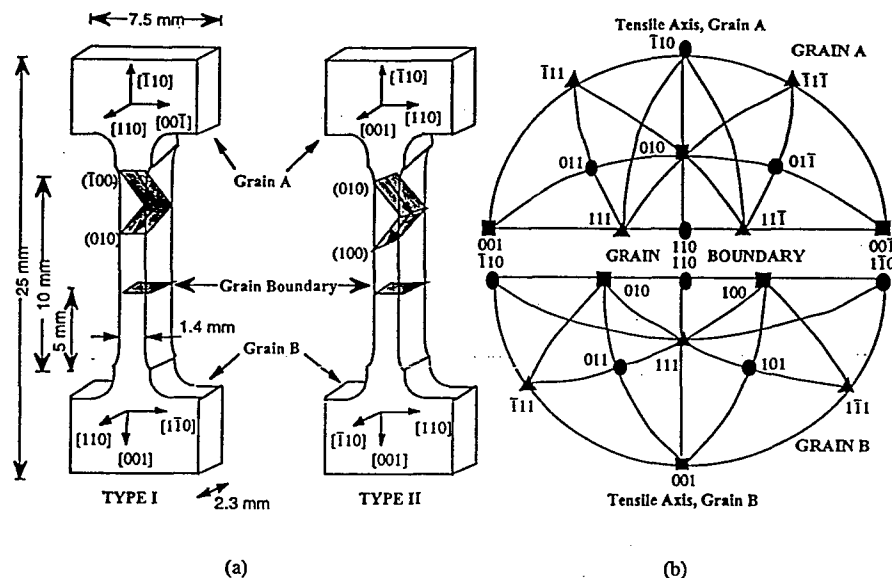
Figure 2. (a) Tensile specimen orientations. approximate dimensions after electropolishing, and slip systems (Grain A) for bicrystal BI-5. Type I and Type II orientations are similar but rotated 90° relative to each other. (b) Half-stereograms representing the orientations of the two bicrystal grains in a Type I bicrystal specimen. As indicated, the grain boundary is parallel to the equator in this split projection.

TABLE 1

Grain Boundary Orientation, Withdrawal Rate, and Boundary Declination for NiAl Bicrystals

Bicrystal I.D.	Grain A Orientation	Grain A Interface	Grain B Orientation	Grain B Interface	Withdrawal Rate (mm/min)	Comments
BI-1	⟨110⟩	{110}	⟨001⟩	{110}	3.5	Grain A declined moderately
BI-2	⟨110⟩	{110}	⟨001⟩	{110}	5.0	Grain A declined completely*
BI-3	⟨110⟩	{110}	⟨001⟩	{110}	0.8	Grain A declined slightly
BI-4	⟨110⟩	{110}	⟨001⟩	{100}	0.8	Grain B declined moderately
BI-5	⟨110⟩	{110}	⟨110⟩	{001}	1.1	Little divergence

*Several new grains also formed.

crystals were tested using the same processing, geometry, specimen shape and preparation, and testing conditions. In order to measure strain distribution along each grain and across the grain boundary, two of the bicrystal samples were marked using a microhardness indentor at 50 μm intervals from the grain boundary towards the sample heads. After indenting, these specimens were annealed at 500°C for 30 minutes before testing in order to relieve stresses induced by the indentor and then cooled to 250°C for testing. Measurements of the spacing between the indentations were made before and at several points during the testing at $\sim 10^{-4}$ s^{-1}.

Results and Discussion

The influences of orientation and withdrawal rate on the divergence of the original boundary plane from the growth axis are summarized in Table 1. By using a slow growth rate and the same growth direction, a {110}-{001} grain interface can be maintained during growth. A top view of BI-5 (Figure 1) indicates that the grain boundary is reasonably planar and orthogonal to the two tensile directions. Tensile directions of ⟨110⟩ and ⟨001⟩ were chosen for comparison with the previous work by Miracle who attempted to observe slip behavior near boundaries parallel to the (001) using compression specimens (5). Furthermore, neither grain experiences any rotation during plastic deformation; such rotations are known to lead to premature fracture due to the torques that develop within the sample (8). As seen in Figures 1 and 2, the grain oriented with its tensile axis along [∼110] will be referred to as "Grain A" and the grain oriented with its tensile axis along the [001] will be referred to as "Grain B". The tensile data for the bicrystal samples (Figure 3) indicate that the yield stress decreases monotonically with
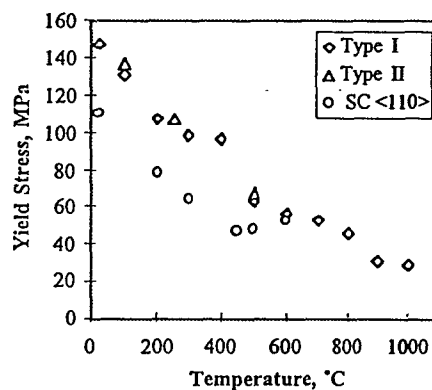

Figure 3. Yield stress (0.2%) versus temperature for Type I and Type II bicrystals and ⟨110⟩ single crystals tested at $\sim 10^{-3}$ s^{-1}.

TABLE 2

Compositions of Bicrystal BI-5 (Type I and II) and sc-$\langle 110 \rangle$

Sample Group	Ni. At %	Al, At %	Si (ppm)	C (ppm)	O (pm)	N (ppm)
BI-5 Type I	50.1	49.8	308	94	70	10
BI-5 Type II	50.0	49.9	416	267	122	20
SC $\langle 110 \rangle$	50.6	49.3	240	180	81	<15

increasing temperature. The differences between the yield stresses for the bicrystals and the $\langle 110 \rangle$ single crystals may be due to slight variations in composition (Table 2), strain rate, "effective" gage length and geometry.

If the data in Figure 3 are re-plotted with the yield stress for $\langle 001 \rangle$ single crystals, it appears that the stresses converge with increasing temperature (Figure 4). Thus, it was anticipated that there might be a temperature where Grain A work hardens enough to increase the load up to the level needed to initiate plastic deformation in Grain B. However, at these temperatures and strain rates, Grain A undergoes strain localization which results in a lowering of the stress in Grain B. The elongation versus temperature (Figure 5) indicates that, above 250°C, there is a jump in elongation as Grain A deforms extensively. Below 250°C, fracture at the grain boundary prevents extensive elongation in Grain A. It should be noted from Figures 3 and 4 that the behavior of Type I and Type II bicrystals is similar over the temperatures tested. Since, for temperatures below 400°C, the CRSS values for $\langle 001 \rangle$ single crystals are significantly higher than those for $\langle 110 \rangle$ crystals (Figure 4), then the bicrystals are expected to behave like $\langle 110 \rangle$ single crystals.

Because it was unclear what would happen near the grain boundary, testing using the specimens which had been indented at 50 μm intervals was performed. The spacing between these points at different periods during testing are shown in Figure 6 (this method is described elsewhere (8)). The two peaks in elongation in Grain A on the right side of Figure 6 indicate the formation of two necks during deformation. Similar multiple necks are common in $\langle 110 \rangle$ single crystals of NiAl when tested at elevated temperatures (8). Since there is clearly no plastic deformation in Grain B, the use of the 5 mm gage length assumed earlier is further justified. The type of fracture depends on both the temperature and strain rate and occurs either at the grain boundary or in Grain A after strain localization (Figure 7). Above 300°C, the fracture always occurred in Grain A, whereas below 100°C, the fracture occurred at the grain boundary. Between 100°C and 300°C, the probability of grain boundary fracture increases
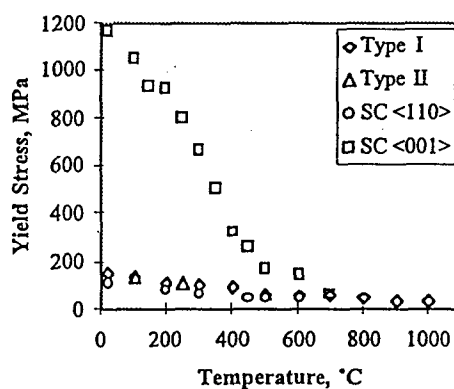

Figure 4. Yield stress (0.2%) versus temperature for $\langle 110 \rangle$ and $\langle 001 \rangle$ single crystals and [001]-[$\bar{1}$10] bicrystals. Strain rate $\sim 10^{-3}$ s^{-1} except for the $\langle 001 \rangle$ tests performed at $\sim 10^{-4}$ s^{-1}.
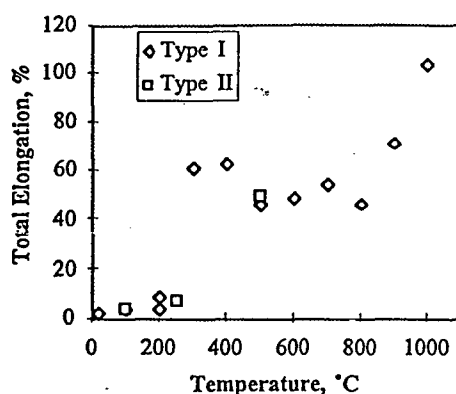
Figure 5. Elongation versus temperature for Type I and Type II bicrystal samples tested at $\sim 10^{-3}$ s^{-1}.

with decreasing temperature and increasing strain rate. A typical specimen that broke at the grain boundary is shown in Figure 8 where the lack of localized plastic deformation in Grain A is apparent.

In the cases where grain boundary fracture occurred, it was common to observe significant strain in Grain A preceding fracture (Figures 5 and 7); this indicates that the boundary strength is greater than the initial matrix strength. Specifically, these fractures occur when the incompatibility stresses that develop at the boundaries reach a critical level. It is clear from Figure 7 that the tests at 10^{-5}s^{-1} were sufficiently slow to allow thermally activated dislocation movement at 150–200°C to relieve the stress concentrations at the grain boundaries. Since decreasing the strain rate does not increase the probability of fracture at the grain boundary, there is clearly no moisture-induced embrittlement in NiAl, unlike FeAl tested in laboratory air (9). It should be noted that hydrogen has been reported to embrittle special boundaries in NiAl bicrystals (10).

The fracture stresses are plotted in Figure 9 and suggest that the intrinsic grain boundary strength decreases from 190 MPa to 160 MPa as the temperature is increased from ambient to 250°C at a strain rate of $\sim 10^{-3}$ s^{-1}. The room temperature tests at three different strain rates seem to indicate that the strength of the boundary is not very sensitive to strain rate and is in the range of 190 to 210 MPa. Analysis of the elastic and plastic constraints at bicrystal grain boundaries in Al (2) and Fe-3%Si (1,11) has shown that additional slip systems may operate near the boundaries in order to accommodate these stresses related to incompatibility. Since there are not five independent slip systems for general plastic
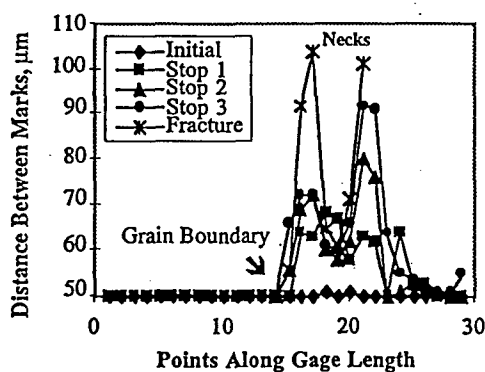
Figure 6. Relative deformation of Grain B (left side) and Grain A (right side) while testing at 250°C and $\sim 10^{-4}$s^{-1}. Initial spacing was 50 μm.
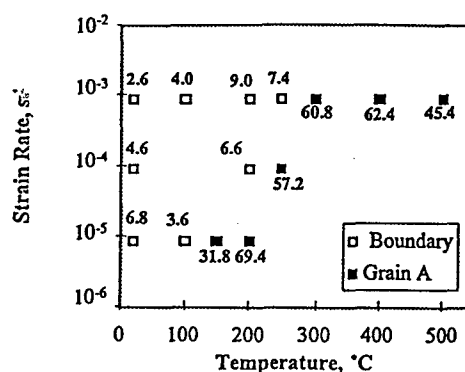
Figure 7. Effects of temperature and strain rate on location of fracture. Numbers indicate percent elongation at fracture.

deformation in NiAl, this accommodation occurs by a thermally activated process (e.g., climb). A plane strain condition appears to hold since deformation occurs only in two directions (Figure 10), and even after extensive deformation, the sample remains rectangular, as noted elsewhere (8). Figure 10 illustrates this effect where orienting the slip planes relative to the face or side of the rectangular tensile sample alters the orientation of the neck with respect to the specimen heads.

At temperatures above 700°C, the different oxide thicknesses on the two grains made the boundary location even more apparent. Since Grain B did not deform in these studies, further bicrystal testing with grains oriented for {557}-{557}, {110}-{557}, and {001}-{001} systems is in progress to examine the effects of geometry, slip transition and compatibility when both grains deform simultaneously.

Conclusions

The present results can be used to draw the following conclusions:

1. NiAl bicrystals with specific orientations can be grown by the Bridgman method with careful selection of growth direction and withdrawal rate.

2. The {001}-{110} grain boundaries in NiAl are not intrinsically brittle and have apparent fracture stresses in the range of 190 to 210 MPa for strain rates from $\sim 10^{-3}$ to 10^{-5} s^{-1}.

3. For a {001}-{110} grain boundary, the temperature range for transition of fracture from intergranular to intragranular varies between 100°C and 300°C depending on strain rate.

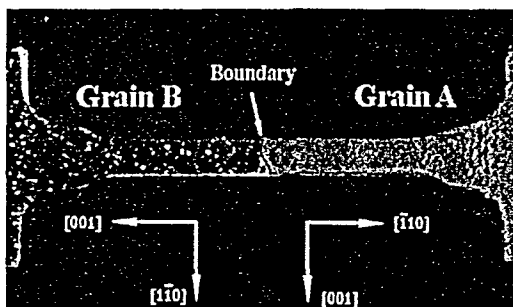4. Unlike Ni$_3$Al and FeAl, there is no apparent environmental embrittlement in NiAl.

Figure 8. Type I sample tested at room temperature and 10^{-3}s^{-1} showing fracture at the grain boundary. Sample halves are brought close together to illustrate the lack of localized deformation in Grain A.
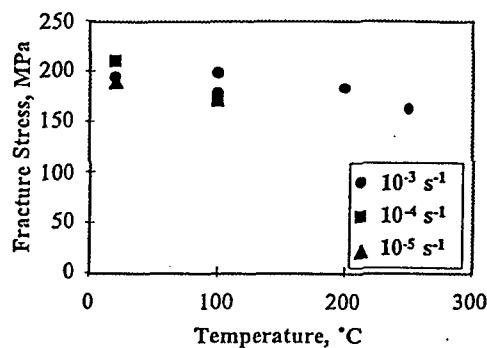
Figure 9. Fracture stress for samples which broke at the grain boundary.
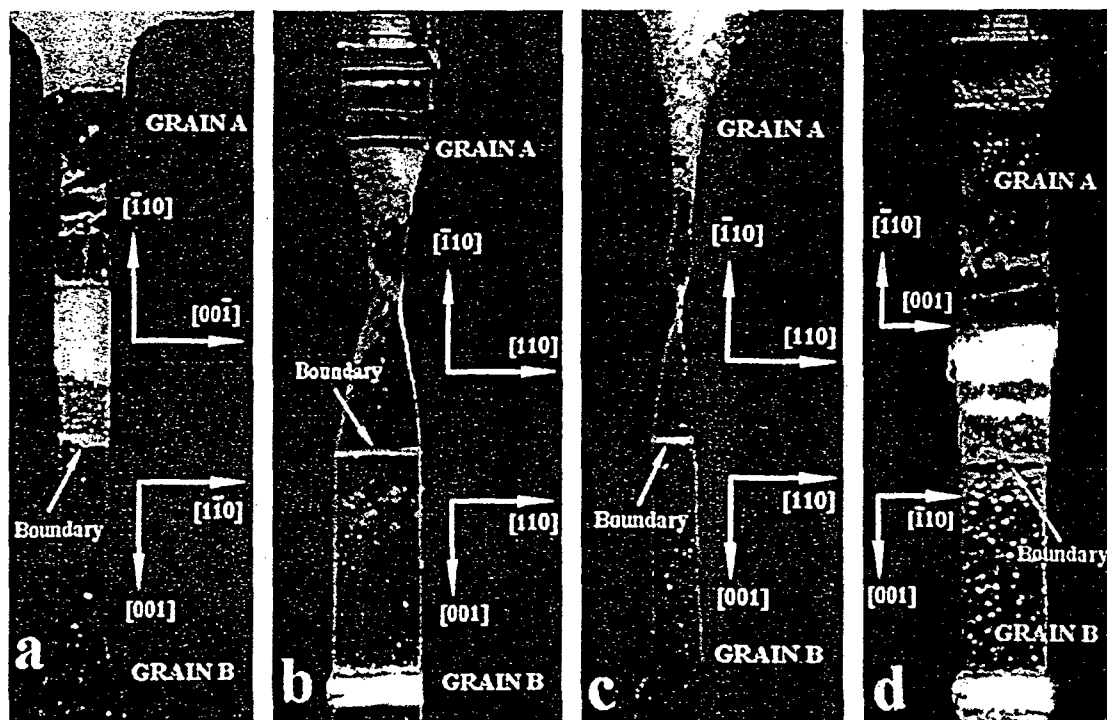
Acknowledgments

Figure 10. Type I and Type II specimens tested at 500°C and 10^{-3} s^{-1} after deformation (a) Type I sample, face view; (b) Type I sample, side view; (c) Type II sample, face view; and (d) Type II sa sample, side view.

References

1. V. I. Levit, et al., Scripta Mat. 34, 1925 (1996).
2. V. I. Levit, et al., TMS Proceedings of Internationl Symposium on Structural Intermetallics (1997) in press.
3. V. Vitek and M. Yan, in Physical Metallurgy and Processing of Intermetallic Compounds, ed. N. S. Stoloff and V. K. Sikka, p. 28, Chapman and Hall, New York (1996).
4. R. W. Fonda, M. Yan, and D. E. Luzzi, in MRS Symposium on High-Temperature Ordered Intermetallic Alloys, ed. J. Horton, I. Baker, S. Hanada, R. D. Noebe, and D. S. Schwartz, Vol. 364, p. 461, MRS, Pittsburgh, PA (1995).
5. D. B. Miracle, Acta Metall. Mater. 39, 1457 (1991).
6. T. J. Moore and J. M. Kalinowski, in MRS Symposium on High-Temperature Ordered Intermetallic Alloys, ed. I. Baker, R. Darolia, J. D. Whittenberger, and M. H. Yoo, Vol. 288, p. 1173, MRS, Pittsburgh, PA (1993).
7. P. Ochmann and H. Vehoff, Mat. Sci. Eng. A192, 364 (1995).
8. V. I. Levit, et al., Mechanisms of High Tensile Elongation in NiAl Single Crystals at Intermediate Temperatures, Recrystallization and Related Phenomena (1996).
9. C. T. Liu, E. H. Lee, and C. G. McKamey, Scripta Metall. Mater. 23, 875 (1989).
10. Bergman and H. Vehoff, Mats. Sci. Eng. A192, 309 (1995).
11. P. Sittner and V. Paidar, Acta Met. 37, 1717 (1989).

Investigation of Localized Deformation in NiAl Single Crystals

Chulho Yang
Graduate student

Vijay B. R. Seelam
Graduate student

Ashok V. Kumar
Assistant Professor

Department of Mechanical Engineering,
University of Florida,
Gainesville, FL 32611

First
Author

Deformation of NiAl single crystals was studied using finite element analysis to investigate the modes of localized deformation. Constitutive parameters and hardening characteristics of the active slip systems were estimated by comparing numerical simulation results with experimental results. Deformation of tensile specimens of NiAl single crystal was simulated when loaded along different crystal orientations to understand the deformation mechanism that result in various localized modes of deformation. In particular, the formation of shear bands and kink bands was studied and the material and geometric characteristics that influence the formation of such localization were investigated.

1 Introduction

NiAl has gained much attention as a potential structural material due to its desirable material characteristics such as high melting point, low density, good oxidation resistance, and excellent mechanical properties at high temperatures including hardness, toughness, thermal stability, and ductility. It has been considered a possible alternative to nickel-based superalloys for building turbine blades where due to lower weight and higher operating temperatures it is expected to provide increased engine thermodynamic efficiency. To find application as a commercial structural material, it should have desirable structural properties over a range of working temperature. However, NiAl has low ductility and poor fracture toughness at ambient temperatures. The tensile plastic strain before fracture at room temperature is typically 0.5–2.5 percent (Lahrman, 1991 and Miracle, 1993). To understand its low ductility, it is desirable to understand the deformation mechanism responsible for its mechanical behavior over a broad range of temperatures. Many modes of nonuniform deformation such as necking, localized shear, kinking etc. have been observed in NiAl single crystals. These localized deformations contribute significantly to the total plastic strain and eventual failure (Miracle, 1993). Significant tensile ductility is obtained only at and above 473 K (Wasilewski, 1967, Lahrman, 1991, etc.). Therefore, many approaches to improve the ambient temperature material properties of NiAl have been investigated (Darolia, 1991 and Darolia et al., 1992). A detailed survey of the literature and a critical review of the physical and mechanical properties of NiAl have been presented by Miracle (1993).

NiAl has a B2 type ordered crystal structure (see Fig. 1) similar to body centered cubic (bcc) crystals. Mechanical properties of NiAl single crystals vary with respect to the orientation of crystal lattice. Plastic deformation in NiAl occurs predominantly due to slip in the $\langle 001 \rangle$ directions along either $\{110\}$ or $\{100\}$ planes when loaded along non-$\langle 001 \rangle$ direction (or soft orientations). NiAl crystal subjected to loading along the $\langle 001 \rangle$ direction (hard orientation) shows high flow stress at low temperatures and enhanced creep strength at elevated temperatures. In this orientation, deformation occurs by non-$\langle 001 \rangle$ dislocation.

Asaro (1983) has reviewed the development and the theoretical basis of crystal plasticity. These theoretical formulations

have since been implemented using finite element method to simulate deformation and to predict and study nonhomogeneous deformation in single crystals. Most of the past studies have used these methods to simulate deformation in fcc (Pierce et al., 1983) and bcc single crystals (Deve et al., 1988). In this paper, we have investigated various modes of localized and diffused deformation observed in NiAl and studied the role of various parameters such as lattice orientation, rate sensitivity, latent hardening ratio etc. in promoting these modes of deformation. A rate-dependent constitutive model for single crystals was implemented into ABAQUS [1], a commercial finite element code that is capable of modeling large deformation and large strains. The rate dependent constitutive equation was integrated using forward gradient method which has been found to be effective (Pierce et al., 1983 and Wenner, 1993) provided sufficiently small time-steps are used for the time integration. For the simulation of localizations (shear band and kink band) we used incompatible elements (Simo and Rifai, 1990) available in ABAQUS. These elements have been found to be particularly suitable for modeling incompressible behavior and for modeling strain localizations (Simo and Armero, 1992) so that the results were not very sensitive to the mesh. Our implementation of the constitutive equation in ABAQUS was verified by reproducing results from other papers where similar constitutive equation was used (Asaro, 1983; Pierce et al., 1983; Deve et al., 1988 etc.).

2 Constitutive Modeling

In this section, we present a constitutive model for the elastic-plastic mechanical behavior of NiAl single crystals. The formulation used here is based on the well-established rate dependent model for single crystals (Pierce et al., 1983 and Asaro, 1983). The following section clarifies the notations and details of the constitutive equation that was implemented for simulating NiAl single crystals.

2.1 Kinematics of Crystalline Deformation. For describing the kinematics of single crystals it is convenient to decompose the deformation gradient (F) of the deformed crystal into two components (Lee, 1969): F^* the elastic stretching and rigid body rotation of the crystal lattice and F^p the deformation solely by plastic shearing so that $F = F^* \cdot F^p$. A particular slip system, α, is specified by the vectors $(s^{(\alpha)}, m^{(\alpha)})$, where, $s^{(\alpha)}$ is the slip direction vector and $m^{(\alpha)}$ gives slip plane normal vector. The vectors $s^{(\alpha)}$ and $m^{(\alpha)}$ are taken to be orthonormal in the undeformed lattice. As the crystal deforms, the slip direction vector $s^{(\alpha)}$ convects with the lattice deformation F^* and de-
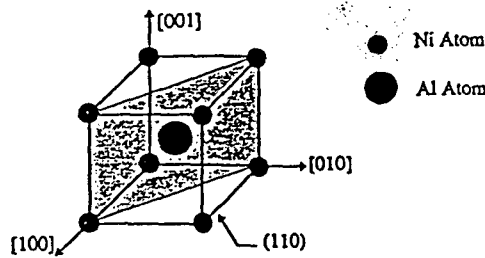
Fig. 1 NiAl crystal structure

formed slip direction $s^{*(\alpha)}$ is given as $F^* \cdot s^{(\alpha)}$ and the deformed slip plane normal vector $m^{*(\alpha)}$ is given as $m^{(\alpha)} \cdot (F^*)^{-1}$.

The total velocity gradient L in the current configuration can be decomposed into D, the rate of stretching and Ω the rate of spin.

$$L = \dot{F} \cdot F^{-1} = \dot{F}^* \cdot F^{*-1} + F^* \cdot \dot{F}^P \cdot F^{P-1} \cdot F^{*-1} \quad (2.1)$$

$$L = D + \Omega = L^* + L^P \quad (2.2)$$

where, L^* is the component of the velocity gradient associated with the elastic deformation and rotation while L^P is the velocity gradient due to plastic shearing. Since plastic deformation occurs solely by shear along the slip planes, the plastic part of the velocity gradient can be written as,

$$L^P = D^P + \Omega^P = \sum_{\alpha=1}^{n} \dot{\gamma}^{(\alpha)} (s^{*(\alpha)} \cdot m^{*T(\alpha)}) \quad (2.3)$$

where, $\dot{\gamma}^{(\alpha)}$ is the rate of shearing on the slip system α, as measured relative to the lattice. Finally, the plastic part of stretching (symmetric) and the spin (skew − symmetric) are given by,

$$D^P = \sum_{\alpha=1}^{n} \dot{\gamma}^{(\alpha)} \cdot P^{(\alpha)} \quad \text{and} \quad \Omega^P = \sum_{\alpha=1}^{n} \dot{\gamma}^{(\alpha)} \cdot W^{(\alpha)} \quad (2.4)$$

where

$$P^{(\alpha)} = \tfrac{1}{2}(s^{(\alpha)} \cdot m^{T(\alpha)} + m^{(\alpha)} \cdot s^{T(\alpha)}) \quad \text{and}$$

$$W^{(\alpha)} = \tfrac{1}{2}(s^{(\alpha)} \cdot m^{T(\alpha)} - m^{(\alpha)} \cdot s^{T(\alpha)}) \quad (2.5)$$

2.2 Constitutive Laws. The Jaumann rate of Kirchhoff stress of single crystal can be related to the elastic rate of stretching by Hooke's law, $\sigma^{\nabla *} = L:D^*$. Here L is the fourth-order tensor of elastic moduli. Jaumann stress rate of Kirchhoff stress $\sigma^{\nabla *}$ with respect to a coordinate that spins with the lattice is defined as

$$\sigma^{\nabla *} = \dot{\sigma} - \Omega^* \cdot \sigma + \sigma \cdot \Omega^* \quad (2.6)$$

$\dot{\sigma}$ is material rate of Kirchhoff stress. The Jaumann stress rate of Kirchhoff stress that spins with the material is given by

$$\sigma^{\nabla} = \dot{\sigma} - \Omega \cdot \sigma + \sigma \cdot \Omega \quad (2.7)$$

The difference between these two expressions is:

$$\sigma^{\nabla *} - \sigma^{\nabla} = \sum \beta^{(\alpha)} \cdot \dot{\gamma}^{(\alpha)} \quad \text{where,}$$

$$\beta^{(\alpha)} = W^{(\alpha)} \cdot \sigma - \sigma \cdot W^{(\alpha)} \quad (2.8)$$

Finally, the constitutive equation may be stated as:

$$\sigma^{\nabla} = L:D - \sum_{\alpha=1}^{n} \dot{\gamma}^{(\alpha)} R^{(\alpha)}, \quad \text{where}$$

$$R^{(\alpha)} = L:P^{(\alpha)} + \beta^{(\alpha)} \quad (2.9)$$

For a strain rate dependent material of the single crystal, the

slip rate of the unit slip system is ~~~~~~~~~~~~~~~~~ ~~ resolved shear stress by power law (Pan and Rice, 1983)

$$\dot{\gamma}^{(\alpha)} = \dot{a}^{(\alpha)} \left[\frac{\tau^{(\alpha)}}{\tau_c^{(\alpha)}} \right] \left[\left| \frac{\tau^{(\alpha)}}{\tau_c^{(\alpha)}} \right| \right]^{(1/m)-1} \quad (2.10)$$

where m is the rate sensitivity parameter, $\tau_c^{(\alpha)}$ is the critical resolved shear stress for the slip system α, $\dot{a}^{(\alpha)}$ is a reference strain rate on each slip systems. The resolved shear stress on the slip system is $\tau^{(\alpha)} = s^{(\alpha)} * \cdot \tau \cdot m^{T(\alpha)}*$. The shear rate in each slip system is uniquely determined by power law Eq. (2.10), and is nonvanishing as long as the resolved shear stress on that system is not identically zero. The critical resolved shear stress $\tau_c^{(\alpha)}$ for each slip system of the material increases with plastic deformation due to work hardening. The hardening curve needs to be determined for each possible slip system so that $\tau_c^{(\alpha)}$ can be expressed as a function of the plastic shear in that slip systems $\tau_c^{(\alpha)} = g(\gamma^{(\alpha)})$. However, when more than one slip system is active, hardening in each slip system is a cumulative effect of slip in all the active slip systems. For a rate dependent model, the rate of increase of the function $\tau_c^{(\alpha)}$ has therefore been specified as (Pierce et al., 1982),

$$\dot{\tau}_c^{(\alpha)} = \sum_{\beta=1}^{n} h_{\alpha\beta} |\dot{\gamma}^{(\beta)}| \quad (2.11)$$

The form of hardening moduli $h_{\alpha\beta}$ matrix commonly used is (Hutchinson, 1970),

$$h_{\alpha\beta} = qh + (1 - q)h\delta_{\alpha\beta} \quad (2.12)$$

where q is the latent hardening ratio. Hardening that occurs in a slip system due to shear in another slip system is referred to as latent hardening as opposed to self-hardening which occurs due to self-activation. The parameter q is the ratio of latent hardening to self-hardening. The hardening rate, h is the rate of change of critical resolved shear stress with shear strain. Two types of hardening curve were used in our implementation to model hardening in NiAl single crystals. For materials that exhibit very small strain hardening, the hardening rate decreases rapidly to zero and the critical resolved shear stress reaches a saturation value τ_s. The hardening curve $\tau_c(\gamma)$ and hardening rate $h(\gamma)$ for single slip in such materials is often represented using the following equations

$$\tau_c(\gamma) = \tau_0 + (\tau_s - \tau_0) \tanh \left(\frac{h_0 \gamma}{\tau_s - \tau_0} \right) \quad \text{and}$$

$$h(\gamma) = h_0 \sec h^2 \left(\frac{h_0 \gamma}{\tau_s - \tau_0} \right) \quad (2.13)$$

For materials that exhibit significant hardening, a power law equation is more appropriate to represent the hardening behavior (Pierce et al., 1982). The hardening curve $\tau_c(\gamma)$ and hardening rate $h(\gamma)$ is given below, where n is the hardening exponent.

$$\tau_c(\gamma) = \tau_0 \left(\frac{h_0 \gamma}{n \tau_0} + 1 \right)^n \quad \text{and}$$

$$h(\gamma) = h_0 \left(\frac{h_0 \gamma}{n \tau_0} + 1 \right)^{n-1} \quad (2.14)$$

3 Determination of Constitutive Parameters

The kinematics of single crystal deformation and constitutive models based on Schmid's law are now well established and have been used to simulate deformation of fcc and bcc single crystals (Pierce et al., 1983; Asaro, 1983; Deve, 1988 etc.). Such models are capable of simulating experimentally observed
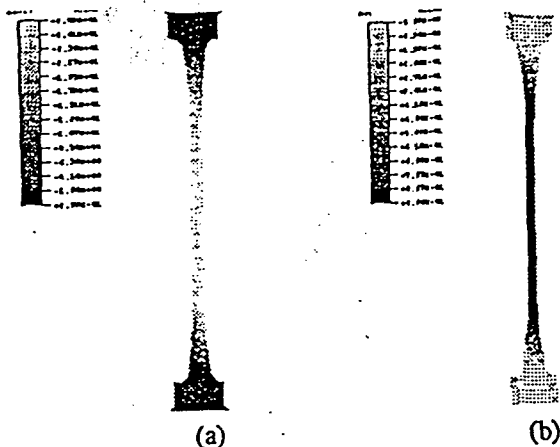
Fig. 2 Deformed specimen at 64 percent nominal strain ([557] orientation). Contour plot of (a) lattice rotation; (b) strain in axial direction

modes of deformation in single crystals. However, the accuracy of the simulated results is limited by the accuracy with which the constitutive parameters can be determined. The deformation pattern obtained numerically for single crystals of different materials vary due to the differences in constitutive parameters and due to differences in the operative slips systems. The factors that most significantly affect the deformation mode include the rate sensitivity parameter (m), the latent hardening (q) and the hardening curve (τ_c versus γ) of the material.

The rate sensitivity parameter m can be determined experimentally. For NiAl, Levit et al. (1996) have reported values of m ranging from 0.02 at ambient temperature to 0.12 at 1073 K. Rate sensitivity has also been found to vary considerably due to impurities such as Si. Presence of impurities lower the rate sensitivity of NiAl.

Experimental evidence (Winton, 1995) suggests that the initial critical resolved shear stress τ_0 is the same for both the $\{110\}\langle001\rangle$ and the $\{100\}\langle001\rangle$ slip systems that are usually activated during plastic deformation of NiAl single crystals. Loading directions such as $\langle557\rangle$ that activate $\{110\}\langle001\rangle$ slip system results in single slip. This provides an opportunity to determine the hardening curve for this slip system from experimentally obtained load-elongation curves. At intermediate temperatures (400–700 K), extremely high tensile elongation (100–350%) has been obtained for specimens loaded along the [557] direction. Determination of the hardening curve (τ vs γ) from the load versus elongation curve is difficult due to the large amount of lattice rotation accompanying the deformation. This lattice rotation changes the Schmid factor continuously during deformation. Furthermore, one has to account for strain localization to accurately determine the true stress and true strain developed in the specimen during the deformation. Levit et al. [17] have experimentally measured strain localization and determined the lattice rotation using electron back scattering methods during tensile elongation along the [557] direction. Based on these results they have calculated an approximate hardening curve (shear stress versus shear strain) for the $\{110\}\langle001\rangle$ slip system. The curve thus obtained exhibits relatively small monotonic hardening followed by a saturation critical resolved shear stress and has a shape that confirms well with the shape of the hardening curve represented by Eq. (2.13).

Several numerical simulations of deformation along [557] direction were performed using the hardening curve in Eq. (2.13) while varying the values of the parameters τ_0, τ_s, h_0. Figure 2 shows the deformed specimen at 64 percent nominal strain showing the contour plots of lattice rotation and strain along the axial direction. The direction of the lattice rotation is such that the Schmid factor decreases. As a result, a higher tensile load is required to produce the resolved shear stress

in yield stress along the tensile direction (referred to as "orientation hardening") prevents further deformation at the neck causing the neck to spread. It can be seen (Fig. 2(b)) that the deformation is more or less uniform within the gage length.

The specimen used in the experimentation and in the above model has a gage length 15 mm long, 1.4 mm wide and 2.4 mm thick. Plane stress conditions were assumed in the model. The nodes along the lower flange edge were fixed so that they do not move in the axial direction. A displacement rate was applied to the nodes along the top flange edge. The central node of the top and lower edge of the flange was fixed not to move in any direction. For all the simulations, the following imperfection or inhomogenity in the width of the specimen was introduced similar to that used by Tvergaard et al. (1981).

$$\Delta h_0 = h_0\left(-\xi_1 \cos\left(\frac{\pi x^2}{L_0}\right) + \xi_2 \cos\left(\frac{m\pi x^2}{L_0}\right)\right) \quad (3.1)$$

Figure 3 shows the close match between the load vs. elongation curve obtained experimentally and numerically. For this simulation the following parameters values were used in the hardening curve: $\tau_s = 38$ MPa, $\tau_0 = 26$ MPa, $h_0 = 110$ Mpa.

The load versus elongation curve obtained for [557] orientation increases to a peak and then decreases gradually to a minimum before increasing again (see Fig. 3). The drop in load after the peak load is due to localized deformation that results in a neck. However, the neck spreads after the initial localization. This behavior has been experimentally observed (Levit et al., 1996) and can be explained in terms of the orientation hardening that results from the large amount of lattice rotation that occurs during single slip. Numerical simulation based on our finite element model confirms this phenomenon.

Tensile elongation of NiAl single crystal along the [110] direction activates the $\{100\}\langle001\rangle$ slip system. However, unlike for [557] direction, elongation in this direction produces double slip. Both the (100) and (010) planes become active simultaneously since the Schmid factor for both these planes are identical. Furthermore, no lattice rotation occurs because these planes are located symmetrically about the tensile axes and identical amount of slip occurs in both slip planes. The load versus elongation curve obtained experimentally (Levit et al.) seems to suggest considerable work hardening. Determining the hardening curve however is not straightforward due to uncertainty about the contribution of latent hardening to the total hardening observed. Simulation of the elongation along [110] using the hardening curve used earlier for $\{110\}\langle001\rangle$ slip system and $q = 1$ yielded poor results at large strains as seen in Fig. 5. The numerically obtained load-elongation curve predicts the initial peak followed by a load drop. However, the load increases at higher strains for the experimental specimen, while it drops due to a sharp neck for the numerical simulation. Increasing the latent hardening parameter moves the load versus elongation curve upwards but does not result in the desired
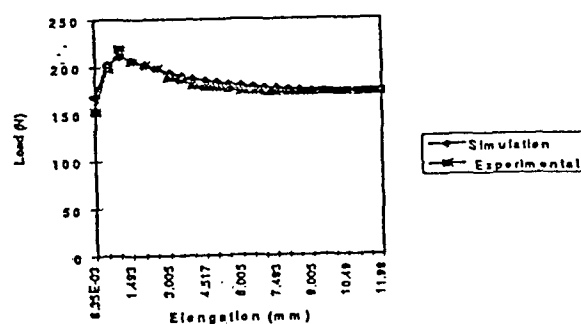

Fig. 3 Load versus elongation for elongation in the [557] direction

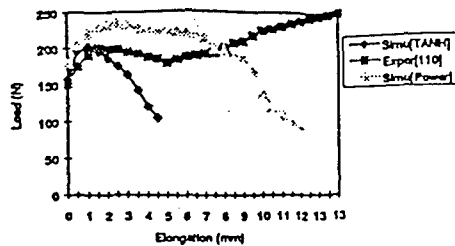/ 9412SSjy08   04-23-98 13:48:44   asmel   ASME: J Materials

Fig. 4 .Load versus elongation for [110] orientation using different hardening curve

increase in load at large deformation. This suggests that there is considerable work hardening for the {100}⟨001⟩ slip system and that the hardening curve for this slip system does not have a plateau as assumed in Eq. (2.13). Simulations were therefore also performed using power law hardening curve represented by Eq. (2.14). Even though the power law equation involves more hardening and a slower drop in hardening rate, the numerically simulated load versus elongation curve still predicts a drop in load followed by necking (Fig. 4). The increase in load at large deformation observed in the experiment was accompanied by spreading of the neck. This requires an unusually high rate of hardening at large strains. It is possible that this increased hardening is associated with cross-slip occurring in {110}⟨001⟩ slip planes at large deformation. Since activation of {110} planes result in non-planar deformation, a 3-dimensional finite element model of the single crystal is required to simulate the deformation. Simulation using 3D finite element model that allowed cross-slip confirmed this hypothesis. The details of the 3D simulation and the corresponding hardening model is the subject of another paper (Kumar and Yang, 1998).

4 Study of Shear Band Formation

NiAl exhibits low ductility and low fracture toughness near room temperature. Significant ductility is obtained only above 200°C. Load versus elongation curve at various temperatures indicates that fracture stress at RT is lower than at 200°C. This seems to suggest that fracture at low temperatures may be initiated by localized deformation such as shear bands. While macroscopic shear band formation has not been observed experimentally in NiAl, it is possible that fracture may be initiated by a tendency toward localization that create stress concentrations. To understand the conditions that lead to shear localization as well as the constitutive parameters that play a significant role, numerical simulations were performed with varying values of constitutive parameters, specimen geometry, orientation and boundary conditions. Previous studies on shear band formation (Pierce et al., 1983; Deve et al., 1988) indicate that both rate sensitivity and latent hardening significantly influence the formation of shear localization. In this study, these properties as well as the effect of hardening were studied.

Results of the numerical simulation indicated that shear band formation is facilitated by low rate sensitivity and low hardening. The underlying cause for the formation of shear bands is orientation softening that creates a band where lattice rotation has made deformation possible at a lower load. As a result, further deformation localizes in the band causing highly localized shear. Shear bands were simulated numerically for elongation in the neighborhood of [110] direction. As mentioned earlier, no lattice rotation occurs for elongation along the [110] direction. However, at orientations a few degrees to either side of the [110] direction, lattice rotation occurs that tries to rotate the lattice back to the [110] symmetric orientation. Due to the specimen geometry and imposed geometric imperfections, nonuniform deformation occurs. Regions where more lattice rotation occurs become softer thus promoting shear band forma-

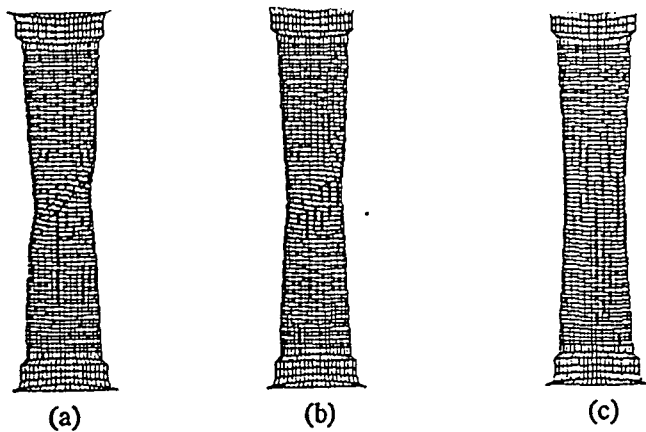

(a)   (b)   (c)

Fig. 5 Deformed mesh with different strain rate sensitivity at 15 percent nominal strain (a) $m = 0.006$; (b) $m = 0.01$; (c) $m = 0.02$

tion. Figure 5 shows shear bands obtained by numerical simulation of elongation 3 deg off from the [110] direction when low work hardening was assumed. In these simulations, a specimen with gage length of 22 mm, 5 mm wide, and 2 mm thick was used. The model assumes plane stress conditions and the following material properties were used: Elastic bulk modulus, $K = 164916$ MPa, Shear modulus, $G = 68660$ MPa. The parameters in the imperfection shape Eq. (3.1) were set to: $\xi_1 = 0.0126$, $\xi_2 = 0.072$, and $m = 5$.

Sharp bands were formed only for low values of rate sensitivity and low hardening. However, as mentioned in the last section, for NiAl single crystals deformation in the {100}⟨001⟩ slip system produces high work hardening even at large deformation. Therefore, shear bands are unlikely to be seen experimentally during tension tests near the [110] direction.

Figures 6 and 7 show the effect of work hardening where the saturation value of critical resolved shear stress τ_s was varied. A moderate value of strain rate sensitivity $m = 0.02$ was used for the results in Fig. 6. These plots shows that no clear shear band forms when the rate sensitivity is high. However, for lower hardening rate ($\tau_s = 50$ MPa) sharp neck-like localization occurs even though the rate sensitivity is high.

In Fig. 7, a lower strain rate sensitivity, $m = 0.006$ was used. No significant localization occurs when τ_s was increase to 120 MPa resulting in a large amount of work hardening.

5 Study of Kinking

Kinking is a highly localized form of deformation that has been observed in NiAl during compression near the hard orientation (⟨100⟩ direction) (Frasier et al., 1973a, b). When com-

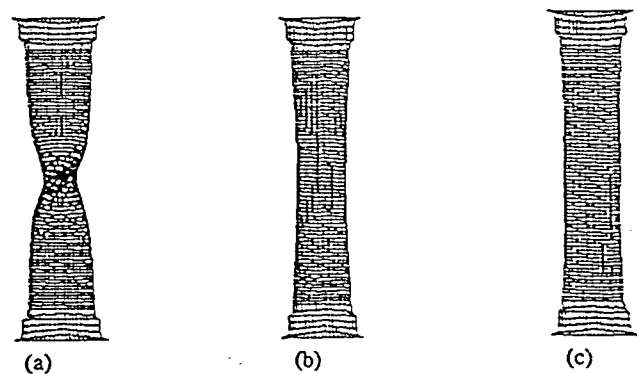
(a)   (b)   (c)

Fig. 6 Deformed mesh with $m = 0.02$ and different work hardening at 15 percent nominal strain (a) $\tau_s = 50$ MPa (b) $\tau_s = 83$ MPa (c) $\tau_s = 120$ MPa
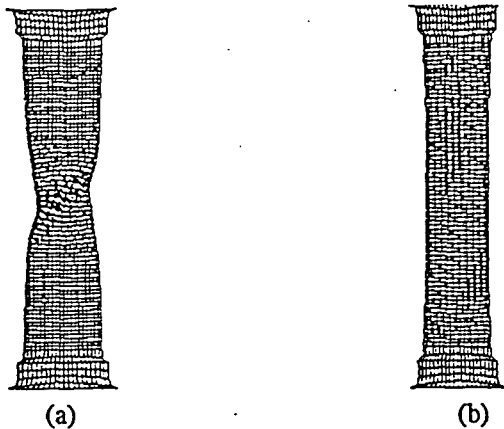
(a)   (b)

Fig. 7 Deformed mesh with m = 0.006 at 15 percent nominal strain (a) τ_s = 60 (Mpa) (b) τ_s = 120 (MPa)

Fig. 9 Load versus elongation curve for 5 deg off from compression axes

pressed along the hard orientation, the resolved shear stress along ⟨001⟩ directions is zero. As a result, glide occurs along other directions such as ⟨111⟩ or ⟨110⟩ (Miracle, 1993). However, if the direction of compression is misaligned slightly from the ⟨001⟩ direction, either {110}⟨001⟩ or {100}⟨001⟩ systems can get activated depending on the direction of misalignment. Such misalignment has been observed to favor kinking. Experimental studies by Fraser et al., 1973, shows that deformation in the kink band occurs on {110} planes due to slip along the ⟨100⟩ direction parallel to the compression axes. However, all three ⟨100⟩ dislocations have been observed experimentally (Miracle, 1993).

Kinking can been explained in terms of orientation softening that occurs due to large lattice rotation. Once a slip system is activated, the lattice rotation increases the resolved shear stress in that system, making it softer so that activation of the other possible systems are unlikely. When nonuniform deformation is induced due to specimen geometry or imperfections, the region where more lattice rotation occurs due to higher strains becomes softer than the rest of the specimen causing further deformation to localize in this region. The exact location of the formation of the band depends on the applied imperfection.

When {110}⟨001⟩ slip system is activated, single slip occurs while double slip occurs when {100}⟨001⟩ system is activated. Significant lattice rotation occurs in both cases. Numerical simulation were performed for both these situations with compressive load applied along directions misaligned by 5–10 deg from
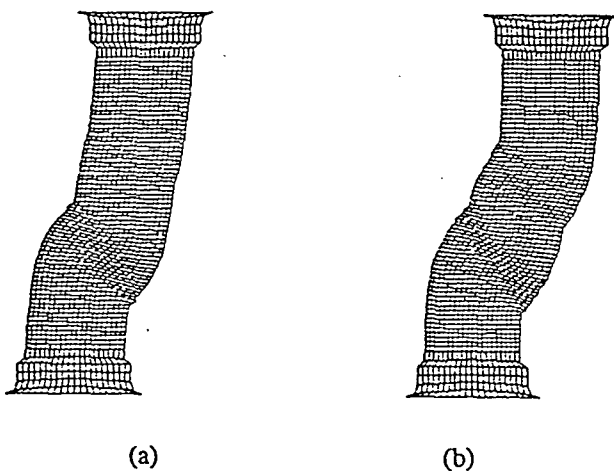
the [001] direction. Figure 8 shows kinking due to single slip along ⟨110⟩⟨001⟩. Kink band starts forming at smaller strains when the angle of misalignment is smaller. Figure 9 shows load versus elongation curve for 5 deg misalignment. Multiple load drops indicate that multiple kink band are formed during the deformation.

Kink bands were obtained during simulation of both single slip or double slip situations. More lattice rotation occurs during single slip than in the double slip case. Figure 10 shows lattice rotation that occurred during the deformation. More than 60 deg of lattice rotation has occurred along the band during single slip. This agrees well with the experimental observation of Fraser et al. (1973) where they have reported slip along {110}⟨001⟩ slip system and ~60 deg lattice rotation in the kink band.

5 Summary and Conclusion

Deformation of NiAl single crystals were studied using finite element simulations. Comparison with experimental data provided information about constitutive parameters such as hardening in different slip systems that are difficult to measure experimentally. Simulation results suggest that significant work hardening occurs in {100}⟨001⟩ slip system while very little hardening occurs in {110}⟨001⟩ plane. The numerically simulated load versus elongation curve matched well with experiment for elongation along the [557] direction. Simulation of elongation in the [110] direction, with the assumption that only {100}⟨001⟩ slip systems are activated, did not agree with experimental data. The increase in load at large deformation observed experimentally requires unusually large work hardening at large deformation. This increase in load is due to activation

(a)   (b)

Fig. 8 Deformed mesh after 7.5 percent nominal strain when loading is (a) 10 deg off from compression axes; (b) 5 deg off from compression axes
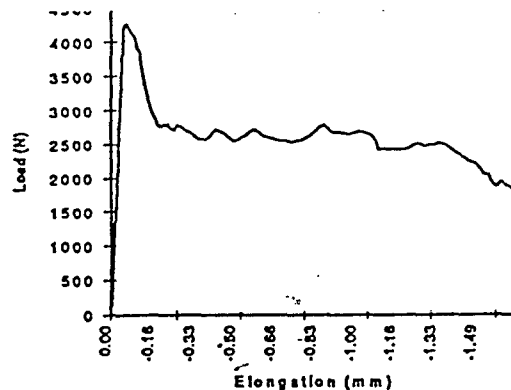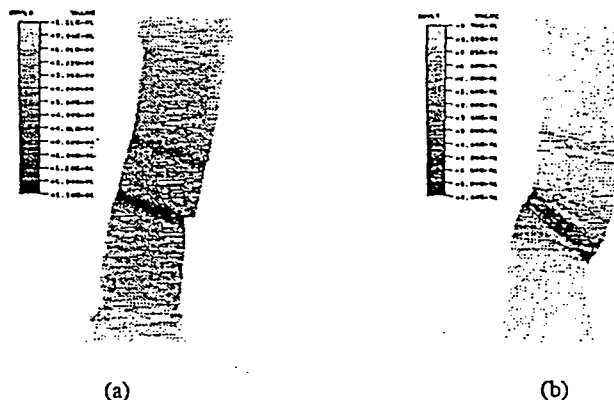

(a)   (b)

Fig. 10 Contour plot of crystal lattice rotation at 2.265 percent nominal strain (a) double slip (θ ≈ 80, 170 deg); (b) single slip (θ = 85 deg)

of $\{110\}\langle001\rangle$ systems. Activation of these slip systems can be modeled only using 3D FEA models.

Simulation of deformation along directions slightly off from the [110] direction shows that the geometrical softening associated with lattice rotation can produce shear localization if the rate sensitivity is very low and the material undergoes very little work hardening. However, since NiAl has much higher values of rate sensitivity and hardening than were used in the simulation, it is unlikely that such bands would be observed experimentally.

Simulation of kinking during compression along directions close to the hard-orientation of the crystal revealed that kink bands may form due to either single slip along $\{110\}\langle001\rangle$ slip system or due to double slip in $\{100\}\langle001\rangle$ slip system. In both cases, the direction of lattice rotation is such that orientation softening occurs which leads to deformation localization. Low rate sensitivity and low hardening promotes kink band formation.

Acknowledgments

References

1 ABAQUS, 1994. Manual Version 5.4.

2 Asaro, R. J., 1979. "Geometrical Effects in the Inhomogeneous Deformation of Ductile Single Crystals," Acta Metall., Vol. 27, pp. 445–453.

3 Asaro, R. J., 1983, "Micromechanics of Crystals and Polycrystals," Advances in Appl. Mech., Vol. 23, pp. 1–115, J. W. Hutchinson, T. Y. Wu, eds., N. Y. Academic Press.

4 Chang, Y. W., and Asaro, R. J., 1981, "Lattice Rotations and Localized Shearing in Single Crystals," Acta Metall., Vol. 29, pp. 241.

5 Darolia, R., 1991, "NiAl alloys for High-temperature structural applications," J. Metals, Vol. 43, No. 3, pp. 44–49.

6 Darolia, R., Lahrman, D. F., Field, R. D., Dobbs, F. R., Chang, K. M., Goldman, E. H., and Konitzer, D. G., 1992, "Ordered Intermetallics—Physical Metallurgy and Mechanical Behaviour," C. T. Lui, R. Cahn and G. Sauthoff, eds., NATO ASI Series E: Applied Sciences, Vol. 213, pp. 229.

7 Deve, H., Harren, S., McCullough, C., and Asaro, R., 1988, "Micro and Macroscopic Aspects of Shear Band Formation in Internally Nitried Single Crystal of Fe-Ti-Mn Alloys," Acta Metall., Vol. 36, No. 2, pp. 341–365.

8 Fraser, H. L., Smallman, R. E., and Loretto, M. H., 1973a, "The Plastic Deformation if NiAl Single Crystals Between 300°K and 1050°K—I. Experimental Evidence on the Role of Kinking and Uniform Deformation in Crystals Compressed Along (001)," Phil. Mag., Vol. 28, p. 651.

9 Fraser, H. L., Loretto, M. H., and Smallman, R. E., 1973b, "The Plastic Deformation if NiAl Single Crystals Between 300°K and 1050°K—II. The Mechanism of Kinking and Uniform Deformation," Phil. Mag., Vol. 28, p. 667.

10 Hill R., and Hutchinson, J. R., 1975, "Bifurcation Phenomena in the Plane Tension Test," J. Mech. Phys. Solids, Vol. 23, p. 239.

11 Hutchinson, J. W., 1970, "Elastic-Plastic Behavior of Polycrystalline Metals and Composites," Proc. R. Soc., Lond. Series A319, pp. 247–272.

12 Kumar, A. V. and Yang, C., 1998, "Hardening Characteristics of NiAl Single Crystals," to be submitted in JOURNAL OF ENGINEERING MATERIALS AND TECHNOLOGY.

13 Lahrman, F., Field, R. D., and Darolia, R., 1991, "High Temperature Ordered Intermetallic Alloys IV," MRS Proc., Vol. 213, p. 603.

14 Lee, E. H., 1969, "Elastic-Plastic Deformation at Finite Strains," ASME Applied Mech., Vol. 36, p. 1.

15 Levit, V. I., Winton, J. S., Yu Gornostyrev, and Kaufman, M. J., 1996, "Mechanism of High Tensile Elongation in NiAl Single Crystals at Intermediate Temperatures."

16 Miracle, D. B., 1993, "The Physical and Mechanical Properties of NiAl," Acta Metall., Vol. 41, No. 3, pp. 649–684.

17 Pan, J. and Rice, J. R., 1983, "Rate Sensitivity of Plastic Flow and Implications for Yield-Surface Vertices," Int. J. Solid Struct., Vol. 19, pp. 973–987.

18 Pierce, D., Asaro, R. J., and Needleman, A., 1982, "An Analysis of Nonuniform and Localized Deformation in Ductile Single Crystal," Acta Metall., Vol. 30, pp. 1087–1119.

19 Pierce, D., Asaro, R. J., and Needleman, A., 1983, "Material Rate Dependence and Localized Deformation in Crystalline Solids," Acta Metall., Vol. 31, No. 12, pp. 1951–1976.

20 Simo, J. C. and Armero, F., 1992, "Geometrically Non-Linear Enhanced Strain Mixed Methods and the Method of Incompatible Modes," International Journal for Numerical Methods in Engineering. Vol. 33, pp. 1413–1449.

21 Simo, J. C. and Rifai, M. S., 1990, "A Class of Mixed Assumed Strain Methods and the Method of Incompatible Modes," International Journal for Numerical Methods in Engineering, Vol. 29, pp. 1595–1638.

22 Tvergaard, V., et al., 1981, "Flow Localization in the Plane Strain Tensile Test," J. Mech. Phys. Solids, Vol. 29, pp. 115–142.

23 Wasilewski, R. J., Butler, S. R., and Hanlon, J. E., 1967, Trans. Metall. Soc. AIME, Vol. 239, p. 1357.

24 Wenner, M. L., 1993, "A Generalized Forward Gradient Procedure for Rate Sensitive Constitutive Equations," Int. J. for Num. Meth. in Engineering, Vol. 36, pp. 985–995.

25 Winton, J. S., 1995, "The Effect of Orientation, Temperature, and Strain Rate on the Mechanical Properties of NiAl Single Crystals," MS thesis, Univ. of Florida.

/ 9412SSjy08   04-23-98 13:48:44   asmel   ASME: J Materials

Study of work hardening models for single crystals using 3-D finite element analysis

Ashok V. Kumar and Chulho Yang
Department of Mechanical Engineering
University of Florida
Gainesville, FL 32611-6300

ABSTRACT

A comparative study of some hardening models that have been proposed for single crystals is presented in this paper. These models are compared by simulating the deformation of FCC single crystals under uniaxial tension using finite element method. During large deformation of single crystals, multiple-slip systems can be activated resulting in a three-dimensional deformation. Therefore, three-dimensional finite element models have been used for the simulation. A rate dependent constitutive model was implemented into a non-linear large deformation finite element program to simulate the deformation of single crystals. The hardening laws are compared to study their ability to predict the three stages of hardening observed experimentally in FCC single crystals.

Shortened Title: Work hardening in single crystals

Corresponding Author: Ashok V. Kumar

Telephone: (352) 392-0816

Fax: (352) 392-1071

Email address: akumar@cimar.me.ufl.edu

1

I. INTRODUCTION

Various rate dependent and rate independent constitutive models have been developed to model the deformation of single crystals (Peirce et al, 1992, 1983). These equations can be incorporated into finite element programs to simulate the deformation of single crystals. Such simulations are required to acquire a better understanding of the causes of many kinds of localized deformation and failures in metals. An important component of constitutive equations used to describe single crystal behavior is the work hardening model. Hardening of single crystals is not very well understood especially during multiple slip when more than one slip system is active. When large deformation is applied on single crystals, various slip systems harden at different rates and the lattice undergoes large rotations often leading to multiple slip. The deformation that occurs in the crystal during multiple slip is three-dimensional and can be accurately modeled only using three-dimensional finite element models. In the past, two-dimensional approximations have been used for finite element analysis, for example, Asaro's 2D planar double slip model (Peirce et al, 1982).

(see attached)

Figure 1. Standard stereographic projection from [100] orientation of FCC crystals

In this paper, the hardening characteristics of FCC single crystals have been studied. The notations used in this paper to refer to the slip systems of a FCC crystal are listed in table 1. The 12 possible slip systems of the FCC crystal (all in the {111}<110> family) are divided into 4 groups and each group has 3 slip directions. The orientation of the load determines which slip system would become active. When the loading axis is inside the triangle of [100], [110], [111] vertices in [100] stereographic projection (figure 1), B4 will be active and it is

2

the "primary" slip system. Only single slip in B4 occurs and the crystal lattice rotates toward slip direction [101]. When loading axis approaches the [100]-[111] border-line, "conjugate" slip system C1 can activate. Most of the hardening laws were proposed and tested for FCC single crystals (Peirce et al., 1983; Bassani and Wu, 1991). In this paper, we will investigate these and other hardening models using three-dimensional finite element analysis.

(see attached)

Table 1. Notation for slip systems of FCC crystals

In the next section, various hardening models that have been proposed for single crystals are summarized. In section III, results of three-dimensional simulation of crystal deformation using various hardening models are presented. Discussion of the results and conclusions are presented in section IV.

II. WORK HARDENING MODELS FOR SINGLE CRYSTALS

In a strain rate dependent constitutive equation for single crystal deformation, the rate of shear, $\dot{\gamma}$, in a slip system is assumed to be related to the resolved shear stress (τ) on that slip system by a power law (Pan and Rice, 1983) given in equation (1).

$$\dot{\gamma}^{(\alpha)} = \mathring{a}^{(\alpha)} \left[\frac{\tau^{(\alpha)}}{\tau_c^{(\alpha)}} \right] \left| \frac{\tau^{(\alpha)}}{\tau_c^{(\alpha)}} \right|^{(1/m)-1} \tag{1}$$

where, m is the rate sensitivity parameter, $\tau_c^{(\alpha)}$ is the *flow stress*, also known as the *critical resolved shear stress*, for the αth slip system and $\mathring{a}^{(\alpha)}$ is a reference strain rate. The shear rate in each slip system is uniquely determined by the power law, eqn (1), and is non-vanishing as long as the resolved shear stress on that system is not identically zero. The flow

3

stress $\tau_c^{(\alpha)}$ for each slip system increases with plastic deformation due to work hardening. The hardening curve needs to be determined for each possible slip system so that $\tau_c^{(\alpha)}$ can be expressed as a function of the plastic shear in that slip system $\tau_c^{(\alpha)} = g(\gamma^{(\alpha)})$. However, when more than one slip system is active, hardening in each slip system is a function of slip on all the active slip systems. For a rate dependent model, the rate of increase of the flow stress $\tau_c^{(\alpha)}$ has therefore been specified as (Hill 1966),

$$\dot{\tau}_c^{(\alpha)} = \sum_{\beta=1}^{n} h_{\alpha\beta} \left| \dot{\gamma}^{(\beta)} \right| \tag{2}$$

The hardening laws that have been proposed so far differ mainly in the definition of the hardening moduli $h_{\alpha\beta}$. From the early 1900's several hardening laws were proposed to explain the deformation process on single crystals. Based on experimental work on aluminum, Taylor (1934) proposed the 'isotropic' hardening law. According to this law all slip systems harden equally when deformation occurs so that $h_{\alpha\beta} = h(\gamma_T)$, where γ_T is the sum of the shear strains on all slip systems. This isotropic hardening is unable to predict the experimental observation that inactive or latent slip systems often harden more than the slip system that is active during deformation.

Hutchinson (1970) accounts for latent hardening by assuming that the off-diagonal terms in the matrix of hardening moduli are different than the diagonal values. Asaro (1983) has also used the same concept in their constitutive model for single crystals, expressing the hardening moduli in the following form, often referred to as the "two-parameter theory.

$$h_{\alpha\beta} = qh(\gamma_T) + (1-q)h(\gamma_T)\delta_{\alpha\beta} \tag{3}$$

4

The parameter h, called the hardening modulus, is the rate of change of flow stress with shear strain during single slip. The second parameter q, is the latent hardening ratio, which is the ratio of the hardening in a latent (or inactive) slip system to the hardening in the active slip system. $\delta_{\alpha\beta}$ is the Kronecker's delta. In Asaro's (1983) model, the hardening modulus, h is assume to be a function of the sum of shear strains (γ_T) in all the slip systems, ie, h=h(γ_T). The hardening curve $\tau_c(\gamma)$ and hardening modulus h(γ) for single slip in such materials is often represented using the following equations

$$\tau_c(\gamma) = \tau_0 + (\tau_s - \tau_0)\tanh\left(\frac{h_0\gamma}{\tau_s - \tau_0}\right) \tag{4}$$

$$h(\gamma) = \frac{d\tau_c}{d\gamma} = h_0 \sec h^2\left(\frac{h_0\gamma}{\tau_s - \tau_0}\right) \tag{5}$$

Latent hardening ratio is often estimated indirectly by measuring the "overshoot" angle, that is the angle by which the tensile axis overshoots the symmetry boundary between stereographic triangles during uniaxial test. If the primary and conjugate slip systems had hardened equally the tensile axis would stop rotating at the symmetry boundary (Asaro, 1983). An alternate method for measuring latent hardening involves first loading the crystal in a single slip orientation in a primary test. Subsequently, the loading direction is changed to activate a previously latent slip system in a secondary test to measure the flow stress in the latent system. The flow stress of the system active during the primary test is compared with the flow stress of the system activated in the secondary test to establish a latent hardening ratio (Fraciosi, (1985), (1980); Bassani, (1994)).

Kocks and Brown (1966) conducted latent hardening tests on aluminum single crystals to obtain latent hardening ratios by comparing flow stress of primary slip system and

secondary slip system. Slip systems that are on the same plane were found to have similar flow stress. Slip systems on different planes than the active system were found to have flow stress 10 to 30 % higher. Jackson and Basinski (1967) conducted tests on copper single crystals and obtained similar results. Nakada and Keh (1966) studied latent hardening of iron single crystals and also found the latent hardening rate to be greater than the self hardening rate.

Many authors have studied the interactions among the slip systems in FCC crystals (Kocks, 1964; Basinski and Basinski, 1979; Franciosi et al., 1980). From a microscopic viewpoint, the hardening of single crystals during deformation can be regarded as the result of dislocation interaction between slip systems. Internal dislocation density and short range interacting dislocation strengths can be considered the main parameters of the hardening analysis.

Franciosi et al. (1982), (1985), expressed flow stress as a function of dislocation interaction coefficients matrix and dislocation density. Contents of the dislocation interaction matrix are classified according to the slip interaction between the slip systems and the resultant dislocation junction such as sessile, glide, hirth lock, no junction and self-hardening.

Weng (1987) has proposed a relation for determining latent hardening ratios between various slip systems of a crystal by considering the angles between the slip direction and slip plane normal of the two slip systems. This relation can account for isotropic hardening, kinematic hardening, strong latent hardening and Baushinger effects. The matrix of latent hardening ratios between all potential slip systems of the crystal are expressed as:

$$g_{ij} = \alpha_1 + (1 - \alpha_1) \cos \theta_{ij} \cos \phi_{ij} + (\alpha_2 \sin \theta_{ij} + \alpha_3 \sin \phi_{ij}) \tag{6}$$

where θ_{ij} is the angle between the slip directions of the i-th and j-th systems. ϕ_{ij} is the angle between the slip plane normals of the i-th and j-th systems. α_1 is the degree of isotropy in work hardening and α_2 represents the anisotropic departure for the latent hardening of coplanar systems and α_3 is the additional departure for systems on intersecting planes.

More recently, Bassani and co-workers (Wu, et al 1991, Bassani et al 1991, Bassani, 1994) have investigated hardening criterion for multi slip condition in FCC single crystals of metals. Based on experimental study of latent hardening in symmetrically and unsymmetrically loaded copper single crystals, they suggest that hardening in secondary slip system may be lower than that in active slip system. The apparent higher flow stress observed in the secondary slip systems by previous investigators are explained to be the result of very high initial hardening rate when these secondary systems are activated. In other words, due to the high hardening rate the flow stress on the secondary system becomes higher than the flow stress of the primary system after a small amount of strain in the secondary system. Variation in hardening behavior with the loading orientation was also studied experimentally. Based on these observations, Bassani and Wu (1991) devised a phenomenological hardening law as follows.

$$h_{\alpha\alpha} = F(\gamma_\alpha)G(\gamma_\beta) \tag{7}$$

$$h_{\alpha\beta} = qh_{\alpha\alpha} \tag{8}$$

where, $h_{\alpha\beta}$ is the instantaneous hardening moduli expressed as a matrix and $h_{\alpha\alpha}$ represents the diagonal terms of the hardening matrix.

$$F(\gamma^\alpha) = (h_0 - h_\infty)\sec h^2\left[\frac{(h_0 - h_\infty)\gamma^\alpha}{(\tau_I - \tau_0)}\right] + h_\infty \tag{9}$$

7

$$G(\gamma^\beta) = 1 + \sum_{\beta=1, \beta \neq \alpha}^{n} f_{\alpha\beta} \tanh(\frac{\gamma^\beta}{\gamma_0}) \qquad\qquad (10)$$

where $F(\gamma^\alpha)$ is the instantaneous hardening modulus under independent single slip on slip system α. G is the function representing interactive latent hardening and it is a function of the shear deformation in all systems except α. The function F is similar to that used in equation (4) except that at large strains the hardening modulus reaches a saturation value of h_∞. The function G accounts for latent hardening by ensuring that every slip system hardens due to slip in other slip systems. The amount of latent hardening is determined by the factors $f_{\alpha\beta}$ whose values depend on the type of dislocation junction formed between slip α and β.

III. THREE-DIMENSIONAL SIMULATION OF DEFORMATION

Simulation of large deformation of single crytals using three-dimensional finite element models provides great insight into deformation modes and work hardening in single crystal. It is also a very useful tool to understand and validate the hardening models and their ability to predict single crytal behavior during large deformation and multiple slip situations. In this section simulation results obtained using two-parameter hardening model, Bassani's models, a modified two-parameter model and multi-parameter models are presented. A rate-dependent constitutive model, eqn (1), for single crystals was implemented into ABAQUS, a commercial finite element program that is capable of modeling large deformation and large strains. The constitutive equation was integrated using forward gradient method which has been found to be effective (Peirce et al 1983 and Wenner, 1993) provided sufficiently small time-steps are used for the time integration. For all the simulation results presented below, a strain rate sensitivity m=0.01 was used. Rate dependent models allow unique determination

8

of slip rates on each slip system even when many potential slip systems are included in the model thus enabling simulation of multiple slip. Furthermore, since three-dimensional finite element models are used, the actual three-dimensional deformation that results due to lattice rotation and unsymmetric slip can be accurately modeled without any approximating assumptions that are typically used for two -dimensional models. Figures 2 shows the finite element mesh for the tensile specimen and figure 3 shows the boundary conditions that were applied. Since the model is rate dependent the load was applied as a rate of displacement for the nodes along the top surface of the specimen.

(see attached)

Figure 2. Specimen used in the simulation

Figure 3: Loading direction and boundary conditions used in simulation

(i)   Two-parameter hardening model

Many researchers have used the two-parameter hardening law described earlier in eqn (3) (eg. Hutchinson 1970, Peirce et al, 1982, 1983). This model is able to predict a higher rate of latent hardening than self hardening by setting the latent hardening ratio, $q > 1$. Asaro (1983) applied it to FCC crystals to model symmetric double slip using an planar model where it is assumed that the two slip planes are normal to the planar model so that the deformation can be modeled as two-dimensional. When loaded in the symmetric orientation, there is no lattice rotation and the results obtained using three-dimensional models matched closely with the results of Pierce et al (1983) who used Asaro's planar double slip assumption. For the simulation, we used material properties that were used by Peirce (τ_o=60.84 MPa, τ_s=1.8τ_o, h_0=8.9τ_o).

9

When loaded along non-symmetric orientation such as [632], significant lattice rotation was observed as expected. Figure 4, shows the flow stress versus time and figure 5 shows the shear strain in all the slip systems at a selected element. For this simulation we assumed isotropic hardening (q=1) so that secondary systems do not harden more than primary. Despite this, it is clear from figure 4 that deformation occurs mainly due to single slip in primary system B4 and that the resolved shear strain in all other slip systems are negligible. The strain rate for B4 slip system suddenly decreases in figure 5 after approximately 10% strain due to strain localization / necking. Figure 6 shows the load versus elongation. The relative high hardening seen during stage I in figure 4 and 6 is due to the assumption that $\tau_s=1.8\tau_o$ (used by Peirce, 1983). Other researchers such as Bassani, have used smaller values of τ_s for stage I.

(see attached)

Figure 4. Flow stress versus time for the two parameter hardening model.

Figure 5. Resolved shear strain vs time for the two-parameter hardening model

Figure 6. Load vs elongation for the two parameter hardening model

This hardening model can predict stage I as seen in figure 4 but is unable to predict stage II and stage III deformation observed experimentally in unsymmetrically loaded crystals. Stage II is attributed to the activation of conjugate slip and the resultant increase in hardening. The rate of hardening is determined by the hardening modulus. The hardening modulus tends to zero at large strains according to this model as per equations (3) and (5) where the hardening modulus is expressed as a function of cumulative strain in all slip systems. Therefore, if the conjugate system activates only at relatively large strain there is no

significant increase in hardening since the hardening modulus becomes very small. Therefore, activation of conjugate or secondary slip systems at large strain does not lead to any substantial increase in hardening.

(ii) Modified two-parameter hardening model

Based on the above observation, a modified two-parameter model was tested in which the hardening modulus for each system is a function of the shear strain in that system alone. This implies that when a new system is activated, there is an increase in the hardening rate of all other slip systems. The hardening modulus then can be expressed as

$$h_{\alpha\beta} = qh(\gamma_\beta) + (1-q)h(\gamma_\beta)\delta_{\alpha\beta} \qquad (11)$$

where $\dot{\gamma}_\beta$ is the shear strain in slip system β alone, h is the hardening modulus evaluated using the function in equation (5) and q is the latent hardening ratio. The material properties and parameters used in the sub-section (i) were used here as well (τ_o=60.84 MPa, τ_s=1.8τ_o, h_0=8.9τ_o). Figure 7 shows the flow stress on primary system as a function of time obtained by finite element simulation. When the conjugate slip system is activated there is an increase of hardening indicating the onset of stage II. The activation of conjugate system can be seen in figure 8, which shows resolved shear strain on all the systems. Load vs. elongation plot (figure 9) also shows increase in hardening upon activation of conjugate system.

(see attached)

Figure 7. Flow stress vs time for the modified two parameter hardening model

Figure 8. Resolved shear strain vs time for modified two-parameter hardening model

Figure 9. Load vs elongation for modified two parameter hardening model

(iii) Bassani's hardening model

The hardening model used by Bassani and Wu (1991) was described briefly in section II, equations (7)-(10). This hardening model was added to our implementation of the constitutive equation, which has a rate dependent formulation. In their study, Bassani (1994) simulated the results within a rate independent framework. For comparison we have simulated uniaxial tension with the initial orientation in a single slip direction [632], using the same values for hardening parameters as Bassani and Wu (1991): (τ_I=1.3τ_o, h_s=1.5τ_o, ho=90 τ_o, γ_o=0.001, q=0). In our simulations we set the rate sensitivity parameter m=0.01. Note that a latent hardening ratio q = 0 was used, implying that secondary slip systems do not harden before they become active. However, this model accounts for latent hardening indirectly through the G(γ) term in the expression for hardening modulus, eqn (7), so that even though secondary slip systems do not harden before they become active, when they do become active there is very high rate of hardening. The rate depends on the amount of slip that has occurred in other slip systems. The lower flow stress in secondary slip systems than in primary slip system facilitates activation of secondary slip systems.

(see attached)

Figure 10. Flow stress vs time for Bassani's hardening model

Figure 11. Resolved shear strain vs time for Bassani's hardening model

Figure 12. Load vs elongation for Bassani's hardening model

The results of our simulation are shown in figures 10, 11 and 12. While the results are qualitatively similar to that of Bassani and co-workers, there were some notable differences due to the rate dependent framework used here. Most notably, the span of stage I is relatively small. Stage II starts after relatively small overall strain as can be seen in figures 10 and 12

12

which show the flow stress and load respectively plotted against the simulation time. The reason for this is that secondary slip systems activate early due to rate sensitivity effect. The rate dependent constitutive law, eqn (1), used in our implementation allows small amounts for strain in secondary slip system even when the resolved shear-stress is slightly below the flow stress. The larger the value of the rate sensitivity parameter (m), the earlier the secondary slip systems activate.

Very fine secondary slip that has indeed been observed (e.g. Kulhmann-Wilsdorf, 1989) in single crystals can only be explained by accounting for rate sensitivity. The results of our simulations indicate that material rate sensitivity does have an important role when Bassani's model is used since even small amounts of secondary slip can lead to significant increase in hardening rate or the onset of stage II. Notice that when secondary slip systems really become active and the rate of strain in these systems becomes large enough to be seen in the shear strain plot (figure 11), there is significant drop in the rate of hardening (figure 10 & 12) that resembles stage III observed experimentally. This is because the high rate of hardening caused by the $F(\gamma)$ term in equation (7) lasts only for very small strains. The contribution due to this term dies out quickly when significant strain occurs in the secondary slip systems.

(iv) Multi-parameter hardening models

In a rate dependent implementation, all twelve slip systems of an fcc crystal can be included in the model. However, when the loading axis is within the stereographic triangle marked B4 in figure 1, the primary slip system is B4, the conjugate slip system is C1 and the two secondary slip systems that could possibly become active are A3 and B5. To reduce computation, only these four slip systems were included in our model. According to equation (2), the increment of flow stress for each slip system is coupled with activation of other slip

13

systems as follows.

$$\begin{Bmatrix} d\tau_c^{(B4)} \\ d\tau_c^{(C1)} \\ d\tau_c^{(A3)} \\ d\tau_c^{(B5)} \end{Bmatrix} = \begin{bmatrix} h(\gamma_{B4}) & q_{B4C1}h(\gamma_{C1}) & q_{B4A3}h(\gamma_{A3}) & q_{B4B5}h(\gamma_{B5}) \\ q_{C1B4}h(\gamma_{B4}) & h(\gamma_{C1}) & q_{C1A3}h(\gamma_{A3}) & q_{C1B5}h(\gamma_{B5}) \\ q_{A3B4}h(\gamma_{B4}) & q_{A3C1}h(\gamma_{C1}) & h(\gamma_{A3}) & q_{A3B5}h(\gamma_{B5}) \\ q_{B5B4}h(\gamma_{B4}) & q_{B5C1}h(\gamma_{C1}) & q_{B5A3}h(\gamma_{A3}) & h(\gamma_{B5}) \end{bmatrix} \begin{Bmatrix} d\gamma_{B4} \\ d\gamma_{C1} \\ d\gamma_{A3} \\ d\gamma_{B5} \end{Bmatrix} \quad (12)$$

In general, each slip system could have a different latent hardening ratio with respect to every other slip system. In equation (12), q_{B4C1} denotes the latent hardening of system B4 due to activation of slip system C1 etc. If we assume symmetry, that is $q_{ij} = q_{ji}$ then there are six ratios that determine the hardening behavior. If we use Weng's formula (equation 16) we can express these six ratios in terms of the three constants $\alpha 1$, $\alpha 2$ and $\alpha 3$, whereupon it can be seen that $q_{B4C1} = q_{C1A3} = q_{C1B5} = q_{A3B5}$.

Similar conclusion can be arrived at from dislocation analysis as well. We know that for FCC single crystals (Franciosi, 1982) the dislocation junction between B4 and C1 as well as that between A3 and B5 is a sessile junction. Similarly, C1 slip system has a glissile junction with both A3 and B5. Both these intersections lead to strong dislocation interactions. On the other hand, the dislocation junction between B4 and A3 as well as B5 results from a weaker dislocation interaction.

It is possible to experimentally determine either the six latent hardening ratios or the three constants in Weng's model. However, for purposes of qualitatively comparing this model with previous models, it is not necessary to determine exact values for these constants because it is possible to determine the limits on their value that will lead to desired behavior. The experimentally observed stage III deformation of single crystals implies that, at large strains, there is very little hardening. This requires that secondary slip systems should not

14

activate significantly even at large strains. We can determine the condition for non-activation of secondary slip systems then use it to select values for the constants to ensure desired behavior.

The condition for activation of secondary slip systems is that the ratio of resolved shear stresses on the currently active slip system and the secondary slip system should become equal to the ratio of their respective flow stresses. During the deformation the loading axis rotates towards the symmetric stable orientation [211]. The ratio of resolved shear stress in the primary slip system to that in secondary slip system when loading is along this stable axis [211] can be easily computed as

$$\left|\frac{\tau^{(p)}}{\tau^{(s)}}\right| = \frac{m_p}{m_s} = \frac{1/\sqrt{6}}{2/(3\sqrt{6})} = K = 1.5 \tag{13}$$

In the above equation m_p and m_s are the Schmid factors for the primary (B4) and secondary (B5 or A3) slip systems when the load is along [211]. Ratio of flow stresses in the primary and secondary slip systems depend on the hardening of these systems. Equation (12) can be integrated to determine the flow stress in each system as follows:

$$\tau_c^{B4} = \tau_0 + H(\gamma_{B4}) + q_{B4C1}H(\gamma_{C1}) \tag{14}$$

$$\tau_c^{C1} = \tau_0 + q_{C1B4}H(\gamma_{B4}) + H(\gamma_{C1}) \tag{15}$$

$$\tau_c^{A3} = \tau_0 + q_{A3B4}H(\gamma_{B4}) + q_{A3C1}H(\gamma_{C1}) \tag{16}$$

$$\tau_c^{B5} = \tau_0 + q_{B5B4}H(\gamma_{B4}) + q_{B5C1}H(\gamma_{C1}) \tag{17}$$

$$H(\gamma_i) = \int_0^{\gamma_i} h(\gamma_i)d\gamma_i = (\tau_s - \tau_0)\tanh\left(\frac{h_0\gamma_i}{\tau_s - \tau_0}\right) = (\tau_s - \tau_0)T(\gamma_i) \text{ and}$$

$$T(\gamma_i) = \tanh\left(\frac{h_0 \gamma_i}{\tau_s - \tau_0}\right)$$

In the above equations we have assumed that no slip has occurred in secondary slip systems (i.e., $\gamma_{A3} = \gamma_{B5} = 0$). All slip systems are assumed to have the same initial flow stress τ_0. The condition for *activation* of secondary systems A3 and B5 can now be stated as $\frac{\tau_c^{B4}}{\tau_c^{A3}} \geq K$ and $\frac{\tau_c^{B4}}{\tau_c^{B5}} \geq K$. Therefore, using equations (14) and (16), the condition for *non-activation* of secondary slip system A3 can be written as:

$$(K-1)\tau_0 + (Kq_{A3B4} - 1)(\tau_s - \tau_0)T(\gamma_{B4}) + (Kq_{A3C1} - q_{B4C1})(\tau_s - \tau_0)T(\gamma_{C1}) > 0 \quad (18)$$

$$\text{or, } q_{B4A3} = q_{A3B4} > \frac{1}{K}\left[1 - \frac{(K-1)}{T(\gamma_{B4})}\left(\frac{\tau_0}{\tau_s - \tau_0}\right) - (Kq_{A3C1} - q_{B4C1})\frac{T(\gamma_{C1})}{T(\gamma_{B4})}\right] = q_{min} \quad (19)$$

The lower bound for q_{A3B4} that would ensure non-activation can be found by considering the maximum value that q_{min} can attain. If $(Kq_{A3C1} > q_{B4C1})$, then this maximum value occurs when $T(\gamma_{B4})$ is maximum ($=1$) and $T(\gamma_{C1})$ is minimum ($=0$). Therefore, the condition for non-activation can be stated as:

$$q_{B4A3} = q_{A3B4} > \frac{1}{K}\left[1 - (K-1)\left(\frac{\tau_0}{\tau_s - \tau_0}\right)\right] \quad (20)$$

Similarly, if $(Kq_{B5C1} > q_{B4C1})$, then the condition for non-activation of B5 can be written as:

$$q_{B4B5} = q_{B5B4} > \frac{1}{K}\left[1 - (K-1)\left(\frac{\tau_0}{\tau_s - \tau_0}\right)\right] \quad (21)$$

From equation (20) and (21), assuming q_{A3B5} and q_{B4C1} to be 1.1, q_{A3C1} and q_{B5C1} to be 1.0 and $\tau_s = 1.8\tau_0$ we can compute lower bounds for q_{B4A3} and q_{B4B5} that will ensure non-

activation of secondary systems.

$$q_{A3B4} = q_{B4A3} = q_{B4B5} = q_{B5B4} > 0.25 \qquad\qquad (22)$$

Simulation was performed the following latent hardening ratios: $q_{B4A3} = q_{B4B5} = 0.5$, $q_{B4C1} = q_{A3B5} = 1.1$, $q_{C1A3} = q_{C1B5} = 1.0$. Stages I, II and III are observed during the simulation using this model as shown in figures 13, 14 and 15. An increase in hardening rate or stage II is observed when the conjugate slip system becomes active (figure 14). Stage III is observed due to the decrease of hardening rate at large strain.

(see attached)

Figure 13. Flow stress vs time for the multi-parameter model

Figure 14. Resolved shear strain vs time for the multi-parameter hardening model

Figure 15. Load vs elongation for the multi-parameter hardening model

IV. DISCUSSION AND CONCLUSION

Constitutive equations for single crystal deformation were implemented into a three-dimensional finite element program to enable simulation of the actual three-dimensional deformation of the crystal due to multiple slip. Using this model we were able to simulate the deformation of FCC crystals along unsymmetrical single slip orientations and predict the resultant crystal rotation and the associated change in resolved shear stress in the various slip systems. Such three-dimensional models were used to perform a comparative study of the various single crystal hardening models that have been proposed.

The two-parameter hardening model was found to be incapable of predicting all the stages of deformation observed in FCC crystals. However, a simple modification of the model where different hardening moduli were used for each slip system, is capable of

17

predicting an increased hardening rate associated with the activation of secondary slip systems. Bassani's hardening model predicted all the three stages of hardening during our simulation. However, due to the rate dependent formulation used here, the conjugate and secondary slip systems activated earlier than in the rate independent formulation (Bassani, 1994). Multi-parameter laws also predicted the three stages of deformation. In this model, the differences in dislocation interaction between various slip systems can be accounted for by assigning appropriate values for latent hardening ratios.

Many fundamental differences were observed between Bassani's model and the multi-parameter models used here. In Bassani's model, the conjugate and secondary slip systems do not harden as long as they do not become active (when q = 0). This implies that these systems will often activate at least by a very small amount even when the resolved shear stress on them is much smaller than that in active systems. If a rate dependent model is used these slip systems activate earlier. The hardening observed during stage II occurs due to very small strains in the conjugate system. Indeed by the time significant strain occurs in the conjugate system the rate of hardening drops substantially. As opposed to this in the modified two-parameter law and multi-parameter laws, stage II is associated with significant activation of the conjugate slip system. Due to the non-zero latent hardening ratios used in these laws, the conjugate systems and secondary slip systems harden even when they are not active. Therefore, they will activate only if there is significant lattice rotation and the associated increase in resolved shear stress in these systems. However, if rate dependent formulation is used very small amounts of slip can occur in these systems even before the resolved shear stress reaches the critical value.

While no attempt has been made here to quantitatively match the results of the

18

simulations with experimental results, it has been shown that except for the two-parameter law all the other models are capable of qualitatively predicting the three stages of deformation. For multi-parameter models, condition for activation of the secondary slip systems were derived that can be used to determine the range of values of the latent hardening ratios that lead to activation or non-activation of secondary slip systems.

ACKNOWLEDGMENT

REFERENCES

[1]   ABAQUS, Users Guides and Theory manual, version 5.5, Hibbitt, Karlsson & Sorensen, Inc., 1995.

[2]   Asaro R. J. (1983) Micromechanics of crystals and polycrystals, *Adv. Appl. Mech.,* **23**, 1.

[3]   Basinski S. J. and Basinski, Z. S. (1979) Plastic deformation and work hardening. In *Dislocations in Solids,* ed. Nabarro, F. R., pp. 262, North Holland, Amsterdam.

[4]   Bassani, J. L. and Wu, T. (1991) Latent hardening in single crystals II. Analytical characterization and predictions, *Proc. R. Soc. London,* A435, 21-41.

[5]   Bassani J.L. (1994) Plastic Flow of Crystals, In *Advances in Applied Mechanics,* **30**, 192-258.

[6]   Franciosi, P. (1985) Concepts of latent hardening and strain hardening in metallic single

crystals," *Acta Metall.*, **33**, 9, 1601-1612.

[7] Franciosi, P., Berveiller, M. and Zaoui, A. (1980) Latent hardening in copper and aluminum single crystals, *Acta Metall.*, **28**, 273-283,

[8] Franciosi, P. and Zaoui, A., (1982a) Multislip in FCC crystals: A theoretical approach compared with experimental data, *Acta Metall.*, **30**, 1627-1637.

[9] Franciosi, P.and Zaoui, A., (1982b) Multislip tests on copper crystals: A junctions hardening effect, *Acta Metall.*, **30**, 2141-2151,

[10] Hutchinson, J. W. (1970) Elastic-plastic behavior of polycrystalline metals and composites, *Proc. R. Soc., London*, **A319**, 247-272,

[11] Jackson, P. J. and Basinski, Z. S. (1967) Latent hardening and the flow stress in copper single crystals, *Can. J. Phys.*, **45**, 707-735,

[12] Kocks, U. F., (1964) Latent hardening and secondary slip in aluminum and silver, *Trans. Metall. Soc.* AIME, **230**, 1160.

[13] Kocks, U. F. and Brown, T. J. (1966) Latent Hardening in Aluminum, *Acta Metall.*, **14**, 87-98.

[14] Nakada Y.and Keh, A. S. (1966) Latent hardening in iron single crystals, *Acta Metall.*, **14**, 961-973.

[15] Peirce D., Asaro R. J. and Needleman A. (1982), An analysis of non-uniform and localized deformation in ductile single crystals, *Acta Metall.* **30**, 1087-1119.

[16] Peirce, D., Asaro, R.J. and Needleman, A. (1983) Material rate dependence and localized deformation in crystalline solids, *Acta Metall.* **31**, 1951-1976.

[17] Weng, G.J. (1987) Anisotropic hardening in single crystals and the plasticity of polycrystals, *Int. J. Plasticity*, **3**, 315-339.

[18] Wenner M. L. (1993) A Generalized Forward Gradient Procedure for Rate Sensitive Constitutive Equations, *Int. J. for Num. Meth. in Engineering*, **36**, 985-995.

[19] Wu, T., Bassani, J. L. and Laird, C. (1991) Latent hardening in single crystals I. Theory and experiments, *Proc. R. Soc. London*, **A435**, 1-19.

Table 1. Notation for slip systems of FCC crystals

Notation	Slip system	Notation	Slip system
A2	$(111)[1\bar{1}0]$	C1	$(1\bar{1}1)[110]$
A3	$(111)[10\bar{1}]$	C3	$(1\bar{1}1)[10\bar{1}]$
A6	$(111)[0\bar{1}1]$	C5	$(1\bar{1}1)[110]$
B2	$(11\bar{1})[1\bar{1}0]$	D1	$(1\bar{1}\bar{1})[110]$
B4	$(11\bar{1})[101]$	D4	$(1\bar{1}\bar{1})[101]$
B5	$(11\bar{1})[011]$	D6	$(1\bar{1}\bar{1})[01\bar{1}]$
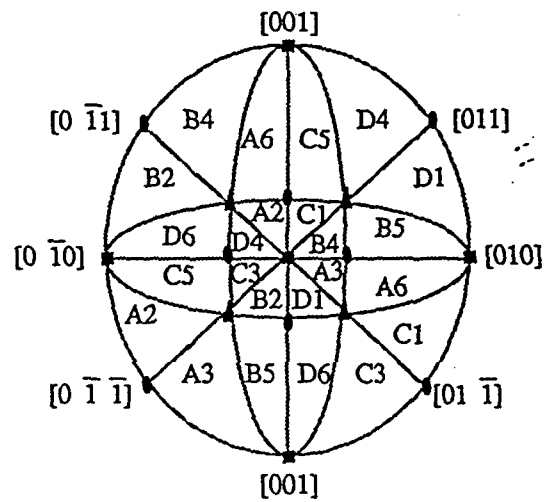
Figure 1 Standard stereographic projection from [100] orientation of FCC crystals
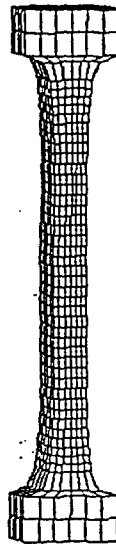
Figure 2. Specimen used in the simulation
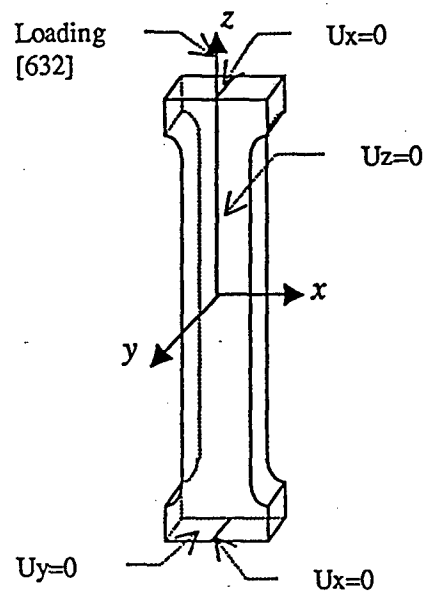
Figure 3: Loading direction and boundary conditions used in simulation
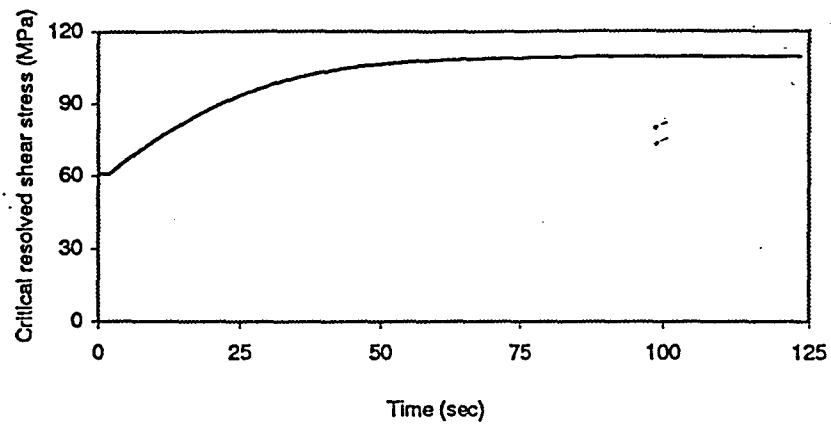
Figure 4. Flow stress versus time for the two parameter hardening model.
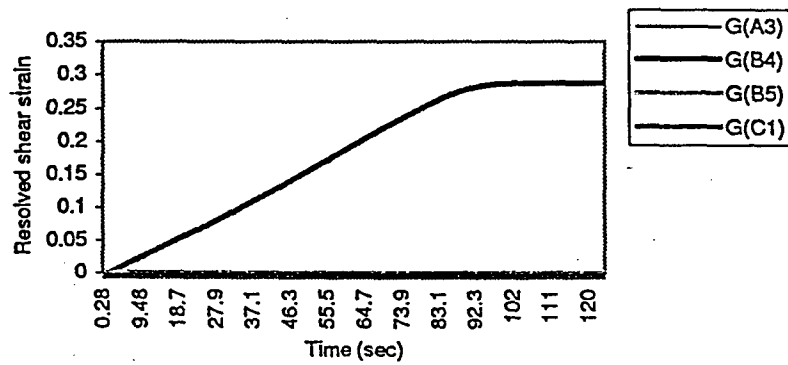
Figure 5. Resolved shear strain vs time for the two-parameter hardening model
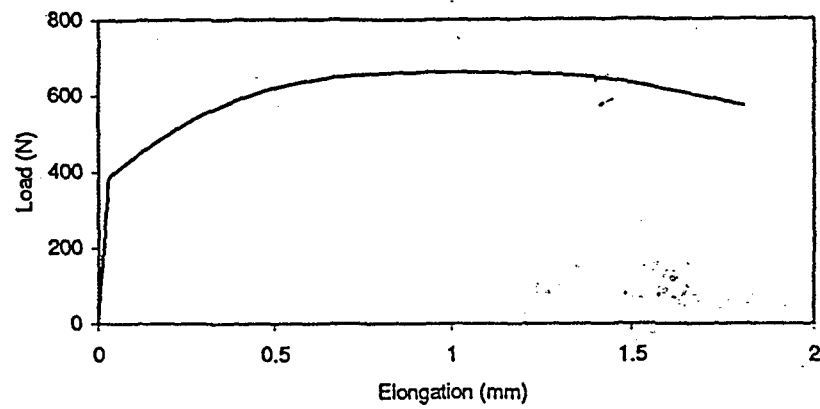
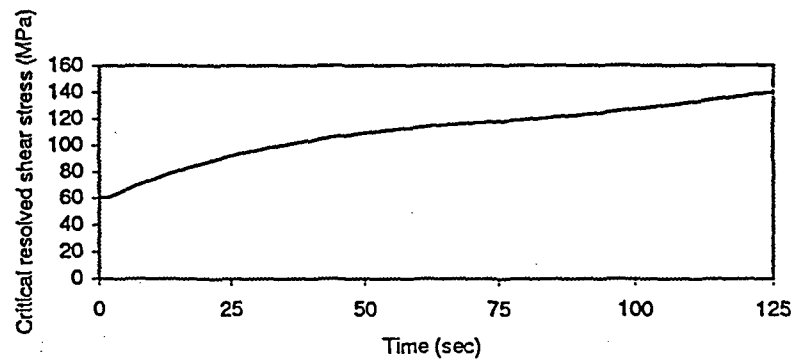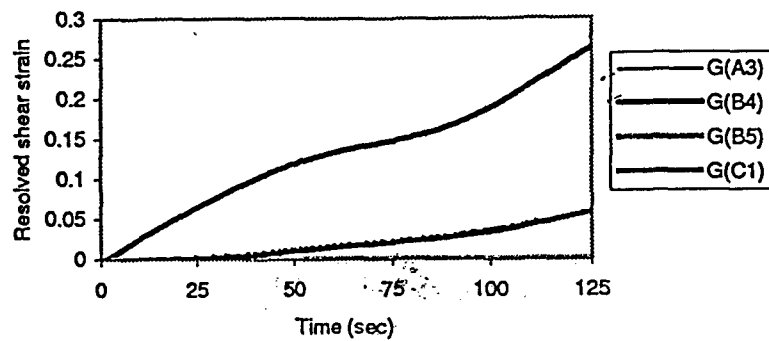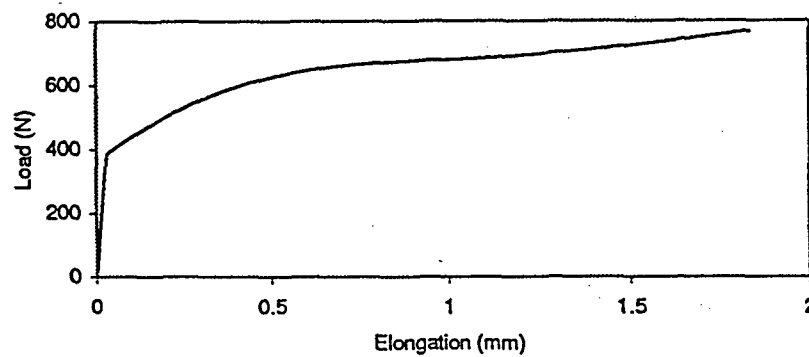Figure 6. Load vs elongation for the two parameter hardening model

Figure 7. Flow stress vs time for the modified two parameter hardening model

Figure 8. Resolved shear strain vs time for modified two-parameter hardening model

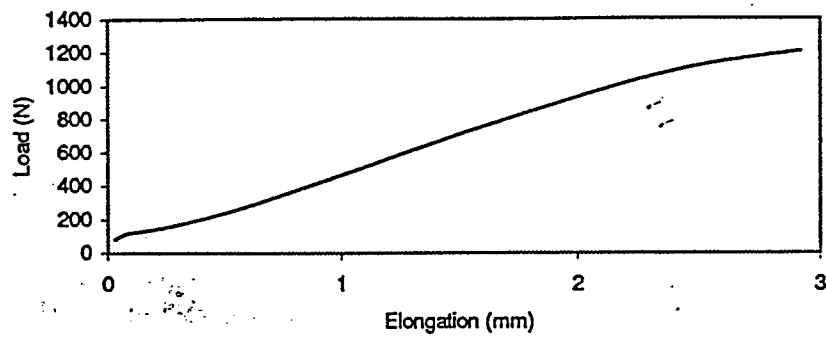Figure 9. Load vs elongation for modified two parameter hardening model

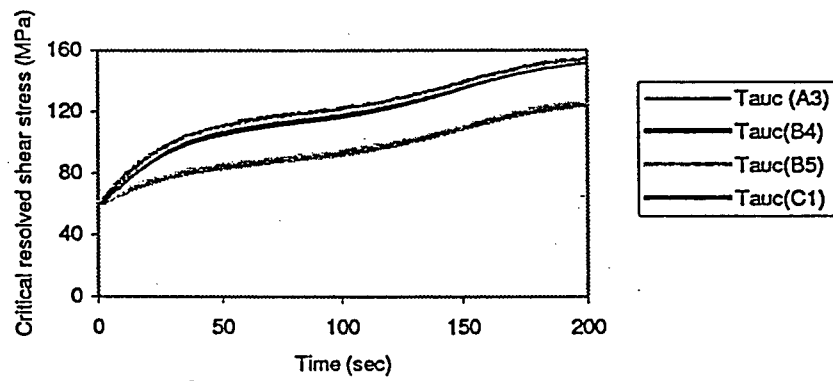Figure 12. Load vs elongation for Bassani's hardening model

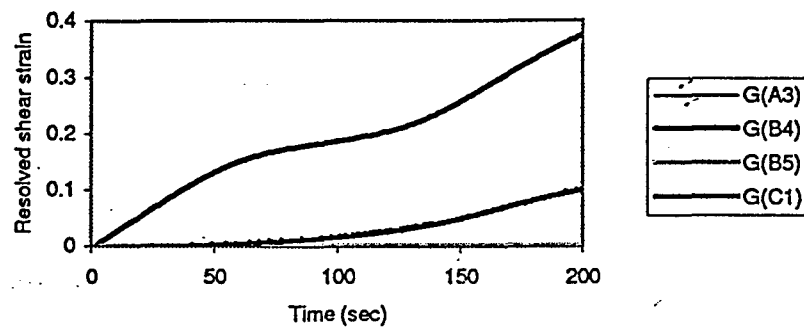Figure 13. Flow stress vs. time for the multi-parameter model

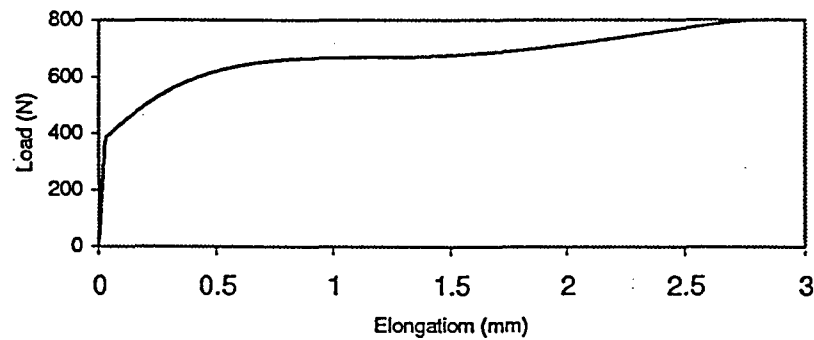Figure 14. Resolved shear strain vs time for the multi-parameter hardening model

Figure 15. Load vs elongation for the multi-parameter hardening model

EFFECTS OF PURITY ON THE PROPERTIES OF β-NiAl SINGLE CRYSTALS

J. Hu[ᴴ], V.I. Levit* and M.J. Kaufman[ᴴ]

[ᴴ]Dept. of Materials Science and Engineering, University of Florida, Gainesville, FL 32611
*AS&M, Inc., MS 188A, NASA Langley Research Center, Hampton, VA 23681

Abstract

The influence of purity on the mechanical properties of β-NiAl single crystals is explored. For this purpose, high purity (HP) single crystals of β-NiAl were grown using a Bridgman technique in high purity alumina crucibles and with high purity nickel (99.98%) and aluminum (99.999%) feedstock. Further purification was attempted using the containerless zone melting apparatus at the University of Tennessee and the results indicated that the Bridgman-grown crystals were of comparable purity before and after zone refining. These crystals contained essentially no metallic impurities and much lower silicon and carbon levels than the "conventional-purity (CP)" crystals used in most recent studies of single crystal NiAl. The mechanical property studies revealed that NiAl behaves similarly to other high purity metals, i.e., the higher the purity, the lower the critical resolved shear stress (CRSS) and the higher the tensile elongations that can be achieved. The effects of heat treatment, deviation from stoichiometry, purity, and test temperature on the tensile properties of NiAl are summarized and the implications of these results on the potential use of this class of materials is discussed.

Introduction

Since the early 60's, the compound β-NiAl has been studied intermittently as a possible structural material for elevated temperature applications (1-10). The obvious drivers include its high melting point, wide solubility range and excellent oxidation resistance especially when doped with elements such as Zr (1). Recent studies have led to an enhanced understanding of the properties of this simple compound and to the realization that it may not be possible to achieve a balance of both high temperature strength and low temperature toughness (3) as it is an intrinsically soft and brittle compound. Even so, it is a simple compound that offers a rather unique opportunity to examine the effects of such things as impurities, thermal vacancies, constitutional defects, intentional alloying additions, prestrain, etc. on both physical and mechanical properties now that its high purity properties have been clarified (4). The influence of purity on the properties of intermetallic compounds tends to be considerably more complex than in, for example, BCC metals; while both are sensitive to tramp impurities (e.g., carbon) and intentional solute additions, the intermetallics are also sensitive to such things as deviations from stoichiometry, which leads to constitutional defects (anti-site atoms and constitutional vacancies), and thermal vacancies. Both of the latter effects are significant in NiAl and should be accounted for in any investigation of impurity effects. The purpose of this paper is to elucidate some of the effects of impurities on the mechanical properties of β-NiAl.

Experimental

The methods of single crystal production, heat treatment and tensile specimen preparation and testing have been described in previous paper (7). For the sake of comparison with other published data, the critical resolved shear stress data (CRSS) was determined from load-displacement diagram by taking the 0.2% offset yield stress times the Schmid factor for the initial orientation. This value may be as much as 25% higher than the actual stress required to initiate the first dislocation sources; the importance of this will become apparent below. The compositions of the single crystals used in this study are given in Table I. In addition to the mechanical tests, selected samples were examined by transmission electron microscopy (TEM) in order to correlate the tensile properties with the dislocation substructures that develop under the various combinations of orientation, temperature, strain and strain rate. For this purpose, the TEM samples were cut from the gage sections with very specific orientations (e.g., parallel or orthogonal to the slip plane) and examined in the TEM using traditional diffraction contrast analysis. The results of these latter efforts will be emphasized in the following.

Table I Chemical composition of the NiAl single crystals examined in the current study. Crystal HP-1 is grown at UF and then processed at the University of Tennessee by Prof. B. Oliver.

Specimen I.D.	Orientation	Ni at.%	Al at. %	Si ppm	C ppm	O ppm	N ppm
UF-NiAl	[110]	50.2	49.7	460	80	-	-
UF-NiAl	[100]	49.7	50.2	260	14	-	-
NiAl-0.3Si	[100],[110]	50.1	49.6	2500	150	88	15
36 T	[111]	50.2	49.7	300	54	78	<15
36 M	[111]	50.0	49.9	300	42	76	<15
36 B	[111]	49.4	50.5	320	86	66	<10
HP-1	[112]	49.6	50.3	320	50	39	<10
UF-NiAl	[123]	49.6	50.3	160	42	n/a	n/a

Results and Discussion

The results and discussion are divided into sections covering the various issues associated with purity effects in NiAl. In the first section, the mechanical properties of NiAl of varying purities and thermal histories are compared. This is followed by a section that compares the dislocation substructures as a function of orientation and purity. Finally, some general discussion concerning the implications of the present results is provided.

Tensile Properties

Soft Orientations The critical resolved shear stress (CRSS), work hardening rate, and tensile elongation of a series of "soft" single crystal specimens tested at room temperature were reported previously (4). As pointed out in that paper (see Table II):

- over 20% tensile elongation can be achieved at RT;
- tensile elongation is dependent on orientation and specimen geometry;
- no obvious difference in CRSS exists between the <001>{110} and <001>{010} slip systems for samples cut from the same crystal (the differences are no more than 5% which is well within the scatter);
- the work hardening rate (WHR) is very low for the single slip (i.e., other than <hk0>) orientations.

Some of these characteristics are apparent in Fig. 1 which compares the shear stress-strain behavior of <111> (single slip) and <110> (double slip) specimens taken from the same high purity NiAl (UF), lower purity NiAl (from Ref. 5) and NiAl-0.3Si (UF). As can be seen, the CRSS, WHR and elongation are all a strong function of purity and orientation.

As seen in Fig. 1, the CRSS in the UF-NiAl is approximately the same for both the single and double slip orientations and is about half that of the CP-NiAl. Furthermore, the attempts at further purification of the UF material by zone melting in Prof. Oliver's facility at the University of Tennessee (10) resulted in similar purity, CRSS and WHR as those in the UF crystal (see HP-1 in Tables I and II); this indicates that the quality of the materials produced in the UF facility are approximately equivalent to the purest NiAl produced to date.

Besides the low CRSS of the UF-NiAl, the Stage 1 WHR for the [111] single slip orientation is less than 100 MPa for the high purity UF-NiAl and is considerably higher for the CP crystal (Fig. 1 and Table II). This is a similar fraction of the shear modulus to that typical of the easy glide stage for pure FCC and HCP metals. The low WHR suggests that the there is little interaction between the dislocations.

Table II Selected mechanical property data for the various UF and one HP NiAl crystals. The subscripts p and .2 represent proportional and 0.2% offset strain values; $d\tau/d\gamma$ and σ_f represent work hardening rate and fracture stress, respectively. Crystal HP-1 is the crystal processed at the University of Tennessee by Prof. B. Oliver.

Spec. ID	Orient.	Schmid Factor	σ_p MPa	τ_p MPa	σ_2 MPa	τ_2 MPa	$d\tau/d\gamma$ MPa	σ_f MPa	El. %
UF-NiAl	[100]	.50	1040	520	-	-	-	1040	0
UF-NiAl	[100]	.50	1120	560	-	-	-	1167	<0.2
UF-NiAl	[111]	.48	122	59	140	68	-	244	15
UF-NiAl	[111]	.48	134	65	156	76	-	213	6
UF-NiAl	[111]	.48	106	51	130	63	-	187	4
UF-NiAl	[779]	.49	108	53	133	65	89	240	20
UF-NiAl	[110]	.50	104	52	117	58	563	237	6
HP-1	[112]	.45	138	62	148	67	153	235	6
UF-NiAl	[123]	.45	82	37	98	44	46	145	24
UF-NiAl	[135]	.41	96	39	115	47	91	266	15

The easy glide stage observed for the UF-NiAl along the [111] axis is considerably longer than any observed for FCC and BCC metals where the latter tend to deform only a few percent before activating a secondary slip system due to the large number of equivalent slip systems. Consequently, the reason for the long easy glide region must be related to the fact that there are only three slip vectors and that the nature of the rotation during single slip as well as latent hardening hinder the activation of secondary slip vectors until relatively large strains are attained. Furthermore, this provides an opportunity for local cross slip as will be discussed below.
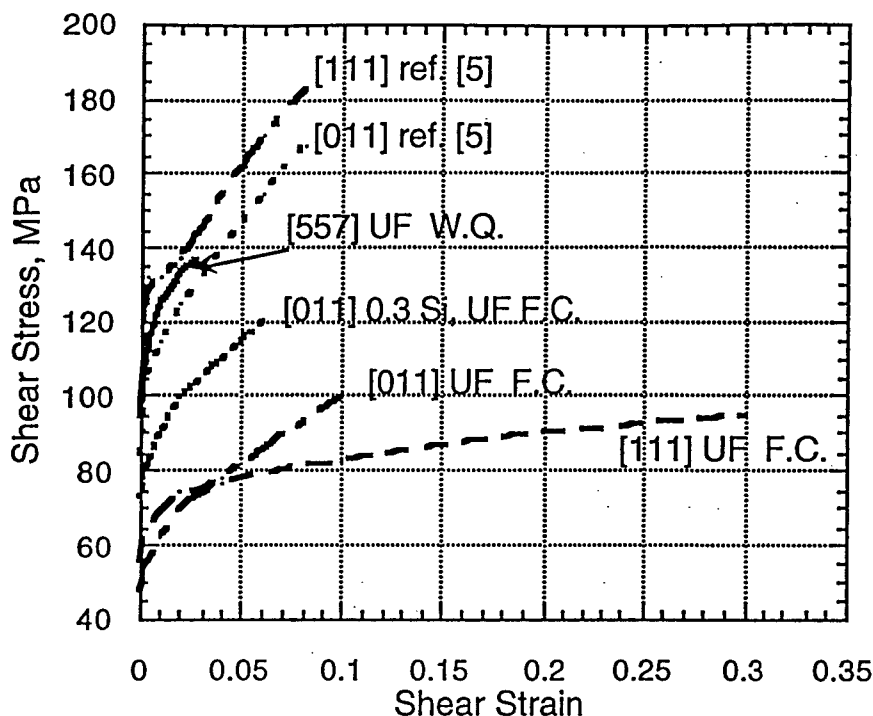
Figure 1: Typical room temperature tensile curves illustrating the differences in properties for the different purity materials. The curves from the "commercial purity material" were estimated from the data published in (5). WQ=water quenched and FC=furnace cooled, both from 1273K.

It is also clear from Fig. 1 that the [011] UF-NiAl crystal exhibits a considerably higher WHR than the single slip orientation (Fig. 1 and Table II). This is expected based on the fact that there are two different slip systems operating from the beginning of the deformation process. As will be shown below, there appears to be considerable entanglement of the two dislocation types as well as considerably greater dislocation debris consistent with the higher WHR.

It can also be seen in Fig. 1 that the WHRs for the WQ, CP and Si-doped NiAl specimens oriented for single slip are all considerably higher than that of the HP crystals. A similar effect is observed when the composition deviates from stoichiometry (Fig. 2). Specifically, the low-impurity, off-stoichiometric UF-Ni48.5Al crystal has similar yield stress vs. temperature behavior as the conventional purity crystals when tested along the hard orientation. Furthermore, soft-oriented [123] crystals of CP Ni-52Al have higher strengths than stoichiometric crystals of the same purity (Fig.3a in Ref.1).

In fact, it is difficult to see a difference in the WHR for the single and double slip orientations of the CP material. In addition, both the CRSS and the WHR for the WQ UF-NiAl are dramatically different from the FC material in the single slip orientation. These results strongly suggest that it is dislocation-impurity or dislocation-point defect interactions rather than dislocation-dislocation interactions which dominate the early stages of deformation in "impure" NiAl.

Temperature Effects on Yield Stress

The temperature dependence of the yield stress for high purity NiAl tested in tension along soft [123], semi-soft [110] and hard ([001]) orientations is shown in Fig. 2 along with some literature data for comparison. For the soft and semi-soft orientations, it is clear that the intermediate temperature plateau is absent in the high purity material although it may be present in the silicon-doped material. Again, this is consistent with the role of interstitials causing DSA in the CP-NiAl.

For the <001>-oriented samples, besides the expected lower yield stress corresponding to the higher purity, the most striking feature is the absence of the plateau at intermediate temperatures. Significantly, this plateau had been correlated with a change in the slip vector from <111> to <110> with increasing temperature (1, 2). Doping with 0.3 at% Si appears to increase the yield stress at temperatures below 773 K and to produce a more abrupt drop between 573 and 773 K although the drop is not as great as in the CP-NiAl. Similarly, deviations from the stoichiometric composition result in a similar effect as observed by comparing the behavior of the UF-Ni50Al with the UF-Ni48.5Al alloys (Fig. 2c).

While it is tempting to speculate that kinking might have been responsible for the observed low yield stresses in the UF-NiAl crystals, such behavior was not observed and, therefore, this is valid yield stress data. This is based on the fact that kinking was observed in some of our other tensile tests on stoichiometric, high purity crystals yet only when the specimens were both misaligned and misoriented (5° from [001]); in these cases, kinking was observed at all temperatures in the range RT to 873K. It is noted that for a misorientation of 5° from <001> towards <111>, the Schmid factor for [001]($\bar{1}$10) slip is 0.087. For the measured CRSS of about 60 MPa at RT, the calculated yield (kinking) stress is around 700 MPa which is consistent with the experimental yield stress determined from the load-elongation curves for these crystals.

At temperatures above 773K, the yield stresses for the HP, CP and Si-doped material all converge suggesting that dislocation climb and cross slip are sufficient to overcome (pass) any obstacles of compositional and dislocation nature. Below 473K, the tensile elongations of the [001]-oriented specimens are typically less than 0.5% and, in many cases, the specimens fractured before any measurable yielding. The specimens typically have ~2% tensile elongation at 473K and 523K, and undergo more than 20% elongation before fracture at and above 573K. Therefore, both the NiAl and NiAl-0.3Si single crystals tested in this work appear to undergo a rather sudden increase in tensile elongation between 523K and 573K. This sudden increase in ductility in [001] specimens coincides with the drop in yield stress, which is clearly more gradual than that reported previously (9, 11).

a
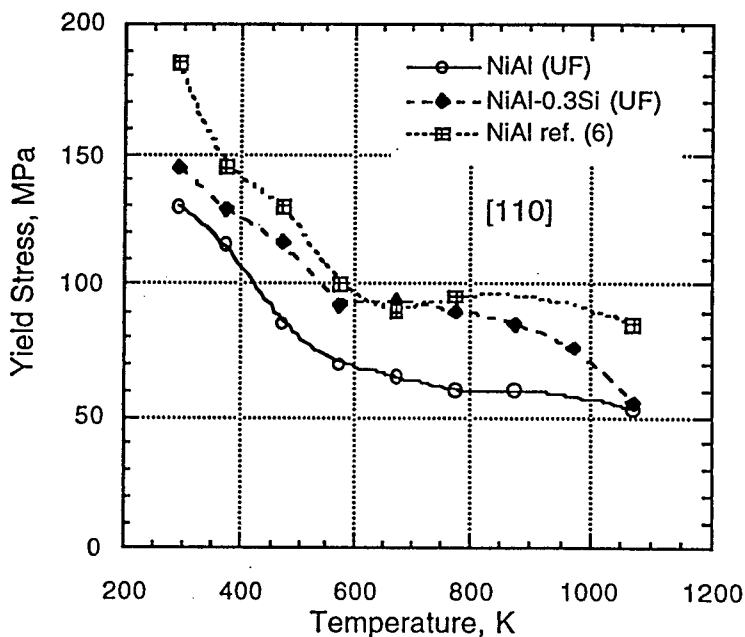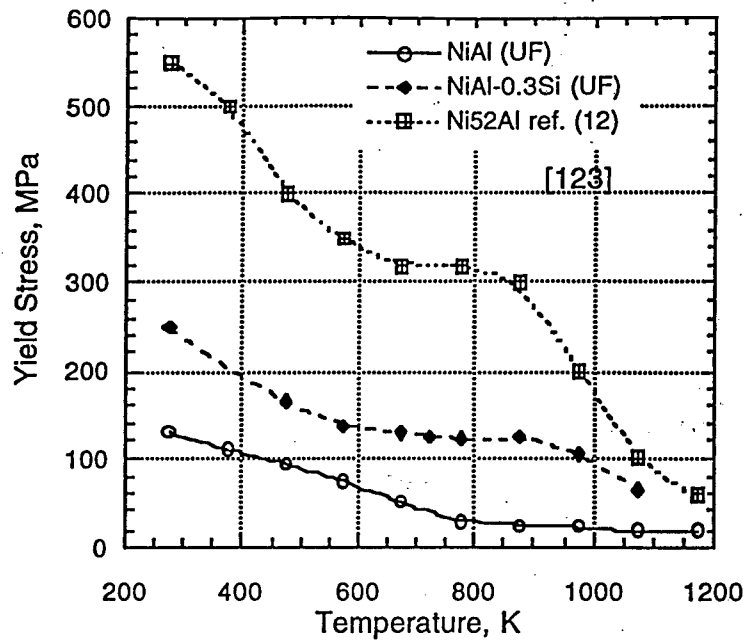
b
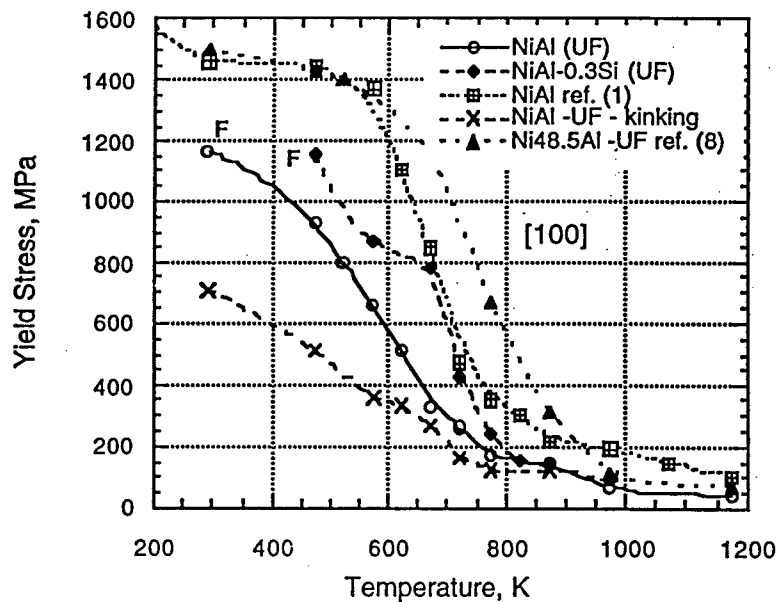
c

Figure 2: Yield stress vs. temperature plots for [110], [123] and [001] orientations. It should be noted that in figure (c), the data points labled F represent fracture stresses.

Dislocation Analysis

[$\bar{5}57$] Crystals The [$\bar{5}57$] orientation was selected for the initial investigation of the slip behavior in high purity NiAl single crystals due to its expected single slip ([001]($\bar{1}$10)) nature. While the dislocation density in the as-homogenized crystals was very low, after about 3% plastic strain, the

dislocation substructure in foils cut approximately parallel to the ($\bar{1}$10) slip plane was non-uniform and contained tangled dislocations in a patch-like arrangement (Fig. 3a). A standard **g.b** analysis indicated that essentially all of the dislocations had the expected [001] Burgers vector and that negligible secondary slip occurred consistent with the low WHR. A trace analysis indicated that the average line direction of the dislocations within these patches was approximately [110], the edge orientation. Furthermore, these patches seemed to be elongated along [110], consistent with [001]($\bar{1}$10) slip.

The dislocations outside of the bands in Fig. 3a tended to be bowed out and were found, using trace analysis, to have a mixed character. These dislocations were heavily pinned and formed edge dipoles sometimes leaving traces of pinched-off loops elongated along the edge direction (arrow points in Fig. 3a). Almost no screw or near-screw segments were observed except for some short segments. This implies that the screw components have considerably higher mobilities than the edge components and probably slip out of the crystal during deformation. Kim [12] also noted the absence of screw segments consistent with the results and calculations of Loretto and Wasilewski [13], who found that screw segments have high elastic energy making them elastically unstable.
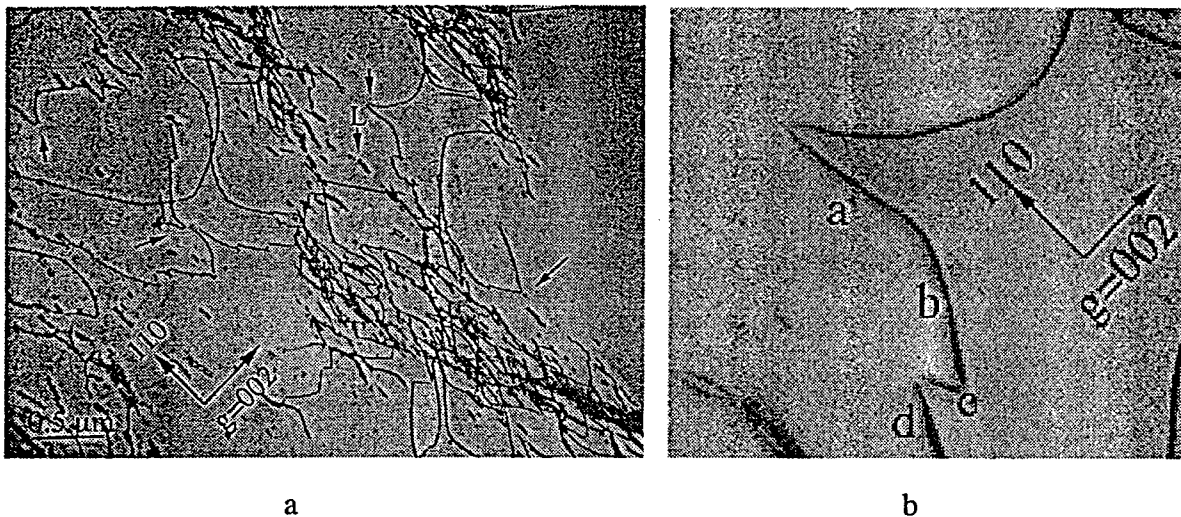

a   b

Figure 3: (a) BFTEMs of dislocations in a [$\bar{5}$57] specimen after 3% tensile strain at a strain rate of 10^{-4} s^{-1}. The foil was cut parallel to ($\bar{1}$10) slip plane and the dislocations are almost exclusively [001] type. (b) Higher magnification images of the dislocation dipoles in (a).

At higher magnification, it is clear that the dipole regions in Fig. 3a are associated with the formation of the [001] prismatic loops elongated along <110>. The higher magnification image in Fig. 3b indicates that cross-slip is indeed relatively easy in NiAl where segments **b** and **d** lie in the ($\bar{1}$10) slip plane approximately along [$\bar{1}$11] while both the **a** and **c** components have line directions that appear, based on trace analysis, to lie out of the primary slip plane. Further work is needed to resolve the exact sequence of events leading to these common geometries. Significant here is the fact that the high purity NiAl tends to cross slip during Stage 1 deformation; this must indicate that the short range stress fields imposed by other "like" dislocations is sufficient to promote cross slip.

The dislocation substructure in a specimen that was water quenched in order to trap thermal vacancies was considerably different from that of the FC material (Fig. 4). The specimen was taken from the gage length of a tensile specimen that fractured after about 2% elongation. As can be seen, the dislocation distribution is somewhat more uniform than in the FC specimen although there is still some localization as indicated by the dislocation tangling, debris and small loops in the patches. Even so, it is clear that the deformation was more uniform in the WQ specimens in spite of their lower ductility. The greater amount of debris outside of the patches indicates that cross slip occurred everywhere in the sample and that dislocation motion was more difficult in the WQ material consistent with the higher CRSS caused by the thermal vacancies.

The **g.b** analysis revealed that the majority of the dislocations in the WQ specimen had the expected [001] slip vector although there was a small, yet significantly higher fraction of secondary [100] and [010] dislocations as compared with the FC material. When the specimen was tilted to the [001] zone (Fig. 4b) so that the primary ($\bar{1}$10) slip plane was edge-on and the primary dislocations displayed only residual contrast (since **g.b**=0), the traces of the patches lying in the [110] direction were apparent as were a significant number of [001] dislocations lying

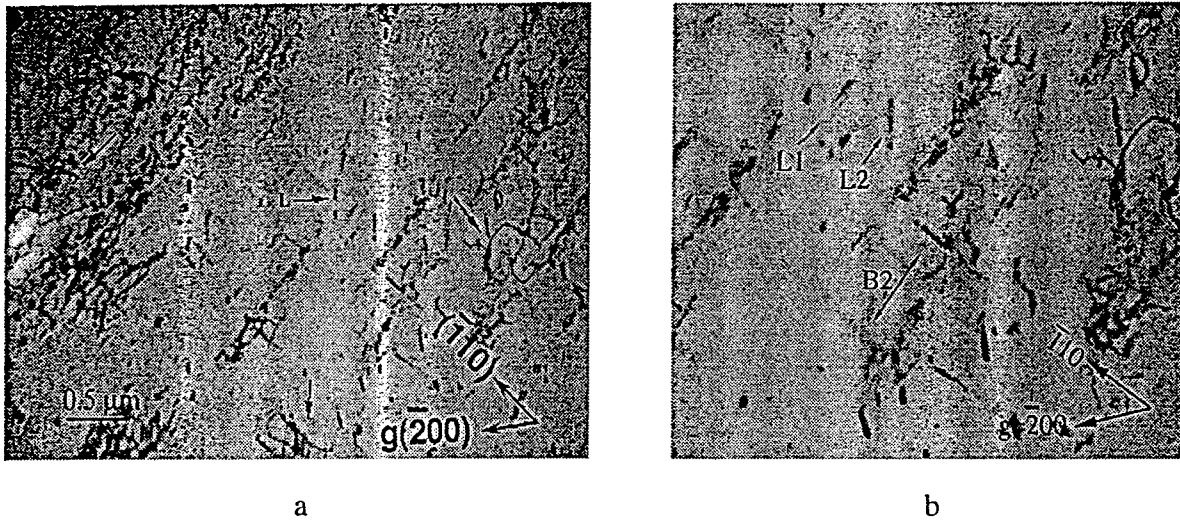a   b

Figure 4: BFTEMs showing dislocations in the WQ [$\bar{5}$57]-oriented NiAl single crystals taken with g=$\bar{2}$00 near B=[001]. (a) Low magnification image showing distribution of patches and debris and (b) higher magnification with loops, etc. indicated (see text).

approximately orthogonal to the ($\bar{1}$10) slip plane. In addition, traces of prismatic [001] loops along both the [110] and [010] directions were observed (L1 and L2, respectively). Since the double cross slip mechanism responsible for the [001] prismatic loops elongated along [110] can not be used to account for the loops elongated along [010], another mechanism must be operative. One possibility involves the operation of the [001](010) slip system which would be expected to leave trailing debris or prismatic loops elongated along <100>. On the other hand, the dislocations lying on (110) must be due to slip on this plane even though the resolved shear stress should be zero for the [$\bar{5}$57] tensile axis. While further work is needed to account for this latter observation, it is clear that the various features indicate that cross slip in NiAl is common. As will be discussed further in a separate paper, the present results indicate that the lower dislocation mobility in the WQ NiAl leads to earlier cross slip, less of a tendency for slip localization (patch development) and lower elongation to fracture. Furthermore, the higher WHR for the WQ specimens (estimated to be approximately 700 MPa) can account for the earlier activation of secondary slip systems as compared with the FC specimens where few secondary dislocations were observed.

While the results on the WQ specimens are not directly related to purity per se, the similarities between the substructures reported after a small amount of strain in the CP material suggest that the effects of thermal vacancies and impurities on dislocation mobility may be somewhat similar. It is noted, however, that caution must be exercised in making general statements since it is clear from earlier studies that interstitials such as carbon can lead to dynamic strain aging and such effects are quite different from those associated with substitutional atoms as well as thermal and constitutional vacancies. Clearly, further work is needed to clarify the similarities and differences between the effects of impurities and thermal vacancies on the deformation behavior of NiAl.

[011] Crystals The dislocation substructures in [011] oriented, FC UF-NiAl crystals deformed a few percent at RT resembled those in the specimens oriented for single slip, i.e., the dislocations formed patches rather than being homogeneously distributed throughout (Fig. 5). The Burger's vector analysis revealed that approximately equal amounts of both [001] and [010] slip vectors were present consistent with the double slip geometry. This is illustrated by imaging with g=110 so that the [010] dislocations are in strong contrast and the [001] dislocations exhibit strong

the lowest line energies correspond to the screw orientations, i.e., u parallel to <011> (15, 16). However, the theoretical calculations to date have not taken into consideration the configuration of the <110> dislocation core structure, which has been observed using HRTEM and WBDF (17) to be either dissociated or decomposed. Therefore, the results from the theoretical modeling may not be very reliable. In addition, there have been no theoretical calculations regarding the Peierls stress for dislocation line configurations other than those with screw or edge character. Significantly, the <111> line directions on {011} planes pass through alternative Al and Ni atom columns which should make its core structure different from those when the dislocation lies along the <001> (edge) or <011> (screw) directions. As a result, it seems reasonable to expect the mobility of <111> line segments to be lower than the other segments. The alternative [$\bar{1}$11] and [111] line segments of <011> dislocations may result from the kink motion of <111> segments. In any case, the preferred line direction of <011> dislocations in this study indicates that a better understanding of both the mobilities and line energies of <011> dislocations is needed.
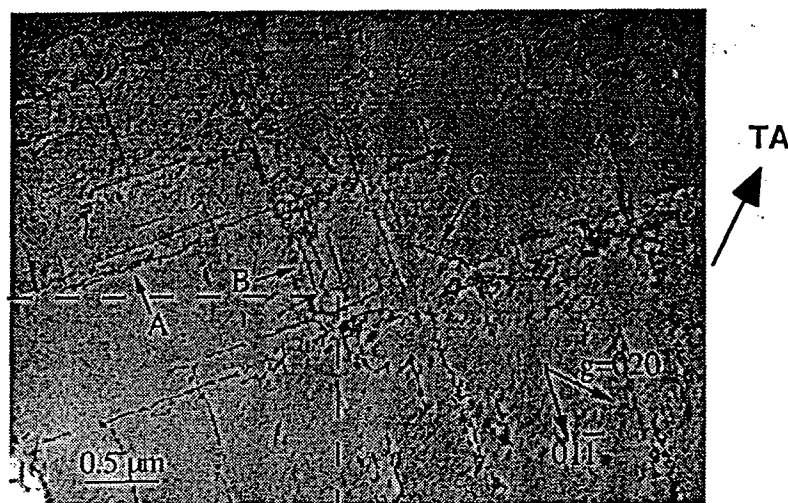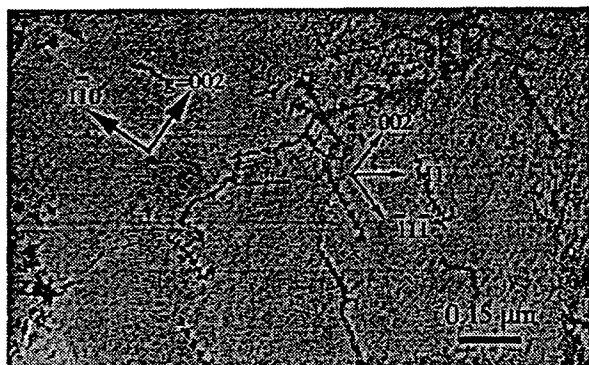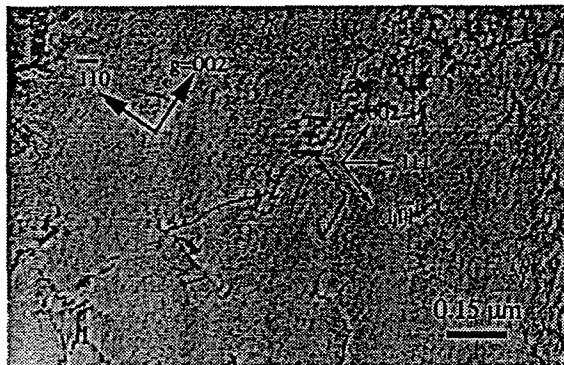
Figure 6: Dislocation substructure in the [001]-oriented NiAl single crystals after 2.5% strain at 573K: (a) Low magnification with g=020 near B=[100]; (b) Higher magnification of outlined region in (a) using g=002 near B=[110]; and (c) Same area as (b) with g=002 near B=[1$\bar{1}$0]. TA = tensile axis. Foil normal near [001].

Unlike <001> slip in the soft-oriented NiAl, <011> slip was relatively uniform as indicated by the lack of dislocation bands in the latter. There were, however, some regions where narrow <011> dislocation bands containing a high density of debris inside them were observed. Since this debris was not formed via mechanisms similar to those described for the soft-oriented crystals, it most likely involved limited cross slip of <011> dislocations. In fact, as will be shown separately, the debris and small loops are actually formed via the interaction between the <011> dislocations.

For comparison, the deformation behavior in <100> oriented NiAl-0.3Si specimens after about 4% elongation at 573K were also investigated using g.b and trace analyses. As in the case of binary

NiAl, the strain occurs by <011> slip almost exclusively as shown in Figs. 7a and b. In fact, essentially no <111> dislocations were observed (Fig. 7b) and only [011](01$\bar{1}$) and [01$\bar{1}$](011) slip systems were operating. This implies that the extent of latent hardening is greater in the Si-doped material.

Although the slip systems were the same in both the NiAl and NiAl-Si specimens, the line directions of these <011> dislocations in the NiAl-Si specimen were less well defined (Fig. 7c) and tended to bow out more both in and out of the slip plane. These features indicate that the <011> dislocations in Si-doped NiAl are more mobile and cross slip more readily. There is also a higher density of debris and small loops in the region where the <011> dislocations are clustered (Fig. 7d). At first glance, these debris and loops could be confused with the edge-on images of other <011> slip systems. However, careful analysis showed that they are distinguishable. In one such [011] dislocation band, the debris and small loops were identified to have either a [010] or [001] Burgers vector; this may indicate that the debris are products of the following dislocation reactions:
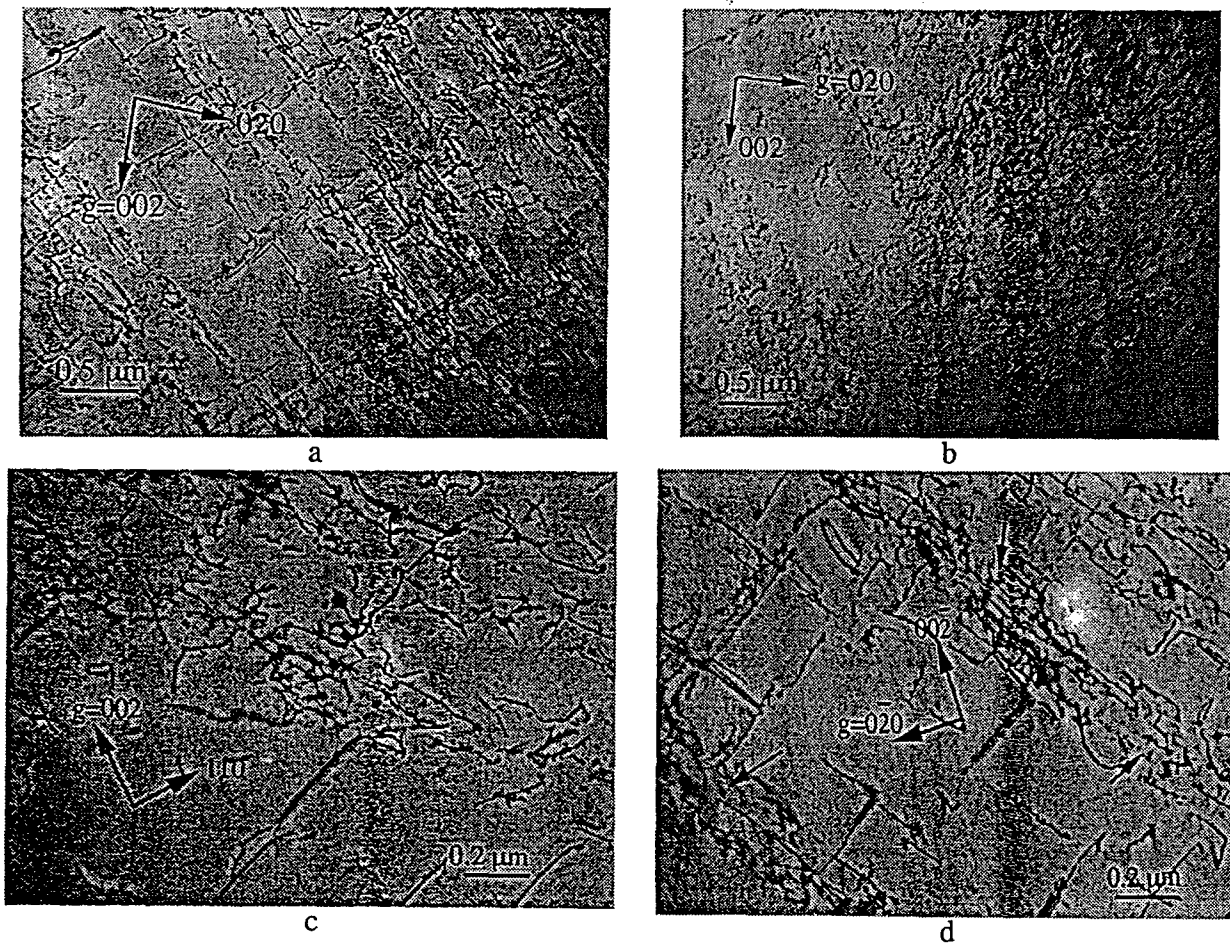
$$a[011]+a[01\bar{1}]=2a[010]$$

$$a[011]+a[0\bar{1}1]=2a[001]$$

Figure 7: BFTEMs of dislocations in [001]-oriented NiAl-Si single crystal after ~4% elongation at 573K: (a) g=002 near B=[100], (b) g=020 near B=[100] showing all the dislocations out of contrast, (c) g=002 near B=[$\bar{1}$10] and (d) g=0$\bar{2}$0 near B=[100]. TEM foil normal parallel to [110].

and occur when [011] and [01Ī] dislocations intersect. This also indicates that the <011> dislocations are reasonably mobile at this temperature. This type of reaction was observed in UF-NiAl specimens deformed at 573K, as shown in the WBDF images shown in Fig. 8. Although, decomposition of [011] dislocations could produce these <001> segments (i.e., a[011]=a[010]+a[001]), it is unlikely that this decomposition would produce the debris and small loops observed.

In the NiAl specimens deformed at 723K, the dislocation substructure consisted primarily of cube dislocations (Fig. 9). However, a small fraction of <011> dislocations on {011} planes were still observed (see arrows in Fig. 9). The dislocation loops are larger than those in the specimens deformed at 573K and were identified as <001> loops. The dislocation density is about the same as that at 573K even though the majority of the dislocations were <001> type.

a

b
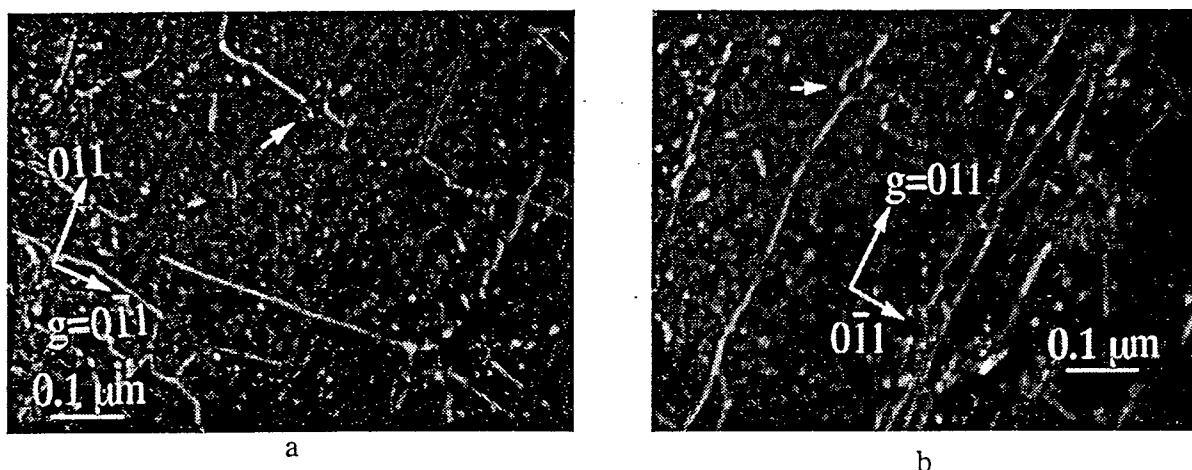
Figure 8: Weak beam dark field (WBDF) images of dislocation substructure in the [001] UF-NiAl specimen after testing at 573K. Foil normal parallel to [100]. The short arrow shows where two <011> dislocations reacted to form two <001> segments. Arrows point to (a) [01Ī] dislocation with [001] segments, and (b) [011] dislocation with [001] segments.

a

b
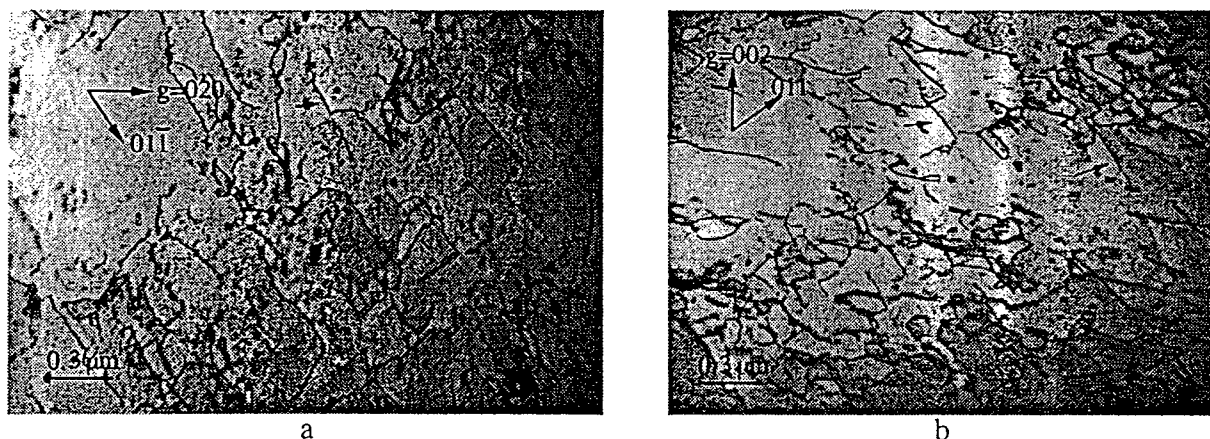
Figure 9: BFTEMs of dislocation substructure in a [001]-oriented UF-NiAl single crystal after deforming about 3% at 723K. Foil normal ~ [100].

The dislocation substructure in the [001]-oriented NiAl specimen deformed at 873K contained many <001> loops and a relatively low dislocation density (Fig. 10). This suggests that the structure had undergone significant dynamic recovery at this temperature. The majority of the dislocations were identified to have <001> Burgers vectors although a small percentage of <011>

dislocation segments bounded between <001> segments were observed (see arrow in Fig. 10) indicating a possible decomposition of the <011> dislocations to produce the <001> dislocations. Among the dislocations identified, less than 10% were <011>, about 45% were [001] and the remaining 45% were either [100] or [010]; this strongly suggests that the cube dislocations result from a decomposition reaction.

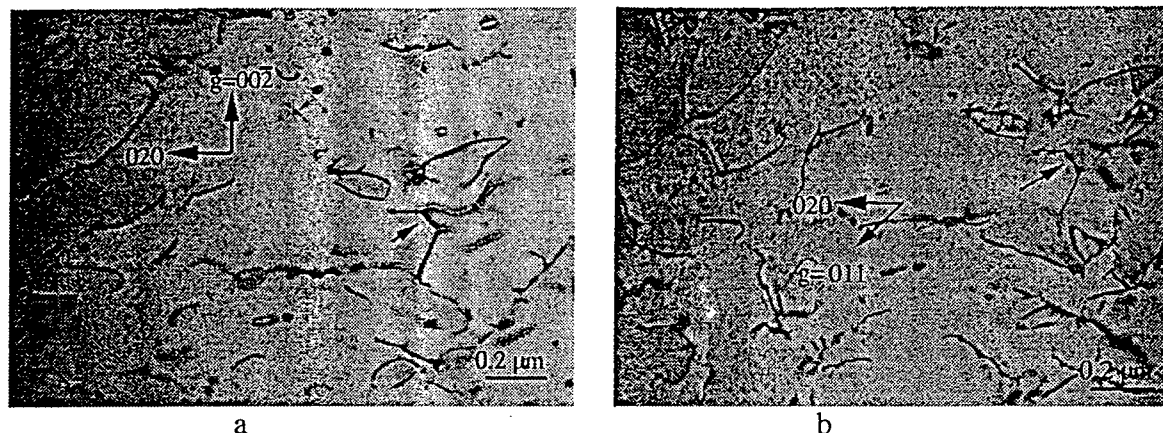a   b

Figure 10: BFTEMs of dislocation substructure in the [001]-oriented NiAl single crystal after deforming 3% at 873K (a) g=00$\bar{2}$ near B=[100], (b) g=011 near B=[100]. Arrows point to a [101] segments. Foil normal near [100].

In the [001] NiAl-Si specimens deformed at 723K, the dislocation substructures were generally similar to those in the binary UF-NiAl specimens (see Fig. 11). However, the NiAl-Si specimens appear to have a higher percentage of <011> dislocations and a higher density of <001> loops. It also appears that the operation of <011> slip systems in NiAl-Si extends to a higher temperature than in binary NiAl. This may suggest that Si stabilizes the <011> dislocations against their decomposition into <001> dislocations. Considering that the transition in the temperature dependence of the yield stress of the NiAl-Si specimens (Fig. 2c) also occurred at higher temperatures than in binary NiAl and that 723K is midway through this transition for the NiAl-Si alloy but about the end for NiAl specimens, it may suggest that the sudden drop in the yield stress correlates with the large fraction of <001> dislocations. However, the instability of <011> dislocations needs to be verified via further experiments. Since the BDTTs of both NiAl and

a   b
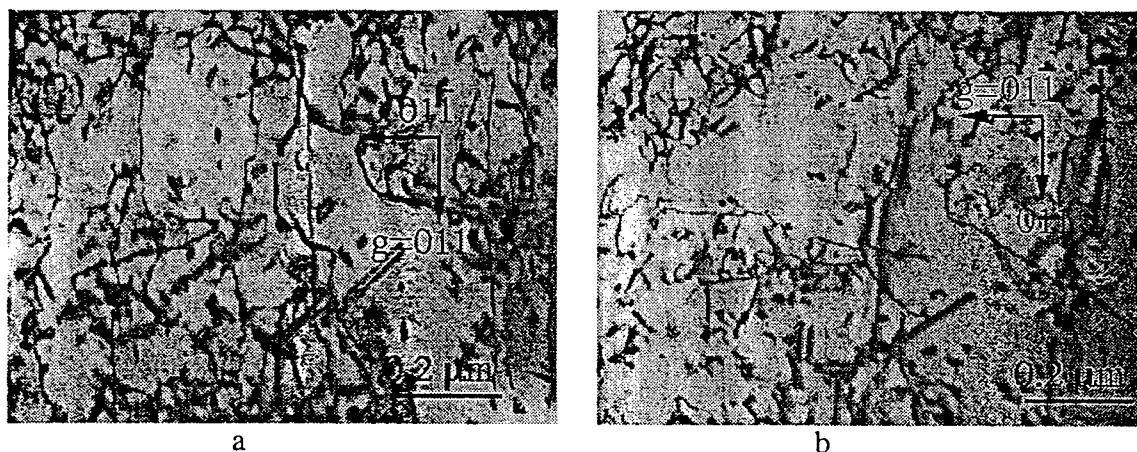
Figure 11: BFTEMs of dislocation substructure in the [001]-oriented NiAl-Si single crystal after deforming 4.5% at 723K: (a) g=011 near B=[100] and (b) g=01$\bar{1}$ near B=[100]. Foil normal [100].

NiAl-Si, as defined by the increase in tensile elongation, was between 523 and 573K, the slip behavior observed in the above specimens indicates that this transition was due to the activation of <011> dislocations rather than the climb of <001> dislocations as suggested by other workers

(18). Since only cube dislocations were observed in <001>-oriented specimens tested below 573K, it was not possible to conclude if there was a <111> to <110> transition in this material as reported in previous studies (18, 19). However, the sudden onset of tensile ductility in hard-oriented NiAl occurs at a temperature and strain rate when <011> dislocations become sufficiently mobile so as to lower the flow stress to below the fracture stress.

General Discussion

The present results indicate that, compared with metals, the properties of intermetallic compounds and ordered alloys are much more sensitive to impurities and other effects such as deviations from stoichiometry, thermal vacancies, etc. Consequently, discussions of purity effects in compounds such as NiAl should be subdivided into

(a) purity as related to general purity including interstitial (e.g., carbon) and substitutional (e.g., silicon and iron) atoms;

(b) purity as related to deviations from stoichiometry which produces either constitutional vacancies or anti-site defects; and

(c) purity as related to vacancy concentration (thermal and/or constitutional).

All three of these "impurity" classes appear to have similar effects on properties; this is in contrast to pure bcc metals where only the first (a) is significant.

The CRSS values of high purity, stoichiometric NiAl are lower than those of "conventional" purity, off-stoichiometric and Si-doped NiAl and that these differences are especially significant at both room and intermediate temperatures when dislocation glide is exclusively responsible for the plastic deformation. Again, it is emphasized that the CRSS values are calculated at 0.2% strain (when possible) in order to be consistent with the literature and in spite of the fact that this value is considerably higher than the threshold stress required to initiate dislocation activity. Further, it is noted that the threshold stresses observed in some of the lower purity NiAl (e.g., the [111] curve for CP-NiAl in Fig. 1) are the result of dislocation-impurity interactions (static strain aging) as pointed out by Hack et al (20) and Weaver, et al. (21). Clearly, the threshold stress in these lower purity crystals corresponds to the stress necessary for dislocations to overcome their impurity atmospheres rather than the stress required to initiate dislocation sources. The positive effect of prestraining on ductility reported for CP crystals must therefore be related to the formation of mobile dislocations that are not trapped by the interstitials. As pointed out in (22), prestraining of HP NiAl led to an increase in the CRSS and a decrease in elongation similar to what would be anticipated in pure metals.

The stress-strain curves for the UF-NiAl in the soft orientation (Fig. 1) indicate that dislocation glide starts at the proportional limit which is about 20-25% lower than the 0.2% offset value. Therefore the CRSS is considerably lower than that calculated at 0.2% strain. This suggests that there is no problem with the nucleation of dislocations in NiAl unlike in more covalent and ionic compounds. Furthermore, Ghosh and Crimp (23) noted, using in-situ straining in the TEM, that the dislocation velocity in the UF-NiAl was considerably (~5X) faster than in the CP-NiAl.

These results suggest that alloying additions to high purity NiAl, impurities and deviations from stoichiometry and thermal vacancies all lead to increases in both the CRSS and the WHR. The beneficial effects of microalloying additions reported by Darolia et al. (24) are difficult to account for in light of the present observations although it can be speculated that the increased elongation might be due to the interaction of the alloying elements with other impurities (e.g., carbon) or to the greater care taken in crystal or specimen preparation and/or handling.

The present results also illustrate the extreme sensitivity of NiAl to Ni/Al ratio; even small deviations (±0.2%) from stoichiometry, which commonly occur during crystal growth due to evaporation of aluminum, lead to significant changes in both CRSS and tensile elongation. Similar effects were reported recently by Kothe et al (25).

Finally, it is apparent that the thermal vacancies introduced by water quenching NiAl have a similar effect to that of the constitutional vacancies that result from the deviations from stoichiometry; both increase the CRSS and the WHR while decreasing the maximum tensile elongation. Recent electrical resistivity measurements indicate that the thermal vacancies annihilate rapidly in the 800-1000K range (26). Consequently, water quenching from above 1000K results in a 30-40% increase in CRSS (Fig. 1) and much lower elongations. Since the furnace cooling treatments used in the current study were sufficiently slow to allow for vacancy annihilation, none of the intermediate temperature anneals (those below 1000K) performed after FC had a significant effect on further reducing the CRSS or on increasing the elongation; this is consistent with the fact that the high purity stoichiometric NiAl with low thermal vacancy concentration has a minimum CRSS and maximum tensile elongation at RT.

Summary

The mechanical properties and slip behavior of pure and impure NiAl single crystals over a range of temperatures and strain rates were reported with an emphasis on understanding the influence of impurities on the deformation behavior of this compound. Based on the results obtained, the following conclusions were drawn:

1. NiAl single crystals deform readily by cube slip on {110} or {100} planes and there is no significant difference between the CRSS of cube slip on these planes for high purity NiAl.

2. The glide of cube dislocations occurs readily in high purity NiAl although the edge components have lower mobility than the screw segments. Cross slip occurs readily in high purity NiAl and leads to the formation of jogs, dipoles and elongated loops.

3. In the highest purity material, the dislocations develop into patches elongated along the edge orientations whereas in lower purity material or high purity NiAl containing quenched-in thermal vacancies, the dislocations and debris are more uniformly distributed throughout the material.

4. Impurities, solute atoms, constitutional defects and thermal vacancies all lead to increased resistance to dislocation motion, increased work hardening rate and decreased ductility. The work hardening rate at ambient temperatures for high purity NiAl in the single slip orientation is quite low and extends to the highest strains achieved to date.

5. The decrease in yield stress with temperature is less abrupt in the higher purity NiAl oriented along the hard orientation compared with the commercially pure and Si-doped NiAl. Silicon does not strongly influence the slip behavior in the case of <001>-oriented crystals.

Acknowledgments

References

1. R. D. Noebe, R. R. Bowman and M. V. Nathal, Inter. Mater. Rev. 38, (1993) 193.
2. D. B. Miracle, Acta Metall. Mater., 41 (1993) 649.
3. J. Hu, PhD Dissertation, University of Florida, 1997.
4. V. I. Levit and M. J. Kaufman, Structural Intermetallics 1997, ed. M.V. Nathal, R.Darolia, C.T.Liu, P.L.Martin, D.B. Miracle, R. Wagner, and M. Yamaguchi, TMS, (1997) 683.
5. D. F. Lahrman, R. D. Field and R. Darolia, High Temperature Ordered Intermetallic Alloys IV, MRS Symp. Proc. Vol. 213 (1991) 603

6. R. D. Field, D. F. Lahrman and R. Darolia, <u>Acta Metall. Mater.</u> **39** (1991) 2951

7. V. I. Levit, I. A. Bul, J. Hu and M. J. Kaufman, <u>Scripta Mater.</u> **34** (1996) 1925

8. R. D. Noebe, private communication (1998)

9. R. Bowman, R.D. Noebe and R. Darolia, <u>HITEMP Review</u> (NASA Conference Publication 10039), (1989) 47-1.

10. D. R. Johnson et al., <u>First International Conference on Processing Materials for Properties</u>, ed. H. Henein and T.Oki, (TMS, 1993) 865.

11. R.T. Pascoe and C.W.A. Newey, <u>Phys. Stat. Sol.</u> **29** (1968) 357.

12. J.T. Kim, PhD Dissertation, University of Michigan (1990).

13. M.H. Loretto and R.J. Wasilewski, <u>Phil. Mag.</u> **23** (1971) 1311.

14. H.L. Fraser, M.H. Loretto, R.E. Smallman and R.J. Wasilewski, <u>Phil. Mag. A</u> **28** (1973) 639.

15. D.I. Potter, <u>Mater. Sci. Eng.</u> **5** (1969/70) 201.

16. C.H. Lloyd and M.H. Loretto, <u>Phys. Stat. Sol.</u> **39** (1970) 163.

17. M.J. Mills and D.B. Miracle, <u>Acta Metall. Mater.</u> **41** (1993) 85.

18. R.D. Noebe and A. Garg, (NASA Technical Memorandum 106981, 1995).

19. J.T. Kim and R. Gibala, MRS Symp. Proc. Vol. 213 (1991) 261.

20. J.E. Hack, J.M. Brzeski, and R. Darolia, <u>Scripta Metall.</u>, **27**, (1992) 1259.

21. M.L. Weaver, M.J. Kaufman, and R.N. Noebe, <u>Scripta Metall.</u>, **29**, 1113 (1993).

22. R.W. Margevicius and J.J. Lewandowski, <u>Acta Metall. Mater.</u> **41** (1993) 485-496.

23. B. Ghosh and M.A. Crimp, <u>High Temperature Intermetallic Alloys VII</u>, C.C. Koch et al., eds., MRS Proceedings, Boston, Vol. 460 (1997) 467.

24. A. Kothe et al., Contribution to the <u>Second International Conference on Ultra-High Purity Based Materials</u>, Saint -Etienne, France (June 13-16, 1995)

25. R. Darolia, D. F. Lahrman and R. D. Field, , <u>Scripta Metall.</u> **26** (1992) 107

26. J.Hu, V. Levit and M.J. Kaufman, <u>High Temperature Intermetallic Alloys VI</u>, J.A. Horton et al eds., MRS Proceedings, Boston, Vol. 364 (1994) 297.

Investigation of strain hardening in NiAl single crystals using three-dimensional FEA models

Ashok V. Kumar and Chulho Yang
Department of Mechanical Engineering
University of Florida
Gainesville, FL 32611-6300

ABSTRACT

Large deformation of single crystals involves activation of multiple slip systems that can often be modeled only using three-dimensional finite element analysis (FEA) models. The main difficulty in extending constitutive models of single crystals to three-dimension is due to the lack of understanding of hardening in single crystals during multiple slip. In this paper, hardening in NiAl single crystals has been studied by implementing a three-dimensional hardening model and constitutive equations into a finite element analysis program. Since the parameters required to describe the hardening model such as latent hardening ratios are difficult to obtain experimentally, a parametric study was conducted to estimate values for these parameters that enable the prediction of the experimentally observed load versus elongation curves.

1. Introduction

An appropriate work hardening model for single crystals is a crucial component of the constitutive equation describing the deformation of single crystals of metals and intermetallic compounds. Incorporation of such models into finite element programs enables the simulation of deformation in these single crystals. Such simulations are necessary to better understand the causes of many kinds of localized deformation and failures in metals. Depending on the orientation of the applied loads and the amount of deformation, multiple slip systems can become active during the deformation. The hardening of single crystals when multiple slip systems are activated is not well understood. Previous study by the authors (Yang, Kumar et al, 1998) and others (Ebrahimi et al, 1997) on single crystals of NiAl showed that multiple slip plays an important role in the deformation process at large strains.

NiAl is an intermetallic compound that has been studied as a potential structural material due to its desirable material characteristics such as high melting point, low density and good oxidation resistance. In addition, it has excellent mechanical properties at high temperatures including hardness, toughness, thermal stability and ductility. However, NiAl has low ductility and poor fracture toughness at ambient temperatures. The tensile plastic strain before fracture at room

temperature is typically 0.5-2.5% (Lahrman, 1991 and Miracle, 1993). Many modes of non-uniform deformation such as necking, localized shear, kinking etc. have been observed in NiAl single crystals. These localized deformations contribute significantly to the total plastic strain and eventual failure (Miracle, 1993). Significant tensile ductility is obtained only at and above 473 K (Wasilewski, 1967, Lahrman, 1991, etc.). Therefore, many approaches have been investigated to improve its material properties at ambient temperature (Darolia, 1991). Miracle (1993) has presented a detailed survey and a critical review of literature on the physical and mechanical properties of NiAl.

Many authors have proposed constitutive models for single crystals (Asaro, 1983, Peirce et al 1983). These theoretical formulations have since been implemented using finite element method to simulate two-dimensional deformation of single crystals. Most of the past studies have used these methods to simulate deformation in fcc (Peirce, et al, 1983) and bcc single crystals (Deve et al, 1988). In these cases, the simulations are often meaningful only for relatively small deformations because at large deformations multiple slip systems can activate making the assumption of two-dimensional deformation invalid.

In this paper, we have studied work hardening in NiAl single crystals at large strains when multiple slip systems are activated. Due to multiple slip a three-dimensional model is required. A three dimensional rate-dependent constitutive model for single crystals was implemented into ABAQUS [1], a commercial finite element code that is capable of modeling large deformation and large strains. The constitutive equation was integrated using forward gradient method which has been found to be effective (Peirce et al 1983 and Wenner, 1993) provided sufficiently small time-steps are used for the time integration.

In the next section, various hardening laws that have been proposed for single crystals are summarized. The crystal structure and plastic deformation modes of NiAl single crystals are described in section 3 along with a summary of results from past research by the authors on deformation localization in these crystals. Three possible modes of deformation at large strain are identified. In section 4, we describe techniques for estimating the latent hardening ratios that would lead to each of these modes of deformation. Results of finite element simulations are presented in section 5 along with comparisons with experimental results. Finally, section 7 contains the summary and conclusions of the paper.

2. Hardening laws

For a strain rate dependent model of single crystal deformation, the slip rate of the α–th slip system is assumed to be related to the resolved shear stress on that slip system by the power law (Pan and Rice, 1983) given in equation (2.1).

2

$$\dot{\gamma}^{(\alpha)} = \dot{a}^{(\alpha)} \left[\frac{\tau^{(\alpha)}}{\tau_c^{(\alpha)}} \right] \left[\left| \frac{\tau^{(\alpha)}}{\tau_c^{(\alpha)}} \right| \right]^{(1/m)-1}$$ (2.1)

where, m is the rate sensitivity parameter, $\tau_c^{(\alpha)}$ is the *critical resolved shear stress* or also known as the *flow stress* for the slip system α, $\dot{a}^{(\alpha)}$ is a reference strain rate on each slip system. The shear rate in each slip system is uniquely determined by power law equation (2.1) and is non-vanishing as long as the resolved shear stress on that system is not identically zero. The flow stress $\tau_c^{(\alpha)}$ for each slip system of the material increases with plastic deformation due to work hardening. The hardening curve needs to be determined for each possible slip system so that $\tau_c^{(\alpha)}$ can be expressed as a function of the plastic shear in that slip system $\tau_c^{(\alpha)} = g(\gamma^{(\alpha)})$. However, when more than one slip system is active, hardening in each slip system is a cumulative effect of slip in all the active slip systems. For a rate dependent model, the rate of increase of the function $\tau_c^{(\alpha)}$ has therefore been specified as (Hill 1966),

$$\dot{\tau}_c^{(\alpha)} = \sum_{\beta=1}^{n} h_{\alpha\beta} \left| \dot{\gamma}^{(\beta)} \right|$$ (2.2)

The hardening laws that have been proposed so far differ mainly in the definition of the hardening moduli $h_{\alpha\beta}$. From the early 1900's several hardening laws were proposed to explain deformation process on single crystals. Based on experimental work on aluminum, Taylor (1934) proposed the 'isotropic' hardening law. According to this law all slip systems harden equally when deformation occurs so that $h_{\alpha\beta} = h(\gamma)$, where γ is the sum of the shear strains on all slip systems. This isotropic hardening is unable to predict the experimental observation that inactive or latent slip systems often harden more than the slip system that is active during deformation.

Hutchinson (1970) accounts for latent hardening by assuming that the off-diagonal terms in the matrix of hardening moduli are different than the diagonal values. In their constitutive model for single crystals, Asaro (1983) has also used the same concept expressing the hardening moduli as:

$$h_{\alpha\beta} = qh + (1-q)h\delta_{\alpha\beta}$$ (2.3)

The hardening modulus, h is the rate of change of flow stress with shear strain during single slip and q is the latent hardening ratio. In Asaro's (1983) model, the hardening modulus, h is assume to be a function of the sum of shear strains that have occurred in all the slip systems, ie, $h = h(\gamma)$. The hardening curve $\tau_c(\gamma)$ and hardening modulus $h(\gamma)$ for single slip in such materials is often represented using the following equations

$$\tau_c(\gamma) = \tau_0 + (\tau_s - \tau_0) \tanh\left(\frac{h_0 \gamma}{\tau_s - \tau_0} \right)$$ (2.4)

3

$$h(\gamma) = \frac{d\tau_c}{d\gamma} = h_0 \sec h^2 \left(\frac{h_0 \gamma}{\tau_s - \tau_0} \right) \tag{2.5}$$

Many authors (Kocks, 1964, Basinski, 1979 and Franciosi et al., 1980) have studied the interaction among slip systems to understand hardening in fcc single crystals. From a microscopic viewpoint, hardening of single crystals is the result of dislocation interactions between slip systems. Internal dislocation density and short range interaction dislocation strengths can be treated as the main parameters of hardening analysis. Franciosi et al (1982) has expressed flow stress mainly as a function of dislocation interaction coefficients [a] matrix and dislocation density ρ. They define [a] matrix using slip interactions classified as sessile, glide, hirth lock, no junction and self hardening according to the slip interactions between the corresponding two slip systems (Franciosi, 1985).

Koiter (1953) proposed a diagonal hardening matrix of the form $h_{\alpha\beta} = h\delta_{\alpha\beta}$. A similar diagonal form has also been used by Bassani and Wu (1991) where each diagonal term is a function of all the slips. The hardening law proposed by Bassani and co-workers (Bassani, 1994) for FCC crystals is based on the dislocation interaction between slip systems. Based on experimental results (Wu, et al 1991), they suggest that initial flow stress on secondary slip systems is lower than the current flow stress on primary systems and that the initial high rate of hardening on the previously latent system leads to a greater flow stress on that system after a small amount of secondary slip.

Bassani et al. (1989) devised phenomenological hardening law based on their observations.

$$h_{\alpha\alpha} = F(\gamma_\alpha)G(\gamma_\beta), \quad \alpha \neq \beta \quad \text{and} \quad h_{\alpha\beta} = qh_{\alpha\alpha} \tag{2.5}$$

where, $F(\gamma_\alpha)$ is the instantaneous hardening modulus under independent single slip α and $G(\gamma_\beta)$ represents the interactive latent hardening. Therefore, G is a function of slip in other slip systems. In their study, the latent hardening ratio q, was assumed to be zero so that latent hardening in slip systems occur only due to the G factor in the hardening formula (2.5).

3. Deformation of NiAl single crystals

NiAl has a B2 type ordered crystal structure (see figure 1) similar to body centered cubic (bcc) crystals. Mechanical properties of NiAl single crystals vary with respect to the orientation of crystal lattice. Plastic deformation in NiAl occurs predominantly due to slip in the <001> directions along either {110} or {100} planes when loaded along non-<001> direction (or soft orientations). NiAl crystal subjected to loading along the <001> direction (hard orientation) shows high flow stress at low temperatures and enhanced creep strength at elevated temperatures.

Figure 1. NiAl crystal structure

When a tensile specimen of NiAl single crystal is loaded along the [110] orientation, the crystal deforms mainly due to slip in two primary slip systems {100}<001> as long as the strains are not very large. The resolved shear stress is identical on both the primary slip systems. Therefore, they activate simultaneously and there is no lattice rotation for this load orientation. At large strains, secondary or cross slip could occur in four {110}<100> slip systems even though these slip systems have a smaller resolved shear stress as compared to the primary slip systems. These four slips systems also have identical resolved shear stress and therefore will activate simultaneously resulting in identical shear in all of them. Slip systems that could be activated in a single crystal of NiAl due to tensile loading along [110] orientation are shown in figure 7. Cross slip can occur due to both rate sensitivity effects as well as due to the differences in the hardening rate between primary and cross slip systems.

Figure 2. Active slips systems of NiAl for loading along [110] orientation

We have used a hardening model for NiAl in which changes in flow stresses of the slip systems in response to shear deformation is expressed using four latent hardening ratios and two hardening moduli as shown below.

$$
\begin{Bmatrix} d\tau_c^{(1)} \\ d\tau_c^{(2)} \\ d\tau_c^{(3)} \\ d\tau_c^{(4)} \\ d\tau_c^{(5)} \\ d\tau_c^{(6)} \end{Bmatrix} = \begin{bmatrix} h_1 & q_{aa}h_1 & q_{ab}h_2 & q_{ab}h_2 & q_{ab}h_2 & q_{ab}h_2 \\ q_{aa}h_1 & h_1 & q_{ab}h_2 & q_{ab}h_2 & q_{ab}h_2 & q_{ab}h_2 \\ q_{ba}h_1 & q_{ba}h_1 & h_2 & q_{bb}h_2 & q_{bb}h_2 & q_{bb}h_2 \\ q_{ba}h_1 & q_{ba}h_1 & q_{bb}h_2 & h_2 & q_{bb}h_2 & q_{bb}h_2 \\ q_{ba}h_1 & q_{ba}h_1 & q_{bb}h_2 & q_{bb}h_2 & h_2 & q_{bb}h_2 \\ q_{ba}h_1 & q_{ba}h_1 & q_{bb}h_2 & q_{bb}h_2 & q_{bb}h_2 & h_2 \end{bmatrix} \begin{Bmatrix} d\gamma_1 \\ d\gamma_2 \\ d\gamma_3 \\ d\gamma_4 \\ d\gamma_5 \\ d\gamma_6 \end{Bmatrix} \tag{3.1}
$$

In the above equation, $d\gamma_1$ and $d\gamma_2$ are the slip in the two primary {100}<001> slip systems henceforth referred to as type a slip systems, while $d\gamma_3$ to $d\gamma_6$ are slip in the {110}<001> slip systems that will be referred to as type b slip systems. As can be seen from the above equations, q_{ab} is the ratio of hardening in a latent type a slip system to hardening in an active type b slip system while q_{aa} is the ratio of hardening in a latent type a slip system to hardening in another active type a slip system. Similar definitions apply to q_{bb} and q_{ba} as well.

We also assume that hardening modulus h_1 is a function of the cumulative strain in all type a slip systems only, ie, $h_1 = h(\gamma_a)$ where $\gamma_a = \gamma_1 + \gamma_2$. Similarly, h_2 is assumed to be a function of cumulative strains in all type b slip systems, $h_2 = h(\gamma_b)$, where $\gamma_b = \gamma_3 + \gamma_4 + \gamma_5 + \gamma_6$. The hardening modulus is assumed to be of the form given in equation (2.4). Therefore, at large value of strain γ, the hardening modulus becomes small and tends to zero. By using seperate hardening modulus for the two types of slip system, the hardening model can predict an increase in the

hardening rate when a previously latent system suddenly becomes active.

At large strains we can identify three possible modes of deformation in the NiAl single crystal loaded along the [110] orientation. These three cases are described below:

Case I: The type *a* slip systems remain the dominant slip systems through out the deformation. This will happen if type *b* systems hardens as fast or faster than type *a* slip systems.

Case II: After a certain amount of deformation, type *b* slip systems become active and slip in type *a* systems becomes negligible. This will happen if type *b* systems harden much less than type *a* through out the deformation.

Case III: After some deformation type *b* slip systems become active and further deformation involves slip in both slip systems. This case can happen if type *a* slip system hardens faster when type *b* is inactive and type *b* hardens faster when both systems are simultaneously active.

4. Estimation of hardening parameters

The parameters used in the hardening model such as the latent hardening ratios and the constants used in the hardening curve (equation, 2.4) are often difficult if not impossible to determine experimentally. In our previous study (Yang, Kumar et al, 1998), we determined the hardening curve for {110}<100> slip systems by conducting a parametric study, comparing experimental data for loading along the [557] orientation with simulation results. Loading in the <557> orientations produce single slip in a {110}<001> slip system thus enabling the determination of the hardening curve for these systems. We have assumed that the hardening curve for {100}<001> systems is identical. However, the values of the four latent hardening parameters need to be determined. While the exact values of these parameters are difficult to obtain, it is possible to predict values of these parameters that will lead to each of the three modes of deformation described above. Then comparison of experimental results with the simulation results for these three modes can help us understand the real mode of deformation.

There is no lattice rotation during deformation when NiAl single crystal is loaded along the [110] orientation. Therefore, the ratio of resolved shear stress in primary slip system (type *a*) to resolved shear stress in secondary slip system (type *b*) is constant.

$$\left| \frac{\tau^{(p)}}{\tau^{(s)}} \right| = K \tag{4.1}$$

K can be obtained by calculating resolved shear stress at each slip system. If m_p is the Schmid factor for primary slip system {100}<001> and m_s is the Schmid factor for secondary slip system

6

{110}<010>, then $\dfrac{m_p}{m_s} = K = \sqrt{2}$

Since the resolved shear stress on primary slip system is higher, the secondary slip system will activate only if the flow stress of the primary is higher by the same factor. Therefore, the condition for activation of secondary slip system can be written as:

$$\frac{\tau_c^{(p)}}{\tau_c^{(s)}} \geq K \tag{4.2}$$

For both type of slip systems to be active simultaneously, the ratio between the flow stresses $\tau_c^{(p)}$ and $\tau_c^{(s)}$ should stay constant and equal to K. At small strains, only the primary slip system is active so resolved shear strain in the secondary slip systems are almost zero ($d\gamma_3 = d\gamma_4 = d\gamma_5 = d\gamma_6 = 0$). The resolved shear stress and strain are the same in both {100}<001> systems, therefore, $d\gamma_1 = d\gamma_2 = d\gamma_p$. Increment in flow stresses in both primary and secondary slip systems are expressed using equation (3.1) as follows:

$$d\tau_c^{(p)} = d\tau_c^{(1)} = d\tau_c^{(2)} = h_1 d\gamma_1 + q_{aa} h_1 d\gamma_2 = h_1(1 + q_{aa}) d\gamma_p \tag{4.3}$$

$$d\tau_c^{(s)} = d\tau_c^{(3)} = d\tau_c^{(4)} = d\tau_c^{(5)} = d\tau_c^{(6)} = (q_{ba} h_1 d\gamma_1 + q_{ba} h_1 d\gamma_2) = 2h_1 q_{ba} d\gamma_p \tag{4.4}$$

where, $h_1 = h(\gamma_a)$ using the definition of hardening rate $h(\gamma)$ used in equation (2.4) and $\gamma_a = \gamma_1 + \gamma_2 = 2\gamma_p$. Integration of incremental flow stress in primary slip system gives the following equation.

$$\tau_c^{(p)} = (1 + q_{aa})(\frac{\tau_s - \tau_0}{2}) \tanh(\frac{2h_0 \gamma_p}{\tau_s - \tau_0}) + \tau_0^{(p)} \tag{4.5}$$

Integration of incremental flow stress in secondary slip system with the same assumptions gives the following formulas for secondary slip system.

$$\tau_c^{(s)} = q_{ba}(\tau_s - \tau_0) \tanh(\frac{2h_0 \gamma_p}{\tau_s - \tau_0}) + \tau_0^{(s)} \tag{4.6}$$

The condition for non-activation of secondary slip systems can then be stated as $\tau_c^{(p)} < K\tau_c^{(s)}$ during the deformation even when $\gamma_p \to \infty$. Using equations (4.5) ad (4.6) this can be expressed as:

$$(1 + q_{aa}) - 2Kq_{ba} < \frac{2(K-1)\tau_0}{\tau_s - \tau_0} \tag{4.7}$$

The above condition does not proclude activation of secondary slip entirely, since the rate sensitive constitutive equation (2.1) allows small strain rates even when the resolved shear stress is

7

below the flow stress. The resolved shear stress in the secondary slip systems are the same due to symmetry. Therefore, the strains are also equal and can be expressed as $d\gamma_3 = d\gamma_4 = d\gamma_5 = d\gamma_6 = d\gamma_s$. Therefore, after activation of secondary slip, we can write the increment in resolved shear stress for each type of slip system as:

$$d\tau_c^{(p)} = (1+q_{aa})h_1 d\gamma_p + 4q_{ab}h_2 d\gamma_s = d\tau_c^{(1)} = d\tau_c^{(2)} \tag{4.8}$$

$$d\tau_c^{(s)} = 2q_{ba}h_1 d\gamma_p + (1+3q_{bb})h_2 d\gamma_s = d\tau_c^{(3)} = d\tau_c^{(4)} = d\tau_c^{(5)} = d\tau_c^{(6)} \tag{4.9}$$

Condition for case I: This case occurs when the deformation is almost entirely due to slip in primary (type a) slip systems. The condition for this can be stated as $Kd\tau_c^{(s)} \geq d\tau_c^{(p)}$ during the entire deformation. Using the above equations (4.8 and 4.9), this condition may be restated as:

$$2Kq_{ba} \geq (1+q_{aa}) \tag{4.10}$$

$$K(1+3q_{bb}) > 4q_{ab} \tag{4.11}$$

Condition for case II: In this case, secondary slip systems are activated and subsequently the primary slip system ceases to be active. Even if the latent hardening ratios satisfy equation (4.7) the secondary slip could activate due to rate sensitivity effect. The condition for case II can be stated as $Kd\tau_c^{(s)} < d\tau_c^{(p)}$ during the entire deformation. From equations (4.8) and (4.9) this condition may be stated as:

$$2Kq_{ba} < (1+q_{aa}) \tag{4.12}$$

$$K(1+3q_{bb}) < 4q_{ab} \tag{4.13}$$

Condition for case III: Both primary and secondary slip systems will be simultaneously active if after activation of secondary slip systems the rate of hardening of secondary systems is K times greater than the rate of hardening in the primary slip systems. In this case, the two systems become active alternately since secondary slip will stop slipping due to high rate of hardening but as soon as primary slip resumes the rate of hardening of primary system increases.

$$2Kq_{ba} < (1+q_{aa}) \tag{4.14}$$

$$K(1+3q_{bb}) > 4q_{ab} \tag{4.15}$$

5. Simulation of crystal deformation

Deformation of NiAl single crystals when loaded along [110] direction was simulated using three-dimensional non-linear large deformation finite element models. The constitutive equations and the hardening model was implemented as a user defined subroutine within ABAQUS finite

element software. The three modes of deformation described in the last section are simulated by selecting hardening modulus that satisfy the conditions for each case.

Case I : The following values of the latent hardening ratios satisfy the conditions for case I (equation 4.10 and 4.11): q_{aa}=1.4, q_{bb} = q_{ab} = q_{ba} = 1.0. The results of the finite element simulation are displayed in figure 3. Figure 3 (a) shows the plot of resolved shear strain (versus time) for each type of slip system. As expected, there is no resolved shear strain on the secondary slip systems indicating that they were inactive during the entire deformation. Figure 3 (b) shows hardening in each type of slip system (flow stress vs time) and figure 4 shows the deformed specimen at the end of the simulation. It can be seen that two necks have formed at the top and bottom of the gauge length of the specimen. The rate of hardening at large strains is not high enough to prevent necking.

(See attached)
Figure 3 (a) Resolved shear strain vs time

Figure 3 (b) Critical resolved shear stress vs time

Figure 4. q_{aa}=1.4, q_{bb}=1.0, q_{ab}=1.0, q_{ba}=1.0, 20 % nominal strain
(a) Deformed mesh (b) Contour plot of Cauchy strain in Y-dir. (c) Contour plot of Cauchy stress in Y-dir.

Case II: Simulation results for two sets of latent hardening ratios are presented for case II. The following values satisfy equations (4.12) and (4.13) : q_{aa}=1.4, q_{ba}=0.2, q_{ab}=1.6, q_{bb}=1.0. In addtion, equation (4.7) predicts that secondary slip systems should activate for these values of latent hardening ratios. Figure 5 (a) shows the resolved shear strains in the slip systems when these values of latent hardening ratios were used. It is seen that secondary slips systems activate early. Due to the activation of secondary slip, significant hardening occurs during the early part of deformation as seen in figure 5 (b). But the rate of hardening becomes very small at large deformation and is not sufficient to prevent localization. Therefore, the specimen necks during the simulation at the top and bottom of the gauge length.

(See attached)
Figure 5 (a) Resolved shear strain vs time

Figure 5 (b) Critical Resolved shear stress vs time

The following set of latent hardening ratios, q_{aa}=1.4, q_{bb}=1.0, q_{ab}=1.9 q_{ba}=0.7, also satisfy the conditions for case II (equations 4.12 and 4.13). For these values of latent hardening ratios, equation (4.7) predicts that secondary slip systems should not activate. However, simulation results (figure 6 (a)) shows that secondary slip systems do become active at large strain. This is due to rate sensitivity which was ignored in the derivation of equation (4.7). Due to rate sensitivity small shear strain rate can exist in secondary slip system even when the resolved shear stress is below flow stress. This further increases the rate of hardening of primary systems relative to secondary.

The activation of secondary slip systems cause a higher rate of hardening at large strain as seen in figure 6 (a). As a result, the specimen does not neck as seen in figure 7 which shows the deformed specimen. When the neck begins to form, the high rate of hardening at large strain prevents further localization and causes the neck to spread. This is precisely the behavior observed experimentally (Winton, 1995) during tests conducted above 473K. The experimental specimens did not neck and significant hardening was observed at large strain.

<div align="center">

(See attached)
Figure 6 (a) Resolved shear strain vs time

Figure 6 (b) Critical resolved shear stress vs time

Figure 7 (a) deformed mesh (b) strain in Y-dir. (c) stress in Y-dir.
(Case II: q_{aa}=1.4, q_{bb}=1.0, q_{ab}=1.9, q_{ba}=0.7, at 40% nominal strain)

</div>

Case III: Two sets of latent hardening ratios that satisfy the conditions for case III are: (a) q_{aa}=1.4, q_{bb}=1.0, q_{ab}=1.2, q_{ba}=0.2 and (b) q_{aa}=1.4, q_{bb}=q_{ab}=1.0, q_{ba}=0.6. The first set of values (Case III a) are selected such that the secondary systems would activate even if the material were rate independent since equation (4.7) predicts that they will activate. The second set of values (Case III b) are selected such that secondary slip systems activate very little (only due to rate dependence). Figures 8 and 9 show the resolved shear stress versus time obtained by finite element simulation for these two sets of values. As expected there is significant activation of secondary slip in case III (a), however the resultant hardening occurs early in the deformation. Very little hardening occurs at large deformation and therefore the specimen necked. For case III (b), very little activation of secondary slip occurs and as a result the rate of hardening is not high enough at large strains to prevent necking.

<div align="center">

(See attached)
Figure 8: Resolved shear strain vs time (Case III (a))

Figure 9: Resolved shear strain vs time (Case III (b))

</div>

Figure 10 shows the plot of load vs time for all the simulations described above. It is seen that except for case II (b), the load drops sharply due to necking and then does not recover. In case II (b) activation of secondary system at large deformation provides higher rate of hardening. Due to the increased flow stress at the neck further deformation is curtailed and the neck spreads leading to the more or less uniform deformation in the gauge length as seen in figure 7. As a result, very large strains can be produced in the specimen without necking. The experimentally observed behavior is very similar to this case.

<div align="center">

Figure 10: Load vs time

</div>

7. Summary

The hardening characteristics of NiAl single crystals have been studied here using the proposed hardening law that is applicable to multiple slip and three-dimensional deformation. Uniaxial loading of NiAl single crystals in [110] direction were simulated using 3D finite element models to study the three possible modes of deformation in the NiAl single crystal. Comparison of simulation results with experimental observation suggests that primary {100}<001> slip systems harden at a faster rate than secondary {110}<001> slip systems during the entire deformation. The activation of secondary slip at large strains due to rate sensitivity effect provides the experimentally observed high rate of hardening at large strains. This high rate of hardening prevents strain localization and causes the neck to spread. Classification of the deformation into various modes and comparison of finite element simulations with experiments enabled us to establish approximate values of latent hardening ratios that lead to the experimentally observed behavior.

8. References

[1]   Asaro R. J., "Micromechanics of crystals and polycrystals", Adv. Appl. Mech., Vol.23 pp.1, 1983

[2]   Basinski S. J. and Basinski Z. S., "Plastic deformation and work hardening" in:Dislocations in solids(F. R. Nabarro ed.) North Holland, Amsterdam, pp. 262, 1979

[3]   Bassani J. L. and Wu T., "Latent hardening in single crystals II. Analytical characterization and predictions", Proc. R. Soc. London, A435, pp. 21-41, 1991

[4]   Bassani J. L., "Plastic Flow of Crystals", Adv. Appl. Mech., vol. 30 pp. 192, 1994

[5]   Crimp M. A., Tonn S. C., Zhang Y., "Dislocation core Structures in B2 NiAl alloys", Material Science and Engineering, A170, pp. 95-102, 1993.

[6]   Darolia R., 1991, "NiAl alloys for high-temperature structural applications", J. Metals, vol. 43, no. 3, pp. 44-49

[7]   Deve H., Harren S., McCullough C. andAsaro R. J., 1988, "Micro and Macroscopic Aspects of Shear Band Formation in Internally Nitried Single Crystal of Fe-Ti-Mn Alloys", Acta metall., vol 36, no.2, pp. 341-365

[8]   Ebrahimi F., and Shrivastava S., 1997, "Crack initiation and propagation in brittle-to-ductile transition regime of NiAl single crystals", J. Material Science and Engineering, in press.

[9]   Franciosi P. and Zaoui A., 1982(a) "Multislip in FCC crystals a theoritical approach compared with experimental data", Acta metall., Vol. 30, pp. 1627-1637,

[10] Franciosi P. and Zaoui A., 1982(b) "Multislip tests on copper crystals :a junctions hardening effect", Acta metall., Vol. 30, pp. 2141 -2151,

11

[11] Franciosi P. , 1985, "Concepts of Latent Hardening and Strain Hardening in Metallic Single Crystals ", Acta metall., Vol. 33, No. 9, pp. 1601-1612

[12] Franciosi P. , 1980, Berveiller M. and Zaoui A., "Latent hardening in copper and aluminum single crystals", Acta metall., Vol. 28, pp. 273-283

[13] Hill R., 1966, "Generalized constitutive relations for incremental deformation of metal crystals by multislip", Journal of Mechanics and Physics of Solids, vol. 14, pp. 95-102.

[14] Hutchinson J. W., 1970, "Elastic-plastic behavior of polycrystalline metals and composities", Proc. R. Soc. London, Sec. A319, pp. 247-272,

[15] Kocks U. F., "Latent hardening and secondary slip in aluminum and silver", Trans. Metall. Soc. AIME 230, pp. 1160, 1964

[16] Koiter W., 1953, "Stress-strain relations, uniqueness and variational theorems for elastic-plastic materials with a singular yield surface", Q. Appl. Maths, vol. 11 pp 350.

[17] Lahrman F., Field R. D. and Darolia R., 1991, High Temperature Ordered Intermetallic Alloys IV, MRS Proc., vol. 213, pp. 603.

[18] Miracle D. B., 1993, "The Physical and Mechanical Properties of NiAl", Acta metall., vol.41, No.3, pp. 649-684.

[19] Nakda Y. and Keh A. S., "Latent hardening in iron single crystals", Acta Metall.,Vol. 14, pp. 961, 1966

[20] Pan J. and Rice J. R., 1983, "Rate Sensitivity of Plastic Flow and Implications for Yield-Surface Vertices", Int. J. Solid Struct, vol. 19, pp. 973-987.

[21] Peirce D., Asaro R. J. and Needleman A., 1983, "Material Rate Dependence and Localized Deformation in Crystalline Solids", Acta metall. vol. 31, no.12, pp. 1951-1976.

[22] Taylor, G. I., "The mechanism of plastic deformation of crystals", Proc. R. Soc., A145, pp. 362, 1934

[23] Wasilewski R. J., Butler S. R. and Hanlon J. E., 1967, Trans. Metall. Soc. AIME, vol. 239, pp. 1357.

[24] Wenner M. L., 1993, "A Generalized Forward Gradient Procedure for Rate Sensitive Constitutive Equations", Int. J. for Num. Meth. in Engineering, vol. 36, pp. 985-995.

[25] Winton J. S., 1995, "The Effect of Orientation, Temperature, and Strain Rate on the Mechanical Properties of NiAl Single Crystals", MS thesis, Univ. of Florida.

[26] Wu T., Bassani J. L. and Laird C., 1991, "Latent hardening in single crystals I. Theory and experiments", Proc. R. Soc. London, A435, pp. 1-19,

[27] Yang C., Kumar A. V., and Seelam V., "Investigation of localized deformation in NiAl single crystals", J. Engg Mat. and Tech., ASME, accepted for publications, 1998.
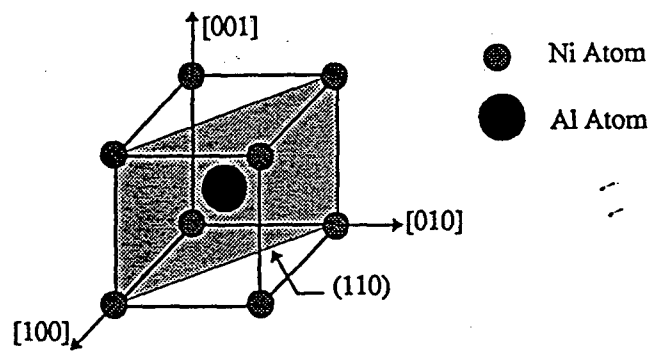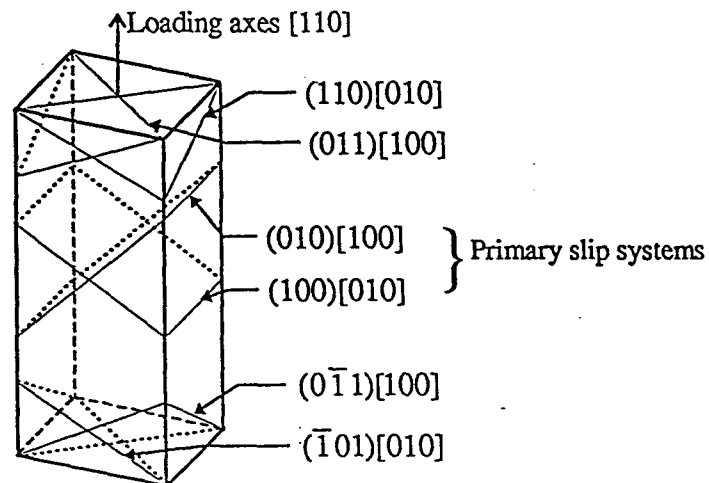
Figure 1: NiAl crystal structure

Figure 2: Active slips systems of NiAl for loading along [110] orientation

Figure 3: (a) Resolved shear strain vs time (Case I)

Figure 3: (b) Flow stress vs time (Case I)

(a)   (b)   (c)

Figure 4: (a) Deformed mesh (b) strain in Y-dir. (c) stress in Y-dir. (Case I: 20 % nominal strain)

Figure 5: (a) Resolved shear strain vs time (Case II (a))

Figure 5: (b) Flow stress vs time (Case II (a))

Figure 6: (a) Resolved shear strain vs time (Case II (b))

Figure 6: (b) Critical resolved shear stress vs time (Case II (b))

Figure 7: (a) deformed mesh (b)strain in Y-dir. (c)stress in Y-dir. (Case II(b) at 40% nominal strain)

Figure 8: Resolved shear strain vs time (Case III (a))

Figure 9: Resolved shear strain vs time (Case III (b))

Figure 10 Load vs time

Figure Captions

Figure 1: NiAl crystal structure

Figure 2: Active slips systems of NiAl for loading along [110] orientation
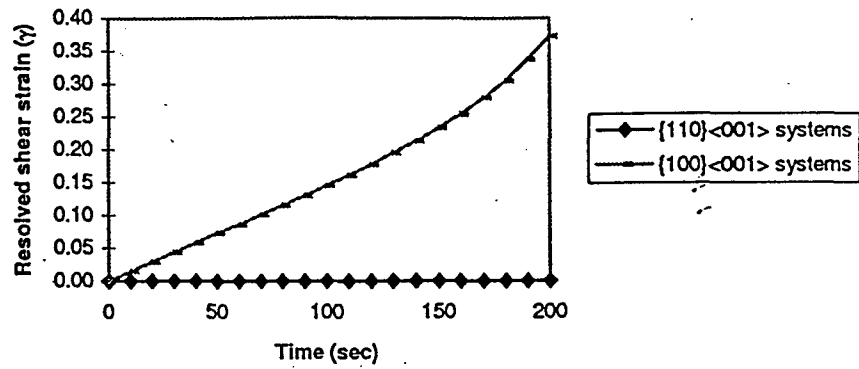
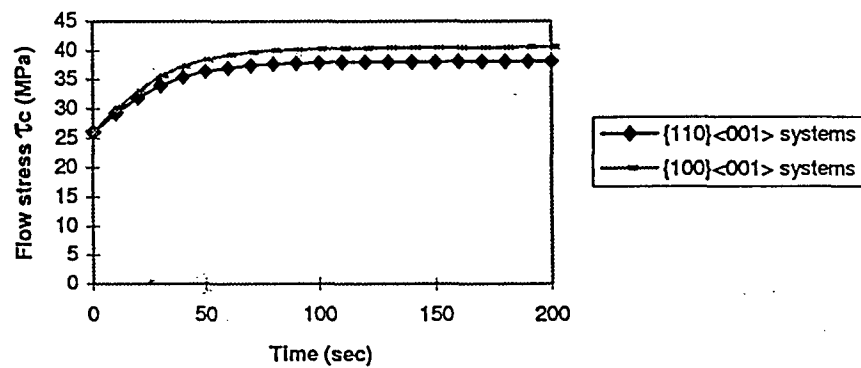Figure 3: (a) Resolved shear strain vs time (Case I)

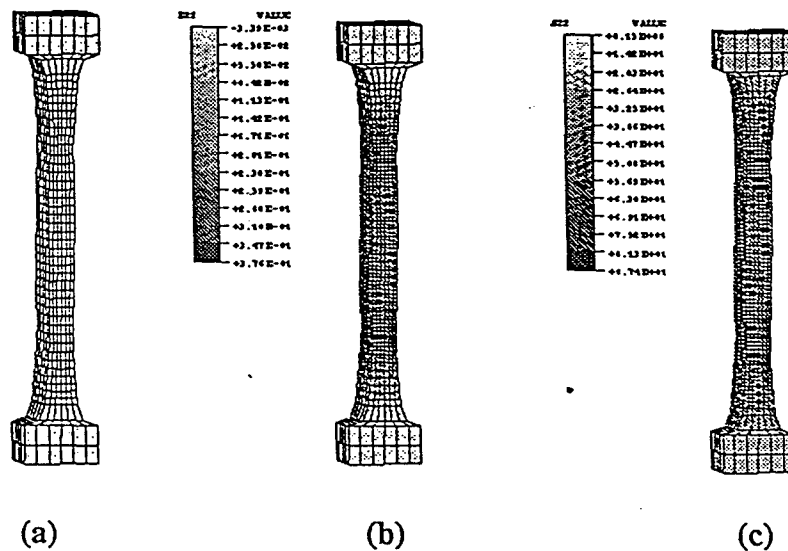Figure 3: (b) Flow stress vs time (Case I)

Figure 4: (a) Deformed mesh (b) strain in Y-dir. (c) stress in Y-dir. (Case I: 20 %
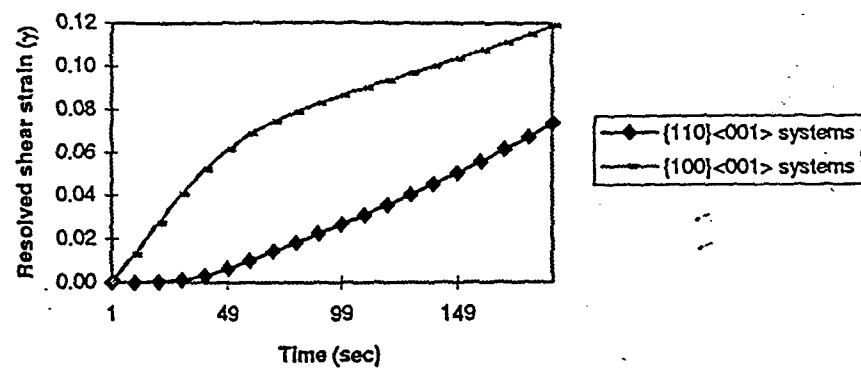
   nominal strain)

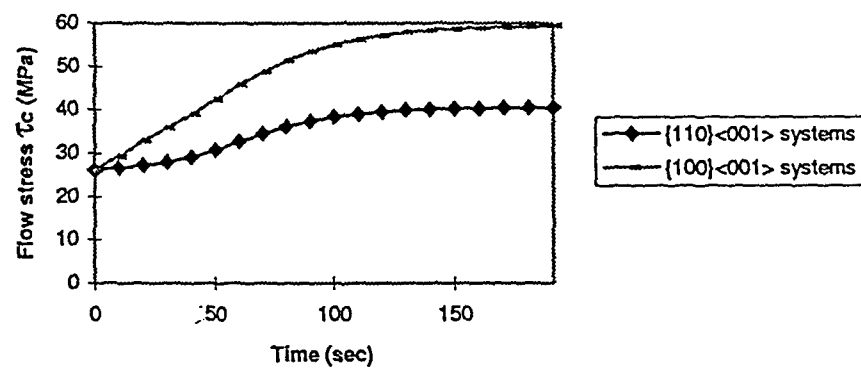Figure 5: (a) Resolved shear strain vs time (Case II (a))

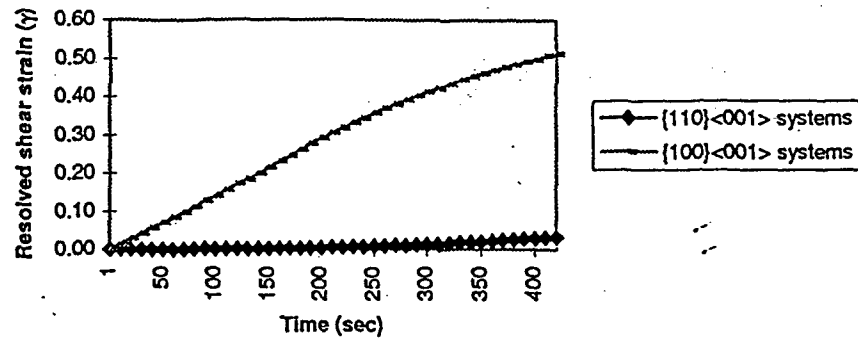Figure 5: (b) Flow stress vs time (Case II (a))
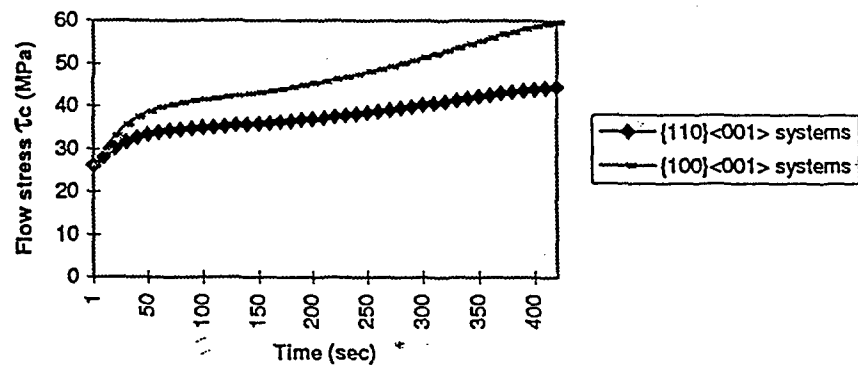
Figure 6: (a) Resolved shear strain vs time (Case II (b))

Figure 6: (b) Critical resolved shear stress vs time (Case II (b))
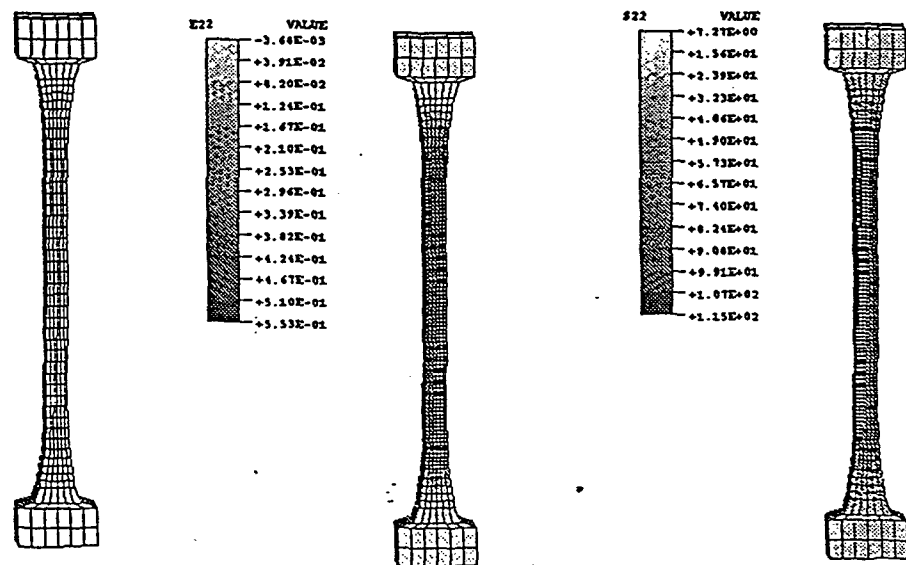
Figure 7: (a) deformed mesh (b)strain in Y-dir. (c)stress in Y-dir. (Case II(b) at 40%
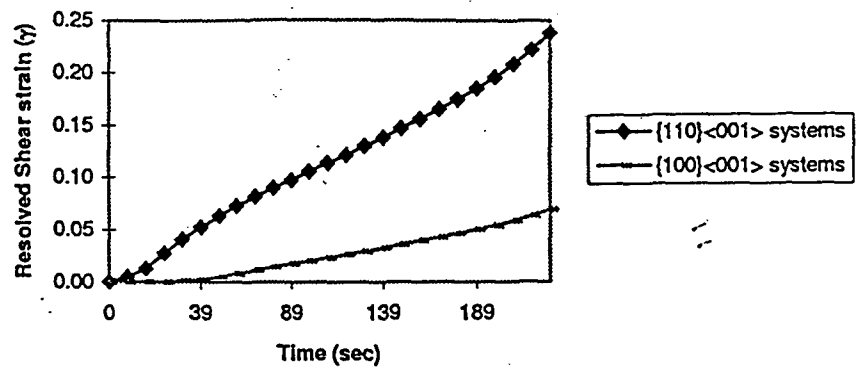
   nominal strain)
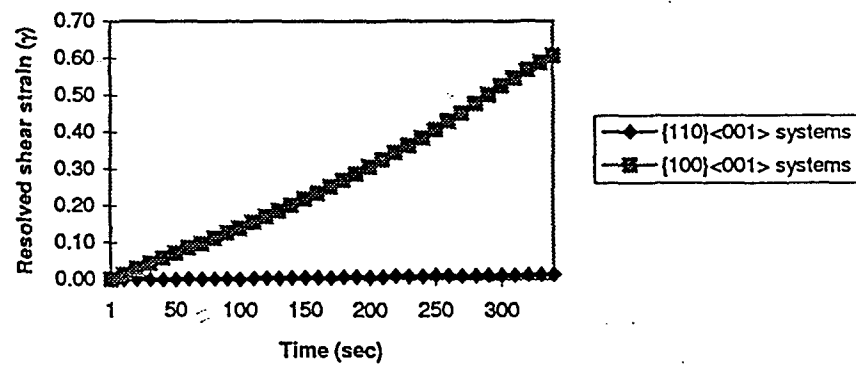
Figure 8: Resolved shear strain vs time (Case III (a))
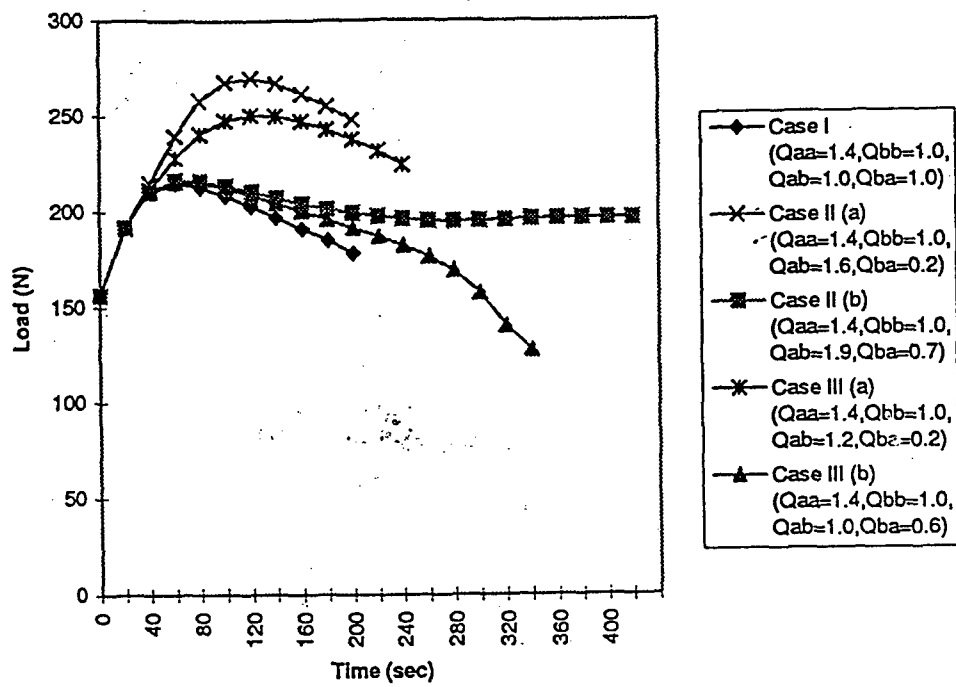
Figure 9: Resolved shear strain vs time (Case III (b))

Figure 10 Load vs time

STRAIN AGING BEHAVIOR IN NiAl MICROALLOYED WITH INTERSTITIAL AND SUBSTITUTIONAL SOLUTES

M.L. WEAVER*, R.D. NOEBE**, AND M.J. KAUFMAN***
*Center for Nonlinear & Nonequilibrium Aeroscience, Florida A&M University, Tallahassee, FL 32306-4005
**NASA-Lewis Research Center, Cleveland, OH 44135
***Department of Materials Science and Engineering, University of Florida, Gainesville, FL 32611

ABSTRACT

Dynamic strain aging has been investigated in polycrystalline NiAl alloys containing combined additions of interstitial and substitutional impurities. The results indicate that strain aging can be enhanced in polycrystalline alloys containing concentrations of silicon or iron in excess of 0.15 at.% in addition to conventional levels of carbon. This co-doping leads to very dramatic strain aging events, comparable to those typically observed in single crystals. This effect will be discussed with respect to conventional theories of strain aging.

INTRODUCTION

Recent research efforts have established that the intermetallic compound NiAl is subject to the phenomenon of strain aging due to elastic interactions between dislocations and interstitial solutes, ely carbon [1-16]. Though this phenomenon can be minimized through the selection of the proper gettering elements [9,12,15], prior investigators have suggested that it can also be enhanced via small additions of various substitutional species [11]. In NiAl single crystals, strain aging manifests itself dramatically dramatically in the form of yield stress plateaus, upper yield points, flow stress transients upon an upward change in strain rate and the Portevin-LeChatelier effect. In polycrystals, however, such manifestations are typically more subtle. In this study, strain aging has been investigated in polycrystalline NiAl alloys containing combined additions of carbon and some common substitutional impurities. The emphasis of this investigation is to identify the role of substitutional impurities on the strain aging behavior of polycrystalline NiAl alloys.

EXPERIMENTAL PROCEDURE

Polycrystalline NiAl alloys in the form of vacuum induction melted (VIM) ingots were prepared from elemental constituents. The resulting VIM ingots were placed in mild steel extrusion cans and extruded at 1200 K at a reduction ratio of 16:1. Post extrusion chemical analyses were conducted using the techniques deemed the most accurate for the particular elements. The results of these analyses are listed in Table 1. Cylindrical compression specimens and round button-head tensile specimens were EDM wire cut or centerless ground from the extruded rods so that the gage lengths were parallel to the extrusion direction. Sample dimensions were 3.1 mm for the tensile gage diameters and 30.0 mm for the tensile gage lengths and 5.0 mm for the compression sample diameters and 10.0 mm for the lengths. All tensile specimens were electropolished prior to testing in a 10% perchloric acid-90% methanol solution that was cooled to 208 K. During some of the compression tests, strain was measured using a clip on strain gage extensometer.

All tensile and compression tests were performed using a screw driven load frame at constant crosshead velocities corresponding to an initial strain rate of 1.4×10^{-4} s^{-1}. Testing was accomplished as follows: the temperature dependence of flow stress was determined by testing all as-extruded alloys in air between 300 and 1100 K by heating the samples in a clamshell type resistance furnace where temperature gradients were controlled to ±2 K. During this phase of testing, the strain rate sensitivity (SRS) was also determined by increasing the strain rate by a factor of ten from the base strain rate at fixed plastic strain intervals. The quantity extracted from these experiments was the SRS, $s = \Delta\sigma/\Delta\ln\dot{\varepsilon}$.

Table 1: Chemical Analyses of NiAl Alloys

Material	at. %				at. ppm			
	Ni	Al	Si	Fe	C	O	N	S
CPNiAl-1	50.10	49.69	0.15	0.00	147	70	<9	<7
CPNiAl-2	50.11	49.84	0.02	0.00	186	94	<9	<8
CPNiAl-3	50.22	49.69	0.02	0.00	431	154	<15	<13
CPNiAl-4	49.51	50.45	0.00	0.00	195	146	<15	<7
NiAl-Fe	50.09	49.28	0.01	0.30	572	148	<9	<13
NiAl-Si	49.49	50.18	0.30	0.00	192	149	<15	<15

Al, Fe, & Ni   Analysis performed using analytical wet chemistry/titration techniques, relative accuracy ±1%

Si   Analysis performed on an Ultraviolet/Visible Spectrophotometer, Shimadzu, Model UV-160, relative accuracy ±10%

C & S   Analysis performed on a Simultaneous Carbon/Sulfur Determinator, LECO Corp., Model CS-244, relative accuracy ±10%

N & O   Analysis performed on a Simultaneous Nitrogen/Oxygen Determinator, LECO Corp., Model TC-136 or Model TC-436, relative accuracy ±10%

RESULTS

Chemistry and Microstructures

Within experimental accuracy (±0.2 at.% for Ni and Al), the Ni and Al contents of both alloys are not significantly different from each other. The major differences between the materials are the residual C, O, N and S contents and the presence of Si and Fe as alloying additions. The microstructures of all the NiAl alloys were similar as observed by optical microscopy and consisted of fully dense recrystallized grains. Nominal linear intercept grain sizes were 20±2 μm.

Mechanical Properties

The temperature dependence of the SRS is presented in Figure 1. In agreement with prior observations, distinct SRS minima were observed in the temperature range 600 to 800 K with SRS becoming negative for NiAl-Si. Coincident with this region of reduced SRS were flow stress transients upon an upward change in strain rate for NiAl-Fe and serrated yielding for NiAl-Si and CPNiAl-1 (Figure 2a). The flow stress serrations observed in NiAl-Si and CPNiAl-1 were preceded by a small critical onset strain, ε_c. In a recent investigation, serrated yielding was observed in single crystal alloys containing the same concentrations of C and Si as NiAl-Si and CPNiAl-1 [9,11,12,17]. No such flow stress transients or flow stress serrations were observed in CPNiAl-3 or CPNiAl-4 (Figure 2b). By plotting the temperature and strain-rate dependence of ε_c, it is possible to derive several kinetic parameters related to the mechanism of strain aging. Following McCormick's formulation [18], ε_c is related to T and $\dot{\varepsilon}$ by the relation:

$$\varepsilon_c^{m+\beta} = K\dot{\varepsilon}\exp(Q/RT) \tag{1}$$

where Q is the activation energy for the onset of serrated flow, R is the gas constant, K is a constant, and the exponent (m+β) is related to the concentration of vacancies and the mobile dislocation density. The exponent (m+β), determined from the slope of a plot of ln $\dot{\varepsilon}$ versus ln ε_c at constant temperature for NiAl-Si was 1.76±0.2 (Figure 3a). The activation energy is then determined from a plot of ln ε_c versus 1/RT (i.e., Q = slope × (m+β), see Figure 3b). This method produces an activation energy of 95 kJ/mol in NiAl-Si which is in good agreement with the activation energies determined for static strain aging in polycrystalline NiAl (70 to 76 kJ/mol) [8-10] and the activation energies for dynamic strain aging in single crystal NiAl [2,3,6,9,12]. Due to a lack of experimental data, it was not possible to estimate the activation energies for strain aging in NiAl-Fe.

Figure 1. Temperature dependence of SRS for NiAl polycrystals: (a) CPNiAl-1, NiAl-Fe, and NiAl-Si; and (b) CPNiAl-2, CPNiAl-3 an CPNiAl-4. Note the significantly reduced SR values in (b).
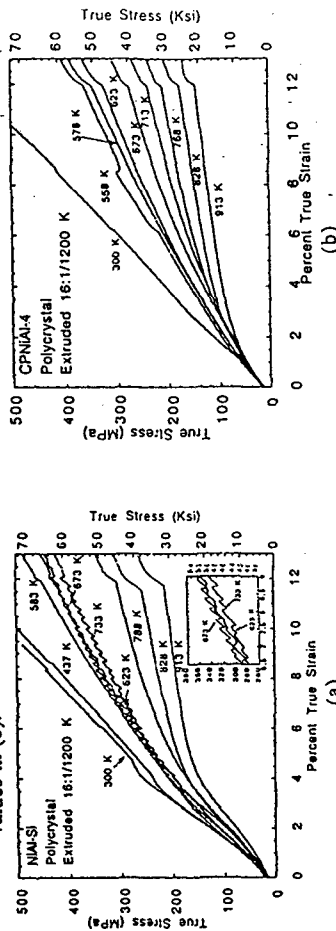
Figure 2 Representative stress-strain curves for NiAl polycrystals: (a) NiAl-Si; and (b) CPNiAl-Flow stress transients as observed for NiAl-Si at 583 K were observed in NiAl-Fe an CPNiAl-2 between 560 and 800 K.
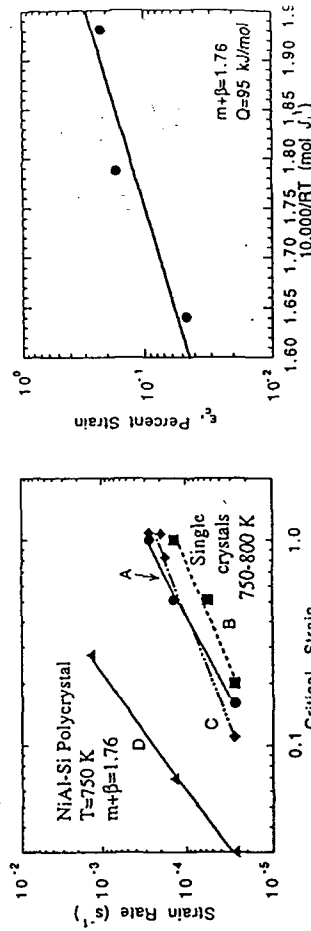
Figure 3. The influence of $\dot{\varepsilon}$ and T on the critical strain for the onset of serrated flow, ε_c fc polycrystalline NiAl-Si: (a) ln $\dot{\varepsilon}$ vs ln ε_c and (b) ln ε_c vs 10,000/RT. Data previously collected for single crystals [9,12] has been included in (a) for comparison purposes.

The typical temperature dependence of the 0.2% offset yield stress, $\sigma_{0.2}$, normalized with respect to the elastic modulus, E, is summarized in Figure 4. The normalized flow stress generally decreased with increasing temperature for all alloys. However, in NiAl-Fe and NiAl-Si, an apparent plateau was observed at intermediate temperatures while no such peaks or plateaus were observed in CPNiAl-3 or CPNiAl-4. Similar peaks have been observed previously in single crystal and polycrystalline alloys exhibiting manifestations of DSA [3,9,11-14,17].
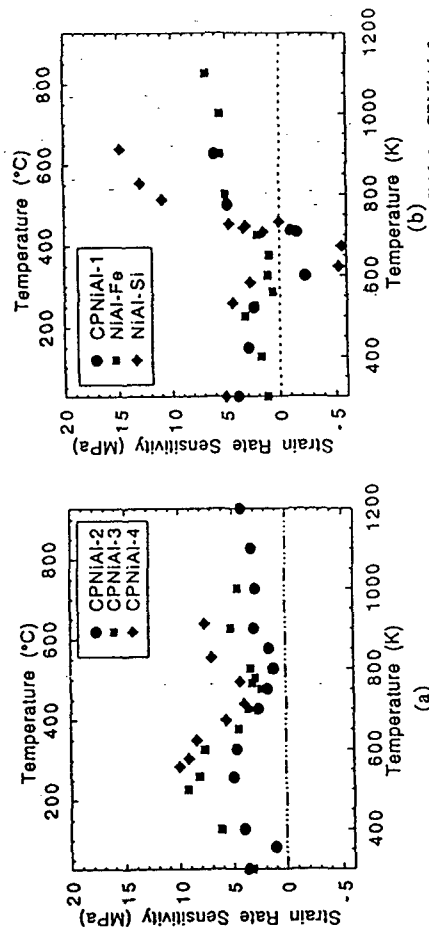

Figure 4   Temperature dependence of $\sigma_{0.2}/E$ for NiAl polycrystals: (a) CPNiAl-2, CPNiAl-3 and CPNiAl-4; and (b) CPNiAl-1, NiAl-Fe, and NiAl-Si. Note the significantly reduced SRS values in (b).
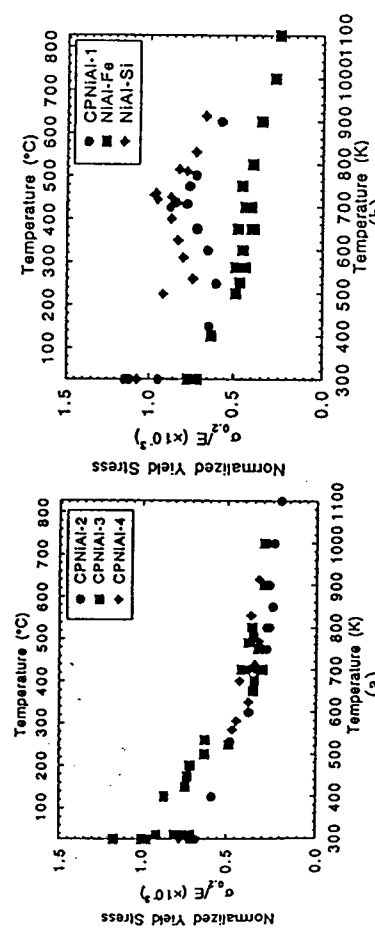
DISCUSSION

It is desirable to determine the species responsible for strain aging. This can be accomplished by analyzing the data generated in this study using equation (1). Typically, when (m+β) is in the range 0.5 to 1 an interstitial specie is responsible for strain aging whereas when (m+β) is in the range 2 to 3, a substitutional specie is responsible. In a prior study of strain aging in single crystals, (m+β) values were observed to lie in the range 0.93 to 1.27 suggesting an interstitial mechanism [9,12]. The results generated in this study are inconclusive. It was noted above that the value for the exponent (m+β) in NiAl-Si was 1.76±0.20 which suggests that either a substitutional specie is causing strain aging or that some other mechanism is operative. Additional inferences can be made by comparing the calculated activation energy data for serrated flow in NiAl-Si with the available diffusion data for NiAl and with the strain aging activation energy data generated in prior investigations [2,3,6,9,10,12]. Average activation energies for the diffusion of substitutional solutes are 225±39 kJ/mol regardless of composition [19]. The activation energies for strain aging reported in prior investigations lie in the range 66 to 134 kJ/mol. The experimentally determined activation energy of 95 kJ/mol in NiAl-Si is at least consistent with the prior results and is within the classical range for the diffusion of interstitial solutes in bcc metals.

In agreement with prior investigations on single crystals [9,11,12], SRS minima, flow stress transients, yield stress plateaus, and serrated yielding have been observed in NiAl polycrystals at intermediate temperatures indicating the occurrence of strain aging. Chemical composition was observed to influence the manifestations of strain aging as follows. (1) At intermediate temperatures (i.e., ~600 to 800 K) the SRS minimum decreases to slightly lower levels and to lower temperature ranges with increasing Si concentration and with small Fe additions. (2) Within the same temperature range, $\sigma_{0.2}/E$ remains relatively unchanged with increasing C concentration and increases significantly with increasing Si concentration. No noticeable increase was observed in NiAl-Fe but there was a detectable increase in scatter. (3) Serrated flow was observed in NiAl-Si and CPNiAl-1 while flow

stress transients were observed in NiAl-Fe and CPNiAl-2. No such behavior was observed in the c alloys. These observations appear to support the hypothesis of Weaver et al. [9,11,12] who obse an increase in serration size in single crystal alloys with increasing Si content and flow stress trans during strain rate change tests of alloys containing high C contents but lower Si contents. / analyzing the available data using equation (1), they suggested that strain aging in NiAl was the r of complex interactions between dislocations and residual C and Si atoms. Recent studies at the Ridge National Laboratory indicating a two-fold increase in Si concentration at dislocation cores and at Johns Hopkins University [21] indicating the preferential segregation of C to dislocat would seem to support these ideas.

From the results presented above, it is impossible to devise a definitive mechanism by w substitutional and interstitial impurities can cause strain aging. In references [9,11,12], it suggested that strain aging could be the result of interaction solid solution hardening (ISSH) an increased lattice distortions caused by the presence of substitutional and interstitial solutes. In ligl the observations at ORNL [20] and Johns Hopkins [21], it is suggested that Si preferent segregates to dislocations and attracts C resulting in small Si-C complexes (i.e., small agglomerate precipitates) which lock dislocations more strongly than Si or C atoms along. Further evidenc support of this hypothesis were provided in diffusion couple studies between NiAl, Ni3Al, and [22,23] which suggested that Si may diffuse as fast as or faster than C in NiAl and may result in formation of complex Ni-Al-Si-C phases. This suggests that some clustering of C with Si, Ni, an may occur resulting in an expansion of the DSA regime and stronger pinning. It is understand that Fe-C complexes could operate in the same manner, however, the overall effects wil minimized. Recent theoretical results suggest that Si will only occupy Al lattice positions whereas other substitutional elements such as Fe or Ga will tend to occupy the site of stoichiometrically deficient host element [24,25]. Assuming that C atoms occupy octahedral sit is theorized that the substitution of smaller Si atoms for Al will result not only in a reduction in size of the octahedral interstices but also into more localized distortions of the lattice. Similar[the cases of Fe or Ga which occupy the stoichiometrically deficient host element sites, the ov distortions in the lattice will be minimized because the tetragonal distortions created by inters atoms can be partially accommodated resulting in reduced strain aging effects. Recently, serr yielding has been reported to occur over a smaller temperature range in both Fe-doped and in doped single crystal alloys [26] which suggests that there might be some validity to this pote mechanism though more work is needed.

CONCLUSIONS

Three of the six polycrystalline NiAl alloys examined in the present study exhibit flow s plateaus, serrated flow and/or flow stress transients during strain rate change experiments in temperature range 600 to 800 K. These observations are consistent with the occurrence of L Compositional analyses suggest that DSA is the result of a complex interaction between substituti solutes, interstitial solutes and dislocations. In this case Si atoms have been shown to stro enhance the occurrence of strain aging in polycrystalline NiAl alloys. Similar additions of F place of Si appear to have the same effect but in a reduced capacity. It is suggested that strain a results from the formation of substitutional-interstitial aggregates.

ACKNOWLEDGMENTS

REFERENCES

1. J. M. Brzeski, J. E. Hack, R. Darolia and R. D. Field, *Mater. Sci. Eng.* A170, 11-18 (1993).
2. J. M. Brzeski, J. E. Hack and R. Darolia, in High-Temperature Ordered Intermetallic Alloys VI, J. A. Horton, I. Baker, S. Hanada, R. D. Noebe and D. S. Schwartz, Eds., Materials Research Society, vol. 364, Pittsburgh, PA, p. 419-424 (1995).
3. J. M. Brzeski, Ph.D. Dissertation, Yale University (1995).
4. J. E. Hack, J. M. Brzeski and R. Darolia, *Scripta Metall. Mater.* 27, 1259-1263 (1992).
5. J. E. Hack, J. M. Brzeski, R. Darolia and R. D. Field, in High-Temperature Ordered Intermetallics V, I. Baker, R. Darolia, J. D. Whittenberger and M. H. Yoo, Eds., Materials Research Society, vol. 288, Pittsburgh, PA, p. 1197-1202 (1993).
6. J. E. Hack, J. M. Brzeski and R. Darolia, *Mater. Sci. Eng.* A192/193, 268-276 (1995).
7. M. L. Weaver, R. D. Noebe, J. J. Lewandowski, B. F. Oliver and M. J. Kaufman, *Mater. Sci. Eng.* A192/193, 179-185 (1995).
8. M. L. Weaver, V. Levit, M. J. Kaufman and R. D. Noebe, in High-Temperature Ordered Intermetallic Alloys VI, J. A. Horton, I. Baker, S. Hanada, R. D. Noebe and D. S. Schwartz, Eds., Materials Research Society, vol. 364, Pittsburgh, PA, p. 425-430 (1995).
9. M. L. Weaver, Ph.D. Dissertation, University of Florida (1995).
10. M. L. Weaver, M. J. Kaufman and R. D. Noebe, *Intermetallics* 4, 121-129 (1996).
11. M. L. Weaver, R. D. Noebe and M. J. Kaufman, *Scripta Mater.* 34, 941-948 (1996).
12. M. L. Weaver, R. D. Noebe and M. J. Kaufman, *Metall. Mater. Trans. A*, in press (1996).
13. M. L. Weaver, R. D. Noebe, J. J. Lewandowski, B. F. Oliver and M. J. Kaufman, *Intermetallics* 4, 533-542 (1996).
14. M. L. Weaver, R. D. Noebe and M. J. Kaufman, *Intermetallics* 4, 593-600 (1996).
15. D. Golberg and G. Sauthoff, *Intermetallics* 4, 143-158 (1996).
16. D. Golberg and G. Sauthoff, *Intermetallics* 4, 253-271 (1996).
17. J. S. Winton, M.S. Thesis, University of Florida (1995).
18. P. G. McCormick, *Acta Metallurgica* 20, 351-354 (1972).
19. R. D. Noebe, R. R. Bowman and M. V. Nathal, *Int. Mater. Rev.* 38, 193-232 (1993).
20. M. L. Weaver, A. J. Duncan and M. K. Miller, unpublished research, Oak Ridge National Laboratory (1996).
21. N. C. Tambakis, T. Lusby and A. J. Melmed, Johns Hopkins University, Quarterly Report, October 15, 1995-January 14, 1996.
22. T. C. Chou and T. G. Nieh, *Scripta Metall. Mater.* 25, 2059-2064 (1991).
23. T. C. Chou and T. G. Nieh, in High-Temperature Ordered Intermetallic Alloys IV, L. A. Johnson, D. P. Pope and J. O. Stiegler, Eds., Materials Research Society, vol. 213, Pittsburgh, PA, p. 1045-1050 (1991).
24. H. Hosoda, K. Inoue and Y. Mishima, in High-Temperature Ordered Intermetallic Alloys VI, J. Horton, I. Baker, S. Hanada, R. D. Noebe and D. S. Schwartz, Eds., Materials Research Society, vol. 364, Pittsburgh, PA, p. 437-442 (1995).
25. I. M. Anderson, A. J. Duncan and J. Bentley, in High-Temperature Ordered Intermetallic Alloys VI, J. Horton, I. Baker, S. Hanada, R. D. Noebe and D. S. Schwartz, Eds., Materials Research Society, vol. 364, Pittsburgh, PA, p. 443-448 (1995).
26. R. Darolia, R. D. Field, R. D. Noebe, A. Garg and W. S. Walston, GE Aircraft Engines/Air Force Office of Scientific Research, Final Report, July 1, 1991 - March 31, 1995.

CHEMICAL POTENTIAL SHIFTS DUE TO CAPILLARITY–UNARY SYSTEMS

N. KULKARNI and R. T. DEHOFF

Department of Materials Science & Engineering, 253A Rhines Hall, University of Florida, Gainesville, Fl 32611, U.S.A.

Abstract—The effect of curvature on the chemical potential for two-phase unary systems at constant temperature, is usually given in the literature by the Gibbs–Thomson equation [1–6],

$$\mu^\beta(H) = \mu^\beta(H = 0) + 2\gamma V^\beta H$$

where H is the local mean curvature of a β particle in equilibrium with an α matrix and V^β, the molar volume of the β phase. It can be shown, based on the above equation, that the corresponding shift in chemical potential for the α phase is [1]:

$$\mu^\alpha(H) = \mu^\alpha(H = 0)$$

Thus the usual form of the Gibbs–Thomson equation that appears in the literature is not rigorous and hence results in a violation of the condition for chemical equilibrium for a curved interface ($\mu^\alpha(H) \neq \mu^\beta(H)$) assuming incompressibility and isotropic stresses in the case of the solid phases [7–9]. A rigorous derivation of the Gibbs–Thomson equation for unary two-phase systems at constant temperature is provided, that gives the correct equation for the chemical potential shift:

$$\mu^\beta(H) = \mu^\alpha(H) = \mu^\beta(H = 0) + 2\gamma H[V^\alpha V^\beta/(V^\alpha - V^\beta)]$$

While the above equation can be approximated ($V^{\alpha\ =\ G} - V^\beta \approx V^G$) in the case of a condensed-gas (G) system to give the usual form of the Gibbs–Thomson equation, a similar approximation for a condensed–condensed system can result in a significant error in both the sign and magnitude of the shift. The corrected expression for the chemical potential shift has an inverse dependence on the difference in the molar volumes ($V^\alpha - V^\beta$) between the two condensed phases. For solid (S)–liquid (L) equilibrium in certain systems the shift may be negative (e.g. $V^{\alpha\ =\ L} < V^{\beta\ =\ S}$ for Bi, Si, Ge) or even approach infinity (e.g. $V^{\alpha\ =\ L} \approx V^{\beta\ =\ S}$ for carbon). A similar dependence is obtained for the pressure shifts in each phase. The present formulation is consistent with the Clausius–Clapeyron equation used to represent unary phase diagrams, which has the same dependence on the relative molar volume. © *1997 Acta Metallurgica Inc.*

1. INTRODUCTION

The assumption of local equilibrium across an interface has been invoked frequently in studying many basic processes in condensed systems such as solidification, growth, diffusion, sintering, coarsening, etc. Gibbs was the first to derive the conditions for equilibrium for planar and curved interfaces [7]. While the condition for thermal equilibrium is identical to that for a planar interface, the conditions for chemical and mechanical equilibrium are in general different [7–9]. The conditions for chemical equilibrium for curved interfaces are modified from the planar case due to the presence of non-isotropic stresses in case of interfaces where one or both of the phases are solid. They are however always identical to the planar case for liquid–liquid interfaces [7–9]. In case of interfaces consisting of solid phases, if it is assumed that the surface stresses (f) present in solid phases are isotropic and equal to γ, the specific interfacial free energy, the conditions

for chemical equilibrium for curved and planar interfaces become the same. The conditions for mechanical equilibrium across a curved interface differ from those across a planar interface by a factor which depends on the product of the local mean curvature (H) and the specific interfacial free energy (γ). These conditions of equilibrium are used in deriving an expression relating the local chemical potential shifts in a system with curvature of the interface, at constant temperature. This expression is classically known as the Thomson–Freundlich or the Gibbs–Thomson relation [1–6]. Although the original Gibbs–Thomson relation applied to liquid–gas equilibria in unary and binary systems [2, 3], it has been assumed to be valid for condensed phase equilibria in unary, binary and multicomponent systems. Some of these formulations contain inaccuracies and inconsistencies, which can result in significant errors in the calculated chemical potential shifts due to curvature. This presentation

focuses on corrections to the Gibbs–Thomson equation applied to unary condensed systems. It is to be noted that Gibb's association with the Gibbs–Thomson relation is only in context with the conditions for equilibrium and *not* the erroneous expression appearing in the literature.

The assumptions of isotropic stresses and incompressibility of solids which are inherent in some of the earlier formulations [1, 6] are also valid in this work, although as pointed out by Cahn [8, 9] hardly practical. Nevertheless it is hoped that a rigorous treatment of the simplest case would lead to adaptation to more general cases based on the framework of the present treatment.

The Gibbs–Thomson relation at constant temperature is usually stated as [1–6]:

$$\mu^\beta(H) = \mu^\beta(H = 0) + 2\gamma V^\beta H \qquad (1)$$

$$\mu^\alpha(H) = \mu^\alpha(H = 0) \qquad (2)$$

where V^β is the molar volume of the β phase. It will be demonstrated later that the relationship between the corresponding chemical potentials for the α phase, predicted from this equation, is that the chemical potential of the α phase does not shift with curvature [2]. Since the condition for chemical equilibrium in the bulk system requires $\mu^\alpha(H = 0) = \mu^\beta(H = 0)$, comparison of Equations (1) and (2) shows that $\mu^\alpha(H) \neq \mu^\beta(H)$. This violates the condition for chemical equilibrium [7]. In this discussion, a self-consistent procedure to evaluate the effects of curvature on thermodynamic properties in unary systems is given, which results in a form of the Gibbs–Thomson equation for which $\mu^\alpha(H) = \mu^\beta(H)$. The significance of this result is briefly explored.

2. PROCEDURE

2.1. Conditions for equilibrium

Consider a two phase ($\alpha + \beta$) unary system. Let r_1 and r_2 be the principal radii of curvature for an α–β surface element. The principal normal curvatures are given by $\kappa_1 = 1/r_1$ and $\kappa_2 = 1/r_2$. Let the local mean curvature across an α–β interfacial element be H where

$$H = \frac{1}{2}(\kappa_1 + \kappa_2) \qquad (3)$$

For each of the principal normal curvatures (κ_1 or κ_2), a vector is defined that is normal to the surface element and points towards the center of curvature. Choose a convention such that the curvature is positive if this vector points into the β phase and negative if it points into the α phase. The local mean curvature H is positive for surface elements that are convex with respect to the β phase, negative for concave elements, and may be either positive or negative for saddle surface elements depending upon the relative values of the curvatures [10].

The variables required to specify this two phase system are:

$$T^\alpha P^\alpha, \ T^\beta, \ P^\beta \text{ and } H.$$

T^α, T^β are the temperatures and P^α, P^β are the pressures in the α and β phases, respectively. An additional variable (H) is required to describe the local mean curvature for this system. The conditions for equilibrium for this two-phase system with a curved interface are according to Gibbs [7]:

$$T^\alpha = T^\beta \qquad (4)$$

$$P^\beta(H) = P^\alpha(H) + 2\gamma H \qquad (5)$$

$$\mu^\alpha(H) = \mu^\beta(H) \qquad (6)$$

$\mu^\alpha(H) = \mu^\beta(H)$ are the chemical potentials of the α and β phases in two-phase equilibrium with an interface of curvature H. It is assumed in this treatment that γ, the specific interfacial energy, is independent of curvature, thereby implying incompressibility of α and β. As mentioned earlier if either α or β or both are solid phases it is necessary to assume that their surface stresses are isotropic and equal to γ, the specific interfacial free energy, for equation (6) to be valid [7–9]. Since there are five variables for this system and three relations among them [equations (4)–(6)], the number of degrees of freedom or independent variables for this system is equal to two.

2.2. Calculation of phase boundary shifts in unary systems

Consider an incremental change in the state of a two-phase system with a curved interface. The change in chemical potential for each of the phases is

$$d\mu^\alpha = -S^\alpha dT^\alpha + V^\alpha dP^\alpha \qquad (7)$$

$$d\mu^\beta = -S^\beta dT^\beta + V^\beta dP^\beta \qquad (8)$$

S^α, V^α and S^β, V^β are the molar entropies and volumes of the α and β phases, respectively. If during this change, the system remains in two-phase equilibrium, then from the conditions for equilibrium [equations (4)–(6)]

$$dT^\beta = dT^\alpha = dT \qquad (9)$$

$$dP^\beta = dP^\alpha + d(2\gamma H) = dP^\alpha + 2\gamma dH \qquad (10)$$

$$d\mu^\beta = d\mu^\alpha \qquad (11)$$

γ is assumed to be independent of curvature. Substituting for dP^β from equation (10), equation (8) can be written as

$$d\mu^\beta = -S^\beta dT^\beta + V^\beta(dP^\alpha + 2\gamma dH) \qquad (12)$$

Equations (7) and (8) are related by the condition

for chemical equilibrium [equation (11)]. Hence

$$-S^\alpha dT^\alpha + V^\alpha dP^\alpha = -S^\beta dT^\beta + V^\beta(dP^\alpha + 2\gamma \, dH) \tag{13}$$

dT^α and dT^β are equal due to the condition for thermal equilibrium [equation (9)]. equation (13) becomes

$$-S^\alpha dT + V^\alpha dP^\alpha = -S^\beta dT + V^\beta(dP^\alpha + 2\gamma \, dH) \tag{14}$$

$$-(S^\alpha - S^\beta)dT + (V^\alpha - V^\beta)dP^\alpha - 2\gamma V^\beta dH = 0 \tag{15}$$

or

$$-\Delta S dT + \Delta V dP^\alpha - 2\gamma V^\beta dH = 0 \tag{16}$$

where

$$\Delta S = S^\alpha - S^\beta \quad and \quad \Delta V = V^\alpha - V^\beta. \tag{17}$$

equation (16) is the general form of the Clausius–Clapeyron relation for a unary two phase system with curved interfaces. Since it represents a single equation among three variables, the unary two phase system with a curved interface has two degrees of freedom, as discussed earlier. Systematic exploration of equation (16) is carried out by comparing equilibrium states in unary two-phase systems in which one of the variables (T or P^α) is constant. This leaves one degree of freedom. This is usually assigned to the curvature H, since one is normally interested in the effect of curvature on other properties. Hence, if P^α is constant in this comparison, one can obtain the dependence of temperature on curvature [3, 10, 11]; if T is constant, the dependence of P^α on curvature is obtained.

2.3. Effect of curvature on pressure

To evaluate the effect of curvature on pressure in a unary two-phase system, compare two systems that are at the same temperature T, but differ in their local equilibrium states on account of a difference in mean curvature H. equation (16) can be written as

$$\Delta V dP^\alpha - 2\gamma V^\beta dH = 0 \quad (dT = 0) \tag{18}$$

Hence the pressure shift in the α phase is

$$dP^\alpha = \frac{2\gamma V^\beta}{\Delta V} dH \tag{19}$$

If α and β are both condensed phases, V^α, V^β and ΔV can be assumed to be independent of the curvature (H). The above equation can be integrated:

$$\int_{P^\alpha(H=0)}^{P^\alpha(H)} dP^\alpha = \int_{H=0}^{H} \frac{2\gamma V^\beta}{\Delta V} dH \tag{20}$$

$$P^\alpha(H) = P^\alpha(H = 0) + \frac{2\gamma V^\beta}{\Delta V} H \tag{21}$$

equation (21) relates the pressure in the α phase in a finely divided system ($P^\alpha(H)$) to that in the same phase in a bulk system ($P^\alpha(H = 0)$) at the same temperature. The corresponding shift in the β phase is obtained by utilizing the condition for mechanical equilibrium across a curved interface [equation (10)].

$$dP^\beta = dP^\alpha + 2\gamma \, dH = \left(\frac{2\gamma V^\beta}{\Delta V} + 2\gamma\right)dH \tag{22}$$

Hence the pressure shift in the β phase is

$$dP^\beta = \left(\frac{2\gamma V^\beta}{V^\alpha - V^\beta} + 2\gamma\right)dH = \frac{2\gamma V^\alpha}{\Delta V} dH \tag{23}$$

The integrated form is given by

$$\int_{P^\beta(H=0)}^{P^\beta(H)} dP^\beta = \int_{H=0}^{H} \frac{2\gamma V^\alpha}{\Delta V} dH \tag{24}$$

$$P^\beta(H) = P^\beta(H = 0) + \frac{2\gamma V^\alpha}{\Delta V} H \tag{25}$$

Subtracting equation (21) from equation (25)

$$P^\beta(H) - P^\alpha(H) = P^\beta(H = 0) - P^\alpha(H = 0)$$

$$+ 2\gamma H \frac{V^\alpha - V^\beta}{\Delta V} = 2\gamma H \tag{26}$$

Thus the condition for mechanical equilibrium across a curved interface [equation (10)] is recovered. equation (21) along with equation (25) gives the correct expression for the pressure shift across a curved interface.

2.4. Effect of curvature on chemical potential

The chemical potential in a unary system is a function of the temperature and pressure for that phase. Since in the comparison between the two states of the system with different curvatures the temperature of the system is constant, the change in chemical potential is given by:

$$d\mu^\alpha = V^\alpha dP^\alpha - S^\alpha dT^\alpha = V^\alpha dP^\alpha \quad (dT^\alpha = 0) \tag{27}$$

Substituting for dP^α from equation (19)

$$d\mu^\alpha = V^\alpha\left(\frac{2\gamma V^\beta}{\Delta V} dH\right) = \frac{2\gamma V^\alpha V^\beta}{\Delta V} dH \tag{28}$$

Similarly the chemical potential shift for the β phase can be obtained by substituting for dP^β from equation (23).

$$d\mu^\beta = V^\beta dP^\beta - S^\beta dT^\beta = V^\beta dP^\beta \quad (dT^\beta = 0) \tag{29}$$

$$d\mu^\beta = V^\beta\left(\frac{2\gamma V^\alpha}{\Delta V} dH\right) = \frac{2\gamma V^\alpha V^\beta}{\Delta V} dH \tag{30}$$

Equations (28) and (30) are identical. Thus the condition for chemical equilibrium is recovered demonstrating the self-consistency of the procedure.

$$d\mu^{\alpha} = d\mu^{\beta} = \frac{2\gamma V^{\alpha} V^{\beta}}{\Delta V} dH \qquad (31)$$

In the case of a *condensed-gas* system, where α is the gas phase, an approximation can be made, since the molar volume of the gas phase is significantly larger than the condensed phase.

$$\Delta V = V^{\alpha=G} - V^{\beta} \approx V^{G} \qquad (32)$$

Hence

$$d\mu^{G} = d\mu^{\beta} = \frac{2\gamma V^{G} V^{\beta}}{V^{G}} dH = 2\gamma V^{\beta} \, dH \qquad (33)$$

Assuming the surface energy (γ) and the molar volume of the condensed phase (V^{β}) to be independent of the curvature, the above equation can be integrated.

$$\int_{\mu^{G}(H=0)}^{\mu^{G}(H)} d\mu^{G} = \int_{\mu^{\beta}(H=0)}^{\mu^{\beta}(H)} d\mu^{\beta} = \int_{H=0}^{H} 2\gamma V^{\beta} \, dH \qquad (34)$$

$$\mu^{G}(H) \equiv \mu^{\beta}(H) = \mu^{\beta}(H=0) + 2\gamma V^{\beta} H$$

$$(condensed-gas\ systems;\ V^{G} \gg V^{\beta}) \qquad (35)$$

The above integrated form of the equation for the chemical potential shift is the same as equation (1), the usual form of the Gibbs–Thomson equation given in the literature. However, it applies *only* to condensed-gas systems. The same approximation for ΔV [equation (32)] that conveniently cancels $V^{\alpha=G}$ in the numerator of equation (33) is no longer valid when applied to *condensed–condensed* systems, as has been done in the literature. For condensed–condensed systems, equation (31) can be directly integrated, since the terms in the integrand are not strong functions of curvature.

$$\int_{\mu^{\alpha}(H=0)}^{\mu^{\alpha}(H)} d\mu^{\alpha} = \int_{\mu^{\beta}(H=0)}^{\mu^{\beta}(H)} d\mu^{\beta} = \int_{H=0}^{H} \frac{2\gamma V^{\alpha} V^{\beta}}{\Delta V} dH \qquad (36)$$

$$\mu^{\alpha}(H) \equiv \mu^{\beta}(H) = \mu^{\beta}(H=0) + \frac{2\gamma V^{\alpha} V^{\beta}}{\Delta V} H \qquad ...$$

$$(condensed-condensed\ systems) \qquad (37)$$

equation (37) is the correct form of the Gibbs–Thomson equation for condensed–condensed systems at constant temperature.

3. DISCUSSION

The widely used form of the Gibbs–Thomson equation for condensed systems [equation (1)] is different from the one derived above [equation (37)]. It can be easily shown that equation (1) is not the correct form of the Gibbs–Thomson equation.

equation (1) can be expressed in a differential form, assuming V^{β} to be independent of H:

$$d\mu^{\beta} = 2\gamma V^{\beta} dH \qquad (38)$$

The chemical potential of the β phase is a function of the temperature and pressure. Since the comparison between the two systems with differing curvatures is made at constant temperature.

$$d\mu^{\beta}(H) = V^{\beta} dP^{\beta} - S^{\beta} dT^{\beta} =$$

$$V^{\beta} dP^{\beta} \ (dT^{\alpha} = d^{\beta} = 0) \qquad (39)$$

The pressure shift in the β phase is obtained by comparing Equations (38 and 39).

$$dP^{\beta} = 2\gamma dH \qquad (40)$$

Integration of the above equation gives the pressure shift in the β phase for a system with a curved interface relative to the same system with a flat interface:

$$P^{\beta}(H) = P^{\beta}(H = 0) + 2\gamma H \qquad (41)$$

In the α phase, the pressure shift is determined by the condition for mechanical equilibrium across the curved interface.

$$dP^{\beta} = dP^{\alpha} + 2\gamma dH \equiv 2\gamma dH \qquad (42)$$

$$dP^{\alpha} = 0 \qquad (43)$$

Thus the form of the chemical potential relation, equation (38), predicts that the pressure in the α phase is not a function of curvature. Hence the chemical potential shift with curvature for the alpha phase is predicted to be

$$d\mu^{\alpha} = V^{\alpha} dP^{\alpha} = 0 \qquad (44)$$

which implies

$$\mu^{\alpha}(H) = \mu^{\alpha}(H = 0) \qquad (45)$$

Since $\mu^{\alpha}(H = 0) = \mu^{\beta}(H = 0)$, comparing Equations (1 and 45) gives $\mu^{\alpha}(H) \neq \mu^{\beta}(H)$. This is a clear *violation* of the condition for chemical equilibrium across a curved interface [7].

Equations (1) and (45) have been derived by Trivedi [1]. An examination of his derivation for the chemical potential shift reveals that in his comparison of systems *both* the temperature and pressure in the α phase are assumed to be constant, i.e. $dT = 0$ and $dP^{\alpha} = 0$. Using this additional assumption ($dP^{\alpha} = 0$), Trivedi has derived Equations (1 and 45), the chemical potential shifts due to curvature for the β and α phases, respectively, which, as discussed earlier, are in violation of the condition for chemical equilibrium. Thus the assumption that $dP^{\alpha} = 0$, leads to an incorrect result for the chemical potential shifts due to curvature. This assumption is therefore *not valid*. equation (35), which has been derived by Herring [4] and Mullins [5] using variational principles, is applicable *only* to condensed-gas system.

It is seen from equation (16), the general form of the Clausius–Clapeyron relation for a unary two phase system with curvature, that there are two independent variables needed to describe the state of the system. If the temperature is maintained constant ($dT = 0$), then equation (16) gives the relation between the change in pressure (dP^α) and curvature (dH). If it is assumed, that both the temperature as well as the pressure are maintained constant ($dT = 0$ and $dP^\alpha = 0$), the two degrees of freedom are assigned. The state of the system is fixed and the variation with H cannot be explored.

The role played by ΔV in shifting phase boundaries in unary condensed systems may be illustrated by considering the effect of curvature on the state of solid–liquid interfaces as exposed in the modified Clausius–Clapeyron equation (16). If two systems with differing curvature are compared at the same pressure in the α phase,

$$-\Delta S\,dT - 2\gamma V^{S=\beta}\,dH = 0 \quad (dP^{\alpha=L} = 0) \quad (46)$$

Thomson's equation for the depression of the melting point is obtained [3, 10, 11].

$$dT = -\frac{2\gamma V^S}{\Delta S}dH \Rightarrow$$

$$T(H) = T(H = 0) - \frac{2\gamma V^S}{\Delta S}H \quad (47)$$

This result is independent of ΔV. Thus the melting point always decreases as the curvature of the solid surface increases. If this result is applied at a series of pressures it may be visualized as a shift in the melting curves to lower temperatures at all pressures, Figs 1 and 2 [3, 10–12]. In a manner similar to that employed in deriving equation (30), the chemical potential shift at constant pressure ($dP^{\alpha i\ L} = 0$) can be shown to be

$$d\mu^L = d\mu^S = \frac{2\gamma V^S S^L}{\Delta S}dH \quad (48)$$

Since the terms in the integrand are not strong functions of curvature the above equation may be integrated to give

$$\mu^L \equiv \mu^S = \mu^S(H = 0) + \frac{2\gamma V^S S^L}{\Delta S}H \quad (dP^L = 0) \quad (49)$$

If the corresponding comparison was made at fixed temperatures, then it is seen that the direction of shift depends upon the sign of the slope of the phase boundary. The sign of the slope in turn depends upon the difference in molar volume between the two phases, $\Delta V = V^L - V^S$. If ΔV and hence the slope is positive, which is the most common case, then the pressure in the liquid phase increases with curvature of the solid–liquid interface, see equation (21). Since $\Delta\mu^L = V^L\Delta P^L$, the chemical potential of the liquid phase increases with curvature of the interface at constant temperature, as is also the deduced in equation (37). The change
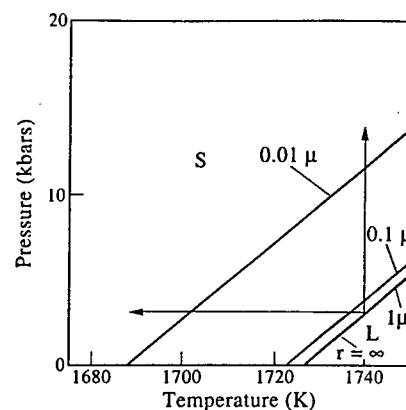

Fig. 1. Capillarity shift for nickel as a function of particle radius. Since the slope (dP/dT) is positive, the pressure shift is positive while the temperature shift is negative.

in chemical potential for the solid phase is the same since the two phases are in equilibrium, see equation (31). For the few cases for which ΔV is negative and the slope of the melting curve is negative, the pressure in the liquid phase *decreases* as the curvature of the solid–liquid interface increases, see equation (21). Accordingly, for this case the chemical potential for the system *decreases* with increasing curvature at constant temperature, equation (37).

The magnitude of the chemical potential shift with curvature at constant temperature varies with $1/\Delta V$. There exist examples of unary phase boundaries for which the slope changes sign at some particular state. For example the graphite–liquid phase boundary for carbon has a vertical slope at approximately 4700 K [13]. For states near this condition, the chemical potential shift with curvature is very large, approaching infinity as the slope changes sign and ΔV becomes zero.

Table 1 lists the correction factors for solid–liquid equilibria for a few elements. The correction
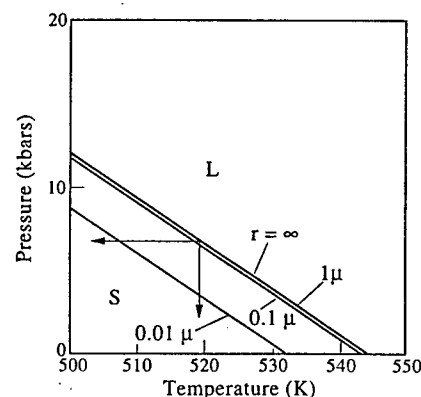

Fig. 2. Capillarity shift for bismuth as a function of particle radius. Since the slope (dP/dT) is negative, the pressure and temperature shifts are both negative.

Table 1. Correction factors for chemical potential shifts in unary systems (solid–liquid equilibrium)

Element	Melting point (K)	Molar volume of solid (V^β) at 298 K (cm³/mole)	Molar volume of solid (V^β) at melting point	Molar volume of liquid at melting point (V^α)	Relative molar volume $\Delta V = V^\alpha - V^\beta$	Correction factor for chemical potential shift $V^\alpha/\Delta V$
Al	933.4	9.99	10.45	11.31	0.86	13.1
Fe	1811	7.1	7.5	7.96	0.46	17.2
Ni	1726	6.6	6.99	7.43	0.44	16.9
Cu	1358	7.09	7.48	7.94	0.46	17.4
Sn	505	16.26	16.5	16.96	0.46	36.9
Ag	1235	10.27	10.83	11.54	0.71	16.3
Pb	600	17.74	18.21	19.4	1.19	16.4
Si	1683	12	12.39	11.19	−1.2	−9.4
Zn	693	9.16	9.50	9.94	0.43	22.7
Ti	1941	10.64	11.12	11.65	0.53	22.1
Bi	544	21.32	21.53	20.75	−0.78	−26.6
Sb	904	18.21	18.51	18.77	0.26	72.2
In	430	15.73	15.88	16.35	0.47	34.8

factor is in the range from 10 to 50 for most elements. Examination of Figs 1 and 2 shows that the chemical potential and pressure shifts become significant for particle sizes smaller than 1 micron. It should be noted that the chemical potentials of *both* the solid and liquid phases at a solid–liquid interface are changed by the same amount. The implications on solidification behavior needs greater review in the light of this analysis.

4. CONCLUSIONS

A rigorous formulation for the Gibbs–Thomson effect in unary condensed systems [equation (37)] has revealed a significant error in the relation widely used in the literature. The correction involves a factor which is inversely proportional to the difference in the molar volumes between the two condensed phases. The pressure and chemical potential shifts are positive for solid–liquid equilibria in most elements at atmospheric pressure, but in a few instances where ΔV is negative, the shifts are negative (e.g. solid–liquid equilibrium in Bi, Si, Ge). Elements for which ΔV changes sign as a function of pressure, are predicted to have an infinite shift where ΔV goes to zero (e.g. graphite–liquid equilibrium in carbon). A similar correction applicable to chemical potential shifts in binary systems will be the focus of an upcoming paper.

REFERENCES

1. Trivedi, R. K., in *Lectures on the Theory of Phase Transformations*, ed. H. I. Aaronson. AIME, Warrendale, PA, 1975, p. 58.
2. Thomson (Lord Kelvin), W., *Phil. Mag.*, 1871, 42(4), 448.
3. Defay, R., Prigogine, I., Bellemans, A. and Everett, D. H., *Surface Tension and Adsorption* XV edn., p. 217, John Wiley, New York, 1966.
4. Herring, C., in *Physics of Powder Metallurgy*, ed. W. E. Kingston, McGraw-Hill, New York, 1951, p. 143.
5. Mullins, W. W., in *Metal Surfaces: Structure, Energetics and Kinetics*, ed. W. D. Robertson and N. A. Gjostein). ASM, Metals Park, OH 1963, p. 17.
6. Lupis, C. H. P., in *Chemical Thermodynamics of Materials*, North Holland (Elsevier Science), New York, 1983, p. 363.
7. Gibbs, J. W., in *The Scientific Papers of J. Willard Gibbs*, Vol. 1, Thermodynamics, Connecticut, 1993.
8. Cahn, J. W., *Acta Metall.*, 1980, 28, 1333.
9. Cahn, J. W. and Larche, F., *Acta Metall.*, 1982, 30, 51.
10. DeHoff R. T. *Thermodynamics in Materials Science.* Chap. 7, Chap. 12. McGraw-Hill, New York, 1993, pp. 132, 355.
11. Thomson, J. J., *Applications of Dynamics.* London 1888.
12. Kaufman L. and Bernstein H. 1970. Computer Calculation of Phase Diagrams. Chap. II. Academic Press, New York. p. 5.
13. Gaskell D. R. 1981. *Introduction to Metallurgical Thermodynamics.* 2nd edn. Chap. 7. Hemisphere Publishing, New York, p. 155.